THE UNIVERSITY OF HULL

NOISE ATTENUATION USING ACOUSTIC RESONATORS:

A MULTIFACTORIAL INVESTIGATION AND

CHARACTERISATION OF PERFORMANCE FACTORS

Being a thesis submitted for the Degree of

Doctor of Philosophy

in the University of Hull

by

Brian Houston

MEng (University of Hull)

June 2024

This work is dedicated to my daughter Summer:

You were yourself an ideology at the beginning of this academic endeavour, you became

a miracle gifted within, you were a constant motivation throughout, and you will be

cherished above all always and forever.

Acknowledgements

Abstract

Unwanted or harmful sound is considered noise. If not addressed, it can cause psychological and physiological harm and have detrimental effects on structures and machinery. Despite the widespread use of acoustic resonators for noise reduction, there remains a lack of comprehensive understanding of the circumstances under which their full potential can be realised. The complexity of this challenge can be attributed to the large number of potential performance-affecting parameters. As a result, the amount of associated literature dealing with such acoustic properties is generally overwhelming.

This thesis compiles comprehensive, application-agnostic information on the performance factors of acoustic resonators, aiming to enhance their effectiveness across a wide range of contexts. Through an extensive literature review, this work identifies and assesses the known influence and significance of performance factors, pinpointing critical gaps in the current understanding. Subsequently, bespoke acoustic experiments are meticulously designed and conducted to evaluate existing theories and enhance the characterisation of performance-defining factors.

The experimental test matrix comprises two distinct acoustic resonator configurations. The first configuration features interchangeable discrete apertures and a variable cavity volume, while the second configuration includes a fixed cavity volume and interchangeable plates with varying distributions of apertures. Acoustic measurements are collected for both configurations under a wide range of geometric and flow conditions variations, which results in a significant database of attenuation performance metrics against corresponding design and environmental variables.

Experimental findings are supplemented with a separate computational fluid dynamic investigative methodology, which is validated against the collected measurements, and utilised to provide additional insight into the intrinsic dynamics in the vicinity of the resonator neck.

Novel insight into the applicability of existing analytical models in an applied context is demonstrated, highlighting and quantifying the significance of previously underappreciated performance factors, and providing empirically derived deductions to improve the current state of the art.

Contents

Nomenclature

Latin Script

Notation	Units	Description
A	m^2	Cross-sectional area
A_O	m^2	Orifice area
A_C	m^2	Cavity area
a	dB/m	Attenuation rate
a	m	Shortest edge length of rectangular cavity
C	$m^4 s^2/kg$	Acoustic compliance
C	-	Courant number
C	m	Circumferential length
C_C	-	Contraction coefficient
C_d	-	Discharge coefficient
c	m/s	Speed of sound
c_{ph}	m/s	Phase velocity
D	m	Diameter
D_C	m	Cavity diameter
D_N	M	Neck diameter
D	-	Acoustic Energy Dissipation Coefficient
d	m	Distance
d	m	Orifice diameter
e	-	Exponential function
F	-	Finite Fourier Transform operation
FRF	-	Frequency Response Function
f	Hz	Frequency
f_c	Hz	Cut-off frequency
$f_{c,mn}$	Hz	Cut-on frequency of mode $m{:}n$
f_r	HZ	Resonance frequency
f'	-	Normalised frequency
G_{xx}	-	One-side auto-spectral density
G_{xy}	-	One-sided cross-spectral density
H	-	Hyperbolic flare constant

He	-	Helmholtz number
IL	dB	Insertion Loss
$Im\{z\}$	-	Imaginary part of complex number z
i	$\sqrt{-1}$	Imaginary unit
j	$\sqrt{-1}$	Imaginary unit
J	-	Bessel Function
J_m	-	Bessel Function of the first kind of order m
j_{mn}	-	Eigenvalue of J_m
K_R	m	Rayleigh conductivity
k	$1/m$	Wave number
$k^{\pm}$	$1/m$	Convective wave number
$k_{r,mn}$	$1/m$	Radial wave number of modes $m{:}n$
k_s	$1/m$	Stokes wave number
k_s'	$1/m$	Effective Stokes wave number
$k_{x,mn}$	$1/m$	Axial wave number of modes $m{:}n$
L	m	Length
L_C	m	Cavity length
L_N	m	Neck length
l	m	Orifice length
l'	m	Length end correction
l_{eff}	m	Effective orifice length
M	kg/m^4	Acoustic inertance
M	-	Mach Number
M_B	-	Bias flow Mach number
M_B^{eff}	-	Effective bias flow Mach number
M_G	-	Grazing flow Mach number
m	-	Exponential flare constant
$\dot{m}$	kg/s	Mass flow rate
N	-	Number of holes
p	Pa	Pressure
p'	Pa	Acoustic Pressure
p_0	Pa	Mean Pressure
$\hat{p}$	-	Complex pressure amplitude
$\hat{p}_{mn}$	-	Complex amplitude of mode $m{:}n$
p_{ref}	Pa	Reference sound pressure

Q_{mn}	-	n-th Eigenvalue of Y_m
q_{mn}	-	n-th Eigenvalue of J_m
q	m^3/s	Acoustic volume velocity
$\hat{q}$	-	Complex volume velocity amplitude
R	m	Radius
R	$J/mol \cdot K$	Specific gas constant
R	-	Reflection coefficient
R	$kg/m^4\,s$	Acoustic resistance
R_C	m	Cavity radius
R_s	$kg/m^2\,s$	Orifice surface resistance
$Re\{z\}$	-	Real part of complex number z
r	m	Radial Coordinate
r	m	Radius
r	$kg/m^2\,s$	Specific acoustic resistance
r_m	m	Mouth radius
r_0	m	Orifice radius
S	m^2	Cross-sectional area at axial position of horn
S_t	m^2	Cross sectional area at throat of horn
Sh	-	Shear number
St	-	Strouhal number
s	J/K	Entropy
T	*Kelvin (K)*	Temperature
T	-	Transmission coefficient
TF	-	Transfer function
TL	dB	Transmission Loss
T_S	s	Sample Length
T	-	Transmission coefficient
t	s	Time
t	m	Wall Thickness
U	m/s	Orifice flow velocity
U_B	m/s	Bias flow velocity
u	m/s	Flow velocity
V	m^3	Cavity volume
V_{pp}	V	Peak-to-peak voltage
v	m/s	Velocity
v'	m/s	Acoustic Particle Velocity

v_0	m/s	Mean Velocity
$\hat{v}$	m/s	Complex velocity amplitude
W	watts (W)	Sound Power
W_i	-	Regression weighting
X	$kg/m^4\,s$	Acoustic reactance
x	$kg/m^2\,s$	Specific acoustic reactance
x	m	Axial coordinate
x, y, z	m	Cartesian coordinate value / vector direction
Y_m	-	Bessel function of the second kind of order m
Z	$kg/m^4\,s$	Acoustic Impedance
z	$kg/m^2\,s$	Specific Acoustic Impedance
z_0	$kg/m^2\,s$	Characteristic Impedance

Greek Script

Notation	Units	Description
α	-	Aspect ratio of perforation distribution
α	-	Absorption coefficient
α	-	Attenuation coefficient
Γ	-	Propagation constant
γ	-	Specific heat capacity ratio
γ	-	Real part of the Rayleigh conductivity
γ_{12}	-	Coherence between signal 1 and signal 2
Δ	-	Delta / Change in magnitude
δ	-	Imaginary part of the Rayleigh conductivity
δ	m	End Correction (due to radiation reactance)
ε	-	Geometrically normalised end correction
ζ	-	Normalised specific acoustic impedance
θ	rad	Circumferential coordinate
θ	rad	Phase angle in radian
θ	-	Normalised specific acoustic resistance
λ	m	Wavelength
μ	$Pa \cdot s$	Dynamic Viscosity
ν	m^2/s	Kinematic viscosity
ν'	m^2/s	Effective kinematic viscosity inc. thermal conductivity losses
$\hat{\xi}$	-	Geometry ratio

$\bar{\xi}$	-	Average of interior and exterior geometry ratios
π	-	Mathematical constant
ρ	kg/m^3	Density
ρ'	kg/m^3	Fluctuating Density
ρ_0	kg/m^3	Mean Density
σ	-	Porosity
σ_{eff}	-	Effective porosity
Φ	-	Pressure ratio
φ	rad	Phase angle
ϕ	m^2/s	Velocity potential
χ	-	Normalised specific acoustic reactance
ψ	-	Orifice interaction function
ω	rad/s	Angular frequency

Subscripts

1	Positions upstream of test section
2	Positions downstream of test section
A	Incident direction sound propagation
ac	Corresponding to acoustic mode
B	Reflected direction of sound propagation
B	Bias Flow
c	Cut-off
$duct$	Duct cavity/Transmission Line
e	External
eff	Effective
G	Grazing Flow
geo	Geometric
$h-h$	Hole-to-hole interaction
$h-w$	Hole-to-wall interaction
i	Incident
i	Inner
int	Interaction
m	Mouth
$neck$	Resonator neck
nl	Non-linear

O	Orifice
o	Outer
op	Corresponding to overall perforation area
opt	Optimum
p	Corresponding to acoustic pressure
qs	Quasi-steady assumption
R	Reflected
rad	Radiation
ref	Reference
res	Resonator cavity
rms	Root mean square
s	Corresponding to surface
sh	Corresponding to single hole
T	Transmitted
t	Corresponding to time
t	Throat
with	With acoustic resonator in-situ
without	Without acoustic resonator in-situ
x	Position/direction x
y	Position/direction y

Superscripts

′	Fluctuating value
‾	Mean Value
^	Complex value

Mathematical notations

arg	Argument (complex analysis)
∅	Diameter
∂	Partial derivative
∇	Nabla operator
Δ^2	Laplace operator
Σ	Summation
∈	Element of
| |	Absolute value

*	Complex conjugate
ln	Natural logarithm

Acronyms

ABSA	Asymmetric Broad target frequency bandwidth Sub-wavelength Absorber
ANSI	American National Standards Institute
BCE	Before the Common Era
CAD	Computer Aided Design
CFD	Computational Fluid Dynamics
CFL	Courant-Freidrichs-Lewy
DLE	Dry Low Emission
DFT	Discrete Fourier Transform
DLN	Dry Low NO_x
DLR	Deutsches Zentrum für Luft- und Raumfahrt
DR	Downstream reflection
EDM	Eldredge and Dowling Method
FFT	Fast Fourier Transform
FRF	Frequency Response Function
HAT	Hot Acoustic Test Rig
H-H	Hole-to-hole interaction
HVAC	Heating, Ventilation and Air Conditioning
H-W	Hole-to-wall interaction
IL	Insertion Loss
IRZ	Inner Recirculation Zone
ISO	International Organization for Standardisation
LBO	Lean Flame Blowout
NVH	Noise, Vibration and Harshness
OEM	Original Equipment Manufacturer
ORZ	Outer Recirculation Zone
PBFIF	Perforate Bias Flow Intermediate Frequency
PVC	Processing Vortex Core
RDR	Reflected downstream reflection
RMS	Root Mean Square
SAM	Sound Absorbing Materials
SPL	Sound Pressure Level

SIDM	Sound Insulation Decoupling Materials
SNR	Signal-to-noise ratio
TDR	Transmitted downstream reflection
TL	Transmission Loss
TMM	Transfer Matrix Method
TPA	Transfer Path Analysis
UAGM	Underwater Acoustic Guided Metamaterials
VBD	Vortex Break Down

List of Figures

List of Tables

CHAPTER 1 - INTRODUCTION

Noise can be considered physically synonymous with sound, a phenomenon which we can sense even before birth (Webb et al., 2015), and one which is intrinsic to our cognitive development. Thus, sound can be attributed to defining our innate existence, and has a profound effect on how we understand and interact with the world around us, and yet irrespective of this significance, the fundamental physics of sound has only been truly comprehended in the past two centuries.

The 6th century (BCE) Greek philosopher and mathematician Pythagoras, is commonly attributed to the origin of quantitative acoustics, due to his observations and experiments on the properties of vibrating strings, and the subsequent derivation of numerical ratios representing the harmonic overtone series (Boyer & Merzbach, 2011). Whilst an assemblage of acoustical hypothesis and experimentation ensued, it was not until the 19th century that the revolutionary work of physicists Hermann von Helmholtz (1821-1894), and Lord Rayleigh (1842-1919), finally demarcated sound as a form of wave motion.

Classification of sound as a form of wave motion led to the explanation of phenomena such as diffraction *(hearing sound around a corner)*, and echoes *(reflected sound with time delay)* (Turner & Pretlove, 1991), and appreciated commonalities with other wave analogies, such as light and electromagnetic radiation etc., expedited an understanding of the mechanics underpinning many contemporary acoustic models.

Acoustic wave theory will be discussed in greater detail in Chapter 2 – Background Theory however, it is pertinent to revisit the opening statement of this section, and clarify the difference between sound, and noise. Both noise and sound can be equally considered a form of energy propagation through a medium consisting of elasticity, mass and consequentially inertia; the mechanism of propagation remains adiabatic for both, and results in the local displacement of the particles of the medium producing local compressions, followed rapidly by local rarefactions, which spread through the medium (Porges, 1977).

Despite often being used interchangeably, noise has additional noteworthy connotations over sound, which are often subjective, and dependant on context. For example, the ANSI S1.1-2013:2.32 standard defines noise as *"(a) Undesired sound. By extension, noise is any unwanted disturbance within a useful frequency band, such as undesired electric waves in a transmission channel or device. (b) Erratic, intermittent, or statistically random oscillation."* (Acoustical Society of America, 2013).

Harris (1994) defined noise as *"A disagreeable or undesired sound, i.e., unwanted sound"*, and many others follow a similarly subjective and equivocal definition. Fink (2019) proposed a new definition of noise, *"Noise is unwanted and/or harmful sound"*. This definition of noise is much more appropriate, as it recognises that noise is not merely a nuisance, but that presents the potential for harm. Fink's interests are predominantly psychological and physiological however, it is important to note that harm caused by noise is not exclusive to living beings, it can also affect physical structures and machinery.

Lord Rayleigh adeptly makes the connection between sound and vibration in the introduction of his book, The Theory of Sound, by stating *"Very cursory observation often suffices to shew that sounding bodies are in a state of vibration and that the phenomena of sound and vibration are closely connected"* (Rayleigh, John William Strutt,3rd Baron, 1926). He goes on to state that *"when a vibrating bell or string is touched by the finger, the sound ceases at the same time the vibration is damped."*

Aside from the fundamental implication, this intrinsic relationship is of great engineering significance, not only because; all things being equal, a quiet machine is preferred by the customer to a noisy one; but also, and importantly because, noise is often an indicator of damaging vibration within a machine (Turner & Pretlove, 1991).

It is for this reason that today, predictive maintenance has reached a sophisticated level in industry, whereby techniques such as vibration monitoring and acoustic emission, has helped the manufacturing industry improve productivity, product quality, profitability and overall effectiveness of manufacturing plants (Scheffer & Girdhar, 2004).

Particular care must be taken when the frequency of vibrations *(or a Fourier component of them)* is near the natural frequency of a dynamic system. Under such resonant circumstances the system will oscillate at a higher amplitude than under the same force applied at other, non-resonant frequencies (Halliday, 2005). This phenomenon of resonance is relevant to all schemes which contains elasticity, mass and inertia, and hence is of great engineering significance; it is for this reason that all machinery should therefore be designed to have natural frequencies well away from any operational frequencies (Porges, 1977).

Whilst the expert exploitation of resonance allows musical instruments to create symphonies, in the context of engineered structures and machinery, it is all too often catastrophic; for example, the first suspension bridge over the Tacoma Narrows in Washington USA, which opened in 1940, gained the alias "Galloping Gertie" thanks to the large vortex-induced vertical vibrations acting on its slender deck. These vertical vibrations were so prominent that motorists crossing the bridge sometimes experienced "roller-coaster like" travel as they watched cars ahead almost disappear from sight and then reappear.

The bridge dramatically collapsed the same year it opened during 42mph winds and to this day the disaster serves as a pertinent reminder of the significance of resonance in structural engineering. It should be noted however, that whilst many refences misquote the cause of failure as the wind providing an external periodic frequency that matched the natural structural frequency; the final action which brought the bridge down occurred in a fundamental antisymmetric torsion mode, more accurately prescribed as an aerodynamically induced condition of self-excitation or "negative dampening" in this torsional degree of freedom (BILLAH & SCANLAN, 1991; Jenkins, 2013), as shown in *Figure 1.*
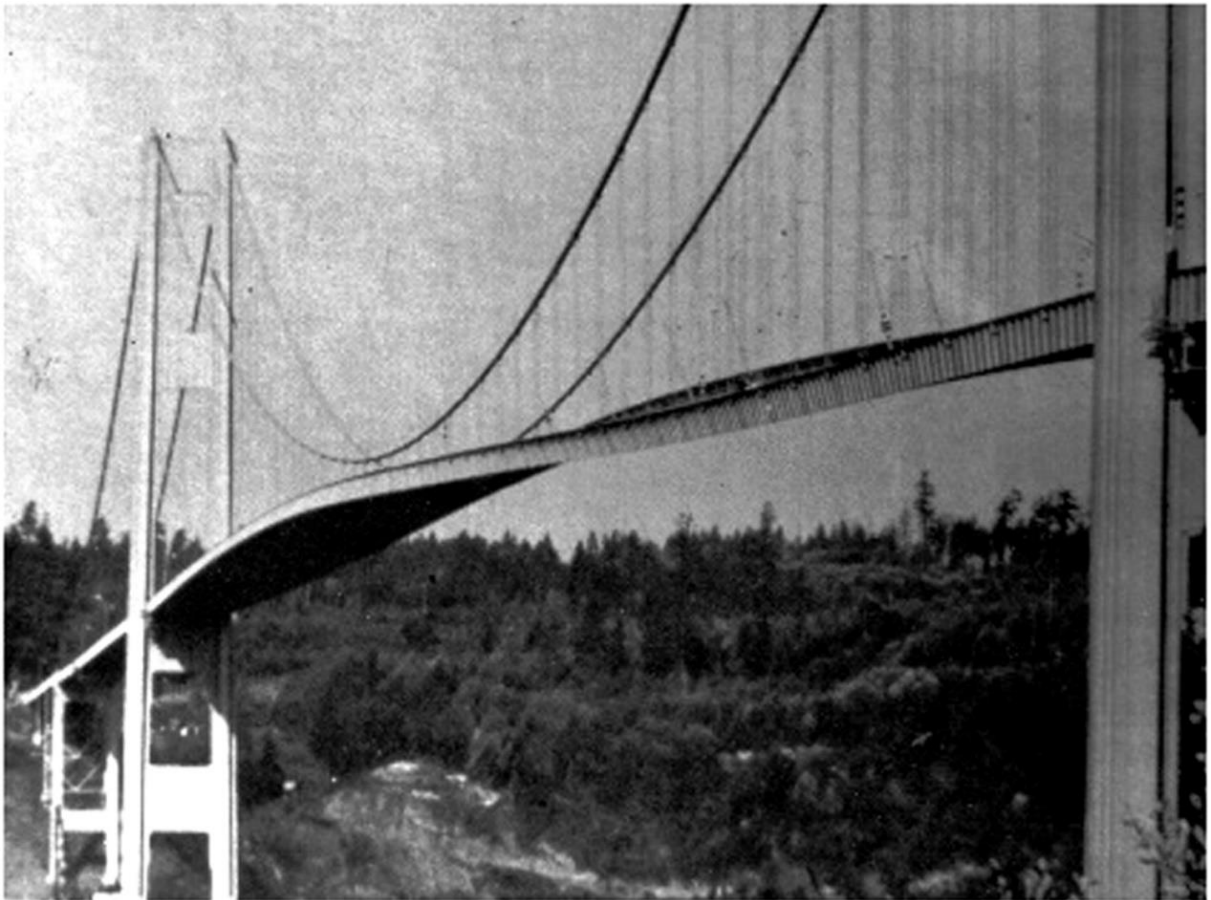
Figure 1 - Photograph of the first suspension bridge over the Tacoma Narrows showing the large twisting motion of the bridge's central span just before it collapsed on November 7, 1940. (University of Washington Structural Research Laboratory et al., 1954)

To this day it is a pertinent objective of structural engineers to understand the fluid structure interactions such as those which caused the catastrophic failure of the Tacoma Narrows bridge, and accomplishing this goal is non-trivial (Green & Unruh, 2006). Mitigation of the potential for disastrous resonance scenarios requires an innate appreciation of the relationship between frequency ratio, dampening coefficient and the resultant resonance transmissibility. This important relationship is shown graphically in *Figure 2*, where it can be seen that the resonance transmissibility rapidly increases as the frequency ratio approaches unity. From this same figure however, the significance of applying

dampening to such a system, and the impact it has on the resonance transmissibility can also be appreciated. Dampening is an important tool in the arsenal of any engineer, as whilst it is ideal to design the natural frequency of any machinery to be well away from the operational frequencies, in reality the possible operational frequencies are not always immediately obvious, and often it is not practicable to account for all possibilities.
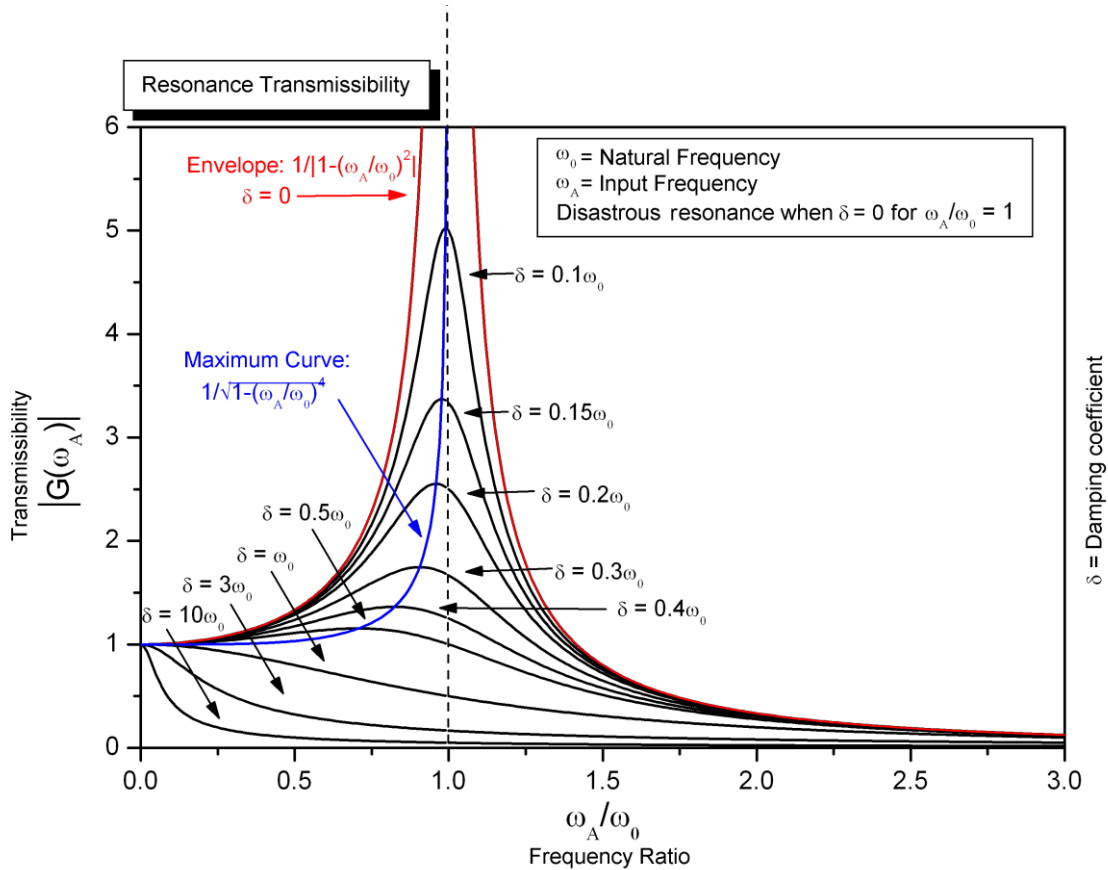
Figure 2 - Resonance effect shown for various input frequencies and damping coefficients (MasterHD, 2008)

Whilst a plethora of noise attenuation, vibration isolation, and resonance dampening technologies exist today, this study focuses on the unique subset of the passive application of acoustic resonators. Passive technology is usually the first alternative to consider in industrial noise control practice (Arenas & Acevedo, 2009), within which two primary approaches to noise attenuation exist: porous materials and resonators. This passive preference can be attributed to a relative simplicity in design, ease of implementation, and consequently lower cost, compared to active dampening alternatives.

In practice any passive noise attenuation device performs silencing work through sound dissipation, reflection, or a combination of both. In the dissipative regime, an acoustically absorptive material acts to convert a considerable amount of the incident sound energy coming into contact with it to heat; whereas the reflective regime relies on a well-defined geometrical structure to reflect a substantial part of the acoustic energy back to the source (Aiman et al., 2018).

An acoustic resonator can be considered a vessel of any shape, containing air *(or other elastic media with mass),* with an opening to the external fluid domain, in the form of a narrow neck or orifice (Yarwood, 1953). From this definition it can be appreciated that acoustic resonators can come in many shapes and sizes, and given that it is principally their geometric characteristics that determine their function, an exhaustive classification is not trivial. Existing literature has however conjointly classified some distinct forms of passive acoustic dampening devices, which are each differentiated by their own acoustical nuances, and each described by their fundamental geometries as shown in *Figure 3.*
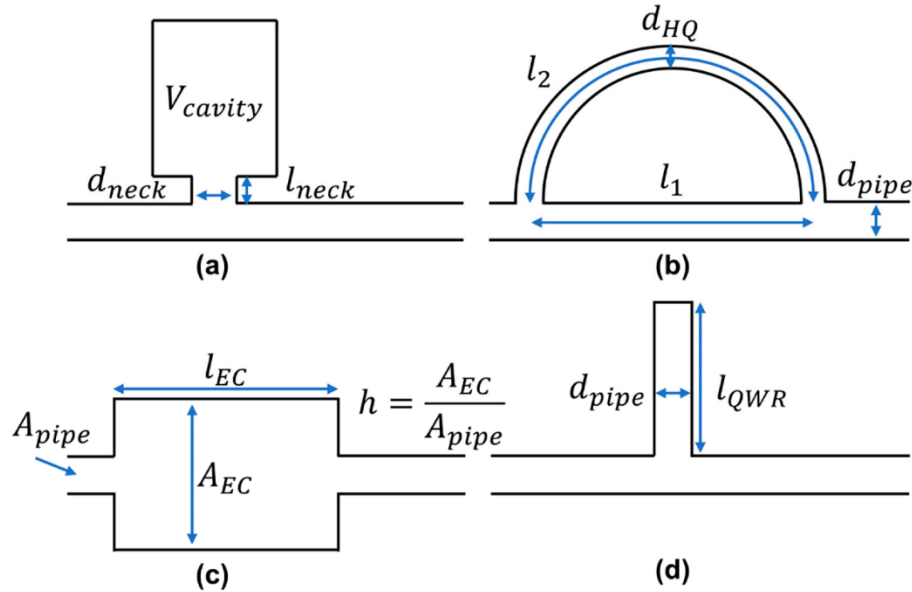
Figure 3 - Schematic of the (a) Helmholtz resonator (HR), (b) Herschel–Quincke tube (HQ), (c) expansion chamber (EC), and (d) quarter wave resonator (QWR). (Sachedina et al., 2020)

This study focuses on the passive application of Helmholtz Resonators, of an archetypical configuration to the schematic shown in *Figure 3(a).* The creator of the Helmholtz Resonator and the devices namesake, Hermann von Helmholtz, played a significant role in the transition from rudimental experimental, to advanced theoretical acoustics; and in his book "On the Sensation of Tone" *(First published in 1862)*, he discusses resonance theory in great detail, and notionally validates fundamental principles of both mathematics and acoustics, such as Ohm's law; where he confirmed through the application of acoustic resonators, that the human ear analyses musical tones according to the laws of simple vibrations, a principle which is of great significance in appreciating how we perceive noise.

Helmholtz prescribes his resonator as a hollow sphere of glass or metal, or tubes, with two openings *(as shown in Figure 4)*. One opening *(a)* has sharp edges, and the other *(b)* is funnel shaped, and adapted for insertion into the ear. The intended function of his device is such that when the resonator is applied to ear, *"most of the tones produced in the surrounding air will be considerably damped; but if the proper tone of the resonator is sounded, it brays into the ear most powerfully"* (Helmholtz, 1954).
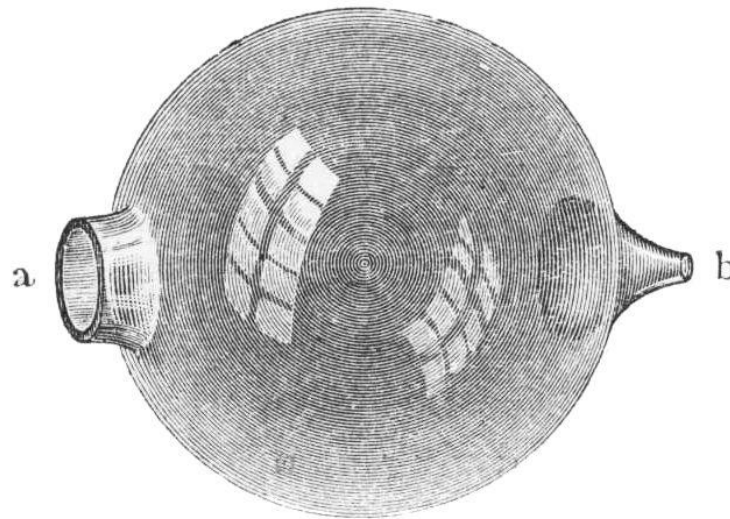
Figure 4 - Helmholtz Resonator as prescribed by Hermann von Helmholtz (Helmholtz, 1954)

In the context of Helmholtz's work, his resonators provided a mechanism to allow a specific frequency of a complex sound to be easily and accurately distinguished, and permitted the distinction between complex sound and pure tones; a principle which was central to his investigations of auditory sensation and perception, and one which is pivotal to a richness of subsequent research which ensued in the fields of psychology, physiology, mathematics, physics and engineering.

As a prelude to the in-depth theory behind the acoustic resonator presented in *Chapter 2 – Background*; and that of the current state of the art in relation to modelling of resonators contained in *Chapter 3 – Literature review*; the functional characteristics of an acoustic resonator can be considered analogous to that of a mechanical system having lumped mechanical elements of mass, stiffness, and resistance (Kinsler & Frey, 1982), allowing its representation by a one dimensional elastic spring and damper model as depicted in *Figure 5.*
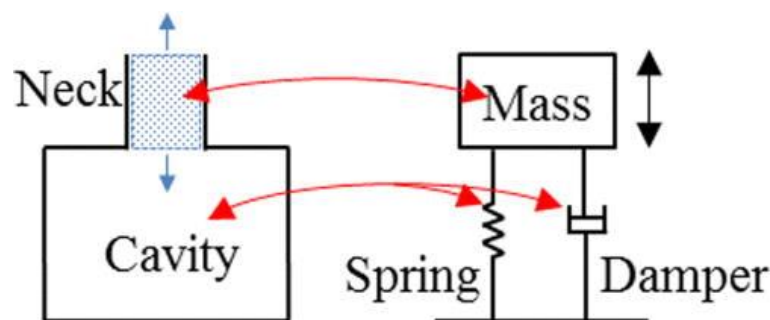
Figure 5 - Helmholtz Resonator depiction and its mass-spring-damper model analogy (Zalluhoglu & Olgac, 2016)

Through this analogy the gas in the neck of the resonator can be considered to move as a single lumped mass, which when acted on by an external force, such as an incident acoustic signal, will oscillate against the volume of gas within the cavity, which in turn acts as an elastic spring and damper.

Furthermore, at the opening there is radiation of sound into the surrounding medium, which leads to the dissipation of acoustic energy, and thus provides a resistance element, in addition to the viscous forces associated with the influx and efflux of gas through the opening (Kinsler & Frey, 1982).

When excited by frequencies or harmonic overtones near to its resonant frequency, relatively small pressure perturbations lead to large oscillating mass fluxes in the resonator neck, which in turn introduce large viscous losses and sound absorption (Dupe`re & Dowling, 2005). It is for this reason that Helmholtz resonators can be extremely effective at noise reduction within the vicinity of their natural resonant frequency.

Because of the relatively simple geometry of a Helmholtz Resonator, supporting a robust and durable construction, coupled with its tuneable characteristics, it has come to be widely used in modern engineering applications to reduce noise centralised in a narrow band at its resonance frequency (CAI & MAK, 2018).   The application of Helmholtz Resonators is particularly prevalent amongst duct-structure systems, such as heating, ventilation and air conditioning systems in buildings, automotive duct systems (inlet & exhaust), gas turbines for power generation and aero-engines; where they are commonly deployed to attenuate noise produced by unavoidable in-ducted elements (MAK, C. M. & YANG, 2000; Cai, Mak et al., 2017a).

As a consequence of the many direct and indirect engineering applications of Helmholtz Resonators as noise attenuation devices, there exists many associated theoretical studies in the field of acoustics, the most pertinent to this study being covered in Chapter 3 – Literature Review; direct application of many simplified theoretical formula for resonant frequency however, often result in a large calculation error, and in some cases even incorrect prediction of the resonant frequency in situ (Li, L. et al., 2017). Hence there is a need for increased academic rigor in the context of many engineering applications of Helmholtz Resonators as noise attenuation devices; and in the subsequent section *(1.1 Motivation),* key engineering applications wherein there is a simultaneous need for further study, and a large application potential for Helmholtz Resonators as noise attenuation devices will be delineated.

1.1   Motivation

In this section the pertinent motivations and justifications for further investigation and evaluation of the application of Helmholtz Resonators as noise attenuation devices, will be presented and discussed in context of distinct industrial applications.

1.1.1   Noise, Vibration, and Harshness (NVH)

In the development of complex products, noise vibration harshness (NVH) problems are unfortunately often discovered only late in the design process; due in part to the fact that the vibration behaviour of complex assemblies is hard to simulate, and effective evaluation is dependent on all components, each of which introduces multiple unknown parameters (Haeussler et al., 2021).

The Transfer Path Analysis (TPA) paradigm is a family of test-based methodologies which can be deployed when the actual vibrating mechanisms are too complex to model or measure directly. TPA concerns a product's actively vibrating components *(such as engines, gearing systems or turbochargers etc.)* and the transmission of these vibrations to the connected passive structures, which results in noise. This technique allows the source excitations to be separated from the structural/acoustic transfer characteristics, allowing engineers to troubleshoot dominant paths of vibration transmission, and then anticipate remedial changes to either the source itself, or the receiving structures that are connected to it (van der Seijs et al., 2016).

In addition to providing a broad review and comparison of TPA methods in a unified notation, Maarten V. van der Seijs (2016) also adeptly states that *"TPA often rises from the need to reduce some sort of undesired noise or vibration, for instance to improve product comfort or lifetime, ensure safety or preserve stealthiness".* This statement provides an inference into some of the industrial applications for which an innate understanding of NVH is pertinent, for example; automotive, aerospace, marine & building acoustics; but also provides three distinct industrial motivators for the study, evaluation and application of NVH mitigation techniques, such as the application of acoustic resonators as noise attenuation devises:

1. Secrecy: Since the 1950s there has been much investigation into how to make military ships and submarines stealthier through the reduction of engine vibration transmission, and the research which ensured typically focuses on the application of absorbers and decoupling mechanisms to mitigate transmission through the passive interfaces (Harrison et al., 1952; Ungar & Dietrich, 1966; Plunkett, 1958; Soliman & Hallam, 1968; Snowdon, 1979). Whilst these applications share some commonalties with the fundamental mechanisms of acoustic resonators; namely the mutual representation by a mass-spring-dampener analogy; the remedial mechanisms are more typically mechanical, as opposed to acoustic.

Acoustic resonators are nevertheless extensively utilised to attenuate noise which perseveres beyond the capabilities of mechanical absorption and decoupling techniques, such as within technical rooms

where noise generating equipment is located, I.e. marine engine rooms, enclosed electric transformer substations, compressor or diesel generator enclosures etc. (Fesina et al., 2015).

More recently however, the development of contemporary metamaterials and metasurfaces has rapidly accelerated the use of acoustic resonators to achieve novel stealth properties, such as echo reduction/acoustic transparency (Gorain & Padmanabhana, 2020; Zhou et al., 2020; Lee, Dongwoo et al., 2021; Zhenjing Zhu et al., 2022; Chen et al., 2020; Yurtseven et al., 2023; Park & Kim, 2019). Such metamaterial developments transfer the research object from air to water, and can be mainly divided into three distinct categories, according to their different functions:

(1) Sound Absorption Metamaterials (SAM), which are categorised by small surface reflections and high loss factors;

(2) Sound Insulation Decoupling Materials (SIDM), whereby impedance mismatching the vibration of the internal structure is blocked from transmitting into the water;

(3) Underwater Acoustic Guided Metamaterials (UAGM), which achieve stealth by directing sound waves to travel along a specific path and thus changing their reflection path (Zhenjing Zhu et al., 2022).

A schematic diagram of the these three main stealth principles can be seen in *Figure 6*; followed by *Figure 7*, which depicts a conceptual diagram of how novel metamaterials can be applied to a submarine hull, utilising miniaturised Helmholtz Resonators within to attenuate reflected sonar signals. Emerging developments such as these, and the importance of the current state of the art of acoustic resonators within the medium of air, is testament to the value added in expanding the current understanding of how to maximise the efficacy of acoustic resonators across a broad range of design and operational parameters.

(a) Sound absorption metamaterial   (b) Sound insulation decoupling metamaterial   (c) Diffractive control metamaterial

Incident Sound Waves   Internal Vibration Noise   Incident Sound Waves   Diffraction Sound Waves
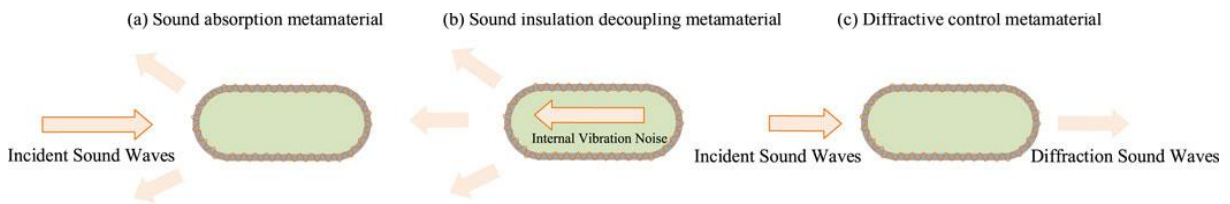
Figure 6 – Schematic diagram of the three main principles of underwater acoustic metamaterials (Zhenjing Zhu et al., 2022).
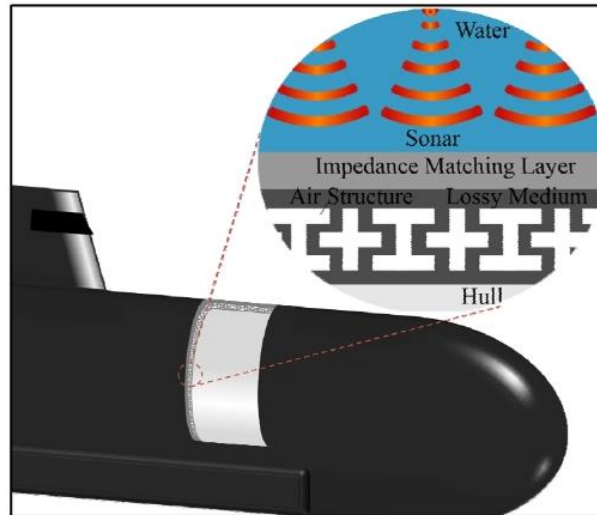
Figure 7 – Conceptual diagram of Helmholtz resonator-based metamaterial applied on a submarine hull (Park & Kim, 2019) .

2. *Safety:* During the rapid advancements in aeroplanes and spacecraft in the 1960s, fatigue and stability *(flutter)* problems began to surface, due to active or induced vibrations. Often tenacious vortex-induced vibrations were the primary source and hence, characterising the passive transfer paths in order to mitigate the impact of catastrophic resonance was of great significance (Bisplinghoff et al., 1955). Such safety concerns can be attributed to mostly external flow phenomena, and would be typically remedied or mitigated through calculated reengineering of the relevant passive structures, principally in consideration of mechanical impedance. Irrespective, the methods of interconnection developed as a consequence, are equally applicable to many complex composite systems, such as electro-mechanical and acoustic-mechanical (On, 1967).

Of equal significance, is that of flow-induced cavity oscillations, and internal cavity resonances; which left unaddressed, can be similarly catastrophic; and for which the application of acoustic resonators is particularly pertinent. Fatigue failure can be further exacerbated within acoustically confined spaces when combined with thermo-acoustic instabilities; which are mainly formed due to in-phase superposition of non-uniform heat release and pressure; and can be observed in combustion systems such as jet engines, rocket engines, ramjets and gas turbines (Deshmukh et al., 2023). Such instabilities left unchecked, will not only lead to a loss of combustion efficiency, increased noise, vibration and harshness, but are also likely result in catastrophic structural failure, and hence are of great safety concern (Li, S. et al., 2016; Poinsot, T., 2017; Nilaj & Sharma, 2017). An example of an early rocket engine developed by NASA which was destroyed by such instabilities can be seen in *Figure 8*, alongside a laboratory burner designed specifically to investigate the problematic perturbances. In adding to NVH ramifications, and safety concerns, there are further performance factors of significance in the investigation and application of acoustic resonators in the context of combustion instabilities, which will be subsequently delineated in *Section 1.1.3*.
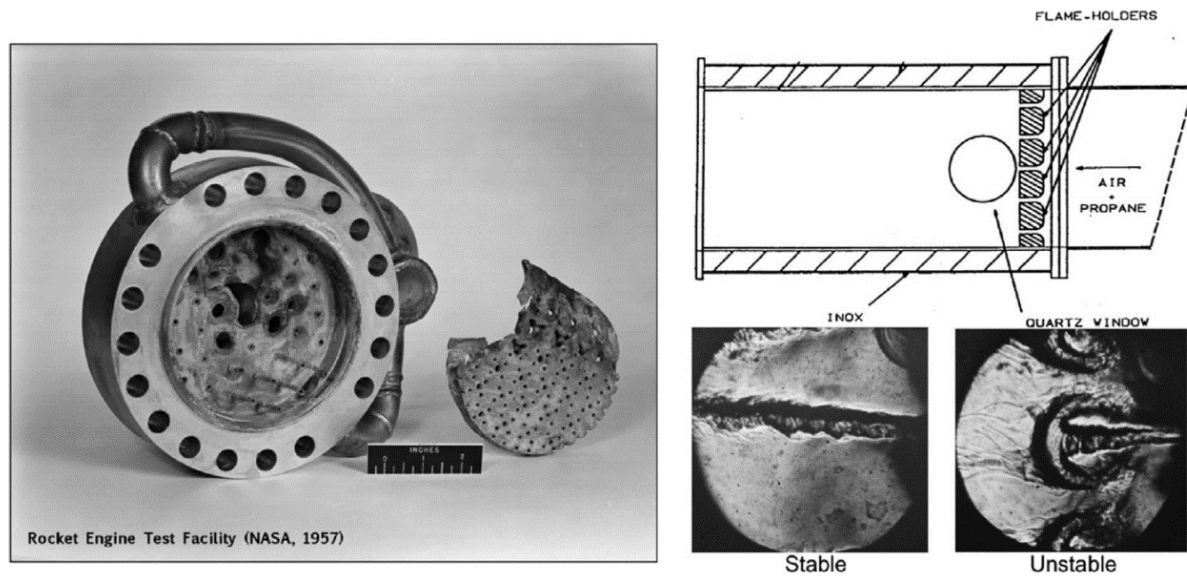
Figure 8 – Rocket engine destroyed by instability during the early years of the US rocket program (left) and a laboratory burner exhibiting both stable and unstable regimes (right) (Poinsot, T. J. et al., 1987).

Following to the aforementioned safety deliberations, it should be noted that audible noise can be just as damaging as any other form of pollution, and is of equal safety concern. It may not only cause irritation or annoyance, but it can also be a danger to health; it is for this reason that legal limits on the exposure to and emission of noise exist in most countries (Turner & Pretlove, 1991), and hence why we must strive to understand and manage it effectively. Acoustic resonators are also particularly well suited to aero-engine liners, both upstream and downstream of the combustor, where they can be designed specifically to reduce the emitted tonal and broadband noise. A well-designed aero-engine liner not only excels in dampening acoustical pressure waves, but importantly can also withstand significant mechanical pressure, and harsh environments, making them inherently safe and reliable (Neubauer et al., 2023).

3. **Comfort:** Beyond any requirements of secrecy and safety, more often contemporary developments and commercial solutions relating to noise, vibration and harshness, are driven by increasing customer expectations of acoustic comfort. In keeping with the aerospace industry, it is within the cabin where the primary customer resides, and hence it is here where concerted engineering efforts on managing acoustic comfort must be applied. In addition to noise induced by the power plant (propeller/engine), in modern aircraft flying at cruise conditions, it is mainly the turbulent boundary layer of the surrounding air which creates cabin noise (Hubbard, 1991; Wilby, 1996). This is because perturbations in the boundary layer excite the fuselage, which in turn causes vibrations in the structure, consequently resulting in transmission to the air within the cabin, and perception by the passenger as sound; which when undesirable has the potential to cause discomfort (Hannink, 2007). Common remedial actions

include the use of dissipative absorbers such as fibrous or porous media (Bies & Hansen, 1997; Cox & D'Antonio, 2016), double wall panels (Basten, 2001), or acoustic resonators.

The application of acoustic resonators to address NVH comfort issues and is nevertheless, not limited to the aerospace industry; with application potential spanning almost every industry in which noise exists. Within few however, is the complexity, breath, and depth of acoustic resonance, and the application of acoustic resonators quite so relevant to comfort, as that of the automotive industry.

The role of noise and vibration factors on vehicle harmony is as multifactorial and complex as our interaction with the vehicle; audio and tactile feedbacks are combined with visual cues and ever-changing driving and boundary conditions. Some NVH elements affect comfort, such as gear whine, boom, tire and wind noise; whilst others like engine noise have a more direct impact on overall appeal and the perception of quality; a summary of which can be seen in *Figure 9*. It is for this reason that automotive companies around the world have invested considerable resources in the past 20 years to understand what role sound and vibration play in a customers' perceptions and to establish realistic targets to ensure commercial appeal. In the past NVH factors would often present collateral damage to other design choices, but nowadays NVH design is often tightly integrated within the early stages of vehicle development (Cerrato, 2009).
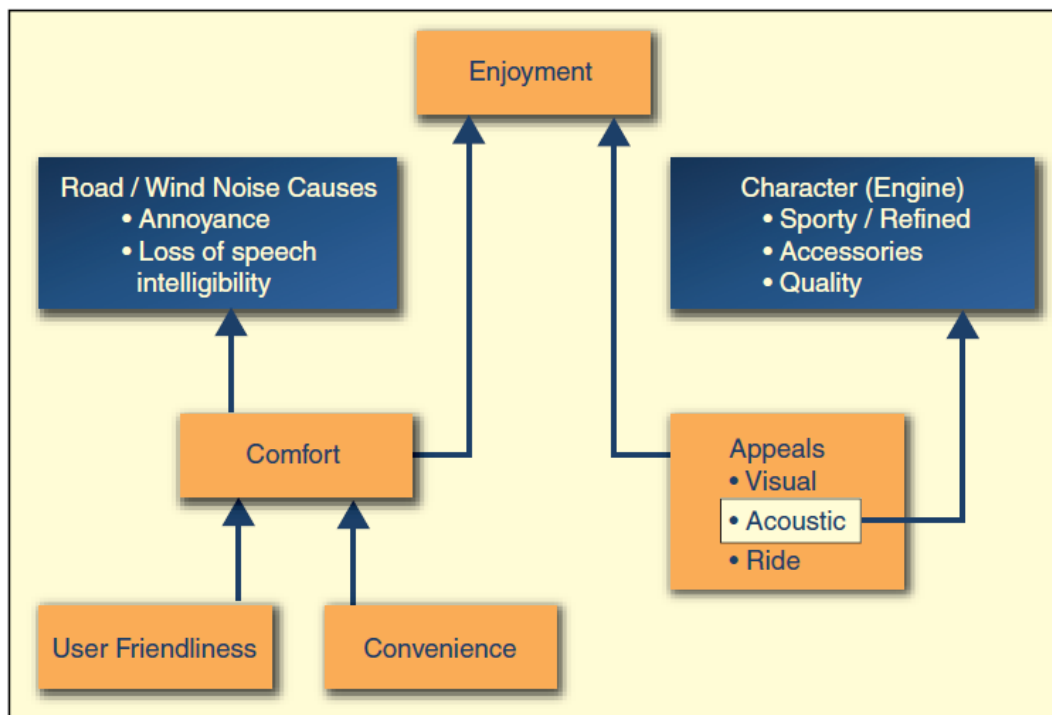
Figure 9 - Impact of NVH on overall vehicle harmony (Cerrato, 2009)

Acoustic resonators play a large part in addressing modern automotive acoustic comfort and quality challenges, with applications spanning multiple flow driven systems; such as intake piping, charge

cooler piping, heating, ventilation and air conditioning (cabin ventilation) ducting, and exhausts; which all have a combination of incoming noise and mean flow, and hence a requirement to "tune" the noise content, by enhancing and/or reducing certain frequencies (Khan, 2014).

Flow generated noise can be both broadband and tonal in nature, and hence automotive attenuation techniques typically exhibit a combination of both absorption and reflection; whereby broadband noise is commonly attenuated through dissipative techniques; and unwanted tones are targeted through reflection by the application of bespoke passive/active acoustic resonators. Noise attenuation devices consisting of both techniques are colloquially referred to as silencers or mufflers; it should be noted however, that no practical muffler or silencer is completely reactive or completely dissipative, as any such device contains some elements with impedance mismatch, and some with acoustic dissipation (Munjal, 1987). Barron (2002) defines a silencer as "an element in the flow duct that acts to reduce the sound transmitted along the duct, whilst allowing free flow of the gas through the flow passage." This definition alludes to the importance on minimising the consequential flow resistance caused by any noise attenuation device; a principle which is particularly pertinent in the automotive sector, where performance is a key product differentiator; but is arguably relevant in any application where the flow is being mechanically driven, as any such restriction will ultimately reduce the overall efficiency of the system. It is for this reason that passive reflective/reactive mufflers based on impedance mismatch are most common in the automotive industry, and dissipative devices based on the principle of conversion of acoustic energy into heat by means of highly porous fibrous linings, are generally reserved for heating, ventilation and air-conditioning systems (Munjal, 1998).

Whilst it is clear that there is significant motivation for advancing the current state-of-the-art in relation to the industrial application of acoustic resonators as noise attenuating devices; many of the lesser understood phenomena, such as the impact of cross-flow over the orifice; are of equal relevance to flow-induced cavity resonance, as they are to duct confined flows. Flow over cavities has received significant interest over the last several years, and the problem of accurate prediction and control over a wide range of flow conditions is not yet solved; due in part to the need to accurately understand the disparate scales of acoustic and vorticial disturbances driving such oscillations, which is a difficult task for fluid dynamicists and aero acousticians alike (Cattafesta et al., 2008).

The underpinning principle of flow-induced cavity resonance can be seen schematically in *Figure 10*, whereby separation of the incoming turbulent boundary layer at the leading edge of the cavity occurs when it encounters an acoustic impedance discontinuity at the onset of the cavity, which in turn establishes a shear layer between the cavity and the external flow, within which vortices are shed periodically from the upstream edge of the cavity (DeMetz & Farabee, 1977). The shear layer spans the cavity and the vortices convect downstream, the shear layer ultimately reattaches near the trailing

edge of the cavity, and as the vortices impinge on the trailing edge, they cause pressure perturbations, which in turn acts as an acoustic source. Resultant acoustic waves consequently emanate from the trailing edge and travel back upstream, where they contribute to the initial acoustic impedance discontinuity magnitude and phase, thus creating a feedback cycle. This mechanism produces resonant frequencies, which are commonly referred to as cavity tones; unlike a Helmholtz Resonator however, there are often multiple tones which can also be accompanied by their corresponding harmonics. This flow-acoustic coupling mechanism has been studied extensively since the 1950s, and founding research established by Rossiter (1964), has led to this phenomenon commonly being referred to as the Rossiter Mechanism.
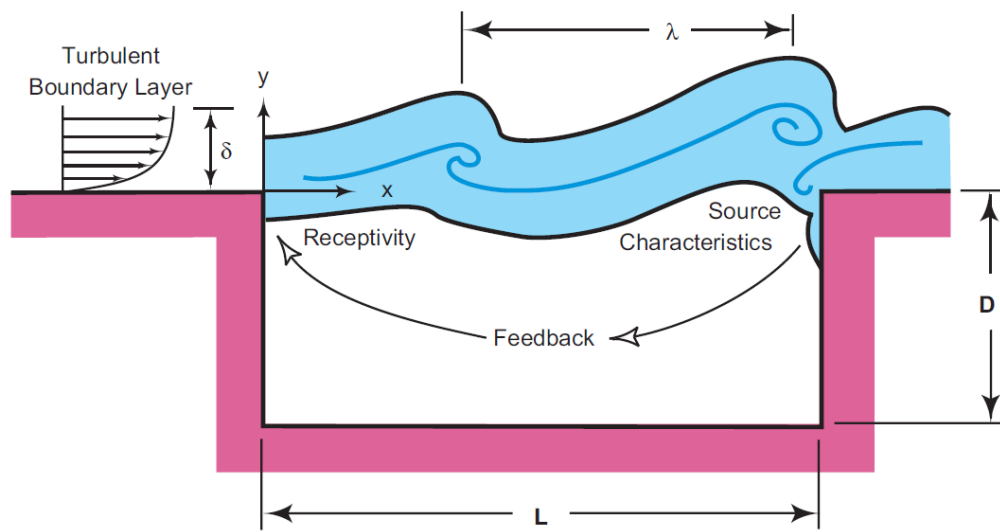
Figure 10 - Schematic illustrating flow-induced cavity resonance for an upstream boundary layer (Cattafesta et al., 2008)

The incoming flow over a cavity, and subsequent addition and removal off mass intermittently, can also make the cavity itself behave as a complex oscillator (Ahuja & Mendoza, 1995). Accordingly, additional tonal frequencies can result from duct resonance (DeMetz & Farabee, 1977; Elder et al., 1982); and furthermore, if the cavity opening has a neck, i.e. high volume to opening area, then distinct tonal responses can also result from volume-dependant Helmholtz oscillation (Meissner, 2002).

A deeper understanding of flow-induced cavity resonance is relevant to a wide array of real-world applications; ranging from aeronautical to automotive, and even less obvious, but equally relevant applications, such as flow in gas transport systems (Bruggeman et al., 1991).

In conclusion, acoustic resonance can be both the cause of, and solution to, numerous industrial noise, vibration, and harness issues; it is however a multi-faceted phenomenon, of which many of the details of physical mechanisms are still not fully understood (DeMetz & Farabee, 1977; Elder et al., 1982; Ahuja & Mendoza, 1995; ROCKWELL & NAUDASCHER, 1978; Rona, 2007). Irrespective of the

substantial academic effort devoted to the topic, a clear understanding of the dependence of the far-field amplitude of cavity noise on parameters, such as geometric properties of cavities, and flow conditions, is seriously lacking (Merino-Martinez & Snellen, 2020). The complexity of the problem can be attributed to the wide variety of possible configurations, in addition to the numerous primary and secondary parameters driving the principle oscillatory phenomena, such as the strong dependence on the boundary layer characteristics, and the inherent three-dimensional nuances of it. All of which serves to motivate this work to advance the current state of the art through thorough experimentation, investigation and characterisation.

1.1.2   Heating, Ventilation and Air Conditioning (HVAC)

Heating, ventilation and Air Conditioning (HVAC) systems are an integral element of almost every structure within which we regularly reside; and in addition to buildings, are equally prevalent in confined modes of transport, such as cars, ships, planes and trains. They play a significant role in maintaining a comfortable environment for humans to live, work and play effectively; however, they also typically consist of mechanical air-movement mechanisms and associated ducting, which are both archetypical examples of sources for resonance induced noise; and such noise produced by HVAC systems is known to result in both psychological and physiological ailments to humans (Hansen, 2007; Alimohammadi et al., 2013). Consequently, engineers and acousticians alike are continually challenged to mitigate the broadband and low frequency tonal noise emanating from HVAC systems (Mak, Cheuk Ming et al., 2009; Fry, 2013; Cai, Mak et al., 2017b).   Dissipative silencers are common noise attenuation practice within the HVAC industry, and are well suited to reducing broadband noise, however, they are not effective at reducing low frequency noise, nor are they efficient at reducing tonal noise. (Denia et al., 2007; Peat, K. S. & Rathi, 1995). Inversely, reactive silencers such as Helmholtz Resonators, are ideally suited to attenuating low frequency, duct-born noise; furthermore, their characteristics of being tuneable, durable and affordable, results in their widespread adoption to address noise attenuation within HVAC systems (Munjal, 2014; Du et al., 2016).

When it comes to the real-world implementation of most HVAC systems, relatively thin-walled, flexible ducts commonly carry both air and any consequential noise generated by associated air-handling units, such as fans, blowers, turbomachinery, and compressors etc. Energy from these noise generating sources is propagated through both airborne and structure-borne paths to the receivers or occupants, as shown schematically in *Figure 11*, and for this reason noise control in buildings is especially challenging due to the sheer number of sources, energy paths, and receiver locations. Due to the complexity and scale of the problem, simulation of the sound environment for a typical building is not viable, and in fact the problem of source identification and quantification is formidable in and of itself

(Ramalingam & Herrin, 2013). In order to rationalise such complex problems, both the International Organisation for Standardisation and the American Society of Heating Refrigeration and Air-conditioning Engineers, recommend considering a system as a number of discrete sources, paths and receivers (ISO, 1998; ASHRAE, 2011). Acoustical engineers in the HVAC industry regularly use the guidance in these documents to support design calculations, but are also aware that much of the tabulated information contained within, is by no means exhaustive; for example, many common duct cross sections are not included, elbows and bends are limited to 90° angles, and the variety of sound absorptive lining materials and thickness are barely considered (Herrin & Ruan, 2019).
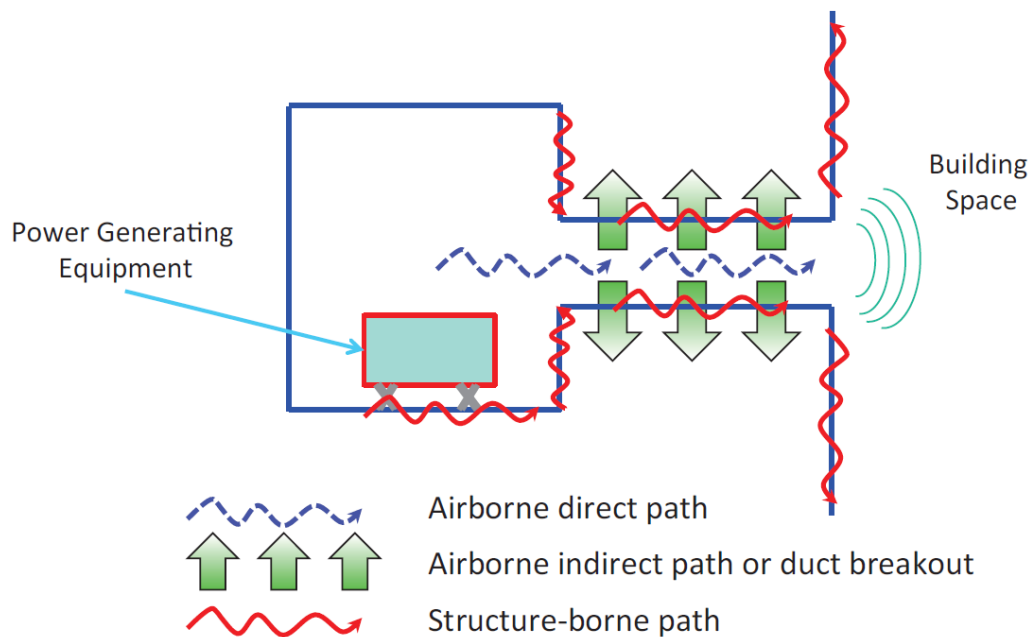
Figure 11 - Schematic showing the airborne direct and indirect and structure-borne energy paths (Ramalingam & Herrin, 2013).

In the early work of Cummings (1978)*,* he recognises that if a silencer were to be placed adjacent to a fan, but designed solely on the basis of duct-borne fan noise transmitted via air outlets to the spaces which they serve, then the intermediate duct-wall radiation would be ignored, and consequential acoustic problems could arise in the intermediate space, irrespective of the presence of the attenuating device. A potential benefit of duct-borne noise breaking out however, is that of the "natural" noise attenuation resulting from the diminution of the internally propagated sound power (Cummings, 1994); that is, provided the breakout does not occur in a noise-sensitive area. It is also important to note that flanking transmission can occur in lined ducts and silencers, whereby breakout, and subsequent breakin can occur; in which case it may be termed "radiation bypass" transmission (Mechel, F. P., 1975). For many years HVAC engineers appreciated the "natural" attenuation effects of air-moving ducts resulting from breakout, but it was not until the later work of Cummings (2001), when a recognition of the reality of breakin occurring was realised, and the consequences valued. As

seen in *Figure 12*, an incoming incident acoustic power flow of W_1, in the absence of breakin, can be equated to the sum of the transmitted acoustic power (W_2), the radiated power (W_o) and that dissipated by dampening in the walls (W_d). In reality however, breakin will also occur, manifesting itself as a power flow of W_i, which splits equally between the upstream and downstream side of the duct.

A comprehensive appreciation of this energy balance is imperative for successful implementation of an acoustic resonator; as any of these power flow elements may result in witnessed tones, or tonal shifts, beyond those of the target frequency of any resonant device; hence any oversight in their contribution to the transmitted acoustic power could significantly reduce the effectiveness of any attempted attenuation.
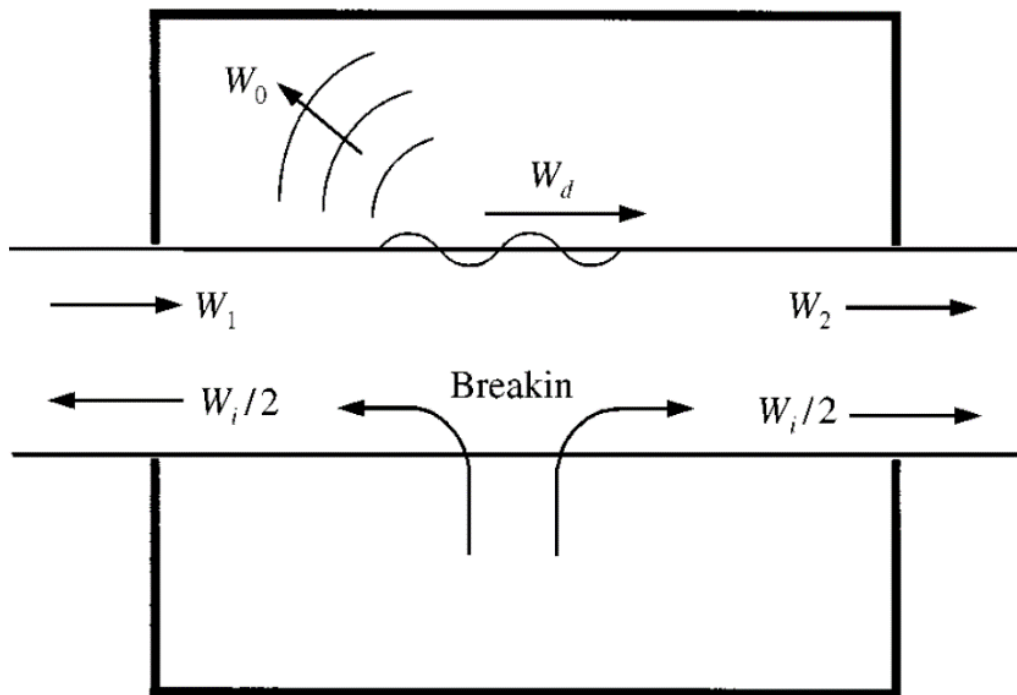
Figure 12 - Power flow in an unlined duct passing through a reverberant enclosure (Cummings, 2001).

Furthermore, and as with the aforementioned NVH cases, whilst an effectively implemented acoustic resonator can serve to mitigate noise, the principles of resonance can all too often contribute to the source of the problem. In the context of HVAC applications, this can occur where any discontinuity within the confined fluid flow has the potential to cause vortex shedding or turbulent eddies, such as the tube bundles within heat exchangers for example. The driving principle can be appreciated from *Figure 13*, which shows the relationship between the Kármán vortex shedding frequency f_w, and the flue gas velocity, V. When the fluctuating velocity component transverse to the mean flow, matches the natural frequency of an acoustic mode within the duct, the resulting resonance can potentially

generate high levels of noise. The problem can also often be exacerbated when the problematic frequencies coincide with the natural frequencies of the structural components, such as the casing, the tubes or even fin-plates etc. In such circumstances, acoustic resonance can result in destructive ducting vibrations, large pressure fluctuations, and in extreme cases may even make it impossible to operate the plant or result in structural damage (Cory, 2005; Shigehiko Kaneko et al., 2014; Dhar, 2016).
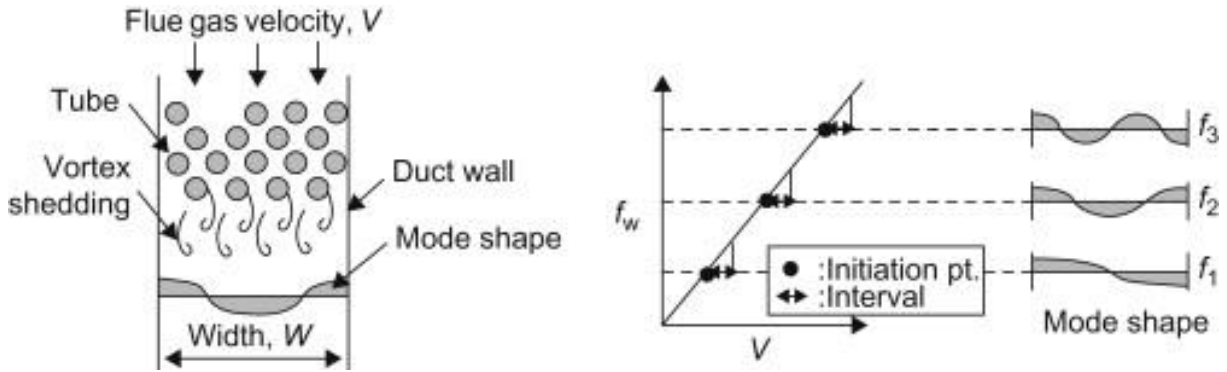
Figure 13 - Overview of acoustic resonance in tube bundle (Shigehiko Kaneko et al., 2014).

Whilst the current state of the art in relation to acoustic resonance and HVAC applications has advanced significantly as of late; the accurate holistic prediction of acoustic performance for even a moderately sized HVAC system remains formidable; due in-part to the scale and complexity of acoustic energy sources, transmission pathways, and receiver locations. The application of acoustic resonators as a corrective response to low-frequency and tonal issues remains prevalent within the industry, however; just as the resonant device itself is sensitive to many fluid dynamic and geometrical factors, within the HVAC industry the noise to be attenuated is often just as nuanced as the corrective device itself.

Given the narrowband response of acoustic resonators, it is imperative to be able to confidently target problematic frequencies; this study seeks to advance the potential for earlier, and more precise implementation of acoustic resonators as noise attenuation devices; and through advances in the understanding of their performance factors, to favour pre-emptive solutions, over the common conservative, and less efficient retrospective remedials.

1.1.3   Combustion Instabilities

As discussed in Section 1.1.1, combustion instabilities can present significant NVH related issues in many industrial combustion-based applications; and in addition to the aforementioned jet engines, rocket engines, ramjets and gas turbines; problematic oscillations can also occur within industrial burners used for heating (Candel, S. M. & Poinsot, 1988), and even in jet engine afterburners (Bloxsidge et al., 1988; Langhorne, 1988). The link between acoustics and flame dynamics was initially

reported as early as the onset of the 19th century, when Higgins (1802) observed that a ducted flame produced oscillatory noise for certain lengths of fuel supply line, which subsequently became colloquially known as the "singing flame" phenomenon. Later Lord Rayleigh (1926) later analysed the singing flame experiment and proposed a criterion for the occurrence of combustion instabilities. Typically, such oscillations will be of the longitudinal, radial or tangential type however, there can also exist mixed modes with the characteristics of all three, each having its own discrete natural frequency (Anderson & Yang, 1995). The occurrence of a combustion driven oscillation, its mode order, and the amplitude; all depend on the thermal diffusivity and heating value of the fuel, the fuel supply rate, the configuration of the fuel supply line, and the dimensions of the combustion chamber (Anderson & Yang, 1995; Putnam, 1971).

Couple these additional factors with the underpinning geometric and thermodynamic factors which impact ducted acoustic resonance phenomenon, and it can be appreciated that combustion instabilities considerably compound the complexity of attenuating unwanted noise. Resonance issues within combustion systems are particularly prevalent and can be primarily attributed to two fundamental causes (Culick, FEC & Yang, 1992; Yang, 2001):

a) Combustion chambers are almost entirely closed and the internal processes tending to attenuate unsteady motions are weak; and

b) The energy required to drive unsteady motions represents an exceedingly small fraction of the heat released by combustion.

Whilst these underlying issues are true for any combustion chamber, they are especially consequential for systems such as gas turbine engines, in which energy intensity is quite high, typically on the order of $100\,\mathrm{MW/m^3/bar}$. In general, less than 0.1% of the energy released in the inherent chemical reactions is sufficient to generate pressure fluctuations having peak amplitudes equal to the mean chamber pressure (Huang & Yang, 2009).

Needless to say, if left unchecked, such significant pressure fluctuations can have catastrophic effects; in Figure 8 the ramifications on a rocket engine can be seen, and Figure 14 shows an example of combustion instability damage in the context of a gas turbine burner.
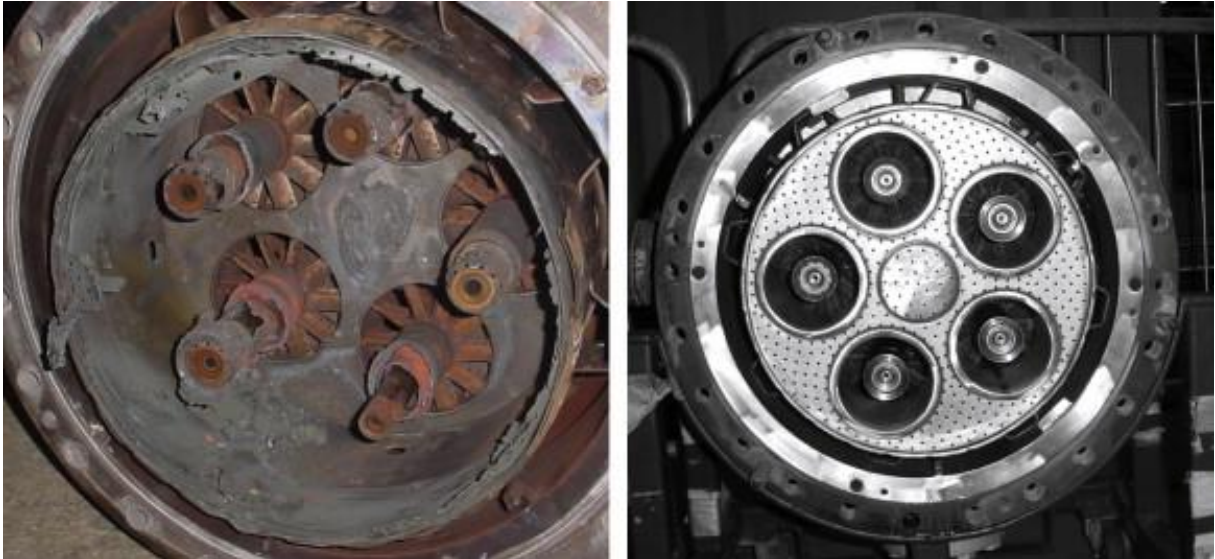
Figure 14 – Gas Turbine Burner assembly (left) damaged by combustion instability and new burner assembly (right) (Goy et al., 2005)

Irrespective of combustion instability resulting pressure and heat fluctuations, inside a combustor is a most hostile environment even under steady state operating conditions. Consequentially, the lifespan of combustor components and downstream turbine blades is limited predominantly by the effects of hot corrosion and creep, pertaining to the constant exposure of high pressure and high temperature reacting flow conditions. Within modern gas turbines pressure ratios can reach 30:1; firing temperatures as high as 2,071°C (Boyce, 2012); and temperatures at the entrance to the turbine of up to 1,650°C (Eliaz et al., 2002).

Such temperatures are much higher than the melting point of many of the components within a typical turbine, therefore effective cooling is essential for their durability. Figure 15 depicts the cross section of a conventional diffusion flame combustion chamber, where it can be seen that around 60% of the incoming air is allocated for the purpose of cooling (Rolls-Royce, 1996).
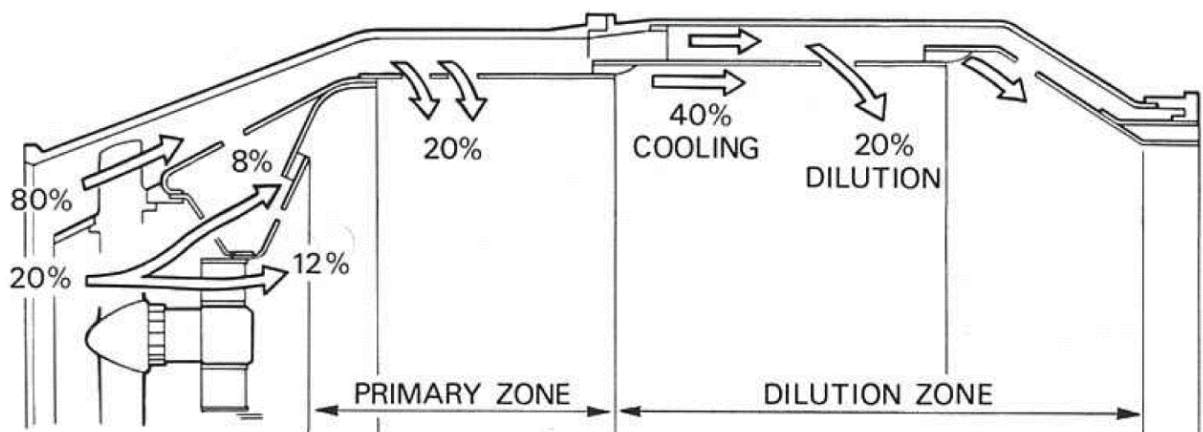
Figure 15 - Apportioning the airflow in gas turbine combustion chamber (Rolls-Royce, 1996)

Of the air not used directly to support the combustion process within the primary zone (approx. 60%), the remaining is introduced progressively into the flame tube downstream, where approximately a third of this air is used to lower the gas temperature in the dilution zone before it enters the turbine; and the remainder is used for the cooling of the walls of the flame tube. The design shown in Figure 15 uses a technique called film cooling, whereby a film of cooling air flowing along the inside surface of the flame tube wall insulates it from the hot combustion gases (Rolls-Royce, 1996). This cooling method not only consumes a lot of air, but has also been shown to be a primary source of resurging related instabilities in early liquid rocket engines (Culick, Fred EC & Yang, 1995).

Contemporary developments in combustion technology require a greater share of the incoming air in order to achieve improvements in combustion efficiency, thereby reducing the amount of air available for the cooling. Consequently, through modern advancements in materials and optimised cooling techniques, wall cooling air consumption has now been reduced by half, to 20% for many combustors now in service (Ballal & Lefebvre, 2010). Figure 16 shows one such example, where the walls are perforated by a large number of small holes with a shallow angle in the combustor mean flow direction, which provides two advantages for the cooling: A larger surface area within the hole for increased heat removal, and the establishment of a thin cooling film along the surface of the wall (Farmer et al., 2003).
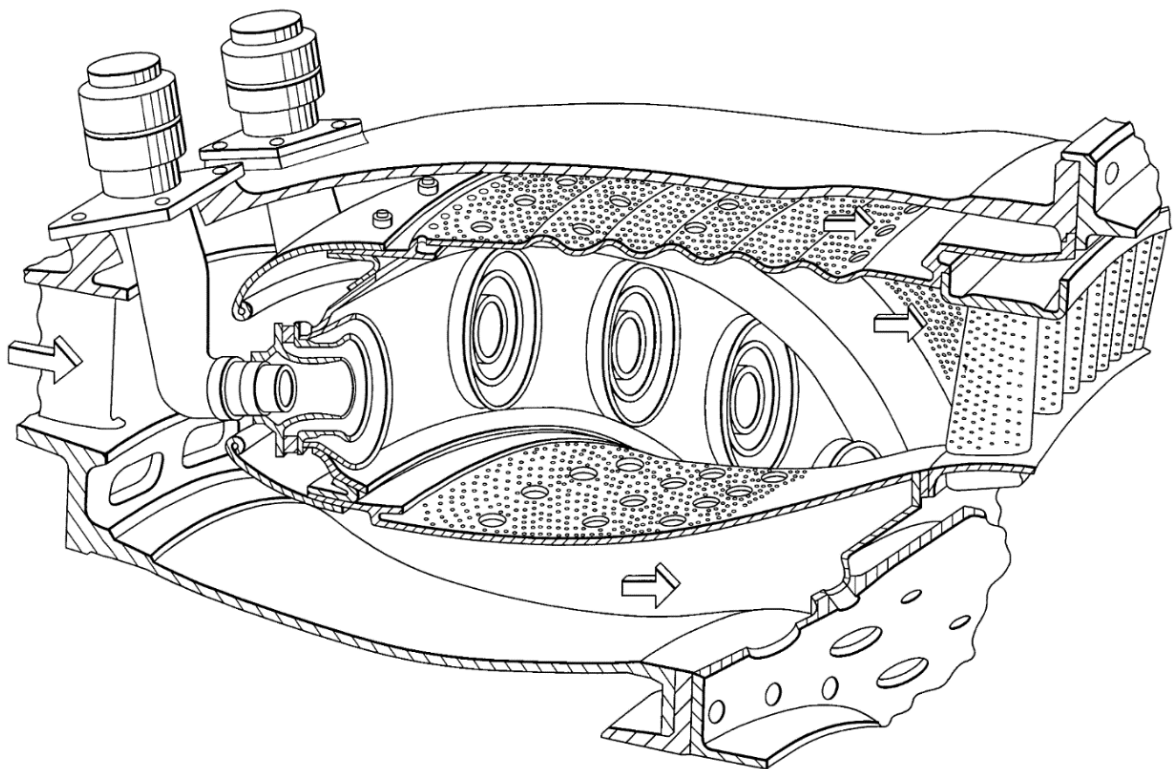
Figure 16 - The GE twin annular premixing swirler (TAPS) combustor with effusion cooling, designed for low emissions and high efficiency (Farmer et al., 2003).

Many modern gas turbine engines, such as the can annular Siemens SGT-750 shown in Figure 17, also commonly employ a double-walled combustor liner to achieve further cooling performance

improvements; allowing both impingement and effusion cooling to employed; whereby impingement cooling enhances the backside external cooling, alongside effusion cooling to create a thin protective film along the internal liner walls. Modern combustors still use large dilution jets to ensure appropriate mixing of the fuel and air, which inherently makes cooling the liner walls through impingement and effusion a difficult challenge, particularly near the dilution holes, where the flows interact. (Shrager et al., 2019).
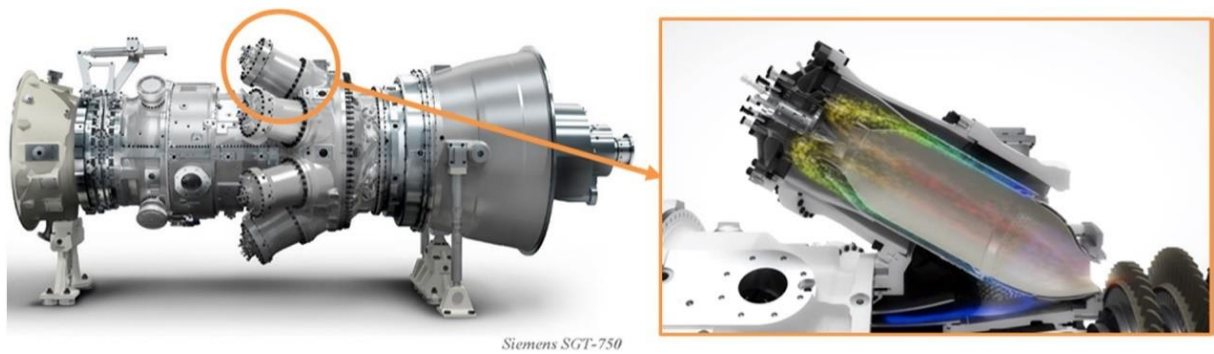
Figure 17 - Siemens SGT-750 gas turbine (left) the can annular combustion chamber (right) (Rashwan et al., 2020)

The careful and calculated apportioning of air consumption and distribution is key not only to effective cooling and durability; but also, to ensure flame and combustion stability. Such unwanted dynamics in conventional diffusion-flame gas turbine combustors, if encountered, can be eliminated largely through relatively simple modifications to the design or operating parameters. Design guidelines are typically based on empirical know-how and commonly are sufficient to avoid the unforeseen occurrence of unwanted dynamics during the engine certification phase. If encountered, simple analysis coupled with empirical guidelines, and a systematic testing and development process, are used to find engineering solutions, without adversely affecting the key combustion system design requirements. Conversely, controlling combustion dynamics in modern Dry Low Emission (DLE) combustion systems remains a substantial challenge for designers (Mongia et al., 2005).

Developments in gas turbine combustion systems, such as Dry Low Emission (DLE) (Liu & Sanderson, 2013) and Dry Low NO$_x$ (DLN) (Evulet et al., 2009), have resulted in a significant reduction in emissions of NO$_x$ compared with traditional diffusion type combustors, which makes them an attractive alternative, irrespective of their inherent instabilities. These emissions reductions have largely been achieved by the combustion of the majority of fuel in a cool and fuel-lean pre-mixed combustion regime, as shown in Figure 18, this regime brings the full-load operating point down on the flame temperature and closer to the lean limit curve.
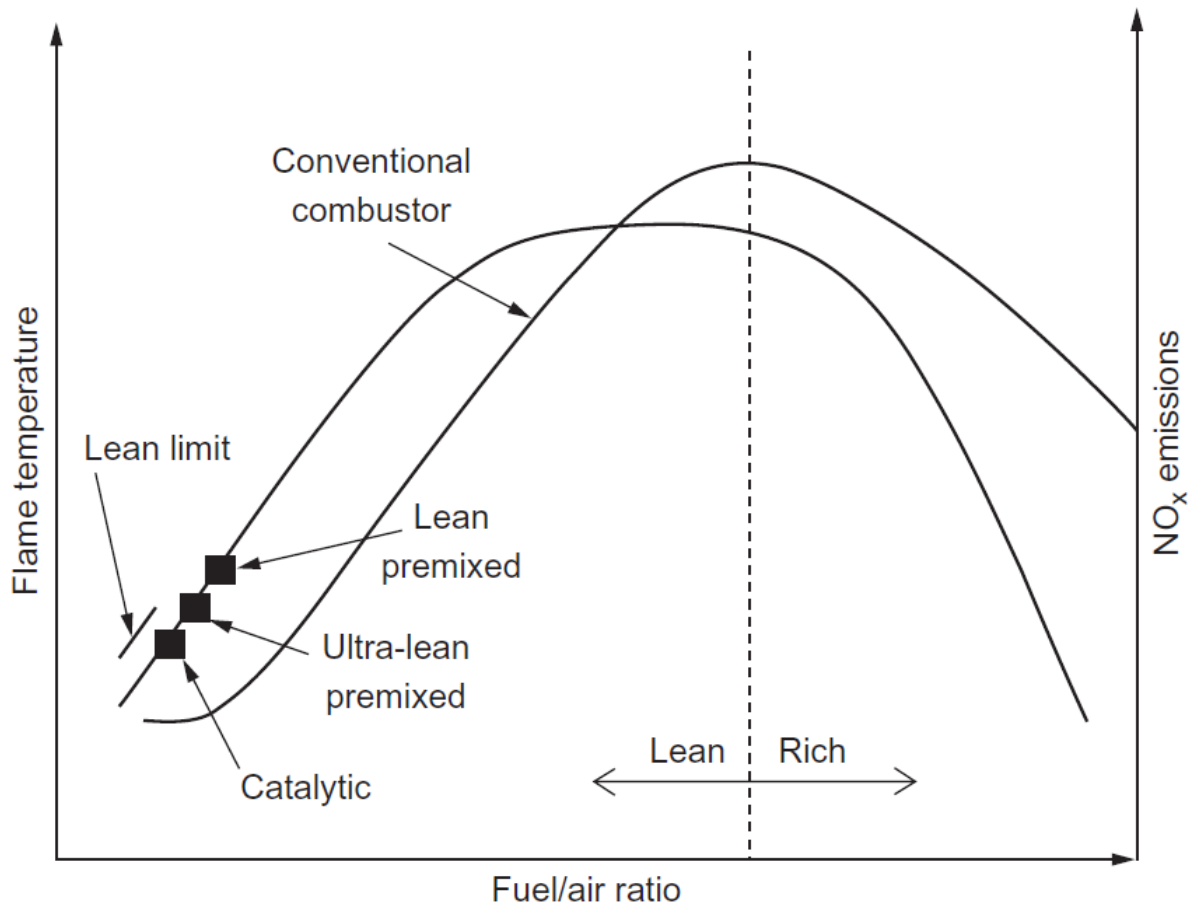
Figure 18 - Effect of fuel-to-air ratio on flame temperature and NOₓ emissions (Boyce, 2012).

Burning so close to the lean limit can however, significantly reduce the stability of the flame and as such significant pressure fluctuations can be formed within the combustor. Such pressure fluctuations can be magnified when fuel heat release is in phase with inherent combustor acoustic frequencies and the resultant oscillations can reduce operating efficiently and increase fatiguing of mechanical components, hence reducing service life and undermining reductions in operational emissions (Houston et al., 2015). As shown schematically in Figure 19, in order to achieve minimum emissions (NOₓ & CO), lean premix burners must operate very close to the lean flame blowout (LBO), thereby action must be taken to ensure that when the engine load is reduced, that flameout does not occur.
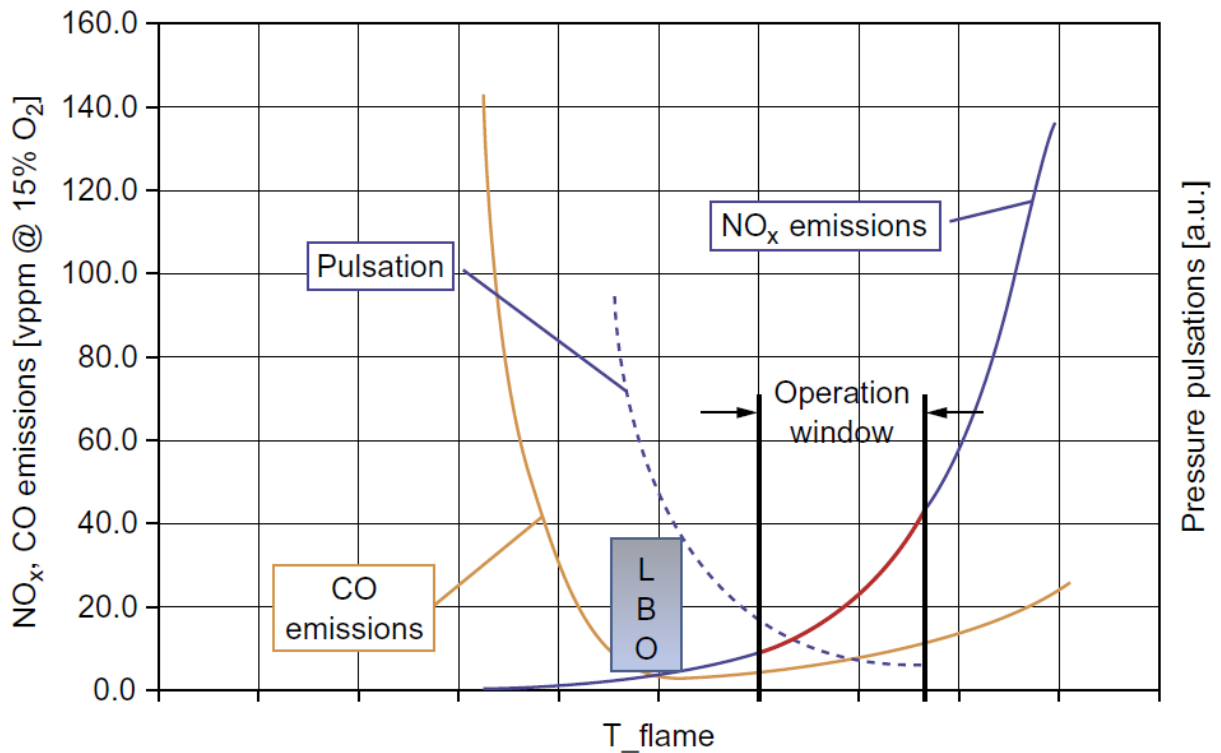
Figure 19 - General emission performance of a lean premix burner (Boyce, 2012).

The main function of the primary zone of the combustion (shown in Figure 15) is to anchor the flame and provide sufficient time, temperature, and turbulence to achieve essentially complete combustion of the incoming fuel-air mixture; and the importance of the primary zone airflow pattern to the attainment of these goals cannot be overstated. Many different types of flow patterns are employed, but one feature that is common to all, is the creation of a toroidal flow reversal that entrains and recirculates a portion of the hot combustion gases to provide continuous ignition to the incoming air and fuel. Lucas combustion group made an important contribution to primary-zone aerodynamics in their early designs for the Whittle W2B (1942) and Welland (1943) engines, and the basic airflow patterns for these combustors is embodied in the concept sketch seen in Figure 20. Here it can be seen that both swirling air, and primary air jets are used to create flow reversal, and the two separate modes merge and blend in such a manner that each one complements and strengthens the other. The result is a strong and stable primary-zone airflow pattern that can provide wide stability limits, good ignition performance, and freedom from the type of flow instabilities that often give rise to combustion pulsations and noise. As a result, these basic aerodynamic features can be found in the combustors designed for many British engines, including the Rolls Royce Nene, Derwent, Dart, Proteus, Avon, Conway and Tyne (Ballal & Lefebvre, 2010).
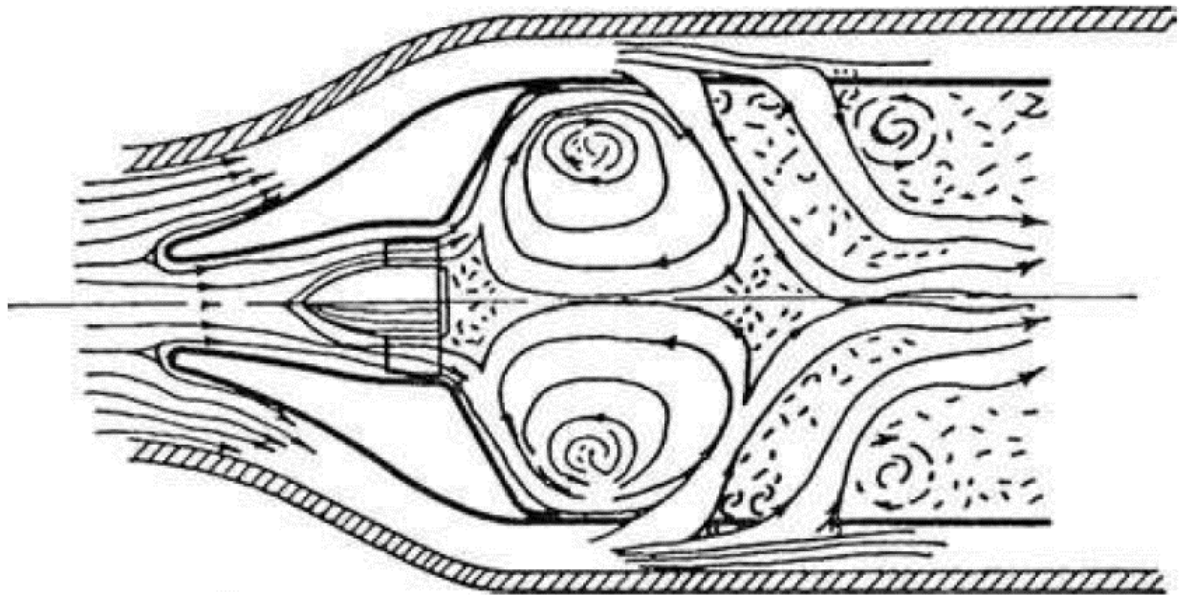
Figure 20 - Lucas primary-zone airflow pattern (Ballal & Lefebvre, 2010).

To avoid flame blowout whilst still ensuring a predominantly lean burn regime, a typical DLE combustor will have two or more fuel circuits. The main fuel (approximately 97% of the total) is injected into the air stream immediately downstream of the swirler, and the pilot fuel is injected directly into the combustion chamber, with little to any premixing. A small proportion of the fuel is always burned richer to provide a stable pilot zone, will the remainder be burned lean; and in both cases swirlers are used to create the required flow conditions in the combustion chamber and to stabilise the flame (Boyce, 2012)

In Figure 21 two DLE burner concepts can be seen: The Siemens Fourth Generation DLE burner (left), and the GE TAPS mixer concept (right); both of which utilise the principle of a separate (but interacting) pilot and lean premix burning zones; to achieve the common goal of all modern combustors still under construction; which is that of robustness, low emissions and fuel efficiency (Akkerman & Law, 2016). Within both systems the swirler retains an integral role as a robust flame holder, which enhances the flame stability. The stabilisation mechanism of the flame lies in two aspects namely; the inner recirculation zone (IRZ) and the outer recirculation zone (ORZ). The IRZ is established by the swirler and governs the flame-vortex interactions through a process of Vortex Break Down, referred to as (VBD) (Altay et al., 2009). Whilst the ORZ is created due to the sudden expansion in the geometry (Taamallah et al., 2015). The swirler centre body ensures robust and strong flame stability across different fuel types, and the process of VBD supports recirculation of unburnt combustion products and mixing with the incoming combustible mixture stream. Another important feature of swirling flow is the so-called Processing Vortex Core (PVC), which from the early investigations of Syred and Beer (1974), was identified as a source of incoherent frequency. When the recirculation zone is not stable,

the PVC takes place and spins around the axis of symmetry, and in doing so the PVC can lead to uncomfortable noise, or worse, if coupled with and acoustic resonance frequency of the combustion chamber. Self-excited combustion instabilities must be tackled by any means to ensure robustness, and previous studies have highlighted several important parameters affecting combustion instability characteristics, such as: the air-fuel equivalence ratio, combustor geometry and varying the fuel composition (Rashwan et al., 2020).
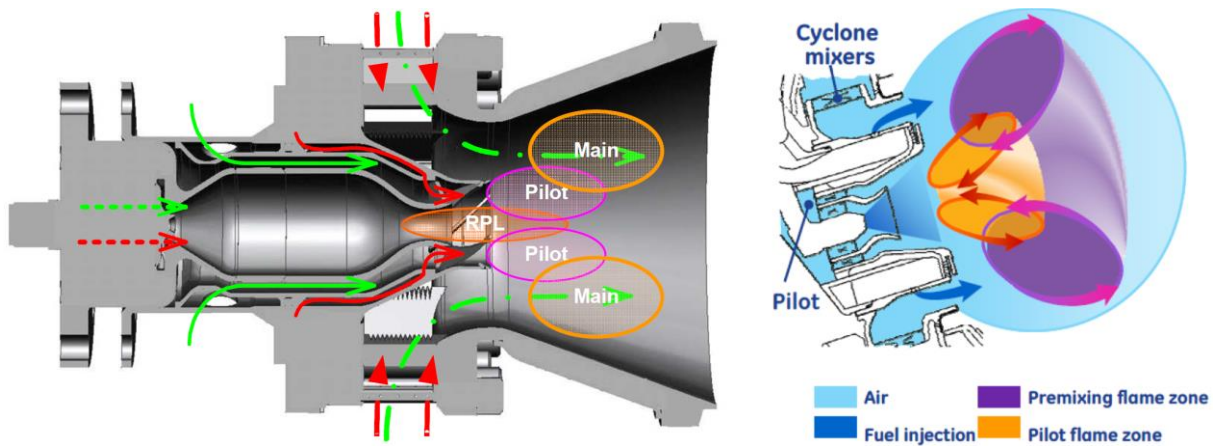
Figure 21 - Associated burning zones for the Siemens 4G-DLE Burner prototype (left) (Carrera et al., 2011) and the GE TAPS Mixer Concept (right) (Herbon et al., 2017)

In Figure 22 it can be seen that improvements in mixing the fuel and air to achieve a homogenous mixture, whilst at the same time leaning out the mixture within the DLE combustor; does indeed achieve the desired effect of a lower peak combustor temperature, and more uniform temperature distribution within the combustion, thus resulting in low thermal NO_x production (Welch, M. et al., 2016).
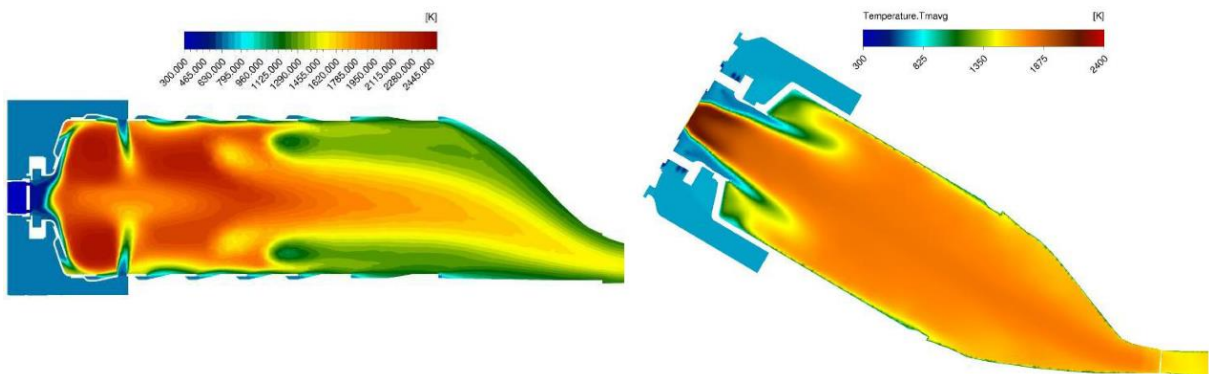
Figure 22 – CFD calculation of temperature distribution within a diffusion flame combustor (left) and DLE lean premixed combustor (right) (Welch, M. et al., 2016)

DLE and DLN combustion systems were specifically developed to reduce NO_x emissions with a primary focus on natural gas as the primary fuel however, over time the development of these combustion

systems has demonstrated the capability to operate on a wide range of fuels, with a much wider range of heating values or Wobble range (Goldmeer et al., 2015; Goldmeer et al., 2017; Cowell et al., 2016). The ability to utilise hydrogen in gas turbines configured with lean premixed combustions systems is a particular area of active research and development for most OEMs currently, with many of the opinion that existing advanced systems will not require significant modification (Goldmeer & Rozas, 2012; Bonaldo et al., 2014; Kurz et al., 2019); albeit lean premixed combustion operating experience with hydrogen is significantly limited, in contrast to conventional combustion (Brun & Allison, 2022). This lack of empirical operational experience puts a much greater onus on the ability to pre-empt and promptly address any unwanted dynamics when burning novel fuels. Therefore, if the benefits of novel fuels are to be fully exploited, the current state of the art in relation to the application of acoustic resonators in this context, must also be advanced accordingly, to ensure effective remedial responses to such unwanted dynamics.

Acoustic resonant devices such as Helmholtz resonators and perforated liners can however be tuned such that they attenuate these dynamics, recouping the efficiency gains and reductions in emissions offered by contemporary combustor technologies. The frequencies at which the magnitude of combustion instability generated pressure waves are most significant are dependent on many factors such as load conditions, fuel properties and the geometry of the combustor itself. As such the successful attenuation of these instabilities through the use of acoustic resonators relies highly on the ability to tune the resonant device to the same frequency as the detrimental dynamic frequency. Helmholtz resonators are well proven to be effective at attenuating pressure fluctuations however, they are most effective at a single peak frequency and their attenuation effect decreases rapidly at frequencies away from this peak frequency. Conversely, attenuation of noise by distributed Helmholtz resonator, i.e. a resonant cavity with multiple small perforations as a neck, takes place across a much wider frequency range, thanks in part to the stronger acoustic resistance of those smaller perforations (Gullaud & Nicoud, 2012; Lahiri, 2014; Noiray et al., 2007). Therefore, even when combustor wall perforations may have been originally designed for the purposes of periphery cooling; such as impingement or effusion cooling; flame stabilisation; or even diffusion; there remains an intrinsic acoustic duality, whereby an underappreciation of the acoustic significance of design parameters may exacerbate combustion instabilities; whilst concurrently an opportunity exists for the effective attenuation of combustion instabilities.

Irrespective of the opportunity for attenuation of unwanted dynamics, both passive methods still require correct tuning to the relevant frequencies, and existing analytical formulations cannot accurately consider all the relevant factors in a gas turbine application. Furthermore, the alternative

of pragmatic experimental design approach is time-consuming and expensive, and often calls for many iterations before arriving at the configuration which is most effective.

The primary challenge of analytical modelling lies in the wide variety of flow and combustion process parameters which can drive instabilities, and the fact that they, as shown in Figure 23, they can be all coupled with acoustic resonant modes.
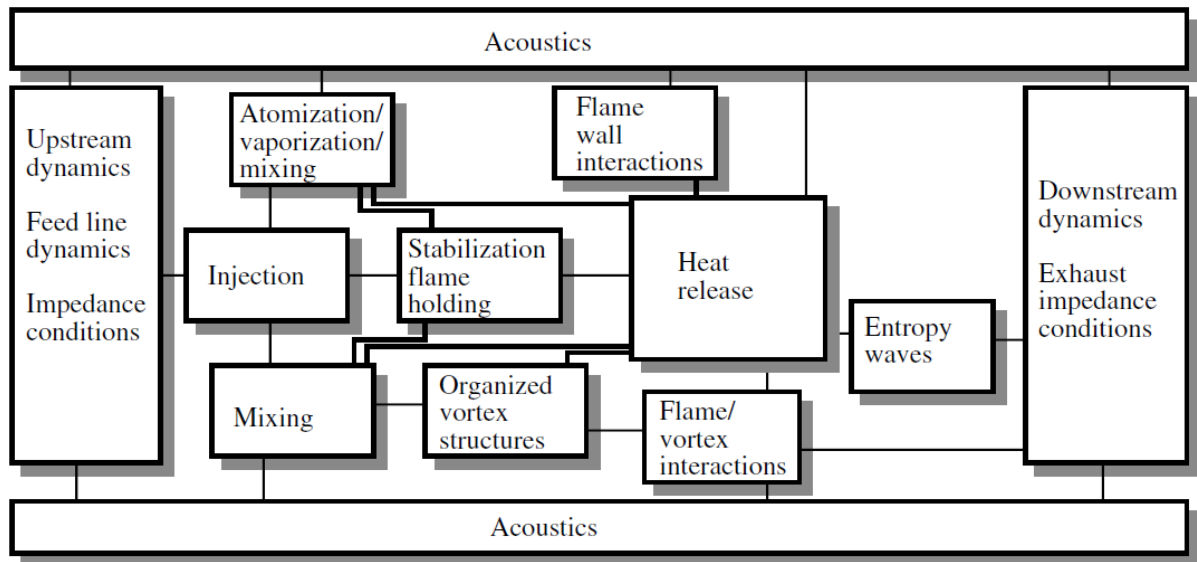
Figure 23 - Basic interactions leading to combustion instabilities (Candel, Sébastien, 2002).

Consequentially, a universal model for predicting combustion instabilities does not yet exist, and a complete solution to the problem can hardly be achieved given the current state of knowledge (Elsari & Cummings, 2003). Irrespective of the fact that we are not yet able to predict combustion instabilities a priori; the phenomenon of combustion dynamics is one of the most important challenges facing the gas turbine industry (Lieuwen & Yang, 2006); and meaningful ductions can still be achieved through fundamental investigations on simplified systems, in combination with practical investigations.

The focus of this study is however, to primarily support more accurate and efficient application of passive acoustic devices to attenuate and control combustion instabilities, amongst other applications; as such, the need to predict instability regimes, is not as imperative as the ability to confidently supress known instabilities. Therefore, through a careful and calculated multifactorial investigation and characterisation of performance factors, noise attenuation using acoustic resonators can effectively support novel product developments, and improvements in existing products efficacy, across a diverse range of invaluable industrial applications.

1.2   Objectives and Scope

Whilst the high potential inherent in the application of acoustic resonators for the reduction in noise is well-know; a comprehensive understanding of under which circumstances this potential can be retrieved in its fullest, remains elusive. The complexity of this topic is compounded by the sheer magnitude of potential performance affecting parameters which exist, and consequently the amount of associated literature dealing with such acoustic properties is in general overwhelming. Typically, existing studies focus on one parameter, which will be practicably limited in the range investigated, with the impact on the performance of noise attenuation being evaluated in isolation.

As such, the primary focus of this investigation is to take a step back and look at the broader picture, and to collect the scatted fragments of information pertaining to acoustic resonator performance factors; with the ultimate goal of providing increased insight and perspective, which supports improvements in their efficacy of application across a wide range of contexts.

The objective of this holistic approach is to identify and determine the influence of the most significant parameters; to provide a comprehensive assessment of the existing models and experimental investigations; to design and implement new experiments where gaps in the current state of the are identified; and consequently, to provide robust suggestions on performance improving factors.

The following section *(1.3 Thesis Outline)* prescribes how this work is structured to achieve these objectives, which can be summarised as follows:

- Conduct a comprehensive literature review to identify and determine the known influence and significance of performance factors.

- Design bespoke acoustic experiments to advance the empirical validation of identified relevant theories in isolation.

- Implement empirical investigations which support an improvement in the characterisation of performance defining interaction effects.

- Compare and critique findings against the current state of the art.

- Draw conclusions and make recommendations on multifactorial influences impacting the efficacy of acoustic resonators as noise attention devices.

The scope of the particular factors investigated is refined by the conclusions from the literature review *(CHAPTER 3 -),* and the experimental scope is defined accordingly at the beginning of the relevant

experimental chapters *(CHAPTER 4 - EXPERIMENTAL METHODOLOGY: DISCRETE RESONATORS,
CHAPTER 6 - CFD INVESTIGATION, & CHAPTER 7 - EXPERIMENTAL METHODOLOGY: DISTRIBUTED
RESONATORS).* Holistically all experimental investigations conducted within this study, are limited to
atmospheric and isothermal conditions, such that they can be practicably empirically evaluated using
the experimental resources available.

1.3 Thesis Outline

This section concludes Chapter 1, which is intended to serve as a preface for the subsequent Chapters;
it introduces the principle of noise, delineates it, and presents its noteworthy connotations. It also
presents the fundamental principles of resonance and the phenomena of natural frequency, including
the significance of its exploitation and consequences of its underappreciation. This leads into the
chronological development of acoustic resonators and an overview of their functional parameters;
followed by a discussion of pertinent industrial applications and justifications for further investigation
across a variety of industrial applications; which forms the motivation of this work. The penultimate
section focuses the opportunities into distinct objectives, and clarifies the intended scope of this thesis.

Chapter 2 serves to provide the prerequisite theory necessary to appreciate the content of the
subsequent chapters, and to permit the effective evaluation of acoustic resonator performance factors,
in the context of noise attenuation. This includes the underpinning principles of acoustic wave theory,
and pertinent conductivity and acoustic impedance models. Experimental measurement strategies,
data processing techniques, and commonly used metrics for investigating and evaluating attenuation
performance are also introduced, defined, and discussed in the context of acoustic resonators.

Chapter 3 provides an executive summary of relevant reviewed literature corresponding to analytical
modelling and empirical modification derivatives, which aims to put into perspective the current state
of the art in relation to the accurate prediction of acoustic resonator performance factors.

Chapter 4 outlines the experimental methodology used to investigate salient performance factors of
discrete acoustic resonators. It clarifies the sub-objectives and investigation strategy used to target the
attainment of novel insight into fundamental discrete resonator noise attenuation characteristics. This
includes the design ethos of the bespoke experimental resonator used in subsequent investigations,
the targeted parameters, and the configuration of associated experimental apparatus and
measurement equipment. The various test cases measured experimentally are clarified, and finally a
qualification procedure is presented, implemented and evaluated, to effectively validate the
experimental methodology. The outcomes from the measurement of the full test matrix of variables
is then presented, evaluated, and discussed in the subsequent results chapter, Chapter 5.

Chapter 6 describes a complementary investigation subsequent to the discrete resonator empirical investigations, which seeks to evaluate the acoustic attenuation characteristics beyond those experimentally practicable, through an implicit unsteady CFD modelling approach. The chapter opens with clarification of the CFD investigation methodology, defining the computational domain, the boundaries and boundary conditions, the meshing regime, physics models and acoustic excitation method. The computational methodology is validated against existing empirically collected test cases and then used to provide additional insight through time-averaged acoustic velocity magnitude contour plots of the resonator cross section, and extrapolation to high sounds pressure levels of excitation beyond those physically achievable with the available measurement apparatus.

Chapter 7 follows a similar structure to that of chapter 4, and outlines the experimental methodology used to investigate the salient performance factors of distributed resonators. Similarly, it clarifies the strategic sub-objectives and seeks to target the attainment of novel insight into fundamental distributed resonator noise attenuation characteristics. The design ethos of an additional bespoke experimental resonator, and associated substantial test matrix is rationalised and explicitly detailed. The commissioned methodology is then evaluated to ensure its inherent nuances are appreciated; and the methodology validated prior to its use in the collection of a large data set of attenuation performance variables. The subsequent impact of geometry variations, flow properties, and interaction effects are presented in Chapter 8, and supported by an interrogation of key findings and accompanying deductions.

The final chapter, Chapter 9, summarises the influence of each investigated parameter separately initially, making recommendations as to how they should be considered in isolation to ensure the maximum efficacy of noise attenuation using acoustic resonators, irrespective of the context of application. Which is then followed by a provision of perspective as to the significance of interaction effects, and concluding recommendations on how to utilise current knowledge to ensure effective and efficient noise attenuation using acoustic resonators, across a range of common and emerging industrial contexts. This chapter concludes with a forward outlook and perspectives section, and makes recommendations for future work which was beyond the scope of this thesis; highlighting the potential to further advance the current state of the art in relation the investigation and characterisation of noise attenuation using acoustic resonators.

CHAPTER 2 - BACKGROUND

The following chapter provides prerequisite background theory necessary to facilitate critique of the content within subsequent chapters. It opens in Section 2.1 with the fundamental principles of acoustic wave theory, which describes the propagation and manipulation of sound (and thus noise). The concept of acoustic conductivity as an analogy to Ohm's law in electricity, commonly referred to as Rayleigh conductivity, is introduced in Section 2.2, prior to detailing the pertinent Acoustic Impedance modelling techniques in Section 2.3. The penultimate Section 2.4, introduces, defines, and discusses relevant experimental methods for empirically examining and evaluating practical acoustic attenuation performance. Finally, Section 2.5 concludes the chapter with a brief executive summary.

2.1   Acoustic Wave Theory

The conservation laws for mass, momentum, and energy underpin the propagation and manipulation of sound within a fluid medium; and in the absence of any additional sources, mass conservation can be described through a partial differential equation (Euler, 1757):

$$\frac{\partial \rho}{\partial t} + \nabla \cdot (\rho \boldsymbol{v}) = 0 \qquad \qquad \textit{[1]}$$

The Gibbs notation is used both here (Gibbs & Wilson, 1913), and subsequently, which uses the Nabla operator ∇ as a convenient mathematical notation for either; the gradient $(grad\ f = \nabla f)$; the divergence $(div\ f = \nabla \cdot f)$; or the rotation/curl $(rot\ f = \nabla \times f)$ (Bronštejn, 2015). Generally known as the continuity equation, this equation relates the velocity of the fluid, to its density, and is valid for all conditions, with the only restriction that the fluid, and its properties must be continuous. This continuum hypothesis disregards the discrete molecular nature of a fluid, and assumes that its macroscopic behaviour is the same as if it were perfectly continuous in structure (Batchelor, 2000). By replacing the local time derivative $(\partial/\partial t)$, with the substantial derivative, this equation can be shown in the following alternative form (Stokes, G., 1849):

$$\frac{D}{Dt} = \frac{\partial \rho}{\partial t} + \boldsymbol{v}\,\nabla \qquad \qquad \textit{[2]}$$

Here the substantial time derivative follows the motion of the fluid, and hence the convective effect of the mean flow is captured. Similarly, it follows from [1] that (Batchelor, 2000):

$$\frac{D\rho}{Dt} + \rho(\nabla \cdot \boldsymbol{v}) = 0 \qquad [3]$$

The conservation of momentum for an ideal fluid was originally defined by Euler (1757) as:

$$\rho \frac{Dv}{Dt} = -\nabla p \qquad [4]$$

This special case for an ideal fluid neglects the effects of gravity, and it is commonly known as the Euler equation; after the defining Swiss mathematician and physicist, Leonhard Euler (1707-1783); it effectively describes the relationship between the pressure and the velocity of the fluid.

For an ideal gas, that is one in which the molecular interaction is neglected; such as air of normal atmospheric temperature and pressure; the conservation of energy is expressed by the equation of state (Clapeyron, 1834), which is also often referred to as the ideal gas law:

$$p = \rho R T \qquad [5]$$

Acoustic motion is considered to be isentropic and as described by Morfey (2000), in an isentropic change of thermodynamic state the entropy remains constant, and an adiabatic process is isentropic provided it is reversable. Therefore, the thermodynamic relationship between density and the pressure can be defined as (Pierce, 1989):

$$\left(\frac{\partial p}{\partial \rho}\right)_S = c^2 \quad \text{with} \quad \frac{Ds}{Dt} = 0 \qquad [6]$$

The system of Equations [3], [4], & [6] together are commonly referred to as the Euler equations, and describe the motion of a compressible, ideal fluid. The pressure, velocity and density field quantities referenced in this system of equations, can also be written as the sum of their mean and acoustic (fluctuating) values:

$$p = p_0 + p' \qquad [7]$$

$$v = v_0 + v' \qquad [8]$$

$$\rho = \rho_0 + \rho' \qquad [9]$$

In most practical applications, the acoustic quantities can be assumed to be much smaller than the mean quantities, which allows the linearisation of the Euler equations as follows:

$$\frac{p'}{p_0} \ll 1 \qquad \frac{v'}{v_0} \ll 1 \qquad \frac{\rho'}{\rho_0} \ll 1 \qquad\qquad [10]$$

The assumption also allows the higher order terms of the Euler equation to be disregarded, such that the approximate acoustic equations can be written as (Goldstein, 1976):

$$\frac{D\rho'}{Dt} + \rho_0(\nabla \cdot \boldsymbol{v}') = 0 , \qquad\qquad [11]$$

$$\rho_0 \frac{D\boldsymbol{v}'}{Dt} + \nabla p' = 0 , \text{ and} \qquad\qquad [12]$$

$$p' = c^2 \rho' \qquad\qquad [13]$$

The acoustic wave equation governs the propagation of acoustic waves through a material and can be obtained from Equations [11], [12] & [13], through initially substituting the fluctuating density ρ' in equation [11] with [13]; then taking the time derivative of Equation [11] and replacing its second term with Equation [12]:

$$\nabla^2 p' - \frac{1}{c^2}\frac{D^2 p'}{Dt^2} = 0 \qquad\qquad [14]$$

Here ∇^2 represents the Laplace operator, sometimes also denoted as Δ, it is named after the French Mathematician Pierre-Simon de Laplace (1749-1827); and it prescribes the summation of the second partial derivatives of a function f, with respect to a given coordinate system, where: $\nabla^2 f = \nabla \cdot (\nabla f) = div(grad\ f)$ (Bronshtein & Semendyayev, 2013).

The general notation described in Equation [14] includes the material derivative (Equation [2]), and hence can be applied to either a stationary or moving medium; under the following assumptions:

- The medium is homogeneous, i.e.: a medium whose properties are spatially uniform and independent of position (Morfey, 2000).

- The medium is an ideal fluid

- Linear Acoustics assumptions can be applied, i.e.: The acoustic signal amplitude is sufficiently small such that the relationship between any two oscillatory quantities is independent of amplitude, propagation is independent, and without interaction (Morfey, 2000).

- The relationship between pressure and density is isentropic.

- The medium is either stationary, on subject to a uniform flow; whereby the magnitude and direction of the velocity is spatially uniform.

By expanding the material derivative in Equation [14], the commonly used form of the convected wave equation can be arrived at as follows (Howe, Michael S., 1998; Howe, M. S., 1975; Morse & Ingard, 1968; Munjal, 1987):

$$\nabla^2 p' - \frac{1}{c^2}\left(\frac{\partial}{\partial t} + \boldsymbol{v}_0\nabla\right)^2 p' = 0 \qquad [15]$$

In a stationary medium $\boldsymbol{v}_0 = 0$, and hence the material derivative can be replaced by the local time derivative, and Equations [14] & [15] reduce to the well-known form of the classical acoustic wave equation (D'Alembert, 1747; Euler, 1766; Pierce, 1989):

$$\nabla^2 p' - \frac{1}{c^2}\frac{\partial^2 p'}{\partial t^2} = 0 \qquad [16]$$

2.1.1   Three-Dimensional Waves

In order to describe wave propagation in a cylindrical duct, the wave Equation [14], can be expressed in cylindrical coordinates; with the axial coordinate x, the radial coordinate r, and the circumferential coordinate θ. The Laplace operator in cylinder coordinates is given by (Bronshtein & Semendyayev, 2013):

$$\nabla^2 p' = \frac{\partial^2 p'}{\partial x^2} + \frac{1}{r}\frac{\partial}{\partial r}\left(r\frac{\partial p'}{\partial r}\right) + \frac{1}{r^2}\frac{\partial^2 p'}{\partial \theta^2} \qquad [17]$$

Therefore, the three-dimensional wave equation can be defined in cylindrical coordinates as:

$$\frac{\partial^2 p'}{\partial x^2} + \frac{1}{r}\frac{\partial}{\partial r}\left(r\frac{\partial p'}{\partial r}\right) + \frac{1}{r^2}\frac{\partial^2 p'}{\partial \theta^2} - \frac{1}{c^2}\frac{D^2 p'}{Dt^2} = 0 \qquad [18]$$

The result is a linear second-order partial differential equation which can be solved by the separation of variables, which introduces a substitution in the form of $p'(x,r,\theta,t) = f_x(x) \cdot f_r(r) \cdot f_\theta(\theta) \cdot f_t(t)$, and reduces the partial differential equation into a set of ordinary differential equations (Bernoulli, 1690). The original derivation of the modal character of a sound field goes back to Duhamel (1849) and Rayleigh (1876); with subsequent detailed discussions provided by Tyler & Sofrin (1962), Morfey (1964), Morse and Ingard (1968). A general solution for a circular duct can be written as:

$$\hat{p}_{mn}(x,r,\theta,t) = \hat{p}_{mn}^{+}e^{-ik_{x,mn}x} + \hat{p}_{mn}^{-}e^{ik_{x,mn}x} \times J_m\big(k_{r,mn}r\big)$$
$$+ Q_{mn}Y_m\big(k_{r,mn}r\big) \times e^{im\theta} \times e^{i\omega t} \qquad \text{[19]}$$

Where the axial and radial wave numbers are related by:

$$\left(\frac{\omega}{c}\right)^2 = k_{x,mn}^2 + k_{r,mn}^2 \qquad \text{[20]}$$

The four elements of the product of Equation [19] describe the spatial (axial, radial, and circumferential) and temporal shape of the mode respectively. The spatial patterns in the axial and circumferential directions are sinusoidal, as is the temporal development; whereas the radial pattern is defined by Bessel functions. J_m is the Bessel function of the first kind, and is commonly referred to as the Bessel function. The Bessel function of the second kind, denoted as Y_m, is interchangeably referred to as either the Weber function, after the German mathematician Heinrich Martin Weber (1842-1913); or the Neumann Function, after the German mathematician Carl Gottfried Neumann (1832-1925). The n-th Eigenvalue of Y_m is denoted by Q_{mn}.

The general solution presented in Equation [19] is a so-called modal solution, whereby a mode can be considered a spatial pattern of vibration, whose shape remains invariant as the vibration propagates spatially (Morfey, 2000). The tangible sound pressure of a time harmonic wave is given by the real part of the superposition of an infinite number of modes:

$$p'(x,r,\theta,t) = \sum_{m}\sum_{n} \hat{p}_{mn}(x,r,\theta,t) \qquad \text{[21]}$$

Where $m \in \{\dots,-2,-1,0,1,2,\dots\}$ and $n \in \{0,1,2,\dots\}$. Each mode is characterised by its circumferential mode order m, and its radial mode order n. The integers m and n describe the number of nodal lines in the circumferential and radial directions respectively. For $m = 0$ and $n = 0$ there are no nodal lines in the transverse direction, hence the sound field is one-dimensional in this mode, with variations in the x-direction only. This special case is referred to as the "fundamental mode", or a plane wave; of which the significance will be delineated further in Section 2.1.4; all additional modes are referred to as "higher order" modes.

In a cylindrical duct, the Q_{mn} value in Equation [19] becomes zero, such that the solution for a time harmonic wave propagating in a cylindrical duct, with hard walls, and uniform flow can be defined as:

$$\hat{p}_{mn} = \big(\hat{p}_{mn}^{+}e^{-ik_{x,mn}^{+}x} + \hat{p}_{mn}^{-}e^{-ik_{x,mn}^{-}x}\big)J_m\big(k_{r,mn}r\big)e^{im\theta}e^{i\omega t} \qquad \text{[22]}$$

In consideration of the mean flow Mach number M, the axial wave number is defined as:

$$k_{x,mn}^{\pm} = \frac{k}{1 - M^2}\left(-M \pm \sqrt{1 - (1 - M^2)\left(\frac{j_{mn}}{kR}\right)^2}\right)$$ [23]

The hard-wall boundary condition demands that the radial velocity vanishes at the wall; hence from Equation [12] it follows that the boundary condition for the acoustic pressure is: $\frac{\partial p'}{\partial r} = 0$ at $r = R$; and consequentially the derivative of J_m vanishes at the wall, therefore for $r = R$:

$$J_m'\left(k_{r,mn}R\right) = 0$$ [24]

Where the radial wave number is:

$$k_{r,mn} = \frac{j_{mn}}{R}$$ [25]

j_{mn} is the n-th root of J_m' or the n-th Eigenvalue of J_m for the hard-wall boundary condition. Some examples of j_{mn} values can be seen in Table 1 however; more extensive tables can be found in mathematical references such as Abramowitz & Stegun (1972).

$m{:}n$	0:0	1:0	2:0	0:1	3:0	4:0	1:1
j_{mn}	0	1.8412	3.0542	3.8317	4.2012	5.3176	5.3314

Table 1 - Eigenvalues of the hard-wall solution for a cylindrical duct, sorted in ascending order of j_{mn} (Abramowitz & Stegun, 1972).

The physical spatial distribution of acoustic pressure within a cylindrical duct for four examples modes can be seen represented schematically in Figure 24. Here the nodal lines of the circumferential and radial patterns are visible in the duct cross-section, and the resulting sound field $p' = p'_{0:0} + p'_{1:0} + p'_{0:1} + p'_{1:1}$. It can be seen that modes of higher circumferential orders (i.e. $m > 0$), result in a rotating transversal pattern which rotates around the x-axis, hence these are often referred to as "spinning modes" (Tyler & Sofrin, 1962). Figure 24 represents a snapshot of the instantaneous acoustic pressure and t=0, and the spinning modes produce the helical pattern of acoustic pressure at the duct surface.
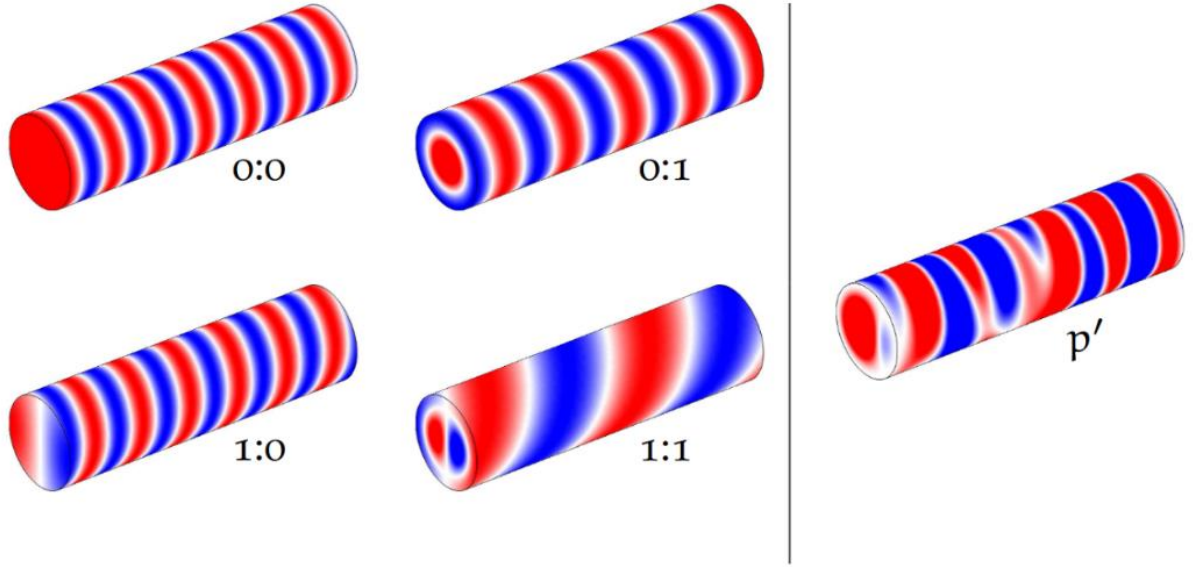
Figure 24 - Schematic representation of the acoustic pressure in a cylindrical duct for four modal components $(m:n)$ 0:0, 1:0, 0:1 and 1:1; and the corresponding sound field p' at a single frequency (Lahiri, 2014).

2.1.2 Cut-On Frequency

Equation *[23]* defines the propagation of a mode in the x-direction through the axial wave number $k_{x,mn}^{\pm}$,which permits two fundamentally different propagation characteristics depending on the evaluation of the square route of the equation, as follows:

$$1 - (1 - M^2)\left(\frac{j_{mn}}{kR}\right)^2 \geq 0 \quad \rightarrow \quad k_{x,mn}^{\pm} \in \mathbb{R} \qquad \qquad [26]$$

$$1 - (1 - M^2)\left(\frac{j_{mn}}{kR}\right)^2 < 0 \quad \rightarrow \quad k_{x,mn}^{\pm} \in \mathbb{C} \qquad \qquad [27]$$

For Equation *[26]* the axial wave number is a real quantity, and under the ideal fluid assumption, will propagate along the duct unattenuated. In Equation *[27]* however, the axial wave number is complex; whereby its imaginary part serves as an attenuation coefficient; and the amplitude of the mode decays exponentially with axial distance from the sources; therefore, the mode is not able to propagate. The point at which a mode starts propagating is a key characteristic frequency, and commonly referred to as the 'cut-on' frequency. At the cut-on frequency the term under the square root in Equation *[23]* vanishes, such that:

$$f_{c,mn} = \frac{j_{mn}}{2\pi R} c\sqrt{1 - M^2} \qquad \qquad [28]$$

The Eigenvalue j_{mn} of the fundamental mode 0:0 is zero and hence the cut-on frequency is also zero, i.e. the fundamental mode is able to propagate at all frequencies. For all other modes the cut-on

frequency is dependent on the duct radius, the mean flow Mach number, the speed of sound, and the Eigenvalue of the associated mode.

Understanding of the cut-on characteristics of any given acoustic transmission line can be advantageous, given that only a limited number of higher order modes are able to propagate at a given frequency, and hence they can be neglected in many cases. It is also important to note that the first higher order mode with the lowest cut-on frequency, also defines the transition between one-dimensional and three-dimensional sound propagation.

2.1.3   Evanescent Modes

Modes which are excited below the cut-on frequency are referred to as evanescent modes, or cut-off modes. The decay of evanescent modes is determined by the imaginary part of the axial wave number (See Equation *[23]*), and the attenuation coefficient has been described by Tyler and Sofrin (1962) as:

$$f_{c,mn} = \frac{j_{mn}}{2\pi R} c\sqrt{1 - M^2}$$

[29]

The unit of attenuation used by Tyler and Sofrin (1962) is the Neper *(Np/m),* which is a logarithmic scaled ratio of field or power quantities. The Neper uses the natural logarithm $\ln$, whereas the decibel used the decadic logarithm $\lg$. The attenuation coefficient can be converted to the attenuation rate a_{mn} in dB/m as follows:

$$a_{mn} = 20 \cdot lg(e^{\alpha_{mn}}) \approx 8.69 \propto_{mn}$$

[30]

When the frequency increases towards the cut-on frequency of a mode, this attenuation decreases accordingly, and given that at any given frequency only a limited number of modes are able to propagate, it is reasonable to neglect all evanescent modes in most practical applications. That being said, if a frequency of interest is close to the cut-on frequency, and the location of interest is in the vicinity of the source, then it may be necessary to consider the impact of evanescent modes; for example, if a measurement microphone is located near a sound emitting source.

2.1.4   Plane Waves

Following from the previous section, it holds that at low frequencies, i.e. below the cut-on frequency of the first higher order mode, that the sound field in a duct is one-dimensional. Under such circumstances the acoustic field quantities of a wave traveling in a x-direction vary with time and distance along the axis, but are constant in any plane normal to the direction of wave propagation;

and are consequently referred to as plane waves. For plane waves the acoustic wave equation ([14]) reduces to (Pierce, 1989):

$$\frac{\partial^2 p'}{\partial x^2} - \frac{1}{c^2}\frac{D^2 p'}{Dt^2} = 0$$

[31]

When the medium is stationary ($v_0 = 0$), a general solution to Equation *[31]* can be defined (D'Alembert, 1747; Euler, 1766; Munjal, 1987; Pierce, 1989):

$$p'(x,t) = f_1\left(t - \frac{x}{c}\right) + f_2\left(t + \frac{x}{c}\right)$$

[32]

Here f_1 and f_2 are arbitrary functions, which have continuous derivatives of the first and second order, and it describes the superposition of two plane waves traveling in opposite directions, with the propagation speed c. The acoustic fluctuations are assumed to be sinusoidal, such that f_1 and f_2 can be approximated by a Fourier series; named after the French mathematician and physicist, Jean Baptiste Joseph Fourier (1768 – 1830). The Fourier series is expressed in complex exponential notation by Fourier (1822) as:

$$f(t) = \sum_{\omega} \hat{p}\omega e^{i\omega t}$$

[33]

Where the coefficient $\hat{p} = Ae^{i\varphi}$ is a complex quantity; with amplitude $A = |\hat{p}|$ and phase, (also known as complex pressure amplitude) $\varphi = \arg\hat{p}$. Applying Equation *[33]* to Equation *[32]* yields the following:

$$p'(x,t) = \sum_{\omega} Re\left\{\hat{p}_{\omega}^+ e^{i\omega\left(t-\frac{x}{c}\right)} + \hat{p}_{\omega}^- e^{i\omega\left(t+\frac{x}{c}\right)}\right\}$$

[34]

Where $\hat{p}_{\omega}^+$ is the complex pressure amplitude of the wave traveling in the positive x-direction, and $\hat{p}_{\omega}^-$ for the wave in the opposite direction. Here the use of complex exponential notation is mathematically convenient however, by taking the real part $Re\{z\}$ of the expression, it can be appreciated that it is only the real part which is physically relevant. Hence it is common practice to omit this explicit notation, whilst still taking the real part.

The sum of all frequency components yields the acoustic pressure however, typically the solution is given for a single frequency wave, or one frequency component independently, or piecewise, and in such circumstances the summation can be dropped. Introducing the wave number as $k = \frac{\omega}{c}$ and

applying the aforementioned simplifications, results in the common notation (Kinsler & Frey, 1982; Munjal, 1987):

$$p'(x,t) = \left(\hat{p}^+ + e^{-ikx} + \hat{p}^- e^{ikx}\right)e^{i\omega t}$$

[35]

This equation describes both the spatial and temporal distribution of the acoustic pressure of a one-dimensional, single-frequency sound wave, in a stationary medium; and dependant on the values of $\hat{p}^\pm$, will result in either:

1. A traveling Wave: $\qquad |\hat{p}^-| = 0$

2. A Standing Wave: $\qquad |\hat{p}^+| = |\hat{p}^-|$

3. A Mixed Wave: $\qquad |\hat{p}^+| \neq |\hat{p}^-|$

The significance of these characteristic behaviours on the temporal development and spatial distribution of resultant acoustic pressure, can be seen graphically in Figure 25.
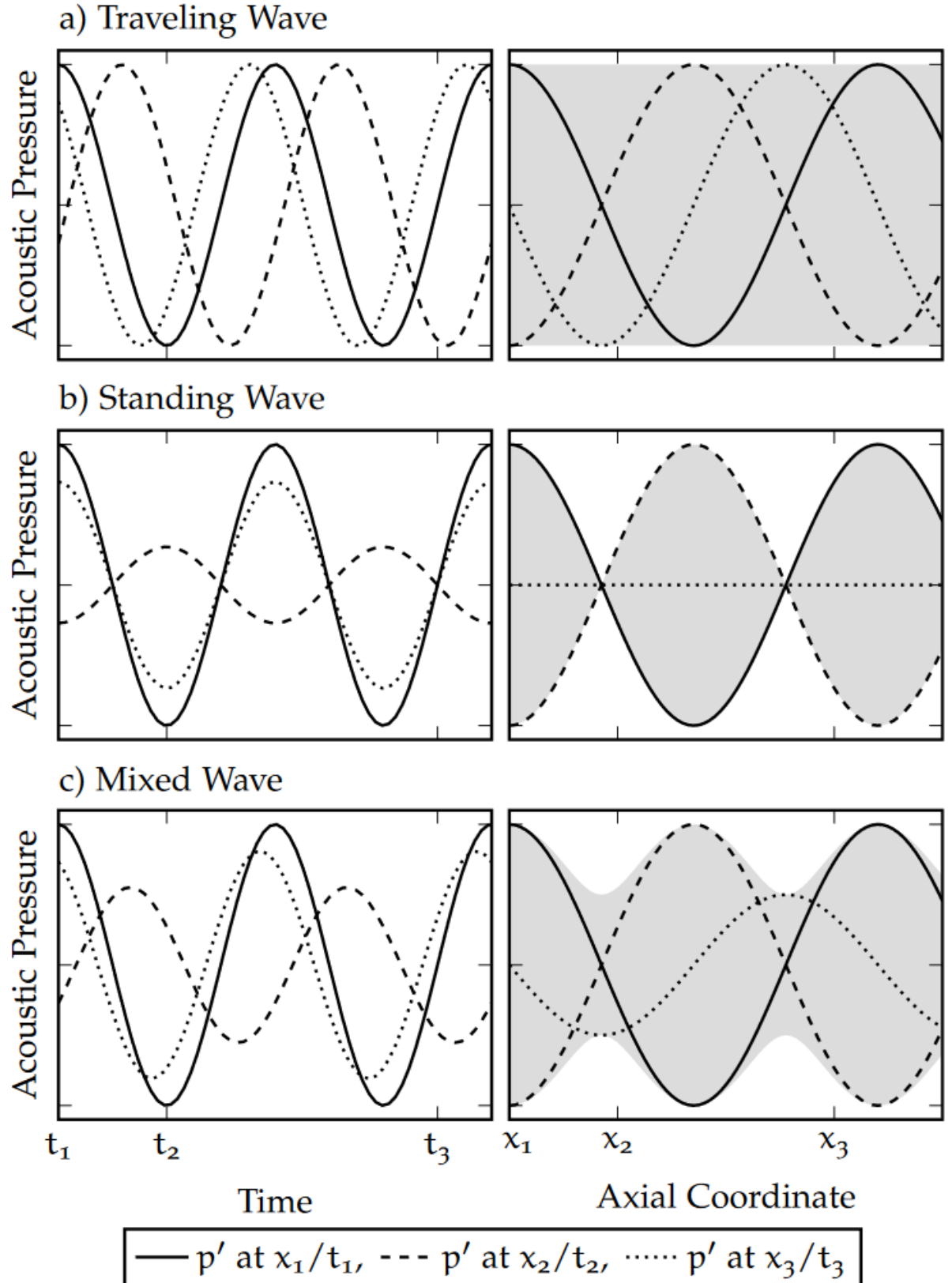
Figure 25 – Illustration of the temporal development (left) and spatial distribution (right) of the acoustic pressure for three characteristic plane wave sound fields: a) Traveling Wave, b) Standing Wave, c) Mixed Wave (Lahiri, 2014).

When a mean flow is introduced in the x-direction, this impacts the propagating speed of the wave, and must be accounted for accordingly within the wave number:

$$k^\pm = \frac{\omega/c}{1 \pm M}$$

[36]

Here the superscript $\pm$ denotes propagation with and against flow direction respectively, where in the flow direction the propagation speed c is increased by the mean flow velocity, whilst it is decreased against the flow direction, i.e. $c \pm v_0$ respectively. In the presence of mean flow, Equation [35] becomes (Kinsler & Frey, 1982; Munjal, 1987):

$$p'(x,t) = \left(\hat{p}^+ + e^{-ik^+x} + \hat{p}^- e^{ik^-x}\right)e^{i\omega t}$$

[37]

2.1.5   Dissipation of Sound

Thus far dissipative effects have been neglected, and in many practical applications their impact on the transmission and manipulation of sound is sufficiently small, that neglecting them reproduces the physical behaviour sufficiently. For certain conditions, and/or more accurate representation, it may be necessary to include such effects; as the absorption of sound results in an attenuation of the wave amplitude with propagation distance, and a change in propagation speed, i.e. phase velocity. Adjusting the wave number accordingly accounts for both, and the adjusted wave number can be used directly within Equation [35], which remains unchanged, where:

$$k = \frac{\omega}{c_{ph}} - i \propto$$

[38]

Where $\alpha = -Im\{k\}$ is the attenuation coefficient in Np/m and $c_{ph} = \omega/Re\{k\}$ is the phase velocity in m/s.

As the attenuation coefficient accounts for the amplitude attenuation, without any dissipation $\alpha = 0$, and the attenuation rate a, can be converted to units dB/m using Equation [30]. The phase velocity represents a possible change in propagation speed, and when c_{ph} is a function of frequency, the propagation is dispersive, i.e. wave of different frequencies propagate at different speeds; and disregarding any absorption leads to $c_{ph} = c$.

2.2 Rayleigh Conductivity

Whilst the electrical conductivity of any element of an electrical circuit is defined by the ratio of the current, to the potential difference; the acoustic conductivity equivalence of an orifice, can be defined by the volume flow through the orifice, against the driving pressure difference. It was Lord Rayleigh (1926) who first introduced the concept of acoustic conductivity as an analogy to Ohm's law in electricity, hence it is commonly referred to as Rayleigh conductivity.

In a practical acoustic context, the pressure on either side of the orifice will fluctuate, which can be represented as a harmonic function of time, whereby:

$$p' = Re\{\hat{p}e^{i\omega t}\}$$

[39]

The pressure difference across the orifice, is equivalent to the electrical potential difference *(i.e. Voltage),* and produces a consequential fluctuating volume velocity through the orifice:

$$q' = Re\{\hat{q}e^{i\omega t}\}$$

[40]

When the flow within the orifice is considered incompressible, and the geometry acoustically compact, i.e. $\lambda \gg r$, then Rayleigh (1926) defines the acoustic conductivity as:

$$K_R = i\omega\rho \frac{\hat{q}}{\hat{p}_1 - \hat{p}_2}$$

[41]

Where: $\rho = mean\ density$

   $\hat{q} = A\hat{v} = acoustic\ volume\ velocity$

   $A = \pi r^2 = orifice\ area$

   $\hat{v} = acoustic\ particle\ velocity$

In an ideal fluid the Rayleigh conductivity can be determined only the geometry of the orifice, and for a circular orifice in a wall of infinitesimal thickness, Rayleigh (1926) defines it as:

$$K_R = 2r$$

[42]

Where r is the orifice radius; for an orifice in a wall of finite thickness however; the Rayleigh conductivity can be expressed as the ratio of the orifice and its effective length:

$$K_{RO} = \frac{A}{l_{eff}}$$ [43]

Where the effective length is defined as the sum of the physical length of the orifice and an end correction for both apertures, $l_{eff} = l + 2l'$.

The additional length l' accounts for the additional mass of the fluid that contributes to the oscillatory motion outside of the orifice, hence it is commonly referred to as 'end correction'; which can be seen schematically, alongside the aforementioned Rayleigh conductivity determining parameters in Figure 26. Rayleigh (1926) also derives an upper and lower limit of the conductivity as:

$$\frac{\pi r^2}{l + \frac{16}{3\pi}r} < K_R < \frac{\pi r^2}{l + \frac{\pi}{2}r}$$ [44]

Hence when $l = 0$, the upper limit coincides with Equation [42], and the end correction can be determined from Equation [44] to be in the range of $0.785r < l' < 0.849r$.
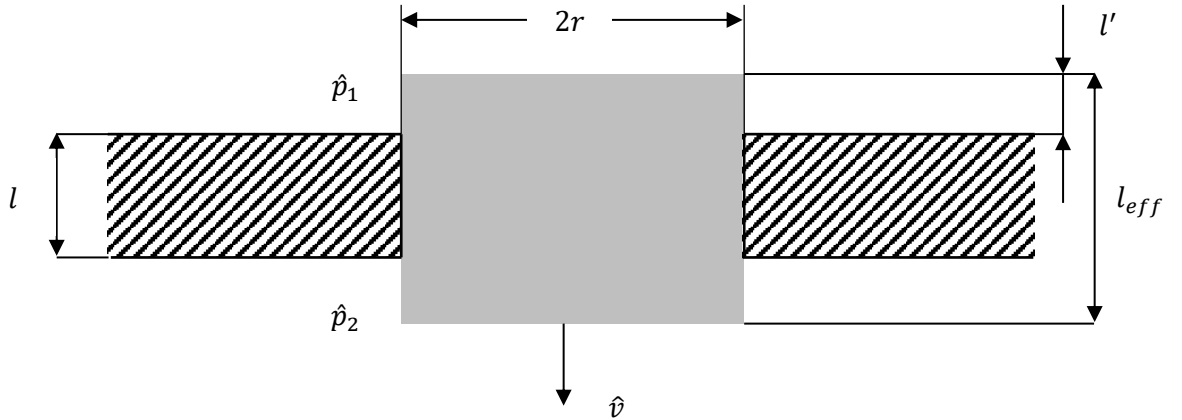
Figure 26 - Schematic representation of Rayleigh conductivity determining characteristics for a single orifice.

In his later work, Rayleigh (1926) suggests $l' \approx 0.82r$ as an appropriate value for an orifice in an infinite wall however, the exact value of the end correction continues to this day to be an ongoing topic of discussion. Given the breadth of academic interest in this particular parameter however, there has arisen some general acceptances: namely an appreciation that the end correction can generally be neglected for cases where $l \gg r$, but that it contributes substantially when $l \to 0$; and that for one end of an orifice in a wall, sometimes referred to as flanged pipe, the end correction length can generally be defined as (Bolt et al., 1949; Crandall, 1926; Ingard, U., 1953; Kinsler & Frey, 1982; Morse & Ingard, 1968):

$$l' = \frac{8}{3\pi}r \approx 0.85r \tag{45}$$

2.3 Acoustic Impedance

Following a similar electro-acoustic analogy to that of the aforementioned Rayleigh conductivity, acoustic impedance is equivalent to electrical impedance, and can be defined as the ratio of driving pressure difference over the consequential volume flow rate through the orifice (Pierce, 1989),

$$Z = \frac{\Delta \hat{p}}{\hat{q}} = \frac{\Delta \hat{p}}{\hat{v}A} \tag{46}$$

Where $z = \hat{p}/\hat{v}$ is known as the specific impedance, which describes the acoustic properties of a medium or material, and can be related to the acoustic impedance $Z = z/A$. It follows that $\hat{v}$ is the normal component of the acoustic particle velocity directed onto the surface A. The specific impedance of a fluid is a characteristic quantity of the medium only, and is therefore referred to as characteristic impedance z_0; and for plane waves $z_0 = \rho c$.

An opportune dimensionless quantity is obtained by the ratio of specific and characteristic impedance, commonly referred to as the normalised specific impedance:

$$\zeta = \frac{z}{z_0} = \frac{Z}{\rho c} = \frac{\Delta \hat{p}}{\hat{v}A\rho c} \tag{47}$$

The impedance is represented mathematically by a complex number, with an $e^{i\omega t}$ time dependency notation as:

$$Z = R \pm iX, \tag{48}$$

$$z = r \pm ix, \tag{49}$$

$$\zeta = \theta \pm i\chi \tag{50}$$

Where the real part is referred to as resistance, and the imaginary part as reactance. When the characteristic dimensions of an acoustic element, such as an orifice, Helmholtz Resonator, or cavity etc., are much smaller than the relevant acoustic wavelength, the characteristic behaviour of the relevant element can be described by three discrete parameters: the resistance R, the inertance M, and the compliance C. It follows that the acoustic impedance can be written as the sum of these three parameters (Kinsler & Frey, 1982):

$$Z = R + i[\omega M - 1/(\omega C)]$$

[51]

These three quantities R, M, and C are commonly referred to as lumped parameters; and when an element exhibits compliance with the acoustically compact assumption, it can be considered as a lumped element.

Upon revisiting mass-spring-damper model analogy discussed during the previous chapter, and depicted schematically in Figure 5, the following mechanical-acoustic comparisons can be made: the resistance represents a linear, massless, viscous damper; the inertance corresponds to a lumped mass; and the compliance describes the reciprocal of the stiffness of a lumped, linear, massless spring (Fahy, 2000). Generally speaking, the resistance describes the energy dissipation, whilst the reactive elements store energy, either in the form of potential energy in a spring-like element, or kinetic energy in a mass-like element (Morfey, 2000).

Upon these underpinning principles, an impedance model can be built to represent a bespoke acoustic system; such as a discrete or distributed Helmholtz Resonator, a perforated plate panel absorber, or even an array of acoustically relevant systems. The subsequent sub-sections will expand upon this theory to provide the prerequisite modelling tools and techniques for key acoustically relevant elements of a typical noise attenuation device.

2.3.1   Impedance of an Orifice

Irrespective of the application, the orifice of any resonant device is crucial to its function and arguably the most nuanced, as such we will start with the impedance of this key element. Neglecting any end effects initially, the normalised specific impedance for a unit length l of an infinite tube filled with a viscous fluid, is defined by Crandall (1926) as:

$$\zeta = \frac{1}{\sigma} \frac{ikl}{F(k_s' r)}$$

[52]

Where ikl is the inviscid impedance of an infinite tube, and represents the inertia of the fluid in the tube, and the function $F(k_s' r)$ introduces the viscous and thermal effects. The division by the porosity σ allows the conversion between the impedance of an array of orifices in a perforated region, to the impedance of a single orifice. It should be noted however, that some sources, such as (Kraft et al., 1999), also divide by the discharge coefficient. In reference to the theories of Stokes (1851), Helmholtz (1863), and Kirchhoff (1868), Crandall (1926) derives:

$$F(x) = 1 - \frac{2J_1(x)}{xJ_0(x)} \qquad\qquad [53]$$

Here J_0 and J_1 are Bessel functions of the first kind, and given that Bessel functions with a complex argument, produce a complex result, it follows that the impedance consists of both a reactive and a resistive part. The effective Stokes wave number k_s', named after the Irish mathematician and physicist Sir Gorge Gabriel Stokes (1819-1903), considers the viscosity and thermal conductivity losses near a highly conducting wall. In order to include both effects, an effective kinematic viscosity $v' = 2.179v$ is used, such that $k_s' = \sqrt{-i\omega/v'}$; and when the heat conduction is neglected entirely, v' can be replaced by v.

Equation [53] does not provide much tangible insight however, dependant on the shear number $Sh = r\sqrt{\omega/v}$, Crandall (1926) and Melling (1973) provide two analytical approximations, which are more physically revealing:

$$\zeta = \frac{8vl}{c\sigma r^2} + i\frac{k}{\sigma}\left(l + \frac{1}{3}l\right) \qquad\qquad for\ Sh < 2 \qquad [54]$$

$$\zeta = \frac{\sqrt{2\omega vl}}{c\sigma r} + i\left(\frac{kl}{\sigma} + \frac{\sqrt{2\omega vl}}{c\sigma r}\right) \qquad\qquad for\ Sh > 10 \qquad [55]$$

When the shear number is small i.e. $Sh < 2$, flow in the orifice is comparable to that of steady flow in a narrow tube, and the consequential resistance is referred to as Poiseuille-type losses; conversely when the shear number is high i.e. $Sh > 10$, flow impedance of the orifice becomes frequency dependant, and a Helmholtz-type resistance prevails. Aside from the obvious introduction of a resistance term, inclusion of the viscosity also affects the mass reactance, which increases from its inviscid value (Melling, 1973; Kinsler & Frey, 1982).

2.3.2   Mass End Correction (Radiation Reactance)

In Section 2.2 the requirement of an effective length representation within the inertance, which is longer than the actual length of an orifice, was introduced and discussed in detail. The additional length is defined by the reactive part of the radiation impedance of a circular piston of an infinite baffle, and as previously discussed, a commonly accepted value for this, considering both apertures of the orifice, is $2l' = 16r/3\pi$ (Kinsler & Frey, 1982).

2.3.3   Resistance End Correction

The idealisation of the effective length of the entrained oscillating mass of fluid within the orifice, leads to a virtual extension which keeps the same typically cylindrical shape; in reality however, fluid is

entrained from the radial direction also. Ingard (1953) considers this reality and subsequently introduces an additional resistive end correction to account for the friction losses on the wall surrounding the orifice. Sivian (1935) makes a similar deduction, however he accounts the additional resistance to friction losses in the shear layer of the emerging jet. Owing to the discussions of Melling (1973), we will take Sivian's expression for the initial purposes of modelling resistance end correction; where, similar to the mass end correction, the additional resistance is captured by extending the length of the orifice, but now in the resistance term of impedance. Sivian demonstrates good agreement with experimental results when using the same additional length as for the reactance, and applying both end corrections to Equation [52] yields (Melling, 1973; Kraft et al., 1999):

$$\zeta = \frac{ik}{\sigma}\left(\frac{l}{F(k_s'r)} + \frac{16r/(3\pi)}{F(k_sr)}\right) \qquad [56]$$

Note that the Stokes wave number corresponding to the fluid external to the orifice considers the viscosity only, i.e. $k_s = \sqrt{-i\,\omega/v}$.

2.3.4   Orifice Interaction

The interaction effect of two adjacent orifices has been studied extensively by Ingard (1953), and he correspondingly introduces a correction factor for the end correction as:

$$\psi(\sigma) = 1 - \sqrt{\frac{\sigma}{2}} \qquad [57]$$

Here the correction factor $\psi(\sigma)$ reduces the end correction with increasing porosity, i.e. with decreasing orifice separation distance. Equation [57] has been used by Guess (1975) and Bellucci et al. (2004); and Melling (1973) presents a comprehensive discussion on the topic, where he refers to a solution that would found by Fok (1941):

$$\psi(\sigma) = \sum_{n=0}^{8} a_n\left(\sqrt{\sigma}\right)^n \qquad [58]$$

Where:

$a_0 = 1$	$a_1 = -1.4092$	$a_2 = 0$
$a_3 = 0.33818$	$a_4 = 0$	$a_5 = 0.06793$
$a_6 = -0.02287$	$a_7 = 0.03015$	$a_8 = -0.01614$

In Figure 27 Equation [57] and Equation [58] can be seen plotted against the porosity; where it is evident that the Fok function predicts a stronger influence of the interaction effects than Ingard's approach. Melling (1973) adds that the interaction effects can be neglected for porosities < 4%, which can be appreciated also from this figure, where the impact is evident to diminish at low values of porosity.
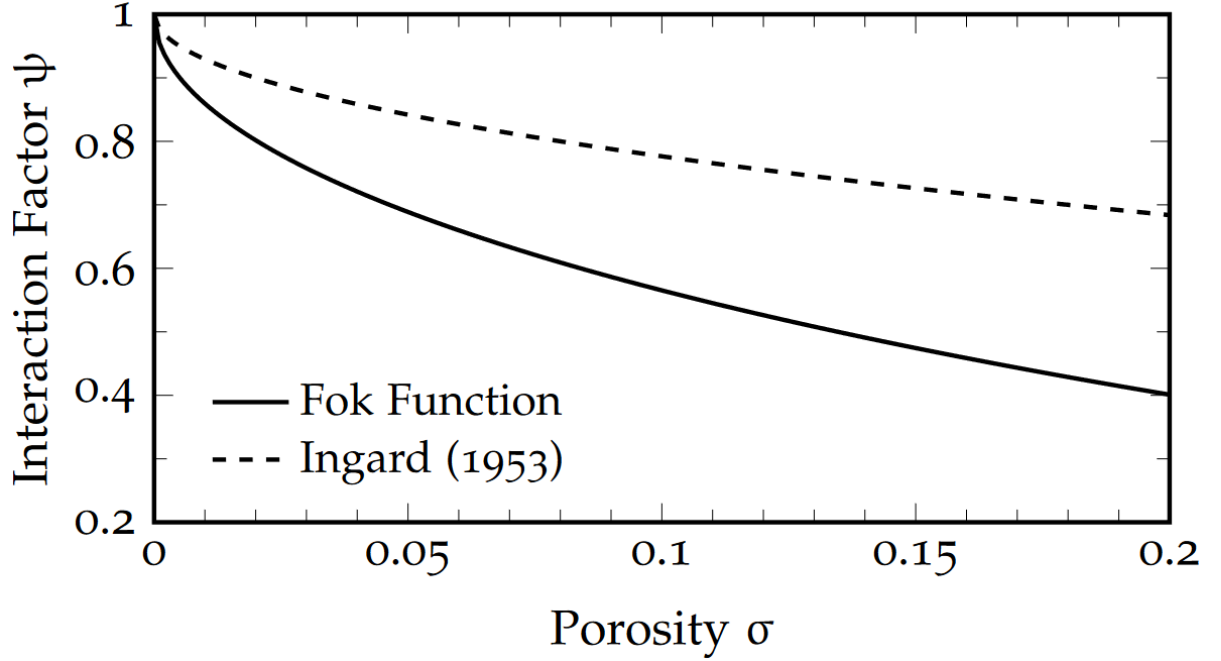
Figure 27 - Orifice interaction factor ψ plotted over the porosity according to Ingard (Equation [57]) and Fok (Equation [58]) (Lahiri, 2014)

Applying the orifice interaction factor ψ correction to Equation [56] yields what will be subsequently referred to as the Melling model (Melling, 1973):

$$\zeta_{Melling} = \frac{ik}{\sigma}\left(\frac{l}{F(k'_s r)} + \frac{16r/(3\pi)}{F(k_s r)}\psi\right) \qquad [59]$$

It should be noted that Lahiri adeptly clarifies that there is a mishandling of the Fok function in Melling's paper (Melling, 1973); whereby Melling defines the Fok function as in Equation [58], but he divides the end correction by ψ, as opposed to multiplying it as shown in Equation [59]. As shown in Figure 27, the Fok function is smaller than unity, and thus it needs to be multiplied in order to get the desired effect. It appears that Melling uses the Fok function as he defines it initially, where in Figure 6 of (Melling, 1973) for example, he plots $1/\psi$ but labels it as ψ. Unfortunately, Melling's erroneous formula has been reproduced by others, for example (Betts, Juan Fernando, 2000; Betts, Juan F. et al., 2000; Lee, Iljae, 2005; Tayong & Leclaire, 2010); however, Kraft et al. (1999) does seem to use it correctly. The correct notation was also used by Randeberg (2000), and the mismatch was also identified by Elnady (2004).

2.3.5   Nonlinear Resistance

For high amplitudes of acoustic signals, it is known that the acoustic behaviour of the orifice becomes nonlinear (Melling, 1973; Sivian, 1935); in other words, the impedance becomes dependant on the amplitude of the oscillation. Numerous works have attempted to address this characteristic within impedance formulation, namely (Bolt et al., 1949; Ingard, U., 1953; Ingard, Uno & Ising, 1967; Ingård & Labate, 1950; Melling, 1973; Sivian, 1935; Tonon & Sirignano, 1970; Zinn, 1970; Zorumski & Parrott, 1971). As an example, Melling (1973) defines a resistance term that depends on the velocity within the orifice to describe the nonlinear behaviour:

$$\theta_{nl} = \frac{1.2}{2c} \frac{1 - \sigma^2}{(\sigma C_d)^2} v'_{rms}$$

[60]

Where v'_{rms} is the root-mean-square value of the acoustic velocity within the orifice; the difficulty with this formulation however, is that the impedance now depends on the acoustic particle velocity, hence it is not possible to directly calculate the impedance when the acoustic pressure is known. The acoustic particle velocity can however be determined iteratively from $|v'| = |p'|/\left(\rho c \sqrt{\theta^2 + X^2}\right)$ (Elnady, 2004); and a first approximation of the acoustic particle velocity can be found from the applied sound pressure level SPL by (Betts, Juan F. et al., 2000):

$$v'_{rms} = \frac{1}{2c\sigma C_d} \frac{p_{ref} 10^{SPL/20}}{\rho c}$$

[61]

Including the nonlinear resistance term in Equation [59] yields the nonlinear Melling model:

$$\zeta_{Melling,nl} = \frac{ik}{\sigma}\left(\frac{l}{F(k'_s r)} + \frac{16r/(3\pi)}{F(k_s r)}\psi\right) + \frac{1.2}{2c}\frac{1 - \sigma^2}{(\sigma C_d)^2}v'_{rms}$$

[62]

Melling neglects the reactance in his model however, generally within a non-linearity regime, the resultant reactance will also be modified (Elnady, 2004; Guess, 1975).

2.3.6   Radiation Resistance

An additional contribution neglected by Melling is that of the resistive part of the radiation impedance; whereas the reactive part of the radiation impedance is already captured through the aforementioned mass end correction. The radiation resistance accounts for the acoustic losses by radiation into the surrounding medium; and the radiation resistance for an array of circular orifices have been defined by Morse and Ingard (1968) as:

$$\theta_{rad} = \frac{1}{\sigma}\left(1 - \frac{J_1(2kr)}{kr}\right)$$

[63]

And when the value of kr is small, Equation [63] can be approximated by (Kraft et al., 1999):

$$\theta_{rad} \approx \frac{(kr)^2}{2\sigma}$$

[64]

Similar to previously, either Equation [63] or Equation [64] cab be simply added to the impedance formulation in order to account for additional radiation resistance.

2.3.7   Grazing Flow Impedance

The common approach to modelling the effect of grazing flow on the impedance is typically a simple additional contribution to the resistance (Bauer, 1977; Guess, 1975; Heidelberg et al., 1980; Rice, 1971), where:

$$\theta_G \approx \frac{0.3M_G}{\sigma}$$

[65]

Whilst the included factor or 0.3 is the most common, some variations can be found, for example Rice (1971) suggests a value of 0.5. More sophisticated models have been investigated, such as (Cummings, 1986a; Grace et al., 1998; Howe, M. S., 1979a; Jing et al., 2001; Kooi & Sarin, 1981; Lee, Seong-Hyun & Ih, 2003) ; and some sources have chosen to focus on the importance of the friction velocity, as opposed to the mean flow velocity (Goldman, A. L. & Panton, 1976; Heidelberg et al., 1980). Peat et al. (2003) did however conclude that the influence of the friction velocity is of negligible significance when the boundary layer is turbulent and fully developed; which is the case for most practical acoustic resonator cases investigated here within; hence the use of mean velocity is deemed adequate for these purposes, and the simple model of Equation [65] should suffice for most cases considered. It should however be noted that Equation [65] does not account for any reduction of the attached mass resulting from the presence of a grazing flow, which will be discussed later.

2.3.8   Bias Flow Impedance

Evaluation of relevant literature leads to two common distinguished approaches to modelling the influence of a steady bias flow on the impedance of an acoustically relevant orifice:

The first approach replaces the acoustic particle velocity of a nonlinear model, with the bias flow velocity (Bauer, 1977; Dean & Tester, 1975; Garrison et al., 1969; Ingard, Uno & Ising, 1967; Mechel, F. et al., 1965; Sullivan, 1979; Zinn, 1970); this method is however, only applicable under the assumption

that the bias flow velocity is much greater than the acoustic particle velocity. In such circumstances, a simple linear relationship of resistance and bias flow Mach number is presented by Sivian (1935) as:

$$\theta_B = \frac{C \cdot M_B}{\sigma} \qquad [66]$$

Which is similar to the aforementioned grazing flow resistance introduced in Equation [65]. Here C is a constant that is empirically derived and is typically in the range of 1-1.5, with a value of 1.15 being recommended by Bauer (1977). It should be noted however, that whilst this value is commonly accredited to Bauer (1977), Bauer himself references Zinn (1970), and both use this term to describe high amplitude effects, as opposed to steady bias flow. This point will be discussed further in Section 3.2.4. Cummings and Eversman (1983) present a derived value for C, deduced from the linearised Bernoulli equation, as $C = (1 - \sigma^2 C_C^2)/C_C^2$, where C_C is the contraction coefficient of the jet.

The second approach combines the effects of the acoustic particle velocity, and the steady bias flow velocity, in one single resistance term; where Premo (1999) suggests a combined velocity term of $\sqrt{(1.15 v'_{RMS})^2 + (2U_B)^2}$; and Betts (2000; 2000) deduces a similar expression of $|1.2 v'_{RMS} + 2U_B|$. Addition to Equation [60] subsequently yields:

$$\theta_B = \frac{1}{2c} \frac{1 - \sigma^2}{(\sigma C_d)^2} |1.2 v'_{rms} + 2U_B| \qquad [67]$$

Both approaches introduced here are predominantly based on empirical deduction and neglect the influence of the bias flow on the reactance. More advanced approaches are presented by Jing and Sun (2000) and Lee et al. (2007); however, neither approach provides a simple parametric description of the impedance, as both require a numerical solution.

2.4 Experimental Methodologies & Performance Criteria

There exist many different methodologies to determining the sound attenuation performance of any given resonator configuration. In the previous section common analytical methods were presented, along with some empirically derived modifications; building upon these fundamental principles, the following section introduces, defines, and discusses experimental methods for investigating and evaluating acoustic attenuation performance. Each metric has its own merits and nuances in application, and as such, this section serves as a prerequisite for the design of experimental methodologies, the consideration of subsequent results, and the associated deductions.

2.4.1 Spectral Analysis

An underpinning commonality between all the following experimentally obtained attenuation performance characteristics, is that they describe the variation of performance in the frequency domain. For each relevant metric, time series data corresponding to acoustic pressure, is recorded by measurement microphones which are strategically positioned within the acoustically relevant spatial domain; with the optimal location dependant on the target performance metric, the geometric parameters of the acoustic domain, and the target frequency spectrum of interest. Conversion of the measured signal is of practical importance, as it permits an understanding of the acoustic response in relation to a discrete problematic tone, or target noise bandwidth; which cannot be intelligibly interpreted from the time domain signal alone, as real-world acoustic measurements are composed of a superposition of all frequencies occurring within the measurement window, as shown in Figure 28.
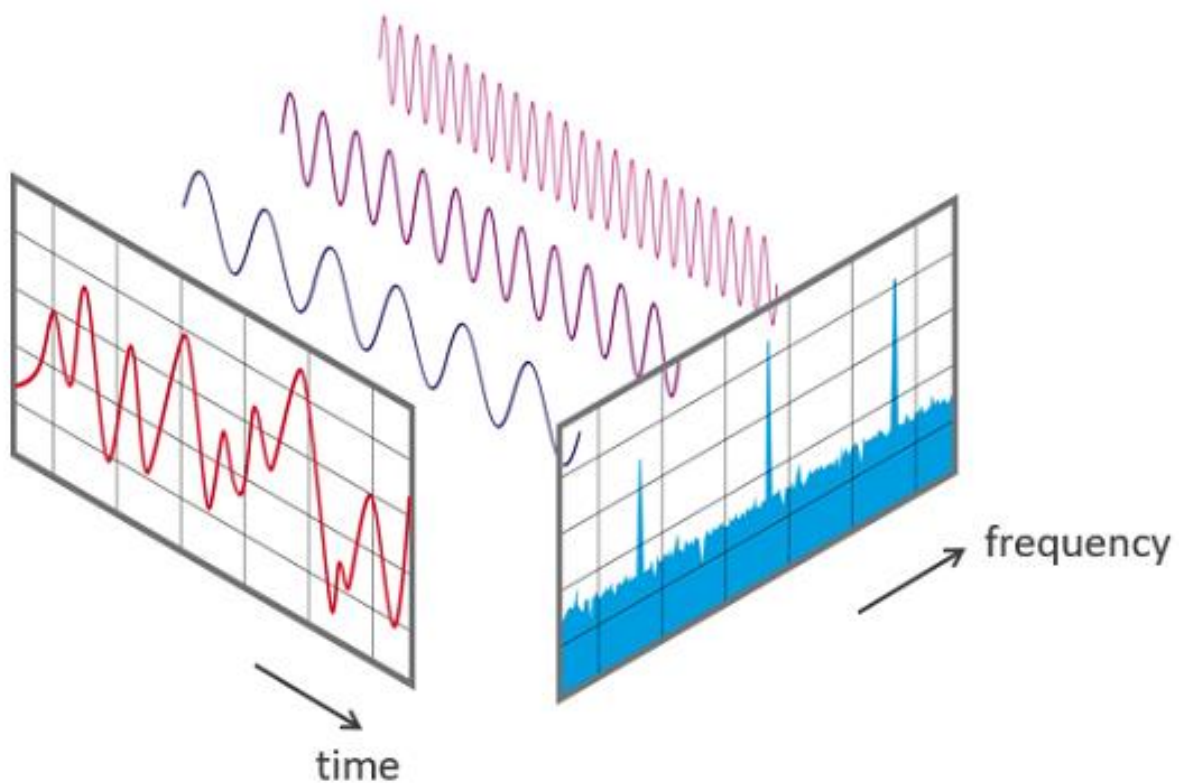
Figure 28 - A view of the acoustic signal in the time and frequency domain (NTi Audio, 2024)

2.4.1.1 Fast Fourier Transform (FFT)

In Section 2.1 the acoustic wave equation was introduced and subsequently that; when under the assumption that acoustic fluctuations are assumed to be sinusoidal; the arbitrary functions in Equation *[32]* can be approximated by the Fourier series; expressed in complex exponentiation form in Equation *[33]*. Sampling the physical acoustic signal occurs at discrete times, and as such results in discrete

numbers, as opposed to a continuous function. Conversion from the time domain through this sampling regime, can be carried out using a discrete Fourier transform (DFT) however; the DFT is very computationally intensive, requiring N^2 complex multiplications and additions; where N is the number of desired terms (Kinsler & Frey, 1982). The Fast Fourier Transform (FFT) is a uniquely efficient algorithm of discrete Fourier transformation, which decreases the processing steps from N^2, to $N \log_2 N$ (Cooley & Tukey, 1965); thus, offering a significant reduction in computation time and effort. Irrespectively, this method requires an assumption of periodicity to effectively capture any given analogue frequency through discretisation. The significance of this assumption can be seen in Figure 29, where the non-periodicity of a discrete harmonic sine signal occurs, when the sample length T_s is not a multiple of sinusoidal signal period; resulting in a discontinuity in the time domain of a combined measured signal. Therefore, for the FFT to work effectively on an acoustic signal, there is a need for the sampling frequency to be at least double that of the studied frequencies; a term known as the Nyquist frequency; beyond which frequencies will either be omitted, or show up as low frequency artefacts (Peters, T. M. & Bates, 1998).
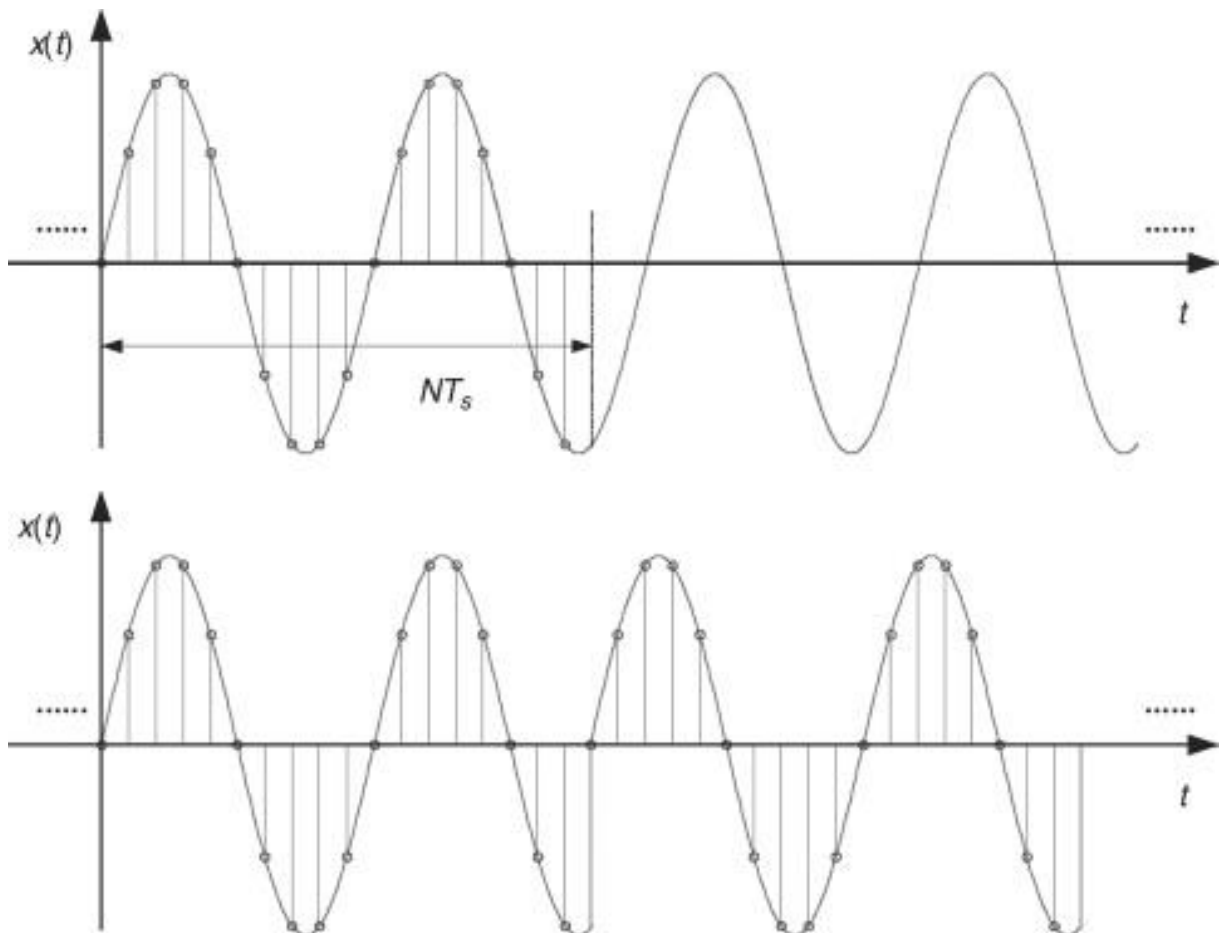
Figure 29 - Periodicity condition of sampling (Kehtarnavaz, 2005)

An appreciation of this inherent limitation is important in ensuring the integrity of subsequently evaluated results, as it can be seen from Figure 30; which shows the outcomes from two FFTs with

equivalent sampling frequencies, with two very different results, despite only 1Hz of signal difference. This provides an example of the consequences of improper sampling, where Figure 30 (a) shows an optimal FFT outcome, when the signal is periodic; and Figure 30 (b) showing the artefacts of numerical leakage, resulting in a smearing of the FFT amplitude across the calculated frequency spectrum.
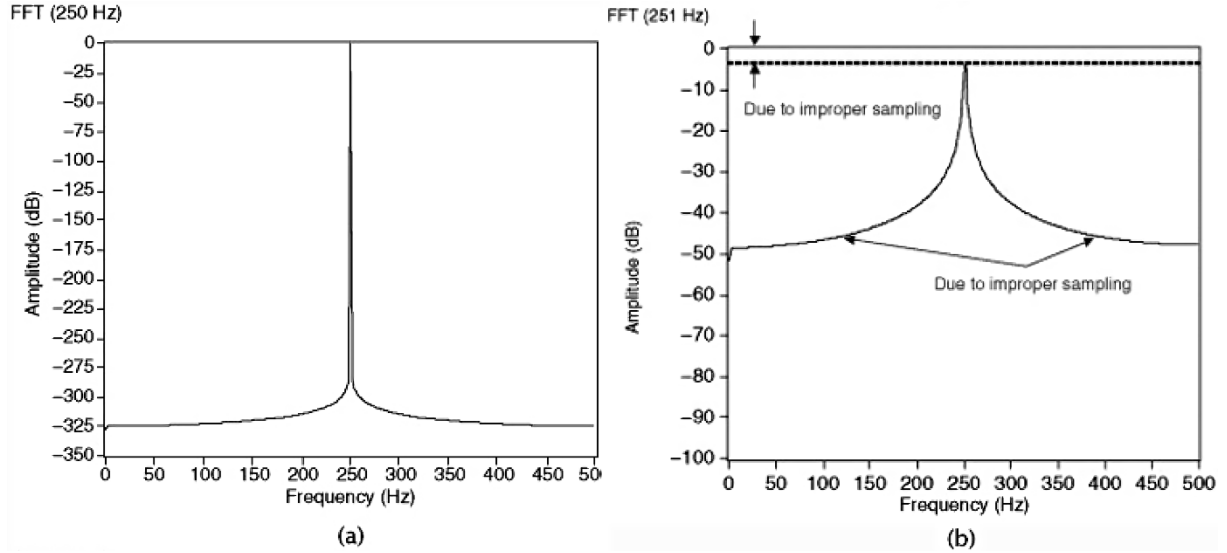
Figure 30 - FFTs of (a) a 250Hz and (b) a 251Hz sinusoid signal (Kehtarnavaz, 2008)

For practical acoustic measurements such as those conducted within this study however, the signal of interest is broadband in nature, and a discrete harmonic signal is often unknown a priori; therefore, the existence of non-periodicity is an inevitable eventuality, irrespective of sample length and period. To prevent smearing of the FFT outcome, a weighting function can be applied to the time signal. This ensures the discrete time samples begin and end with zero amplitude, and hence can be repeated periodically without a sharp transition, and the associated FFT artefacts, as shown in Figure 31.
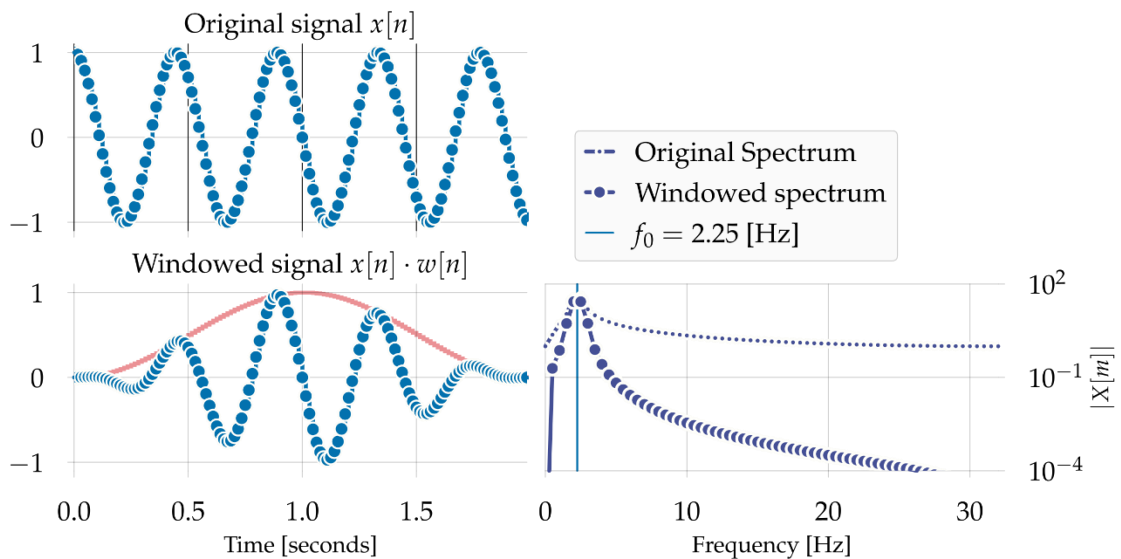
Figure 31 – (NTi Audio, 2024)Effects of windowing on resultant FFT spectrum (McFee, 2023)

2.4.1.2 Segment Averaging

When conducting real-world acoustic measurements, the existence of non-periodicity, and stochastic signals, will result in variance between respective samples, irrespective of sample length and period. When spectral density estimation is critical to effective analysis, an averaging over serval signal segments can be utilised to reduce the variance of the resulting spectrum, which is known as the Bartlett (1948) method. Welch (1967) provides an extension of the Bartlett method, in which he proposes to apply a window function to each segment prior to averaging, which addresses the leakage occurring from non-period signals. However, because applying a windowing function attenuates the signal at the beginning and end of each segment, more averages must be taken to ensure the same statistical accuracy of the estimated spectrum, compared to not using windowing functions; hence requiring longer measurement times. Welch (1967) addresses this by allowing the respective segments to overlap, thus reusing some of the data attenuated by the window function, and providing more segments for the averaging process, whilst keeping the overall length the same. This process can be seen schematically represented in Figure 32; which shows how a 2s acoustic signal can be split into three individual 1s segments, with a 50% overlap, prior to the application of a window function.
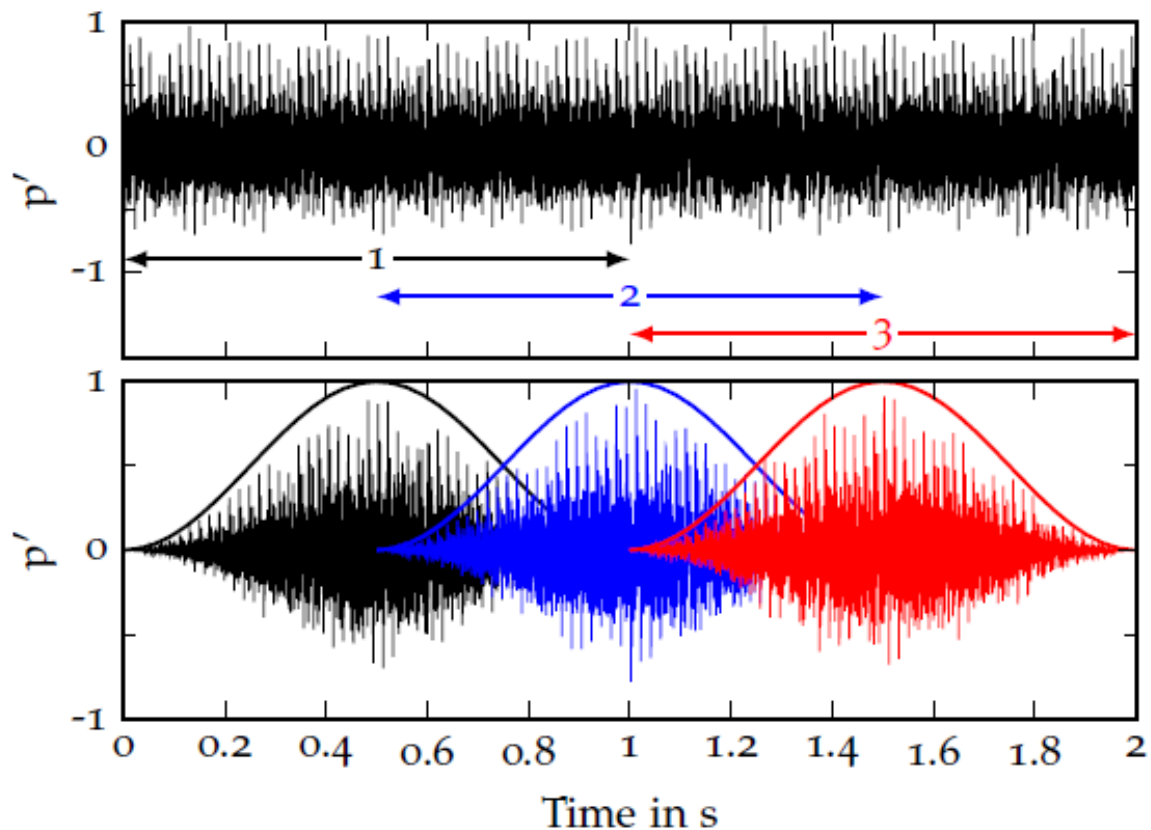
Figure 32 - Illustration of the Welch method. Top: A two second time series signal is split into 3 segments of one second length with 50% overlap. Bottom: Each segment is modified by applying the Hann window function. (Lahiri, 2014)

The window segment applied in Figure 32 is the common Hann window function, which is named after the Austrian meteorologist Julius Ferdinand von Hann (1839-1921), and is commonly referred to as the Hanning window (Blackman & Tukey, 1958). For a discrete time series of $x(n)$, with N samples, it is defined as: (Bendat & Piersol, 2011)

$$X(k) = \sum_{n=0}^{N-1} x(n) \cdot e^{-i2\pi kn/N}$$

[68]

Where $k = 0,1,2,\dots,N-1$

The losses introduced from windowing can be corrected by multiplication with $\sqrt{8/3}$, and the one-sided auto-spectral density, or auto spectrum for short, is then given by averaging over all segments s, and normalising with the number of samples: (Bendat & Piersol, 2011)

$$G_{xx} = \begin{cases} \dfrac{2}{SN} \sum_{s=1}^{S} |X_s(k)|^2 & for\ k = 1,2,\dots,(N/2)-1 \\ \dfrac{1}{SN} \sum_{s=1}^{S} |X_s(k)|^2 & for\ k = 0,(N/2) \end{cases}$$

[69]

Where S is the number of segments, and therefore the one-side cross-spectral density of the two signals $x(n)$ & $y(n)$, or cross spectrum for short, is given by: (Bendat & Piersol, 2011)

$$G_{xy} = \begin{cases} \dfrac{2}{SN} \sum_{s=1}^{S} [X_s^*(k) \cdot Y_s(k)] & for\ k = 1,2,\dots,(N/2)-1 \\ \dfrac{1}{SN} \sum_{s=1}^{S} [X_s^*(k) \cdot Y_s(k)] & for\ k = 0,(N/2) \end{cases}$$

[70]

Where X^* is the complex conjugate of X, and for an acoustic signal, the resultant spectrum is commonly scaled to the root-mean-square value by division with $\sqrt{2}$. (Lahiri, 2014)

2.4.1.3   Rejection of Flow Noise

Under a flowed regime, the measured pressure perturbations are a superposition of both acoustic sound pressure, and the flow induced turbulence noise. A method of rejecting the stochastic turbulent flow noise from the evaluated signal is presented by Chung (1977), whereby the basic premise is that the flow noise at three differing spatial measurement locations in an acoustic transmission duct are uncorrelated; whilst the sound pressure is entirely coherent. The coherence between any two signals

x and y is calculated from the aforementioned auto-spectral and cross-spectral densities, as follows: (Bendat & Piersol, 2011)

$$\gamma_{xy}^2 = |G_{xy}|^2 / (G_{xx} \cdot G_{yy})$$

[71]

Which leads to the definition of a "noise-free" auto-spectral density G'_{xx} of: (Chung, 1977)

$$G'_{11} = G_{11} (\gamma_{12} \cdot \gamma_{31}) / \gamma_{23}$$

[72]

Where the indexes 1,2 and 3 refer to the three spatially different signals; where index 1 refers to the target microphone, index 2 is an arbitrary reference microphone, and index 3 relates to the incoming acoustic signal.

Equation [72] results in a real valued auto spectrum, with units of Pa^2 however, plane wave decomposition (Section 2.4.2.3) requires phase information also. To address this, the phase information is added by using the incoming signal as an arbitrary, but fixed for all microphones, phase reference. Therefore, inserting Equation [71] into Equation [72], and adding the phase of the cross correlation between the target signal and the incoming signal yields:

$$G'_{11} = \frac{|G_{12}| \cdot |G_{13}|}{|G_{23}|} e^{i arg(G_{13})}$$

[73]

The complex pressure amplitude at the position of the target microphone x_1 is then given by $\hat{p}(x_1, f) = \sqrt{G'_{11}(f)}$. (Lahiri, 2014)

2.4.1.4   Linear Regression Smoothing

Additional smoothing can be subsequently applied to the resultant acoustic spectrum in order to remove any remaining unwanted measurement noise; which can be particularly useful when attempting to statistically evaluating peak attenuation frequency and magnitude experimentally. Within this study the final step in data processing is to apply a locally weighted, linear least-squares regression data smoothing strategy; which ensures that any remaining outliner points do not skew any trend deductions, based upon peak absorption frequency and magnitude which is taken across a wide-ranging set of experimental data. This method is considered local because each smoothed value is determined by the neighbouring data points within a defined span; and within the defined span a regression weight is computed for each data point using the following tricube function: (The MathWorks, 2023)

$$W_i = \left(1 - \left|\frac{x - x_i}{d(x)}\right|^3\right)^3 \qquad\qquad [74]$$

Where: x is the predictor value associated with the response value to be smoothed; x_i are the nearest neighbours of x as defined by the span; and $d(x)$ is the distance along the abscissa from x to the most distant predictor within the span.

Employing this method means that the data point to be smoothed will have the largest weight, and hence the most influence on the fit, and all data points outside of the determined span will have a weight of zero, and therefore no influence on the fit. Following the computation of the regression weights, a weighted linear least-squares regression can then be performed on the data using a first-degree polynomial. This method is very effective at removing unwanted measurement noise, whilst still maintaining the integrity of the underlying trend in the data. It is noteworthy however, that the value of the span must be carefully selected, in order to ensure that unwanted noise is sufficiently removed, whilst still maintaining the sought-after peak attenuation magnitude; and the specific values deployed within this study, along with their respective significance, will be discussed in greater detail within subsequent experimental methodology chapters.

2.4.2 Acoustic Attenuation Performance Criteria

Within the following sub-section, an overview of the most pertinent acoustic attenuation performance criteria will be introduced, their obtainment perquisites defined, and the corresponding nuances of their use in the evaluation of experimentally obtained acoustic attenuation performance delineated.

2.4.2.1 Frequency Response Function

The Frequency Response Function (FRF) is a complex value, containing both magnitude and phase information; it describes the relationship between the complex amplitudes of the acoustic pressure in the duct and the resonator cavity. The maximum amplitude of the FRF indicates the resonant frequency of the resonator, as a result of the perturbations in the duct; and the magnitude indicates the amount of attenuation of these perturbations. The frequency response function can also be described by the impedance of the resonator necks and volume as follows:

$$FRF = \frac{p'_{res}}{p'_{duct}} = \frac{Z_2}{Z_1 + Z_2} \qquad\qquad [75]$$

Where: Z_1 is the impedance of the inner apertures, and Z_2 is the impedance of the cavity volume (and outer apertures if present). In addition to identifying the resonator's natural modes, or resonant frequencies; the shape of the FRF curve around the resonance peak, also indicates the corresponding

quality factor, or selectivity of the resonant response. The FRF is a fundamental concept in understanding the acoustic response of any given resonator configuration, to a specific excitation sound field; and the interaction insight is critical in the design and optimisation of acoustic resonator properties to target unwanted dynamics.

2.4.2.2   Insertion Loss

Insertion Loss (IL) is defined as the difference between the measured acoustic pressure response with, and without, the influence of the sound attenuating device, an acoustic resonator in this case. In the context of this investigation, the acoustic resonator must be removed from the test rig in to collect the reference response, i.e. the duct response. This baseline response is subsequently computed along with the resonator case response, as shown in Equation [76].

$$IL = 20 \cdot \log_{10}\left(\frac{p'_{without}}{p_{ref}}\right) - 20 \cdot \log_{10}\left(\frac{p'_{with}}{p_{ref}}\right) \qquad [76]$$

Where $p'_{without}$ corresponds to the acoustic pressure measurement in the absence of any resonant device; p'_{with} is the equivalent acoustic pressure measurement with the acoustic resonator in situ; and p_{ref} is the reference acoustic pressure of $20 \times 10^{-6}Pa$. Because the same measurement location and microphone is used in the derivation of this metric, it is not as susceptible to phase mismatching or calibration error as alternative multi-microphone, multi-location metrics. As a direct consequence of this benefit, however, is the detriment that the insertion loss technique cannot effectively give an appreciation of the incident and reflected components, which contribute to the overall value of insertion loss.

2.4.2.3   Decomposition Method

The spectral analysis of the duct acoustics at any given measurement microphone location, yields the complex pressure amplitude for each frequency within the measurement range; and below the plane wave cut-off frequency; the corresponding measured sound pressure is a superposition of two waves travelling in opposite directions. The decomposition of this superposition is a powerful tool in providing a deeper understanding of duct acoustics, as it permits evaluation of the incident and reflected components respectively. Mathematically the acoustic pressure measured by a microphone at a distance x along a duct, under the plane wave assumption, can be described by Equation [77]:

$$p(x,t) = p(x) \cdot e^{j \cdot \omega \cdot t} = \left[A \cdot e^{-j \cdot k \cdot x} + B \cdot e^{j \cdot k \cdot x}\right] \cdot e^{j \cdot \omega \cdot t} \qquad [77]$$

Where:

        P *is pressure [Pa]*

        x *is the position within the duct [m]*

        t *is time [s]*

        A *is the complex amplitude of the incident wave [Pa]*

        B *is the complex amplitude of the reflected wave [Pa]*

        j *is the imaginary unit, $\sqrt{-1}$*

        k *is wave number, $k = \omega/c$ [m⁻¹]*

        ω *is angular frequency [s⁻¹]*

        c *is the velocity of sound in the duct [m/s]*

        e *is the base of natural logarithm*

Transforming the measured pressure data from the time domain, into the frequency domain, yields the finite Fourier transform of Equation [77], as shown in Equation [78].

$$F_p(\omega) = F_A(\omega) \cdot e^{-j \cdot k \cdot x} + F_B(\omega) \cdot e^{j \cdot k \cdot x} \qquad [78]$$

Where:

        F_p *is the finite Fourier transform of pressure $p(x, t)$*

        F_A *is the finite Fourier transform of the amplitude of incident wave*

        F_B *is the finite Fourier transform of the amplitude of reflected wave*

An archetypical experimental acoustic attenuation investigation methodology can be generically considered to consist of three main sections: an upstream section, from which an acoustic excitation signal, and/or mean flow, is delivered; an absorption section within which the attenuating device or medium is present; and downstream section which typically transitions to an anechoic (non-reflecting) termination. The impedance change at the interface between these sections will result in a partial reflection of the propagating acoustic excitation signal; furthermore, most real anechoic terminations are non-perfect, and consequentially downstream reflections have the potential to also propagate upstream, and impact the acoustics within the absorption section under investigation. It is therefore beneficial to investigate the respective incident and reflected components of the corresponding acoustic pressure, both upstream and downstream of the absorption section; which for a generic experimental methodology consisting of two upstream, and two downstream measurement microphones, is schematically represented by Figure 33;
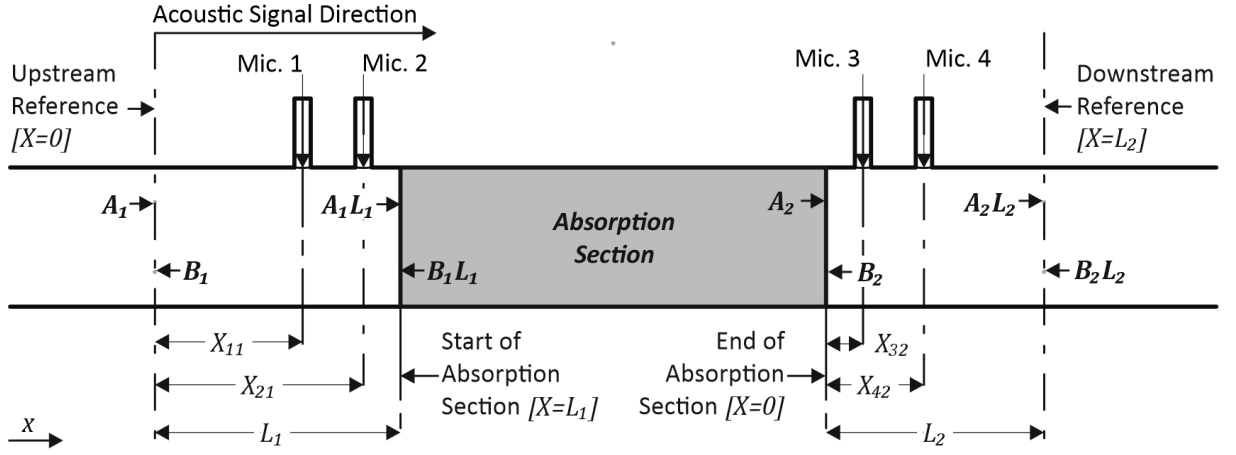
Figure 33 – Schematic representation of an acoustic absorption section of interest, with upstream and downstream measurement microphones, and key dimensions required for plane wave decomposition

In Figure 33 the subscripts of 1 & 2 denote the upstream and downstream parameters respectively, and any preceding subscripts identify the specific microphone with which the parameter is associated. Using this notation, and dropping the ω from Equation [78], the finite Fourier transforms of acoustic pressure for each of the four microphone locations becomes:

$$F_{P11} = F_{A_1} \cdot e^{-j \cdot k \cdot x_{11}} + F_{B_1} \cdot e^{j \cdot k \cdot x_{11}} \qquad \qquad \text{Mic. 1} \qquad [79]$$

$$F_{P21} = F_{A_1} \cdot e^{-j \cdot k \cdot x_{21}} + F_{B_1} \cdot e^{j \cdot k \cdot x_{21}} \qquad \qquad \text{Mic. 2} \qquad [80]$$

$$F_{P32} = F_{A_2} \cdot e^{-j \cdot k \cdot x_{32}} + F_{B_2} \cdot e^{j \cdot k \cdot x_{32}} \qquad \qquad \text{Mic. 3} \qquad [81]$$

$$F_{P42} = F_{A_2} \cdot e^{-j \cdot k \cdot x_{42}} + F_{B_2} \cdot e^{j \cdot k \cdot x_{42}} \qquad \qquad \text{Mic. 4} \qquad [82]$$

Where the finite Fourier transform of the complex amplitudes corresponding to the incident and reflected upstream and downstream components are:

F_{A_1} *incident upstream wave system*

F_{B_1} *reflected upstream wave system*

F_{A_2} *incident downstream wave system*

F_{B_2} *reflected downstream wave system*

For both the upstream and downstream wave systems the reference distance $X = 0$, is taken to be the upstream side of the respective section, with the total length of the section being defined as L. If Equations [79]-[82] are solved for the unknown finite Fourier transforms of the amplitudes of incident and reflected waves, both entering the absorption section upstream $X = L_1$, and exiting the absorption section downstream $X = 0$, then the upstream and downstream incident and reflected amplitudes can be defined as:

$$F_{A_1 L_1} = \frac{F_{P11} \cdot e^{-j \cdot k \cdot x_{21}} - F_{p21} \cdot e^{-j \cdot k \cdot x_{11}}}{e^{j \cdot k \cdot d_1} - e^{-j \cdot k \cdot d_1}}$$ *Upstream incident* [83]

$$F_{B_1 L_1} = \frac{F_{P21} \cdot e^{j \cdot k \cdot x_{11}} - F_{p11} \cdot e^{j \cdot k \cdot x_{21}}}{e^{j \cdot k \cdot d_1} - e^{-j \cdot k \cdot d_1}}$$ *Upstream reflected* [84]

$$F_{A_2} = \frac{F_{P32} \cdot e^{-j \cdot k \cdot x_{42}} - F_{p42} \cdot e^{-j \cdot k \cdot x_{32}}}{e^{j \cdot k \cdot d_2} - e^{-j \cdot k \cdot d_2}}$$ *Downstream incident* [85]

$$F_{B_2} = \frac{F_{P42} \cdot e^{j \cdot k \cdot x_{32}} - F_{p32} \cdot e^{j \cdot k \cdot x_{42}}}{e^{j \cdot k \cdot d_2} - e^{-j \cdot k \cdot d_2}}$$ *Downstream reflected* [86]

Where:

$d_1 = x_{21} - x_{11}$, *the distance between upstream microphones*

$d_2 = x_{42} - x_{32}$, *the distance between downstream microphones*

One noteworthy restriction for this two-microphone method, is the fact that the solution becomes singular when $ks = n\pi$, where s is the spacing between microphones and $n = \{0, 1, 2, …\}$; and for $n = 1$ this corresponds to a spacing of one-half wavelength. If this corresponding frequency is ensured to be beyond both beyond the planar wave cut off frequency of the experimental rig, and beyond the measurement range of interest, any inherent effects can be effectively mitigated, but should remain duly noted regardless.

It is also important to consider the impact of introducing a mean flow in the duct when decomposing the signal, as the presence of a mean flow will alter the propagation speed of the acoustic wave. The presence of grazing flow in the duct will increase the propagation speed by the mean flow velocity, in the direction of the mean flow, and consequently decrease it against the flow direction. As such the convective effect of the mean flow can be factored into the wave number, and represented effectively through a mean flow adjusted wave number, as shown in Equation [87]:

$$k^{\pm} = \frac{\omega / c}{1 \pm M}$$ [87]

Where $\pm$ denotes the direction in, and against, the flow direction respectively. When processing the experimental data, if the magnitude of grazing flow condition is $\neq 0$, then the formulations for the finite Fourier spectra *(Equations* [83]-[86]*)*, should be modified in accordance with the corresponding value of wave number, as specified in Equation [87].

2.4.2.4   Transmission Loss

The rudimental form of the Transmission Loss (TL) can be considered as the difference between the upstream and downstream acoustic pressure however, this approach neglects to evaluate the

significance of the reflected components of the signal. As a result, the decomposed signal derived incident transmission loss is the preferred metric, as shown in Equation [88]:

$$TL = 20 \log_{10} \left| \frac{F_{A_1}}{F_{A_2}} \right|$$

[88]

Where the finite Fourier transform of the complex amplitudes corresponding to the incident upstream and downstream components are:

F_{A_1} = upstream incident signal

F_{A_2} = downstream incident signal

When using decomposed signal derived metrics care must be taken to avoid phase mismatching and calibration error caused by the use of multiple microphones simultaneously; in addition to a careful consideration of the separation distance, and the potential for the aforementioned singularity artefacts. Such factors can however be alleviated through careful consideration of microphone separation distance, and the use of additional upstream and downstream microphones if available, can permit improved spatial averaging. In this work only two upstream and two downstream microphones were available; their separation distance was however chosen specifically to minimize the impact of spatial factors within the target measurement range for the corresponding experimental methodologies.

2.4.2.5   Reflection Coefficient

Reflection Coefficient is defined as the ratio of the reflected pressure wave, to that of the incident pressure wave, as shown in Equation [89]:

$$R = |R| \cdot e^{j \cdot \theta} = \frac{F_{B_1}}{F_{A_1}}$$

[89]

Where: R = Reflection Coefficient

θ = Phase angle in radians

F_{A_1} = Finite Fourier transform complex amplitude of upstream incident signal

F_{B_1} = Finite Fourier transform complex amplitude of upstream reflected signal

2.4.2.6   Absorption Coefficient

The Absorption Coefficient can also be determined from the Reflection Coefficient, as shown in Equation [90]:

$$\alpha \,=\, 1 - |R|^2 \hspace{4cm} [90]$$

2.4.2.7   Transmission Coefficient

Transmission Coefficient is defined as the ratio of the downstream incident pressure wave and the upstream incident pressure wave, as shown in Equation [91]:

$$T \,=\, \frac{F_{A_2}}{F_{A_1}} \hspace{4cm} [91]$$

Where F_{A_1} = *Finite Fourier transform complex amplitude of upstream incident signal*

F_{A_2} = *Finite Fourier transform complex amplitude of downstream incident signal*

2.4.2.8   Dissipation Coefficient

Conventionally transmission loss and reflection/absorption coefficients are considered independent of each other, however in a practical situation both metrics should be considered of equal importance; and the rigorous evaluation of a resonator's attenuation performance should ideally consider both metrics simultaneously.   In an experimental situation it is traditionally the magnitude of the attenuation of downstream perturbations which is chosen as the key performance defining characteristic however, in many practical contexts, for example where the target dynamics initiate from an upstream combustion instability; the reflection of unwanted dynamics back upstream can be just as significantly detrimental on the source flame dynamics, as the downstream transmitted perturbations are on physical components.   As such it is often desirable to consider a performance metric which can simultaneously appraise the magnitude of both transmission and reflection, in the ultimate evaluation of the total performance of a resonator design, which can be achieved through the calculation of dissipation coefficient, as described in the following sections.

2.4.2.8.1   Basic Definition Dissipation Coefficient

By considering the both the transmission and reflection coefficients simultaneously, the performance of the resonator can be evaluated by appreciating the fact that that in energy terms, the sum of reflection, transmission, and dissipation is unity, as shown in Equation [92]:

$$R^2 + T^2 + D = 1 \qquad\qquad [92]$$

Where:

R = *Pressure reflection coefficient, as defined in Section 2.4.2.5*

T = *Pressure transmission coefficient, as defined in Section 2.4.2.7*

D = *Acoustic energy dissipation coefficient.*

In the presence of a mean flow, it is important to consider the fact that the corresponding propagation direction of transmission and reflection are opposing, and as such the effect of cross-flow will act differently on each metric. Therefore, in the presence of a mean flow, the dissipation can be evaluated as shown in Equation [93]:

$$D = 1 - \left(\frac{(1-M)^2}{(1+M)^2} \cdot |R|^2 + |T|^2 \right) \qquad\qquad [93]$$

Where:

M = *Mach number of mean grazing/cross-flow*

2.4.2.8.2 Dissipation in applied experiments

The definition of dissipation coefficient as described in Equation [92] and Equation [93] applies the assumption that all the acoustic energy entering the measurement section equals the acoustic energy going out. However, in a practical application this assumption does not always hold true; for example, the existence of mean flow and/or bias flow, along with the associated interaction effects, may add additional flow generated noise, which is not accounted for in the basic definition of dissipation coefficient. Furthermore, the assumption of a perfectly non-reflecting downstream outlet is rarely achievable in practice, especially under high grazing flow conditions, where the effectiveness of the anechoic termination is often reduced. The significance of these assumptions can be demonstrated in the schematic shown in Figure 34; where the non-perfect anechoic termination is represented by downstream reflection P_{DR}. This outlet reflection inevitably results in an incident wave traveling back up the duct in the opposite direction to the source signal, and accordingly it too will be partially reflected and dissipated by the absorption section, resulting in an additional upstream reflection component P_{TDR}, and downstream transmission component P_{RDR}.
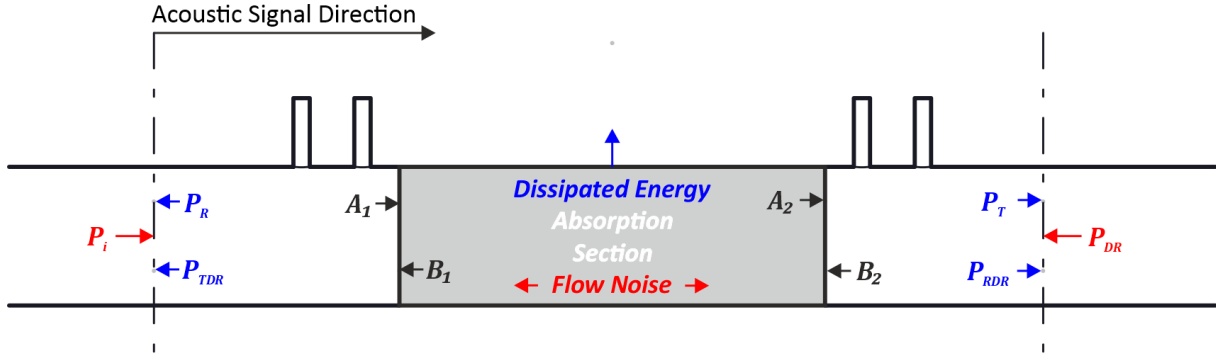
Figure 34 – Schematic representation of an applied dissipation investigation with a reflecting outlet and additional flow induced noise

The significance of the additional flow generated noise, is that as the noise propagates from the resonator both upstream and downstream, and thus will contribute to an amplification of the measured reflected and transmitted signals. This apparent increase in reflected and transmitted signal amplitude will consequentially result in higher transmission and reflections coefficients, which will in turn result in a decrease of the calculated dissipation coefficient, when calculated using Equation [93]. When the magnitude of the additional flow generated noise is small relative to the acoustic excitation signal, the effect of this error may be trivial. If the magnitude of the flow generated noise is however not insignificant, and/or the magnitude of dissipation is small, this over-prediction of the transmission and reflection coefficients will result in an under prediction of the dissipation coefficient. Furthermore, at frequencies far from the peak absorption frequency, where the dissipation coefficient should be expected to be zero, an apparent negative dissipation coefficient may also be witnessed due to this error.

The contribution to practical dissipation error attributed to reflections emanating from downstream of the absorption section can in part be accounted for, if the assumption is made that both components of the upstream and downstream traveling waves are in phase. Under this assumption Equation [93] can still be applied, as the respective upstream and downstream, incident and reflected waves, can be considered as superposition of their corresponding components. For the representative system shown in Figure 34, the calculation of Dissipation coefficient according to Equation [93], becomes equivalent to Equation [94]:

$$D = 1 - |R|^2 - |T|^2 = 1 - \left(\frac{\sqrt{P_R^2 + P_{TDR}^2}}{P_i}\right)^2 - \left(\frac{\sqrt{P_T^2 + P_{RDR}^2}}{P_i}\right)^2 \qquad [94]$$

As with the flow noise however, calculation of the dissipation coefficient through this method, in the presence of any downstream reflections, will result in an underprediction of the true dissipation, with an error proportional to the magnitude of downstream reflections. This is due to the underpinning

assumption that the only acoustic energy entering the absorption section, is that of the applied upstream incident acoustic signal, thereby neglecting the contribution from any downstream reflections to the total acoustical energy within the absorption section. Therefore, to reduce this error it is necessary to include the reflected signal from downstream within the derivation of the dissipation coefficient, a significance which becomes clear when considering the derivation of the dissipation coefficient under the assumption of conservation of acoustic energy; thereby the dissipation coefficient can be defined holistically as Equation [95], and for the representative experimental methodology according to Equation [96]:

$$D = \frac{Acoustic\ Energy\ Dissipated}{Acoustic\ Energy\ entering\ test\ section}$$

$$= \frac{Acoustic\ Energy\ entering\ test\ section - Acoustic\ Energy\ exiting\ test\ section}{Acoustic\ Energy\ entering\ test\ section}$$

$$= 1 - \frac{Acoustic\ energy\ exiting\ test\ section}{Acoustic\ energy\ entering\ test\ section}$$

[95]

$$D = 1 - |R|^2 - |T|^2 = 1 - \frac{P_T^2 + P_R^2 + P_{RDR}^2 + P_{TDR}^2}{P_i^2 + P_{DR}^2}$$

[96]

It should be noted however, that it is not practicable to differentiate between the respective components of a decomposed wave magnitude resulting from differing sources. For example, consider the representative measurement methodology depicted schematically in Figure 33 & Figure 34; if using the decomposition method described in Section 2.4.2.3, the measured acoustic field can only be decomposed into the constituent components of the wave traveling downstream F_A, and the wave traveling upstream F_B. As such, the theoretical components of P_R & P_{TDR}, which are both traveling upstream from the absorption section, would be measured simultaneously as F_{B_1} in the applied measurements. Similarly, the practicable Finite Fourier transforms of complex amplitude, can be considered equivalent to the idealistic components in the presence of a non-reflecting boundary, according to Equations [97] - [100]:

$$F_{A_1} = P_i \qquad [97]$$

$$F_{A_2} = P_T + P_{RDR} \qquad [98]$$

$$F_{B_1} = P_R + P_{TDR} \qquad [99]$$

$$F_{B_2} = P_{DR} \qquad [100]$$

Consequently, by applying the assumption that all signals are in phase, the dissipation coefficient can be defined for use in a practical experiment with two upstream, and two downstream microphones, and a non-perfect downstream termination, as defined by Equation [101]:

$$D = 1 - \frac{\left|F_{A_2}\right|^2 + \left|F_{B_1}\right|^2}{\left|F_{A_1}\right|^2 + \left|F_{B_2}\right|^2} \qquad [101]$$

Irrespective of the reduction in dissipation error through the consideration of the reflected downstream contributions, there still exists practical errors which cannot be effectively captured by the dissipation coefficient metric. This is due to the inherent assumption that all secondary waves traveling either upstream or downstream, are in phase with their primary counterparts, which cannot be wholly applied practically. In reality however, secondary waves and even higher orders of waves, have the potential to couple with the incident sound field in different phases; a nuance which cannot be sufficiently represented using the aforementioned decomposition methods, which are only currently capable of decomposing a sound field into one superimposed signal in each propagation direction.

2.5 Background Summary

Within the previous chapter the foundations of acoustic wave theory have been introduced in order to convey the fundamental mechanisms of noise propagation, manipulation, and ultimately attenuation. Upon these underpinning principles is built an introduction to the concept of acoustic conductivity as an analogy to Ohm's law in electricity, which facilitates the subsequent introduction to Acoustic Impedance modelling techniques. Acoustic Impedance modelling techniques and their nuances are discussed in relation to typical acoustic resonator performance defining characteristics, including factors pertaining to a broad range of application contexts.

This theoretical background content within this chapter serves to support; an appreciation of, and ability to rigorously critique, current state of the art in the subsequent literature review chapter; and to underpin the definition of the experimental methodologies and performance criteria definitions delineated in the preceding subsection.

The empirical insight provided within this section is also intended to serve as a refence point for development of the following experimental methodologies, and to support an informed deliberation of the subsequent results, interpretations, and conclusions.

72

CHAPTER 3 - LITERATURE REVIEW

In the previous chapters relevant literature has extensively been reviewed and referenced in order to underpin the fundamental prerequisites needed to appreciate, evaluate, and predict acoustic resonator performance factors, covering a wide variety of operational circumstances and application contexts. The following sections will explore and discuss how this prior literature has been interpreted, applied, and advanced, summarising the current state of the art in effective acoustic resonator performance prediction approaches.

3.1 Rayleigh Conductivity Models

3.1.1 Howe's Model

Howe investigated the Rayleigh conductivity of a circular orifice in an infinitely thin wall, in the presence of bias flow, and he analytically derives a formulation of the Rayleigh conductivity which includes the absorption caused by vorticity shedding (Howe, M. S., 1979b; Howe, Michael S., 1998). He assumes the bias flow velocity is not sufficiently high that the fluid can no longer be treated as incompressible, but not sufficiently low that the viscous effects can be neglected in their entirety. His hypothesis is that a vortex sheet forms in the orifice due to the bias flow injection, and it prevails downstream of the orifice, at the same speed as that of the bias flow; where the inlet side of the flow field resembles that of a potential sink at the centre of the orifice, and on the outlet side; that of an axisymmetric jet flow, with a potential core and a shear layer. Viscosity is neglected except for at the rims of the orifice, where the acoustic perturbations trigger periodical shedding of vortex rings, which are determined to be a contributing factor for the attenuation of acoustic energy. The radius of the vortex rings coincides with the orifice radius and remains constant when traveling downstream, thus forming a cylindrical vortex sheet, his assumptions can be summarised as follows:

- The frequency of the sound is low, so that the wavelength is much larger than the orifice radius, i.e. the orifice is acoustically compact: $\lambda \gg r$
- The Mach number of the bias flow is low, such that the fluid can be considered incompressible: $M_B \ll 1$
- The Reynolds number of the bias flow is high, such that viscosity is only considered at the rims of the orifice: $U_B\, r/v \gg 1$
- The wall is infinitely thin: $t = 0$

Based on these assumptions, Howe defines the Rayleigh conductivity as (Howe, M. S., 1979b; Howe, Michael S., 1998):

$$K_R = 2r(\gamma + i\delta)$$

Where:

$$\gamma + i\delta = 1 + \frac{\frac{\pi}{2}J_1(St)e^{-St} + iK_1(St)\sinh(St)}{St\left[\frac{\pi}{2}J_1(St)e^{-St} - iK_1(St)\cosh(St)\right]}$$

St is the Strouhal number, J_1 and K_1 are the modified Bessel functions of the first and second kind respectively, γ is the inertia of the medium in the orifice, and δ represents the flow resistance which contributes to acoustic absorption. Both terms are based on the Strouhal numbers, under the assumption that the vorticity convection velocity is equal to that of the mean flow velocity within the orifice $U_{\bar{B}}$, and the orifice radius r_0: $St = \omega r_0/U_{\bar{B}}$. Figure 35 shows the real and imaginary parts of Equation *[103]*, where it can be seen that, at high Strouhal numbers $\delta \to 0$, i.e. the vorticity shedding has a negligible influence, and δ reverts to its value in the absence of the flow; and the maximum of the imaginary part, is found at a Strouhal number just beyond unity.
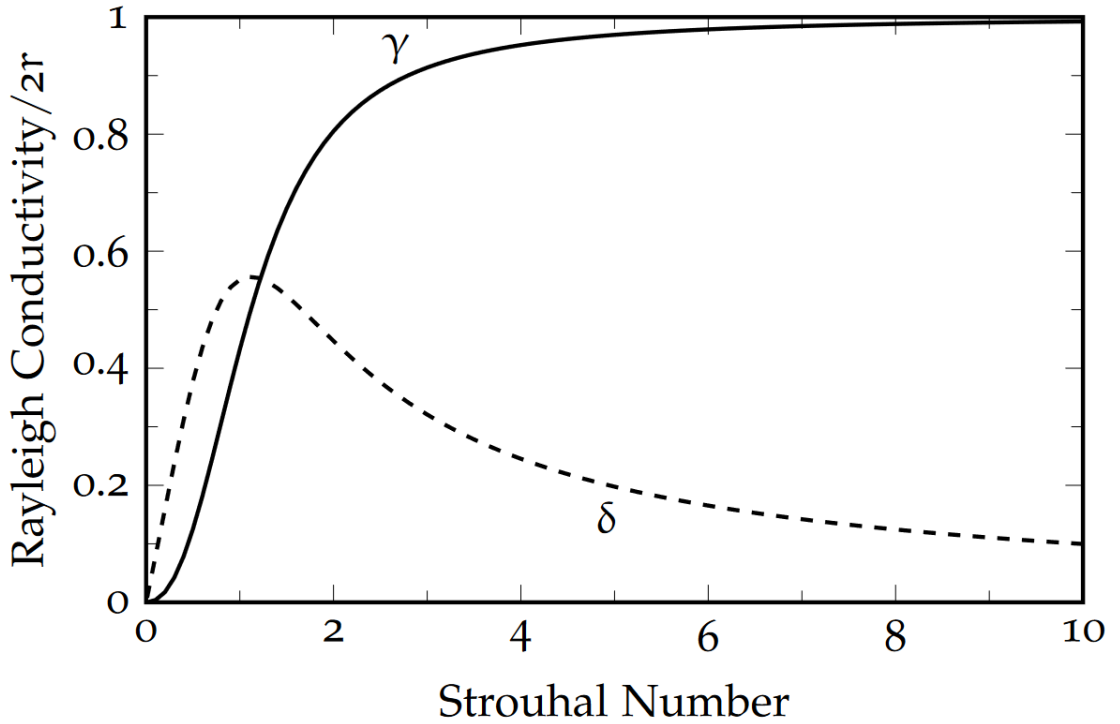
Figure 35 - Real part γ and imaginary part δ of the normalised Rayleigh conductivity plotted over the Strouhal number (Lahiri, 2014).

Howe's assumption of an infinitely thin wall does not hold for any practical application however, subsequent modified versions have shown good agreement with experimental results (Hughes & Dowling, 1990; Eldredge & Dowling, 2003; Mendez & Eldredge, 2009), making it a foundation for current work where bias flow through the orifice has acoustic relevance.

3.1.2   Jing and Sun's Model

Jing and Sun (1999) proposed a method to include the wall thickness in Howe's model and expressed their argumentation in terms of impedance. The relation between the normalised specific impedance ζ and the Rayleigh conductivity is given by:

$$\zeta = \frac{ikA}{K_R}$$

<div align="right">[104]</div>

Where for a circular orifice $A = \pi r^2$ with bias flow $K_R = 2r(\gamma + i\delta)$ and, after splitting the real and imaginary parts by multiplication with $(\gamma - i\delta)/(\gamma - i\delta)$ yields:

$$\zeta = \frac{k\pi r\delta}{2(\gamma^2 + \delta^2)} + i\frac{k\pi r\gamma}{2(\gamma^2 + \delta^2)}$$

<div align="right">[105]</div>

The additional thickness adds a mass inertance to the system such that the impedance for a circular orifice with bias flow, with viscosity neglected, and of finite thickness, can be defined as (Jing & Sun, 1999):

$$\zeta_{Jing} = \frac{k\pi r\delta}{2(\gamma^2 + \delta^2)} + i\left(\frac{k\pi r\gamma}{2(\gamma^2 + \delta^2)} + kt\right)$$

<div align="right">[106]</div>

Here the δ term represents the acoustic resistance due to the bias flow, the γ term represents the end correction when a bias flow is present, and the t term adds the mass inertance of the fluid within the orifice. Hence the effective length of the orifice is represented by the sum of the end correction length of the orifice, and the thickness $l_{eff} = l' + t$; and adding the conductivities reciprocally $1/K_R = 1/K_1 + 1/K_2$, yields the Rayleigh conductivity for a circular orifice of finite thickness, with bias flow, as:

$$K_{R_{Jing}} = 2r\left(\frac{1}{\gamma + i\delta} + \frac{2t}{\pi r}\right)^{-1}$$

<div align="right">[107]</div>

As this model considers the tangible thickness of real-world applications, it is an improvement over the basic Howe model, and has generally shown good agreement with experimental results as a result (Jing & Sun, 1999; Eldredge & Dowling, 2003; Andreini et al., 2012; Scarpato et al., 2012; Scarpato et al., 2013).

3.1.3   Luong and Cummings

The foundation of the Luong et al. (2005) model is the Rayleigh conductivity modelling efforts of Howe (1979b; 1998) and Equation *[102]*; which is subsequently modified with a Bernoulli-type equation from the work of Cummings (1984; 1986b), the assumption is made that the steady pressure drop across the orifice is much larger than the acoustic pressure, and it excludes any reversal of the flow within the orifice against the flow direction:

$$l_{eff}\frac{dv'}{dt} + \frac{1}{2C_c^2}(U_b + v')|U_b + v'| = \frac{\Delta p_0 + pcos(\omega t)}{\rho}$$

[108]

Where l_{eff} represents the effective thickness of the orifice, $pcos(\omega t)$ represents the acoustic pressure difference across the orifice, v' and U_b are the acoustic particle velocity and mean bias flow velocity in the orifice respectively; and the term $1/(2C_c^2)(U_b + v')|U_b + v'|$ is the pressure drop across the orifice. A simplified expression of Rayleigh conductivity is presented as:

$$K_{R_{Luong}} = \frac{A}{l_{eff}}\left(\frac{\omega l_{eff}/U_{\bar{B}}}{\omega l_{eff}/U_{\bar{B}} + i/C_c^2}\right)$$

[109]

Where A/l_{eff} is the Rayleigh conductivity without flow (Equation [43]), and $U_{\bar{B}}$ is the mean velocity in the plane of the orifice. From comparison with experiments, Cummings (1986b) recommends a contraction coefficient of $C_c \approx 0.75$; and Luong et al. (2005) confirm agreement between Howe's (1979b) linear theory, and their approach is best for this particular choice of C_c. This model, and Equation *[109]* presents a good approximation for both the linear, and non-linear regime; whereby the principal effect of nonlinearity is expressed in a small reduction of the steady bias flow velocity; and it holds true so long as flow reversal does not occur, i.e. providing acoustic velocity is no larger than the bias flow velocity.

3.1.4   Mendez's Application

Mendez et al. (2008; 2009) derived an acoustic impedance model for perforated liners based on the work of Luong et al. (2005), and in reference to the Cumming's Equation *[108]*; in which pressure drop caused by particle velocity through an orifice is defined as:

$$\Delta P = \rho l_{eff}\frac{dU}{dT} + \frac{\rho U^2}{2C_c^2}$$

[110]

The "acoustic impedance jump model" as it's coined, is obtained by linearisation of Equation *[110]* by the orifice velocity U:

$$Z = \frac{\partial(\Delta P)}{\partial U} = \frac{\rho U}{\sigma C_c} + i\frac{\rho\omega l_{eff}}{\sigma} \qquad [111]$$

The numerical model prescribed in Equation *[110]* is then integrated into their LES code (AVBP); and acoustic impedance results obtained from their model are subsequently shown to be in high agreement with those of experimental results (Mendez & Eldredge, 2009).

3.2   Acoustic Impedance Models

The fundamentals of Impedance modelling have already been introduced previously in Section 2.3, where much of the early developments can be attributed to the work of Crandall (1926). In the following sub-sections, contemporary contributions and modifications of the acoustic impedance modelling methods introduced in the previous section will be summarised.

3.2.1   Maa's Model

Maa (1998) proposed an acoustic impedance model based on Crandall's work (Crandall, 1926), which focused on the application of modelling micro-perforated panel absorbers (MPP absorbers), with medium shear numbers. He states that the acoustic impedance of an MPP absorber is determined by the porosity of the plate, thickness of the plate, orifice size and the cavity geometry; and defines the normalised specific acoustic impedance and reactance of such perforated liners as approximately (Maa, 1998):

$$r = \frac{8\mu l}{\sigma\rho c r^2}\left(\left(1 + \frac{Sh^2}{32}\right)^{0.5} + \frac{\sqrt{2}}{16}Sh\frac{r}{l}\right) \qquad [112]$$

$$x = \frac{kl}{\sigma}\left(1 + \left(9 + \frac{Sh^2}{2}\right)^{-0.5} + \frac{1.7r}{l}\right) \qquad [113]$$

His model effectively predicts acoustic impedance for MPP absorbers when the shear number is $1 < Sh < 10$, and the orifice aspect ratio d/l is close to unity, which are common conditions for many tangible MPP absorbers, making it well suited to many physical applications. The same cannot be said however for plates with large perforations, where the shear number can easily exceed the threshold of applicability, even at relatively low frequencies of noise.

3.2.2   Atalla's Model

Atalla and Sgard (2007) propose an alternative method, which builds upon the Johnson-Allard approach (Johnson et al., 1987; Champoux & Allard, 1991); whereby the perforated screen is treated as an "equivalent fluid", and the density of the medium is modified by the dynamic tortuosity of the perforated region. He presents an acoustic impedance model for a perforated panel, backed with an air cavity, under exposure to a normal incidence acoustic signal as (Atalla & Sgard, 2007):

$$z = \left(\frac{4l}{d} + 8\frac{l'}{d}\right)\frac{R_s}{\sigma\rho c} + \frac{1}{\sigma}(2l' + l)ik - icot(kL_c) \qquad [114]$$

Where $R_s = \sqrt{\mu\omega\rho/2}$ represents the orifice surface resistance, l' represents the end correction length, $l' = 0.85r\left(1 - 1.14\sqrt{\sigma}\right)$ when $\sigma < 0.16$. Contrary to Maa's model (Maa, 1998), which is only applicable to micro-perforated panel absorbers, Atalla's mode is appropriate for perforations of both large and small diameters.

3.2.3   Bellucci's Model

Bellucci et al. (2002; 2004) introduces an impedance model based on that of Crandall (1926) model given in Equation [52]; they neglect the thermal conductivity losses however, such that the normalised specific impedance of a perforation, without end correction, and without flow yields:

$$\zeta = \frac{1}{\sigma}\frac{ikl}{F(k_s r)'} \qquad [115]$$

Where the function F is as defined in Equation [53]. Bellucci et al. (2002; 2004) use a common approximation of Equation [115] for large shear numbers, $Sh > 10$:

$$\zeta = \frac{1}{\sigma}ikl\Gamma \quad \text{where} \quad \Gamma = \left[\left(1 + \frac{\sqrt{2}}{Sh}\right) - i\left(\frac{\sqrt{2}}{Sh}\right)\right] \qquad [116]$$

Several additional terms are added to capture the effect of bias flow and the relevant end corrections; and a combined end correction consisting of contributions from the radiation reactance l'_{rad}, the orifice interaction l'_{int}, the bias flow l'_{B}, and nonlinear effects of high amplitudes l'_{nl}. Including both apertures yields:

$$l'_{Bellucci} = l'_{rad} \cdot l'_{int} \cdot l'_{B} \cdot l'_{nl} \qquad [117]$$

The contributing terms have been compiled from various sources, and listed by Bellucci et al. (2004) as:

$$l'_{rad} = 2 \cdot 0.8216r \left(1 + \frac{(0.77He)^2}{1 + 0.77He}\right)^{-1} \qquad \text{(Norris \& Sheng, 1989)} \qquad [118]$$

$$l'_{int} = 1 - \sqrt{\sigma/2} \qquad \text{(Ingard, U., 1953)} \qquad [119]$$

$$l'_B = \frac{0.3(6/St^2) + 1}{6/St^2 + 1} \qquad \text{(Jing \& Sun, 2000; Peters, M. et al., 1993; Rienstra, 1983)} \qquad [120]$$

$$l'_{nl} = 1 - 0.3/St_{ac}^{0.6} \qquad \text{(Peters, M. et al., 1993)} \qquad [121]$$

Here both the Helmholtz and Strouhal numbers are based on the orifice radius, where; $He = kr$; $St = \omega r/U_B$; the acoustic Strouhal number $St_{ac} = \omega r/|\hat{v}|$; and the coefficients for l'_B and l'_{nl} have been obtained empirically from experimental data.

The effect of bias flow and nonlinear effects on the acoustic resistance is accounted for by (Bellucci et al., 2004):

$$\theta_{Bellucci} = \frac{\xi}{c\sigma} G\left(\frac{U_B}{|\hat{v}|}\right)|\hat{v}| \qquad [122]$$

Where both $G(x)$ and ξ are piecewise functions and have different expressions depending on the relative magnitude of mean bias flow velocity U_B, and acoustic particle velocity U_{ac}. Keller and Zauner state $G(x)$ as:

$$G(x) = \begin{cases} \frac{2}{\pi}\left(x \cdot \arcsin(x) + \frac{\sqrt{1-x^2}}{3}(2+x^2)\right) & \text{If } |x| \leq 1 \\ |x| & \text{If } |x| > 1 \end{cases} \qquad [123]$$

The term ξ is evaluated according to the ratio of bias flow velocity to acoustic particle velocity as follows (Bellucci et al., 2002):

$$\xi \begin{cases} 1/C_d^2 & \text{If } U_B = 0, St_{ac} \leq (ST_{ac})_{qs} & [124] \\ 0.5\left(\frac{3\pi}{4}\right)St_{ac}^{1/3} & \text{If } U_B = 0, St_{ac} > (ST_{ac})_{qs} & [125] \\ \frac{\pi}{2}\frac{\delta St}{\gamma^2 + \delta^2} & \text{If } U_B \geq |\hat{v}| & [126] \\ \frac{\xi_0(1-G) + \xi_B\left(G - \frac{4}{3\pi}\right)}{1 - \frac{4}{3\pi}} & \text{If } 0 < U_B < |\hat{v}| & [127] \end{cases}$$

In Equation [127] the term ξ_0 refers to either Equation [124] or Equation [125], depending on the value of ST_{ac}; ξ_B refers to Equation [126]; γ and δ are, respectively, the real and imaginary part of Howe's Rayleigh conductivity, as stated in Equation *[103]*. The limit of the quasi-steady assumption for the

acoustic Strouhal number is given by $(ST_{ac})_{qs} = 0.61/C_d^6$, and adding Equations [117] and [122], to Equation [115], results in:

$$\zeta_{Bellucci} = \frac{\xi}{c\sigma} G\left(\frac{U_B}{|\hat{v}|}\right)|\hat{v}| + \frac{ik}{\sigma}(l\Gamma + l'_{Bellucci}) \qquad \qquad [128]$$

This equation only describes the impedance of the perforation; Bellucci (2004) also includes cavity reactance, and determines the acoustic particle velocity $|\hat{v}|$ iteratively, with a Newton-Raphson method; where the particle velocity is approximated, as suggested by Betts et al. (2000):

$$|\hat{v}| = \frac{1}{2\sigma C_d}\left(\frac{p'_{ref} 10^{SPL/20}\sqrt{2}}{\rho c}\right) \qquad \qquad [129]$$

Bellucci et al.(2004) present a comparison of their model with experimental collected data obtained from measurements of reflection coefficient of a perforated plate with normal sound incidence, and the results show good agreement between their model and the collected results across the range of parameters investigated, which can be seen in Table 2.

f	Hz	50 - 600
SPL	dB	N/A
M_B	-	$0 - 0.023$
σ	%	$1.03 - 2.31$
d	mm	$4 - 13.8$
t	mm	1.5 - 43

Table 2 - Parameter range of experimental data investigated by Bellucci et al. (2004)

3.2.4   Betts' Model

An impedance model was proposed by Betts (2000; 2000) which is based on Equation [59] with a modification to capture nonlinear effects, as proposed by Melling's Equation [60] (Melling, 1973). Betts then modifies the non-linear term to include the bias flow, as shown in Equation [67]. He does not however, use the exact solution of Equation [59], but rather a combination of the low and high shear number approximations; by combining both approximations, he proposes an intuitive impedance formulation without Bessel functions, which can be applied to all frequencies. As a result, half of the Poiseuille viscous term is added to the Helmholtz approximation, such that (Betts, Juan F. et al., 2000):

$$\zeta_{Betts} = \frac{4vl}{c\sigma C_D r^2} + \frac{\sqrt{2\omega v l}}{c\sigma C_d r} + \frac{1-\sigma^2}{\sigma C_d}\left|M_B^{eff}\right| + i\left(\frac{kl}{\sigma C_d} + \frac{\sqrt{2\omega v l}}{c\sigma C_d r} + \frac{16r\psi}{3\pi}\right) \tag{130}$$

Where M_B^{eff} is the effective bias flow Mach number, considering the acoustically induced flow, as well as the steady bias flow (Betts, Juan F. et al., 2000).

$$M_B^{eff} = \frac{1}{2c\sigma C_d}\left(\frac{p'_{ref} 10^{SPL/20}\sqrt{2}}{\rho c}\right) + M_B \tag{131}$$

Betts refers to this model as the Perforate Bias Flow Intermediate Frequency (PBFIF) model, and he compares the model to impedance measurements of a perforated plate, with normal sound incidence, across the parameter range detailed in Table 3; which demonstrates good between his model and the experimental results.

f	Hz	1000 - 1300
SPL	dB	120 - 140
M_B	-	$0 - 0.0175$
σ	%	$0.9 - 16.5$
d	mm	$0.24 - 1.48$
t	mm	$0.51 - 1.02$
d_c	mm	272

Table 3 - Parameter range of experimental data compared to Betts model (Betts, Juan F. et al., 2000)

3.3 Empirical Modelling

3.3.1 Bauer's Model

Bauer (1977) proposed his empirical acoustic impedance model by simply combining the viscous resistance term $\frac{\sqrt{8\mu\rho\omega}}{\rho c\sigma}\left(1 + \frac{l}{d}\right)$ of Ingard (1953), the grazing flow resistance term $\frac{0.3M_B}{\sigma}$ of Dean (1975), the bias flow resistance term $1.15M_B/\sigma$ of Zinn (1970), and a constant end correction length of $0.25d$ of Rice (1971), leading to:

$$\zeta_{Bauer} = \frac{\sqrt{8\mu\rho\omega}}{\rho c\sigma}\left(1 + \frac{l}{d}\right) + \frac{0.3M_B}{\sigma} + \frac{1.15M_B}{\sigma} + i\frac{k(l + 0.25d)}{\sigma} \tag{132}$$

3.3.2 Wang's Model

Wang (2019) presents a model for the prediction of resonant frequencies of distributed Helmholtz resonators which effectively captures hole-to-hole interaction effects. His model was initially derived

based on high resolution computational simulations for twenty-five distributed Helmholtz resonators, upon which regression analysis of the resulting response surface was undertaken.

He obtained a time-accurate, three-dimensional, numerical solution for the propagation of a white noise signal in an impedance tube, in the absence of any mean flow or bias flow; and under the assumption that the acoustic perturbations may be considered to remain in the laminar flow regime. Under these assumptions, and with sufficient temporal and spatial resolution, his simulations can be considered to be a direct numerical solution to the governing Navier-Stokes equations.

A two-microphone transfer function was employed for acoustic analysis as per Seybert (1977), and the normalised specific impedance of the plate absorber was taken as defined by Kuttruff (2007):

$$z = r + ix = (1 + R)/(1 - R)$$

[133]

Where r is the normalised specific acoustic resistance, x is the normalised specific acoustic reactance, and R represents the reflection coefficient. As his simulations represented a distributed resonator mounted at the end of an impedance tube, the acoustic energy absorbed was considered as that not reflected, and the resonance frequency of the resonator to coincide with an acoustic reactance value of zero (Kuttruff, 2007):

$$\alpha = 1 - |R|^2 = \frac{4r}{(1 + r)^2 + x^2}$$

[134]

The range of geometric variations investigated can be seen in Table 4, and an example of six perforated plates in Figure 36; where each case has intentionally the same values of porosity, plate thickness, and cavity dimensions; such that the significance of the ratio of hole separation distance to hole diameter $(x/d, y/d)$, can be effectively evaluated; where x is the hole pitch in the horizontal direction, and y is the hole pitch in the vertical direction, and d is the diameter of the hole.

Case No.	Diameter of the Impedance Tubes and Perforated Plates (mm)	Diameter of the Hole, d (mm)	x/d	y/d	Effective Porosity, σ_{eff}
1	90	2	1.2	1.2	0.545
2	90	2	1.5	1.5	0.349
3	90	2	2	2	0.196
4	90	2	2.5	2.5	0.126
5	90	2	3	3	0.087
6	90	2	4	4	0.049
7	90	2	5	5	0.031
8	135	3	1.2	1.2	0.545
9	135	3	1.5	1.5	0.444
10	135	3	2	2	0.250
11	135	3	2.5	2.5	0.160
12	135	3	3	3	0.111
13	135	3	4	4	0.063
14	135	3	5	5	0.040
15	180	4	1.2	1.2	0.545
16	180	4	1.5	1.5	0.444
17	180	4	2	2	0.250
18	180	4	2.5	2.5	0.160
19	180	4	3	3	0.111
20	180	4	4	4	0.063
21	180	4	5	5	0.040
22	135	3	1.5	5	0.105
23	135	3	2	5	0.079
24	135	3	3	5	0.052
25	135	3	4	5	0.039

Table 4 - Geometric Features of plates resolved by CFD (Wang et al., 2019)
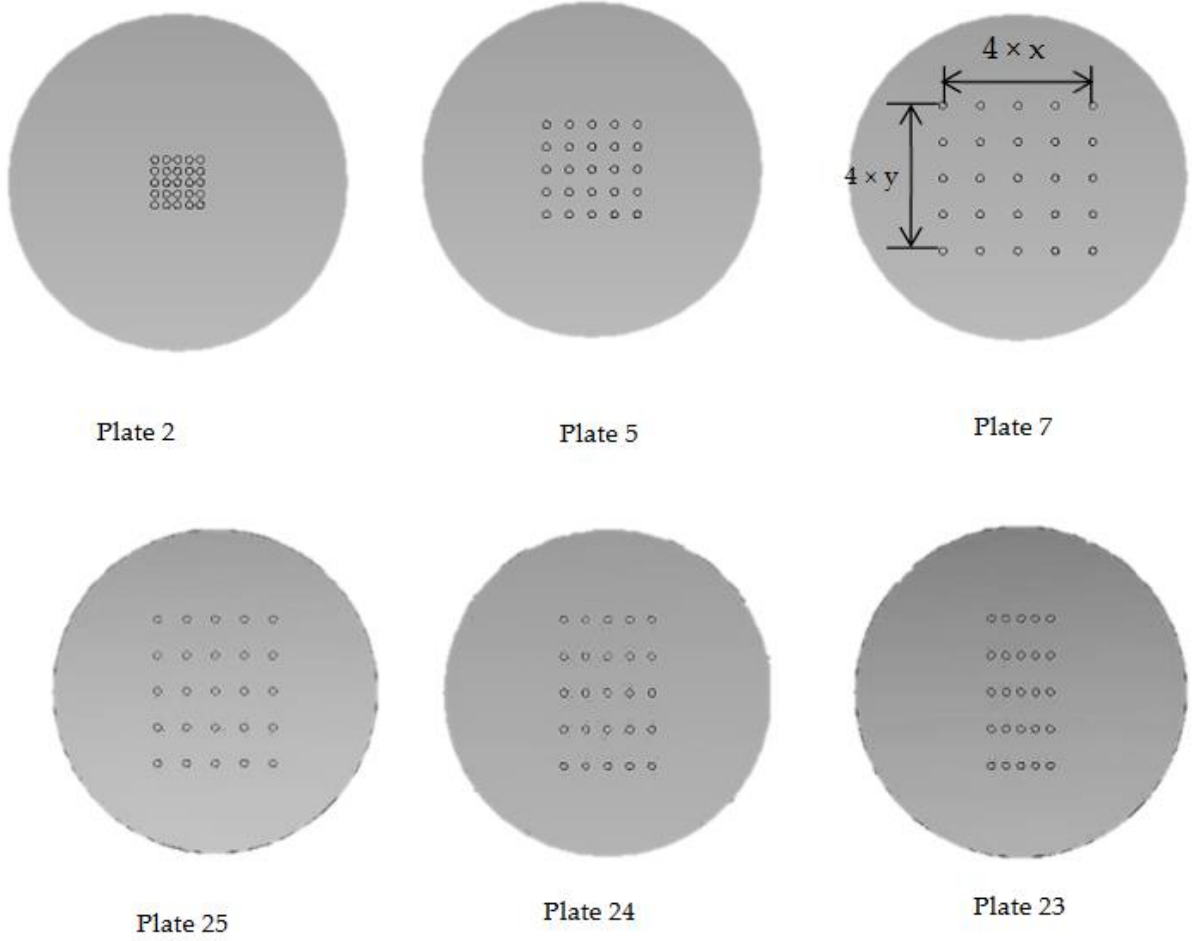
Figure 36 - A schematic example of six perforated plate configurations (Wang et al., 2019)

The porosity of the plates is defined as the ratio of the total opening area to the whole surface area of the perforated plate, $\sigma = nA_0/A_p = A/A_p$; where n is the number of holes, A represents the total opening area of all holes, A_0 is the cross section of a single hole, and A_p stands for the total surface area of the perforated plate backed by a cavity.

A new parameter is introduced, referred to as "effective porosity", which depicts the uniformity of hole distribution in a perforated plate; it is equal to the classical porosity if all holes are equally distributed however, it will be larger if some or all holes are more densely distributed in a local area of noise dampening surface. Effective porosity is defined as:

$$\sigma_{eff} = \pi d^2/4xy \qquad\qquad [135]$$

Where d is the diameter of the hole, x and y are the hole separation distance in two directions (as shown in Figure 36), $\pi d^2/4$ is the opening area in a rectangular perforation region, whose area is xy.

The obtained normalised specific acoustic reactance curves for the twenty-five cases evaluated can be seen in Figure 37, within which all cases investigated demonstrate a shift towards lower resonant frequencies, with a decreasing distance between individual holes. In consideration of the classic Helmholtz resonator equation $f = \frac{v}{2\pi}\sqrt{\frac{A}{Vl}}$ (Pierce, 1989), these reductions in resonant frequency imply that the end correction length increases, with decreasing hole separation distance.
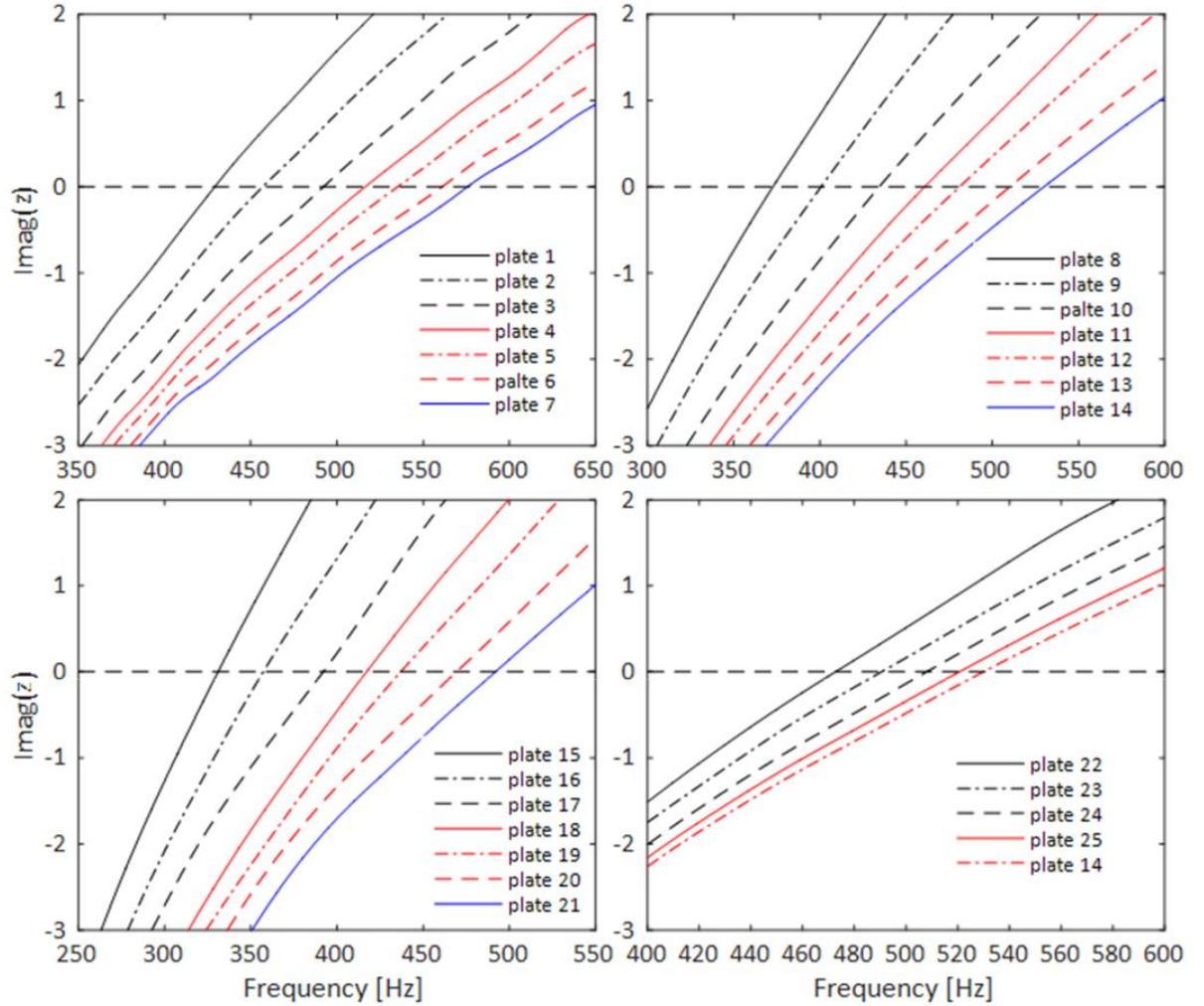
Figure 37 - CFD obtained resonance frequencies of perforated plates No. 1-25 (as listed in Table 4) (Wang et al., 2019)

Interestingly, this is contrary to Fok's function, which suggests that the hole interaction effect reduces the overall acoustic end correction length (Fok, 1941). Reviewing the computed acoustic velocity magnitude in the vicinity of the perforations of Plate No. 7, Figure 38, it can be seen that the corresponding oscillating masses for each orifice are so far apart that they have negligible interaction. By contrast, for plate No. 2, Figure 39, the acoustic velocity does not diminish so rapidly when neighbouring holes are very close, as a result of the combined momentum of the interacting jet flows from the neighbouring holes. This observation gives rise to an extra acoustic radiation effect from the perforation area as a whole to the acoustically relevant downstream space; and leads to the

introduction by Wang of an additional radiation effect, coined "acoustic radiation effect due to the overall perforation area". Subsequently he deduces that the acoustic radiation effect of a perforated plate is treated as a superposition of two radiation effects simultaneously: the "individual hole radiation effect", and the "overall perforation region radiation effect".
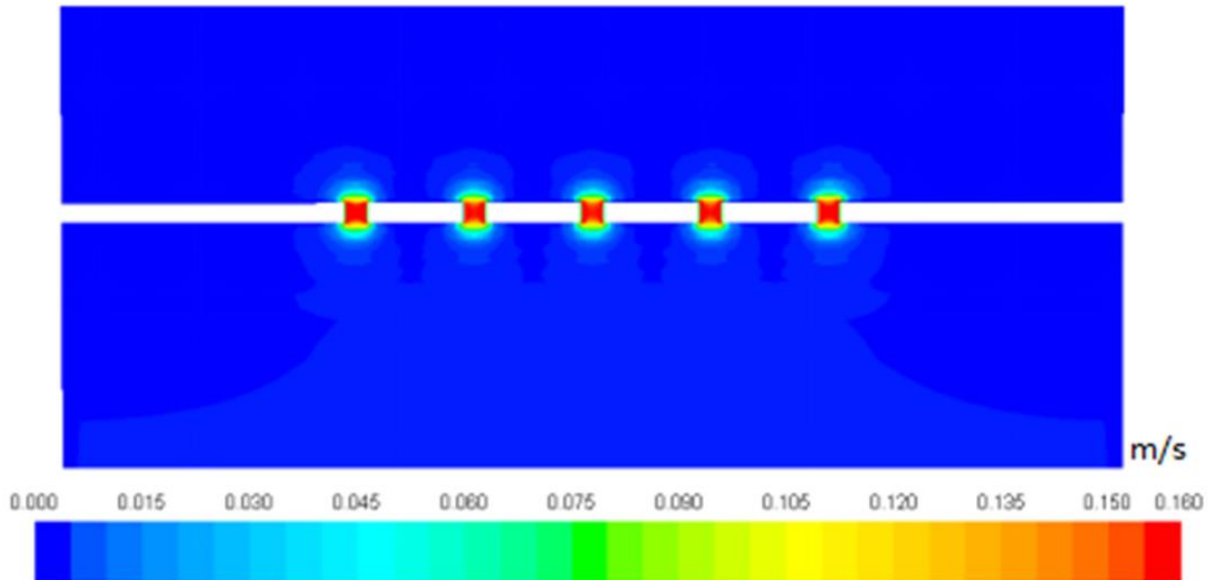
Figure 38 - Acoustic velocity magnitude contour near perforated plate No. 7 absorber (Wang et al., 2019)
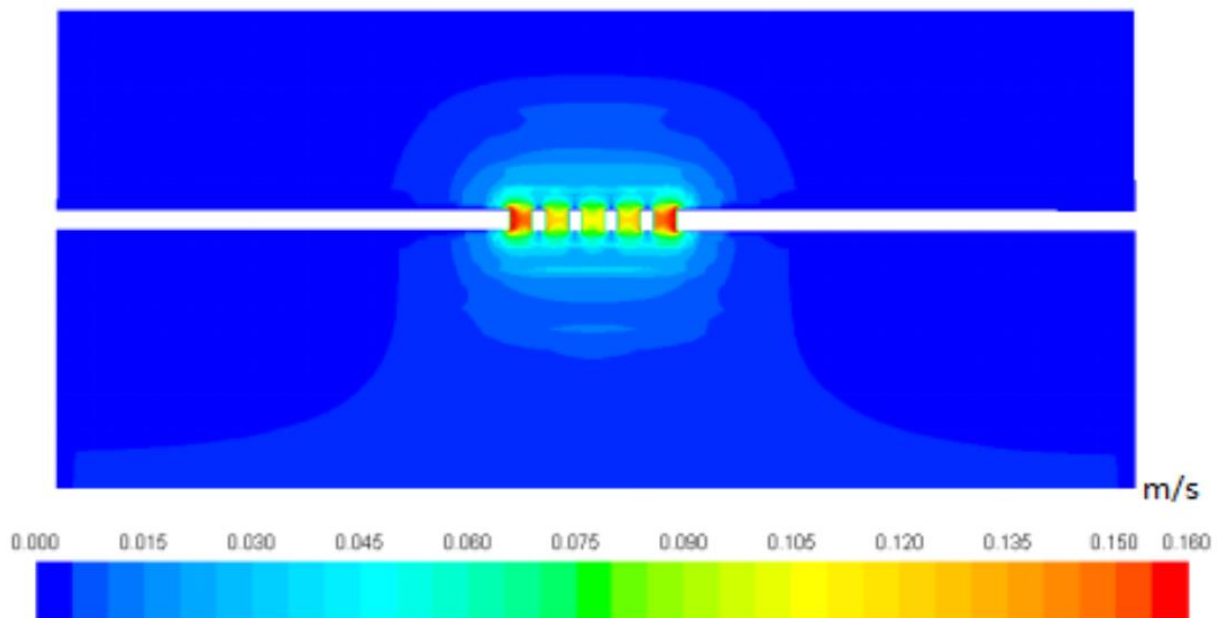
Figure 39 - Acoustic velocity magnitude contour near perforated plate No. 2 absorber (Wang et al., 2019)

Wang's model builds upon the work of Ingard (1953) and Kuttruff (2007), whereby the end correction length due to a single hole radiation effect is derived to be:

$$l_{sh} = 0.96\sqrt{A_0} \hspace{3cm} \text{[136]}$$

In consideration of an extreme case where all perforations are just next to each other ($x/d = 1$), the orifices can be considered as approximately a single large hole, in terms of acoustic radiation, therefore he proposes that the acoustic end correction due to the overall perforation area follows a similar form as the individual hole:

$$l_{op} = C \cdot 0.96\sqrt{A} \hspace{3cm} \text{[137]}$$

Where A_0 is the area of an individual perforation, A is the overall opening area of all orifices, and C is a correction parameter, introduced to consider the extent to which the perforation region is acting like a single hole. C is large when the holes are close together and diminishes when the holes are far apart. By assuming that the acoustic end correction lengths caused by these effects are additive, Wang proposes the following simple model for combined end correction length:

$$l' = l_{sh} + l_{op} = 0.96\sqrt{A_0} + C \cdot 0.96\sqrt{A} \hspace{3cm} \text{[138]}$$

Where l' represents the total end correction length, l_{sh} is the end correction length due to the acoustic radiation effect near an individual hole, and l_{op} stands for the end correction length due to the acoustic radiation effect of the overall perforation area. The correction factor C was investigated for all twenty-five cases, and using regression analysis, a model connecting the overall perforation area, to the effective porosity was obtained as follows:

$$l_{op} = 0.96\sqrt{A}\left(0.78\sqrt{\sigma_{eff}} - 0.11\right) \hspace{3cm} \text{[139]}$$

Which leads the total end correction effect being:

$$l' = l_{sh} + l_{op} = 0.96\sqrt{A_0} + C \cdot 0.96\sqrt{A}\left(0.78\sqrt{\sigma_{eff}} - 0.11\right) \hspace{2cm} \text{[140]}$$

And it follows that the resonant frequency of a distributed Helmholtz resonator, in consideration of hole-to-hole interaction effects, can be described by:

$$f_r = \frac{c}{2\pi}\sqrt{\frac{A}{Vl_{eff}}} = \frac{c}{2\pi}\sqrt{\frac{A}{V(l+l')}} = \frac{c}{2\pi}\sqrt{\frac{A}{V\left(l + 0.96\sqrt{A_0} + 0.96\sqrt{A}(0.78\sqrt{\sigma_{eff}} - 0.11)\right)}} \quad [141]$$

The model was fitted to the computed numerical results, which spans an effective porosity range of 3.14-55% and an aspect ratio range of 0.4:1-1:1; and as shown in Figure 40, the later term l_{op} reduces to zero when $\sigma_{eff} \approx 2\%$, which suggests that this is the threshold where the individual holes become far enough apart that there is no interaction effects, and the holes can be effectively considered to radiate in isolation.
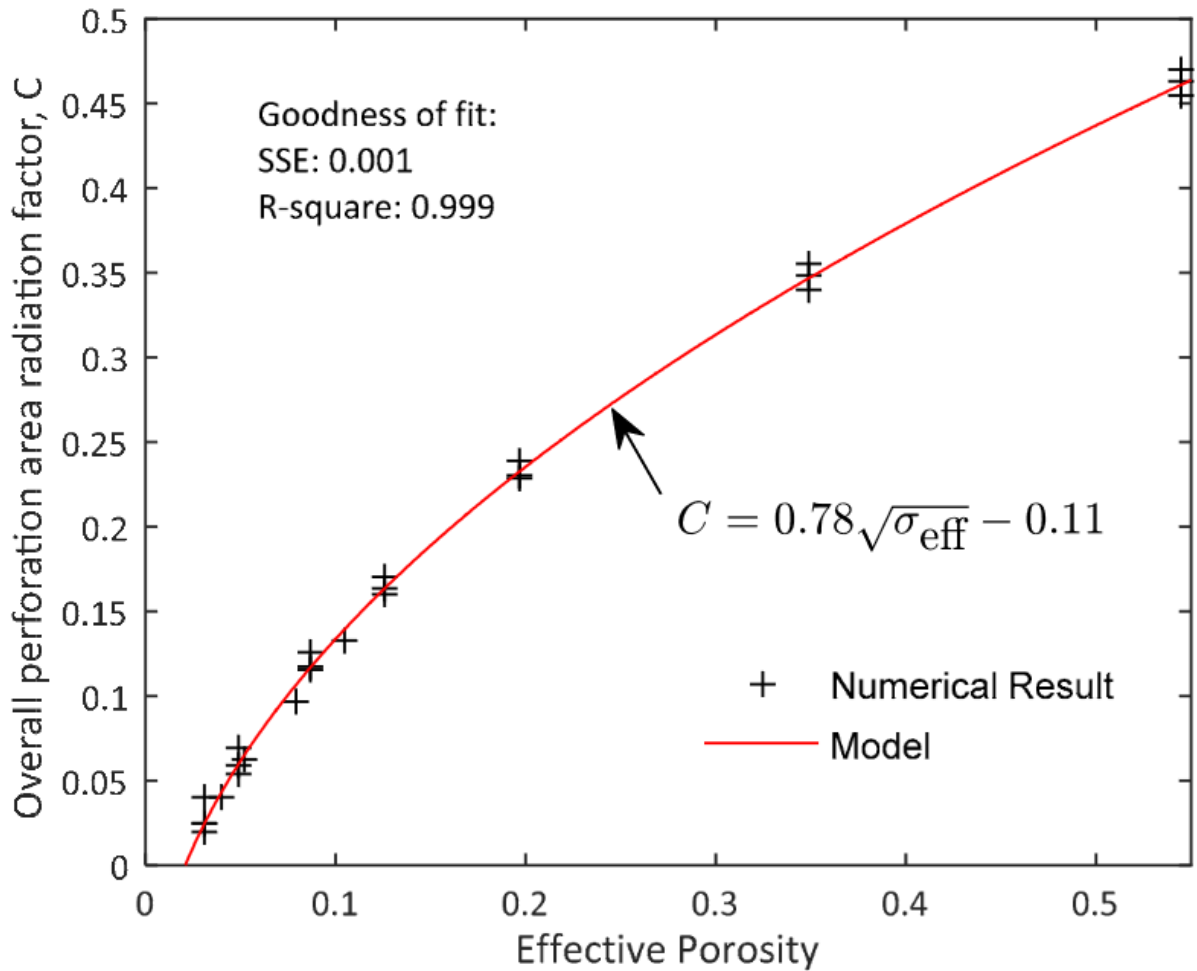
Figure 40 - Proposed model for end correction factor as a function of effective porosity (Wang et al., 2019)

His model was derived based on numerical results alone, but was validated against experimental results collected from eighteen of the distributed Helmholtz resonators prescribed in CHAPTER 7 -. The porosity of these examples ranged from 3.38% to 13.5% and perforation aspect ratios of 1:1 to 1:3, and the results of the caparison can be seen in Figure 41 and Table 5. Both experimental and model results demonstrate an increase of end correction length for cases with small hole separation distances

and therefore, large hole-to-hole interaction effects; whereby in contrast, Fok's function can be seen to consistently underestimate the required end correction for cases where interaction effects are prevalent. Wang's model demonstrates a tendency to also underpredict the required end correction value for the cases investigated with large hole separation; and this error is expected to be a contribution of some hole-to-wall interaction effects, as the outer holes of the array reach closer proximity to the wall of the resonant cavity; a feature which is not captured by this model. Irrespective, it does prove to be effective at capturing hole-to-hole interaction effects and provides an accessible advancement in the accuracy of resonant frequency predictions using the modified classical Helmholtz resonator frequency Equation [141].
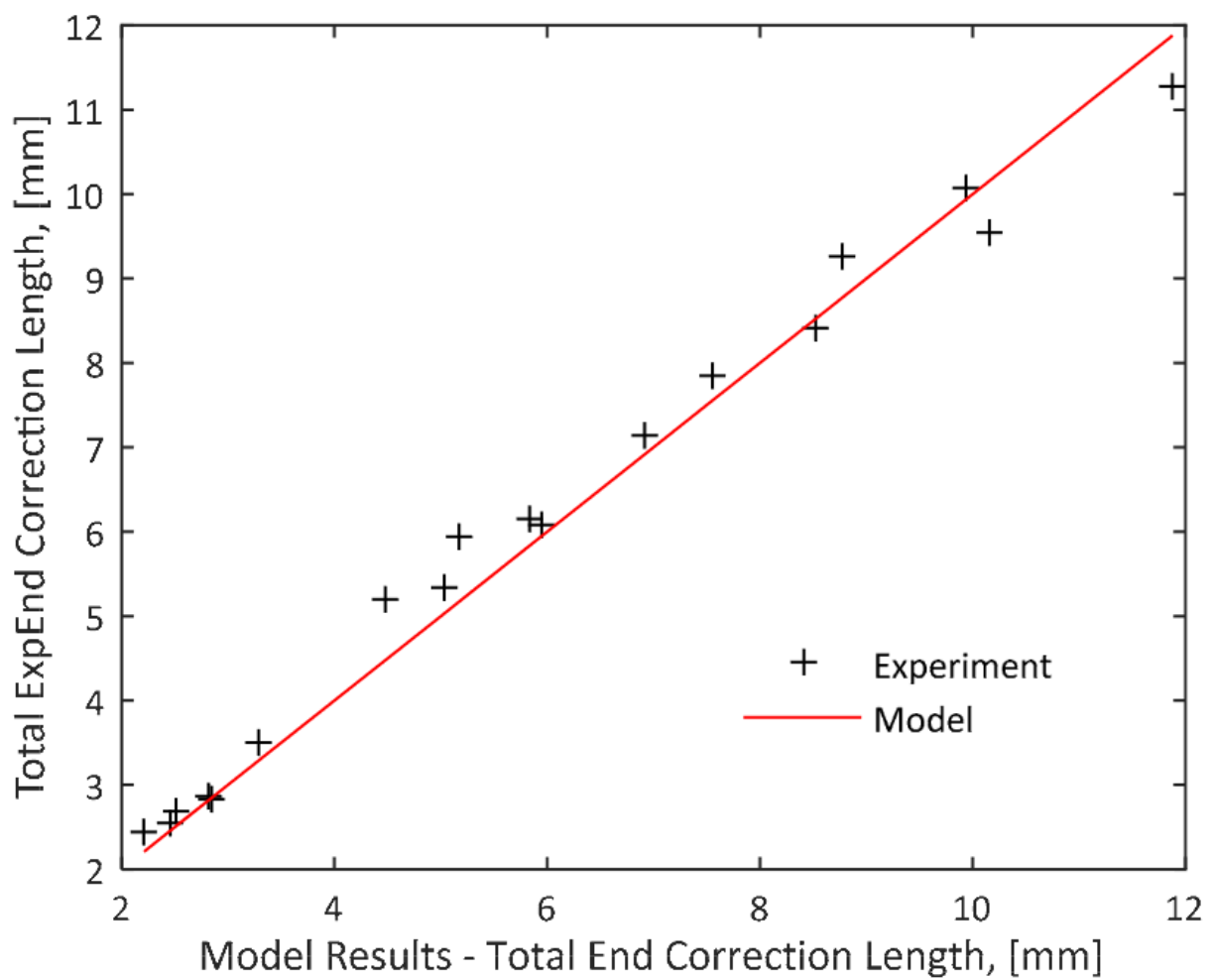
Figure 41 - Validation of the Wang's model against experimental results (Wang et al., 2019)

Case #	σ_{eff}	f_r Exp. (Hz)	f_r Model. (Hz)	l' Fok (mm)	l' Exp. (mm)	l' Model (mm)	Model Relative Error (%)
1	0.0436	579	595	<1.7	2.45	2.21	-9.80
2	0.0582	573	579	<1.7	2.54	2.45	-3.59
3	0.0873	556	554	<1.7	2.82	2.86	1.18
4	0.0623	563	575	<1.7	2.71	2.51	-7.04
5	0.0831	554	557	<1.7	2.86	2.80	-1.92
6	0.1247	520	531	<1.7	3.52	3.29	-6.41
7	0.0982	683	719	<2.55	5.19	4.49	-13.5
8	0.1309	676	691	<2.55	5.34	5.03	-5.79
9	0.1963	644	649	<2.55	6.09	5.95	-2.34
10	0.1402	650	683	<2.55	5.94	5.18	-12.8
11	0.1870	642	654	<2.55	6.14	5.83	-5.10
12	0.2805	606	613	<2.55	7.14	6.92	-3.02
13	0.1745	778	790	<3.4	7.86	7.55	-3.88
14	0.2327	757	753	<3.4	8.41	8.52	1.31
15	0.3491	719	700	<3.4	9.54	10.15	6.37
16	0.2493	728	744	<3.4	9.26	8.78	-5.20
17	0.3324	703	707	<3.4	10.07	9.93	-1.37
18	0.4987	671	655	<3.4	11.29	11.88	5.21

Table 5 – Comparison of experimental and fitted model results (Wang et al., 2019)

3.4   Literature Review Summary

All of the aforementioned analytical and empirical acoustic impedance models can be used to obtain acoustic impedance for a variety of different acoustic resonator configurations, and application contexts however, they all lack the ability to capture the full fidelity and complexities inherent in real-world applications. The true acoustic attenuation performance of an applied device is dependant not only on the normal incident Rayleigh conductivity, but is also intrinsically linked to the surrounding boundaries, such as the signal incidence angle; the geometric parameters of both the device; and those of the surrounding environment; as these factors all introduce additional acoustic nuances, not captured by any idealist model.

Therefore, whilst these models can provide invaluable insight into attenuation performance characteristics, they cannot be used as a standalone method for the accurate prediction of attenuation performance in complex, real-world applications, where the acoustic and flow field conditions void many of the assumptions of the aforementioned models. To make a rigorous assessment of any given parameter, it is therefore necessary to conduct supporting experimental measurements, under carefully controlled specific conditions tuned to the performance defining parameters of interest. Hence, in the subsequent chapters such experiments will be discussed, designed, implemented and their results evaluated, to provide further insight into the effectiveness of existing modelling methods.

91

CHAPTER 4 - EXPERIMENTAL METHODOLOGY: DISCRETE RESONATORS

Within this chapter an experimental design methodology is applied and described, to outline a systematic method of design and deployment of an efficient experimental regime, targeted specifically on gaining novel insight into fundamental discrete resonator sound attenuation characteristics.

The aim of this methodology is to rationalise a comprehensive set of acoustic experiments, which can contribute to a greater understanding of the objective points outlined in *Section 4.1.*

The planning for implementation of this experimental design methodology is initiated and discussed within *Section 4.2*, where there within the investigation strategy is outlined, and the necessary exploratory tools and techniques are identified.

Following identification of the required tools and techniques, the explicit measurement methodologies to be employed are specified within *Section 4.3*, including details of the Discrete Resonator design, the Impedance Tube utilised for non-flowed experiments, the cross-flow measurement rig, and the associated measurement apparatus.

Section 4.4 clarifies the experimental variables, providing justification and specification of the chosen test cases, such as cavity volume variations, neck dimeter variations and alternative neck geometry cases.

Prior to the commencement of any explorative investigation pertaining to discrete resonator sound attenuation characteristics, a comprehensive evaluation of the proposed measurement methodology is conducted; investigating salient characteristics of the measurement apparatus and methods as a prerequisite. The results from these commissioning exercises are considered as a 'Qualification of Measurement Procedures' and presented separately for the Impedance Tube *(Section 4.5)* and the cross-flow rig *(Section 4.6).*

A summary of the experimental methodology design and evaluation for Discrete Resonators can be found in *Section 4.7,* which serves as a preamble for the collected results presented, described, and discussed in CHAPTER 5 - RESULTS & DISCUSSION: DISCRETE RESONATORS.

4.1 Objectives

- Qualify fundamental resonator geometrical considerations, such as cavity volume and neck diameter variation.

- Evaluate the intrinsic interconnectivity of geometrical factors, i.e. Diameter Ratio (r_O/R_C), Cavity Volume, and neck geometry sensitivity.

- Obtain insight into interaction effects of nearby walls *(Hole-to-Wall)*.

- Quantify impact of Cross/Grazing Flow on attenuation performance.

- Investigate potential saturation factors.

4.2 Investigation Strategy

The principal investigation strategy is to design parametric Helmholtz resonator, and then evaluate its inherent sound attenuation performance across a carefully constructed test matrix, consisting of both geometric and environmental variations. To achieve this effectively, the resonator must be purposefully designed, such that it can cater for a large degree of experimental variation, whilst ensuring a high degree of measurement capability, accuracy and repeatability.

Whilst the resonator design will facilitate geometrical variation permutations and in-resonator measurement methods; variations in environmental conditions and in-duct measurement methods, will require alterations to measurement apparatus and test rigs, as such the resonator is designed to be readily interchangeable between required experimental rigs.

The resultant variable volume Helmholtz resonator is employed initially within an isothermal atmospheric Impedance tube, primarily to allow the parametric evaluation of acoustic attenuation characteristics, against varying geometric conditions.

Once a comprehensive test matrix of parametric geometric variations has been collected, the results can then be evaluated for inherent interdependences in the parameters, and their consequential impact on the acoustic performance of a discrete Helmholtz resonator as a sound attenuation device. For example, to evaluate the effects of diameter ratio r_0/R_C *or* Hole-to-Wall interaction effects, the neck diameter is varied for a given fixed resonator diameter and neck length, however; the significance of cavity volume on the cases evaluated, must also be considered concurrently.

In order to investigate the effects of neck geometry on resonator performance, and potential end correction implications, a sequence of alternative neck geometry inserts are produced and subsequently evaluated, each with a varied termination geometry.

Whilst all of the previous points of interest can be effectively evaluated within an Impedance Tube, in order to understand the significance of a cross/grazing flow on the resonators sound attenuation characteristics, a separate cross-flow rig is required. The equivalent resonator geometric parameters will be investigated within this flow rig, such that the impact of cross-flow existence (and variation in magnitude), can be considered alongside the non-flowed Impedance Tube evaluated cases.

In order to investigate potential saturation characteristics occurring for high sound pressure levels, a CFD simulation strategy is employed, allowing pressure levels beyond those practicable within the experimental apparatus available to be investigated. This CFD method will be initially validated against the standard impedance tube collected cases, then extrapolated to more extreme values, allowing additional insight to be gained beyond existing known conditions. This CFD investigation will be presented in its entirety within CHAPTER 6 -.

The chosen metrics for subsequent evaluation of the defined discrete resonator cases, will be those of sounds pressure level (SPL) and Frequency Response Function (FRF). The SPL will be evaluated both in the temporal domain, as RMS SPL; and in the frequency domain, as a measure of the in-situ acoustic pressure distribution; unless otherwise specified, a reference sound pressure of $p_{ref} = 20 \times 10^{-6} Pa$ is used in the derivation of the corresponding SPL. The FRF will be evaluated as a representation of the acoustic attenuation performance of each case investigated.

4.3   Discrete Resonator Measurement Methodology

In the following section *(Section 4.3.1),* information will be presented on the variable volume Helmholtz resonator employed within subsequent discrete resonator investigations; including its geometric properties, measurement facilities, and its acoustically significant design considerations.

Information pertaining to the employed acoustic test rigs, such are their dimensions, acoustic signal generation and measurement capabilities, in addition to acoustically significant design considerations, can be found respectively in *Sections 4.3.2 & 4.3.3.*

Section 4.3.4 clarifies the specific measurement apparatus used for all subsequent discrete resonator investigations, in addition to the typical measurement configuration.

4.3.1 Resonator Design

For all subsequent discrete resonator investigations, a variable volume Helmholtz resonator is employed, as detailed in Figure 42. The resonator body has a fixed internal diameter of 50mm, and a sliding piston which facilitates the change in resonator volume. The maximum cavity length, limited by the construction of the resonator, is 150mm, which corresponds to a maximum volume of 294,524mm^3.
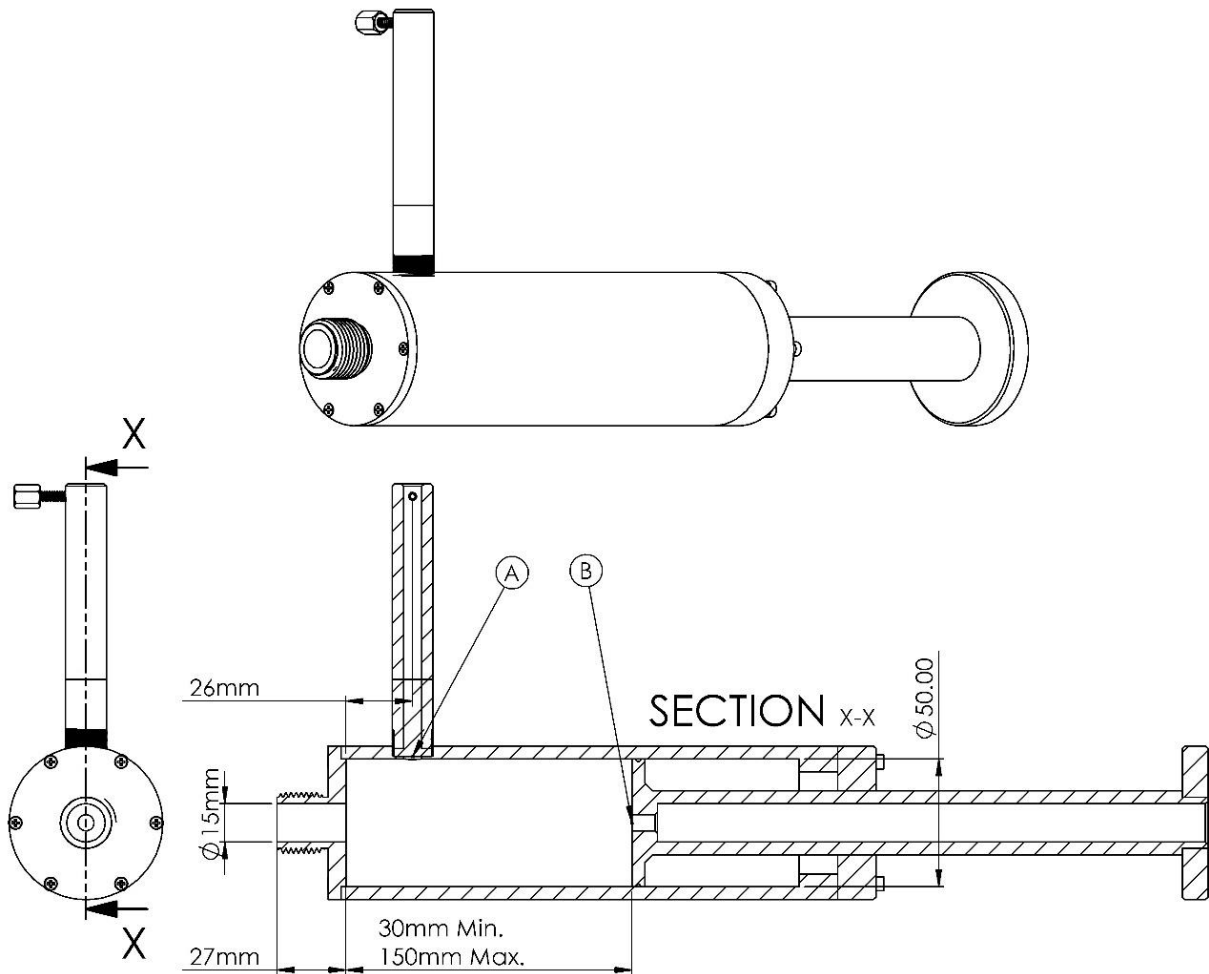
Figure 42 - Schematic of Variable Volume Helmholtz Resonator, including key dimensions & measurement locations: [A] - Tangential with Resonator wall, [B] - Flush with Piston wall.

The neck length is fixed at 27.15mm and a maximum diameter of 15mm, which we will herein refer to as the 'baseline neck'. This baseline neck also doubles as the mounting method of the resonator to the measurement section of either the Impedance tube *(Section 4.3.2)* or the Cross-Flow rig *(Section 4.3.3)*. The approach to varying the neck diameter is through machined inserts which fit within the baseline neck, allowing the effective neck diameter to be reduced from the baseline 15mm, whilst keeping the neck length fixed *(Section 4.4.2)*.

Within the resonator cavity there are two probe locations which are available for acoustic measurements, one which is machined flush with the cavity wall *(Figure 42 [A]),* and another which terminates flush with the piston wall *(Figure 42 [B])*. The depth adjusting piston contains an elastomer O-Ring around its circumference to ensure an airtight and acoustic seal between the active cavity, and the passive rear void. The piston shaft is incremented to aid the manual setting of any given cavity volume, which can be read from the alignment with the rear resonator end cap. This rear resonator cap functions as a bearing surface for the adjusting piston, ensuring proper coaxial alignment between the piston and the resonator body, and contains a small vent hole, in order to relieve the pressure from the passive void during cavity depth adjustments. These two probe locations and the depth adjusting piston can be seen pictorially in *Figure 43*.

Figure 43 - *Variable Volume Helmholtz Resonator Images, showing; [A] Flush Bored Cavity Wall Probe location, [B] Incremented Cavity Depth Adjustment Piston and vent hole, [C] Piston Wall Probe location*

4.3.2   Impedance Tube Configuration

The Impedance Tube used for this study is of a 72mm x 72mm cross section aluminium construction, with a corresponding planar wave cut-off frequency of ≈2,400Hz. The acoustic excitation signal is generated by a box mounted cone speaker at one side of the 2.266m long square section duct, inclusive of a 311mm tapered transition section, which acts as an anechoic termination for reflected signals travelling back up the duct. On the opposite side of the duct is the measurement section where the cylindrical variable volume Helmholtz resonator detailed in *Section 4.3.1* is attached. Multiple duct wall microphone probe locations are available for both 1/2" and 1/4" measurement microphones, and when a port is not being used, it is plugged flush with the duct wall, to ensure no acoustic significance. A qualification of the acoustic significance of the available measurement locations for both the Duct and the Resonator, can be seen in *Sections 4.5.1, 4.5.2* respectively, a schematic overview of the Impedance Tube can be seen in *Figure 44*, and a detail view of the measurement section, inclusive of acoustically significant dimensions can be seen in *Figure 45.*
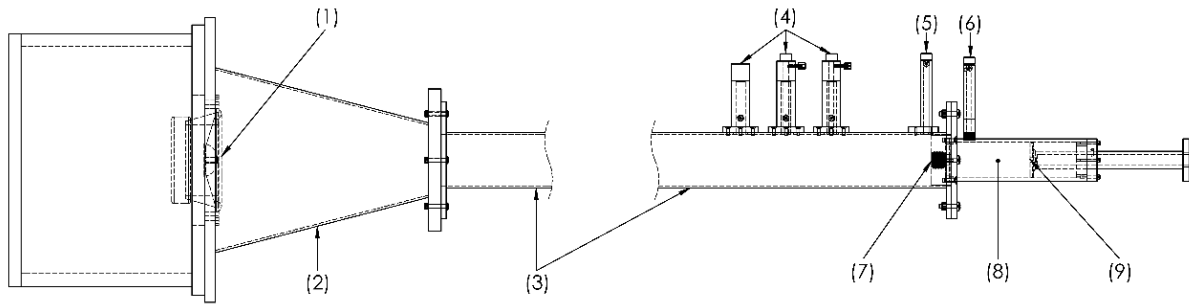
Figure 44 - Impedance tube rig overview schematic: (1) box mounted loudspeaker, (2) transition duct/anechoic section, (3) square section duct, (4) duct wall mounted measurement microphone ports, (5) near-neck, duct wall mounted measurement microphone port, (6) resonator wall mounted measurement microphone port, (7) resonator neck, (8) resonator cavity, (9) adjustable resonator cavity wall piston.
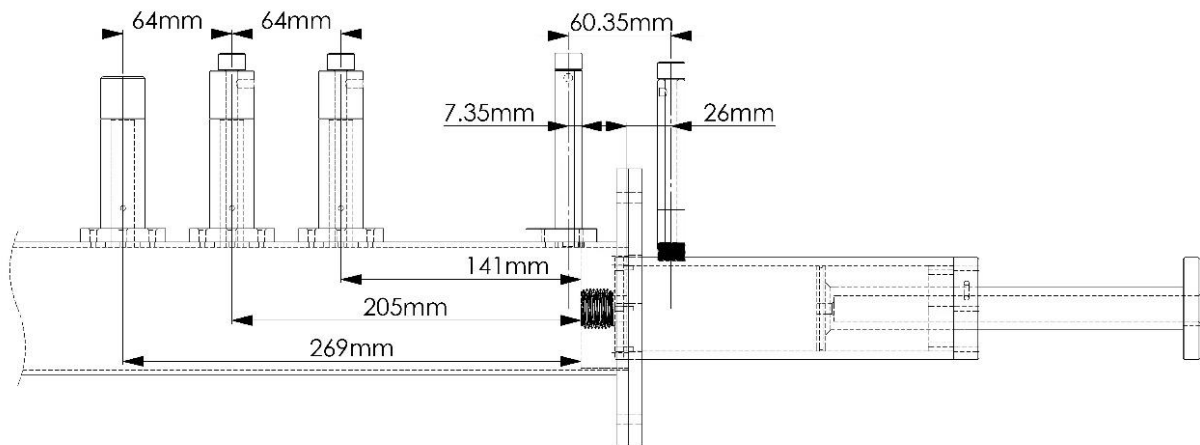
Figure 45 - Impedance Rig measurement section detail view & acoustically significant dimensions.

When the variable volume Helmholtz resonator is attached to the square section impedance tube, an additional interface adapter is required for the termination of the impedance tube. This interface adapter is specifically designed to fit within the 72mm x 72mm impedance tube, allowing the variable volume resonator to be mounted via its threaded baseline 15mm neck, and retaining all existing measurement locations. The dimensions of this adapter are such that that the neck terminates flush with the acoustic end of the impedance tube, as can be seen pictorially in *Figure 46*.
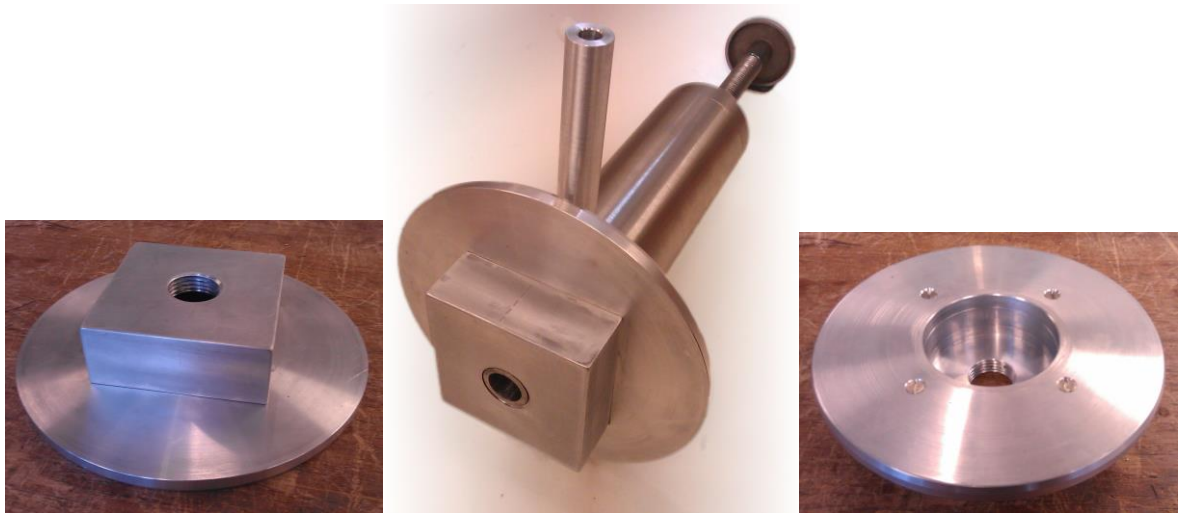
Figure 46 - Variable Volume Helmholtz Resonator Square Impedance Tube Interface adapter

An evaluation of this rigs acoustic excitation methodology, measurement location sensitivity and repeatability of the resonator's geometric variations, can be seen in detail in *Section 4.5 - Impedance Tube Qualification of Measurement Procedures.*

4.3.3   Cross-flow Rig Configuration

The cross-flow rig used for subsequent discrete resonator attenuation performance evaluations, consists of a series of 62mm internal diameter sections of stainless-steel pipe, with a corresponding planar wave cut-off frequency of ≈2,800Hz. The cross-flow is provided by a large three phase *(18.5kW)* floor standing centrifugal fan, which feeds the acoustic duct via a flexible hose to isolate mechanical vibration and connects to a large dissipative silencer to mitigate the transfer of unwanted fan noise within the duct. The acoustic excitation signal is provided by a single enclosed cone speaker, feeding the duct approximately 6m downstream from the silencer. The adjacent downstream section is the measurement section, where a test section can be added accordingly, via integrated mounting flanges.

For this investigation, the measurement section consists of a central resonator mounting section, which allows the same variable volume Helmholtz resonator as detailed in *Section 4.3.1,* to be mounted via its threaded duct-side end cap, with its baseline 15mm neck terminating flush with the internal wall of the pipe. Both upstream and downstream from the resonator section, are two probe sections, which allow the application of measurement microphones to capture duct acoustics either side of the resonator section. The duct is anechoically terminated with an ISO 7235 design (ISO-7235, 1991), approximately 6m downstream from the measurement section to mitigate any acoustically significant reflections back upstream. *Figure 47* shows a schematic overview of the rig configuration, including the measurement section (*Figure 47[C]*) and Anechoic Termination *(Figure 47 [D]).*
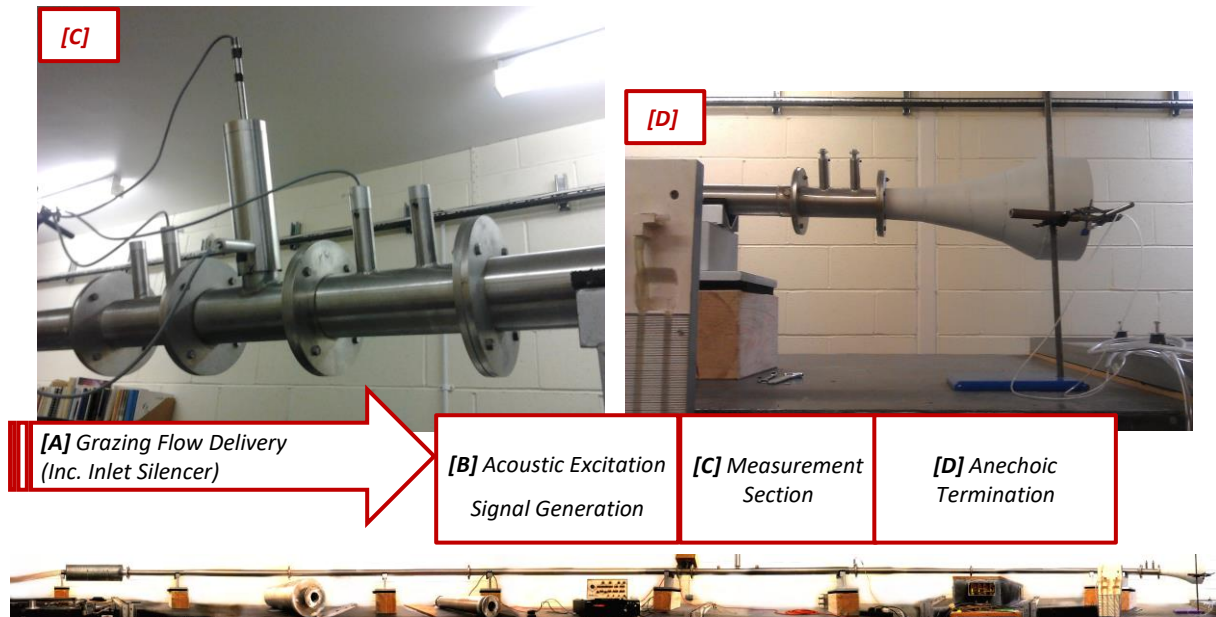
Figure 47 - Schematic showing Hull's Discrete Resonator Grazing Flow Rig Configuration

An evaluation of this rigs cross-flow delivery capability, acoustic excitation characteristics, and the interaction of cross-flow induced noise over generated measurement white noise, can be seen in detail in *Section 4.6 - Flow Rig Qualification of Measurement Procedures.*

4.3.4 Measurement Equipment

The following equipment list details the experimental apparatus used for discrete resonator experiments, including those conducted in the Impedance Tube and on the cross-flow rig.

Equipment List:

- Impedance Tube (As detailed in *Section 4.3.2* & shown in *Figure 48*)
- Cross-flow Rig (As detailed in *Section 4.3.3* & shown in *Figure 47*)
- Tektronix AFG 3022B Dual Channel Arbitrary/Function Generator (250MS/s, 25MHz)
- 2 x Bruel & Kjaer ¼" condenser microphones with preamplifiers
- Bruel & Kjaer 4 Channel microphone power supply (200V) Type 2829
- 2 x Bruel & Kjaer measuring amplifier (20-20,00Hz) Type 2609
- Sony Integrated Stereo Amplifier TA-FE330R 160W Super Legato Linear (70W + 70W)
- Agilent U2781A 6-Slot USB Modular Instrument Chassis
- Agilent U2542A 4 channel simultaneous sampling board (16 Bits, 500KS/s)
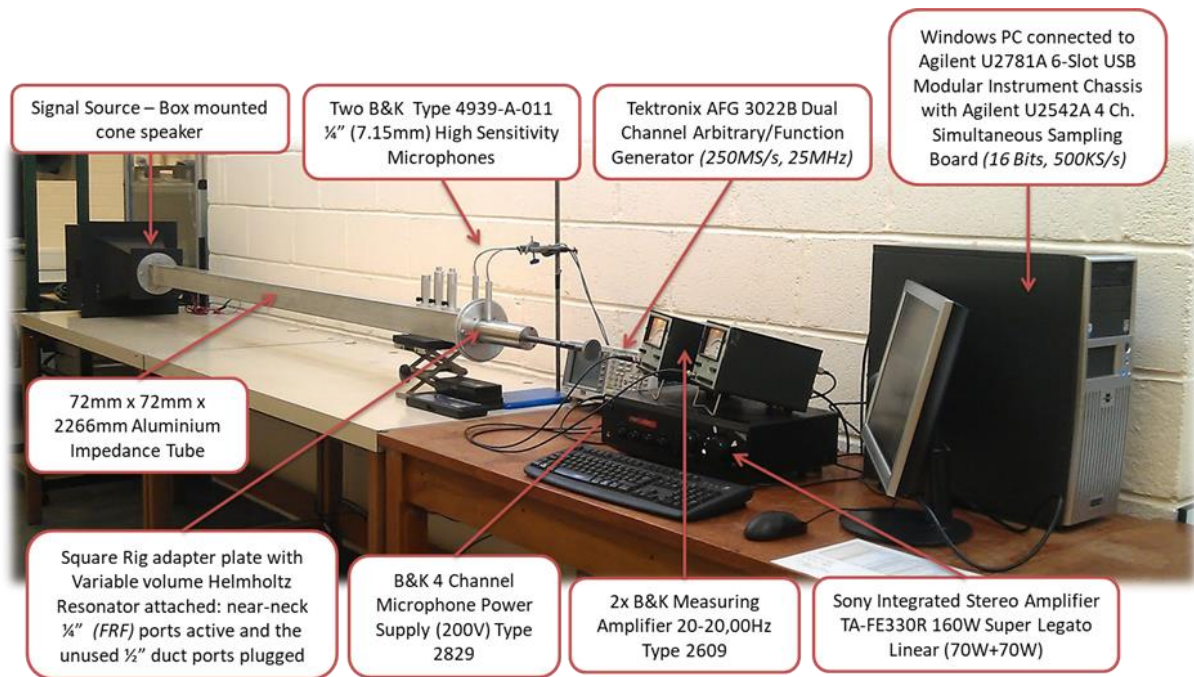
Figure 48 – Discrete resonator associated Measurement Equipment

4.4   Discrete Resonator Test Cases

In the following section the rationale and specification of all investigated discrete resonator variations are presented, including a total of 14 cavity volume variations, 5 standard neck diameter variations, and 14 alternative neck geometry variations. These variations present a total number of discrete resonator experimental permutations of 266, from which the results of subsequent experimental evaluation can be found in *CHAPTER 5 - RESULTS.*

4.4.1   Cavity Volume Cases

In order to support subsequent investigations, it is necessary to make measurements with a variety of resonator cavity volumes, and as the resonator diameter is fixed, this shall be achieved via a distribution of cavity length *(and hence volume)* cases.

The ultimate bounds of measurable cavity volumes, are defined by the confines of permissible piston movement within the cavity body, as can be appreciated from *Figure 42*. The maximum permissible cavity length for this resonator design is ≈150mm, limited only by contact between the piston and piston-side end cap. The minimum cavity volume has a practicable limit of ≈30mm imposed through the inability to use the wall mounted measurement microphone probe location beyond this length, as seen in *Figure 43[A].* It should be noted however, it is possible to measure smaller cavity volumes than 30mm, if only the piston mounted probe location is required. In the interest of ensuring a robust investigation, we shall choose to limit the minimum cavity volume, in preference of ensuring multiple

measurement locations throughout all resonator neck, and volume permutations. The solution of the ideal resonator frequency Equation [142], using these practical cavity length limits and the known neck characteristics, allows an initial perception of the upper and lower limits of measurement frequency, which are 567.67Hz & 253.87Hz respectively, for the baseline Ø15mm neck.

$$f = \frac{c}{2 \cdot \pi} \sqrt{\frac{A}{V \cdot l}}$$ [142]

In addition to ensuring that the full range of measurement capability of the equipment available is deployed for subsequent investigations, it is also desirable to ensure that there is a good distribution of data points within this range, in order to support the effective deduction of any underlying trends or defining characteristics etc. To support this ethos, we can solve the ideal resonant frequency equation for the length of cavity, and by specifying a predefined target frequency, an even distribution of measurement cases in the frequency domain can be ensured. Using the upper limit of cavity volume and the baseline neck properties, Equation [143] can been used to define a series of resonator cavity length cases, initiating from the nearest viable multiple of 10Hz resonant frequency, and incrementing in multiples of 20Hz target frequency. The end result is 14 cases of defined cavity lengths (and volumes) which can be used across all subsequent investigations, as detailed in *Table 6.*

$$L_C = \frac{A_O}{A_C l_O} \left(\frac{c}{2 \cdot \pi \cdot f} \right)^2$$ [143]

Volume Case #	Length of Cavity (mm)	Volume of Cavity (mm³)
1	36.42	71,506
2	39.39	77,341
3	42.74	83,921
4	46.54	91,377
5	50.86	99,872
6	55.82	109,610
7	61.55	120,850
8	68.19	133,900
9	75.98	149,190
10	85.18	167,260
11	96.17	188,820
12	109.42	214,840
13	125.60	246,620
14	145.67	286,020

Table 6 – Discrete Resonator Cavity Volume Cases

4.4.2   Standard Neck Diameter Cases

In addition to the baseline Ø15mm neck, an additional 4 standard neck diameter cases have been created by utilising neck inserts to facilitate a reduction in neck diameter to 12mm, 9mm, 6mm and 3mm. The baseline neck and available neck inserts can be seen pictorially in *Figure 49*, and the full range of neck diameters and corresponding neck diameter ratios r_0/R_C are clarified in Table 7.

Figure 49 - Baseline Resonator neck, and additional machined neck inserts

The standard neck diameter insets are fabricated from aluminium and turned to an outside diameter which is equal to the internal diameter of the baseline neck (~15mm). The outer diameter is machined to a high tolerance, 0.005mm Interference fit, to allow sufficient residual stress for a secure fitment, without the need for any additional fasteners which could be considered acoustically significant. The overall length of the inserts is ensured to be identical to that of the baseline neck (27.15mm), such that the resonator cavity volume is not affected, and the neck termination can be deemed equivalent to that of the baseline neck.

	Baseline	Insert	Insert	Insert	Insert
Neck Diameter (mm)	15	12	9	6	3
Diameter Ratio (r_0/R_C)	0.3	0.24	0.18	0.12	0.06

Table 7 - Measured Neck Diameter Cases

4.4.3   Alternative Neck Geometry Cases

In order to support the effective experimental investigation of neck geometry variations on subsequent resonator attenuation performance, a set of additional neck inserts have been designed and manufactured, for deployment within the variable volume Helmholtz Resonator detailed in *Section 4.3.1*. These neck inserts have been designed specifically to fit within the standard Ø15mm x 27.15mm baseline neck and themselves have a baseline 5mm neck diameter across all cases, such as to provide an additional neck diameter ratio, and compliment the standard range detailed in Table 7. In addition to the baseline 5mm diameter cylindrical neck, there are 5 variations of conical termination geometries, 5 variations of radii termination geometries, and three additional terminations based around common horn geometries: exponential, hyperbolic and tractrix. All geometry variations terminate on one side of the neck only, such that their effects can be investigated experimentally on either duct-side or resonator-side termination independently. These alternative geometry neck cases can be seen schematically in *Figure 50*, and pictorially in *Figure 51.*
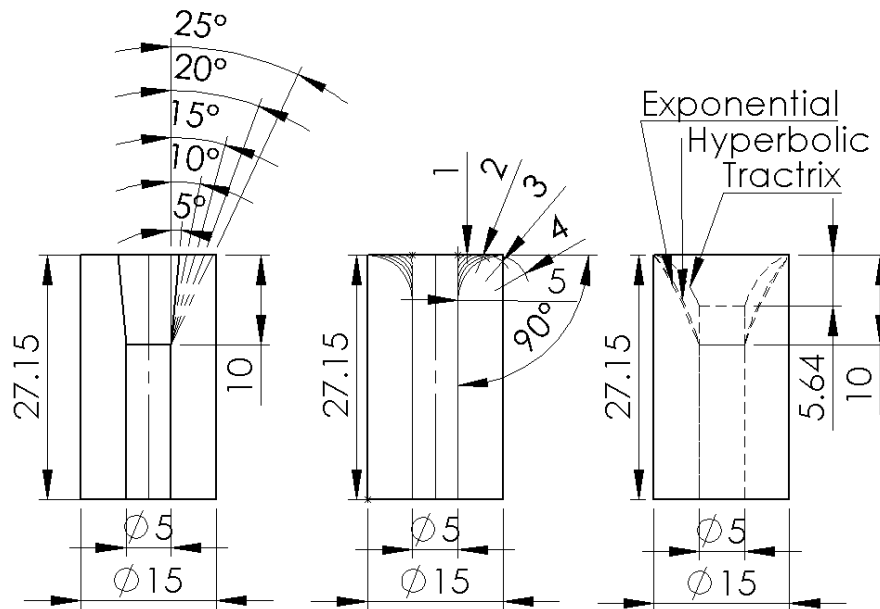
Figure 50 – Schematic representation of available neck geometry variation inserts showing; [Left] – x5 conical termination variations, [Centre] – 1x Baseline Cylindrical 5mm neck & x5 radii termination variations & [Right] – x3 horn profile termination variations
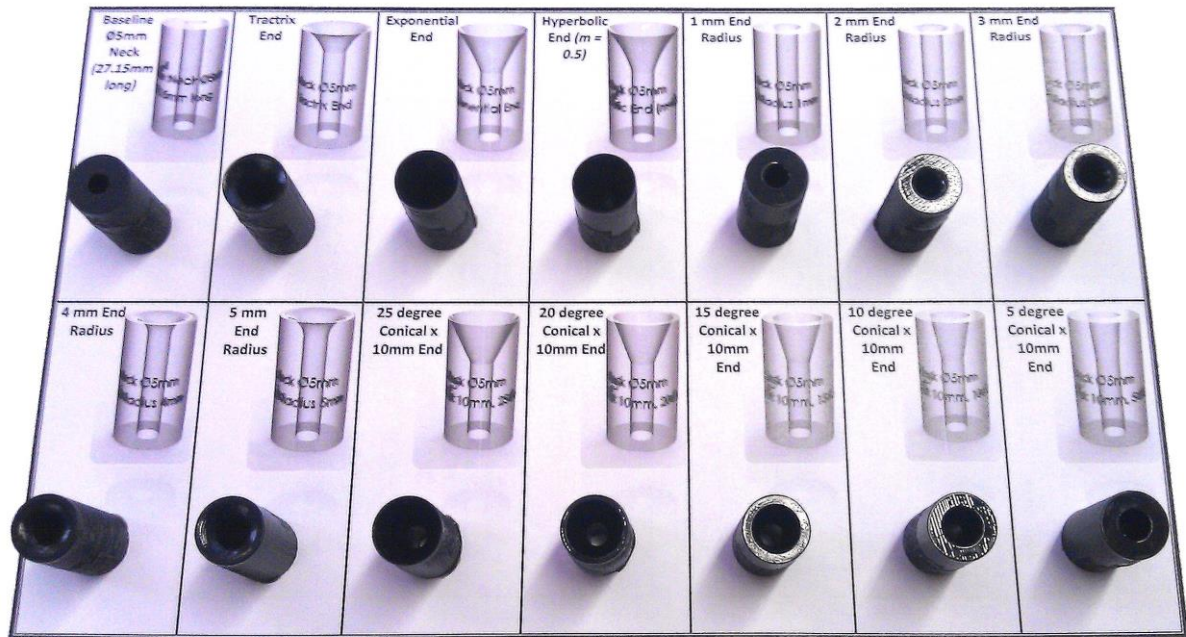
Figure 51 – Image of 3D Printed Alternative Geometry Case Neck Inserts

4.5   Impedance Tube Qualification of Measurement Procedures

In the following section information will be presented pertaining to the effective prerequisite commissioning of the discrete resonator impedance tube, prior to its application in the collection experimental data corresponding to the experimental test cases, described in *Section 4.4.* An innate understanding of the experimental nuances of the employed measurement procedure is imperative in ensuring appropriate academic rigor during the subsequent evaluation of collected results.

As such, the following section will investigate fundamental characteristics of the Impedance Tube rig, such an evaluation of the Acoustic Excitation Methodology *(Section 4.5.2),* an evaluation of the possible measurement locations and their corresponding sensitivity *(Sections 4.5.1 & 4.5.2),* and a repeatability analysis relating to the manually adjusted geometric parameters of the resonator *(Section 4.5.4).*

4.5.1   Evaluation of Duct Measurement Location Sensitivity

In order to qualify the significance of any spatial variations in observed acoustic response within the impedance tube duct, and to appreciate the significance on any subsequently derived resonator performance metrics, an initial investigation has been conducted whereby all available measurement locations have simultaneously deployed for measurement of a common case.

For this qualification case, the baseline $\emptyset$15mm neck is utilised, and the cavity volume is set to the middle volume case (Volume Case #7), with the same acoustic excitation signal and settings, as

presented in *Section 4.5.2.* Clarification of the available measurement locations, and their notations, can be seen in *Figure 52,* and the results from the measurement, presented in terms of the distribution of measured SPL in the Frequency Domain, can be seen in *Figure 53.*
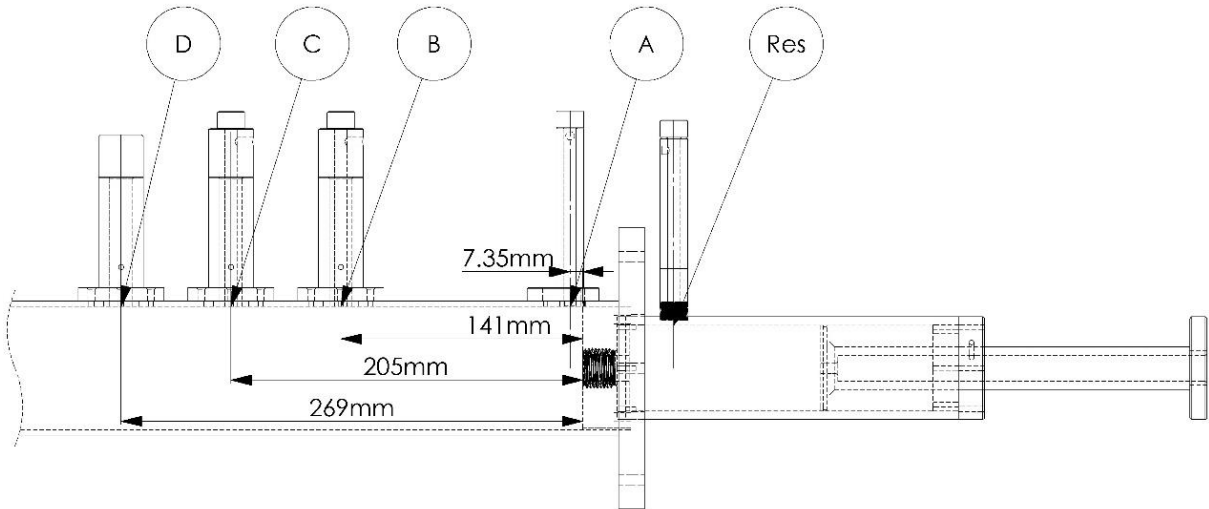
Figure 52 – Schematic showing available in-duct measurement locations, and comparative in-resonator measurement locations: [Res.] = In-Resonator wall, [A] = Duct wall near-neck (7.35mm from end), [B] = Duct wall 141mm from end, [C] = Duct wall 205mm from end, [D] = Duct wall 269mm from end.
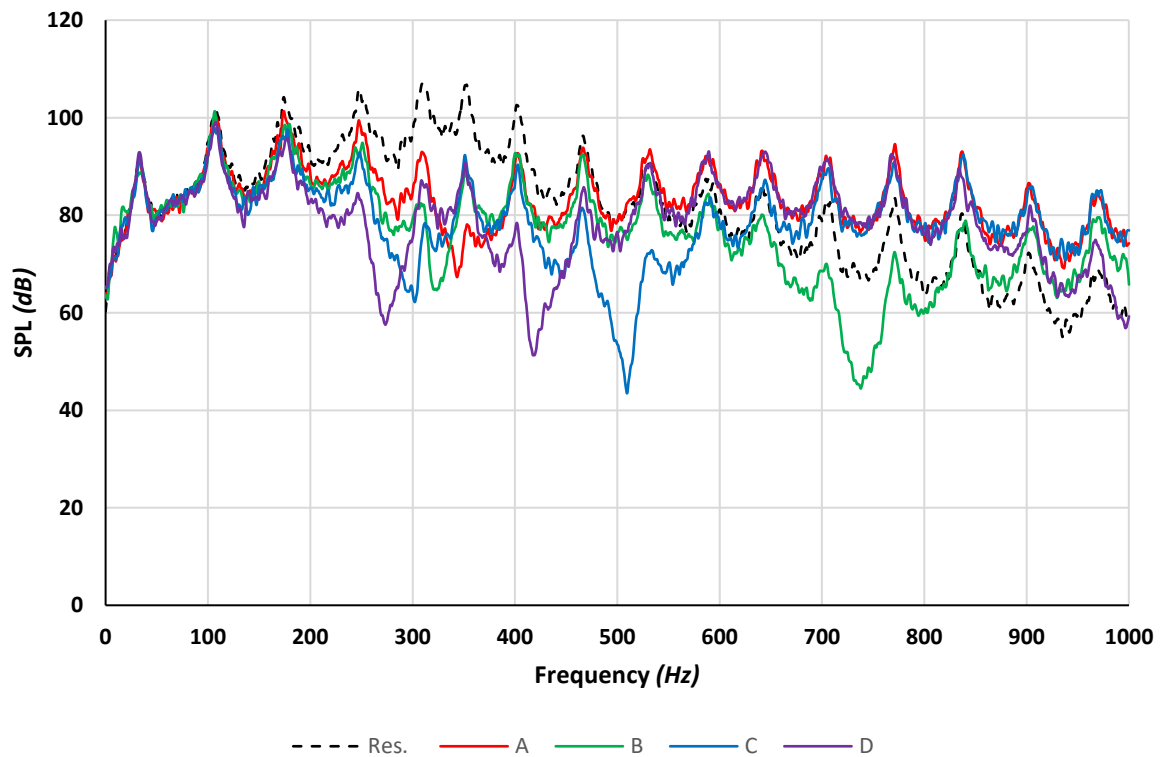
Figure 53 - Measured SPL of Acoustic Excitation Signal according to each available Impedance Tube duct wall measurement location, and a comparative in-resonator measurement.

From this initial investigation it can be seen that the measured response for a common signal, is not equal at all measurement locations, confirming the existence of non-planar waves within the duct, and indicating the significance of spatial sensitivity in measurements.

A similarity between all cases can be seen in the region of 200Hz-450Hz, in that the measured duct acoustic pressure around this frequency is consistently lower at all observed locations, than the equivalent magnitude within the resonator. This phenonium can be considered to be indicative of the resonant frequency for this particular resonator case, resulting in the attenuation of the magnitude of these frequencies within the duct.

What is however more revealing, is the observed existence of multiple significant dips in measured amplitude, which are unique to each measurement location, and which are indicative of the presence of standing waves and/or boundary interference within the duct. Lack of appropriate appreciation of such spatial characteristics would introduce significant potential for error any deduced resonator performance metrics, if not duly accounted for.

Figure 54 shows an example of this, whereby each duct measurement location was used to derive the frequency response function (FRF) of this initial resonator case, and here too the spatial significances can be observed, as both shifts in observed peak response frequency are witnessed, and the inclusion of additional indicated peaks are indicated.
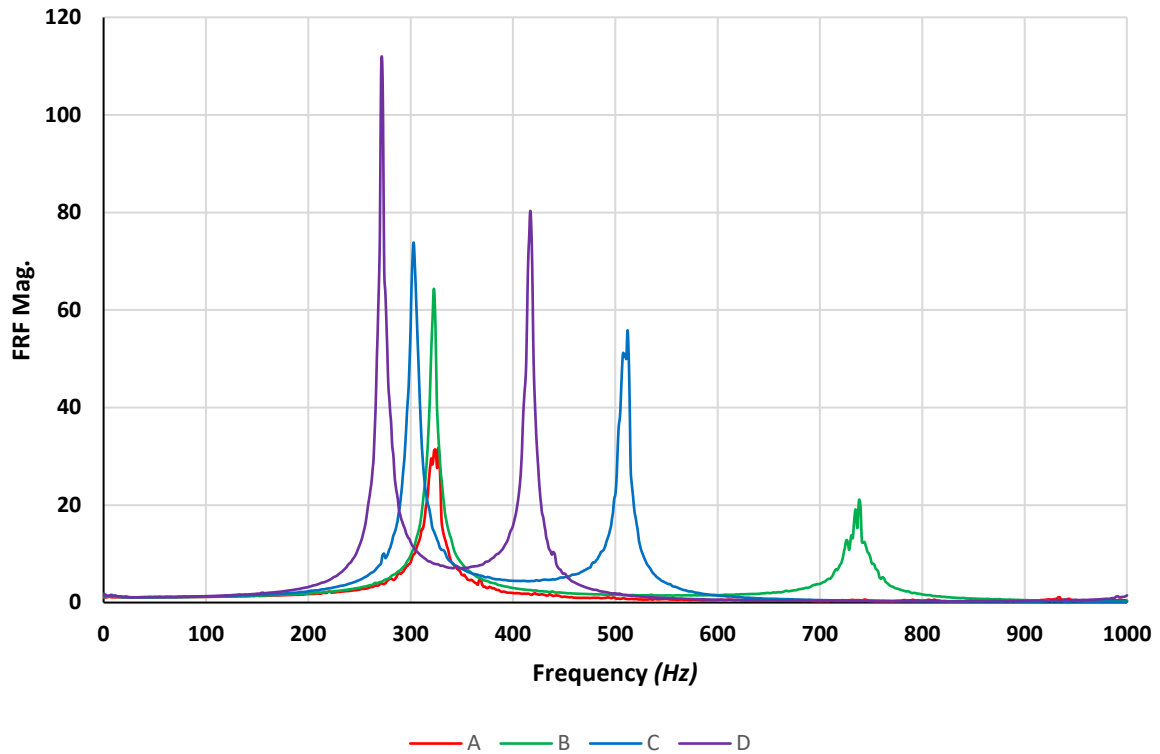
Figure 54 - FRF derived using in-resonator wall measurement and Duct Wall locations A, B C, & D.

From careful comparison of the measured resonator response seen in *Figure 53*, and the corresponding measured duct SPL spectra, it can be appreciated that the most likely true resonator response for the investigated case is in the region of 200Hz-450Hz; a response which is further validated by the FRF results witnessed in *Figure 54*. It can also be noted that the near-neck measurement location [A], is the only location to not exhibit multiple peaks, in addition to exhibiting the best coherence with the observed resonator response.

As the end of the impedance tube is a solid wall, and hence cannot be anechoically terminated, the best mitigation to boundary interference and spatial sensitivities, is to ensure the measurement distance is minimised. For example, if we consider the measurement distance from an acoustically significant feature, such as the end of the duct in terms of its corresponding ¼ wavelength, it can be surmised that location 'A' may succumb to boundary interference resulting from duct-end reflections in the region of 11kHz, a frequency far beyond the upper limit of interest for these discrete resonator cases.

As such it can be concluded that for measuring discrete resonator performance in an impedance tube, under incident Gaussian White Noise acoustic excitation, and using FRF as the primary performance metric, a near-neck duct wall measurement location should be used. Hence, duct measurement location [A] will be used exclusively in the evaluation of attenuation performance for all subsequent discrete resonator impedance tube investigations.

4.5.2   Evaluation of Acoustic Excitation Methodology

The acoustic excitation methodology for the investigation of resonator performance in the impedance tube, consists of the generation of a continuous Gaussian Noise signal from a Tektronix AFG3022B Series Signal Generator *(As shown in Figure 48)*, which is subsequently amplified and used to drive a box mounted loudspeaker as the sound source.

In order to appreciate evaluate the resultant acoustic excitation environment seen by the resonator, an initial acoustic measurement sample was recorded from within the duct, at the wall location nearest the resonator *(Figure 44 - [5])*. From which the RMS value of the SPL in the duct could be deduced from the time-domain as 94.67dB, and the distribution of sound pressure level across the frequency domain, as shown in *Figure 55.*
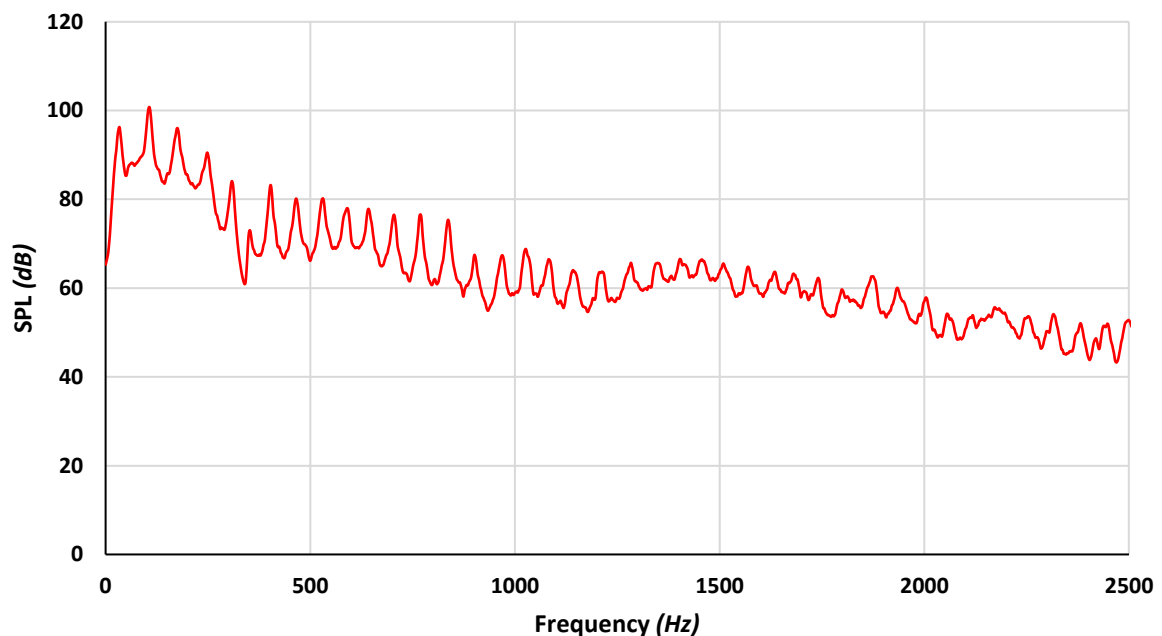
Figure 55 - Measured SPL of Gaussian Noise Acoustic Excitation Signal in Impedance Tube Duct

It can be gleaned from Figure 55 that there exists within the Impedance Tube duct acoustic excitation frequencies beyond those of the plane wave cut-off frequency of the duct of approximately 2,400Hz. This is due to the fact that the excitation signal itself has no corresponding band-pass filter applied, and as such it should be appreciated that there will exist higher order modes of acoustic excitation spatially within the geometry of the duct, and the resonator accordingly.

Irrespective, the measured sound pressure level across the bandwidth of measurement interest *(nominally 100Hz – 600Hz),* can be considered sufficient to excite the relevant resonator configuration, such that a clear resonant response can be observed, especially in that there is no competing noise

generation within the Impedance Tube due to the no-flow scenario, and hence a signal to noise evaluation is not necessary.

It is however pertinent to further investigate the significance of any inherent spatial variations in the measured acoustic pressure field as a result of the existence of higher order excitation modes, in particular any which may exist within the measurement bandwidth of interest. As such, the subsequent sections will investigate the acoustic significance of available measurement locations.

4.5.3 Evaluation of Resonator Measurement Location Sensitivity

As discussed in the previous section, in which an evaluation of duct measurement location sensitivity was presented, it is just as pertinent to evaluate potential resonator measurement locations; thus, considering any inherent spatial considerations or acoustic significances, which left unappreciated, could compromise the integrity of subsequent sound attenuation performance evaluations.

The variable volume Helmholtz resonator employed for this study has, by design, two potential in-resonator measurement locations, as seen in *Figure 56*; one is flush with the cylindrical surface of the resonator cavity wall, at a fixed axial distance of 26mm from the resonator neck; and the other is flush with the variable volume adjustment piston wall, and hence its distance from the neck varies according to the set cavity length/volume case.
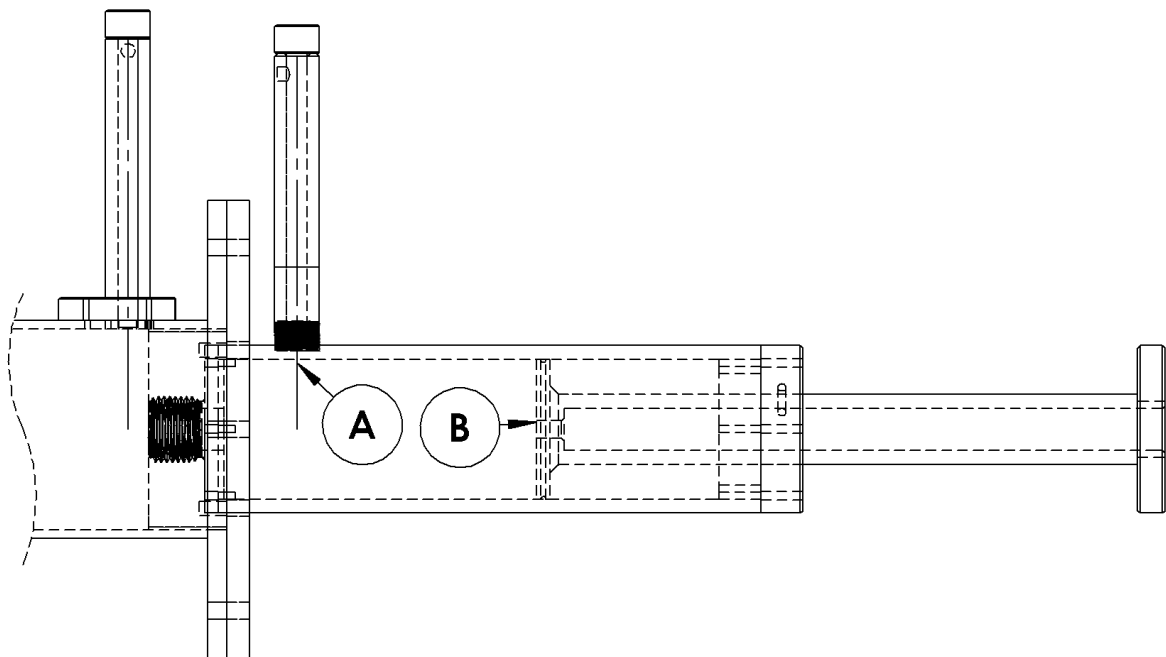
Figure 56 - Schematic showing available in-resonator measurement locations: (A) - Tangential with Resonator wall & (B) - Flush with piston wall

In order to appreciate the acoustic significance of these two locations in terms of a deduced frequency response function, the baseline Ø15mm resonator neck and the previously investigated Volume Case #7, will be utilised to provide a direct comparison of measured response. This initial investigation was also extended to the largest (Case #14) and smallest (Case #1) cavity volumes, such that any significances which may occur towards the extreme geometry cases can be fully appreciated, the results of which can be seen in *Figure 57.*
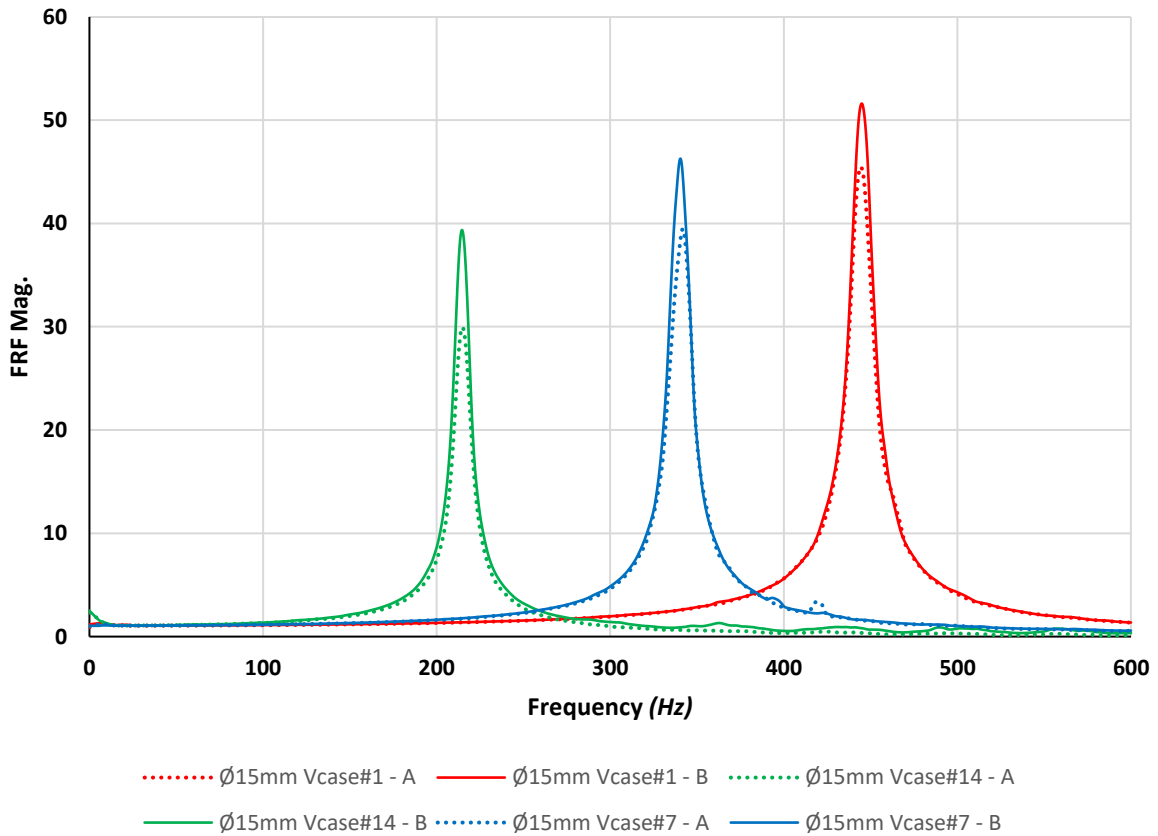
Figure 57 – FRF for Ø15mm neck and various cavity volume cases, using varied in-resonator measurement locations: (A) - Tangential with Resonator wall & (B) - Flush with piston wall

From these results it can be seen that there is a comparable FRF response derived using both in-resonator locations, in terms of both peak response and distribution, which also holds true across all investigated cavity volume cases. It can however be noted that the peak FRF magnitude is consistently larger for all cases using location B (Piston Wall), and that the distribution for these responses, is more normal within the near-resonant bandwidth, when compared to those deduced from location A (Resonator Wall). Given that the same duct measurement location (Duct wall, near neck) has been used for both derivations of FRF, it can be reasoned that the measured acoustic pressure response is larger in magnitude at the piston wall, than it is at the cavity wall. This is likely due to the predominantly perpendicular incident nature of the incoming pressure field at the piston wall, as opposed to the primarily tangential incidence at the measurement location within the cavity wall.

Irrespective, from Figure 57, it can be appreciated that either location could be used with confidence for the standard Ø15mm neck and all cavity volume cases under investigation, so long as each location is used exclusively, when extrapolating any trends or characterisations relating to FRF magnitude.

In order to exhaustively evaluate the significance of these measurement locations, it is appropriate to also investigate the lower extremities of neck diameter and equivalent neck diameter ratios. As such, the smallest available neck diameter of 3mm, was also deployed for the equivalent measurement methodology, and the results from this investigation can be seen in *Figure 58.* For the Ø3mm neck cases, there is a much more prominent variation in the FRF witnessed from each corresponding resonator measurement location. The FRF magnitude variation is consistent with that observed from the Ø15mm neck cases however, there is a more prominent shift in the indicated peak FRF frequency observed for all volume cases corresponding to the Ø3mm neck. This too could be a result of the difference between measuring acoustic pressure normal incidence to the excitation source at location B, and the grazing incidence at the resonator wall (location A). It can also be seen from *Figure 58* that there are additional tones noted in frequencies above 250Hz, which are evident across all cases, but notably more prominent in the FRF responses derived from the piston wall (B), and in particular the smallest volume case (Case#1). Given that volume case #1 exhibits the shortest cavity length, and hence closest proximity of the resonator piston to the neck, it can be considered that these tones are a true artefact of the Ø3mm neck and are suspected to be a consequence of evanescent modes; a theory which will be further investigated in CHAPTER 6 - CFD INVESTIGATION.

In addition, the FRF responses derived from the piston wall indicate the existence of infrasonic resonant tones, which are not picked up by the resonator wall derived responses, nor are they prominent in the acoustic excitation signal. As both locations were exposed to the same acoustic excitation and data processing methodology, it can consequently be assumed that these artefacts measured at the resonator wall, are subtle nuances of the physical phenonium of this geometry configuration, and that the resonator piston wall measurement location, offers improved measurement resolution, over the cavity wall location, for an equivalent case.

Consequently, it can be concluded that whilst either in-resonator measurement location can be shown to produce a quality representative FRF response for the extremities of measurements cases within this targeted range, each location should not be treated as interchangeable in subsequent investigations; due to subtle variations in observed peak FRF magnitude and frequency. It can also be concluded that when the magnitude of acoustic significances is small in magnitude, the piston wall measurement location offers superior resolution for an equivalent excitation condition and data processing methodology, making it the preferable measurement location for exploratory threshold investigations.
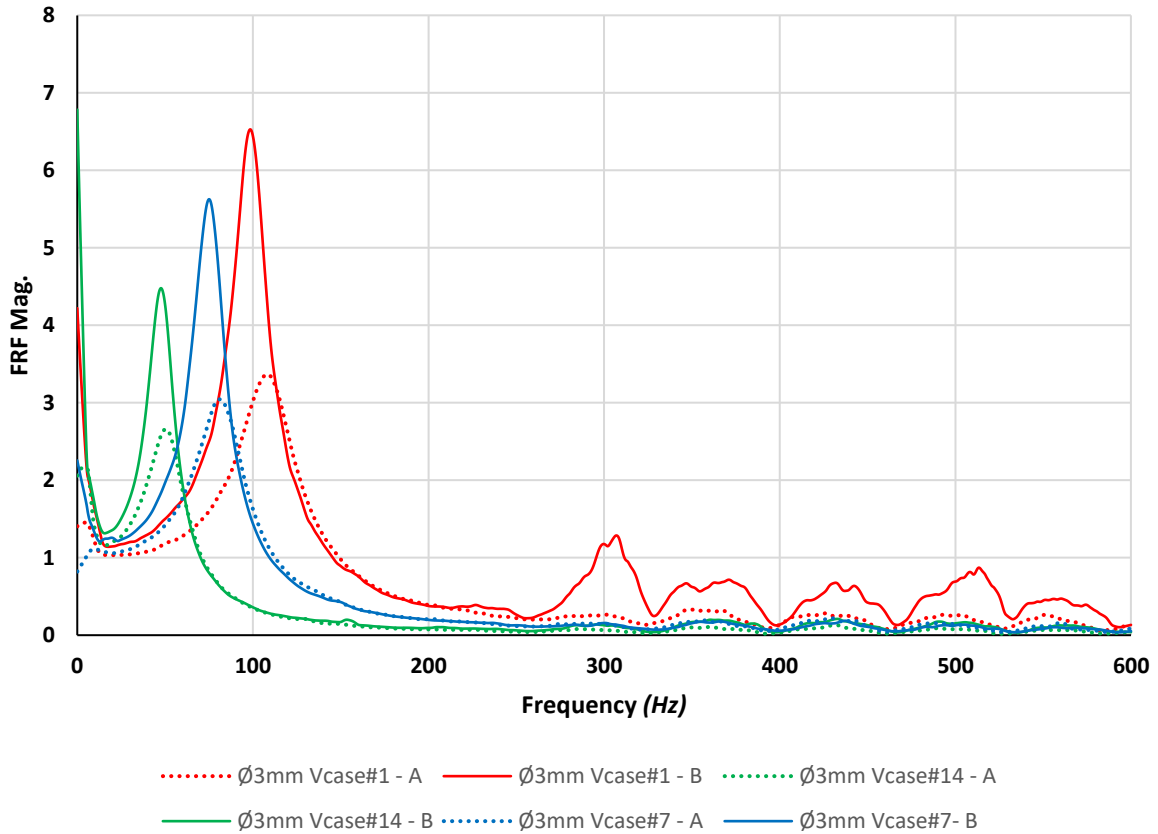
Figure 58 - FRF for Ø3mm neck and various cavity volume cases, using varied in-resonator measurement locations: (A) - Tangential with Resonator wall & (B) - Flush with piston wall

4.5.4   Repeatability Analysis

As adjustment of the variable volume Helmholtz resonators volume requires the careful manual setting of cavity length to set the relevant cavity volume case # for investigation, it is thus beneficial to consider the statistical significance of any characteristic human error imposed by this experimental methodology, on the subsequent results.

To glean an insight into this experimental significance, both the extremities of available neck diameters (Ø15mm & Ø3mm) cases, and all volume cases, were remeasured 6 months after the original measurements were taken. For this investigation, exactly the same rig, operator and data processing regime was used in both cases; ensuring that any observed differences in measured peak frequency, are an honest representation of the combination of human setting error, and minor environmental changes. Therefore, the results from this qualification investigation can be considered an accurate representation of experimental repeatability. The tabular results from each case can be seen in Table 8, and plotted in Figure 59.

Case #	Neck Diameter (mm)	Measured Peak Frequency (Hz)		Experimental Absolute Difference [Hz]	Experimental Percentage Difference [%]
		[Run 1]	[Run 2]		
1	15	444.03	443.88	0.15	0.03%
2	15	425.87	426.79	-0.92	-0.21%
3	15	407.56	410.61	-3.05	-0.74%
4	15	391.54	392.61	-1.07	-0.27%
5	15	375.82	375.82	0.00	0.00%
6	15	357.82	358.89	-1.07	-0.30%
7	15	336.46	340.27	-3.81	-1.12%
8	15	321.66	321.81	-0.15	-0.05%
9	15	302.89	305.79	-2.90	-0.95%
10	15	286.10	287.93	-1.83	-0.64%
11	15	267.64	269.47	-1.83	-0.68%
12	15	250.40	251.16	-0.76	-0.30%
13	15	232.39	233.00	-0.61	-0.26%
14	15	213.93	215.15	-1.22	-0.57%
1	3	109.10	108.34	0.76	0.70%
2	3	104.06	103.76	0.31	0.29%
3	3	100.56	100.10	0.46	0.46%
4	3	94.60	93.69	0.92	0.98%
5	3	92.16	91.71	0.46	0.50%
6	3	87.28	85.45	1.83	2.14%
7	3	81.94	80.26	1.68	2.09%
8	3	76.60	76.90	-0.31	-0.40%
9	3	72.63	71.72	0.92	1.28%
10	3	67.75	67.44	0.31	0.45%
11	3	64.39	63.63	0.76	1.20%
12	3	59.81	58.90	0.92	1.55%
13	3	55.39	54.02	1.37	2.54%
14	3	50.81	50.20	0.61	1.22%

Table 8 - Results of discrete resonator repeatability analysis for min and max neck diameter, and all volume cases.
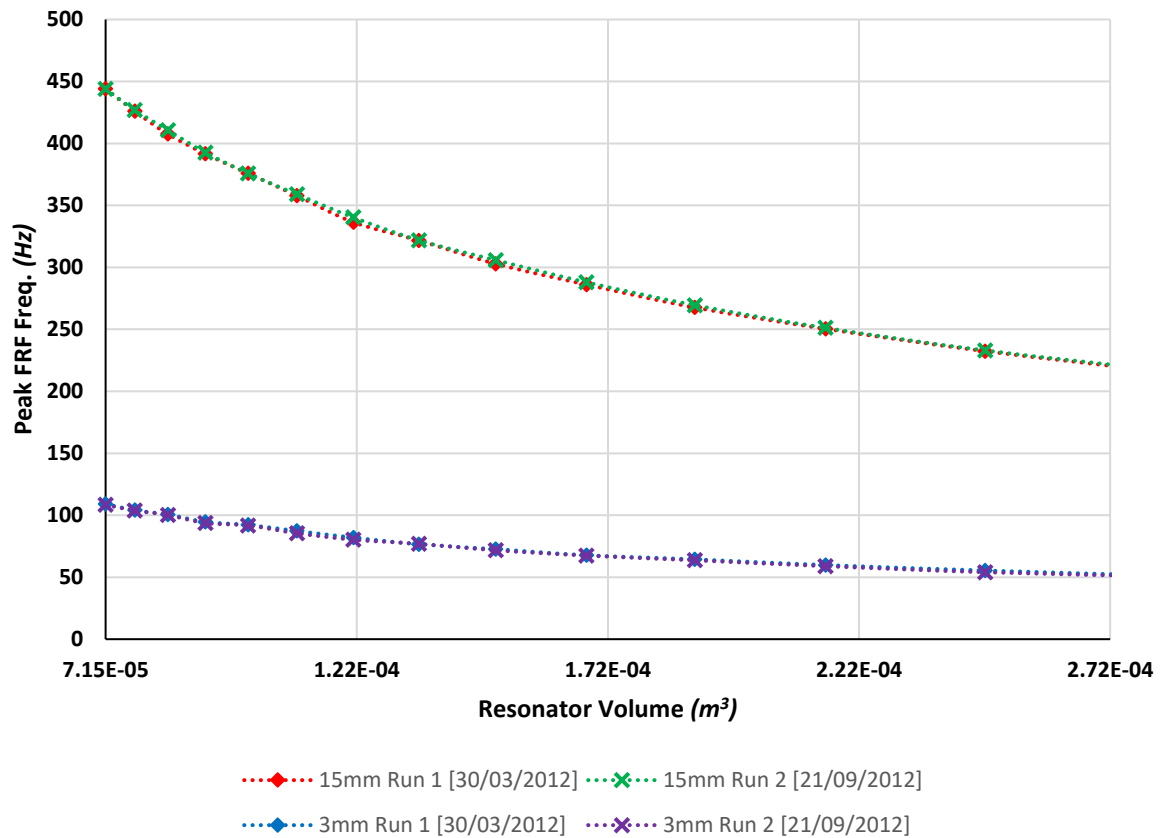
Figure 59 - Repeat measured peak FRF magnitude across all volume cases & extremes of neck diameter

From these results it can be seen that good measurement repeatability can be achieved for the manual cavity volume specification across the full range of cavity volumes defined in this experimental methodology. A summary of the key statistical findings can be seen in *Table 9*, where it can be concluded that an average absolute experimental repeatability of approximately 1Hz, or 0.75%, is a good representation of this experimental method, and an earnest consideration in the evaluation of subsequent characterisation exercises.

	Experimental Absolute Difference [Hz]	Experimental Percentage Difference [%]
15mm Neck	-1.36	-0.43%
3mm Neck	0.78	1.07%
Average	1.07	0.75%

Table 9 - Summary of repeatability analysis

4.6   Flow Rig Qualification of Measurement Procedures

As with *Section 4.5,* in the following section information will be presented pertaining to the effective prerequisite commissioning of the discrete resonator cross-flow measurement rig, prior to its application in the collection experimental data corresponding to the measurement test cases, described in *Section 4.4.*

Inclusive of this is an evaluation of the Acoustic Excitation Methodology *(Section 4.6.1),* an evaluation of the cross-flow delivery methodology *(Section 4.6.2),* and an evaluation of the acoustic signal to flow generated noise *(Section 4.6.3).*

4.6.1   Evaluation of Acoustic Excitation Methodology

The acoustic excitation methodology for the investigation of resonator performance in the cross-flow rig, is equivalent to that of the impedance tube, as described in *Section 4.5.2.* It also consists of the generation of a continuous Gaussian Noise acoustic excitation signal, which is subsequently amplified and used to drive a box mounted loudspeaker, which is in turn side branch mounted to the flow rig, as shown in *Figure 47 [B].*

In order to appreciate evaluate the resultant acoustic excitation environment seen by the resonator within the flow rig, an initial acoustic measurement sample was recorded from within the duct, at the upstream duct wall location, nearest to the resonator test section seen in *Figure 47 [C].* From this initial measurement the RMS value of the SPL in the duct could be deduced from the time-domain as 78.74dB, and the distribution of sound pressure level across the frequency domain, as shown in *Figure 60.*
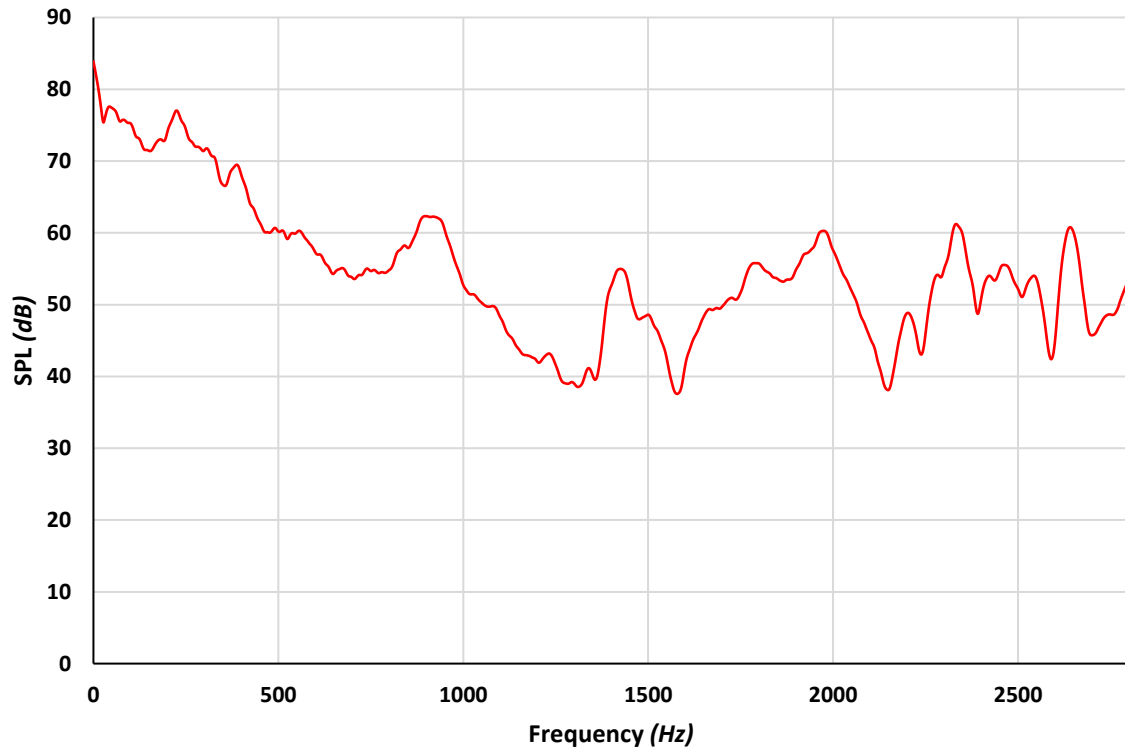
Figure 60 - Measured SPL of White Noise Acoustic Excitation Signal in Flow Rig

As with the Impedance Tube excitation signal, there can be seen to be excitation frequencies present beyond those of the plane wave cut-off frequency of the duct of approximately 2,800Hz. This is also due to the lack of any applied low-pass filter to the acoustic excitation signal and will subsequently result in the existence of higher order modes of within the duct.

Irrespective, the measured sound pressure level across the frequency bandwidth of interest (nominally 100Hz-600Hz), remains the primary interest for initial measurements. Similarly, the measured SPL and distribution of signal frequencies within this region, can be considered sufficient to excite any of the relevant resonator configurations specified in this measurement methodology. Unlike the Impedance Tube however, the significance of any cross-flow generated noise must also be considered, and this will be evaluated in *Section 4.6.3* accordingly.

4.6.2 Evaluation of Cross-flow Delivery Methodology

In order to characterise the cross-flow delivery capabilities of the discrete resonator flow rig, the velocity profile was measured at two key locations, the measurement section, and the anechoic termination. Measurement of the cross-flow velocity at various radial locations at both axial locations, allows evaluation of the condition of the flow development within the rig, in addition to the determination of maximum and average cross-flow velocity. The resultant cross-flow velocity profile at the measurement rig and the anechoic termination, can be seen in *Figure 61 & Figure* 62 respectively.
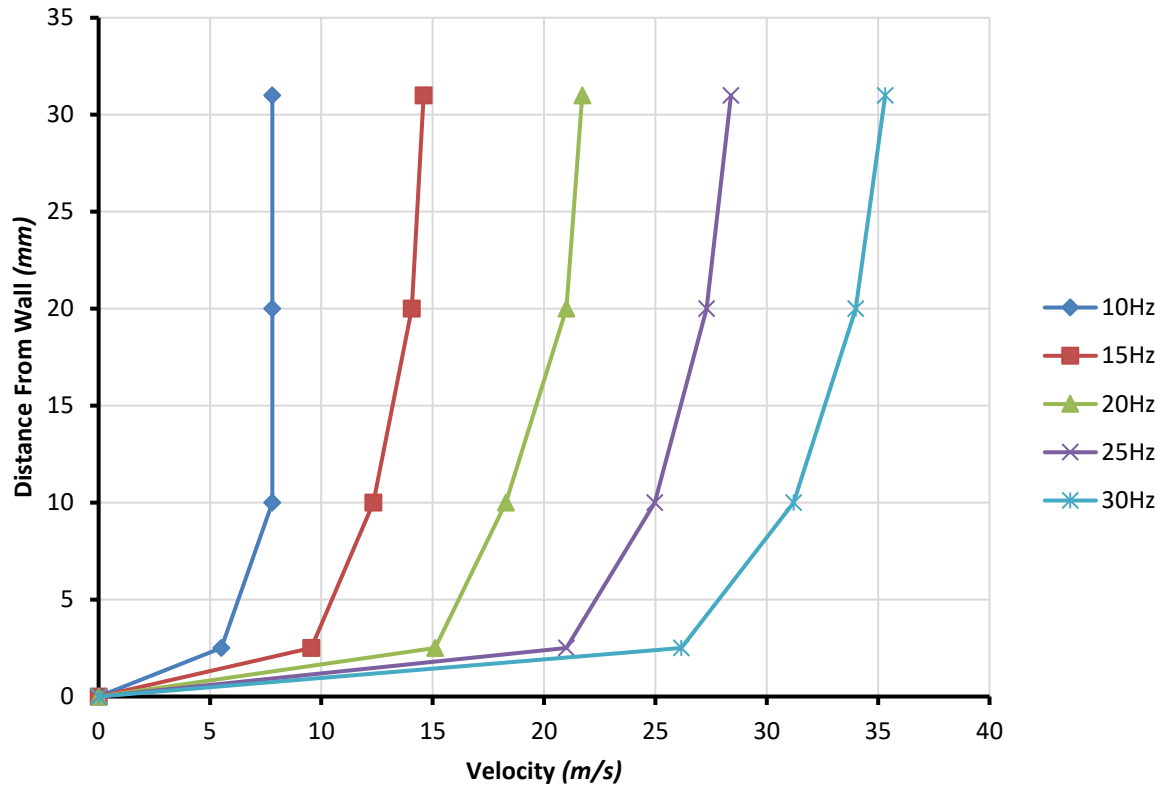
Figure 61 - Cross-flow Velocity Profile, as measured at resonator port, for 5Hz increments in supply fan motor controller driving electrical frequency.
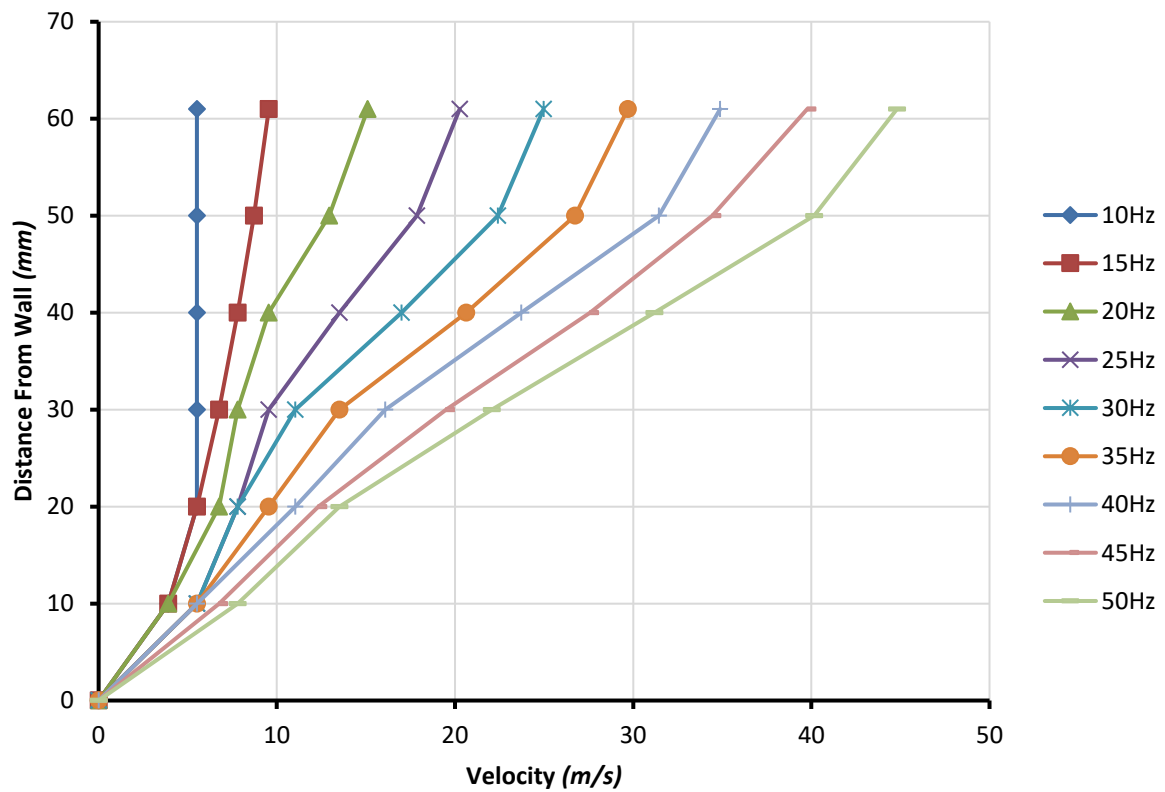
Figure 62 - Cross-flow Velocity Profile, as measured at Anechoic Termination outlet, for 5Hz increments in supply fan motor controller driving electrical frequency.

From the measured velocity profile, the geometric properties of the duct at each location, and the thermodynamic properties at the time of measurement, the relevant mass flow rate for each condition and location can be determined. The measured velocities and corresponding calculated mass flow rates for both locations, can be seen in *Table 10 and Table 11* respectively.

Fan Frequency (Hz – Electrical)	Max Velocity (m/s)	Mean Velocity (m/s)	Mass Flow Rate (kg/s)
10	7.80	6.25	6.40E-02
15	14.59	10.81	7.48E-02
20	21.71	16.31	8.97E-02
25	28.39	21.87	1.17E-01
30	35.32	27.25	1.32E-01

Table 10 - Table Showing Cross-flow delivery velocity, and corresponding mass flow rate, at resonator port location

Fan Frequency (Hz – Electrical)	Max Velocity (m/s)	Mean Velocity (m/s)	Mass Flow Rate (kg/s)
10	5.52	4.79	6.40E-02
15	9.55	6.24	7.48E-02
20	15.10	8.08	8.97E-02
25	20.26	10.73	1.17E-01
30	24.97	12.71	1.32E-01
35	29.70	15.13	1.55E-01
40	34.88	17.54	1.77E-01
45	39.77	19.67	2.04E-01
50	44.81	22.85	2.33E-01

Table 11 - Table Showing Cross-flow delivery velocity, and corresponding mass flow rate, at Anechoic Termination outlet location

A comparison of the derived mass flow rate at both investigated locations, in relation to the corresponding variable-frequency motor controller driving frequency, can been seen in *Figure 63*, and the direct correlation between locations and delivery rates, both validates the measurement method, and rig configuration; in regards to the delivery cross-flow.
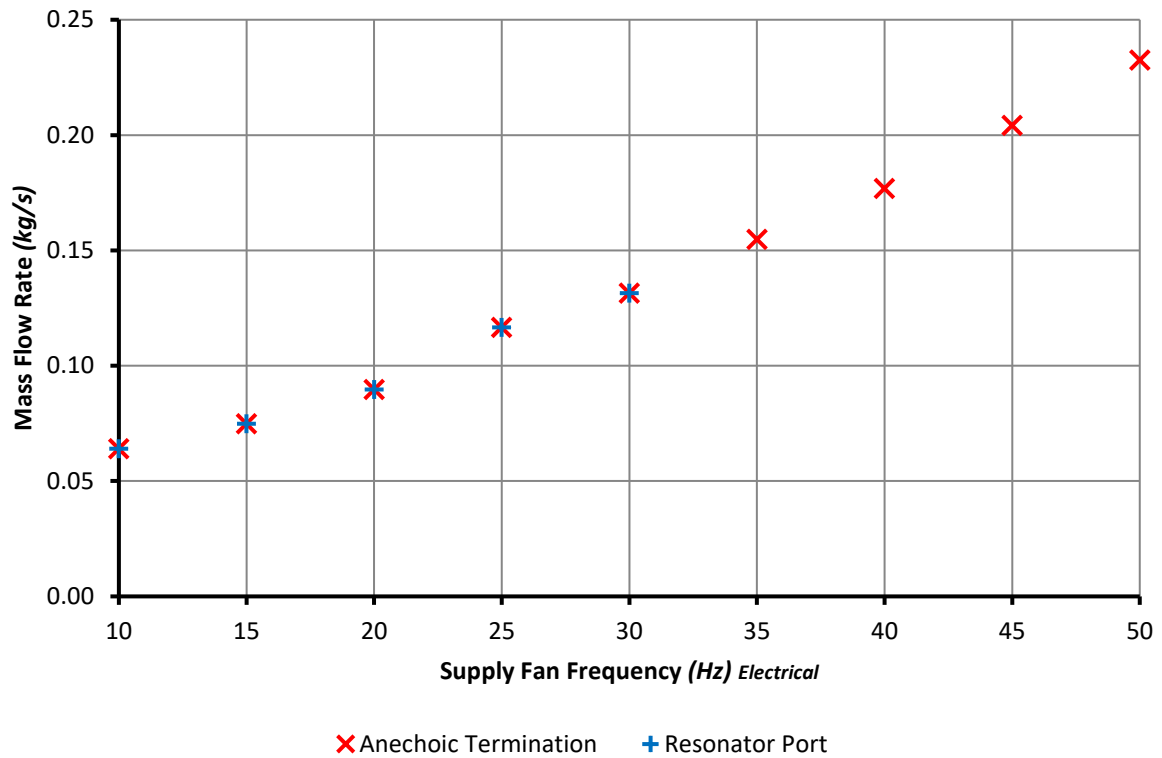
Figure 63 - Calculated Mass Flow Rate location comparison, against driving fan electrical frequency (Hz)

The results of this investigation signify that there is a fully developed flow within the measurement section of the rig, with a relatively small boundary layer and an expected velocity profile at both locations. These results also allow the mapping of cross-flow supply properties to the driving electrical frequency to the supply fan, which is set via the digital motor controller interface to vary the fan's rotational frequency. This mapping ensures that a known and repeatable delivery mechanism is achievable, with only minor seasonal variations in velocity and mass flow rate expected, as a result of air density variations.

4.6.3   Evaluation Acoustic Signal to Flow Noise Comparison

In order to appreciate the significance of any flow generated noise on the acoustic excitation experienced by any subsequent discrete resonator cases under investigation, the equivalent investigation described in *Section 4.6.1,* was repeated in the presence of varying cross-flow delivery magnitudes. The results from this investigation, this time focused on the frequency domain of primary interest, can be seen in Figure 64. From these results it is evident that the cross-flow delivery mechanism within this rig generates its own acoustic noise, and to a magnitude which surpasses the acoustic signal generation capability. Regardless, it can be seen that the resultant flow generated noise presents in itself, an effective distribution of excitation frequencies within the measurement bandwidth of interest.
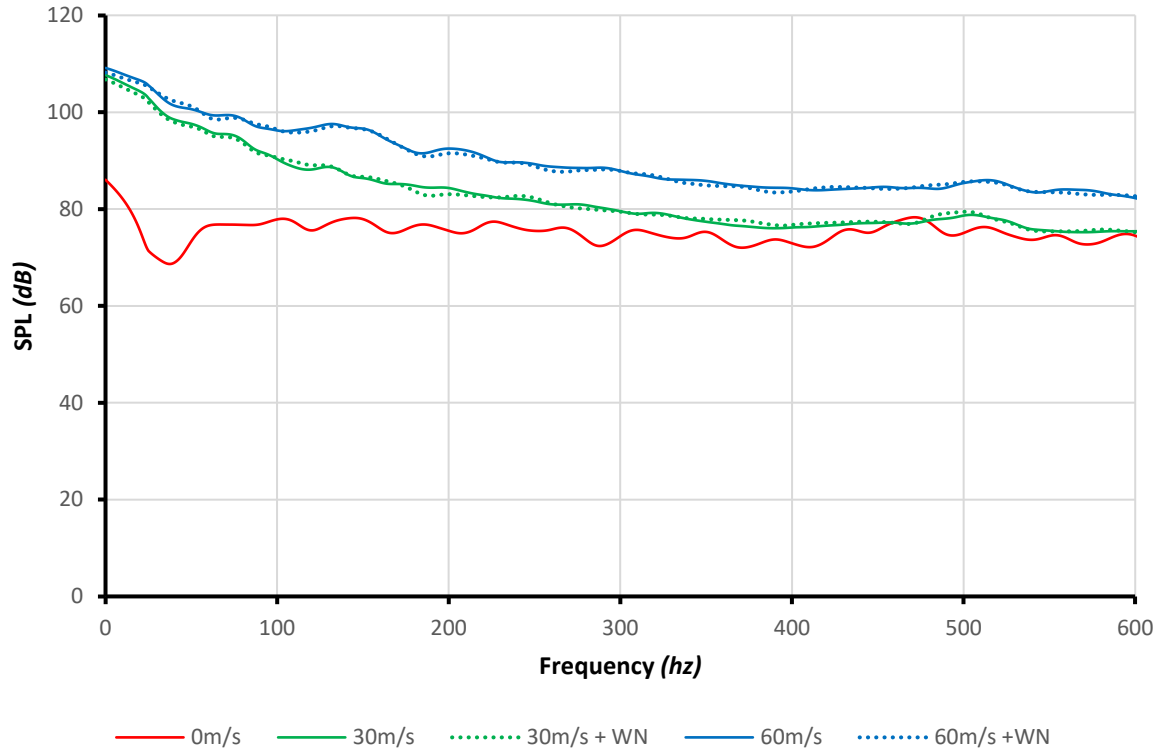
Figure 64 - Measured SPL of Acoustic Excitation Signal, in the presence of cross-flow of varying magnitude

Furthermore, it can be noted that the significance of the superposition of the acoustically generated noise signal on the flow generated noise, is negligible; indicating that the flow noise alone should be sufficient to the excite the discrete resonator cases within the range of planned experimental test cases. It should be noted however, that there remains within this excitation methodology, excitation frequencies beyond those of the planar wave cut off frequency of this rig.

4.7   Discrete Resonator Experimental Methodology Summary

Within the previous chapter a systematic experimental design methodology is applied to facilitate the development of a robust experimental regime, which is focused on gaining novel insight into fundamental discrete acoustic resonator noise attenuation characteristics. Following a comprehensive explanation of the target investigation strategy, and the necessary tools and techniques required to permit effective evaluation, the resultant parameters, permutations, and measurement methodologies are explicitly defined.

The ensuing test matrix consists of 14 defined cavity volumes; 5 standard cylindrical necks of fixed length, and varying diameter; 14 additional neck geometries, consisting of an alternative baseline cylindrical neck, fixed length, common nominal diameter, and varying termination geometries; and a

defined grazing flow delivery methodology, with a characterised mean flow velocity, mass flow velocity and velocity profile.

Initial qualification investigations are conducted using the intended experimental methodology, which serves as a validation of the targeted design and implementation strategies and provides additional insight into the salient characteristics of the measurement apparatus and methods. The conclusions drawn from the closing qualification exercises, serve to set the scene for an effective and rigorous evaluation of collected experimental results in the subsequent chapter, and the subsequent characterisation of key noise attenuation performance factors.

CHAPTER 5 - RESULTS & DISCUSSION: DISCRETE RESONATORS

In the following Chapter the measurement results obtained from the aforementioned experimental design methodology will be presented, discussed and evaluated in relation to coherence with the current state of the art in relation to known acoustic resonator attenuation performance factors.

Conventional geometric factors will initially be investigated; with a particular focus on practical implications of exceeding the thresholds parameters of common assumptions which underpin typical modelling methods; and the impact on peak resonant frequency predictions and noise attenuation potential.

It begins with Section 5.1, within which evaluation of attenuation performance characteristics are obtained through impedance tube measurements, under exposure to a white noise acoustic excitation signal, for a large test matrix of seventy variations in neck diameter and cavity volume. The results from which facilitates an evaluation of the accuracy of predictions using the current state of the art, and the inherent limitations of commonly applied assumptions. Subsequent to comparison with existing modelling methods, a new empirical model for effective end correction is proposed, which factors in sensitivity to spatial factors not currently captured by existing models.

In Section 5.2, attenuation performance factors associated with neck termination are investigated, leading to a comparison with existing acoustic horn theory, and highlighting the potential of alternative neck termination geometry to improve the acoustic attenuation performance of Helmholtz resonators.

The final experimental investigation of this Chapter, Section 5.3, investigates the impact of varying degrees of grazing flow on the acoustic attenuation performance of a representative geometry case, and serves as a preamble to later grazing flow investigations on distributed resonators, seen in CHAPTER 8 - RESULTS: DISTRIBUTED RESONATORS.

5.1 Neck Diameter & Cavity Volume Effects

The results of the measured Frequency Response Function (FRF) for all seventy standard neck diameter and cavity volume variations are presented in Figure 65 - Figure 69. Here each discrete plot shows the FRF magnitude against frequency for each of the fourteen measured cavity volume variations, according to Table 6; and each plot corresponds to one of the five standard cylindrical neck geometries, as detailed in Table 7.
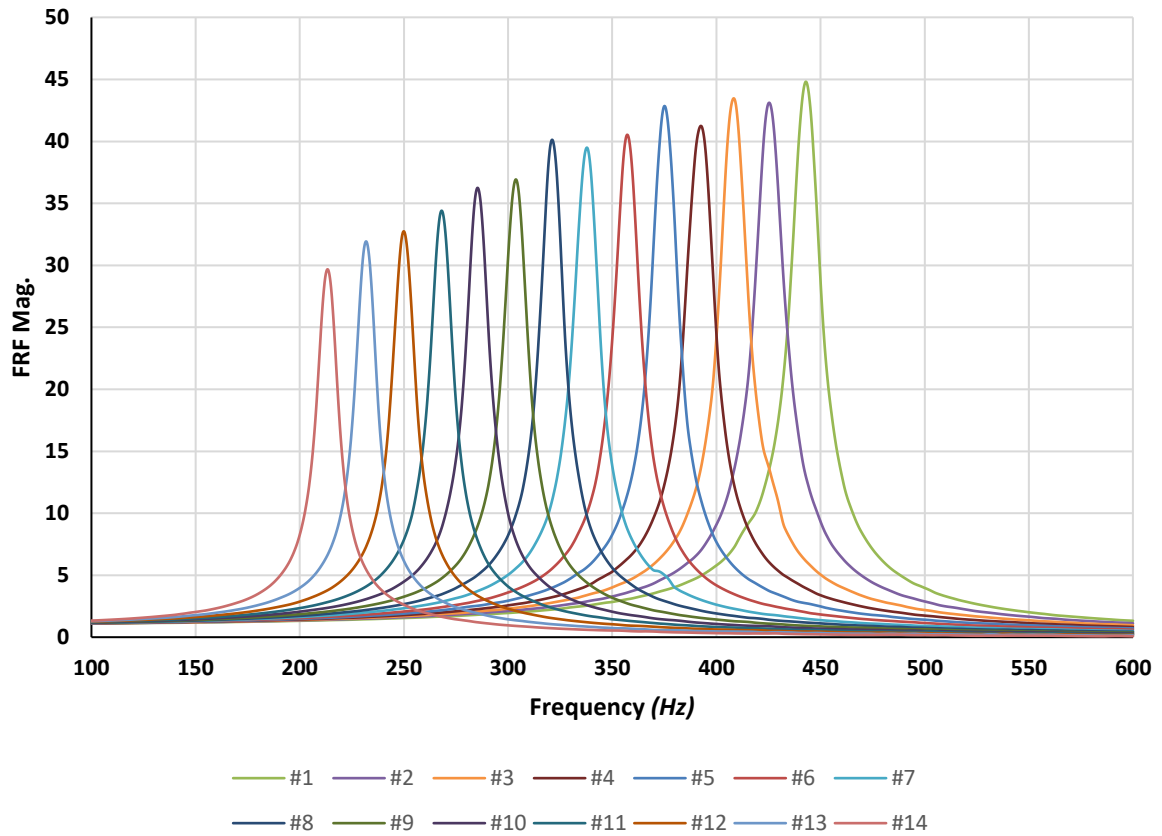
Figure 65 - FRF Magnitude for Neck Ø15mm and Cavity Volume case #1-14
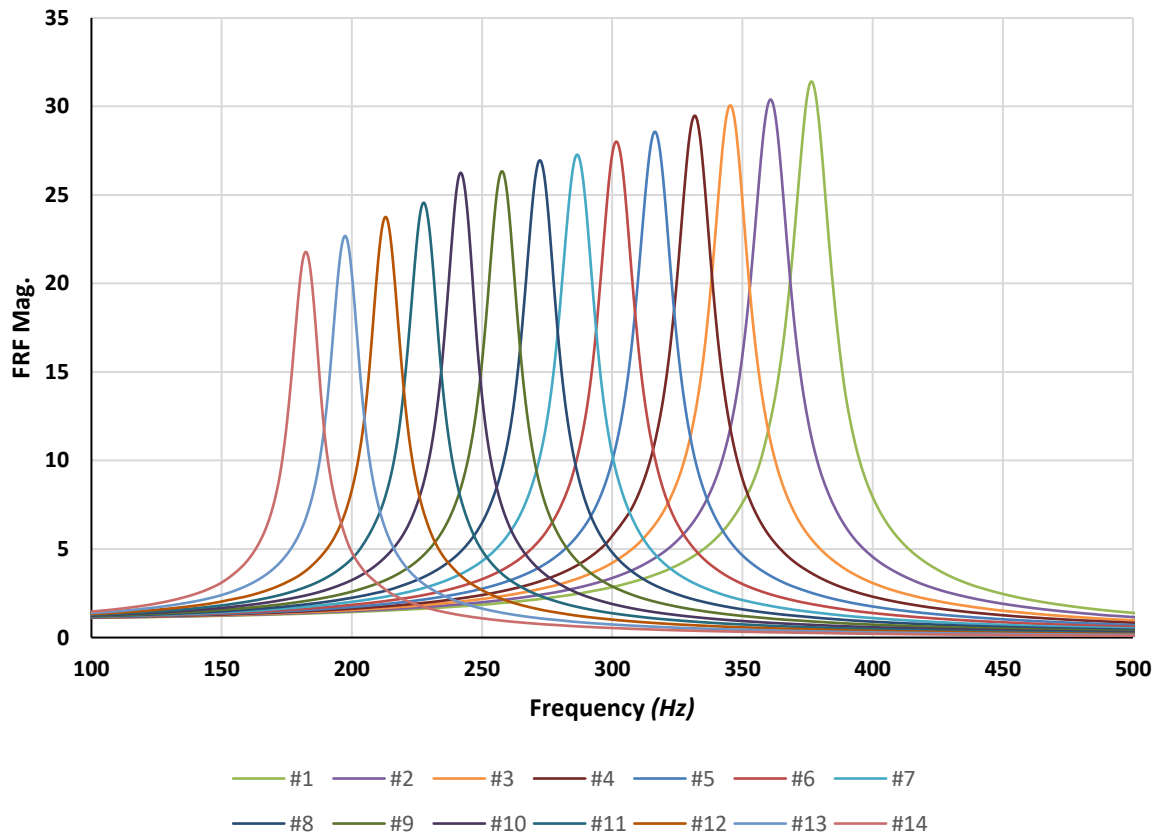
Figure 66 - FRF Magnitude for Neck Ø12mm and Cavity Volume case #1-14
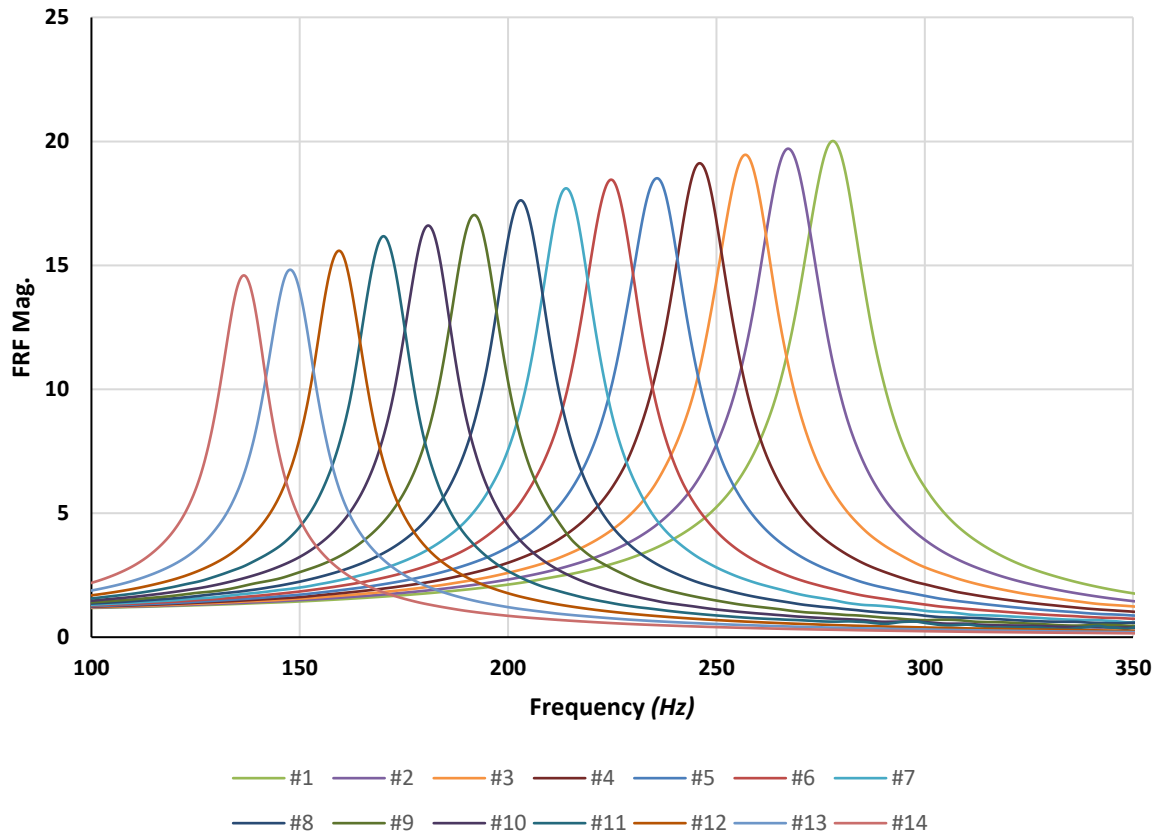
Figure 67 - FRF Magnitude for Neck Ø9mm and Cavity Volume case #1-14
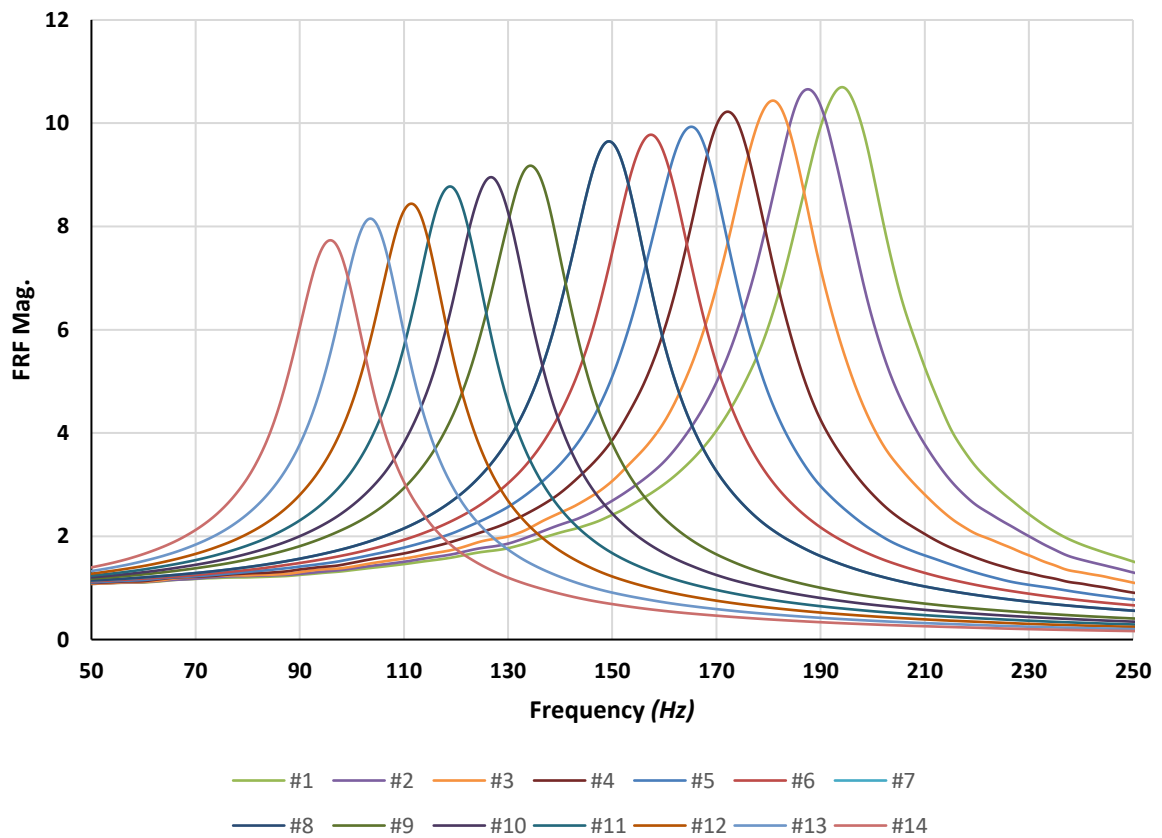
Figure 68 - FRF Magnitude for Neck Ø6mm and Cavity Volume case #1-14
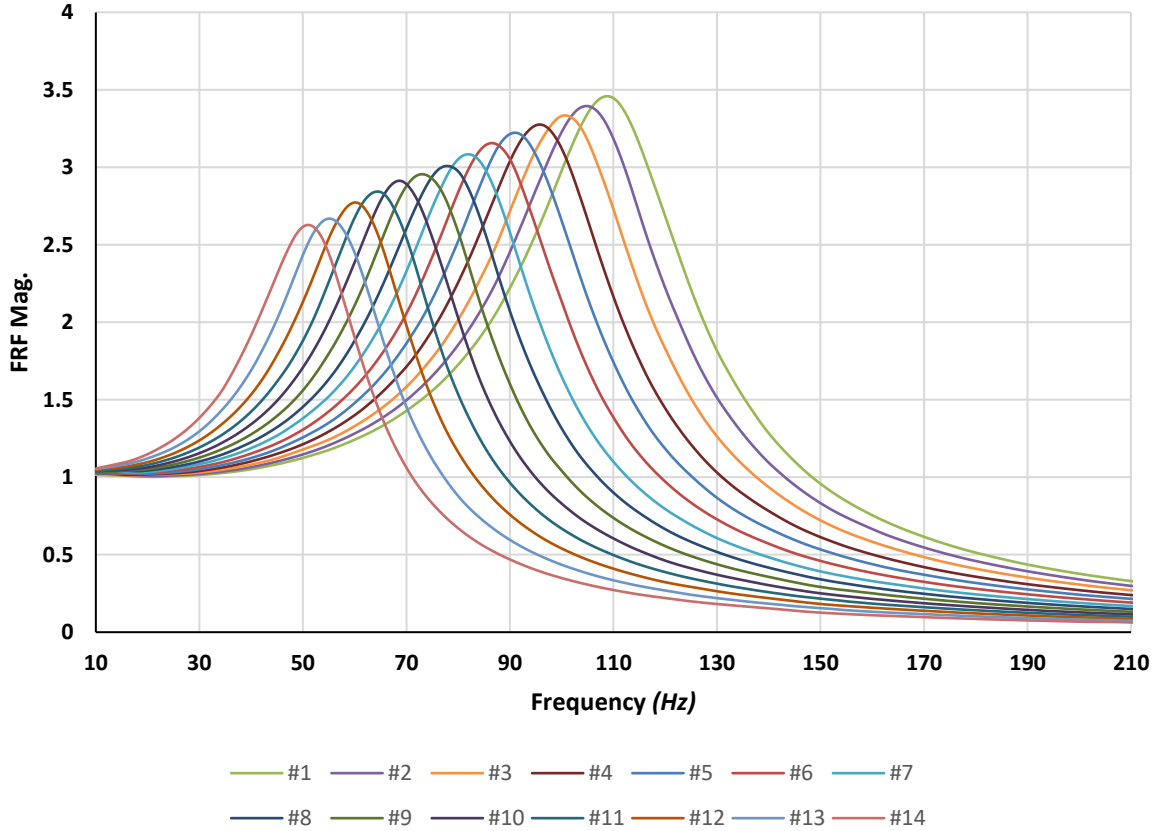
Figure 69 - FRF Magnitude for Neck Ø3mm and Cavity Volume case #1-14

By plotting the measured peak attenuation FRF magnitude against the peak resonant frequency for all measured cases, as shown in Figure 70, an overview of the full spread of results obtained from the experimental design methodology can be appreciated. Here too it can be seen that the trends apparent from Figure 65 - Figure 69, whereby a reduction of the cavity length, and subsequently cavity volume; not only reduces increases the resonant frequency as expected, but also tends to produce a proportionally larger attenuation potential; evidenced by an increase in FRF magnitude.

This observation is of practical significance, as if a particular detrimental frequency is to be targeted for attenuation by an acoustic resonator, the designer of the mitigation mechanism has some choices to make in terms of the geometric parameters of the device. From these results it can be appreciated that within the range of parameters investigated, there exists multiple permutations which could all equally effectively attenuate the same detrimental frequency; for example, attenuating a target frequency of circa 250Hz could practically be achieved with a resonator of either a Ø9mm, Ø12mm or Ø15mm neck, and the corresponding cavity volume; however, the relevant Ø15mm neck case exhibits an approximately 55% larger FRF magnitude than the equivalent Ø9mm neck case; hence if the design scope permits it, this particular permutation would result in a greater attenuation efficacy.
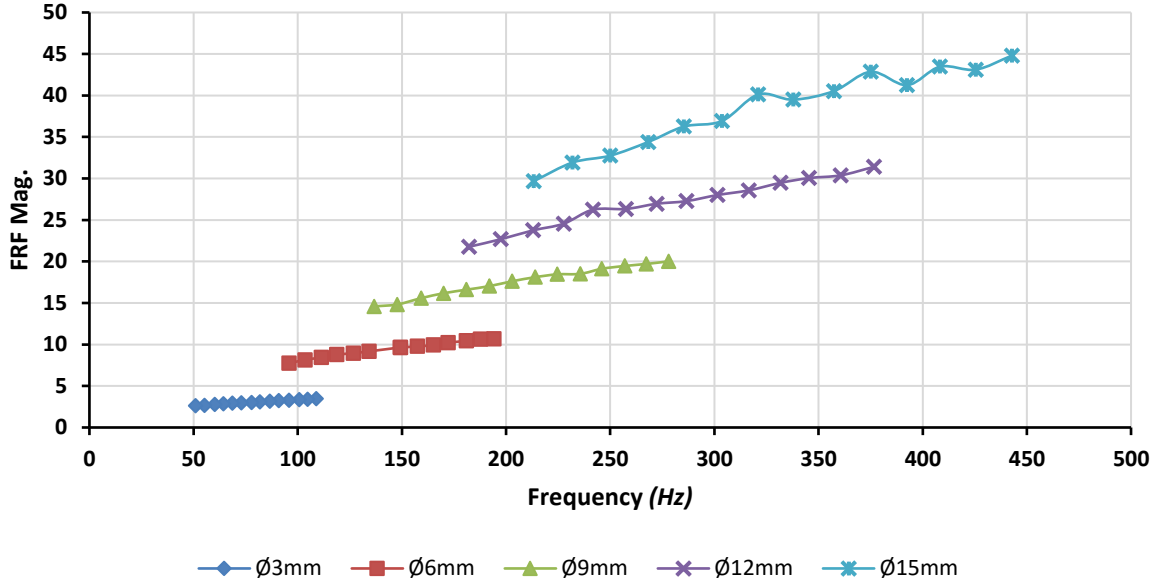
Figure 70 - Peak FRF Magnitude for all investigated Cavity Volume Cases and Neck Diameters

For the purposes of brevity, and subsequent comparison with analytical prediction methods, the measured peak absorption frequency values for all cases invested can be seen in numerical form in Table 12, along with the corresponding geometric characteristics of both the resonator necks, and cavity volumes for each case.

Measured Peak Absorption Frequency (Hz)								
	Neck Properties			1.5	3	4.5	6	7.5	r_o
				0.06	0.12	0.18	0.24	0.3	r_o/R
Cavity Properties				0.04	0.08	0.13	0.17	0.21	r_o/a
				9.05	4.53	3.02	2.26	1.81	L_n/D_n
#01	71,506	36	0.73	98	193	278	372	445	
#02	77,341	39	0.79	95	184	268	357	428	
#03	83,921	43	0.85	91	177	257	343	410	
#04	91,377	47	0.93	87	169	245	328	393	
#05	99,872	51	1.02	83	163	235	314	376	
#06	109,610	56	1.12	79	155	224	300	358	
#07	120,850	62	1.23	75	147	213	285	340	
#08	133,900	68	1.36	71	140	202	270	323	
#09	149,190	76	1.52	67	132	191	256	305	
#10	167,260	85	1.70	63	125	180	240	287	
#11	188,820	96	1.92	59	117	169	226	270	
#12	214,840	109	2.19	55	110	158	211	251	
#13	246,620	126	2.51	52	102	147	196	233	
#14	286,020	146	2.91	48	95	136	181	215	
	$V_c\ (mm^3)$	$L_c\ (mm)$	L_C/D_C						

Table 12 - Resonant Frequency across all measured Neck Diameter and Cavity Volume Cases

5.1.1   Comparison with Modelling Predictions

As discussed in previous chapters, accurate prediction of the resonant frequency of an acoustic resonator is not trivial, and dependant on very many geometric and thermodynamic factors. Within this chapter we are focused on principal geometric parameters, under atmospheric and isothermal conditions; as such, and in consideration of the experimental methodology, the solution of the ideal resonator frequency, Equation [142], can be used as a baseline comparison against the measured results. In determination of the effective length parameter for use in the subsequent calculations however, the commonly accepted value of additional acoustic radiation end effect of $2l' = 16r_0/3\pi$ (Kinsler & Frey, 1982), assumes a circular piston of infinite baffle; and this assumption is not appropriate for the physical dimensions of the measurement methodology employed; where the dimensions of the resonator, and the duct, are by design not acoustically insignificant.

Ingard (1953) recognises that whilst this end correction represents a good approximation when the aperture is very small compared to the cross section of the resonator cavity, it can be in considerable error when the cavity geometry has an acoustical influence on the aperture impedance. He also adds that a careful analysis should actually consider different end corrections on the two sides of the aperture, such that the total end correction is the sum of an interior end correction δ_i, and an external end correction δ_e, i.e. $\delta = \delta_i + \delta_e$. Ingard (1953) goes on to define more sophisticated mass end corrections for circular apertures in a circular tube, circular apertures in a rectangular tube, and rectangular apertures in a rectangular tube; and deduces that for geometric ratios of proportionally of $\xi < 0.4$, the end correction on one side of the aperture can be written approximately as:

$$\delta_{i/e} \cong 0.48\sqrt{A_0\big(1 - 1.25\xi_{i/e}\big)} \qquad\qquad [144]$$

Where $\sqrt{A_0}$ replaces r_0 with a more convientant and geometry agnostic representation, allowing application to non-circular apertures; for a circular aperture in a circular cavity $\xi = r_0/R_C$, with R_C being the cavity radius; and for a circular aperature in a rectangular duct $\xi = r_0/a$, with $2a$ being the shorter edge length of the rectangular cavity. Using this modified end correction, the peak absorption frequency for each measured case can be estimated according to Equation *[145]*.

$$f_r = \frac{c}{2\pi}\sqrt{\frac{A_0}{V(l + \delta_{h-w})}} \qquad\qquad [145]$$

Where δ_{h-w} represents the hole-to-wall end correction, corresponding to the sum of the Ingard (1953) mass end correction, Equation *[144]*, calculated for both the internal and external aperture of the

resonator neck under investigation. The results of the two-sided end correction calculations according to Ingard's (1953) theory, can be seen in Table 13; and the corresponding predictions of peak absorption frequency plotted against the measured results are shown in Figure 71 for the full measured data set.

Ingard Hole-to-Wall End Correction Factor					
r_0 (mm)	1.5	3	4.5	6	7.5
A_0 (m^2)	7.45E-06	2.98E-05	6.55E-05	1.25E-04	1.86E-04
r_0/R_C	0.06	0.12	0.18	0.25	0.31
$\delta_{int}/\sqrt{A_0}$	0.44	0.41	0.37	0.33	0.30
r_0/a	0.04	0.09	0.13	0.18	0.21
$\delta_{ext}/\sqrt{A_0}$	0.45	0.43	0.40	0.37	0.35
$\delta_{h-w}/\sqrt{A_0}$	0.90	0.83	0.77	0.70	0.65

Table 13 – Calculation of Ingard hole-to-wall end correction for both sides of the measured apertures, according to Equation [144]
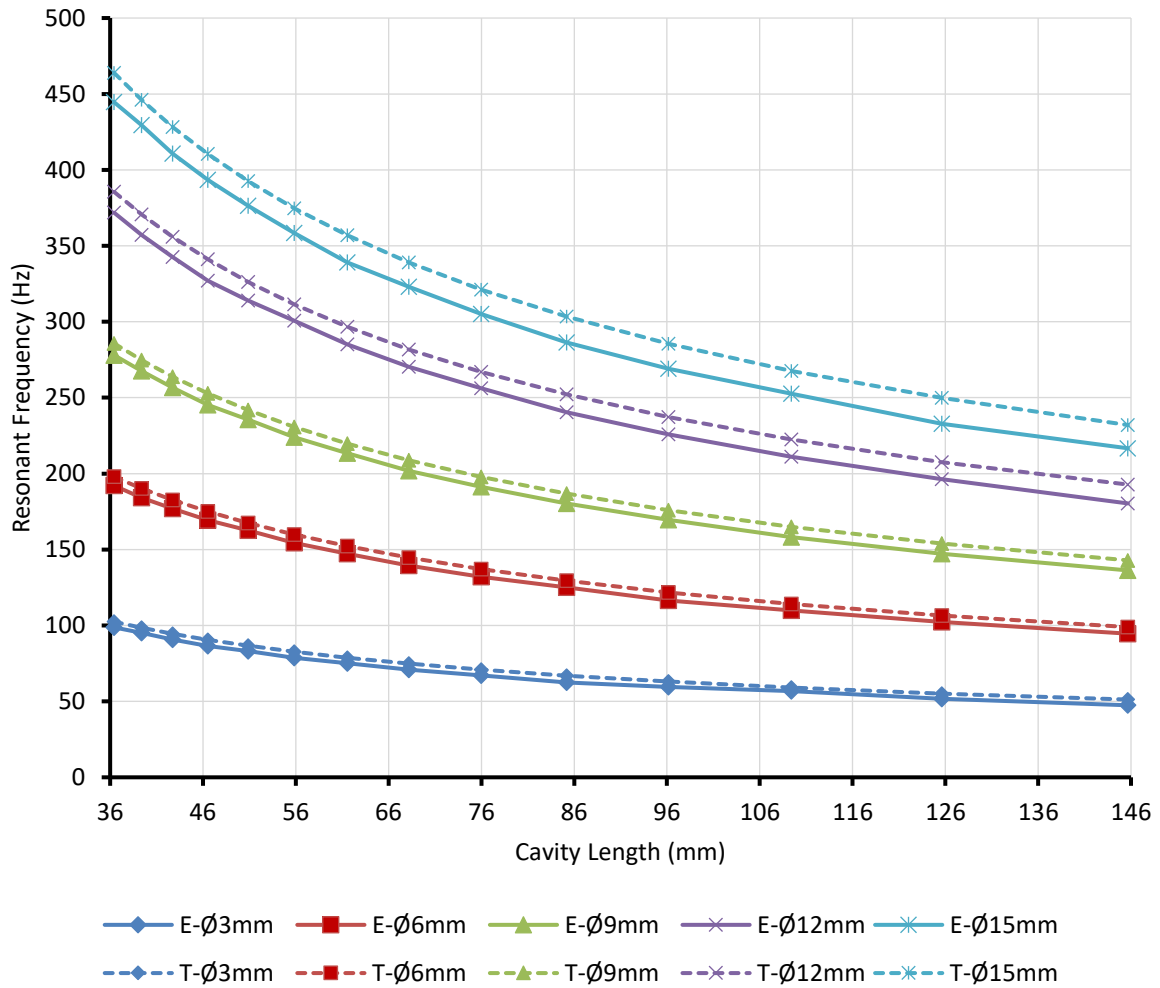
Figure 71 – Resonant Frequency against Cavity Length, for all measured cases of Neck Diameter and Cavity Volume, where E=Experimental & T=Theoretical, as calculated using Equation [145].

From these results it can be seen that whilst the theory is generally in alignment with the measured results across the full data set, in all cases the theory overpredicts the resonant frequency, and the difference increases with increasing neck diameter. This observation is contrary to the Hole-to-Wall interaction theory, whereby the standard infinitely baffled value of $0.96\sqrt{A_0}$ is reduced proportional to an increase in the value of the geometry ratio ξ. The magnitude of the difference in prediction and measurement for each case can be seen numerically in Table 14; where the minimum error of 3.04Hz corresponds to the 3mm neck diameter; the largest error of 19.30Hz, the 15mm diameter neck; with an average overprediction error of +8.8Hz across the full test matrix.

Ingard Hole-to-Wall Calculated Peak Absorption - Measured Peak Absorption (Hz)								
			1.5	3	4.5	6	7.5	r_0
	Neck Properties		0.06	0.12	0.18	0.24	0.30	r_0/R_C
Cavity Properties			0.04	0.08	0.13	0.17	0.21	r_0/a
			9.05	4.53	3.02	2.26	1.81	L_n/D_n
#01	71,506	36	0.73	4.00	5.20	7.73	13.55	19.30
#02	77,341	39	0.79	3.72	5.83	6.82	13.52	17.78
#03	83,921	43	0.85	3.75	4.94	7.27	12.88	18.40
#04	91,377	47	0.93	3.93	5.71	7.42	13.01	16.88
#05	99,872	51	1.02	3.66	4.96	6.50	12.37	16.28
#06	109,610	56	1.12	3.69	4.83	6.65	10.96	16.44
#07	120,850	62	1.23	4.02	5.30	6.33	11.70	16.90
#08	133,900	68	1.36	4.05	4.86	6.79	11.83	16.46
#09	149,190	76	1.52	3.62	4.73	6.33	11.35	16.17
#10	167,260	85	1.70	3.65	4.90	6.48	11.61	16.78
#11	188,820	96	1.92	3.04	4.61	6.48	11.44	15.27
#12	214,840	109	2.19	3.55	4.77	6.46	11.55	17.41
#13	246,620	126	2.51	3.58	4.18	6.32	11.53	16.96
#14	286,020	146	2.91	3.45	4.36	6.31	11.81	17.43
	$V_c\ (mm^3)$	$L_c\ (mm)$	L_C/D_C					

Table 14 - Difference in peak absorption frequency between measured and predicted values, according to ideal resonator with Ingard two-sided hole-to-wall end correction.

These results indicate that using the standard end correction value for an infinitely baffled tube would actually reduce the overprediction error evident from this comparison test matrix however, Ingard (1953) has already validated this interaction modelling experimentally, and demonstrated good agreement between theory and measurements, albeit for less extreme geometry variations. As such it can be reasonably deduced that the cause of the discrepancy is in fact an additional factor, not currently captured by Ingard's model. In the following sub-section, we will introduce an additional correction factor, with the goal of capturing the salient parameters contributing to the observed differences between measurement and prediction.

5.1.2   Improvement in Modelling Predictions

In the aforementioned hole-to-wall modelling efforts by Ingard (1953), the ideal resonator assumption, with an empirical end correction modification, provides a convenient and accessible solution for expedient prediction of peak attenuation frequency. As shown in Figure 71 and Table 14 however, the inherent assumptions are a limiting factor which determines the accuracy and thus the threshold of applicability of this model. Ingard (1953) determined from his own experiments that his model is provides a reasonable approximation for geometric ratios of proportionally of $\xi < 0.4$; as this is the observed limit of linear proportionality between the inner and outer mass end correction of the aperture, and the geometric ratio ξ. Critically however, a uniform velocity distribution assumption is also applied, and the impact of viscosity is neglected; therefore, the standalone application of this end correction is also inherently limited to that of apertures with negligible thickness. Inclusion of the additional reactance and resistance elements can nevertheless be modelled accordingly as lumped parameters, through impedance modelling techniques; as per the previous discussions in Section 2.3. This additional accuracy does however come at the cost of calculation complexity, as solution subsequently becomes dependant on additional variables, such as frequency and/or field values etc.

As such a new model is proposed, which captures the nuances of the geometry variations which are limiting factors of the existing modelling techniques, whilst retaining the limitation of the solution to the case of zero total reactance, i.e. the peak resonant frequency of the acoustic system. The assumption is made that Equation *[144]* holds true across the investigated range in terms of aperture to cavity geometric ratio of ξ; and that additional correction factors are required to account for the other relevant geometric factors. Utilising iterative regression analysis in Excel, the additional geometric factors omitted by others, can be evaluated for an alternative empirical end correction modification, which more accurately varies the predicted results according to the measured results. Through systematically analysing the significance and sensitivity of the additional known geometric factors, and iteratively evaluating and modifying the model, an optimised alternative definition was arrived at, as shown in Equation *[146]*:

$$\delta_{geo} = \left(\sqrt{L_C/D_C} \left(1 - \sqrt{D_n/L_n} \right) - \left(0.25 - \bar{\bar{\xi}} \right) 2\pi \sqrt{L_C} \right) \sqrt{A_0} \qquad [146]$$

Where $\bar{\bar{\xi}}$ represents the average of interior and exterior geometric ratios, and for the geometry under investigation here experimentally, this corresponds to:

$$\bar{\bar{\xi}} = \frac{1}{2}\left(\frac{r_0}{R_C} + \frac{r_0}{a}\right) \qquad\qquad [147]$$

Calculation of Equation *[146]* for the full set of geometric variables investigated, yields an additional correction factor which varies according to the spatial parameters of the neck and cavity of the resonator, including the relationship between the length and diameter of both. The resultant surface for the test matrix investigated experientially can be seen in Figure 72.
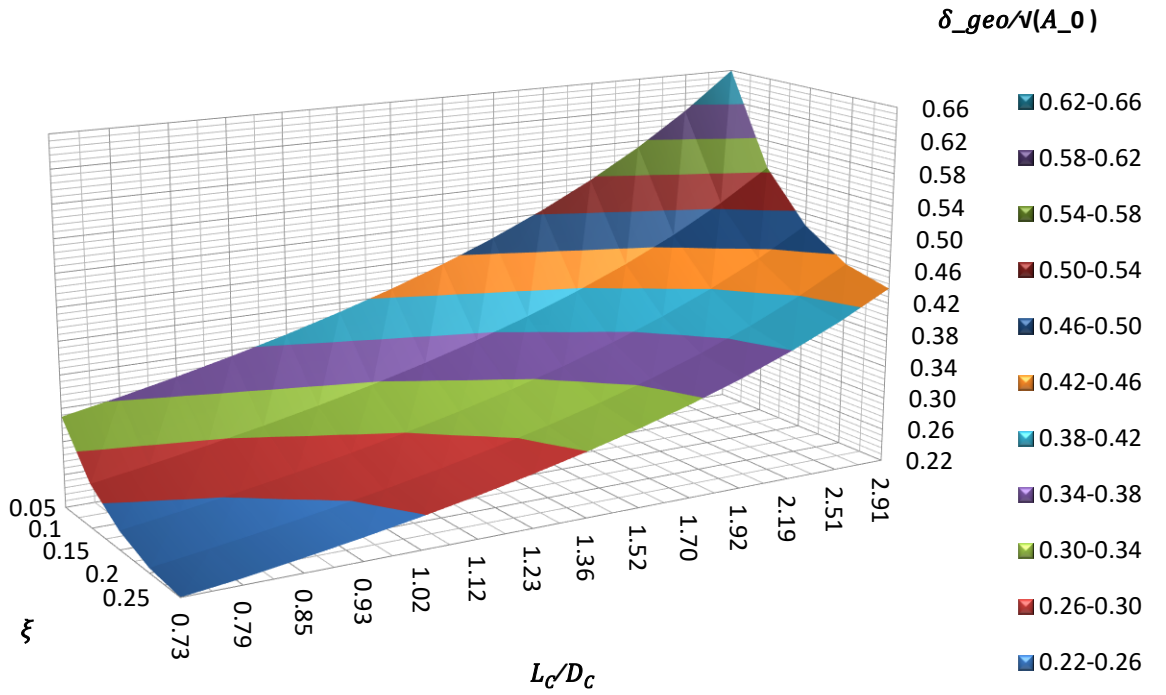
Figure 72 – 3D surface plot of geometric correction factor δ_{geo} against the geometric ratios of proportionality of both the neck $\bar{\bar{\xi}}$, and resonator cavity L_C/D_C.

Modification of Equation *[145]* to include the additional proposed correction factor yields Equation *[148]*, which now includes both hole-to-wall effects, and the observed pertinent spatial factors, in one simple formulation for peak resonant frequency:

$$f_r = \frac{c}{2\pi}\sqrt{\frac{A_0}{V\left(l + \delta_{h-w} + \delta_{geo}\right)}} \qquad\qquad [148]$$

Upon a repeat comparison between the predicated peak absorption frequencies using the additional end correction factor according to Equation *[148]*, and the measured values, can be seen numerically in Table 15, and graphically in Figure 73. Here it can be seen that the additional correction factor is effective at capturing the spatially driven additional end correction factors not previously captured by

Ingard's (1953) method alone. A shift from a global overprediction in the peak absorption frequency of the aforementioned method, has moved towards a reduced overprediction for the small neck diameter cases, and a slight underprediction for the majority of the larger neck diameter cases; with and average difference of only 0.34Hz across the full measured test case of seventy geometry variations.

These results show that the proposed additional empirically derived end correction presents a robust solution for the improved accuracy of discrete resonators with neck diameter ratios of $0.04 < \xi < 0.3$, and length over dimeter ratios for both the neck and resonator cavity of $1.81 < L_N/D_N < 9.05$, and $0.73 < L_C/D_C < 2.91$ respectively.

Equation [148] Calculated Peak Absorption - Measured Peak Absorption (Hz)								
			1.5	3	4.5	6	7.5	r_0
	Neck Properties		0.06	0.12	0.18	0.24	0.3	r_0/R_C
Cavity Properties			0.04	0.08	0.13	0.17	0.21	r_0/a
			9.05	4.53	3.02	2.26	1.81	L_n/D_n
#01	71,506	36	0.73	2.47	0.63	-0.62	-0.71	0.17
#02	77,341	39	0.79	2.19	1.27	-1.07	-0.68	-0.97
#03	83,921	43	0.85	2.37	0.69	-0.90	-1.11	-1.04
#04	91,377	47	0.93	2.25	1.32	-0.73	-0.93	-1.57
#05	99,872	51	1.02	2.13	0.28	-1.63	-1.96	-2.54
#06	109,610	56	1.12	2.31	0.46	-1.46	-2.53	-1.99
#07	120,850	62	1.23	2.34	0.49	-1.60	-2.03	-2.05
#08	133,900	68	1.36	2.37	0.52	-1.27	-1.68	-2.09
#09	149,190	76	1.52	2.25	0.09	-1.55	-2.23	-2.43
#10	167,260	85	1.70	2.28	0.28	-1.37	-1.87	-1.55
#11	188,820	96	1.92	2.24	0.16	-1.34	-1.81	-3.10
#12	214,840	109	2.19	2.19	0.19	-1.30	-1.74	-1.12
#13	246,620	126	2.51	2.07	-0.08	-1.42	-1.66	-0.96
#14	286,020	146	2.91	2.11	-0.04	-1.37	-1.42	-0.33
	$V_C\ (mm^3)$	$L_C\ (mm)$	L_C/D_C					

Table 15 - Difference in peak absorption frequency between measured and predicted values, calculated using modified empirical end correction according to Equation [148].
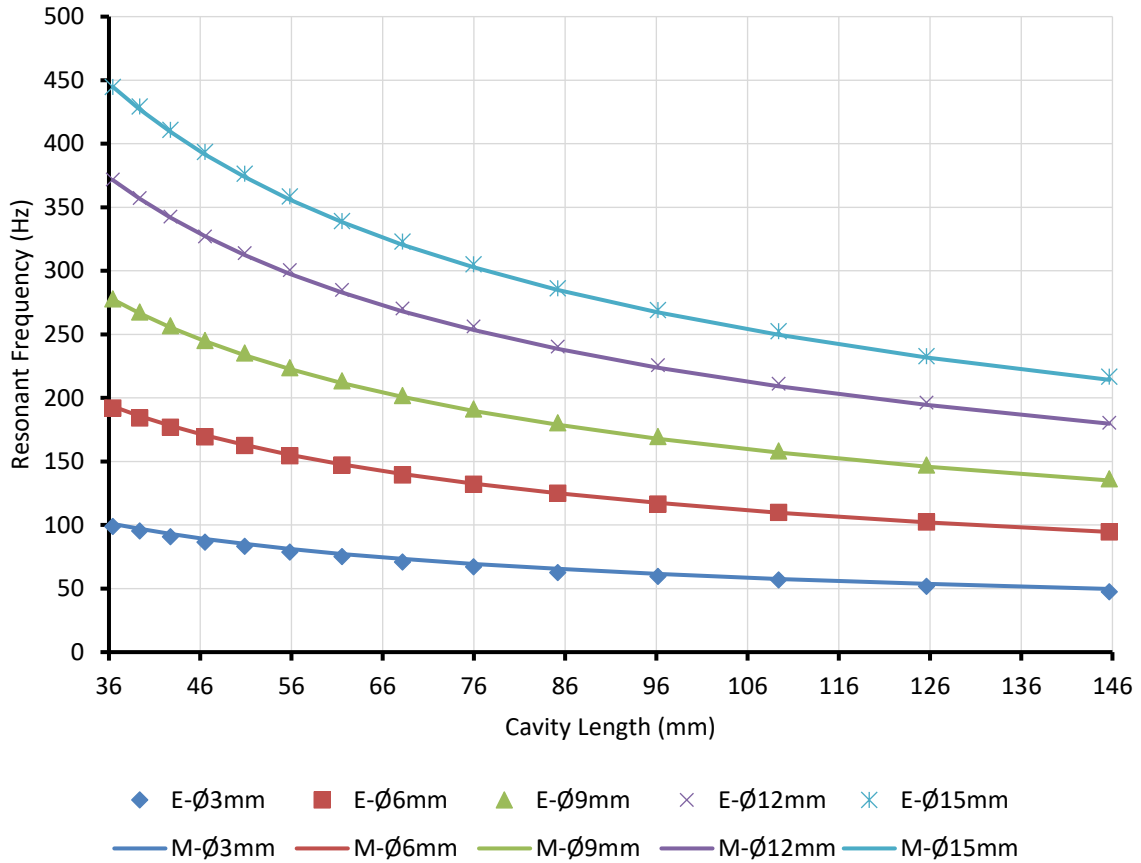
Figure 73 – Resonant Frequency against Cavity Length, for all measured cases of Neck Diameter and Cavity Volume, where E=Experimental & M=Modelled, as calculated using Equation [148].

5.2 Neck Termination Geometry

In this section the results obtained from impedance tube measurements of alternative resonator neck geometries will be presented and evaluated; the impedance tube configuration is as per Section 4.3.2; and the investigated neck geometries are as detailed in Section 4.4.3. The subsequent results are presented in terms of the FRF obtained from exposure to a white noise excitation signal, allowing a spectral evaluation of peak absorption frequency and magnitude of the relative geometry cases, against a baseline Ø5mm cylindrical neck control case.

Three differing categories of neck termination geometry are investigated separately; firstly, a chamfered edge, referred to as a conical termination; secondly varying degrees of edge radii are investigated; and finally, several common horn geometries are evaluated. In all cases presented, the alternative neck termination geometry is located at the duct side of the resonator neck; and the extremes of available cavity volume cases are investigated in parallel, in order to consider the observed results sensitivity to cavity volume, and aspect ratio.

5.2.1   Conical Neck Termination

A comparison of the results obtained from measurements with varying degrees of conical neck termination; ranging from the straight control Ø5mm case, to a maximum of 25° conical taper angle; can be seen for the smallest cavity volume case #1, in Figure 74; and for the largest cavity volume case #14, in Figure 75. Here it can be seen that with increasing taper angle, there is a clear increase in both the peak absorption frequency, and magnitude, indicating that the attenuation performance potential of the resonator has been improved as a result of the tapered termination.

From direct comparison of Figure 74 and Figure 75, it can be appreciated that the sensitivity to the equivalent neck geometry variations is greater for the smaller cavity volume case of #1, than it is for the larger cavity volume case of #14. The observed sensitivity is approximately double in terms of peak absorption frequency shift, with an observed 25.2Hz increase in peak absorption frequency over the control Ø5mm neck resulting from of the 25° tapered neck; compared to an equivalent 12.5Hz increase for the large volume case. Similarly, there is an observed 1.73 increase in FRF magnitude for volume case #1, compared to a 1.00 equivalent increase in magnitude for volume case #14. These observations agree with the general trends presented in Section 5.1 relating to neck diameter and cavity volume variations, where here too it can be seen that neck diameter variations are more dominant for small cavity volumes.
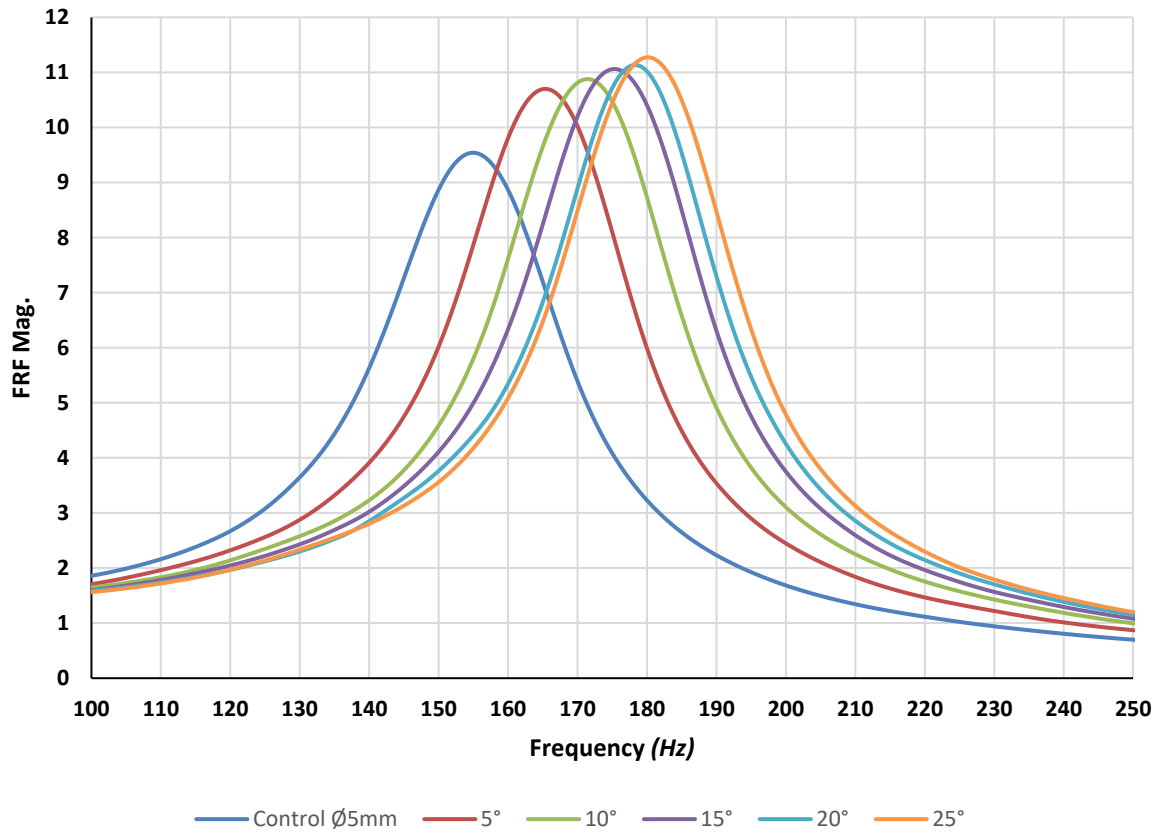
Figure 74 - FRF against varying degrees of Conical Neck Termination for Volume #1
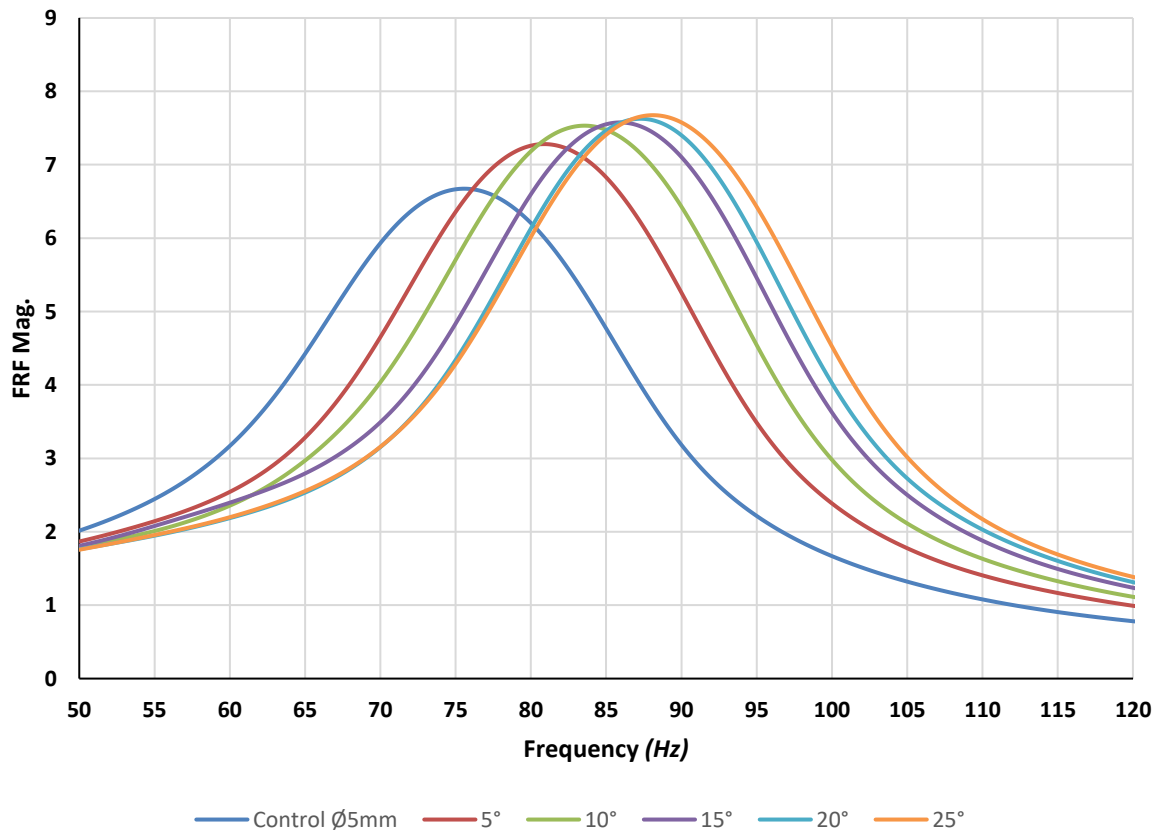
Figure 75 - FRF against varying degrees of Conical Neck Termination for Volume #14

These findings agree with the work of Tang (2005), who investigated both theoretically, and experimentally, the acoustical properties of Helmholtz resonators with tapered geometry on the internal, cavity side of the neck. Figure 76 shows a schematic representation of the geometry investigated by Tang (2005), and the nomenclature he uses in the derivation of analytical reasoning of his findings. His work opens with a theorisation that a smoother area change from the neck towards the cavity will reduce the flow resistance and draws reference to the fact that the low-frequency plane wave theory suggests that a reduction of this resistance, gives rise to a higher sound transmission loss; that is, so long as this resistance is higher than that of the surrounding medium.
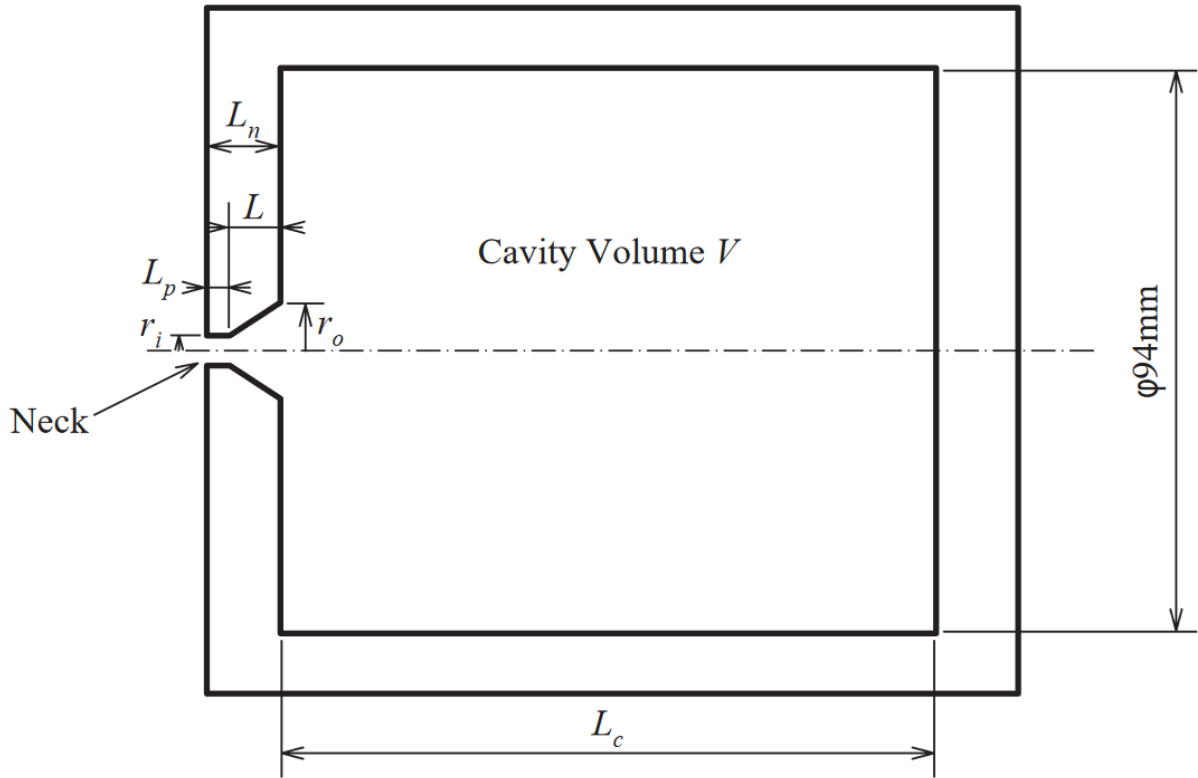
Figure 76 - Schematic of the tapered neck Helmholtz resonator and the nomenclature adopted by Tang (2005)

Tang (2005) states that, whilst it is not easy to find exactly the resistance R_0, one expects it increases relatively quickly with frequency and thus k in general, as the pressure loss for incompressible flow through enlargement suggests that R_0 is proportional to the squared velocity (Streeter et al., 1985). Therefore, under the assumption that the wavelength concerned is much larger than any length dimension of the resonator, and R_0 is finite, it can be deduced that the acoustic impedance is approximately:

$$Z \approx \frac{r_i^2}{r_o^2} R_0$$

[149]

Which infers that the resistance is likely to be reduced by the tapering of the neck however, it should be noted that the additional resistance due to radiation out of the neck is unchanged under this simplified assumption; and as shown with the previous results, any geometry variation can have a measurable impact on the radiation resistance. Irrespective, the current deduction tends to suggest a considerable improvement of the noise attenuation capability of a Helmholtz resonator at its resonant frequency through tapering of the neck. Tang (2005) goes on to derive a solution for the approximation of the resonant frequency of a resonator with a tapered neck, based on the geometry and nomenclature shown in Figure 76, and the zero-reactance assumption, as follows:

$$f_r = \frac{c}{2\pi} \sqrt{\frac{\pi r_i^2}{L_n V} \left[\frac{r_i L}{r_o L_n} \left(1 + \frac{\pi r_o^2 L_p}{V} \right) + \frac{L_p}{L_n} \right]^{-1}} \qquad [150]$$

In reality L_n should be replaced by the effective length, and Tang (2005) suggests that the common value of $L_n + 16 r_i / 3\pi$ should be used, in reference to Kinsler (1982); for his cases investigated, a small value of $\xi = 0.05$, infers that the error induced from this simplification should be small, albeit not negligible; in fact Tang (2005) goes on to determine that the depth analysis end correction of Chanaud (1997) results in approximately a 4% improvement in estimation, over the conventional simplified end correction. It can also be directly deduced from Equation *[150]* that the resonant frequency decreases as the straight neck length increases, irrespective of wither the tapered length is kept fixed or not, which is later confirmed experimentally by Tang (2005). Equation *[150]* uses the radii as opposed to the previously preferable area-based formulations, which were geometry agnostic, however in practical applications, the mechanical chamfering process renders this notation trivial. Tang (2005) states that the above conclusions may not apply where the neck inlet is larger than its outlet, that is $r_i > r_o$, and that this condition is not recommended in practical terms; as it tends to introduce additional unfavourable flow separation at the neck inlet in applied applications, where the neck is typically exposed to fluid flow. Irrespective, for the no-flow normal incident signal circumstances of the impedance tube measurements conducted here, there can be seen coherence in the results obtained, regardless of the location of the conical taper neck termination.

In conclusion, both the theoretical deduction and the experimental results indicate that a reduction of the acoustic impedance through a tapering of the neck, increases the noise attenuation potential of a Helmholtz Resonator. The greater the degree of taper, the better the absorption will be, and the greater the corresponding increase in resonant frequency will be over the non-tapered equivalent case. The comparative effects of neck taper on peak absorption frequency and magnitude, decrease with increasing resonator cavity volume.

5.2.2 Radial Neck Termination

The results from varying degrees of neck termination radii for both the small cavity volume #1, and large cavity volume #14, can be seen in Figure 77 and Figure 78 respectively. Here the neck termination radius is increased from the baseline Ø5mm cylindrical control neck in increments of 1mm, up to a maximum 5mm radius, as shown in Figure 50. The experimental methodology is as per the conical neck cases and the observed trends are also similar in nature. Therefore, it can be deduced that the aforementioned theory is correspondingly applicable for these radial neck termination cases; in that the smoother area change from the acoustic transmission line to the neck of the resonator, reduces the flow resistance; and thus, gives rise to a higher sound absorption potential for resonator.

It can be seen that the shift in peak absorption frequency resulting from the radial neck termination, even at the largest measured case of 5mm, is approximately 40% less significant than that observed from the chamfered cases; with a maximum increase of 9Hz in peak frequency observed for the small #1 volume case, and 4.7Hz for the #14 large cavity volume case. This can be appreciated upon comparison of the relative change in neck volume between the corresponding cases; as shown in Figure 50, the conical neck cases are all fixed at 10mm in length; whereas the radial neck terminations finish tangential with the end face of the neck, therefore only altering the baseline cylindrical neck geometry up to a depth equal to the corresponding radius. To put this into context, the maximum 25° conical taper neck termination increases the acoustically relevant volume within the vicinity of the neck by 111%, adding an additional volume of 594mm^3 to the baseline ideal piston volume of the Ø5mm cylindrical case of 533mm^3; compared to the largest 5mm radius case, which only contributes to an equivalent 23% increase, equating to an additional 122mm^3. Irrespective, for the small volume case #1, the 5mm radius case still increases the FRF by 1.62, which is 94% of the equivalent increase resulting from the maximum 25° chamfer case; whereas whilst an increase in FRF magnitude is still evident for the large cavity volume case #14, it is only 50% that of the equivalent maximum tapered conical neck case.

Keller and Zauner (1995) made similar observations, when they conducted experiments on a resonator with a neck of Ø9mm, 100mm length, and an end termination of a 15mm radius, swept 40° from normal to the axis of the neck; they found an increase of 55% relative attenuation, and a frequency shift of 6-7Hz. They account the higher peak frequency values to an effective reduction of the effective length resulting from the rounding of the edges and confirm that the loss coefficients are decreased by 25-40% of the values for sharp edges.
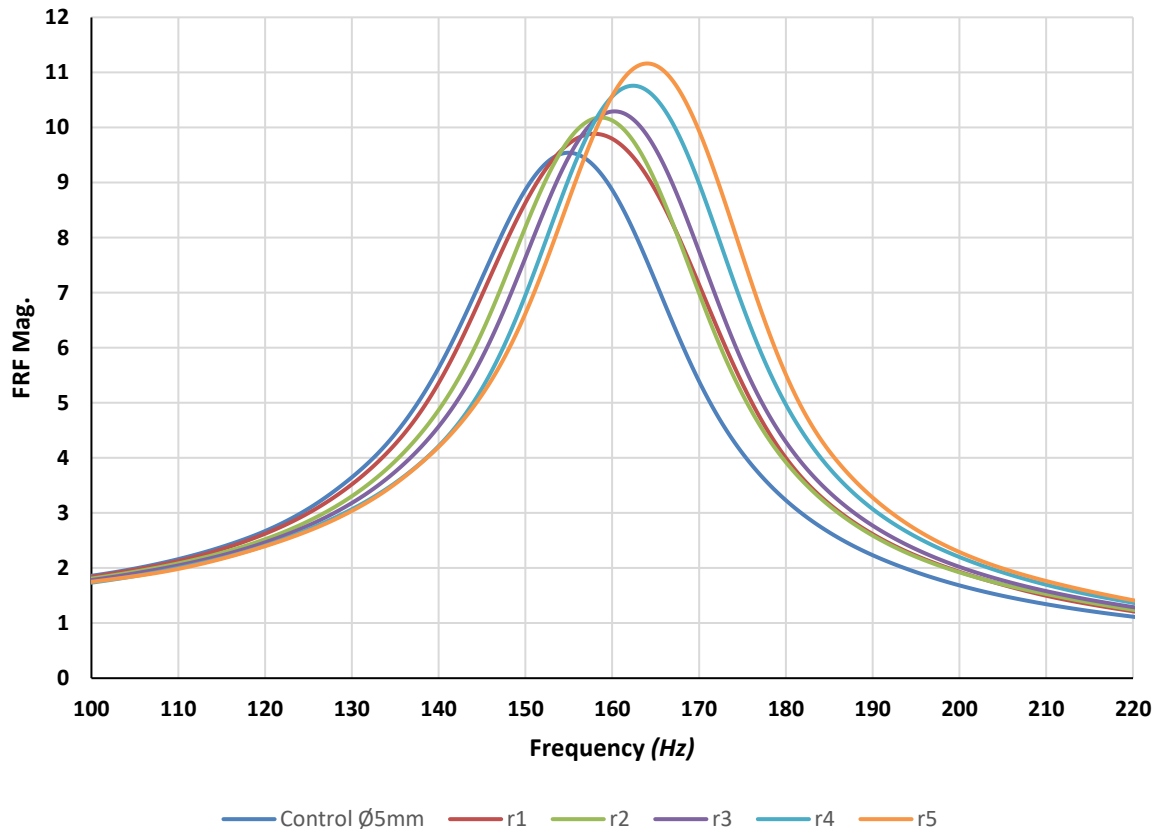
Figure 77 - FRF against varying size of edge radii of Neck Termination for Volume #1
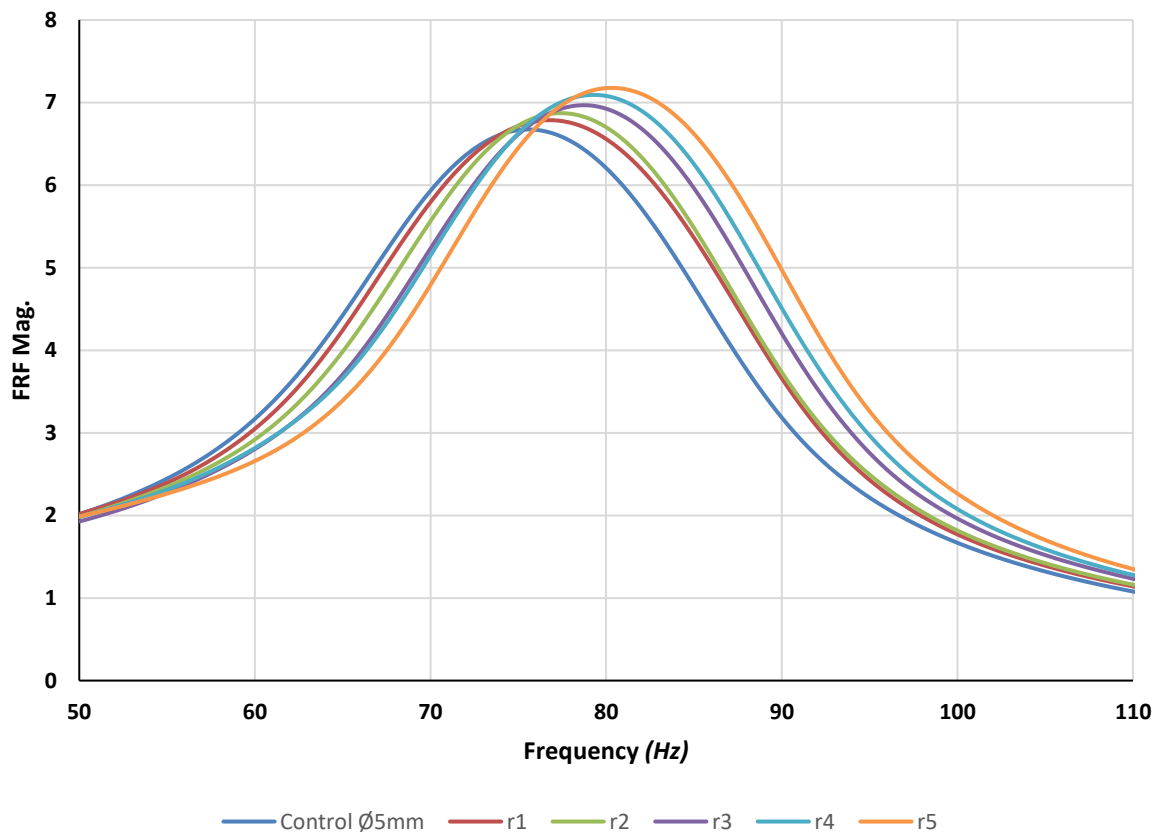
Figure 78 - FRF against varying size of edge radii of Neck Termination for Volume #14

5.2.3   Horn Geometry Termination

The final alternative neck geometry cases investigate the impact of employing common horn geometries as neck terminations. The experimental methodology remains as with the previously investigated cases, and similarly the geometries under investigation are clarified in Figure 50. Before interpreting the results, it is first beneficial to briefly discuss the basic principles of a horn, where, and why they are commonly employed. One of the most prevalent and relevant applications of acoustical horns, is that of electroacoustics, within which there are two important applications; firstly, controlling the loading of the electromechanical driver; and secondly directivity control. Both of which ultimately serve to increase the acoustic output of a mechanical driver; as increasing the loading of the driver over that of free air increases efficiency and hence the output; and concentrating the sound into a certain solid angle increases the output further (Kolbrek, 2008). As with the many nuances of acoustic resonators, the problem of sound propagation and manipulation in horns, is a complicated one, and has not yet been rigorously solved analytically; irrespective there has been, and remains, a large academic effort applied in advancing the current state of the art, which is testament to the potential benefits in understanding and application of the principles. This short supplementary investigation aims to provide some insight into the potential effects of acoustical horns on the attenuation performance potential of acoustic resonators.

The results from three common horn geometries are experimentally investigated; exponential, hyperbolic, and tractrix; can be seen for both the small cavity volume #1, and the large cavity volume #14, in Figure 79 and Figure 80 respectively. As with all previously investigated alternative neck termination geometries, the modification of the termination results in an increase in peak attenuation frequency, and an equivalent increase in peak FRF magnitude, thus attenuation potential. Across both volume cases investigated, the significance of the tractrix curve termination on both FRF frequency shift, and magnitude increase, is lesser than that of the exponential and hyperbolic terminations; for which there is only marginal differences. Similar to the aforementioned conical and radial case comparison, the tractrix horn geometry, as seen in Figure 50, expands faster than the exponential and parabolic equivalents, and thus results in a lesser degree of geometry modification over the baseline, hence a lower shift in frequency and magnitude can be appreciated. Comparison of the exponential and hyperbolic curves are noteworthy, as a deviation from trend witnessed in all prior cases within this investigation is observed, whereby the exponential curve produces a greater frequency shift, but a lesser FRF magnitude shift, than the hyperbolic equivalent case, which demonstrates the largest FRF magnitude increase of all cases investigated here within.
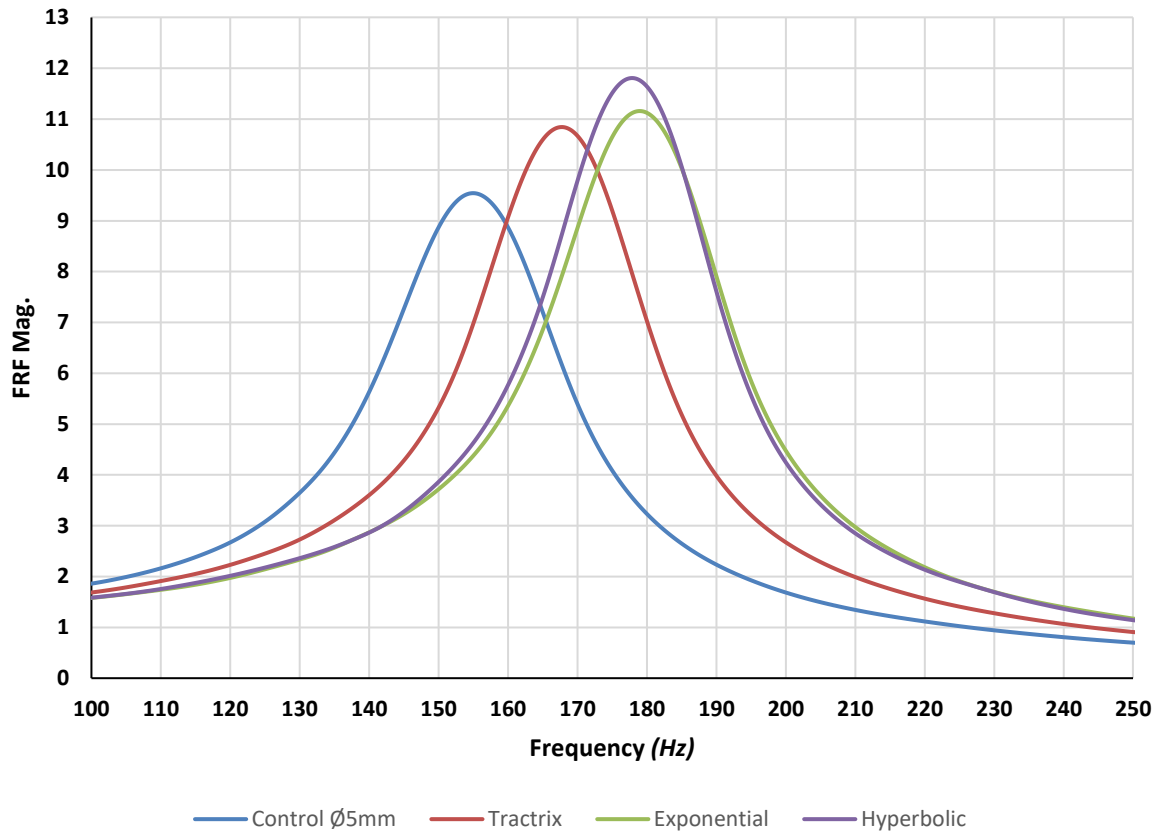
Figure 79 - FRF against varying horn geometry Neck Termination for Volume #1
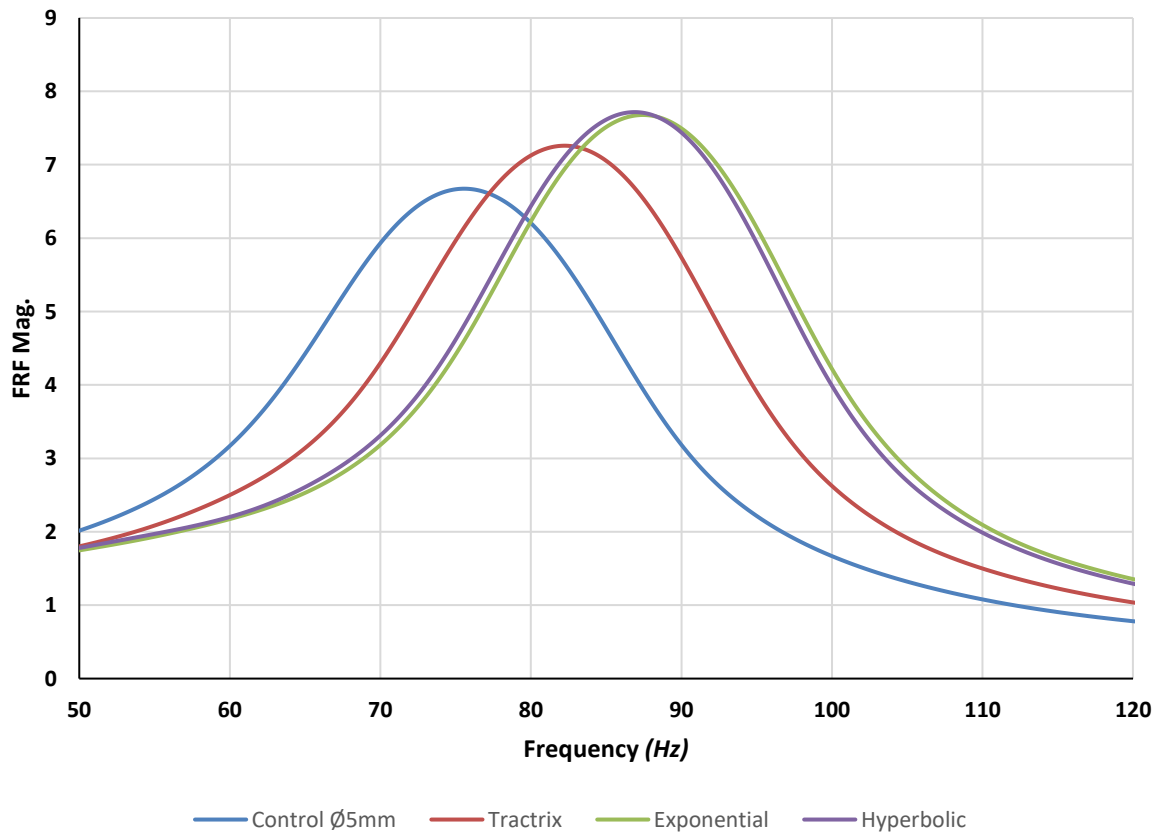
Figure 80 - FRF against varying horn geometry Neck Termination for Volume #14

5.2.4 Alternative Neck Geometry Summary

A summary of all alternative neck geometry cases investigated can be seen plotted in terms of peak FRF frequency and magnitude, for both cavity volume #1 and #14, in Figure 82 and Figure 83 respectively; with the numerical values summarised in Table 16.

Whilst this section concluded with an investigation into horn geometries, it is worth noting that from an acoustics point of view, the aforementioned conical necks, and even the radial terminations, can also be considered as acoustic horns; and correspondingly much of the associated acoustic theory can also be applied to such geometries. Initially academic investigations into the acoustics of horns were all born from the learnings of Lord Rayleigh (1926), who is his own words stated within Articles 265 and 280 of his classical treatises, first published in 1878, "when the section of pipe is variable, the problem of the vibration of air within cannot be generally solved" (Rayleigh, John William Strutt,3rd Baron, 1926). In subsequent years his works attracted mainly academic interests however, at the turn of the century more general interest was aroused by early gramophones, for which external conical horns were integral to their function.

Whilst the theory of the conical horn was originally investigated by Lord Rayleigh, the first serious attempts to establish a practical working formula for the exponential horn were not made until 1919 and the years following; with the basic formulae for the transmission of sound waves through horns being presented in modern terms by Salmon (1946) and others. The advent of the moving coil loud-speaker in 1927 and electrical amplification stimulated further advances in the design of horns, including the contributions of Beranek (1954), which lead to and understanding of the acoustical resistance and reactance against frequency at the throats of a series of infinite horns of different contours with identical cross sectional areas at the throats, at a given point along the axis of the horn, as shown in Figure 81 (Dinsdale, 1974).

In 1919, Webster (1919) presented a convenient one-dimensional solution to the complex three-dimensional problem of representing acoustic properties within horns, by assuming that the sound energy was uniformly distributed over a plane wave-front perpendicular to the horn axis, and considering only the motion in the axial direction; leading to the so called "Webster's Horn Equation", which can be seen in Equation *[151]*, and can be solved for a large number of practical cases (Kolbrek, 2008).

$$\frac{d^2\phi}{dx^2} + \frac{d\ln S}{dx}\frac{d\phi}{dx} - k^2\phi = 0 \qquad\qquad [151]$$

Where: $k = 2\pi f / c$ is the wave number or spatial frequency in radians per meter; ϕ is the velocity potential; and S is the cross-sectional area of the horn, as a function of x. The solution of Equation *[151]* can be solved in a general from using Equation *[152]*:

$$\phi = Au + Bv$$

[152]

Where A and B represent the outgoing (diverging) and reflected (converging) wave, respectively, and u and v depend on the specific horn type (Kolbrek, 2008). In the case of an infinite horn, there is no reflected wave, and hence the solution is simplified, as $B = 0$. Subsequent solutions can be presented in terms of absolute acoustical impedance $Z = \rho_0 c / S_t$, such that the specific impedance (impedance per unit area) can be found by multiplying by the throat area S_t; and the normalised throat resistance by multiplying by $S_t / \rho_0 c$.
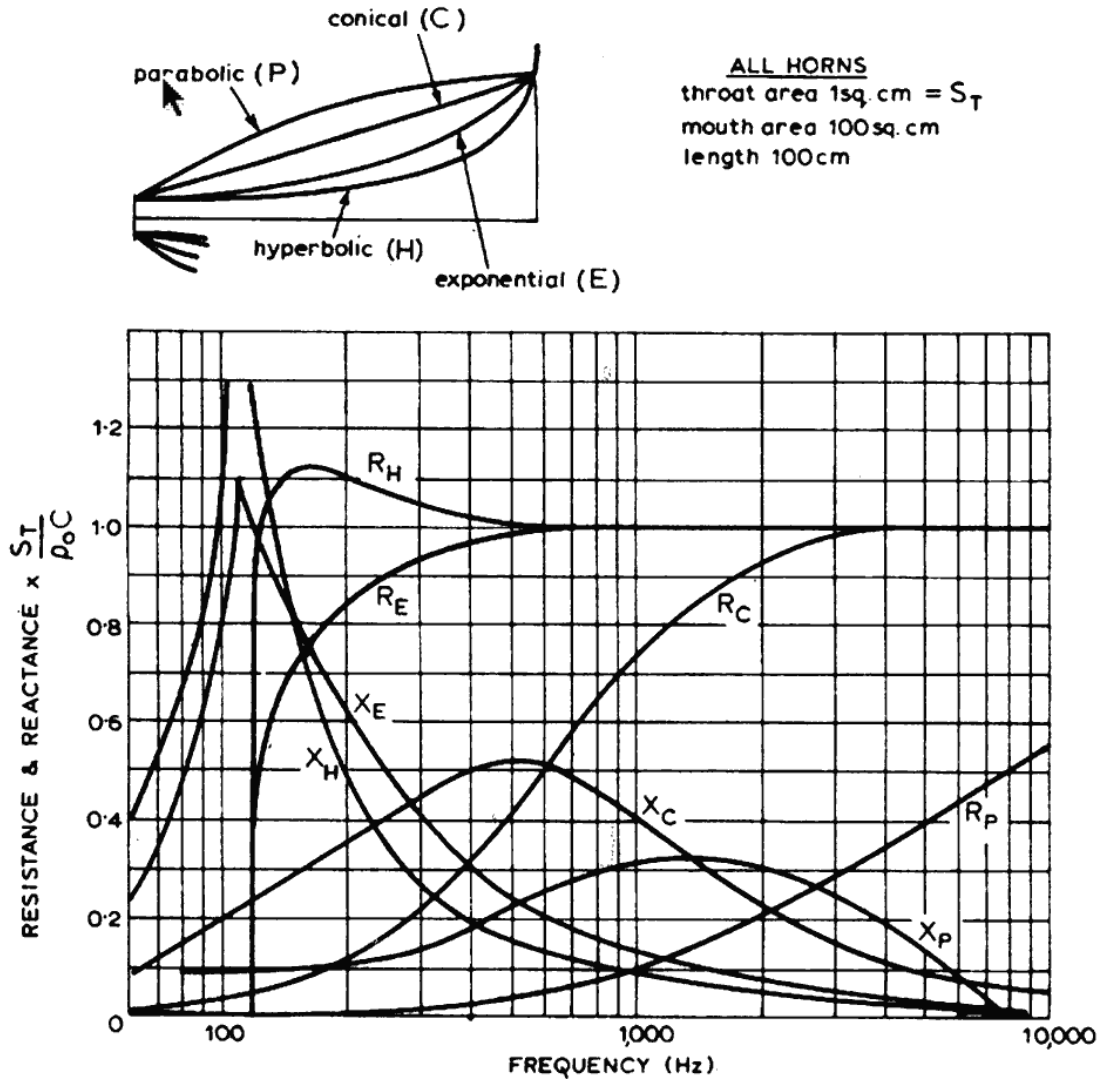
Figure 81 - Acoustical resistance and reactance against frequency at the throats of a series of infinite horns of different contours (Beranek, 1954).

Theoretically the current state of the art permits, under the aforementioned assumptions of Webster (1919), the calculation of the impedance at the throat of an infinite horn geometry corresponding to the investigated conical, exponential, and hyperbolic horn geometries, as shown in Equations *[156]*, *[157]*, & *[158]* respectively.

$$Z = \frac{\rho_0 c}{S_t}\left(\frac{k^2 x_0^2 + jkx_0}{1 + k^2 x_0^2}\right) \qquad\qquad Conical \qquad [153]$$

$$Z = \frac{\rho_0 c}{S_t}\left(\sqrt{1 - \frac{m^2}{4k^2}} + j\frac{m}{2k}\right) \qquad\qquad Exponential \qquad [154]$$

$$Z = \frac{\rho_0 c}{S_t}\left(\frac{\sqrt{1 - \frac{1}{f'^2}}}{1 - \frac{1 - H^2}{f'^2}} + j\frac{\frac{H}{f'}}{1 - \frac{1 - H^2}{f'^2}}\right) \qquad\qquad Hyperbolic \qquad [155]$$

Where m is the exponential flare constant, H is the hyperbolic flare constant, and f' is the normalised frequency = f/f_c. Under the assumption of plane wave fronts, the cross-sectional area of the corresponding wave fronts for relative horn geometries are defined in Equations *[156]*, *[157]*, & *[158]* respectively:

$$S(x) = S_t\left(\frac{x + x_0}{x0}\right)^2 \qquad\qquad Conical \qquad [156]$$

$$S(x) = S_t e^{mx} \qquad\qquad Exponential \qquad [157]$$

$$S(x) = S_t\left(\cosh\frac{x}{x_0} + H\sinh\frac{x}{x_0}\right)^2 \qquad\qquad Hyperbolic \qquad [158]$$

For a finite horn however, both parts of Equation *[152]*, which requires the pressure and volume velocity at both the mouth and the throat of the horn, solution of the required expressions rapidly becomes complicated, and whilst it has analytically addressed by Stewart & Lindsay (1930), we will focus in this study on the observed practical effects of finite horns.

Of additional noteworthy significance, is that whilst in a uniform tube the wave fronts can exist in planar form, the same cannot be said for the horn geometry; where for a circular horn, the wave-fronts are spherical, with centres at the apex; which has been shown experimentally for an exponential and conical horn by Hall (1928; 1932). An appreciation of this understanding can be accounted to the to the development of the remaining geometry investigated, the Tractrix horn; where the tractrix curve was first employed for horn use by P.G.A.H. Voight, and patented in 1926 (Voigt, 1926). The equation

for the tractrix curve is given in Equation *[159]*, where r_m is the mouth radius; and because the radius is not a function of x, as with the previous horn geometries, the calculation of the contour is not so trivial.

$$x = r_m ln \frac{r_m + \sqrt{r_m^2 - r_x^2}}{r_x} - \sqrt{r_m^2 - r_x^2}$$ *[159]*

The theory of the tractrix horn was later investigated by Lambert (1954) and it was found that the assumption that sound waves travel through the horn as spherical wave-fronts with constant radius, tangent to the wall at all times, was not true; in fact, it was found that the wave-front was neither spherical or planar (Kolbrek, 2008).

In conclusion, all of the alternative geometries investigated can be seen to ultimately improve the noise attenuation properties of an acoustic resonator over the basic cylindrical straight neck geometry; that is, so long as the shift in peak absorption frequency can be accurately predicted and accounted for accordingly when targeting an unwanted dynamic frequency. The underpinning principle is that a gradual change in geometry from the duct to cavity, serves to reduce the impedance of the neck and thus improve the acoustic loading of the resonator cavity, and thus the attenuation potential. The potential gains in performance are proportional to the degree of geometry modification supporting effective transitioning, for which there is a greater significance for smaller volume cavities, where the neck properties are more dominant in defining the ultimate performance. In both volume cases investigated, the hyperbolic horn yields the greatest potential attenuation performance improvement.
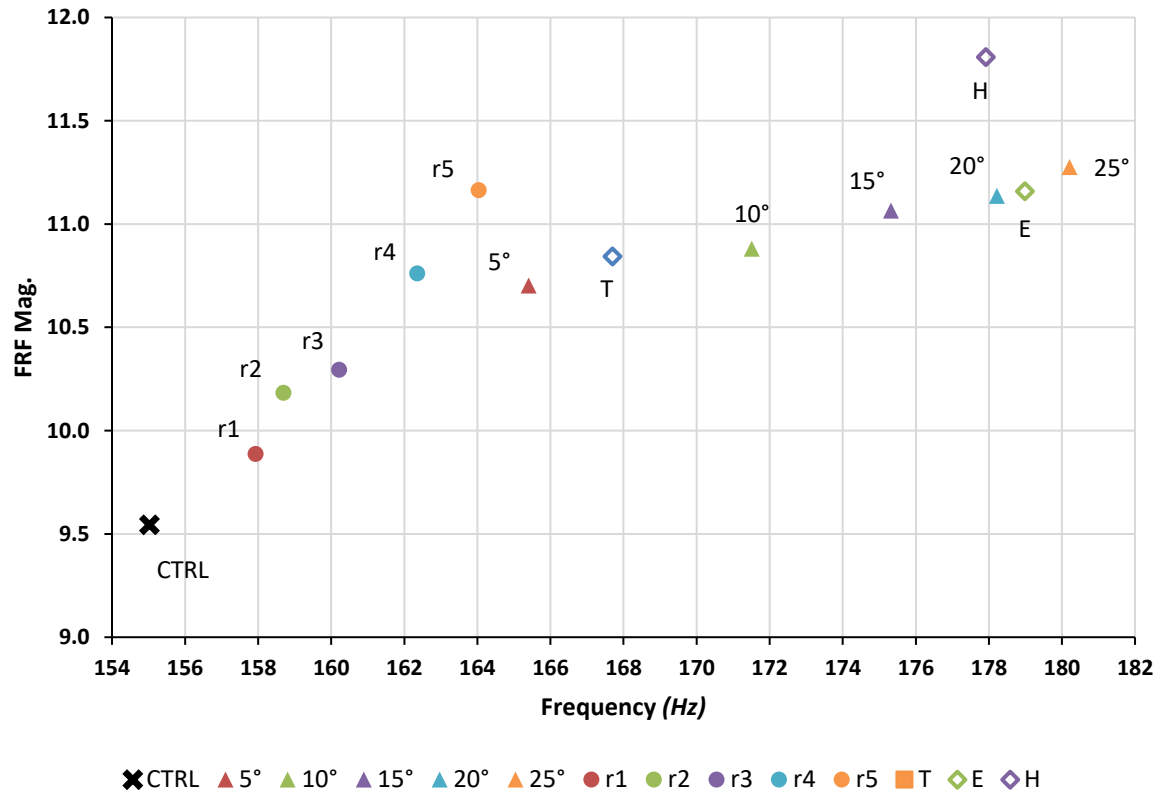
Figure 82 - Peak FRF Magnitude and Frequency for all investigated geometry cases, using volume case #1
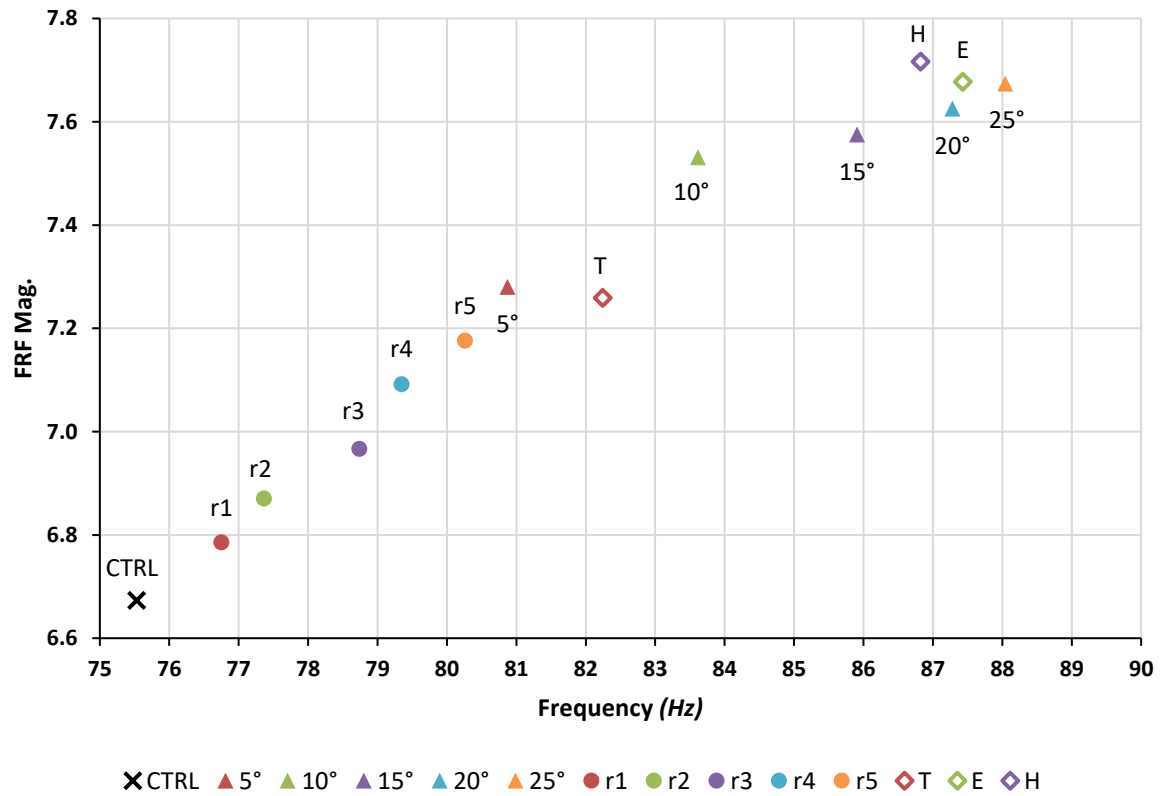
Figure 83 - Peak FRF Magnitude and Frequency for all investigated geometry cases, using volume case #14

ID	Detail	Peak FRF Frequency *(Hz)*		Peak FRF Magnitude	
		#1	*#14*	*#1*	*#14*
CTRL	Control Ø5mm cylinder	155.0	75.5	9.54	6.67
5°	5° Conical Taper	165.4	80.9	10.70	7.28
10°	10° Conical Taper	171.5	83.6	10.88	7.53
15°	15° Conical Taper	175.3	85.9	11.06	7.58
20°	20° Conical Taper	178.2	87.3	11.14	7.63
25°	25° Conical Taper	180.2	88.0	11.28	7.67
r1	1mm Radius	157.9	76.8	9.89	6.79
r2	2mm Radius	158.7	77.4	10.18	6.87
r3	3mm Radius	160.2	78.7	10.29	6.97
r4	4mm Radius	162.4	79.3	10.76	7.09
r5	5mm Radius	164.0	80.3	11.16	7.18
T	Tractrix Curve	167.7	82.2	10.84	7.26
E	Exponential Curve	179.0	87.4	11.16	7.68
H	Hyperbolic Curve (H=0.5)	177.9	86.8	11.81	7.72

Table 16 - Summary of Peak FRF Frequency & Magnitude for all measured alternative geometry neck variations

It should be noted that these deductions have been made in the absence of flow, which has a great potential to reduce the potential gains, and potentially even introduce detrimental factors, such as increased flow separation, or the generation of additional unwanted tonal noise. Furthermore, the manufacturing implications of these intrinsic geometry modifications are not trivial, and in many applied contexts the additional complexity of manufacturing could render the potential performance improvements unattainable in practice.

Irrespective, with contemporary advancements in manufacturing technologies, such as the 3D printing techniques employed in this investigation, it may become more economically and technically viable to apply these learnings to novel applications; and to benefit from the knowledge transfer of classical acoustic horn theory, and electroacoustics, to the effective implementation with the context of acoustic resonators for the purposes of noise suppression.

5.3 Grazing Flow

In the following section the impact of a grazing, or cross-flow, i.e. a flow perpendicular to the neck axis, is investigated in relation the impact on peak resonant frequency and noise attenuation capacity of single neck, Helmholtz resonators. An initial comparison with the previously presented impedance tube collected results is made, followed by presentation of the subsequently collected flowed experiments, concluding with a discussion of findings, and comparison with the current state of the art.

5.3.1   Impedance Tube & Cross-flow Rig Comparison

In order to ensure that the results obtained from the cross-flow rig detailed in Section 4.3.3, and qualified in Section 4.6, are comparable with those previously collected from the non-flowed Impedance Tube, a direct comparison of the measured FRF for a representative case is made, the results of which can be seen in Figure 84. Here the Ø15mm, Cavity Volume #7 case was chosen for comparison; with the upstream, and piston wall acoustic pressure measurement locations being utilised to determine the corresponding FRF; under zero cross-flow magnitude, and an acoustic excitation methodology according to Section 4.6.1.

From Figure 84 it can be seen that the results obtained from the separate experimental rigs yield an identical match in terms of peak frequency, and a negligible difference in peak FRF magnitude. The flow rig obtained FRF spectrum does however indicate a slightly noisier response than the impedance tube obtained results, which can be in-part attributed to the properties of the rig itself, the minor differences acoustic excitation hardware and consequential power spectral density, and the lack of any microphone coherence correction applied to these measurements. Regardless, the strong consistency in peak frequency, magnitude, and spectral distribution between the respective rigs for the equivalent case, gives sufficient confidence in the variable volume resonator measurement methodology; therefore, subsequent comparisons can be confidently made between results obtained from either rig.
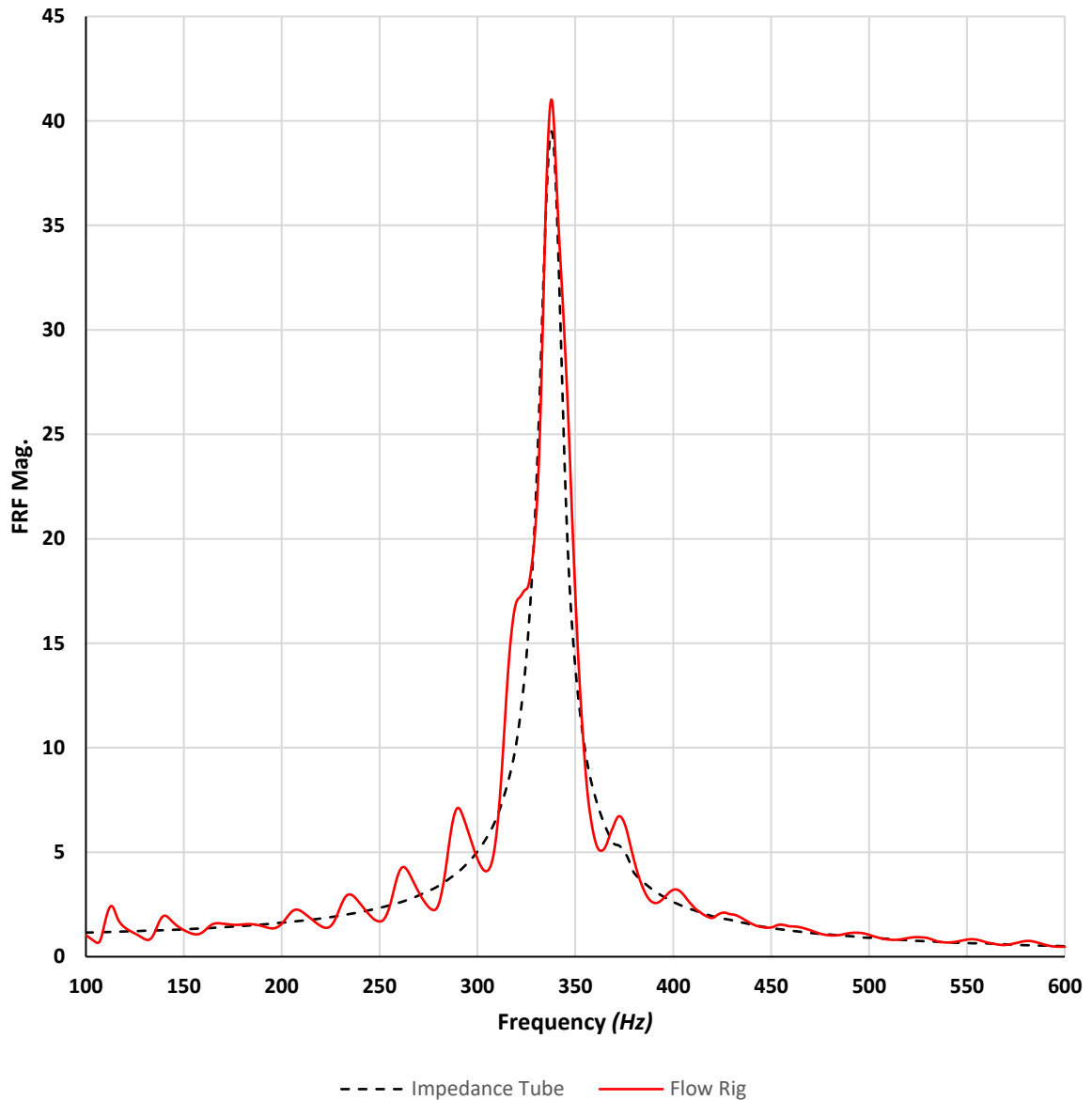
Figure 84 - Comparison between Impedance Tube & Grazing Flow Rig derived FRF, for Ø15mm Neck, Volume Case #7.

5.3.2 Grazing Flow Results

The measured FRF spectrum against varying grazing flow magnitude; ranging from 0m/s to 60m/s, in 15m/s increments; can be seen for a resonator with Ø15mm neck diameter, and the minimum #1, the median #7, and the maximum #14 cavity volume cases, in Figure 85, Figure 86, and Figure 87 respectively. In all cases it is evident that the magnitude of FRF is immediately reduced in the presence of grazing flow, with a rapid transition from 0-30m/s, and negligible variation in observed response for magnitudes between 30-60m/s; which can be attributed to the aforementioned expectation of resultant increase in resistance, corresponding to the magnitude of grazing flow velocity.

In addition to an observed reduction in FRF magnitude, a shift in peak frequency can also be observed, indicating an additional modification to the reactance of the resonator in the presence of grazing flow. The resultant shift in frequency is difficult to accurately quantify directly from the FRF response alone; due in part to the reduction of magnitude and quality factor, which diminishes rapidly with the onset of grazing flow; and the additional measurement noise, which results in a less prominent peak attenuation frequency. Regardless, it can be observed that, for the small volume case #1, Figure 85, there is an immediate reduction in the peak attenuation frequency for the 15m/s case, above which point an increase can be seen, which is proportional to grazing flow magnitude.
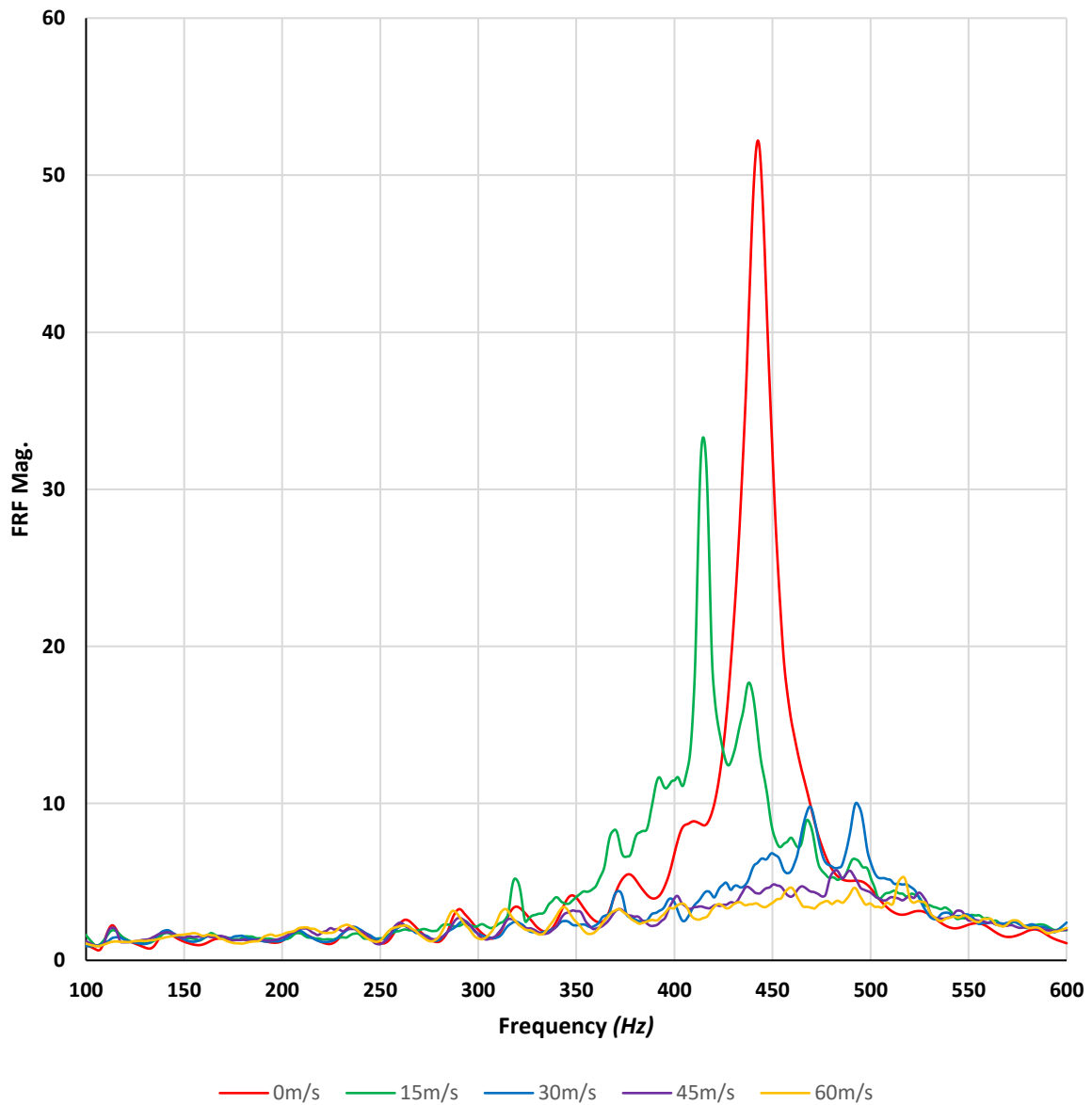
Figure 85 - Impact of Grazing Flow on FRF Magnitude for Ø15mm Neck, Volume Case#1

For the median volume case #7, as seen in Figure 86, a general increase peak absorption frequency can be seen to be proportional to grazing flow magnitude between 0-30m/s, above which point the variation between cases is negligible.
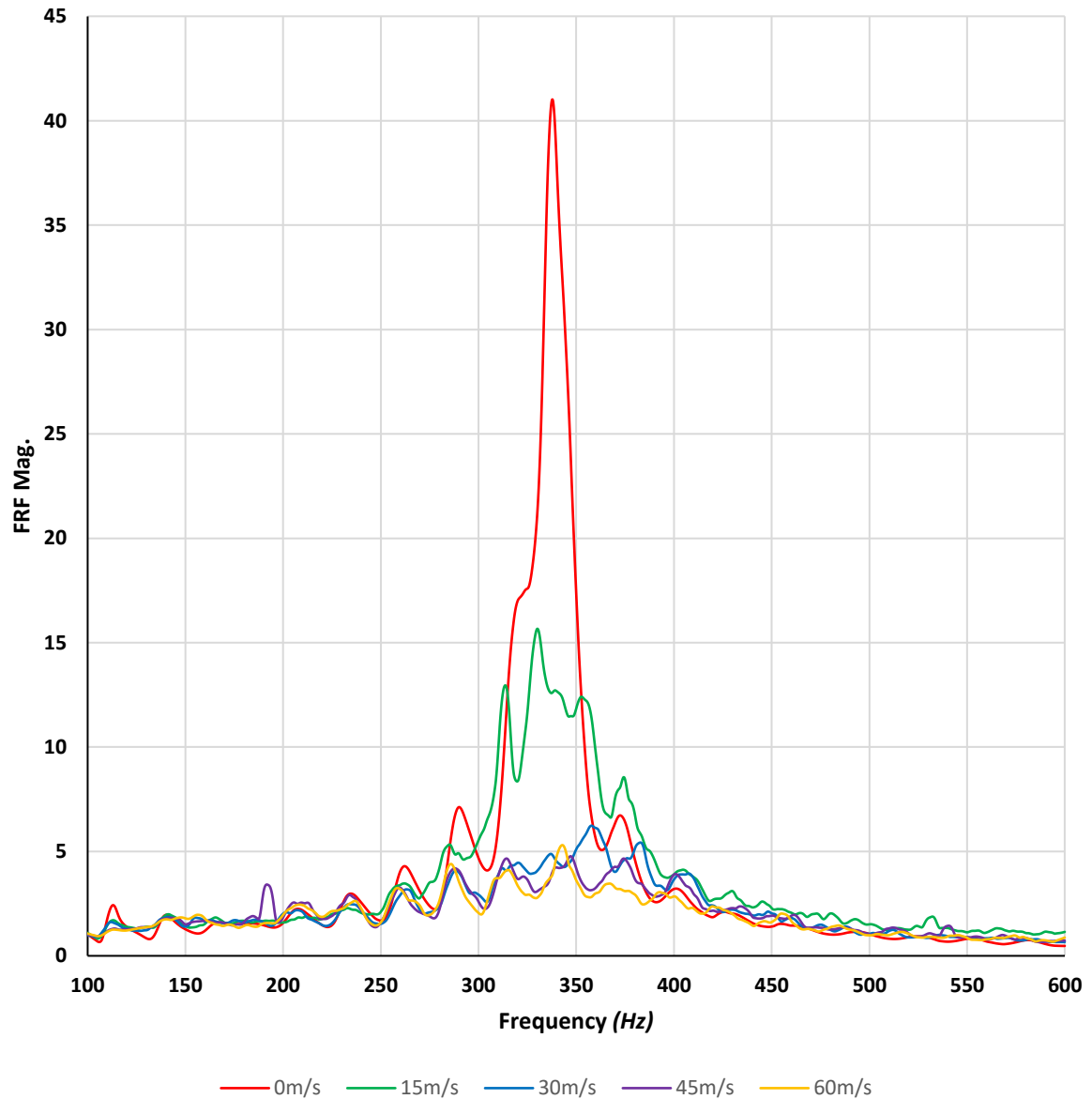
Figure 86 - Impact of Grazing Flow on FRF Magnitude for Ø15mm Neck, Volume Case#7

For the largest cavity volume case #14, as seen in Figure 87, there appears to be a slight increase in peak attenuation frequency for the 15m/s case, after which point there is negligible shift in frequency with increasing grazing flow magnitude; however a dominant response can be observed around 200Hz for higher magnitude cases, which is lower than the non-flow resonant frequency of ~215Hz.
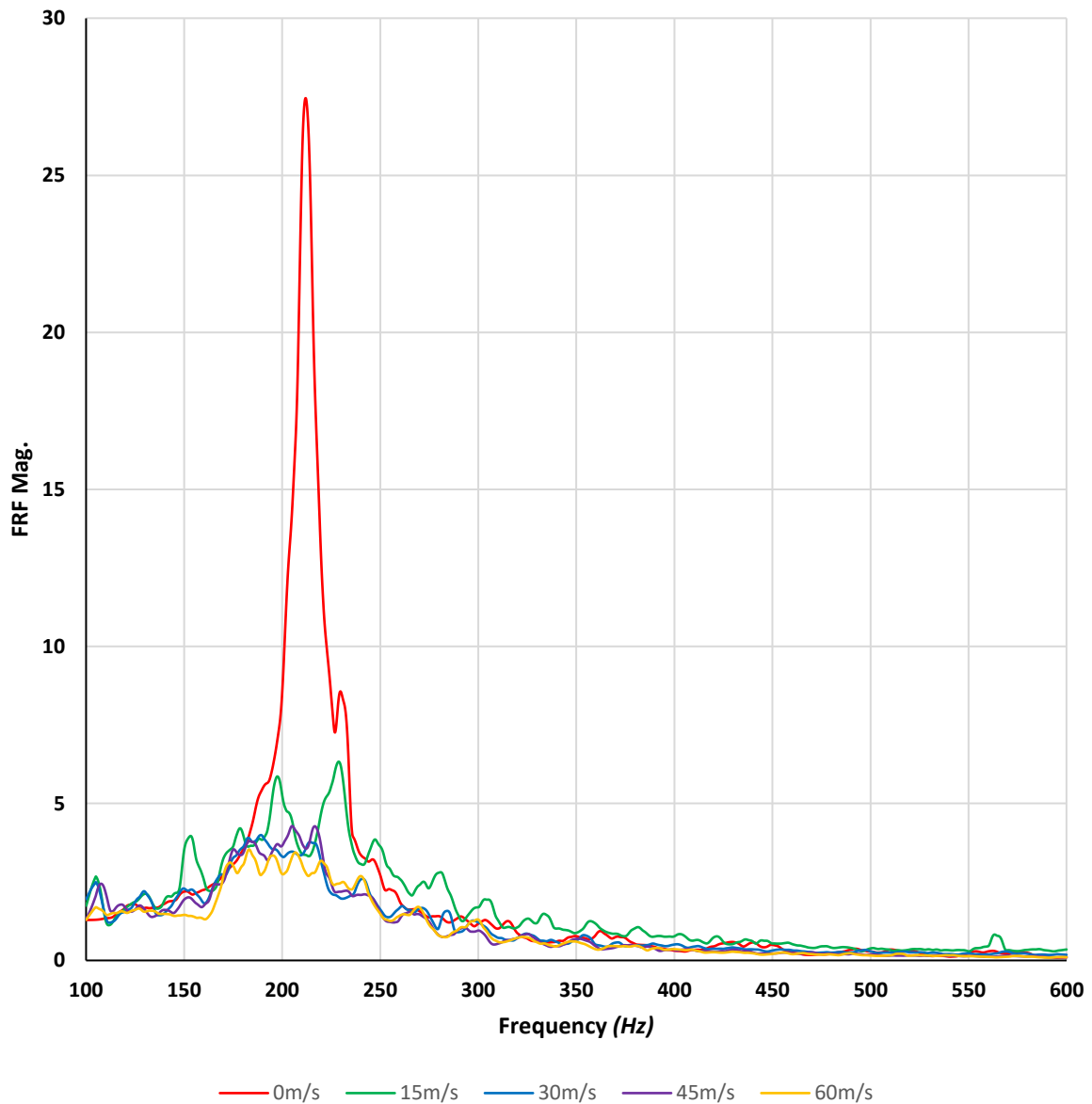
Figure 87 - Impact of Grazing Flow on FRF Magnitude for Ø15mm Neck, Volume Case#14

In order to further the insight into the impact of grazing flow on the observed attenuation properties of the resonator configurations investigated, decomposition of the incident and reflected signals at both upstream and downstream locations would be beneficial; however, for measurement methodology deployed here, only one upstream, and one down measurement location was available. Consequently, it is not possible to investigate the incident and reflected signals upstream and downstream respectively for these cases; however in the later distributed resonator investigations of CHAPTER 7 - & CHAPTER 8 -, such methods have been deployed for grazing flow investigations, and will be discussed in greater detail within these sections.

By evaluating the measured SPL at the upstream, downstream, and in-resonator measurement locations concomitantly, an appreciation as to the attenuation properties and resonant response can however be obtained, as shown in Figure 88. Here it can be seen that there is a strong singular tone

existing both upstream and downstream of the resonator, which also aligns with the observed peak FRF response of the resonator for this case. This tone was not observed in the earlier flow rig acoustic excitation qualification exercise; where it can be seen from Figure 64, that the measured acoustic signal in this frequency range, was flat in the absence of a resonator. This clearly indicates the existence of a discrete flow generated tonal noise under these particular set of circumstances, specific to this case geometry, and the grazing flow magnitude. The existence of this strong tone amongst the excitation signal, especially given the close proximity to the non-flowed resonant frequency, is likely to dominate any minor modifications to reactance due to end correction effects. Therefore, it is reasonable to deduce that this observed reduction in peak attenuation is a direct result of the unique flow generated noise under these conditions, and independent from any underlying trends in end correction modification etc.

What is also evident from Figure 88, that is not so obvious from the FRF response seen in Figure 85, is that there is a notable broadband attenuation of the downstream signal, in relation to the upstream signal, at frequencies beyond the peak response frequency. This is also indicative of an increase in resistance, and demonstrates that whilst both the peak attenuation magnitude, and quality factor are reduced as a result of the flow, additional damping effects can be introduced due to the interaction between the acoustic oscillations and the fluid flow.
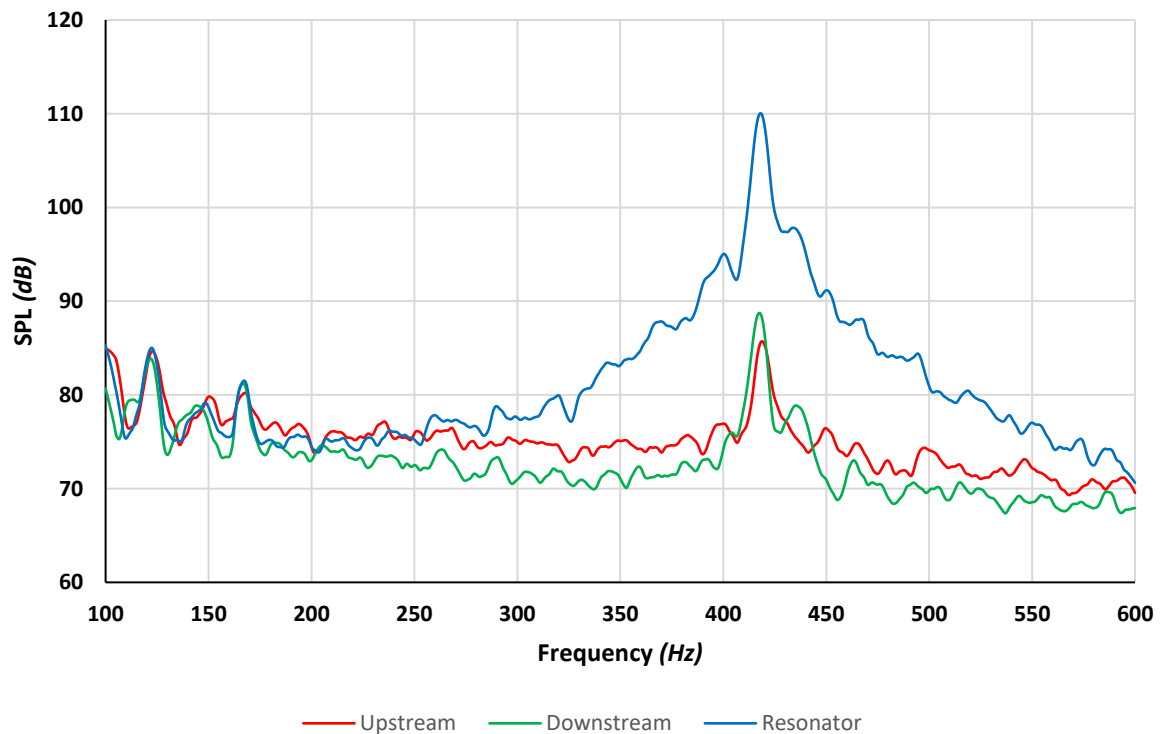
Figure 88 - Measured SPL against Frequency, under 15m/s grazing flow, for Ø15mm Neck, Volume case #1

5.3.3   Grazing Flow Summary

It can be seen that the impact of grazing flow on end correction is less prevalent than the effects on the resistance; an observation that has been shared with previous experimental studies (Goldman, A. L. & Panton, 1976; Goldman, A. & Chung, 1982; Kooi & Sarin, 1981). A comparatively large degree of scatter in frequency shift variation is observed, leading to similar deductions as to that of Cummings (1986a), who made a similar observation in his end-correction data for grazing turbulent pipe-flow, relative to the more obvious coherence between cross-flow magnitude and resistance. Cummings (1986a) also deduced that from his own experiments, and prior art, that the physics of the flow/acoustic interaction is quite complex, and that attempts to parametrise the orifice impedance partially masks the true nature of the mean flow effects at an orifice. This conclusion is supported by the significance of the flow generated noise evident in the small cavity volume case #1, where it can be seen that the presence of a strong flow generated tone, has the ability to dominate the resonant response, and deviate from the expected analytically described trend for this particular case. Sun et al. (2002) made a comparison of their own grazing flow experiments, with the quasi-steady state model of Rice (1976), the linearised potential flow model of Jing et al. (2001), and the empirical equation of Lewis and Garrison (1971); which confirmed generally good agreement in relation to acoustic resistance predictions, and are in alignment with these experimental findings.

In regards to reactance, its absolute value was also shown to decrease towards a constant at high grazing flow speed, with the high grazing flow speed being reasonably well predicted by the empirical model of Lewis and Garrison (1971), with the lower grazing flow reactance aligning better with Rice's (1976) model (Sun et al., 2002). Rice (1976) drew a conclusion that the orifice inductive mass reactance end correction is not a function of grazing flow; contrary to the widely held notion that grazing flow removes the effect of the orifice inductive end correction; and rather proposed that the experimentally observed total inductance reduction with grazing flow, may be occurring within the slug flow within the orifice itself, as opposed to externally within the end correction. This notion is also commented on by Herse and Walker (1979), who stated that due to the vena contracta effect of the grazing flow, a slug-mass type oscillatory flow no longer exists within the orifice, and that this assumption remains conjecture. Herse and Walker (1979) also observed loud resonant tones radiating from single orifice Helmholtz resonators investigated experimentally, which they accounted to interaction between the grazing flow shear layer, and the resonant cavity; with their measurements showing that the tones radiated at a Strouhal number equal to 0.26.

As commented by Massenzio et al. (2008), most existing literature on this topic employs semi-analytical models which make use of a Strouhal number in order to predict resonance leading to the

highest sound pressure level, i.e. the critical phenomena. Massenzio introduces a novel double coincidence model which introduces the wavelength of the shear layer, as opposed to the Strouhal number; and links both aeroacoustics tones and acoustic eigenfrequencies of the cavity; which ultimately highlighted the high potential for many resonant interactions. Whilst such a model can be useful for a draft study purpose to roughly predict the onset of aeroacoustics resonances, in a practical application it would require the definition of the eigenfrequencies of an open cavity under no-flow conditions to be done either analytically or numerically; and definition of the momentum thickness of the flow over the cavity, again to be defined either analytically or numerically.

In conclusion there is a clear proportionality between the magnitude of acoustic resistance of Helmholtz resonators, and that of grazing flow magnitude; which is dependent on frequency and amplitude at low grazing flow conditions; and increases linearly with high grazing flow magnitudes. In the absence of non-linear effects, the acoustic resistance can in general be accurately predicted in relation to grazing flow magnitude; which results in a decrease in peak absorption magnitude and quality factor of any given resonator response; but does offer a greater broadband dissipation potential, than and non-flowed acoustic resonator. The corresponding values of acoustic reactance are much smaller than those of resistance, and in general tend towards zero for increasing grazing flow speeds, meaning that the impedance of Helmholtz resonators at high grazing flows, is almost linear. In general, it can be seen that increasing grazing flow serves to reduce the effect of acoustic radiation through two key principles; an end correction modifying local neck flow; and an effective removal of acoustic radiation. Both phenomena tend to reduce the effective length, and thus cause an increase in peak attenuation frequency, from the onset of moderate grazing flows, and with diminishing rate of change to a transition point; at which point grazing flow dominates the resonator behaviour, over the sound particle velocity field. Particular attention must however be paid to non-linear effects, which occur due to the interaction between grazing flow shear layers and the resonator cavity. The coupling of flow induced aeroacoustics phenomena and acoustic properties of resonators, can result in uncharacteristic alterations in attenuation performance, and even the generation of additional noise, in the form of powerful tones. Furthermore, whilst current models provide indicative insight as to the potential onset of non-linear effects, confident clarification of such nuances remains reserved for numerical and experimental investigations.

5.4   Summary of Discrete Resonator Results

In this chapter the acoustic attenuation performance characteristics of single neck Helmholtz resonators were investigated across a range of seventy geometric variations of neck diameter and cavity volume, fourteen alternative neck geometries; and exposure to a grazing flow.

Neck diameter and cavity volume analysis showed that existing approaches to modification of the ideal resonator frequency equation, are limited to a narrow range of practical geometries; and consequently, can result in significant prediction error when applied to resonator geometries outside of their thresholds of applicability. Contemporary impedance models can vastly improve prediction accuracy across a broader range of conditions, but improvements in fidelity come at the cost of additional solution complexity; thereby reducing their accessibility in many practical and pragmatic applications. The strategic design of an experimental methodology focused on advancing understanding of geometric factors, has permitted the development of a new empirical end correction modification; one which complements the existing understanding of hole-to-wall factors, and permits its application to a larger range of practical resonator geometries; whilst retaining the accessibility and implementation benefits of the ideal resonator frequency equation.

Experimental investigations into alternative neck geometries have demonstrated that, using additive manufacturing techniques, small scale acoustic horn geometries can be applied to resonator neck terminations; and that they can offer tangible and predictable attenuation performance improvements.

Investigations into the impact of a grazing flow has shown that with increasing grazing flow magnitude, the acoustic resistance of a resonator increases, which in turn causes; a decrease in peak attenuation magnitude; a reduction in quality factor; and an increase in broadband dissipation. Acoustic radiation is reduced with increasing grazing flow magnitude; until the grazing flow velocity dominates the acoustic particle velocity field; after which point the impedance becomes almost linear. The initial reduction in acoustic radiation occurs under moderate grazing flows, and results in a shift towards higher peak attenuation frequencies. Aeroacoustics-acoustic coupling results in deviations from these general trends; including the generation of additional strong tonal noises. The onset of non-linear characteristics can be estimated with current theory however, resultant attenuation performance cannot currently be predicted by simplified analytical solutions; and a comprehensive characterisation of such performance factors requires rigorous numerical or experimental investigations.

CHAPTER 6 - CFD INVESTIGATION

In this Chapter a computational fluid dynamic (CFD) investigative methodology is developed, discussed, and deployed; utilising the commercial CD-adapco (2011) Star-CCM+ software suite; to further evaluate noise attenuation performance factors of discrete Helmholtz resonators. The Chapter opens with the subsequent Section 6.1, which presents the proposed CFD investigation approach, and discusses important prerequisites to building an effective methodology, such as the computational domain, boundaries and boundary conditions; the meshing regime; physics models; and the acoustic excitation signal.

Section 6.2 presents a validation of the proposed CFD methodology, initially through an evaluation of the Courant-Freidrichs-Lewy (CFL) stability criterion for a characteristic geometry case; followed by a closer investigation of the significance of neck geometry and timestep assumptions; and concluding with validation against a representative sample of experimental results, as detailed in the previous chapters.

Subsequent to validation of the developed methodology, Section 6.3 exploits the additional benefits of a spatial solution of the resonator's fluid dynamics, and through visualising the distribution of time-averaged acoustic particle velocity within the acoustically relevant fluid, provides additional insight into the underpinning attenuation performance characteristics.

This investigative methodology is then applied to select representative geometry variations, to further advance the prior Chapter's evaluation of the effects of neck diameter and cavity volume variations, and alternative neck termination geometry variations.

Following which, a supplementary investigation is conducted, which evaluates the effects of increasing the sound pressure level (SPL) of the acoustic excitation signal, to amplitudes beyond that which is physically viable using the available experimental apparatus, as detailed in Section 4.5.2.

Finally, Section 6.4 provides a summary of the results obtained from the deployed CFD methodology; and discusses the subsequent observations in relation to their coherence with the prior experimentally invested characteristics, and the current state of the art, in relation to the understanding and prediction of acoustic resonator performance factors.

6.1   CFD Investigation Methodology

6.1.1   Computational Domain

In order to minimise the computation effort required to effectively represent the internal fluid dynamics of the discrete resonator impedance tube rig, the inherent rig symmetry is exploited, and only a quarter section is defined as the computation domain for subsequent investigation.

In addition, and by the same rationale, the upstream duct section is significantly shorted, and does not extend into the region where the additional duct measurement ports exist in the physical rig; as given that the near-neck duct location was determined as the most appropriate location in *Section 4.5.1*, this duct location only will be used for comparison purposes with the experimental results.

In Figure 89, a computer-generated representation of the CFD computational domain can be seen within a scale model of the experimental discrete resonator impedance tube rig for context. Here it can be seen much of the physical intricacy of the physical rig can be omitted, when only modelling the internal, acoustically relevant fluid domain.
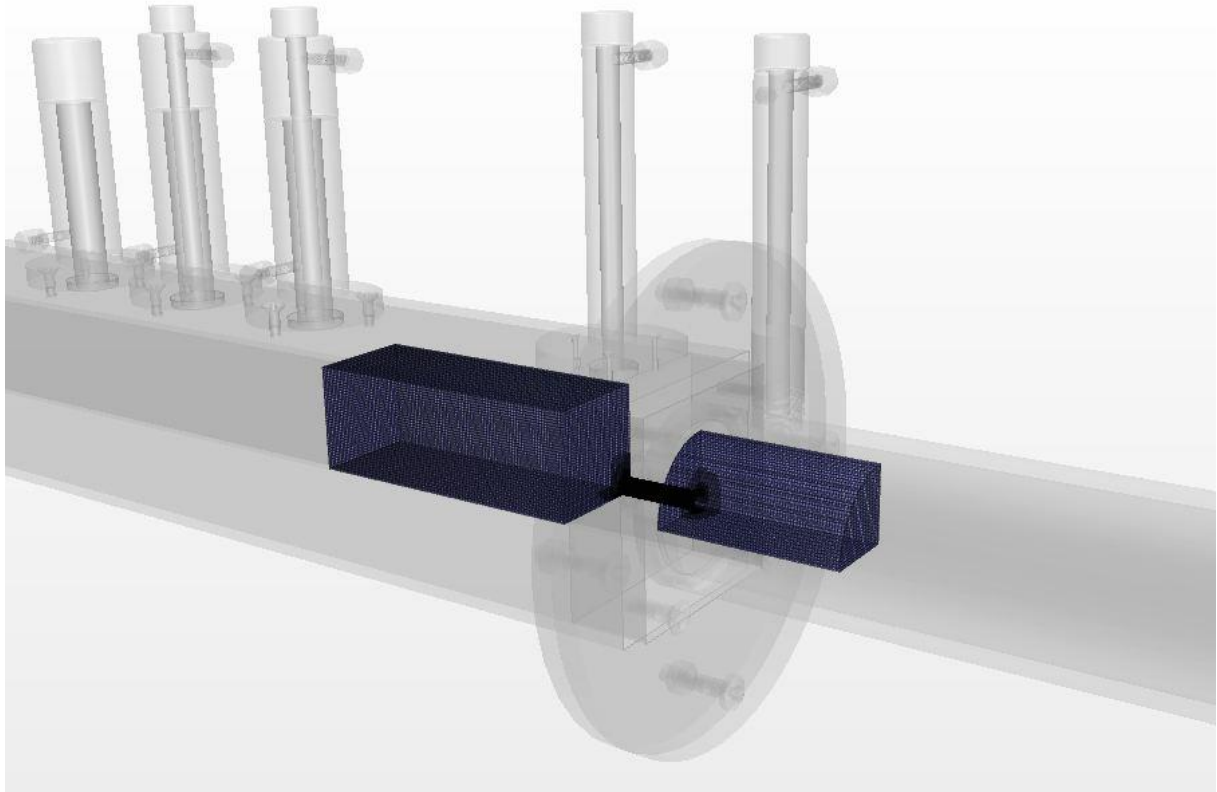
Figure 89 - CAD Representation of the CFD Computational Domain within the Experimental Discrete Resonator Impedance Tube Rig (Ø9mm Neck, Volume Case#7)

Figure 90 shows a schematic vertical section view of the computational domain, including highlighting the geometric parameters which can be varied to represent different experimental results collected for the equivalent isothermal atmospheric measurements conducted in the physical impendence tube. Parametric definition of the CFD domain ensures that subsequent models can be efficiently adapted to match experimental dimensions.
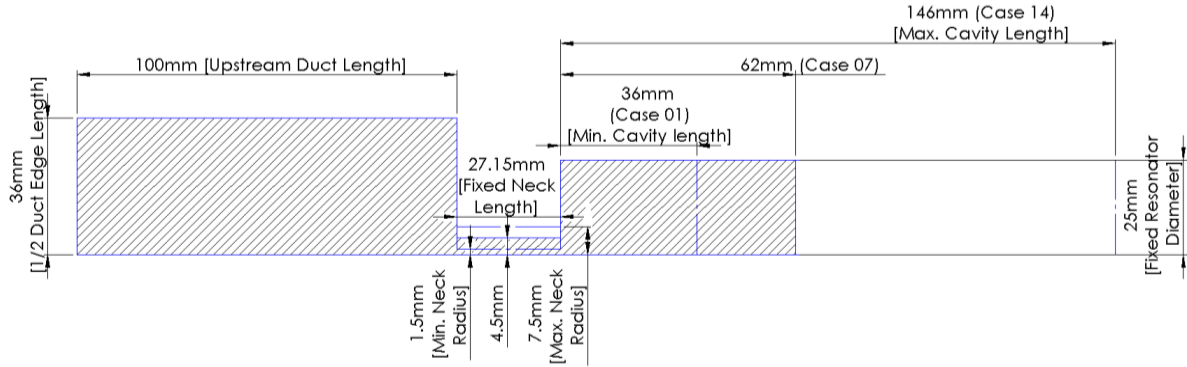
Figure 90 - Schematic vertical section representation of the parametric CFD Computation Domain

6.1.2 Boundaries & Boundary Conditions

As with an experimental investigation, the boundaries which define the scope of acoustic interest, must be carefully considered, in order to ensure the integrity of any deductions made from the investigation. In regards to a CFD study, a suitable boundary condition must be applied to all exterior surfaces of the volume of interest as a prerequisite for numerical solution.

In the context of this investigation, the "Inlet" represents both the source of the incoming acoustic excitation signal, and the termination for any subsequent reflections. As such, it is equally pertinent to ensure that it functions as an effective anechoic termination, otherwise there is potential for constructive/destructive interaction with the generated noise, resulting in either skewing of results, or falsification.

A full fidelity representation of a suitable sized transition duct, and an anechoic termination, could achieve the same results as experimentally however, at great cost to computational demand. Thankfully contemporary CFD tools such as those deployed in this study, enable the possibility of highly dissipative terminations to effectively represent an anechoic termination, without the need to geometrically represent it. By applying a "Free Stream" (Non-reflecting) transient-wave transmissive boundary condition to the inlet of this model, reflected pressure waves can be allowed to freely exit the computational domain; thus, ensuring that only the applied incident, and consequent generated acoustic signals remain for investigation.

All walls which represent a physical wall in the experimental equivalent are specified as a "No-Slip" wall; meaning that the fluid velocity will equal the wall velocity at the interface, which for the purposes of representing an equivalent impedance tube experiment, is zero at all walls. Due the fact that the CFD simulation will be solving for a compressible ideal gas (Air), a wall temperature must also be specified for all walls, which is also set to 293K in order to be comparable to atmospheric isothermal experiments.

A symmetry boundary condition is applied to both horizontal and vertical internal symmetry planes. This boundary definition limits the fluxes across the planes to be zero and sets the normal components of all variables to be zero on the plane. As with the inlet non-reflecting boundary condition, this offers the benefit of reducing the computational domain for which the governing fluid dynamics must be solved, and hence reducing the compute resource requirement. Within the comparable physical experimental configuration these symmetry planes also exist; and as they intercept through the axial centreline along which the incident acoustic wave propagates, this representation should not limit subsequent simulation's ability to adequately capture three dimensional nuances of any given acoustic response. A summary of all applied boundary conditions can be seen in Table 17.
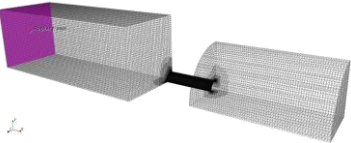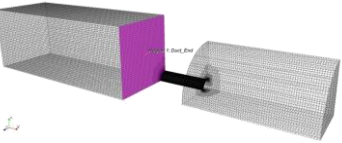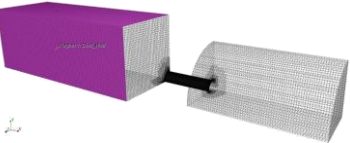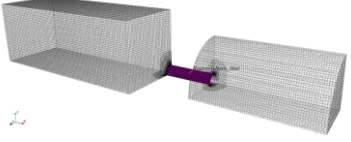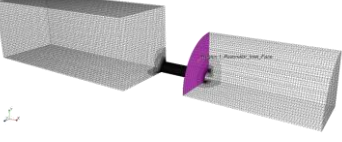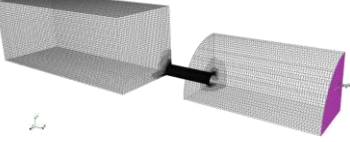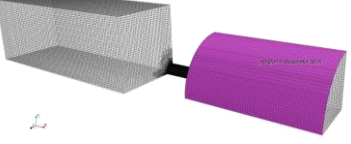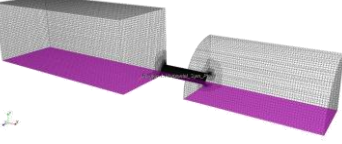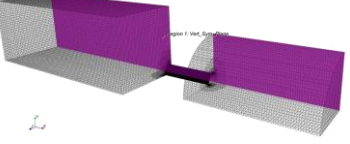
A) Inlet	B) Duct End	C) Duct Wall
Free Stream Boundary Condition *(Non-Reflecting)*	Wall *(No-Slip)*	Wall *(No-Slip)*
D) Resonator Neck	E) Resonator Inlet Face	F) Resonator Piston Face
Wall *(No-Slip)*	Wall *(No-Slip)*	Wall *(No-Slip)*
G) Resonator Wall	H) Horizontal Symmetry Plane	I) Vertical Symmetry Plane
Wall *(No-Slip)*	Symmetry Boundary Condition	Symmetry Boundary Condition

Table 17 - Clarification of boundary definitions; name, locations and applied boundary conditions

6.1.3   Meshing Regime

A hexahedral template mesh is used as the foundation of the volume mesh for subsequent numerical solution, which is then cut with the geometry surface defined by the parametric model, and further refined by custom boundary specific mesh conditions and volumetric mesh controls. As the neck of the resonator is particularly pertinent in defining the fluid dynamics which drive any given resonators acoustic response, here an additional boundary meshing regime is applied, in the form of a prism layer mesher. This results in a projection of the core mesh back to the associated wall boundaries via prismatic cells, which are generated according to user specified parameters, which can be seen in *Table 18.* The resultant layer of cells at the boundary serves to improve the accuracy of the flow solution in these areas, as the prediction of flow features such as pressure drop etc., are dependent on resolving the velocity and temperature gradients normal to the wall. These gradients can be steep and sudden in the viscous sublayer of a turbulent boundary layer and may be underrepresented if the mesh is too course in such areas. In addition to the prism meshing regime within the neck region, additional mesh refinement within the neck is obtained by specifying the boundary specific mesh conditions of a minimum size of cells (0.1mm), and target size (0.2mm), directly on the neck wall boundary *(*Table 17-*D)*. The final step in refining a meshing regime, which is sufficiently robust to permit a reasonable study of parametric variations, was to define some geometrically linked volumetric mesh controls, as detailed in *Table 19.*

Volume Mesh Type	*Trimmer/Cut Mesh*
Maximum Cell Size	*5mm*
Prism Layers	*Neck Wall only*
Number of Prism Layers	*5*
Prism Layer Stretching	*1.5*
Prism Layer Thickness	*0.1mm*
Surface Growth rate	*1.1*
Surface Size	*1mm Minimum & 1mm Target*
Template Growth Rate	*Slow*

Table 18 - General Mesh Conditions for all CFD Investigations
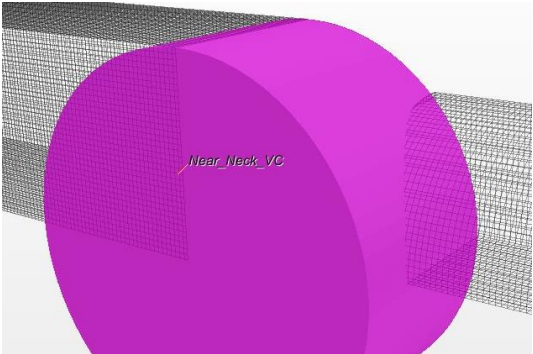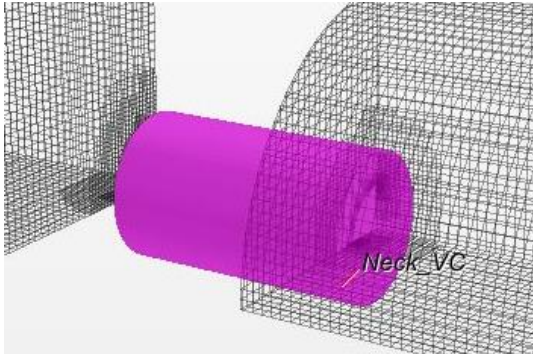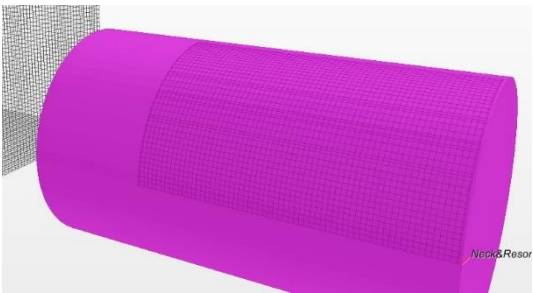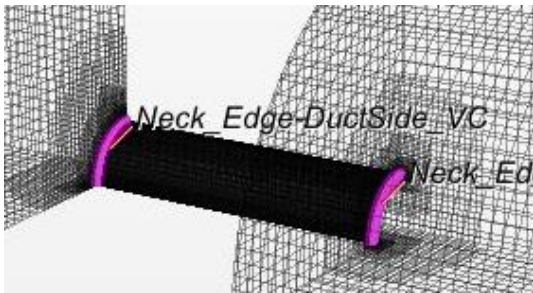
A) **Near Neck**	B) **Neck Volume**
Custom Isotropic Size – 1mm	Custom Isotropic Size – 0.5mm
C) **Resonator Volume**	D) **Neck Exit Edges**
Custom Isotropic Size – 1mm	Custom Isotropic Size – 0.1mm

Table 19 - Volumetric Controls applied to all CFD simulations

The outcome of this meshing regime and mesh controls, can be seen visually on the resultant volume mesh for a representative median case in *Figure 91 & Figure 92*. These figures show a simulation geometry which corresponds with the Ø9mm neck, and volume case #7; for all other geometric variations the meshing regime is kept consistent, and all volumetric controls are scaled with geometry variations accordingly; as a result the number of cells caries across neck diameter and volume cases as shown in *Table 20.*
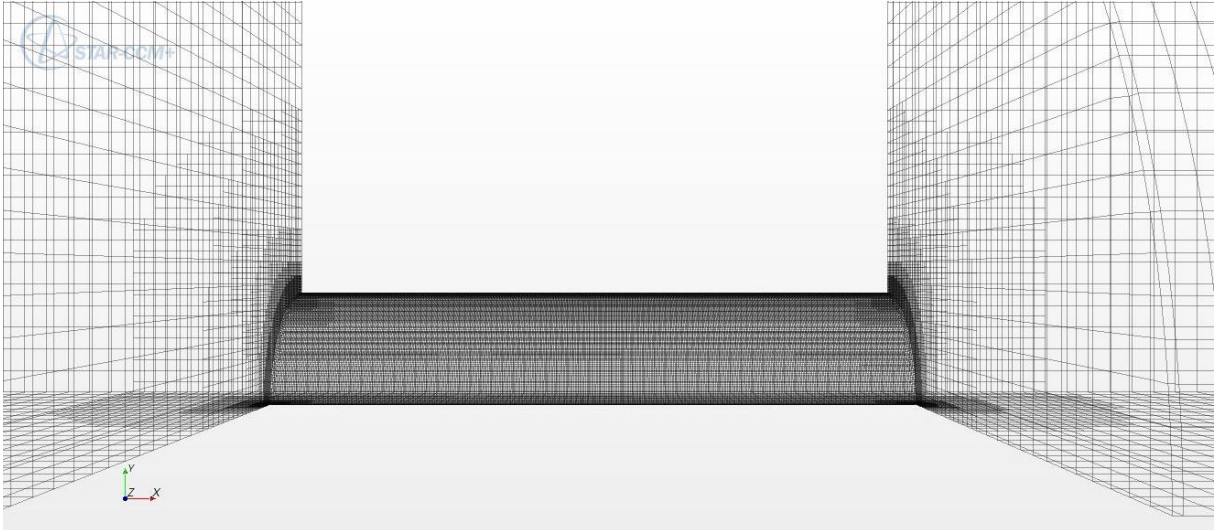
Figure 91 - CFD Neck Region Mesh Detail for Ø9mm Neck Case
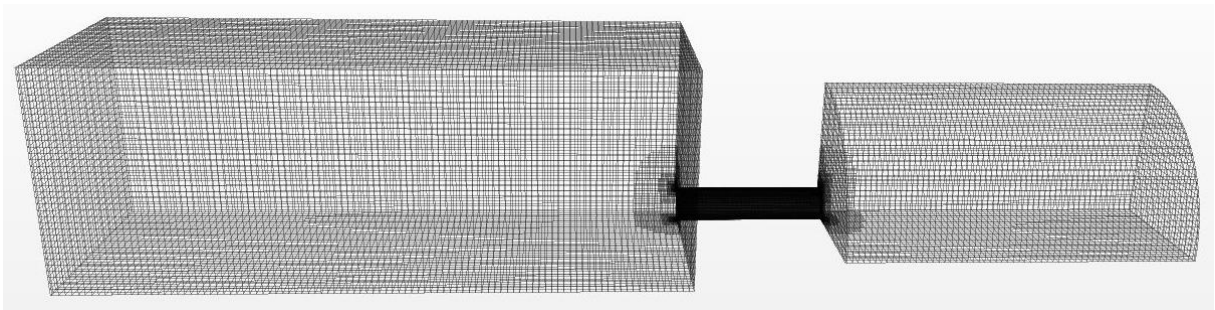
Figure 92 - CFD Volume Mesh Detail for Ø9mm, Volume #07 Case (615,841 cells)

	Ø3mm	Ø6mm	Ø9mm	Ø12mm	Ø15mm
Volume Case #1	279,420	446,535	607,073	790,829	949,007
Volume Case#14	334,647	502,863	663,608	848,188	1,004,533

Table 20 - Number of cells in resultant volume mesh, for each neck diameter, and min/max volume cases.

6.1.4   Physics Models

As the primary interest of this investigation is to evaluate the acoustic attenuation characteristics beyond those experimentally practicable, and hence potentially non-linear; it is necessary to ensure that any applied models are capable of resolving both the acoustic, and flow fields within the domain of interest. The medium within which the acoustics are propagating is represented as atmospheric air, henceforth a compressible gas, and specifically characterised within this study by a reference pressure of 101,325Pa, and Temperature of 293K. An accurate representation of the acoustic wave propagation within the medium is intrinsic to this simulation strategy, a goal which is rationalised through the solution of the governing compressible Navier-Stokes equations.   This is achieved through the integration of the governing equations of fluid flow across the computational domain; made

practicable by discretisation according to the meshing regime; which results in the conversion of the integral equations into a system of algebraic equations; thereby allowing for an iterative numerical solution to found.

This Implicit Unsteady modelling approach has the consequence of requiring careful consideration of an appropriate timestep over which to solve the flow field within the computational domain. The choice in timestep definition for this investigation was initially pragmatically defined as 1×10^{-4}s, such that the highest equivalent acoustic frequency of interest for this geometry (500Hz), would be resolved across a total of 20 discrete timesteps; thereby introducing a practical low band-pass filter, in the sense that frequencies higher than this within the computational domain could be considered insufficiently resolved. Evaluation of the results presented in subsequent sections indicated this timestep was sufficient to effectively characterise both the acoustic and fluid flow fields for the lower resonant frequency cases; however, for some of the following cases, this timestep was further reduced to 5×10^{-5}s in order to permit a higher resolution investigation, at the expense of increased compute time, and hence slower solution.

As these simulations are representing acoustic excitation only, the most pertinent velocity scale is that of the particle velocity. Under the excitation signal investigated, this velocity will be typically less than 1m/s for the acoustic field, hence the flow regime within the computational domain can be considered to be principally laminar flow, with a corresponding Reynolds Number $Re < 1$. Therefore, a segregated flow solution, i.e. separate solution of pressure and velocity, with 2nd order convection, and solving for temperature, is determined to be a good balance between compute resource requirement and fidelity of results.

Due to the importance of time dependence in accurately capturing the acoustic field, and the potential to numerical error when dealing with small magnitude permutations, a double precision solver is utilised, as is a 2nd order temporal discretisation of the solution.

6.1.5   Acoustic Excitation Signal

The approach to acoustic excitation within the simulations was designed to be equivalent to that used in experimental methodologies, in that the resonator is exposed to a random noise, in order to trigger an unknown response. For the CFD simulations, the equivalent noise which would be generated experimentally by a signal generator or flow generated noise, must be engineered and explicitly specified as an inlet condition. To achieve this goal, a white Gaussian noise sample signal was generated using Matlab, consisting of 100,000 points.

This generated signal is assumed to cover a time of 10s, and therefore 10,000Hz; and is then cleaned by filtering out frequencies within which are beyond the scope of measurement interest of 500Hz. This approach mitigates unwanted noise from entering the simulation, thus improving stability, allowing larger time steps, and requiring less compute time for sufficient data to be comparable with typical measured experimental data.

After filtering, the signal is then multiplied by a scalar value in order to give a resultant signal magnitude comparable with measured cases typical input signal. For all baseline simulations in this work, which are intended to be comparable with isothermal atmospheric Impedance tube tests, a scalar multiplier of 10 is used, which results in an RMS value of 1.39Pa (96.8dB) in the duct. In addition to the pressure specification, the Mach Number, which is based on acoustic velocity in this case, and the temperature, must also be provided in order to satisfy the energy equations at the free stream (non-reflecting) inlet boundary. In *Figure 93* a graphical representation of this signal shows the significance of the various signal conditioning steps. The final full 10 seconds of filtered and amplified signal, and corresponding Mach Number and Temperature tables, are those which are used as the inlet boundary specification for all subsequent CFD instigations.
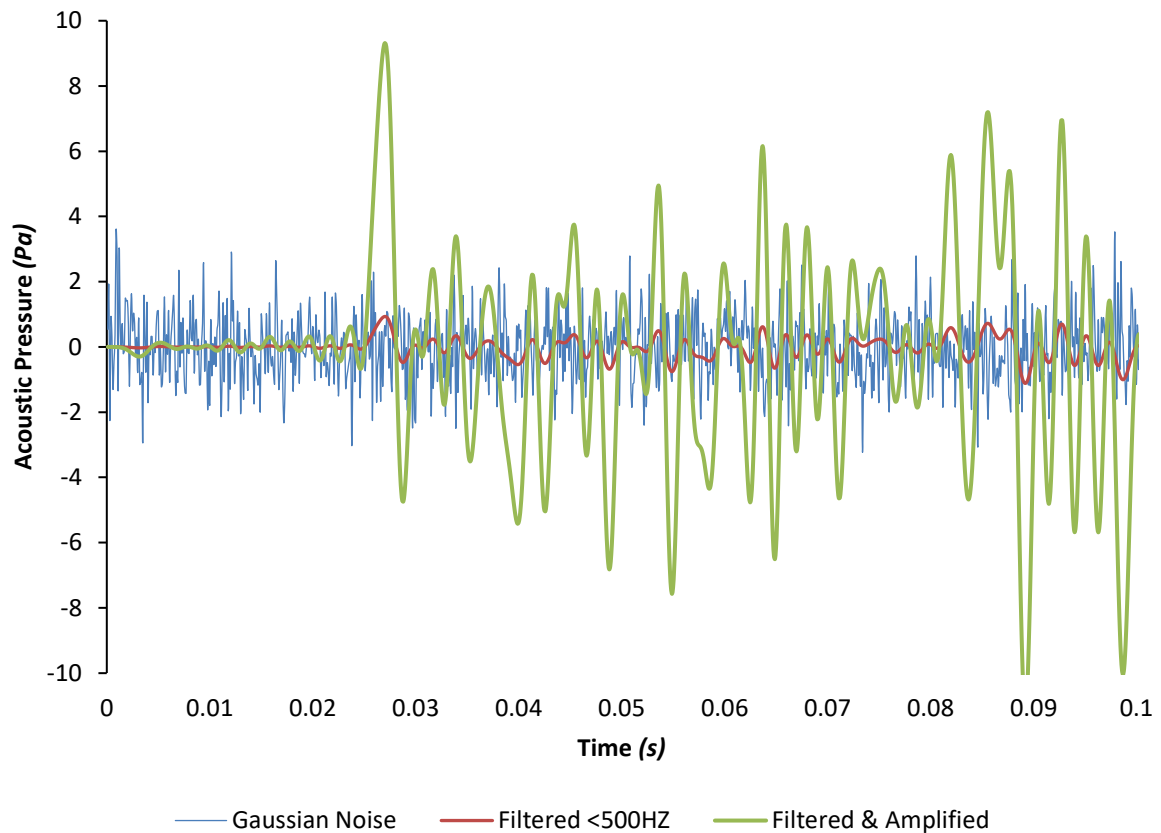
Figure 93 - Snapshot comparison of CFD Acoustic Excitation Signal, over 0.1s duration

6.2   Qualification of CFD Procedures

6.2.1   Methodology validation

Prior the evaluation of any CFD produced results, the Courant-Freidrichs-Lewy (CFL) stability condition is utilised to provide confirmation that the specified time step requirements for the proposed transient simulations, are appropriate for both the specified meshing regime, and the flow velocities resulting from the acoustic excitation. The Courant Number *(Equation [160]),* which can be calculated from the flow velocity u, the timestep Δt, and a characteristic dimension of the mesh Δx, was evaluated during the initial solution of a representative case, and shown to be consistently < 1.

$$C = u \frac{\Delta t}{\Delta x}$$

[160]

The Courant number provides an indicative insight into how much flow field information travels through a computational grid cell in a given unit of time, and as such a Courant number > 1, indicates that the information propagates through more than one cell per timestep, and could consequently introduce inaccuracies, instabilities, or even divergence of the solution.

In *Figure 94* a snapshot of the initial solution for a representative case *(Neck Ø9mm, Volume Case #7)* can be seen at solution time $t = 1s$. This scalar plot was observed throughout the initial simulations to ensure a reliable and robust simulation regime had been specified. The results of this initial evaluation showed that the Courant number consistently remained sufficiently low, and that as expected, the highest values occurred around the sharp exits to the neck, where the mesh size was the smallest, and the velocities amongst the highest.
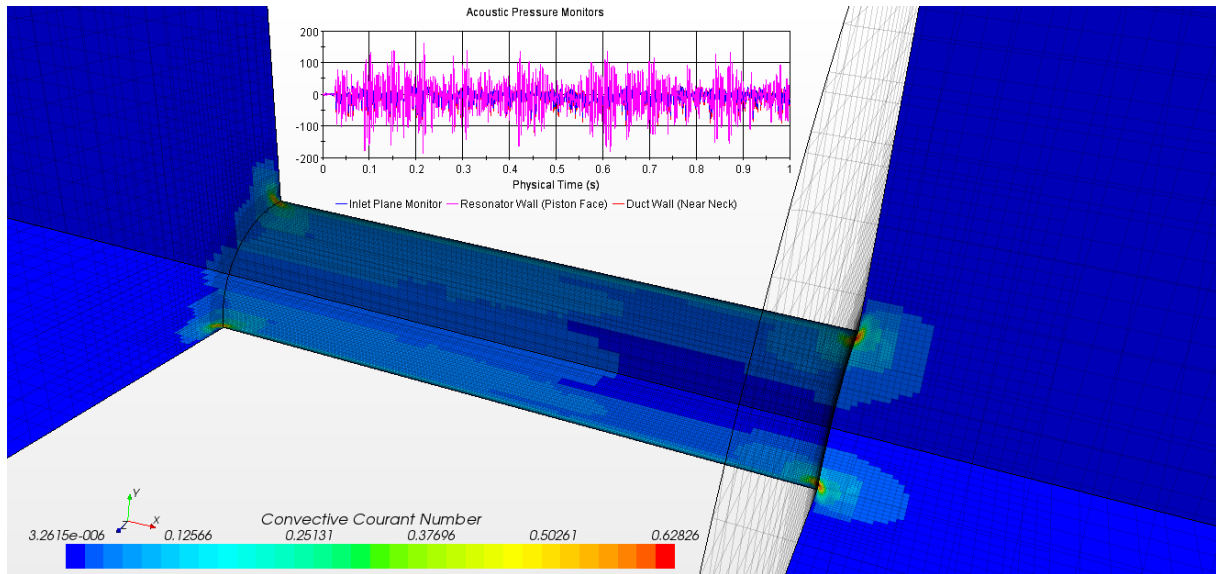
Figure 94 - Scalar plot of Courant Number during initial simulation for Ø9mm neck, volume case #7, at a solution time of t=1s.

6.2.2   Confirmation of Resonator Geometry

During the evaluation of initial cases, it was found that all CFD solutions were consistently converging on resonant values lower than those of the corresponding measured cases. After a thorough analysis of potential causes, it was hypothesised that the idealistic resonator geometries applied in the CFD model, may not be sufficiently representative of the physical artefacts used to collect the experimental results. In fact, as all initial CFD simulations were consistently predicting lower resonant frequencies than those measured, it was deduced that there must be either an under representation of the true resonator neck diameters, or an over representation of the neck length or cavity volume.

The assumed neck dimeters corresponding to each of the neck inserts, relate to the diameter of twist drill and subsequent reamer used to create the hole. As with any practical manufacturing process, there are inherent tolerances; and even when striving for a high tolerance manufacturing process, the practicable limitations of the process may still be acoustically significant.

In order to evaluate this hypothesis, an initial investigation was conducted, whereby the density of the material used to construct the inserts *(2720kg/m³),* and the measured outer diameter *(15.2mm),* was used to determine the mass of a "Control Neck Insert", i.e. a representative solid cylinder. Each of the discrete neck inserts could then be weighed on a highly accurate set of measurement scales, where their mass could then be determined to the nearest 1000th of a gram. Once the mass of the inserts was known, it could then be subtracted from the control mass, in order to evaluate the "missing mass" corresponding to the neck volume. This approach allows for any axial variations in diameter or other internal defects to be accounted for; for example a piece of removed swarf may have scraped away additional material during boring which would not be detectable from the exterior surfaces, or a drift

169

in the concentricity of the drill may have resulted in a reduction of the circularity of the hole etc.; irrespective of the cause, this method allows for an effective diameter to be considered through representation of the missing mass, as an idealised cylinder. As shown in *Table 21*, the results from this investigation did indeed conclude that the evaluated neck diameters were consistently determined to be larger than the ideal values used in the initial CFD models, thus in-part explaining the reason for convergence on under-predicted peak resonant frequencies for the initial cases investigated.

Assumed Neck Ø *(mm)*	Measured Weight *(g)*	Measured Outer Diameter *(mm)*	Measured Length *(mm)*	Effective Neck Ø *(mm)*
12	4.417	15.2	27.0	12.53
9	8.659	15.2	27.1	9.12
6	11.21	15.2	27.2	6.24
3	12.824	15.2	27.3	3.34

Table 21 - Effective Neck Insert Diameters, as determined by weighing technique

To ensure appropriate rigor in these deductions, an alternative optical metrology method was also employed as a comparison. This technique consisted of taking high resolution images of the neck inserts on a calibrated imagining table, before then utilising metrology software to fit and calculate an effective diameter for both sides of the neck. An overview of this process and the metrology software overlay can be seen in *Figure 95.*
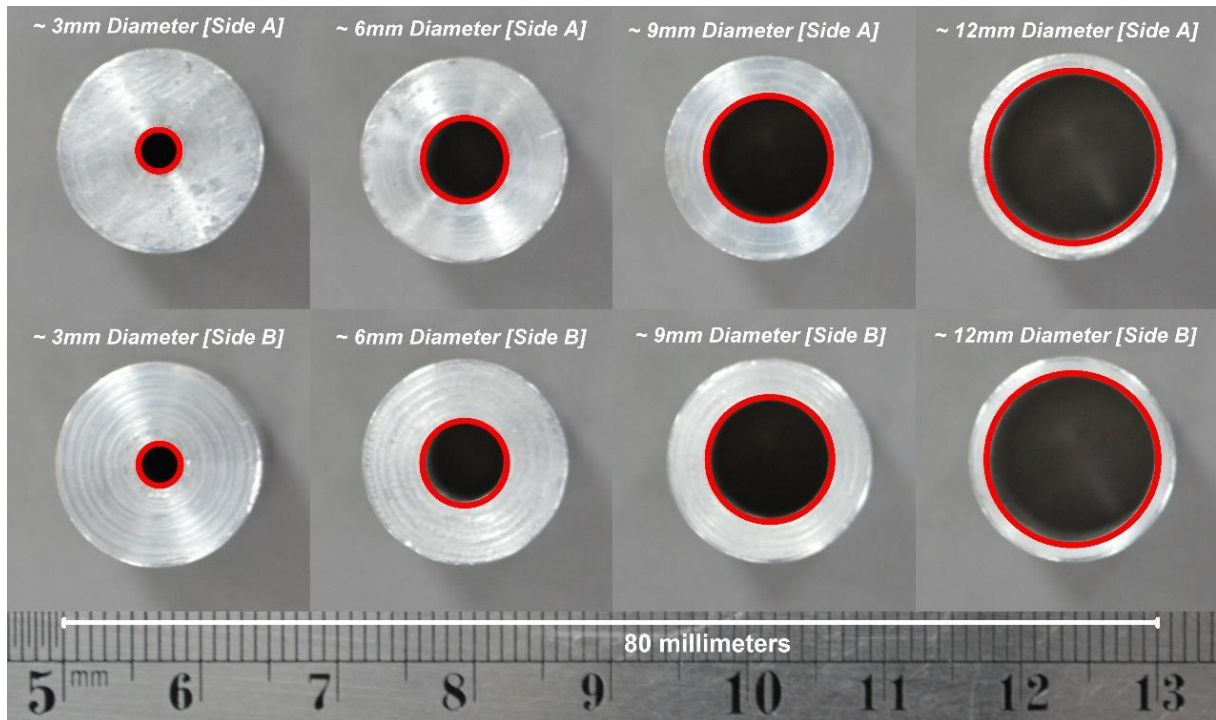
Figure 95 - Overview of optical neck diameter measurements and metrology software overlay

The conclusion from this method of evaluation was also in agreement with the weighing approach, similarly, concluding that in all cases the actual neck diameter of the inserts was indeed larger than the ideal values. There was, however, some small variations in deduced diameter between the two techniques; and by iteratively solving for all suggested diameters, it was found that the optically determined values showed slightly better coherence with the experimental results. As such the average measured diameters shown in *Table 22*, will be those used in all subsequent CFD evaluations, unless otherwise specified.

Assumed Neck Ø *(mm)*	Side A radius *(mm)*	Side B radius *(mm)*	Average Measured Ø *(mm)*
12	6.315	6.293	12.61
9	4.565	4.565	9.13
6	3.058	3.102	6.16
3	1.529	1.551	3.08

Table 22 - Effective Neck Insert Diameters, as determined by optical measurement technique

6.2.3   Significance of Timestep

In *Section 6.1.4* the rationale for the chosen time step of 1×10^{-4}s was presented however, it was also alluded to that for some of the cases exhibiting resonant responses closer to the specified cut off frequency of 500Hz, it was necessary to decrease this timestep to 5×10^{-5}s. In this section the significance of this choice is evaluated through a direct compassion of equivalent case solution, using both simulation time step regimes on the corresponding cases. The results from this evaluation can

be seen in Figure 96, whereby it can be seen that for the small volume case #1, the resonant frequency and magnitude are both under predicted by the larger time step solution of 1×10^{-4}s. Irrespective of direct comparison with experimental results, it can alone be appreciated that for the lower frequency dynamics cases of cases #7 & #14, there is very good coherence between both applied timesteps. Between these two cases, only a maximum difference of 1.83Hz is witnessed in peak attenuation Frequency, and a maximum difference of 1.22 in FRF magnitude.

Careful consideration the results from comparison of volume case #1 show that the onset on resonance is comparable, as is the change in slope, until in the region of 360Hz; beyond which point the magnitude of the 1×10^{-4}s case decreases from the expected trend. From this evidence is clear that the despite there clearly still being frequencies within the simulation below the cut off frequency of 500Hz, they are likely being numerically dampened in region close to cut off, which has the inherent consequence of skewing resultant FRF derivations.
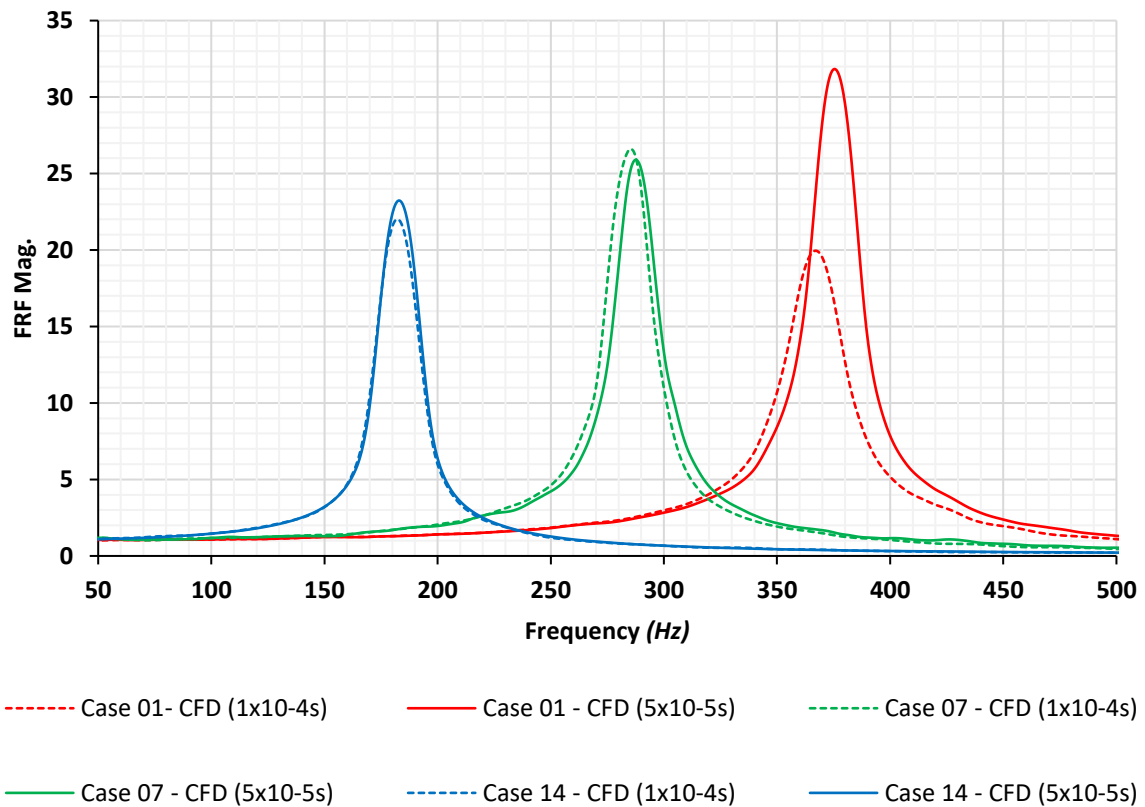
Figure 96 - Significance of CFD Time Step Specification on the solution of a Ø12mm Neck Case, across Min, Median & Max Cavity Volume Cases (#1, #7 & #14)

As a result of these findings, it can be concluded that the originally proposed time step of 1×10^{-4}s can be confidently applied to the test cases within this study which exhibit frequency dynamics of less than 300Hz *(i.e. Neck Diameters <12mm),* and for the remaining higher frequency dynamics cases, a smaller timestep of 5×10^{-5}s should be used in preference.

6.2.4   Validation against experimental cases

In the following section, the developed CFD simulation methodology will be applied to the direct simulation of existing experimental discrete resonator test cases, for the purpose of validation of the proposed simulation regime. A simulation was conducted for each available neck diameter, and for each diameter case the minimum, median, and maximum volume cases *(Cases #1, #7 & #14)* were evaluated.

FRF was used as a comparison metric and derived by taking a probe points of acoustic pressure within the computational domain, identical to those of the experimental measurement methodology. The resultant temporal pressure data was then post processed using the same methodology and parameters as the experimental results also, thus ensuring direct equivalence of the results under comparison.

The results from this validation exercise showed good coherence between the CFD model's predictions of both peak absorption frequency, and FRF magnitude; as seen in both the corresponding FRF comparison plots *(Figure 97, Figure 98, Figure 99, Figure 100 & Figure 101),* and the corresponding peak value tables *(Table 23, Table 24, Table 25, Table 26 & Table 27).*

Within the results for the smallest neck diameter of 3mm *(Figure 97 & Table 23),* there can be seen to be a general trend of underprediction of the resonant frequency by the CFD model, albeit of magnitude of <2Hz. The maximum difference in predicted FRF magnitude is 0.57 for volume case #1, which could be perceived to be insignificant however, given the magnitude of FRF is small for these cases, this small absolute difference equates to an 8.5% difference in prediction. It is also noteworthy that FRF magnitude is overpredicted for volume cases #1 & #7, whereas it is slightly underpredicted for the large volume case #14. Across the cases there is an average frequency difference of 1.48Hz, and an FRF magnitude difference of 0.31.
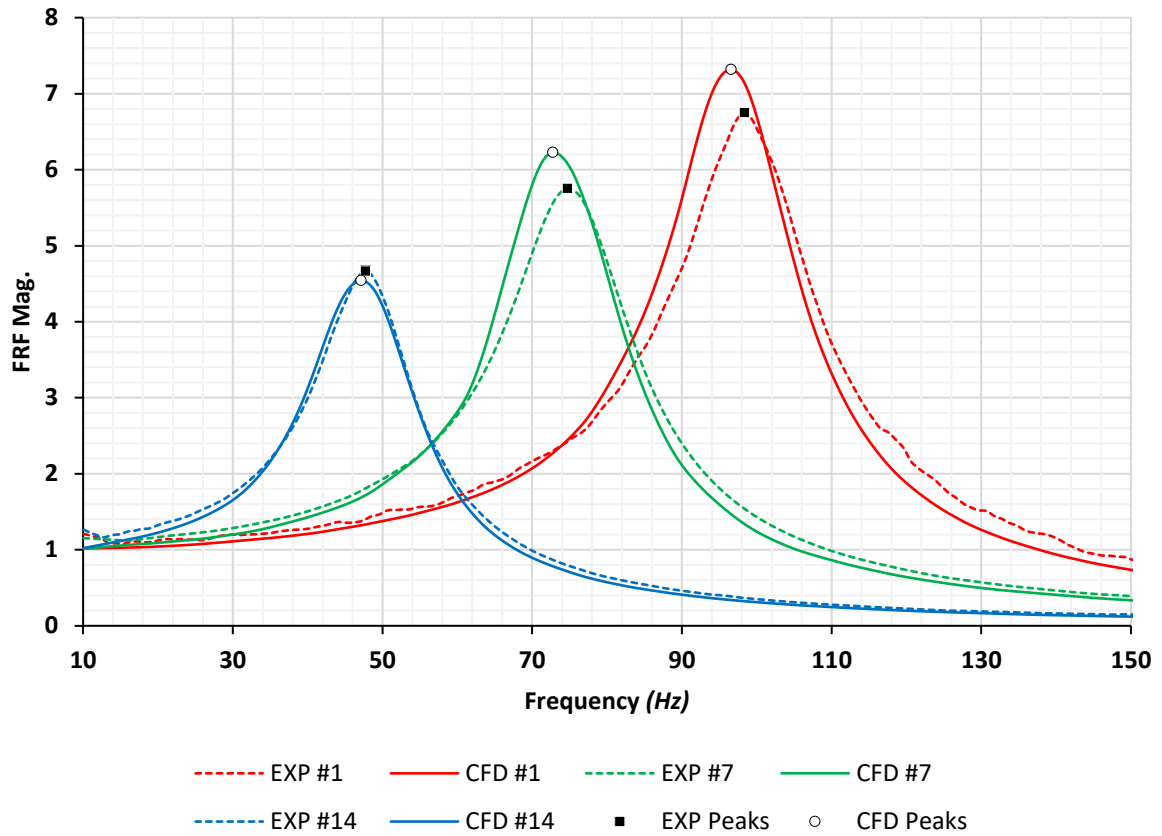
Figure 97 - Comparison of CFD & Experimentally derived FRF, for Neck Ø3mm & Min, Median & Max Cavity Volume Cases (#1, #7 & #14)

	Volume #1		Volume #7		Volume #14	
	Frequency (Hz)	FRF Mag.	Frequency (Hz)	FRF Mag.	Frequency (Hz)	FRF Mag.
Experiment	98.42	6.75	74.77	5.75	47.76	4.67
CFD	96.59	7.32	72.78	6.23	47.15	4.54
Difference	1.83	-0.57	1.98	-0.48	0.61	0.12
	1.9%	-8.5%	2.7%	-8.3%	1.3%	2.6%

Table 23 - Comparison of CFD & Experiment peak FRF frequency, magnitude and difference, for Neck Ø3mm & Min, Median & Max Cavity Volume Cases (#1, #7 & #14)

The results for the 6mm diameter neck *(Figure 98 & Table 24)* are in very close agreement with the experimental results, across both metrics and all cases; with an average peak absorption frequency difference of 0.05Hz, and an average FRF magnitude difference of 0.25. The maximum Frequency prediction error is a 0.76Hz underprediction for volume case #1, which also exhibits the largest FRF magnitude error of 0.91, or 5.4%.
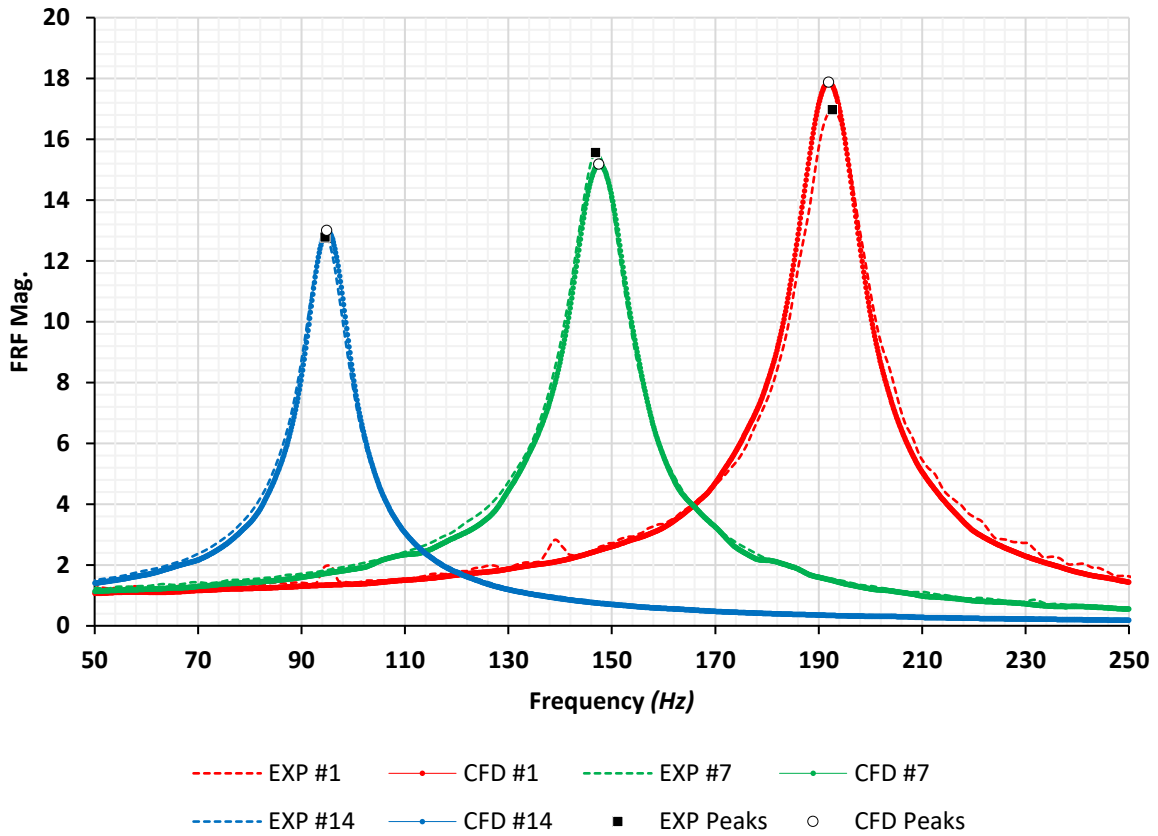
Figure 98 - Comparison of CFD & Experimentally derived FRF, for Neck Ø6mm & Min, Median & Max Cavity Volume Cases (#1, #7 & #14)

	Volume #1		Volume #7		Volume #14	
	Frequency (Hz)	**FRF Mag.**	**Frequency (Hz)**	**FRF Mag.**	**Frequency (Hz)**	**FRF Mag.**
Experiment	192.72	16.96	146.94	15.55	94.60	12.78
CFD	191.96	17.87	147.55	15.17	94.91	12.99
Difference	0.76	-0.91	-0.61	0.38	-0.31	-0.22
	0.4%	-5.4%	-0.4%	2.4%	-0.3%	-1.7%

Table 24 - Comparison of CFD & Experiment peak FRF frequency, magnitude and difference, for Neck Ø6mm & Min, Median & Max Cavity Volume Cases (#1, #7 & #14)

In *Figure 99 & Table 25*, which correspond to the 9mm diameter neck, a similar trend of good correlation can be witnessed in terms of peak absorption frequency, with an average difference of 0.56Hz across the cases, and a maximum difference for case #1 of 1.98Hz. What is more pertinent in the 9mm diameter cases, however, is a greater variation of FRF magnitude between the model and measurements. There is an average underprediction across these volume cases of 2.5, with the largest variation also being accounted for by the case #1, which is underpredicted in magnitude by 4.11, equivalent to 18% of the measured signal.
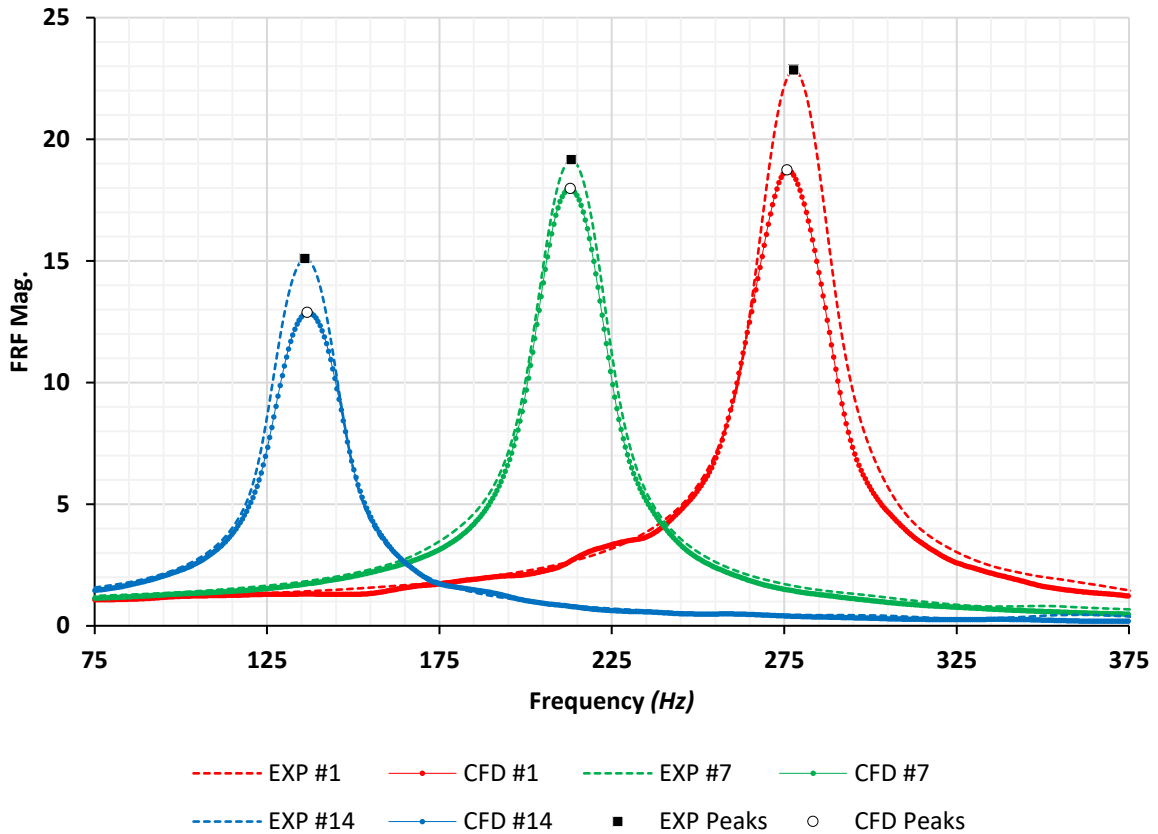
Figure 99 - Comparison of CFD & Experimentally derived FRF, for Neck Ø9mm & Min, Median & Max Cavity Volume Cases (#1, #7 & #14)

	Volume #1		Volume #7		Volume #14	
	Frequency (Hz)	FRF Mag.	Frequency (Hz)	FRF Mag.	Frequency (Hz)	FRF Mag.
Experiment	277.86	22.84	213.32	19.15	136.11	15.09
CFD	275.88	18.73	213.01	17.97	136.72	12.88
Difference	1.98	4.11	0.31	1.18	-0.61	2.21
	0.7%	18.0%	0.1%	6.2%	-0.4%	14.6%

Table 25 - Comparison of CFD & Experiment peak FRF frequency, magnitude and difference, for Neck Ø9mm & Min, Median & Max Cavity Volume Cases (#1, #7 & #14)

In *Section 6.2.3* it was shown that for a neck diameter of 12mm, volume case #1 required the reduction in standard time step from 1×10^{-4}s, to 5×10^{-5}s, in order to fully resolve the higher frequency dynamics defining the resonators response. In *Figure 100 & Table 26* it can be seen that when comparing the resultant CFD predictions for all simulated 12mm diameter neck case, to their experimental equivalence, there is a good agreement across all cases, including the higher frequency resonance of case #1. The peak frequency error does still lie with case #1, and to the tune of a 3.66Hz (1%) over prediction. The peak FRF magnitude error however, occurs for the largest volume case of #14, and equates to a 2.23 (10.6%) overprediction. Due to the fact that volume case #14 overpredicts the

magnitude, whereas the other cases underpredict it, the average FRF magnitude deviations is actually quite low, at 0.12 across all volume cases; compared to the consistent overprediction of the peak absorption frequency, which results in an average error of 2.5Hz.
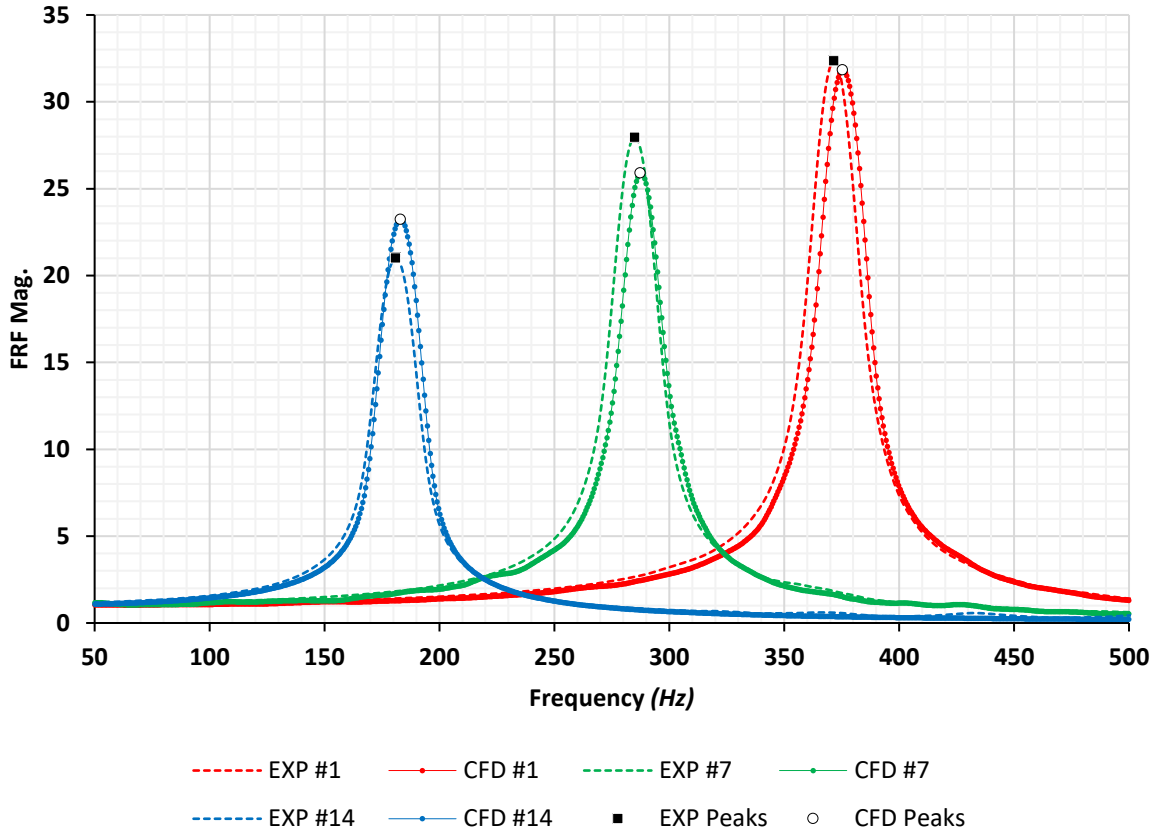
Figure 100 - Comparison of CFD & Experimentally derived FRF, for Neck Ø12mm & Min, Median & Max Cavity Volume Cases (#1, #7 & #14)

	Volume #1		Volume #7		Volume #14	
	Frequency *(Hz)*	**FRF Mag.**	**Frequency** *(Hz)*	**FRF Mag.**	**Frequency** *(Hz)*	**FRF Mag.**
Experiment	371.70	32.36	285.03	27.95	180.97	21.00
CFD	375.37	31.83	287.48	25.90	183.11	23.23
Difference	-3.66	0.53	-2.44	2.05	-2.14	-2.23
	-1.0%	1.6%	-0.9%	7.3%	-1.2%	-10.6%

Table 26 - Comparison of CFD & Experiment peak FRF frequency, magnitude and difference, for Neck Ø12mm & Min, Median & Max Cavity Volume Cases (#1, #7 & #14)

The initial CFD simulations of the baseline neck of assumed 15mm diameter, did not converge on a result matching that of the experimental results as expected; however, an accurate effective diameter for this case could not be concluded from the previous metrology exercises, which applied to the neck inserts only. Irrespective, given the proven faithfulness of this CFD methodology's ability to predict

peak absorption frequency for these discrete cases, it was therefore possible to use the CFD model as a tool to iteratively find the most representative neck diameter for the 15mm neck cases.

The results shown in *Figure 101 & Table 27* are those relating to the conclusion of an iterative batch run of neck variation simulations for the nominal 15mm case, in which the diameter was varied, until a match with the experimental results was found. This investigation utilised volume case #7 and converged on a neck diameter of 15.38mm as the ideal representation.

From these results it can be seen that this value of neck diameter, and the existing simulation methodology, provides an excellent correlation with measured results across all volume cases. The maximum prediction error was only marginally largest for volume case #1, and of magnitude 0.92Hz. Volume case #14 presented the largest difference in FRF magnitude by some way, to the value of a 2.41 (5.4%) overprediction by the CFD model. Across all volume cases, the average peak absorption frequency difference was 0.1Hz, with an average FRF magnitude difference of 0.71.
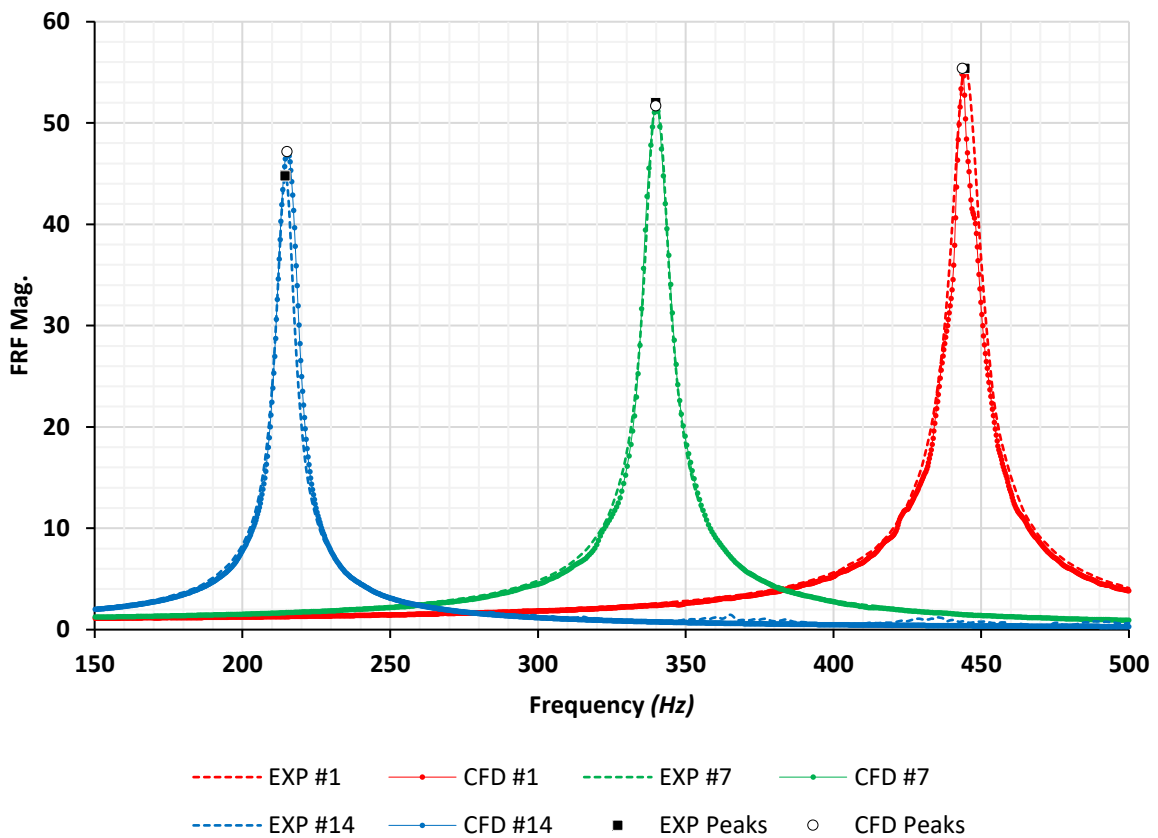
Figure 101 - Comparison of CFD & Experimentally derived FRF, for Neck Ø15mm & Min, Median & Max Cavity Volume Cases (#1, #7 & #14)

	Volume #1		Volume #7		Volume #14	
	Frequency (Hz)	FRF Mag.	Frequency (Hz)	FRF Mag.	Frequency (Hz)	FRF Mag.
Experiment	444.64	55.35	339.97	51.97	214.54	44.73
CFD	443.73	55.36	339.97	51.67	215.15	47.15
Difference	0.92	-0.01	0.00	0.30	-0.61	-2.41
	0.2%	0.0%	0.0%	0.6%	-0.3%	-5.4%

Table 27 - Comparison of CFD & Experiment peak FRF frequency, magnitude and difference, for Neck Ø15mm & Min, Median & Max Cavity Volume Cases (#1, #7 & #14)

Across all cases simulated and evaluated, the largest difference between measured and simulated peak absorption frequency occurred with the 12mm diameter neck cases, and the largest error in FRF magnitude occurred for the 9mm diameter cases. Across all cases the average difference between CFD and experimental peak absorption frequency and FRF magnitude was only 0.13Hz and 0.27 respectively. These values are within the range of experimental tolerances, and as such should allow the use of this CFD simulation methodology with confidence, as a mechanism for the deeper investigation and evaluation of discrete resonator sound absorption characteristics, and subsequently to investigate conditions beyond what is experimentally practicable.

6.3 CFD Results & Discussion

6.3.1 Time Averaged Acoustic Velocity Magnitude Investigations

As demonstrated in the previous section, the CFD simulation methodology employed here is capable of fully resolving the fluid dynamics of the resonators investigated here within; and has shown an ability to accurately predict the corresponding acoustic response when exposed to an excitation signal. Subsequent to the aforementioned validation against measured cases, the full potential of a spatial solution can now be exploited to provide a greater insight of the underpinning performance factors, one such example of this is to plot the time-averaged acoustic velocity magnitude against the location in the system. The following figures (Figure 102 - Figure 104) show the spatial distribution of time-averaged acoustic velocity magnitude throughout the transition duct, the resonator neck, and the cavity; where $X = 0$ is the entrance to the neck, and $Y = 0$ is the axial centreline; from which it can be seen that for the equivalent acoustic excitation signal, the resultant flow regime within the neck and surrounding volume, varies significantly between the investigated geometry cases.

In Figure 102 the time-averaged acoustic velocity magnitude can be seen for a Ø6mm neck, with a median cavity volume of case #7. From this plot it can be immediately appreciated the inherent

weakness of the fundamental Rayleigh (1926) end correction approach; which was discussed initially in Section 2.2, and shown graphically in Figure 26; in which the additional entrained mass of the oscillating fluid volume within the vicinity of the neck, is idealised as a virtual extension of the same geometry as the neck. This idealistic assumption masks the underlying fluid dynamics in the vicinity of the neck however, Ingard (1953) identified that to truly define the end correction, the particular diffraction problem dealing with the transmission of sound through the resonator aperture must be solved; and that the difficulty arises from the fact that the velocity distribution in the aperture is not known a priori; hence pre-CFD solutions typically employed a uniform velocity distribution assumption.

Irrespectively, many early works still attempted to empirically model the additional radial entrainment characteristics, in addition to the simplified axial movement; through modifications of acoustic reactance and resistance terms as discussed in Chapters 2 & 3. Furthermore, analytical solutions and empirical corrections have been extensively shown to provide reasonable predictions of the resultant acoustic response of complex underpinning three dimensional phenomena, regardless of the inherent simplified assumptions; and in the previous chapter it was shown that the current state of the art, could be further advanced to provide very accurate predictions of attenuation performance, across a large range of geometric variations.

Through a numerical solution of the acoustically relevant flow field however, the full fidelity of the end correction dynamics can be appreciated; and the aforementioned approach of plotting the time-averaged acoustic particle velocity magnitude, provides a novel appreciation of the true three-dimensional acoustic energy diffraction mechanisms. By plotting the spatial distribution of time-averaged acoustic particle velocity across the computational domain, the resultant contour plot provides an indication of the kinetic energy contributing to the individual attenuation characteristics of each simulated geometry variation.

The results obtained for the Ø6mm Neck, Volume Case #7, shown in Figure 102; and the Ø9mm Neck, Volume Case #1 shown in Figure 103; can be seen to exhibit similar results; whereby it is evident that the diffraction gradient from cylindrical axial oscillation within the neck, to planar axial propagation in the duct and resonator cavity, is quasi-spherical; and hence consists of both axial and radial end correction elements, as expected by the current theory.

At this point it is pertinent to compare the relative ideal quasi-empirical end correction introduced in Section 5.1.2 for each case, where the total end correction was defined as the sum of the Ingard hole-to-wall end correction δ_{h-w}, and the newly proposed geometric proportionality end correction δ_{geo}, where:

$$\delta_{total} = \delta_{h-w} + \delta_{geo}$$ [161]

The value of $\delta_{total}/\sqrt{A_o}$ for the Ø6mm Neck and Volume Case#7 is 1.19, and the corresponding value for the Ø9mm Neck, Volume Case #1 is 1.02. Whilst the diffraction profile between the two cases is visually similar; closer inspection of the magnitude contours, in relation to the spatial dimensions; supports the rationale that the latter case entrains less fluid volume outside of the vicinity of the neck, and thus should have a correspondingly lower end correction length to model it effectively in an ideal resonant frequency solution.
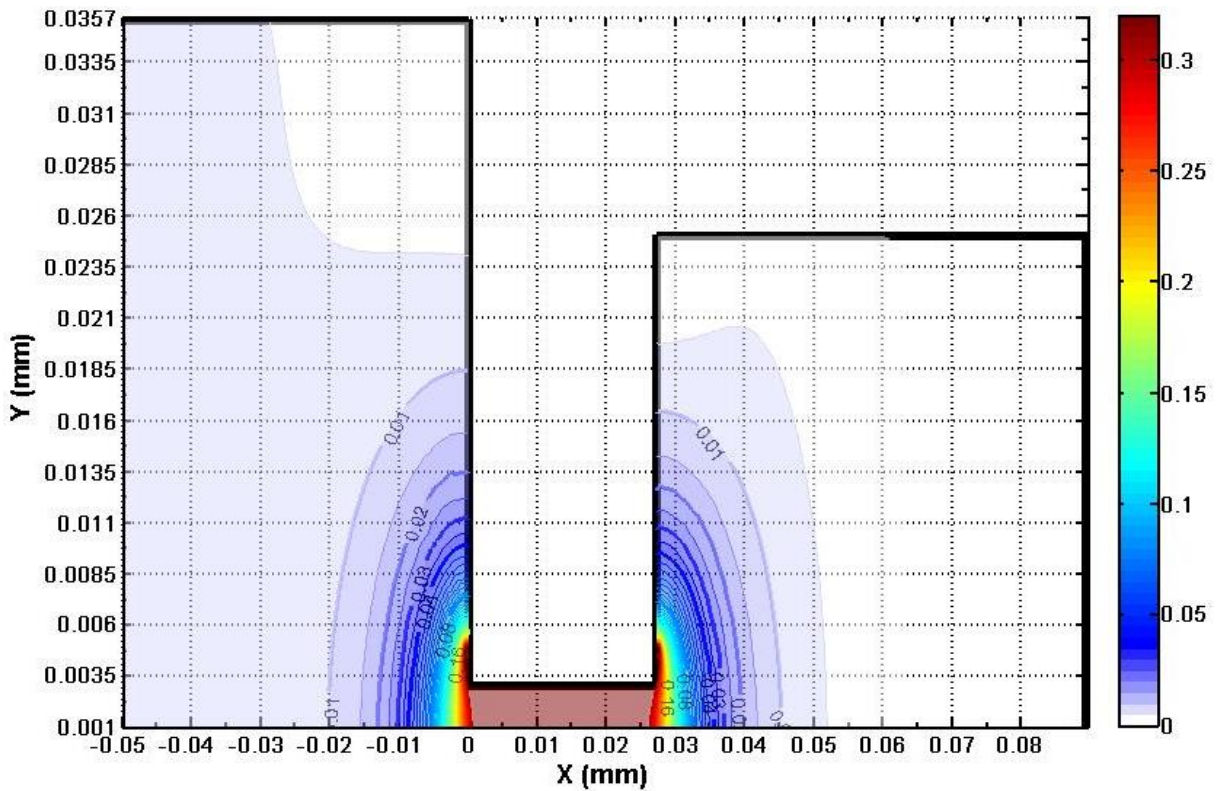
Figure 102 - Time-Averaged Acoustic Velocity Magnitude (m/s) for 6mm Neck, Volume Case #7

That observed deviations from experimental and numerical results and one-dimensional analytical predictions, indicates the significance of multi-dimensional wave propagation at frequencies for which, theoretically, only the planar mode should propagate; hence it is pertinent to discuss the localised problem of diffraction in the vicinity of the neck aperture, in relation to the acoustic wave theory presented in Section 2.1. Principally we can deduce that at area discontinuities, such as the apertures of the resonator neck, multi-dimensional waves are excited at all frequencies; however, for frequencies well below the cut-off frequency, the multi-dimensional waves decay in a short distance and have little impact on the holistic attenuation characteristics. At higher frequencies approaching that of the first radial mode however, multi-dimensional effects begin to dominate, causing a breakdown of the one-dimensional plane wave propagation assumptions inherent to most analytical

methods.   (Selamet & Radavich, 1997). In the context of the carefully designed experimental and numerical investigations here within, the excitation signal conditioning and measurement methodology mitigates the existence of non-planar wave propagation within the transition duct; however, and irrespectively, we can see that in the local vicinity of the neck aperture, there must exist a transition region between the area discontinuities, where the plane-wave propagation assumption cannot be applied. Similar observations on the local significance of multi-dimensional waves can be found in existing literature using both finite element and boundary element methods, such as: Young and Crocker (1975) for a simple expansion chamber, and (1977) for exhaust mufflers, including flow-reversing chambers and Helmholtz resonators; and by Sahasrabude et al. (1995) for sudden area discontinuities. In the latter reference of Sahasrabude, he found that the optimal axial length following an area discontinuity, necessary to ensure plane wave conditions at the respective termination, to be 1.5 times the diameter; and he attributes observed errors between experimental and analytical models with $L/D < 1.5$ to the non-decay of the evanescent modes at the exit plane.
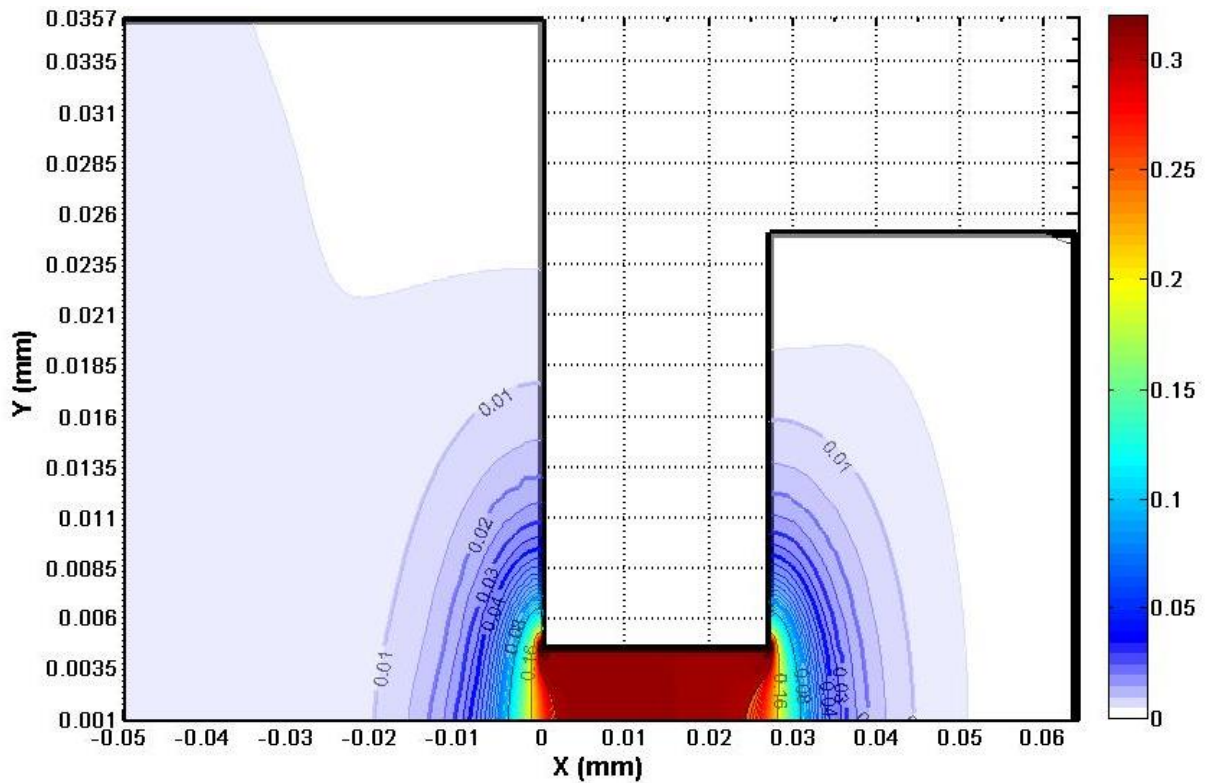
Figure 103 - Time-Averaged Acoustic Velocity Magnitude (m/s) for 9mm Neck, Volume Case #1

To put the aforementioned deduction into the context of the resonator cases investigated, the cavity volume cases of #7 and #1, shown in Figure 102 & Figure 103, have L/D values of 1.23 and 0.73 respectively; hence it can be assumed that the not all evanescent modes may have fully decayed before reaching the back wall of the resonator cavity; a notion which is supported by the transition profile of the time-averaged velocity magnitude contours in the respective figures. It should also be noted that, as discussed in the previous chapter, the equivalent neck-to-cavity geometric proportionality also

effects end correction; and whilst it has been shown that empirical corrections can effectively represent these effects within 1-D models to a certain extent; the ultimate cause for the geometric sensitivity is the fact that the end correction is composed of three dimensional evanescent cross modes (Chanaud, 1997); similarly this notion is supported by previous results, when evaluating the diffraction pattern in the radial (Y) direction.

The minimum cavity length investigated in this study is volume case #1 ($L = 36cm$), which corresponds to a L/D value of 0.73; more extreme values of L/D ratios for cavity dimensions have been investigated by Kang and Ji (2008), who found that for a L/D ratio of 0.1, the sound waves propagate in the radial direction only; as the short cavity cannot decay 3D waves sufficiently, and consequently it is not possible to introduce an effective acoustic length correction for the axial wave propagation. Dickey (1996) also recognised that multi-dimensional wave propagation into the cavity volume was prevalent at the neck aperture, and similarly investigates extremes of cavity geometry theoretically. His study focuses on the one-dimensional limit for small cavity length-to-diameter ratios, and he ultimately deduces that as the L/D ratio is decreased below unity; such that the volume approaches a "pancake" configuration; axial gradients in the volume become negligible, and an additional one-dimensional solution may be obtained, in which purely radial wave propagation is considered.

The effects of L/D ratio on the acoustic attenuation performance of concentric expansion chambers has been extensively investigated, and findings here within can also be shown to correlate well with these results relating to acoustic resonator geometric factors. For example, Craggs (1976) showed using finite element models that the peak absorption frequency of an expansion chamber was not only defined by the respective radii at the sudden expansion, but the chamber length also. El-Sharkawy and Nayfeh (1978) later verifies Cragg's findings using a three-dimensional analytical solution for concentric chambers; and their findings also agreed well with the experimental measurements of Eriksson et al. (1983) , for L/D ratios of 0.3 to 0.9. Ih and Lee (1985) developed a three-dimensional model for circular chambers that incorporated mean flow and allowed for offset inlet and outlet locations, which showed good correlation with experimental values for L/D values ranging from 0.33 to 1.35. Selamet and Radavich (1997) also commented that these works indicate that a very short-length concentric expansion chamber no longer exhibits typical broadband behaviour, in fact acting rather like a resonator; and in the aforementioned work of Ih and Lee (1985), they developed an expression for the L/D ratio where the acoustically short chamber resonance appears.

The maximum cavity volume #14 investigated in this study corresponds to a L/D ratio of 2.91, which is far beyond the scope of the aforementioned studies; and it can be seen from Figure 104 that, when coupled with the Ø9mm neck, the resultant diffraction pattern for this extreme case is noticeably different to the previously presented cases. Here it is evident that within the spectrum of frequencies

stimulated at the aperture of the neck, there are evanescent modes which do not decay as quickly as the others, resulting in a portion of the oscillating neck volume projecting much further into the cavity volume. This observation provides a supporting rationale for the increasing value of the new empirical end correction introduced in the previous chapter for the large values of L/D, which for this particular case corresponds to $\delta_{total}/\sqrt{A_o} = 1.27$.
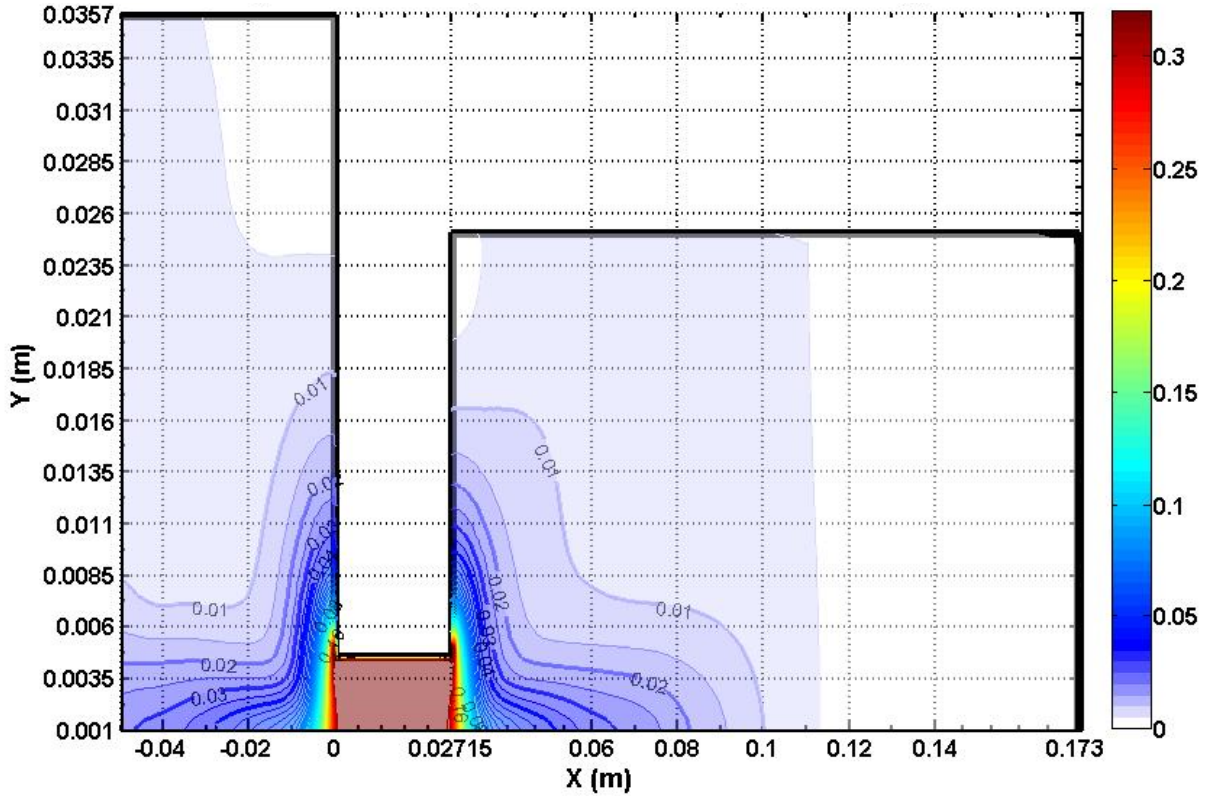
Figure 104 - Time-Averaged Acoustic Velocity Magnitude (m/s) for 9mm Neck, Volume Case #14

To further validate this observation, similar prior art corresponding to concentric expansion chambers can be referred to, and the work of Selamet and Radavich (1997) provides particularly strong supporting evidence; as they conducted a robust analysis consisting of: (1) a two-dimensional, axisymmetric analytical solution; (2) a three-dimensional computational solution based on the boundary element method; and (3) experiments on an extended impedance tube set up, which investigated fixed chamber diameters and varying chamber length-to-diameter ratios from $L/D = 0.2 \ to \ 3.5$. Figure 105 shows an example of their boundary element solution for the largest L/D case of 3.5, and the instantaneous pressure contours for three discrete frequencies, each corresponding to peaks of maximum transmission loss. From Figure 105(a) it can be seen that at very low frequencies, the contours are planar as expected; Figure 105(b) shows the onset of some non-planar contours at the area discontinuities with increasing frequency, which decay rapidly downstream; and Figure 105(c) shows that when the frequency increases closer towards the propagating, or cut-off frequency for the

first radial mode, the modes do not decay as quickly and the multi-dimensional effects spread throughout the length of the chamber (Selamet & Radavich, 1997).
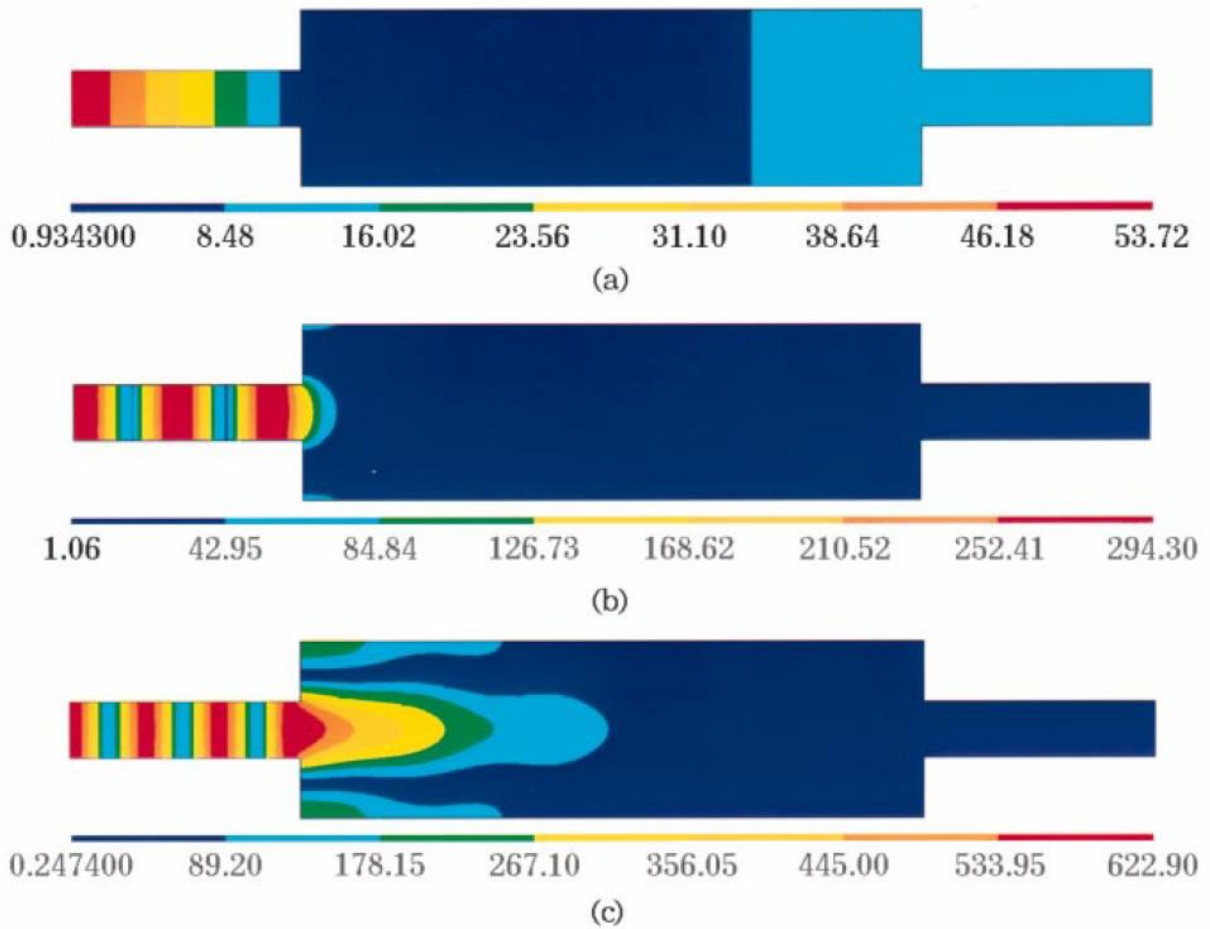
Figure 105 – Pressure contours for an expansion chamber with $l/d = 3.525$ for three frequencies of maximum transmission loss: (a) 160Hz; (b) 2,080Hz; (c) 2,714Hz (Selamet & Radavich, 1997)

It can therefore be concluded that the distended end correction profile observed in Figure 104 can be attributed to the stimulation of frequencies close to the cut-off frequency by the area discontinuity of the neck aperture, which subsequently decay slower than the typical exponential evanescent rate; and propagate further into the cavity volume.

6.3.2 Alternative Neck Geometry Investigations

In the previous Chapter, within Section 5.2, the effect of varying the neck termination geometry on the noise attenuation characteristics of the resonator was investigated. It was found that introducing any modification to the neck termination which reduces the suddenness of area expansion, ultimately results in a reduction in neck resistance, and a consequential increase in attenuation magnitude; at the same as shifting the peak absorption frequency to higher frequencies. As shown previously, a CFD supported numerical solution of the acoustically relevant volume can provide additional insight into

resonator performance, beyond what can be achieved through analytical modelling techniques. Furthermore, the inherent assumptions required to permit many analytical solutions can in many cases mask the performance defining characteristics, either limiting the understanding of applicability, or introducing errors in prediction accuracy.

Irrespectively the developed computational model is still built upon inherent assumptions and as such, the chosen design methodology parameters must still be validated prior to their application in supporting subsequent deductions. As such, the resultant FRF response, obtained using the equivalent measurement locations to the prior experimental methodology, can be seen in Figure 106; where excellent replication of the observed experimental results for the equivalent cases can be seen to be replicated effectively by the CFD modelling efforts.
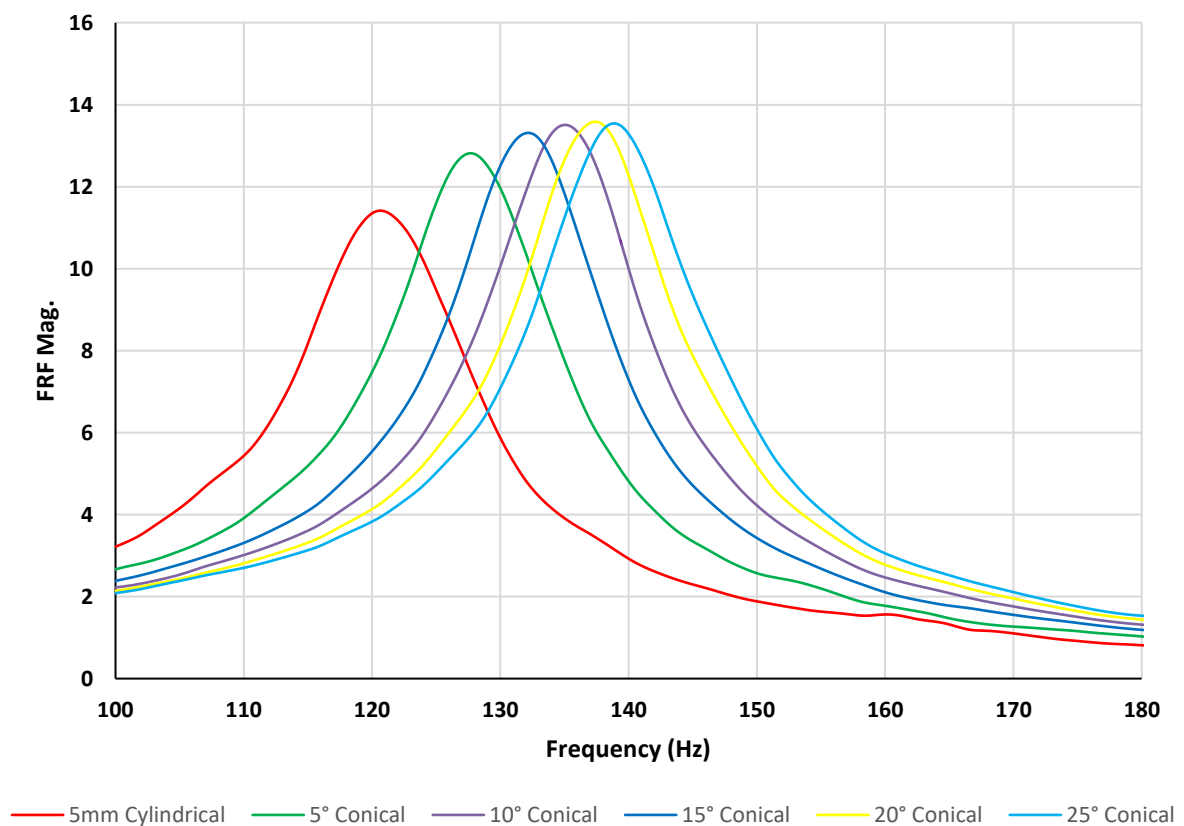
Figure 106 – CFD Simulated FRF against varying degrees of Conical Neck Termination, for Volume #7

With confidence that the CFD modelling methodology can effectively replicate the acoustic response on the conical neck terminations in terms of FRF magnitude and frequency, the previous time-averaged acoustic velocity magnitude methodology can be subsequently deployed to provide additional insight into the neck dynamics, as shown in Table 28. Here it can be seen that the cylindrical neck exhibits the behaviour of stimulated higher order evanescent modes in the vicinity of the aperture however, as the

magnitude of neck tapper increases, the distended profile of the end correction can be seen to decrease proportionally.
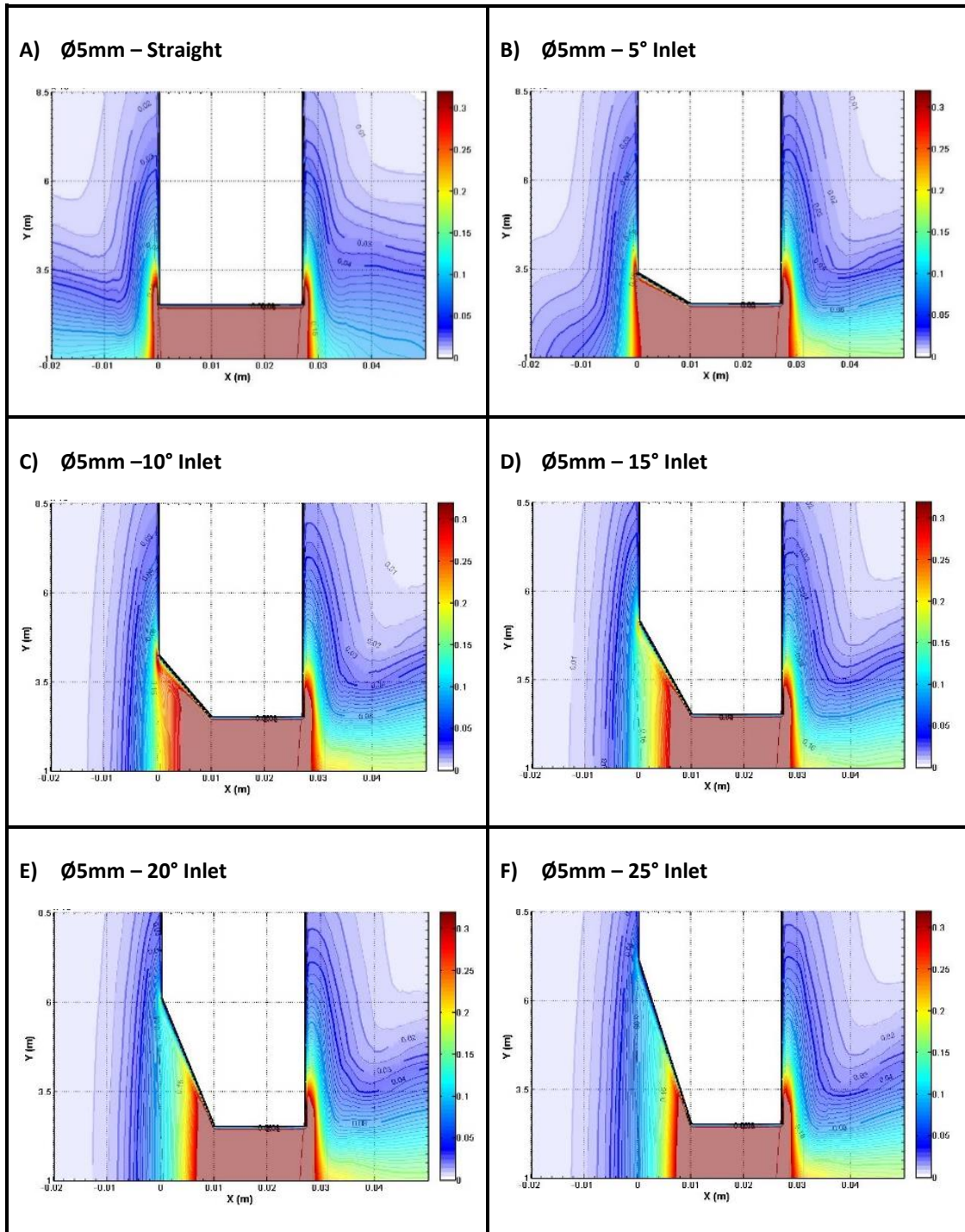
Table 28 - Time-Averaged Acoustic Velocity Magnitude (m/s) for Ø5mm Neck, Volume Case #7: (A) Straight Neck, (B) 5° Inlet, (C) 10° Inlet, (D) 15° Inlet, (E) 20° Inlet, (F) 25° Inlet

These results are ultimately supportive of the experimental and theoretical deductions discussed in Section 5.2.1. It can be seen that the commonly applied analytical assumption of plane wave propagation aligns well with the observed time-averaged acoustic velocity magnitude contours within the conical section; and that the reduction of severity in the area discontinuity results in a lack of

stimulation of evanescent modes. Although a direct comparison has not been made here, these findings are supportive of the analytical approximation of the resonant frequency of a resonator with a tapered neck derived by Tang (2005), shown in Equation *[150]*. In addition, it can be concluded that with an evident reduction in evanescent modes at the aperture, and a regular quasi-hemispherical diffraction profile, the depth analysis end correction of Chanaud (1997) should give a reasonable approximation of the additional entrained inertial end correction at the conical neck exit.

6.3.3   High SPL Saturation evaluation

A fundamental benefit of a computational simulation of acoustic performance, over an experimental evaluation, is the ability to investigate factors which are not easily practicable with common experimental apparatus. One such example of this is the investigation of high SPL induced non-linear effects. The experimental methodology employed within this study was focused predominantly on isothermal atmospheric impedance tube measurements, with a white noise acoustic excitation signal of 94.67dB RMS. This value of excitation SPL was chosen partly to ensure a strong excitation of the acoustic resonator at all investigated resonant frequencies; and partly to be well within operational limits of the associated hardware; thus, ensuring that the signal could be reliably sustained, and replicated over long periods of experimental investigation. In order to increase the SPL of the excitation signal sufficiently high to investigate any potential non-linear effects, would have risked the integrity of subsequent investigations, whereas to investigate such factors numerically using a CFD model carries no such risk. As such the CFD methodology provides a convenient opportunity to exceed the physical design limitations and investigate potential performance factors beyond those physically practicable.

In Figure 107 the instantaneous acoustic pressure (horizontal X-Z plane) and velocity magnitude (vertical X-Y plane) can be seen for the Ø9mm neck, cavity volume #7 case. As previously shown within this chapter, the availability of a spatial solution of these variables provides convenient visual clarity as to the underlying acoustic characteristics of the neck aperture, far beyond what is appreciable from an equivalent one-dimensional analytical solution. Unlike the previously presented time-averaged acoustic velocity plots however, the plotting of instantaneous values cannot be used to deduce the general acoustic response, as at different solution times, the resonator will be exposed to different frequencies with the white noise excitation signal. Irrespectively, it can be seen from Figure 107 that, under the investigated parameters, this resonator is exhibiting an expected linear response; evident by the planar wave fronts within the entirety of the neck; and the decaying aperture diffraction profiles. Increasing the RMS value of the acoustic excitation signal to 136dB however, as shown in Figure 108, significantly changes the observed response to the equivalent spectrum; and demonstrates transition

into a non-linear regime. At such a high SPL the formation of vortices at the neck apertures can be seen, which permeate into both the neck and cavity.
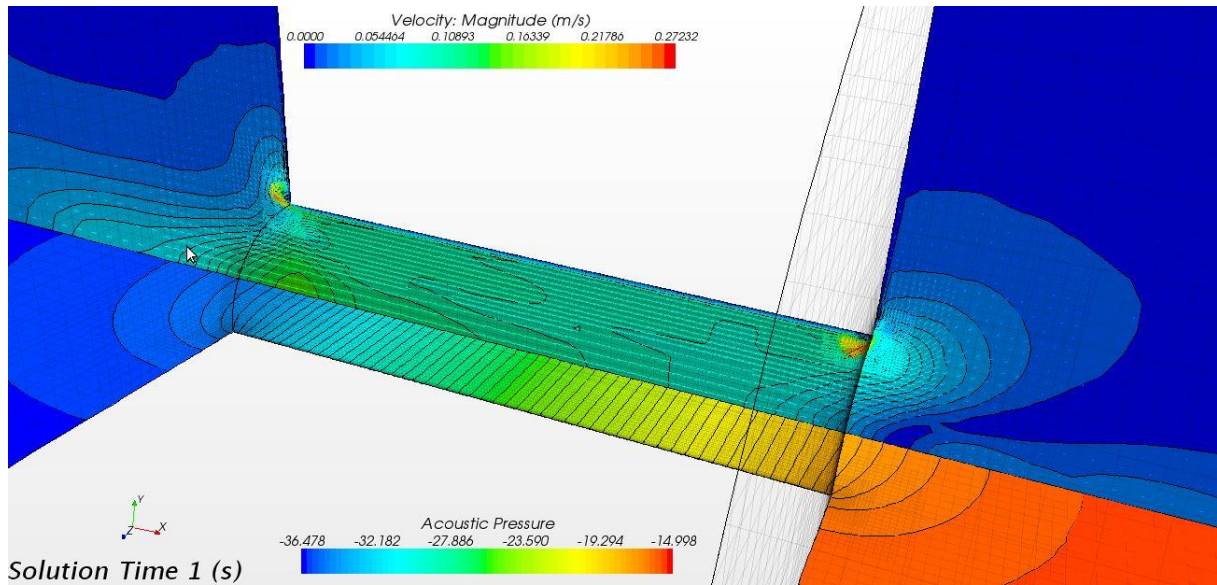
Figure 107 – Instantaneous Acoustic Pressure and Velocity Magnitude for Ø9mm neck, volume case #7, under 96dB RMS acoustic excitation
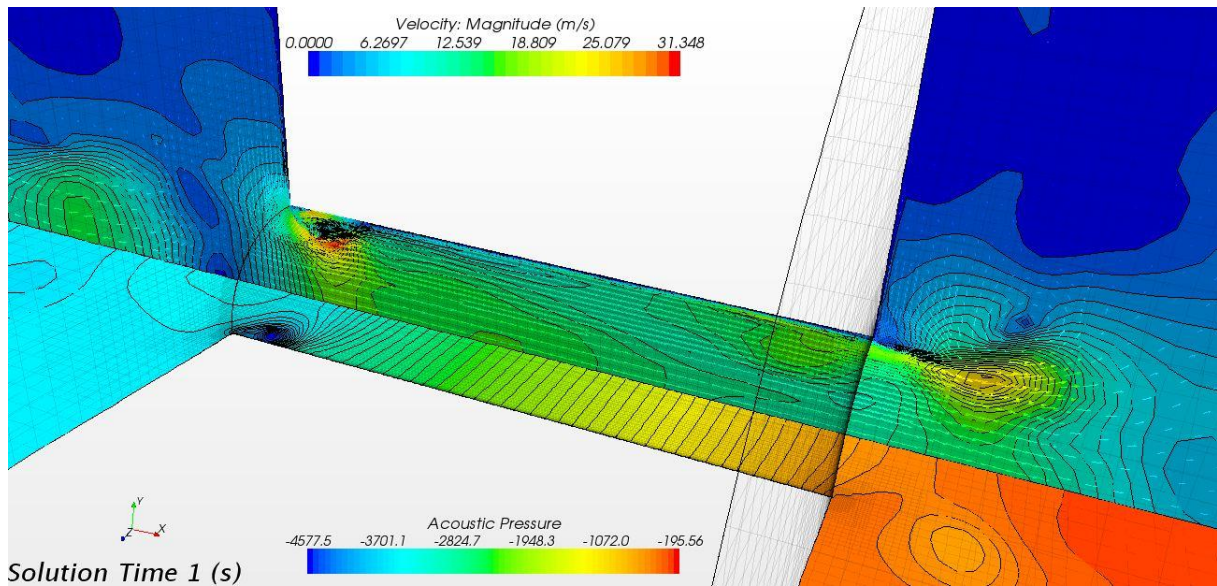
Figure 108 - Instantaneous Acoustic Pressure and Velocity Magnitude for Ø9mm neck, volume case #7, under 136dB RMS acoustic excitation

Clearly such a significant variation in the resonator dynamics will have an equally significant effect on the overall acoustic attenuation performance; and the impact on acoustic impedance modelling was introduced initially in Section 2.3.5, with a subsequent evaluation of current approaches discussed in more detail within CHAPTER 3 - LITERATURE REVIEW.

High SPL saturation effects will also be revisited experimentally later in section 8.1 however, it is important to conclude here that; whilst the presented CFD methodology is does not advance the

current state of the art in relation to non-linear effects; an underappreciation of the transition to a non-linear regime could inevitably compromise the integrity of any deductions here within or otherwise, if not considered accordingly. This transitional limit has been shown to be independent of frequency and orifice diameter, and is suggested by Tran et al. (2009) and Lahiri (2014) to be ≈115dB; Heuwinkel et al. (2008) found a limit of 110dB for a single tone at 310Hz; and Lee and Kwon (2004) concluded a lower limit of 102dB for a broadband excitation signal. All of the above transitions are supported by the experimental and numerical results presented here thus far, indicating that at under the circumstances investigated, non-linear effects can be considered negligible. It should be noted however, that Bodén and Zhou (2012) showed that the non-linear effects cannot be neglected entirely below this limit; and just as the often-neglected evanescent modes have been shown to impact end correction; an underappreciation of non-linear effects could undoubtably reduce prediction accuracy, or mask important performance defining characteristics.

6.4   CFD Investigation Summary

An implicit unsteady computational modelling methodology has been developed and implemented, which replicates the experimental methodology of the previous chapter. Rigorous refinement of the model and subsequent comparison with experimental results has demonstrated an aptitude of the modelling methodology to accurately predict the acoustic attenuation performance characteristics of tangible resonator configurations.

A novel post processing approach of time-averaging acoustic velocity magnitude under broadband excitation, has provided advanced insight of intrinsic dynamics in the vicinity of the resonator neck, including: the significance of multi-dimensional evanescent cross modes on the effective inertial end correction; the relationship between geometric parameters and the decay of evanescent modes; and the effects aperture edge geometry modification.

Finally, a brief investigation into effects of high SPL, confirms that at sufficiently high magnitude, the neck dynamics transition to a non-linear dominated regime.

CHAPTER 7 - EXPERIMENTAL METHODOLOGY: DISTRIBUTED RESONATORS

Within this chapter an experimental design methodology is applied and described, to outline a systematic method of design and deployment of an efficient experimental regime, targeted specifically on gaining novel insight into fundamental distributed resonator sound attenuation characteristics.

The aim of this methodology is to rationalise a comprehensive set of acoustic attenuation performance defining parameter investigations, which can contribute to a greater understanding of the objective points outlined in Section 7.1.

The planning for implementation of this experimental design methodology is initiated and discussed within Section 7.2, where there within the investigation strategy is initially summarised, and followed by a systematic exercise of experimental design parameter definition. The fundamental principles of acoustic impedance modelling detailed in CHAPTER 2 - BACKGROUND, and the current state of the art in relation to attenuation defining characteristics presented in CHAPTER 3 - LITERATURE REVIEW, are utilised to inform the design process; ensuring that the resultant test cases defined for subsequent investigation are optimised to support additional insight into key attenuation performance defining criteria.

Following the definition of key experimental parameters, the explicit measurement methodologies to be employed are specified in Section 7.3, including the geometric properties of the bespoke resonator, the acoustic flow rig and measurement section specifications, bias flow delivery procedure, data collection and processing apparatus.

Section 7.4 clarifies the physical experimental variations, providing applied justifications for mounting methods, integration requirements within the measurement section, and specification of the chosen test cases, such as inner/outer plate specifications.

The subsequent Section 7.5 describes the rationale behind the measurement strategy prior to the collection of any experimental results and explains how the investigation objectives are aimed to be addressed via targeted empirical evaluation.

As with CHAPTER 4 - EXPERIMENTAL METHODOLOGY: DISCRETE RESONATORS, the preceding Section 7.6 provides a comprehensive qualification of the experimental methodology, and uncovers the salient characteristics of the measurement apparatus, as a prerequisite for the subsequent evaluation of results, followed by a summary of the Chapter in Section 7.7.

7.1   Objectives

- Saturation Effects/Sound Pressure Level

- Neck Length versus diameter factors (L/D)

- Hole Spacing factors (Hole-to-Wall [H-W] & Hole-to-Hole [H-H])

- Cross-flow Impact

- Bias Flow Impact

- Combined Cross-flow/Bias Flow interaction effects

7.2   Investigation Strategy

In order to investigate the performance factors relevant to the aforementioned investigative objectives of *Section 7.1*, a bespoke distributed resonator was designed and fabricated to allow strategic experimental measurements to be collected via an acoustic wind tunnel. As with *CHAPTER 4 - EXPERIMENTAL METHODOLOGY: DISCRETE* RESONATORS, an experimental design methodology approach was taken here also; with the primary driving factor of interest being the investigation of Hole-to-Wall (H-W) & Hole-to-Hole (H-H) interaction effects. The results of this methodology yielded 36 different inner plate specifications, consisting of 3 neck diameter variations, and 12 different hole patterns. Introducing grazing flow and bias flow permutations provides an additional 42 condition variations per inner plate geometry, which results in a total Distributed Resonator Test matrix size of 1512 individual cases. This comprehensive test matrix is designed so that it provides sufficient factor variations to both demonstrate significant resultant performance variations; and sufficient intermediate cases to evaluate pertinent trends where possible. The systematic steps of this experimental design methodology are delineated in the subsequent sub-sections.

7.2.1   H-W & H-H parameter optimisation

In Section 2.3.4 the significance of orifice interaction was introduced, followed by delineation of the current state of the art in relation to modelling such performance defining factors in CHAPTER 3 - LITERATURE REVIEW. From which it is clear that significant impact on a resonator's attenuation performance can be attributed to both H-W & H-H interaction effects; irrespective of this known significance, all previous studies indicate a need for further investigation; and as of yet a comprehensive understanding of such factors impact on resonator performance has not been achieved.

In Section 5.1.1 an end correction factor approximation which considered H-W effects for cylindrical apertures, centred within a cylindrical cavity, as defined by Equation *[144]*, was investigated experimentally. Here it was shown that the Ingard approximation resulted in an underprediction of the required mass end correction for the cases investigated experimentally, and subsequently an empirical modification was developed within the following subsection (5.1.2). Irrespectively the work of Ingard proved to be a reasonable approximation of the trending variation in witnessed attenuation performance; and therefore his work will be utilised here within as a best guess approach to speculate resultant H-W & H-H factors at the experimental design stage.

For circular resonators consisting of multiple distributed apertures the respective H-W & H-W contributions to mass end correction are defined by Ingard as:

$$\frac{\delta_{h-w}}{\sqrt{A}} = \frac{4}{\sqrt{\pi}} \frac{R}{r_o} \sum_{m=0}^{\infty} \sum_{n=1}^{\infty} \frac{J_1^2(q_{mn} r_o/R) J_m^2(q_{mn} a/R)}{(q_{mn})^3 [1 - (m/q_{mn})^2] J_m^2(q_{mn})} \qquad \text{(Hole-Wall)} \qquad [162]$$

$$\frac{\delta_{h-h}}{\sqrt{A}} = \frac{4}{\sqrt{\pi}} \frac{R}{r_o} \sum_{m=0}^{\infty} \sum_{n=1}^{\infty} \frac{(-1)^m J_1^2(q_{mn} r_o/R) J_m^2(0.5 q_{mn} L/R)}{(q_{mn})^3 [1 - (m/q_{mn})^2] J_m^2(q_{mn})} \qquad \text{(Hole-Hole)} \qquad [163]$$

Where J_m is the Bessel function of the first kind, and q_{mn} is the eigenvalue of the Bessel function J_m. In Equation *[162]* a corresponds to the eccentricity of the aperture, i.e. the distance from the axial centreline of the cavity; and in Equation *[163]* L corresponds to the centre-to-centre hole distance of the respective apertures for with the H-H interaction is being calculated. As with before, a robust analysis should consider both the internal and external end corrections; and the geometric parameters required for H-W and H-H calculation, for a cylindrical resonator, with distributed cylindrical apertures, are schematically represented for a generic resonator in Figure 109.
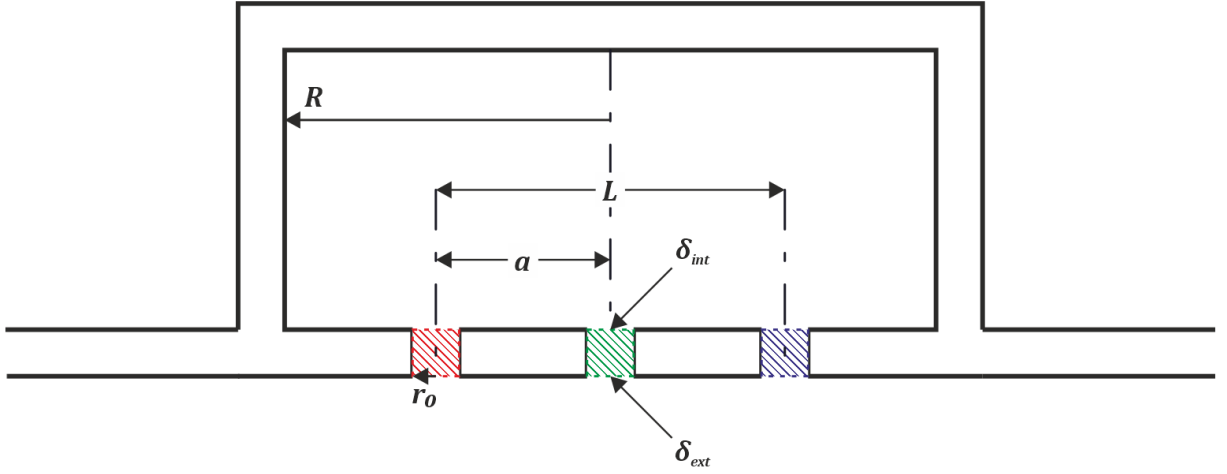
Figure 109 - Schematic representation of H-W & H-H parameters for a resonator with cylindrical cavity and distributed cylindrical apertures.

According to equation *[162]*, when the aperture is located at the centre of the cavity, i.e. $a/R = 0$, the H-W associated correction factor is at its maximum value; and as the aperture is moved away from the centre of the cavity, the radiation reactance decreases to a local minimum at $a/R = 0.5$, prior to increasing again as $a/R \rightarrow 1$; with the rate of change being defined by the ratio r_0/R. The H-H attributed correction factor, as described by Equation *[163]*, decreases as the distance between the two corresponding apertures increases; the largest value occurs when the two apertures just touch each other; and similarly, the rate of change is dependent on the ratio r_0/R.

The equivalent H-W and H-H interactions for a distribution of cylindrical holes, within a rectangular cavity, are described by Equation *[164]* and Equation *[165]* respectively :

$$\frac{\delta_{h-w}}{\sqrt{A}} =$$

$$\frac{8}{\pi^{2.5}} \frac{1}{\xi} \sqrt{\frac{1}{\alpha}} \sum_{m=0}^{\infty} \sum_{n=0}^{\infty} \frac{J_1^2\left(\sqrt{m^2 + n^2/\alpha^2}\,\pi\xi/2\right)}{\nu_{mn}(m^2 + n^2/\alpha^2)^{1.5}} \cos^2\left(\frac{m\pi x}{L_x}\right) \cos^2\left(\frac{n\pi y}{L_y}\right) \qquad \text{[164]}$$

$$\frac{\delta_{h-h}}{\sqrt{A}} =$$

$$\frac{8}{\pi^{2.5}} \frac{1}{\xi} \sqrt{\frac{1}{\alpha}} \sum_{m=0}^{\infty} \sum_{n=0}^{\infty} \frac{J_1^2\left(\sqrt{m^2 + n^2/\alpha^2}\,\pi\xi/2\right)}{\nu_{mn}(m^2 + n^2/\alpha^2)^{1.5}} \cos\left(\frac{m\pi x}{L_x}\right) \cos\left(\frac{m\pi x'}{L_x}\right) \cos\left(\frac{n\pi y}{L_y}\right) \cos\left(\frac{n\pi y'}{L_y}\right) \qquad \text{[165]}$$

Where J_m is the Bessel function of the first kind, $\xi = 2r_0/L_x$ is the ratio of the hole diameter to the cavity width, $\alpha = L_x/L_y$ is the aspect ratio of the rectangular plate, and x, y, x', y' are four coordinates of the centre of two holes; as shown schematically represented for a generic rectangular resonator, with distributed cylindrical apertures, in Figure 110.
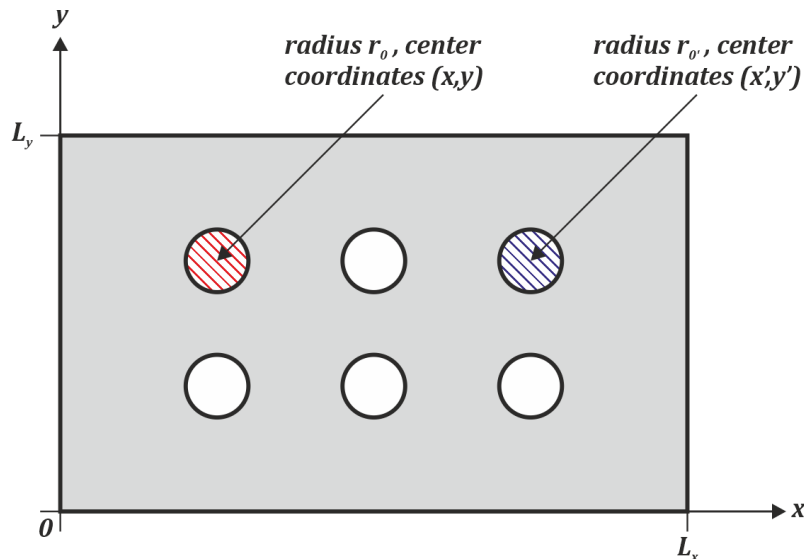
Figure 110 – Schematic representation of H-W & H-H parameters for a resonator with rectangular cavity and distributed cylindrical apertures.

As the primary aim of this experimental methodology is to investigate the contribution of H-W & H-H effects on overall resonator performance, the aim is to, where possible, constrain all other performance relevant factors, so that any witnessed variations can be accounted solely to H-W & H-H effects. To begin the main geometric properties of the resonator box are defined; starting with the length and depth, which are specified based on the existing configuration of the acoustic wind tunnel intended to be used in these experiments, and a pre-existing opening in the acoustic duct where a new distributed resonator design could be conveniently mounted. Whilst the ideal number of holes cannot be defined a priori, it can be appreciated that a greater number of holes will result in a stronger acoustic response, and hence a greater clarity in the experimental evaluation of performance factors can be supported. There must also however, remain sufficient space between the holes to permit enough variation of hole pitch and diameter parameters, in order to observe H-W & H-H performance alerting characteristics; consequentially the required aspect ratio, number of holes, and pitch values for the baseline case parameters were rationalised around these requirements, and the resultant baseline parameters are defined in Table 29.

Variable	Description	Value	Units
L_x	width of resonator box	59.4	mm
L_y	depth of resonator box	50.0	mm
α	aspect ratio	0.842	-
N	Number of holes	32	-
$Pitch_x$	Pitch in x direction	10	mm
$Pitch_y$	Pitch in y direction	7	mm

Table 29 - Table showing baseline distributed resonator geometric parameters

196

As both Equation *[164]* & Equation *[165]* include infinite series terms, before each equation can be used to calculate the theoretical H-W & H-H contributions, it is first necessary to carry out a convergence study. In order to determine an appropriate number of modes with which to calculate the H-W end correction, Equation *[164]* can be solved for the geometric variables of the baseline case, as specified in Table 29.

In Figure 111 the results of this computation can be seen that for the lower-left-most hole *(x=10 & y=5.2),* and for this case a clear convergence can be seen around 100 modes, and hence in all future uses of Equation *[164]* a truncated number of 100 x 100 modes will be used.
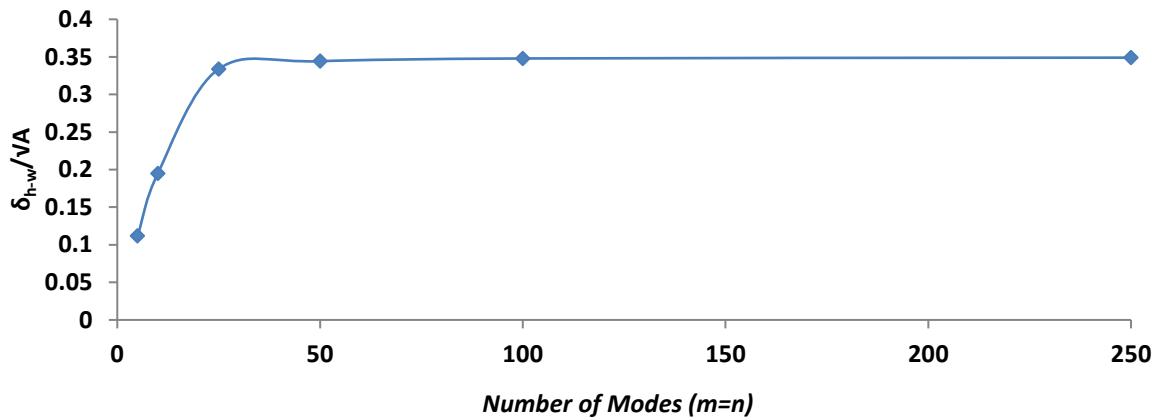
Figure 111 - Convergence Plot for number of modes when calculating H-W contribution

Similarly, it is necessary to carry out the same exercise for Equation *[165]* to ensure that the same number of modes is appropriate in this case also. From Figure 112, which corresponds to the convergence study for the interaction between the lower-left-most hole and the hole immediately to its right, it can be clearly seen that a truncated number of modes of 100 x 100 is sufficient for these calculations also.
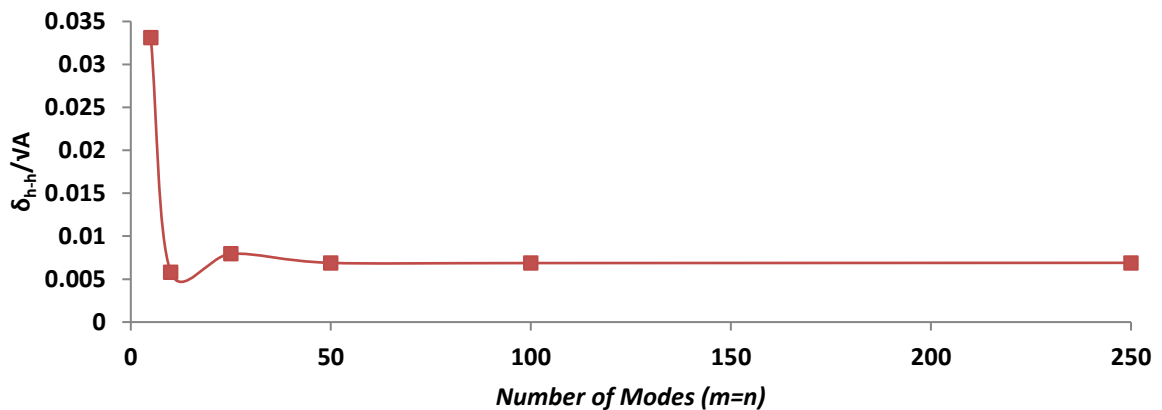
Figure 112 - Convergence Plot for number of modes when calculating H-H contribution

It can be seen from Equation *[164]* that the H-W effect varies exponentially with the distance of a hole from a nearby wall. By calculating the H-W end correction for each hole in the initial case (Table 29) then *Figure 113* can be created, which shows the variation of H-W effect across the inner plate surface. From this it is clear that, as expected, the H-W effect is greatest at the outer holes nearest the cavity wall, and subsequently decreases exponentially towards the centre of the plate. As a result of this effect, in order to witness the greatest possible variation of H-W effect, it will be necessary to vary the distance of the outer holes from the walls of the resonator as much as practicable.
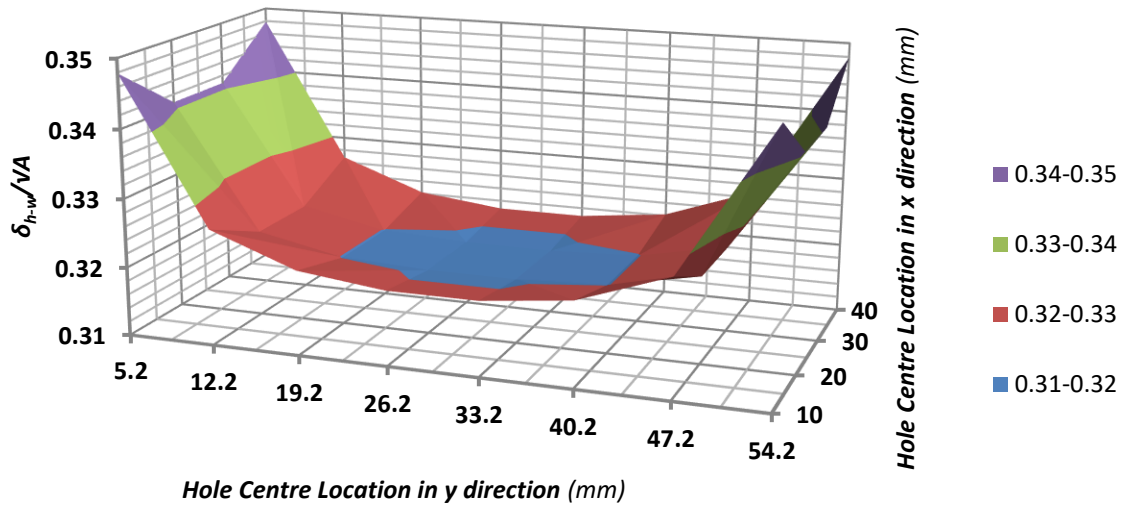
Figure 113 - 3D surface plot of H-W variation across holes in initial example case

In a similar manner it can be appreciated that the H-H interaction will decrease exponentially with increasing separation distance between two given holes; the process of calculation of H-H interaction for a full resonator is however significantly more arduous compared with H-W interaction; as for each hole, the interaction effect of that hole with all other surrounding holes must be considered. Starting with one hole only and using Equation *[165]* to calculate the H-H interaction of that hole with all others, a surface plot can be produced to show the distribution of H-H interaction across the plate surface, as shown in *Figure 114*.
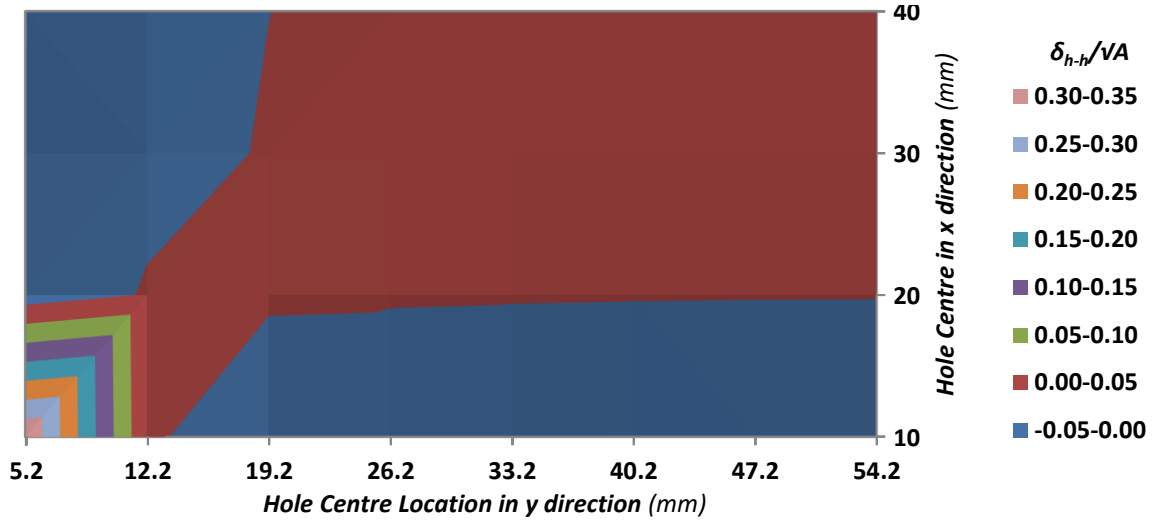
Figure 114 - H-H interaction between single hole and surrounding holes

It is noteworthy that for the surface shown in *Figure 114* the lower left corner is not a feasible case as at this point the two holes are overlapped and in fact under these conditions the value corresponds to the H-W interaction only, as when *x'-x=y'-y=0* Equation *[165]* becomes equal to Equation *[164]*. Furthermore, it is of little practical relevance to consider any case where the two holes would overlap *[i.e. x'-x=y'-y<D]*

If this strategy is applied to each hole of this initial case, an appreciation of the H-H interaction across all holes of the perorated section can be computed. The results of this investigation can be seen in Figure 115, and from this it is evident that the largest H-H interaction is witnessed at the centre of the perforated section, where there is a large number of holes in close proximity to each other.
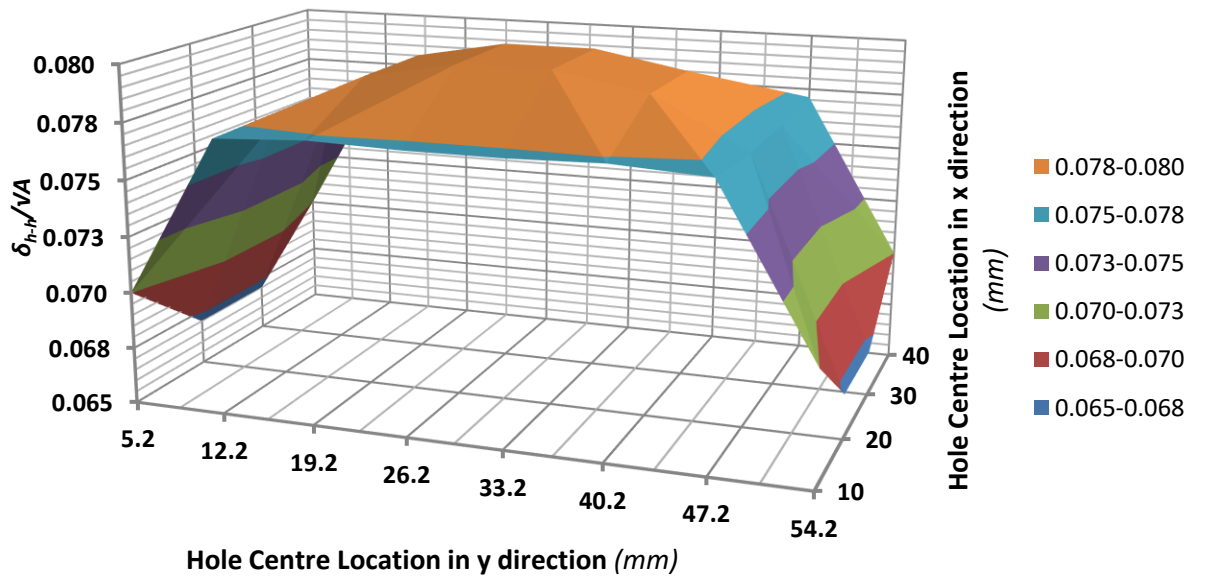
Figure 115 - 3D surface plot of H-H variation across holes in initial example case

As with the H-W interaction effects, in order to ensure the best possible measurement of H-H effects, the design of experimental parameters should seek to maximise the variation of hole spacing across the respective test cases. With this in mind, and in consideration of the baseline distributed resonator geometric parameters specified in Table 29, the remaining required parameters for subsequent experimental investigation are defined as per Table 30.

Variable	Description	Value	Units	Value Type	Dependant on
L_x	width of resonator box	59.4	mm	Constraint	-
L_y	depth of resonator box	50.0	mm	Constraint	-
α	aspect ratio	0.842	-	Constraint	L_x & L_y
N	Number of holes	32	-	Constraint	-
N_x	Number of holes in x-direction	4	-	Constraint	-
N_y	Number of holes in y-direction	8	-	Constraint	-
D	Hole Diameter	1-5	mm	Control Variable	Manufacturing & scaling factors
$Pitch_x$	Pitch in x direction	10	mm	Target Variable	L_x, D & N_x
$Pitch_y$	Pitch in y direction	7	mm	Target Variable	L_y, D & N_y

Table 30 - Table showing Distributed Resonator Experimental Design Variables

In order to maximise the variation of pitch in both the x and y directions and thus the consequent H-W & H-H interactions, it is first necessary to define the hole diameter variations because, as shown in Table 30, these variables are dependent on the hole diameter and box dimensions. A minimum of three variations is sufficient to indicate any apparent trends and as such a total of three differing hole diameters will be defined for this study. The values of 2mm, 3mm & 4mm are chosen because, as with the resonator dimensions, they are comparable with existing resonator box designs currently applied practically, and furthermore by keeping the hole dimension an integer value it ensures ease of manufacture, regardless of the method used. With the control variable of hole diameter defined, the last remaining step in defining the full test matrix is to determine the variations of pitch in both the x and y directions. By setting the limits of a minimum of 0.2mm separation distance *(minimum manufacturing tolerance)* between holes; a limit of 0.5mm between a hole wall and resonator wall *(combined manufacturing and assembly tolerance);* and setting three pitch variations in the y-direction and four variations in the x-direction; the final test matrix can be arrived at, as shown in Table 31, which consists of a total of thirty-six unique test cases.

Case #	L_x (mm)	L_y (mm)	α	D (mm)	ξ	Pitch$_y$ (mm)	Pitch$_x$ (mm)
01	50	59.4	0.842	3.0	0.06	7.7	15
02	50	59.4	0.842	3.0	0.06	7.7	12
03	50	59.4	0.842	3.0	0.06	7.7	9
04	50	59.4	0.842	3.0	0.06	7.7	6
05	50	59.4	0.842	3.0	0.06	6.0	15
06	50	59.4	0.842	3.0	0.06	6.0	12
07	50	59.4	0.842	3.0	0.06	6.0	9
08	50	59.4	0.842	3.0	0.06	6.0	6
09	50	59.4	0.842	3.0	0.06	4.2	15
10	50	59.4	0.842	3.0	0.06	4.2	12
11	50	59.4	0.842	3.0	0.06	4.2	9
12	50	59.4	0.842	3.0	0.06	4.2	6
13	50	59.4	0.842	4.0	0.08	7.7	15
14	50	59.4	0.842	4.0	0.08	7.7	12
15	50	59.4	0.842	4.0	0.08	7.7	9
16	50	59.4	0.842	4.0	0.08	7.7	6
17	50	59.4	0.842	4.0	0.08	6.0	15
18	50	59.4	0.842	4.0	0.08	6.0	12
19	50	59.4	0.842	4.0	0.08	6.0	9
20	50	59.4	0.842	4.0	0.08	6.0	6
21	50	59.4	0.842	4.0	0.08	4.2	15
22	50	59.4	0.842	4.0	0.08	4.2	12
23	50	59.4	0.842	4.0	0.08	4.2	9
24	50	59.4	0.842	4.0	0.08	4.2	6
25	50	59.4	0.842	2.0	0.04	7.7	15
26	50	59.4	0.842	2.0	0.04	7.7	12
27	50	59.4	0.842	2.0	0.04	7.7	9
28	50	59.4	0.842	2.0	0.04	7.7	6
29	50	59.4	0.842	2.0	0.04	6.0	15
30	50	59.4	0.842	2.0	0.04	6.0	12
31	50	59.4	0.842	2.0	0.04	6.0	9
32	50	59.4	0.842	2.0	0.04	6.0	6
33	50	59.4	0.842	2.0	0.04	4.2	15
34	50	59.4	0.842	2.0	0.04	4.2	12
35	50	59.4	0.842	2.0	0.04	4.2	9
36	50	59.4	0.842	2.0	0.04	4.2	6

Table 31 - Table showing all 36 H-W & H-H test cases

7.2.2   Scaling Considerations

As all measurements carried out in this study are conducted under isothermal atmospheric conditions, and as such it is important to consider how these results will compare with alternative scenarios which commonly apply acoustic resonators in order to attenuate noise under dynamic thermal or pressure conditions, such as combustors, or downstream from combustion systems. Aside from the isothermal atmospheric measurement conditions, a key defining geometric characteristic of the measurement

section is the diameter, which is constrained by the existing rig specifications at Ø165mm; which corresponds with a plane wave cut-off frequency of approximately 1,200Hz. With this in mind it is necessary to keep measurement dynamics lower than this frequency, so that where possible, only planar waves exist in the measurement rig. Ensuring the existence of only plane waves within the measurement section is a prerequisite assumption for subsequent decomposition of measured responses and has the additional advantage or reducing measurement microphone location specific errors. Furthermore, it also allows direct comparison of collected measurements with existing theories and models, many of which commonly rely on plane wave assumptions.

In order to consider the impact of thermodynamic scaling on the resonant frequency of a classic resonator, we can revisit the earlier definition provided by (Pierce, 1989), in terms of the speed of sound, where $c = 2\pi f/k$.

$$f_r = \frac{c}{2\pi}\sqrt{\frac{A}{VL}} \hspace{3cm} [166]$$

Rearranging Equation *[166]* in terms of the wave number k, yields Equation *[167]*, from which it can be seen that wave number is only dependant on geometry parameters, and independent of environment temperature and pressure.

$$k_r = \sqrt{\frac{A}{VL}} \hspace{3cm} [167]$$

As such, one viable approach to comparing acoustic response and corresponding dynamics across varying thermodynamic environments is to scale according to the wave number, as defined by Equation *[168]*:

$$k = \frac{\omega}{c} = \frac{2\pi f}{c} \hspace{3cm} [168]$$

If the target dynamics frequency at isothermal atmospheric conditions is specified as 1,000Hz for example, then using the extreme thermodynamic conditions of the Hot Acoustic Test Rig (HAT) (A joint facility of DLR and TU Berlin) (Lahiri, 2014); and by keeping the wave number constant; the equivalent dynamics frequency can be speculated as shown in Table 32.

Variable	Description	Atmospheric Value	HAT Value	Units
T	Temperature	293	723	K
R	Gas Constant	287	290	J/kg/K
γ	Specific Heat Ratio	1.4	1.33	-
c	Speed of Sound	343	528	m/s
k	Wave Number	18.3	18.3	1/m
f	Dynamics Frequency	1,000	1,654	Hz

Table 32 - Table showing typical atmospheric and extreme HAT thermodynamic conditions

It can therefore be deduced that, whilst the dynamics frequencies which can be evaluated within the isothermal atmospheric test rig are limited to a maximum of 1,200Hz by the plane wave cut-off characteristic of the rig, investigated dynamics can be scaled to an elevated temperature equivalent environment beyond this experimentally practicable limit.

Furthermore, by applying the reverse process and assuming a target dynamics frequency for elevated thermodynamics, and taking any known geometric properties, the corresponding geometric parameters needed to evaluate the dynamics under alternative thermodynamic conditions can be reasonably speculated, by scaling according to a constant dimensionless wave number, $k \cdot l$. This approach is of practical significance when considering the fitness of purpose from findings obtained experimentally between varied thermodynamic contexts.

7.2.3   Optimisation of Resonator Dimensions

As a result of the H-W & H-H parameter optimisation efforts, acoustic test rig integration, and thermodynamic scaling considerations, the only remaining geometry variables are the length of the holes and the resonator cavity height. As shown in Figure 116, in order to facilitate the fitment of a resonator box of edge lengths $L_x = 50mm$ & $L_y = 59.4mm$ to the existing Ø165mm rig, it is necessary to have a resonator box in the form of an annular sector.
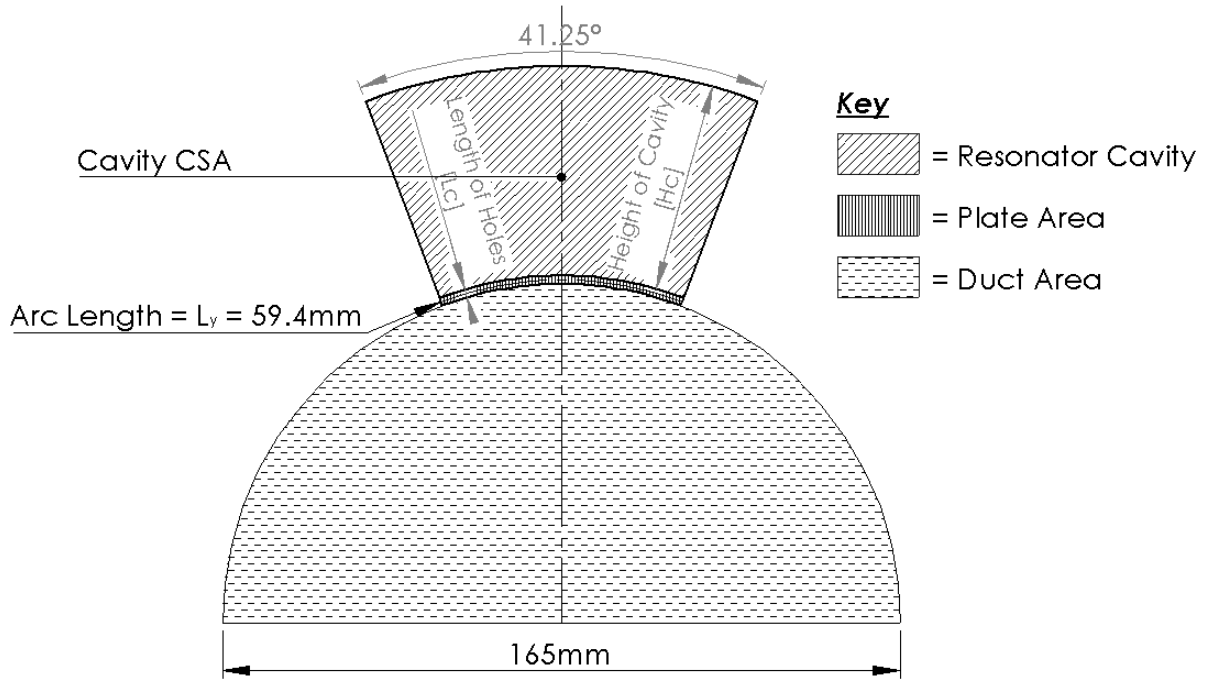
Figure 116 - Schematic drawing of measurement rig and resonator cross section

The significance of this design is that the inner wall of the resonator must be formed to the same curvature as the inner wall of the existing acoustic measurement rig. Consequentially the hole length is initially set to 2mm; due to primarily the practical limitations of standard sheet metal material availability, and the process capability of bending this thickness of material accurately to the relatively small, required radius of 82.5mm.

Constraining the hole length leaves only the cavity height variable undefined and therefore the final step of design optimisation is to tune this cavity dimension to give the desirable expected response frequency range. By using impedance modelling approaches discussed in CHAPTER 2 - BACKGROUND and CHAPTER 3 - LITERATURE REVIEW, the expected acoustic response from the proposed test cases can be speculated; which is achieved by applying the fundamental premise that every acoustically relevant component of the resonator is represented by its impedance, Z, according to Equation *[169]*:

$$Z = \frac{p}{u \cdot A} = \frac{p}{V} \qquad [169]$$

The impedance characterises the relationship of a driving force given by the acoustic amplitude p, on the specific face A, and the resulting acoustic volume flow V of the fluid downstream of that face. Recalling that the impedance is a complex number, and can be split into its corresponding real and imaginary parts according to Equation [48]; where R is the real part and is called resistance; and X is the imaginary part called reactance; which can each be calculated for the distributed resonator orifices according to Equations *[170]* & *[171]* respectively:

$$R_{O_{total}} = \frac{1}{N_O A_O} \left(\underbrace{(8\mu\bar{\rho}\omega)^{1/2}\left(1 + \frac{l_O}{d_O}\right)}_{=R_V \, (\text{dissipation due to viscosity } \mu)} + \underbrace{\bar{\rho}\bar{c}\frac{1}{8}\left(\frac{\omega}{\bar{c}}d_O\right)^2}_{=R_R \, (\text{radiation})} \right) \qquad [170]$$

$$X_{O_{total}} = \frac{1}{N_O A_O} \left(\bar{\rho}\omega l_O + \underbrace{\bar{\rho}\omega\delta}_{radiation} \right) \qquad [171]$$

Where: $A_O = \frac{\pi}{4}d_O^2$ is the area of a single orifice; N_O is the total number of orifices corresponding to a single resonant cavity; and end correction is calculated according to Equation [136]. The contribution due to viscous loss is taken from Ingard (1967); the radiation terms arise from the fact that an acoustic wave leaving an orifice induces an acoustic pressure field downstream of the orifice, and therefore the impedance of an open end is not zero. The relationship between this near field acoustic pressure and the acoustic velocity at the orifice is considered by the radiation impedance, and the derivation of the radiation terms both for the resistance and the reactance is described by Morse & Ingard (1968). The acoustic properties of the cavity volume are characterised by reactance only, and can be calculated according to Equation *[172]* (Munjal, 1987):

$$X_{Volume} = -\rho c^2 \frac{1}{\omega V_c} \qquad [172]$$

By applying this lumped acoustic impedance modelling approach, a speculative acoustic response can be determined from the calculated FRF according to Equation [75]; which can be used in conjunction with the known geometric parameters of Table 31, and hole length of 2mm; in order to pragmatically evaluate a rational cavity depth value for subsequent investigations. Noting that the aforementioned approach uses only a basic end correction value, and hence will not effectively evaluate the nuances of H-W & H-H factors, the upper limit of the proposed geometry should include a factor of safety to mitigate the potential of dynamics beyond the physical plane wave cut-off frequency.

Through this pragmatic modelling approach a cavity height of 51mm was arrived at, which subsequently results in a resonator cross sectional area of 4,038.91mm² and a volume of 201,945.5mm³. It can be seen in Figure 117 that this cavity depth results in expected dynamics for the Ø4mm cases in the region of ≈1kHz, and lower end dynamics for the Ø2mm cases in the ≈650Hz region. This indicates that upper dynamics should remain within the plane wave cut-off frequency limit of 1,200Hz with a 200Hz tolerance permitted for as yet undefined characteristics, whilst also maximising the experimental variation expected to be seen between corresponding geometries; thereby giving the best possible chance to clarify performance defining variables, and any intrinsic trends observed within the experimental range of geometric factors investigated.
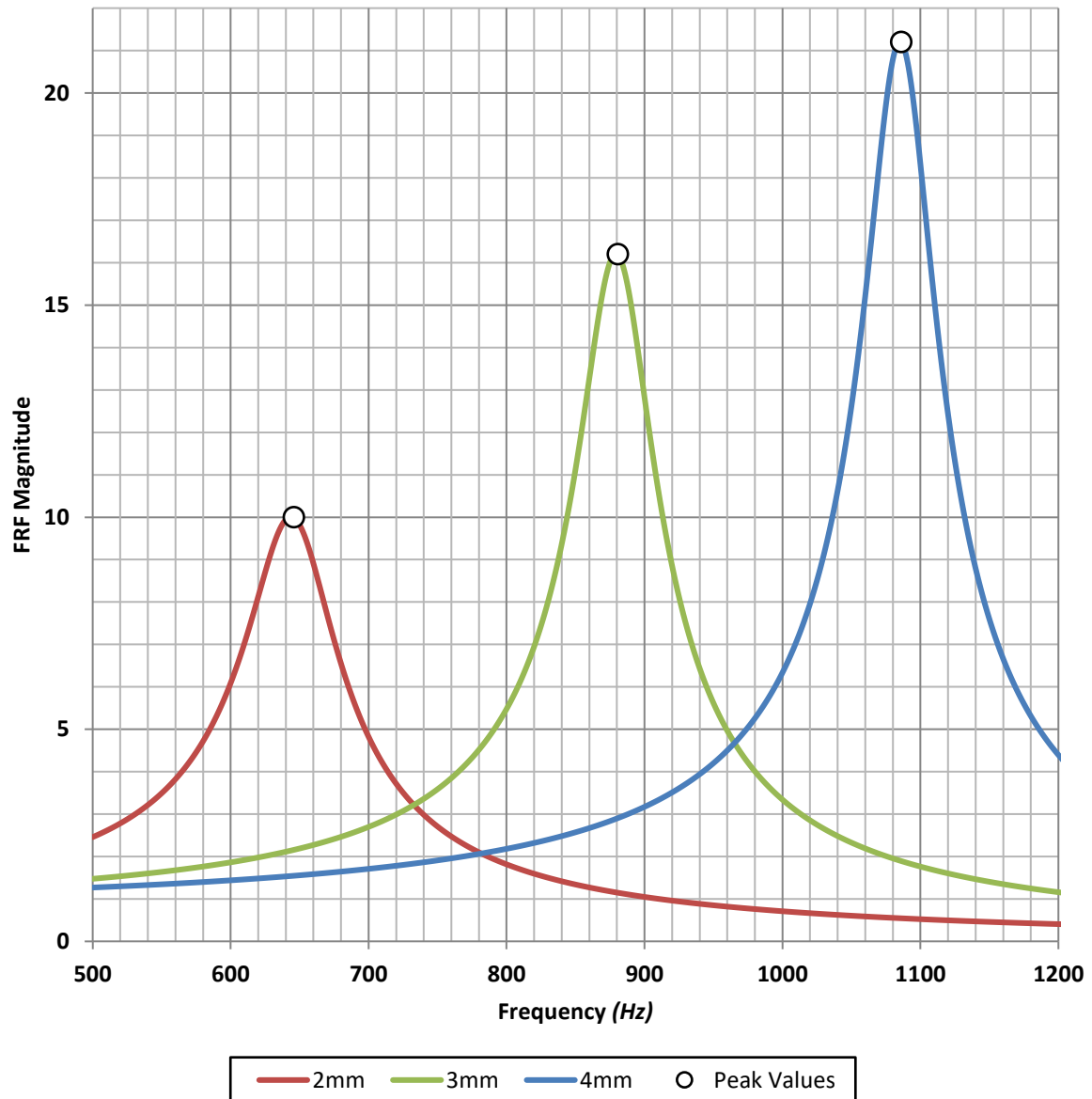
Figure 117 – Analytical FRF Magnitude for proposed distributed resonator test cases

7.3 Measurement Methodology

All of the measurements detailed in this report have been collected using the large acoustic flow rig at Hull's Acoustic Research Centre. All measurements are carried out under isothermal atmospheric conditions with an average temperature of 20°C and ambient pressure of 101,300Pa. The following sections detail the flow rig specifications, measurement equipment, measurement criteria, the distributed resonator design and test case specifications, processing methodology, and acoustic excitation signal specifics.

7.3.1   Acoustic Flow Rig Specifications

The large acoustic flow rig installed at Hull's Acoustic Research Centre is over 30m in length with a 1m x 1m cross section, lined with lead to aid acoustic isolation. The schematic drawing shown in Figure 118 highlights the main functional components of the installation.
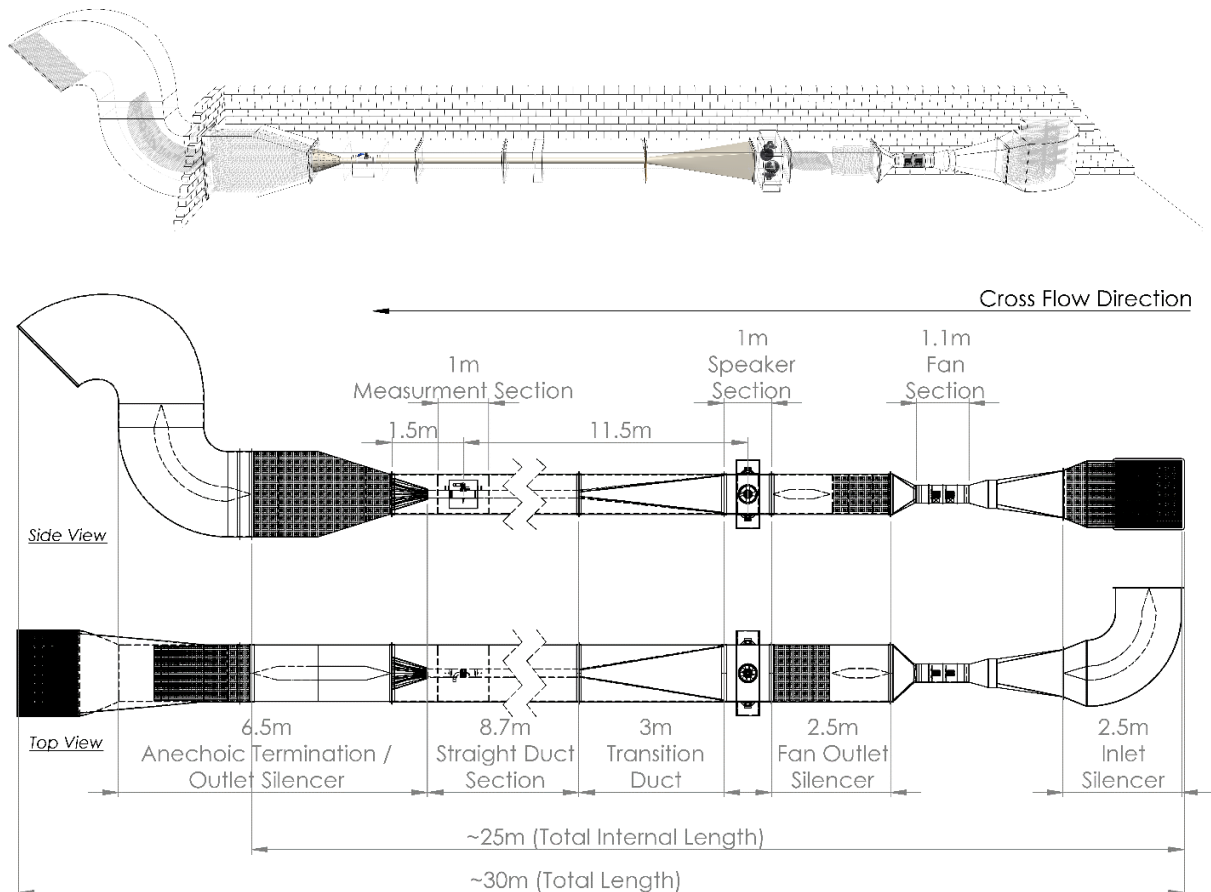
Figure 118 - Schematic of Hull's large acoustic flow rig

In order to facilitate perforated liner measurements for Siemens Industrial Turbomachinery *(Lincoln)* in 2011, the main 1m x 1m cross was retrofitted with a Ø165mm cylindrical duct. In Figure 119 this duct can be seen on top of the main wind tunnel section prior to installation. A transition duct was fabricated to reduce the cross section immediately downstream from the sound source section down to 165mm, as visible on top of the original rig on the right of Figure 119. An additional conical anechoic termination was also fitted downstream from the new measurement section, which terminates into the original rig's anechoic termination, as show on the left of Figure 119.

Cross-flow is pulled from outside of the facility through an inlet silencer to eliminate unwanted environmental noise and passed through an additional silencer to reduce fan induced noise. An acoustic signal can be generated in the sound source section immediately afterwards which consists of four radially mounted and enclosed 600W drivers.

Figure 119 - Image showing Ø165mm test section before installation inside main 1mx1m duct [Left - Anechoic Termination & Measurement Section, Right - Transition Duct]

7.3.2   Design of bespoke Distributed Aperture Test Resonator

The key dimensions for the bespoke distributed resonator intended for these investigations were specified in *Sections 7.2.1-7.2.3*, through careful deliberation of design for manufacture and assembly factors, and fitness for purpose for the defined experimental objectives; the final detailed design of this bespoke distributed resonator can be seen in Figure 120. A key characteristic feature of this experimental resonator design is the ability to easily interchange the inner and outer plates, whilst retaining sufficient in-situ measurement capability. This design ethos ensures the experimental agility of the design, allowing the efficient measurement of a large number of acoustic attenuation performance defining parameters. The interchangeable inner plates allow the investigation of the full H-W & H-H test matrix detailed in Table 31, along with investigation neck length versus diameter factors (L/D) through the multiple neck diameters contained within this proposed test matrix. The interchangeable outer plates permit the investigation of bias flow factors, and the modular design is considerate of the potential need for future modifications, to permit additional investigations beyond the scope of this initial study.
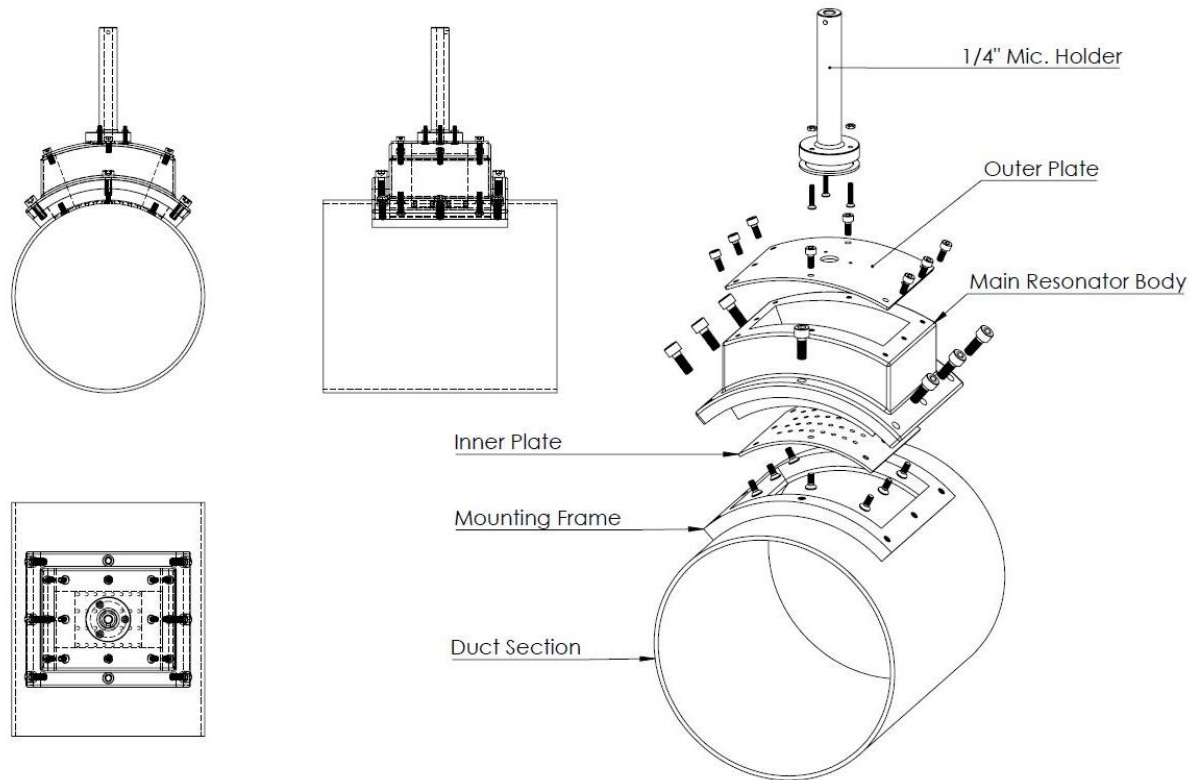
Figure 120 - Assembly CAD drawing of final distributed resonator design

The mounting frame is bonded to the existing acoustic duct section and serves the purpose of providing sufficient wall thickness to receive the main resonator body securing bolts, without requiring any protrusion into the internal cavity of the duct. Furthermore, the design is such that the mounting frame aids accurate and repeatable location of the main resonator body and also ensures that the inner surface of the test plate remains flush with the inner wall of the duct, mitigating any unwanted or inconsistent acoustic artefacts emanating from the interface. The main resonator body and the mounting frame are constructed from high quality stainless steel to both ensure the longevity of the components, and to ensure that the repeated use of the retaining bolts does not prematurely wear out the internal threads; which can be seen pictorially in Figure 122, and schematically in Figure 121.
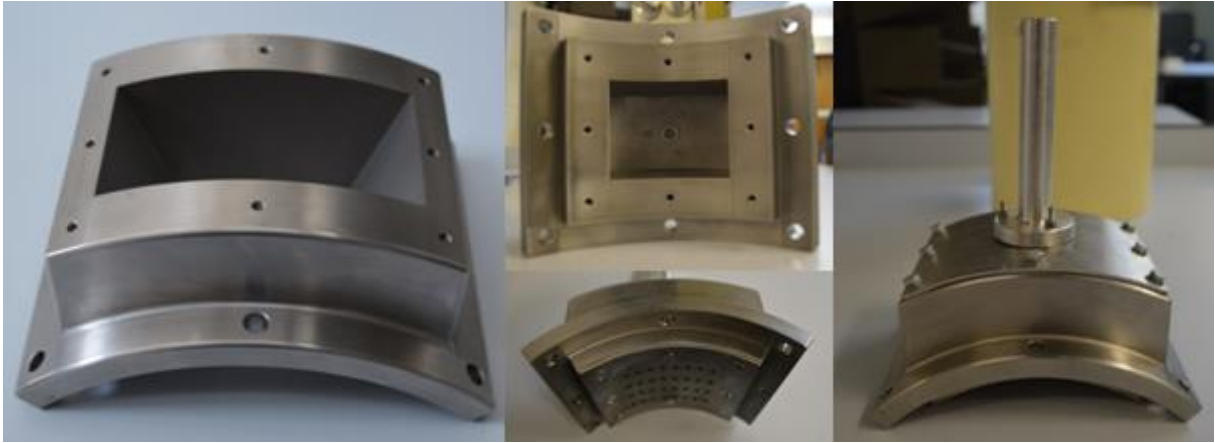
Figure 121 - Images of fabricated HFD Resonator components
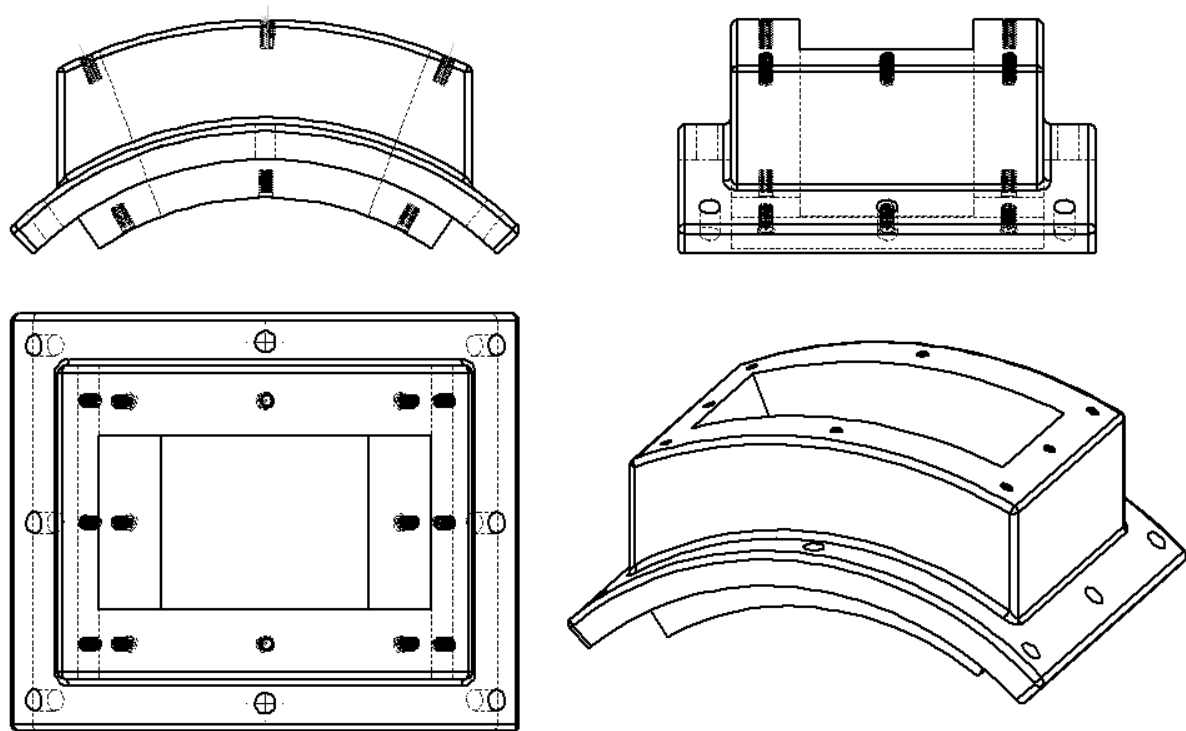
Figure 122 – Schematic CAD drawing of distributed resonator main body

7.3.3   Measurement Section Specifications

The distributed resonator design shown in *Section 7.3.2* is fixed to a 524mm long blank section of
Ø165mm tube, which forms the removable test section of the existing acoustic rig. The measurement
section is held in place by two foam lined heavy-duty stainless-steel compression bands, allowing
convenient removal of the section, whilst still ensuring a secure and air-tight fitment to the main flow
rig section. As shown in schematically in Figure 123, and pictorially in Figure 124, there are an
additional three 1/4" in-duct microphone measurement locations fixed circumferentially in the same

plane as the in-resonator microphone, which allows multiple locations for the derivation of FRF, and can also be used to check for the presence of higher order modes in the duct.

There are also two upstream and two downstream measurement locations available either side of the measurement section, mounted directly into the existing duct. These ports are designed for 1/2" microphones however, using a reducer can also be adapted to accept 1/4" microphones. When not in use a 'dummy microphone' insert is used to blank off the relevant measurement location to both seal the rig, and to mitigate the generation of unwanted aero-acoustic noise. Static pressure taps and an access port for Pitot tube measurements are also available both upstream and downstream of the measurement section, which can be used to determine the corresponding grazing flow velocity and pressure drop within the duct either side of the measurement section.
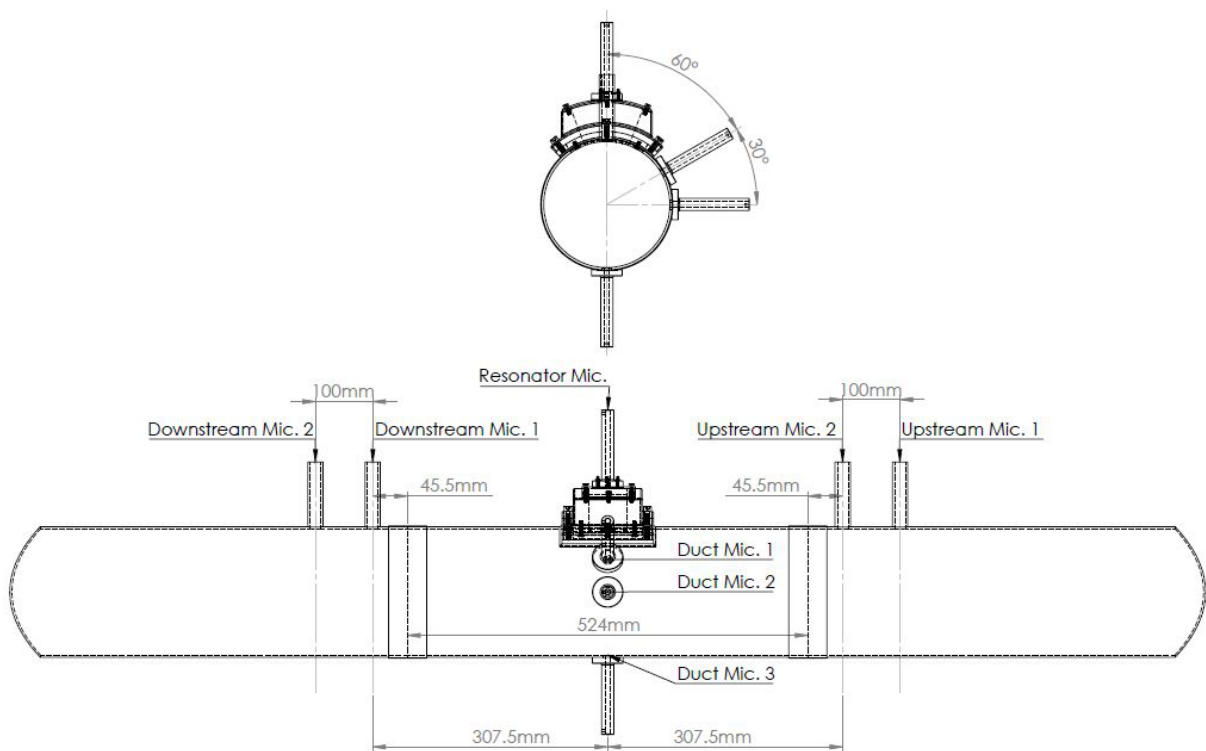
Figure 123 - CAD Drawing of flow rig measurement section including distributed resonator
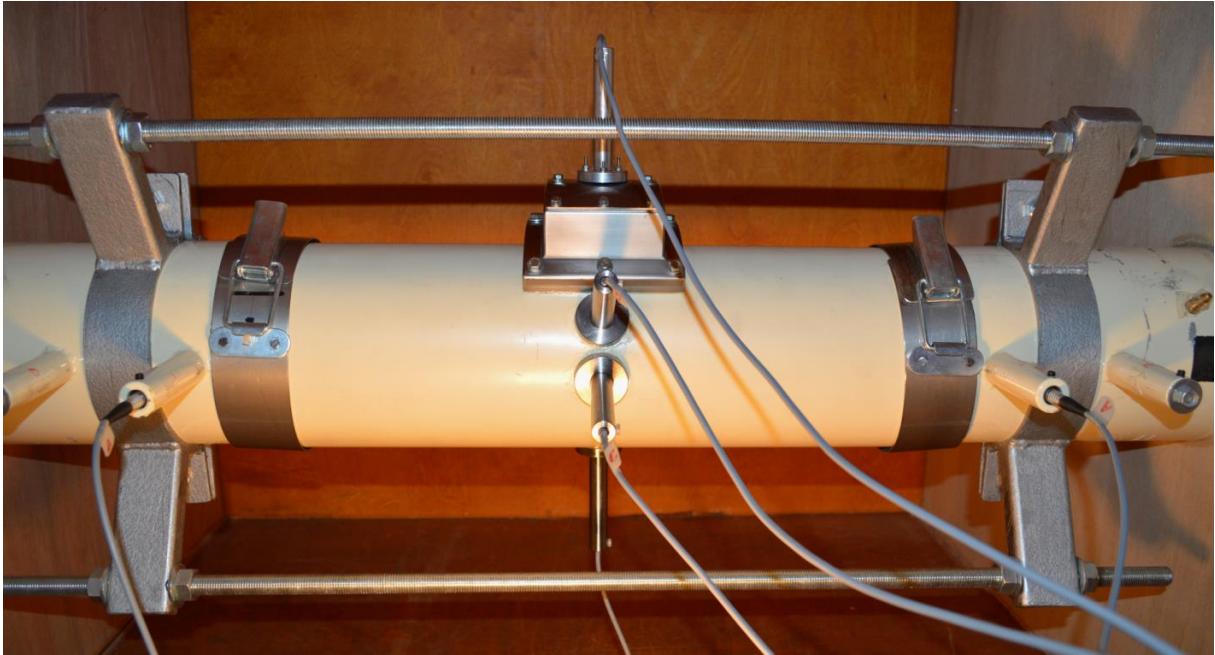
Figure 124 - Image of distributed resonator installed in measurement section of flow rig

7.3.4   Bias Flow Delivery Procedure

A bespoke method of bias flow introduction was integrated to the aforementioned existing acoustic flow rig specifically to address the delivery of bias flow through the new distributed resonator, for which the delivery interface can be seen in *Figure 125*. This new approach has the advantage of over the previous method; of pressurising the entire measurement section with a centrifugal fan and venting off excess mass flow; in that bias mass flow can be measured directly; rather than calculated as a function of pressure drop as previously. Furthermore, as the previous method used a centrifugal fan to drive the bias flow delivery and pressurise the measurement section, there was a practical limit to the minimum bias flow that could be provided by these means. In contrast however, the current approach facilitates delivery of bias flow via a compressed air feed, and as such it can be regulated right down to effectively zero mass flow.

A further benefit of the current bias flow delivery method is the integration of multi-location, surface mounted pressure taps, in both the resonator cavity and plenum section; allowing improved accuracy in the measurement of pressure drop across the resonator.
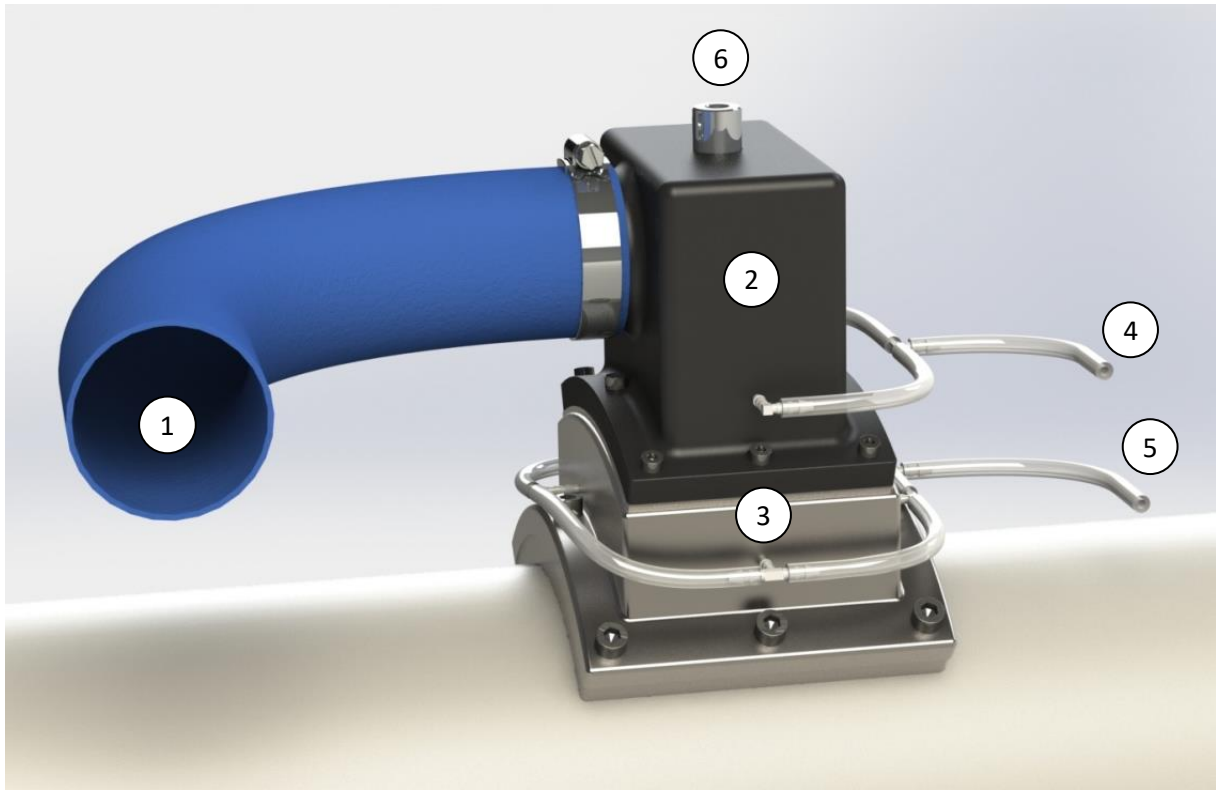
Figure 125 - CAD model of bias flow delivery system: 1) Bias Flow Delivery Hose; 2) Bias Flow Plenum; 3) Distributed resonator body; 4) Plenum Static Pressure Tap; 5) Resonator Static Pressure Tap; 6) In-Resonator Measurement Microphone Port

One downside to using compressed air is the additional flow generated noise which can occur from a sudden expansion as it leaves the supply line at high pressure; in order to alleviate this noise, the blue tube shown in *Figure 125* extends 10m downstream from the resonator. This supply hose is reinforced high pressure 54mm ID water hose, the large diameter, bend radii and upstream length is intended to ensure that the volume upstream of the resonator is sufficient to negate any significant resonant properties within the current measurement range. An additional advantage to this configuration is the improved access to the measurement section of the previous approach, allowing for expedient changes in plate configurations. The bias flow delivery components can be seen installed in situ within the measurement section of the acoustic rig in Figure 126, with bias flow being delivered *(as indicated by the inflated hose)*. This system has been tested and shown to be able to consistently delivery mass flows of up to 8g/s and pressures of up to 10bar.
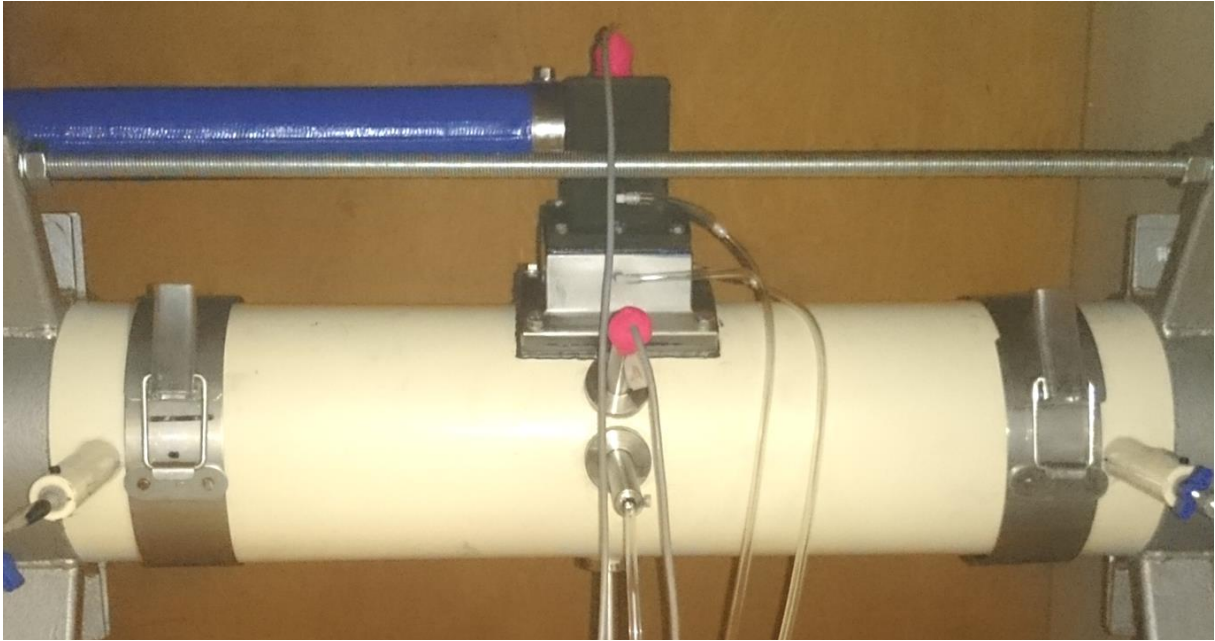
Figure 126 - Image showing the Bias Flow delivery system installed, and in operation within the distributed resonator test section

The amount of bias flow delivered to the resonator is controlled via an analogue flow regulator, as shown in *Figure 127*. Using this flow regulator, the amount of bias flow can be manually controlled from almost zero up to the maximum of 8g/s. The exact amount of mass flow delivered can be read manually via the externally mounted Rotameters, as also shown in *Figure 127*. Three Rotameters of differing scales are configured in series so that the full range of bias flow available can be utilised if necessary *(0 - 8g/s)*. Where the bias flow supply leaves the last Rotameter, it then travels 10m downstream in a 25mm ID pipe, before then stepping up to the 54mm ID hose, this additional length also helps to suppress the flow generated noise resulting from the flow regulator and Rotameters. Also mounted on the external bias flow instrumentation board are six digital manometers, each of which provides independent pressure measurements from the distributed resonator test rig: with specifications and measurement locations according to Table 33.

In order to ensure an effective subsequent combined flow test matrix, it is important to initially quantify the bias flow parameters according to the corresponding pressure drop, and to ensure that the resultant bias flow properties are as comparable as reasonably practicable across inner plate designs. To achieve this goal, the outer hole diameter and number of open holes was varied across inner neck diameter cases, ensuring an optimal compromise between all flow factors. As all inner plate designs of common neck diameter exhibited almost exactly the same neck velocities, regardless of hole spacing, there are only three different outer plate configurations needed to satisfy the full distributed resonator test matrix. The resultant outer plate configurations for each corresponding inner plate neck diameter, and the measured mass flow, and neck velocities for each configuration, can be seen in *Table 34*.
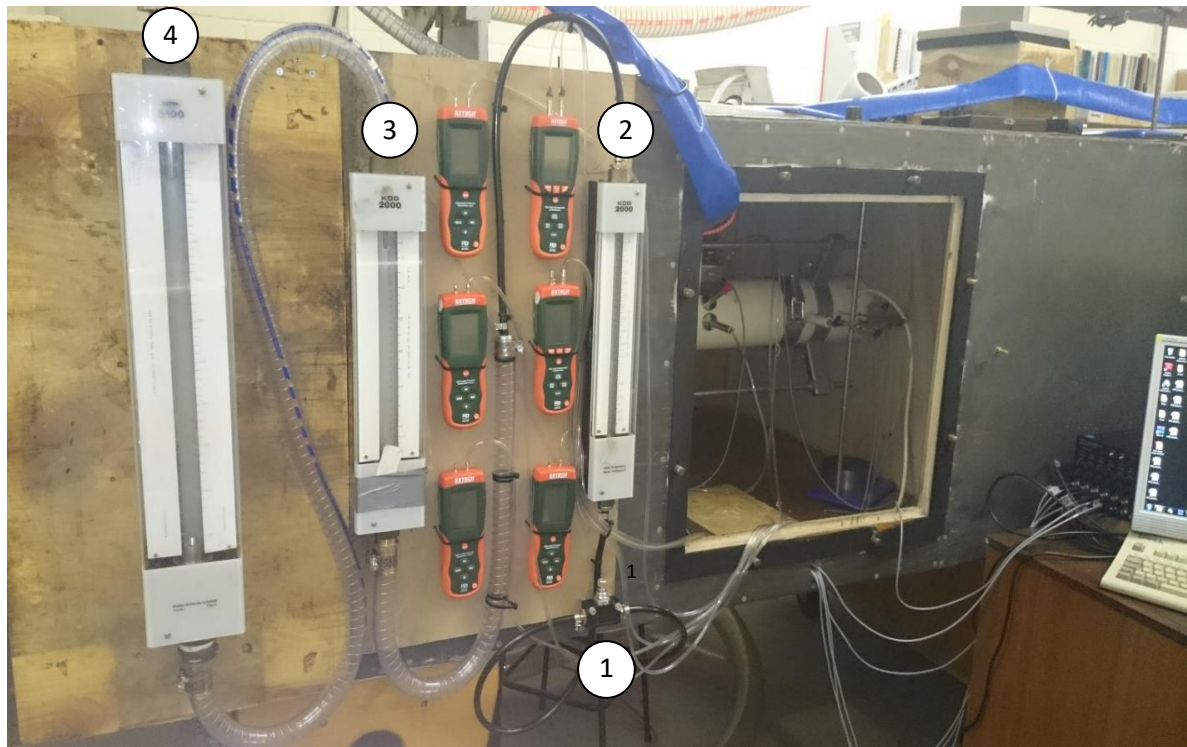
Figure 127 - Image showing delivery of bias flow into measurement section and bias flow metering system: 1) Analogue Flow Regulator; 2) Small Rotameter [0.1 -1.04 g/s]; 3) Medium Rotameter [0.5 - 4.3 g/s]; 4) Large Rotameter [1 - 9.9 g/s]

Model	Range	Measurement	Probe Location
Extech HD750	5psi (34kPa)	Plenum Pressure	Bias Flow Plenum Wall x 2
Extech HD755	0.5psi (3.4kPa)	Resonator Pressure	Resonator Wall x 2
Extech HD755	0.5psi (3.4kPa)	Upstream Static Pressure	Upstream Duct Wall Tap
Extech HD350	0.7252psi (5kPa)	Cross-flow Velocity	Upstream Centre Mounted Pitot Tube
Extech HD350	0.7252psi (5kPa)	Downstream Static Pressure	Downstream Duct Wall Tap
Extech HD700	2psi (13.8kPa)	Test Section Static Pressure	Measurement section side mic. port

Table 33 - Table Showing Digital Manometer configurations

	2mm x12 Outer Plate			2mm x20 Outer Plate			1mm x 20 Outer Plate		
	Plates 1-12			Plates 13-24			Plates 25-36		
D_p (%)	$\dot{m}$ (g/s)	U_o (m/s)	U_i (m/s)	$\dot{m}$ (g/s)	U_o (m/s)	U_i (m/s)	$\dot{m}$ (g/s)	U_o (m/s)	U_i (m/s)
0	0	0	0	0	0	0	0	0	0
1	1.6	34.6	5.8	2.7	35.8	5.6	0.7	35.9	5.6
2	2.2	49.3	8.2	3.8	50.8	7.9	0.9	48.6	7.7
3	2.7	59.6	9.9	4.6	61.9	9.7	1.1	61.0	9.5
4	3.0	68.5	11.4	5.4	72.9	11.4	1.3	71.6	11.2
5	3.4	75.9	12.6	5.9	79.6	12.4	1.5	79.6	12.4
Pressure Ratio (Φ)									
	30.31			31.37			37.74		

Table 34 - Bias mass flow rate & neck velocity for distributed resonator test matrix

7.3.5   Data collection & processing specifics

All experimental data collected in relation to the distributed resonator test cases is collected under atmospheric isothermal conditions; with the sampling frequency and sample size shown in *Table 35*, and subsequent spectral analysis conducted according to Section 2.4.1.

Variable	Value	Units
Sampling Frequency	*40,000*	*Hz*
Sample Size	*200,000*	*-*
Number of Samples	*12*	*-*
Average Temperature	*23*	*°C*
Average Atmospheric Pressure	*101,300*	*Pa*

Table 35 - Table showing experimental acoustic data sampling configuration for distributed resonator test cases

7.3.6   Measurement Equipment

All measurements included in this report have been collected using the following equipment:

Equipment List

- *Hull ARC acoustic flow rig*

- *Ø165mm x 524mm Blank Tube Section*

- *Ø165mm x 524mm measurement section with distributed resonator and x4 1/4" Microphone Holders (1 in-resonator & 3 in-duct)*

- *Tektronix AFG 3022B Dual Channel Arbitrary/Function Generator (250MS/s, 25Mhz)*

- *Cambridge Audio Ltd. SR707 – Professional Power Amplifier*

- *G.R.A.S. Sound & Vibration – Power Module, Type 12AG*

- *x4 Brüel &Kjær Type 4937-A-011 ¼" Measurement Microphones*

- *x2 Brüel &Kjær Type 4190-B-001 ½" Measurement Microphones*

- *Agilent Technologies – U2781A, 6-Slot USB Modular Instrument Chassis*

- *x2 Agilent Technologies 4 Channel Simultaneous Sampling Board, 16Bits, 500KS/s*

- *Windows PC running Windows Vista OS*

Figure 128 shows some the measurement equipment used next the measurement section of the acoustic flow rig, with the distributed resonator test section visible inside.
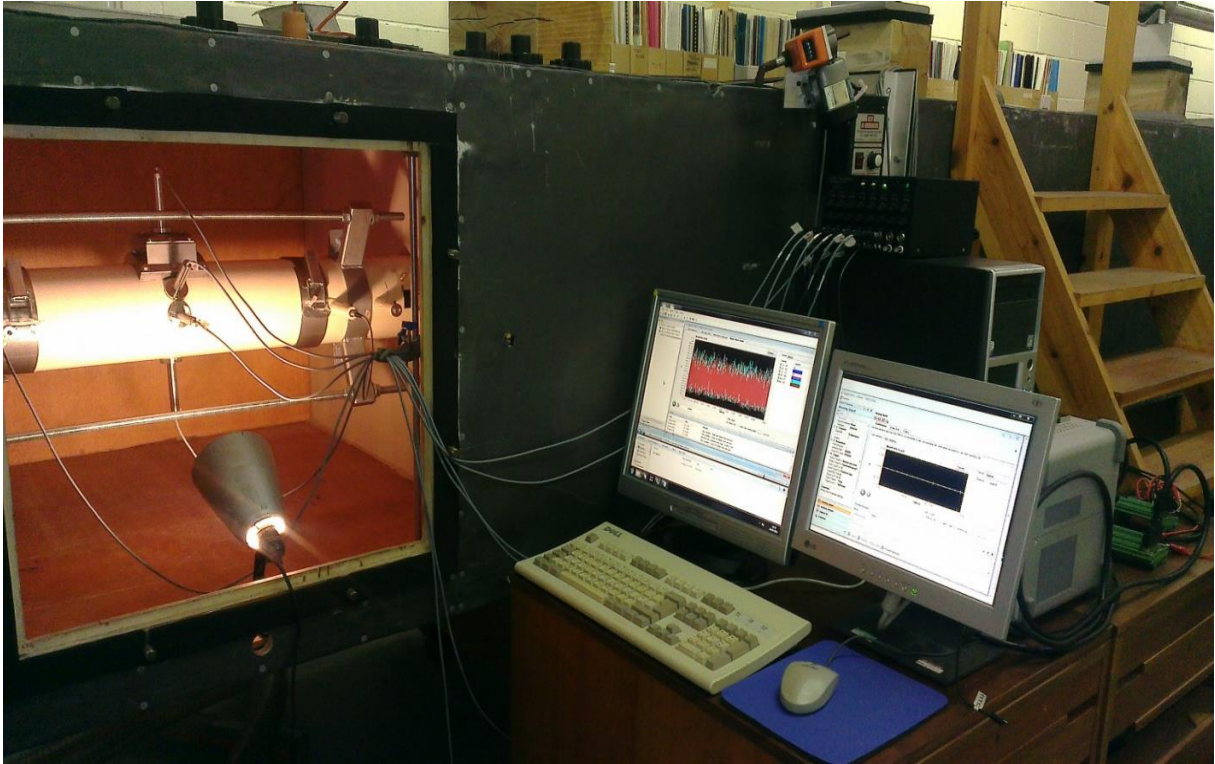
Figure 128 - Image of distributed resonator measurement section & measurement equipment

7.4 Distributed Resonator Test Cases

In order to facilitate the effective analysis of all desired characteristic factors of distributed acoustic resonator performance, as described in *Section 7.3*, there are three key component variations utilised by the resultant experimental resonator design. These are: the variation of the inner plate configuration; both single and multi-hole test cases; and the outer plate variations, which are required for bias flow analysis. All proposed experimental test articles to be deployed in this targeted analysis are described in the following sections.

7.4.1 Multi-holes

As shown in Table 31, the proposed experimental test matrix consists of a total of 36 inner plate variations; consisting of: 3-hole diameter variations; 3 Pitch$_y$ variations; and 4 Pitch$_x$ variations; giving a total of 12-hole spacing permutations for each hole diameter. In order for the desired plate area to be exposed to the resonator cavity it is necessary to have extra material to form a mounting surface to the inner radius of the main resonator body. The final form of the inner plates can be seen in Figure 129, which are designed to be fabricated via laser cutting from 2mm stainless steel sheet material, which is then cold rolled to the correct radius; and finally the mounting holes must be countersunk, so that the fixing tapered machine screws finish flush with the surface of the plate when mounted, thus ensuring no impact on the grazing flow.
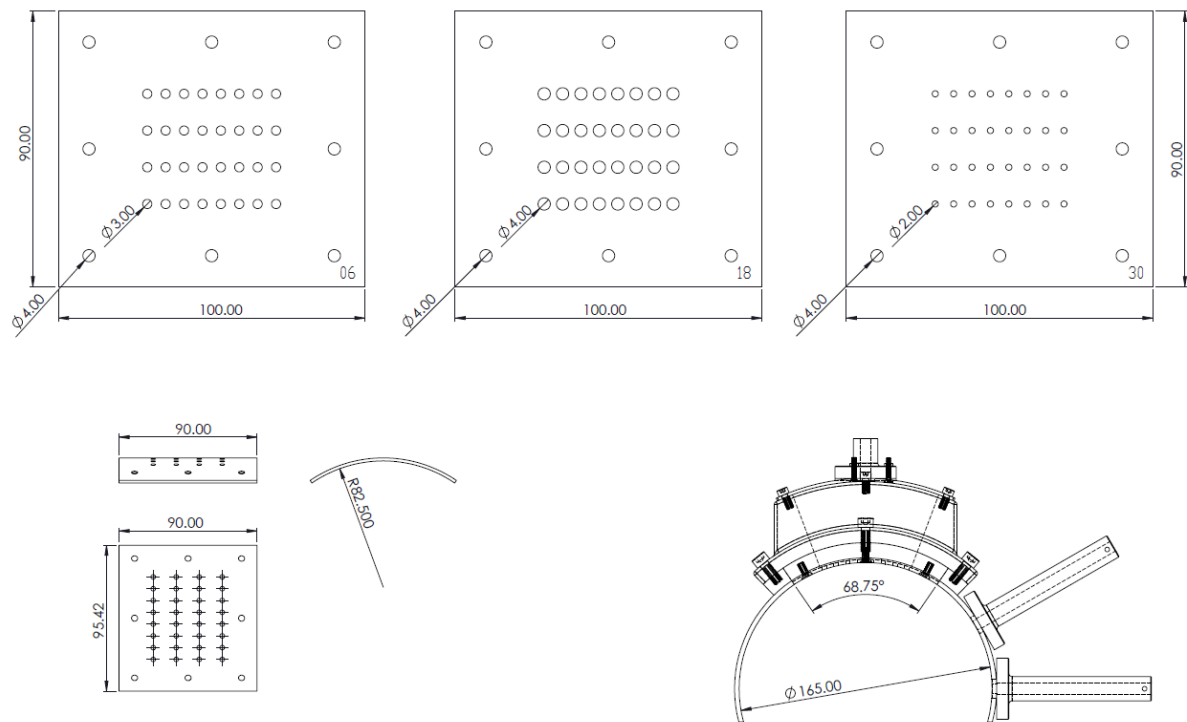
Figure 129 - Engineering drawings showing distributed resonator inner plate manufacturing and assembly requirements

The full produced set of x36 H-W & H-H inner test plates can be seen in Figure 130 after laser cutting, cold rolling and countersinking; where the plates shown are arranged in increasing numerical order according to the with case numbers identified in Table 31; with Case #01 on the top left and Case #36 on the lower right of Figure 130.

Figure 130 - Image of all 36 test plates after laser cutting and cold rolling

The engineering drawings shown in Figure 131 - Figure 133 detail the flattened plate surface exposed to the resonator cavity (the acoustically relevant surface), and the hole spacing configurations for each of the x36 inner plate test cases.

218

Case #	01	02	03	04	05	06	07	08	09	10	11	12
Length (Lx)	50	50	50	50	50	50	50	50	50	50	50	50
Height (Ly)	59.4	59.4	59.4	59.4	59.4	59.4	59.4	59.4	59.4	59.4	59.4	59.4
Alpha (Aspect Ratio) [Lx/Ly]	0.842	0.842	0.842	0.842	0.842	0.842	0.842	0.842	0.842	0.842	0.842	0.842
Hole Diameter	3	3	3	3	3	3	3	3	3	3	3	3
Xi (Aperture Ratio) [D/Lx]	0.06	0.06	0.06	0.06	0.06	0.06	0.06	0.06	0.06	0.06	0.06	0.06
Pitch (x Direction)	7	7	7	7	5.5	5.5	5.5	5.5	4	4	4	4
Pitch (y Direction)	10	8	6	4	10	8	6	4	10	8	6	4

Figure 131 – Distributed resonator inner test plate cases #1 - #12

Case #	13	14	15	16	17	18	19	20	21	22	23	24
Length (Lx)	50	50	50	50	50	50	50	50	50	50	50	50
Height (Ly)	59.4	59.4	59.4	59.4	59.4	59.4	59.4	59.4	59.4	59.4	59.4	59.4
Alpha (Aspect Ratio) [Lx/Ly]	0.842	0.842	0.842	0.842	0.842	0.842	0.842	0.842	0.842	0.842	0.842	0.842
Hole Diameter	3.5	3.5	3.5	3.5	3.5	3.5	3.5	3.5	3.5	3.5	3.5	3.5
Xi (Aperture Ratio) [D/Lx]	0.07	0.07	0.07	0.07	0.07	0.07	0.07	0.07	0.07	0.07	0.07	0.07
Pitch (x Direction)	7	7	7	7	5.5	5.5	5.5	5.5	4	4	4	4
Pitch (y Direction)	10	8	6	4	10	8	6	4	10	8	6	4

Figure 132 - Distributed resonator inner test plate cases #13 - #24

Case #	25	26	27	28	29	30	31	32	33	34	35	36
Length (Lx)	50	50	50	50	50	50	50	50	50	50	50	50
Height (Ly)	59.4	59.4	59.4	59.4	59.4	59.4	59.4	59.4	59.4	59.4	59.4	59.4
Alpha (Aspect Ratio) [Lx/Ly]	0.842	0.842	0.842	0.842	0.842	0.842	0.842	0.842	0.842	0.842	0.842	0.842
Hole Diameter	2.5	2.5	2.5	2.5	2.5	2.5	2.5	2.5	2.5	2.5	2.5	2.5
Xi (Aperture Ratio) [D/Lx]	0.05	0.05	0.05	0.05	0.05	0.05	0.05	0.05	0.05	0.05	0.05	0.05
Pitch (x Direction)	7	7	7	7	5.5	5.5	5.5	5.5	4	4	4	4
Pitch (y Direction)	10	8	6	4	10	8	6	4	10	8	6	4

Figure 133 - Distributed resonator inner test plate cases #25 - #36

7.4.2 Single Hole Case Specifications

In order to provide baseline measurement data for subsequent CFD simulations (outside of the scope of this study) for which the complexity and computational cost associated with meshing and simulating a full distributed resonator configuration would be prohibitive; and the intended saturation studies (Section 8.1.1), for which the additional sensitivity of a single hole case is beneficial; a special case has been defined using the inner plate #13 with only one single hole exposed, for which the properties can be seen in Figure 134.
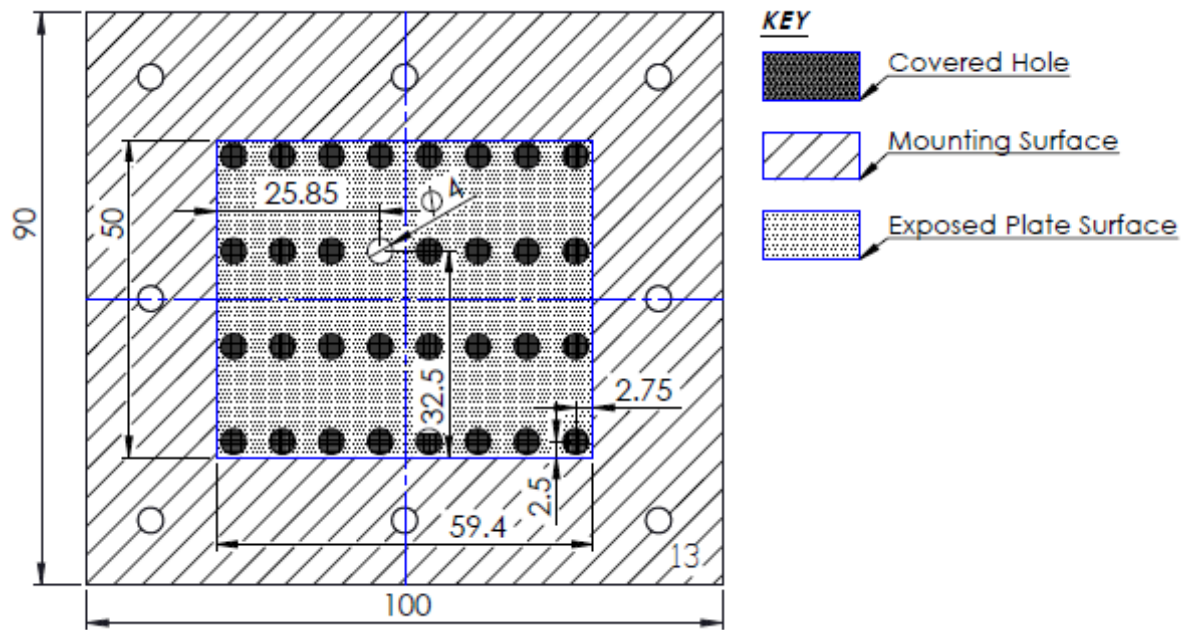
Figure 134 – Engineering drawing detailing the inner plate #13 single hole configuration

The applied approach to realising the single hole case is to use a heavy-duty adhesive tape to mask off the redundant holes. Figure 135 shows how this strategy was implemented practically; where on the right of the figure the internal surface of the plate can be seen with the section of tape removed around the target hole, and of the left of the figure the reassembled resonator can be seen with the single active hole open to the internal cavity.
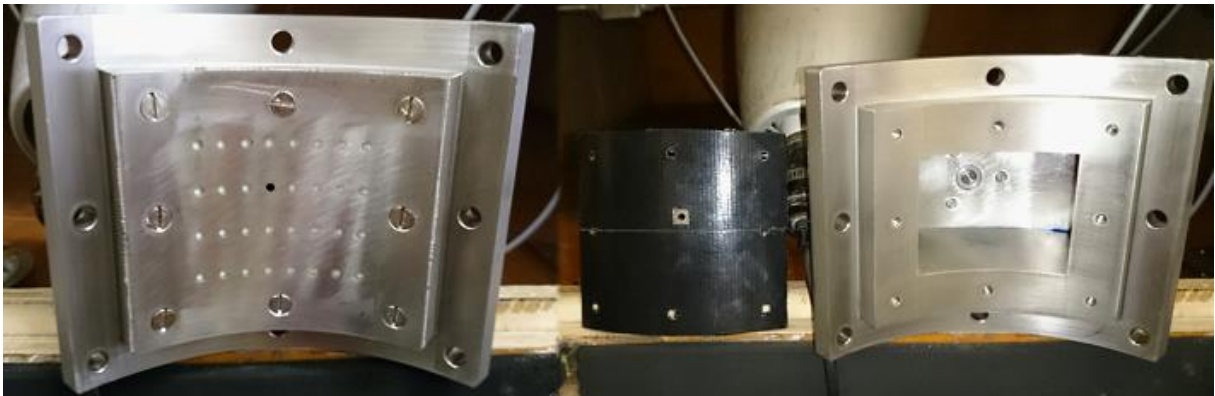
Figure 135 - Image Showing Single Hole Configuration for plate #13

7.4.3   Outer Test Plate Specifications

As with the inner test plates, the outer plates must be also laser cut, cold rolled to the correct bend radius, and then countersunk.   The exterior mounting holes for the outer plate do not require countersinking, as they are not exposed to any cross/grazing flow, whereas the internal fixtures for the measurement microphone holder must be countersunk on the internal surface of the plate. A total of

four outer plate variations have been produced for the scope of this investigation, as detailed in Table 34, and shown schematically in Figure 136.
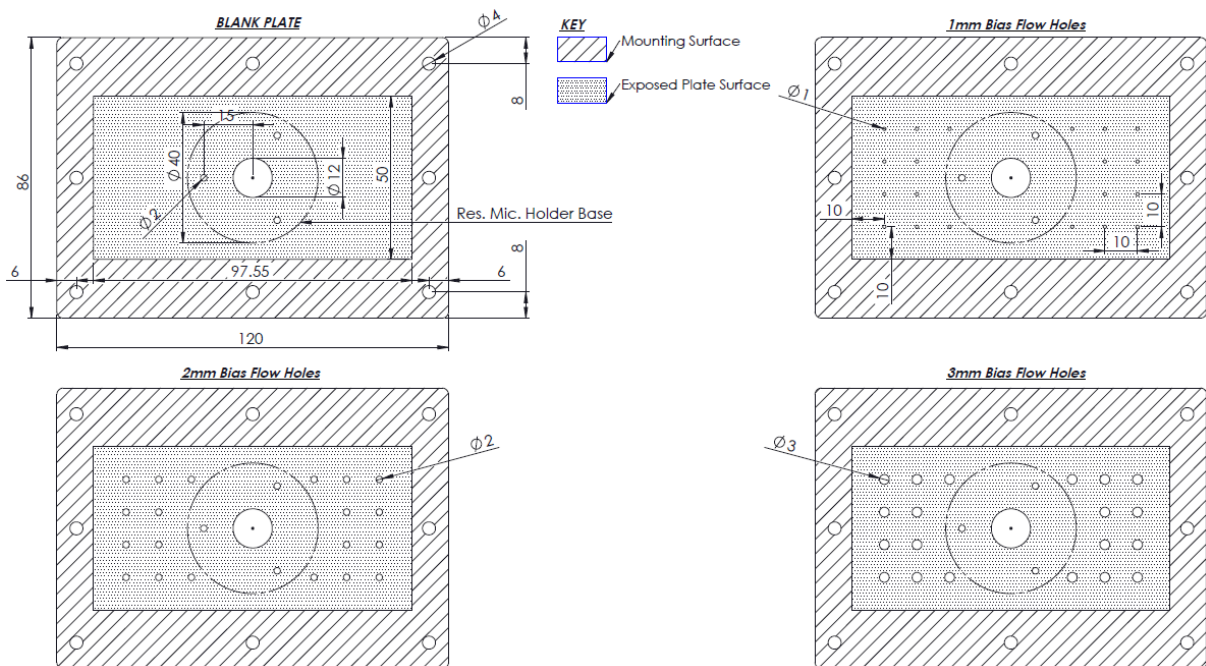
Figure 136 – Schematic engineering drawing showing outer plate design requirements

7.5 Measurement Strategy

In order to address each of the objectives of this investigation outlines in Section 7.1, a systematic approach to the experimental data collection is required. The following sections detail the specific measurement strategies employed, with the goal to ensure a methodical regime of experimental data collection is implemented, which effectively supports the subsequent evaluation and analysis of the targeted acoustic attenuation performance factors.

7.5.1 Saturation Effects/Sound Pressure Level

To investigate the potential of resonator saturation resulting from high acoustic excitation sound pressure levels (SPL), a range of acoustic excitation amplitudes need to be measured for representative test cases; followed by evaluation of relevant attenuation performance metrics for each SLP condition investigated. As the maximum SPL is ultimately dependant on the hardware limitations of the rig, due diligence must be taken when pursuing high SPL conditions, in order to mitigate any damage to the measurement equipment. Indicators of excessive loading of the installed acoustic signal generation hardware include initiation of over current protection systems *(Fuses, Residual Current Devices etc.);* component overheating; and any observed distortion of the expected signal. All of the aforementioned indicators need to be carefully monitored when seeking the maximum permissible sound pressure

level, and for the full distributed resonator test matrix, an optimal sound pressure level must be maintained throughout the subsequent experiments. An optimal SPL can be considered one which is concurrently; sufficiently higher than flow generated noise SPL, such that consistent excitation is facilitated across the relevant frequency domain; and yet suitably below the onset of non-linear resonator response *(i.e. saturation).* As such the intended initial SPL measurement strategy is as follows:

1) Vary acoustic SPL for a single hole case under acoustic excitation only *(Plate #13).*
2) Vary acoustic SPL for representative extreme cases of H-W & H-H factors *(Plate #1, #13, #24, #25 & #36),* in closed configuration *(i.e. with the blank outer plate fitted, and no bias flow),* and under acoustic excitation only *(i.e. no cross-flow).*

From this study and the preceding cross/bias flow noise evaluations, a preferred SPL level for the acoustic excitation signal can be defined and applied to all subsequent measurements. This chosen level should offer the best compromise between signal to noise ratio, and the onset of saturation factors for the full test matrix, and should be consistently used as the acoustic excitation, unless stated otherwise.

7.5.2   Neck Length versus Diameter Factors (L/D)

In order to investigate the significance of the ratio between neck length and neck diameter, it is desirable to test several cases where the expected peak response frequency is comparable between cases, and only the neck length over diameter ratio (L/D) is varied. For the intended test matrix only one neck length is available *(2mm),* however three neck diameters are available *(2mm, 3mm & 4mm).* Irrespective, an initial appreciation of L/D variation can be determined by varying the cavity volume, to give a common peak attenuation frequency, and then comparing the relative resultant attenuation performance between the corresponding cases. For the existing distributed resonator design, the cavity volume is fixed, and not easily modified without the need to manufacture a new resonator body. For the purpose of an initial insight into any possible significance on resonator performance however, the cavity can be rudimentarily modified, by reducing its volume through inserting additional material within the cavity, thus reducing the acoustically relevant fluid volume. Given that the resonator cavity can only be easily reduced and not increased, the measurement strategy is as follows:

1) Measure the response for a representative 4mm neck diameter case *(Plate #18)* $[L/D = 1/2].$
   a. Calculate the expected volume reduction required to shift the response frequency of a representative 3mm neck diameter case *(Plate #6)* $[L/D = 2/3]$ to match that of the 4mm case *(Plate #18)* $[L/D = 1/2].$

  b. Modify the cavity volume based on target volume reduction.

2) Measure the resultant 3mm case, revaluate steps 1a & 1b, and repeat *(if necessary).*

  a. Calculate the expected volume reduction required to shift the response frequency of a representative 2mm neck diameter case *(Plate #30)* $[L/D = 1]$ to match that of the 4mm case *(Plate #18)* $[L/D = 1/2]$.

  b. Modify cavity volume based on target volume reduction.

3) Measured the resultant 2mm case, revaluate steps 2a & 2b, and repeat *(if necessary).*

4) Evaluate the relative measured acoustic response across all three L/D ratio cases.

7.5.3   H-W & H-H Factors

As presented in Section 7.2.1 - H-W & H-H parameter optimisation H-W & H-H , the 36 inner plate configurations were designed with the target of maximising the H-W & H-H variations across the available cases. Therefore, it is expected that the two extremes of hole spacing pattern for each neck diameter case, should exhibit measurable differences in both peak attenuation magnitude and phase. The measurements used for the analysis of H-W & H-H factors should initially be closed cases, and under acoustic excitation only, hence any variation in observed acoustic response can be solely attributed to the effects of H-W & H-H factors. A relative comparison between the observed acoustic response from each measured test case can then be compared; thus, providing further experimental insight into the significance of these factors, facilitating critique of current analytical modelling methods, and supporting the progression of the current state of the art in relation to H-W & H-H factors; the measurement strategy required to support this goal is:

1) Measure the acoustic response of all 36 inner plate variations in a closed resonator configuration *(i.e. with the blank outer plate fitted, and no bias flow),* under acoustic excitation only *(i.e. no cross-flow).*

2) Make a relative comparison of the acoustic response of all measured cases across the targeted frequency domain, evaluating any experimental observed trends.

3) Extract then compile values of peak attenuation frequency and magnitude for all cases, to support comparison with, and critique of, current analytical methods.

4) Calculate predicted H-W & H-H contributions for all measured cases using current analytical methods.

5) Compare analytically derived predictions with experimental results and modify/calibrate existing formulations as necessary to achieve cohesion between calculations & measurements.

7.5.4   Grazing Flow Factors

In order to rigorously evaluate the impact of grazing flow factors on a distributed resonators attenuation performance, it is necessary to capture and detail the transient phase, such that current assumptions inherent in analytical end correction modelling approaches can be efficiently critiqued. To effectively support the advancement of insights in relation to the onset of grazing flow impact on end correction assumptions, measurements will be conducted with the grazing flow magnitude ranging from zero, to the maximum permissible magnitude; followed by a relative evaluation of the impact on attenuation performance for each investigated case. Similar to the H-W & H-H investigations, the goal is to obtain further experimental insight into the significance of these factors, to facilitate the critique of current analytical modelling methods, and support the progression of the current state of the art in relation to grazing flow factors; the measurement strategy required to support this goal is:

1) Vary grazing flow magnitude for closed resonator *(i.e. with the blank outer plate fitted, and no bias flow)*, single hole case *(Plate #13)*, with concurrent acoustic excitation.
2) Vary grazing flow Magnitude for closed *(i.e. with the blank outer plate fitted, and no bias flow)* representative extreme cases of H-W & H-H factors *(Plate #1, #13 & #25),* with concurrent acoustic excitation.

7.5.5   Bias Flow Factors

In order to gain an appreciation of the impact of bias flow through the resonator on resultant resonator performance, it is necessary to experimentally evaluate a target test matrix in which the only significant variable is the magnitude of bias flow. As with the measurement strategy for grazing flow, the bias flow impact will be evaluated by analysing the two extreme hole spacing cases for each neck diameter case; and similarly the goal is to obtain further experimental insight into the significance of these factors, to facilitate the critique of current analytical modelling methods, and to support the progression of the current state of the art in relation to bias flow factors; the measurement strategy required to support this goal is:

1) Vary Bias Flow Magnitude for a single hole case, under acoustic excitation and with zero grazing flow *(Plate #13)*
2) Vary Bias Flow Magnitude for representative HFD Resonator Cases *(Plate #1, # 13 & #25)* under acoustic excitation and with zero grazing flow.

7.5.6   Combined Flow Factors

In order to effectively investigate the impact of combined grazing flow and bias flow interaction effects on a distributed resonators acoustic attenuation performance, both parameters need to be varied simultaneously; therefore a systematic combined flow test matrix is required, which defines the variation in flow parameters, and can be implemented on any given geometric test case variation; this test matrix is defined as shown in Table 36:

Plate XX		Bias Flow						
Cross Flow		*Pressure Drop Across Resonator (d p)*						
Hz	*m/s*	Closed	0%	1%	2%	3%	4%	5%
0	0							
10	12							
15	17							
20	23							
25	29							
30	34							

Table 36 - Table showing combined flow test matrix for single inner plate configuration

The implemented investigative strategy yields a test matrix of 42 unique flow permutations for each investigated inner plate configuration, of which there are 36 configurations available. This results in a total of 1512 individual test permutations, providing a comprehensive test matrix for the subsequent evaluation of all targeted flow impact objectives. In the derivation of this experimental design methodology for distributed resonator attenuation performance factors, the objective acoustic excitation and flow targets embodied are as follows:

- Maintain a high Signal-to-Noise Ratio (SNR) in presence of flow generated noise
- Target neck velocities of < 15m/s
- Target Bias Mass Flow magnitudes of < 5g/s

In summary, the strategic approach to the determination of combined flow factors impact on resonator performance is as follows:

1) Measure all 1512 combined flow cases.
2) Make a relative comparison of the acoustic response of six representative extreme cases of H-W & H-H factors *(Plate #1, #13 & #25)* across the targeted frequency domain, evaluating any experimental observed trends.
3) Compare existing theory with experimental results and investigate potential to modify/calibrate existing formulations as necessary to achieve improved cohesion between predictions & measurements.

7.6   Qualification of Measurement Procedures

As the flow rig used in this investigation is novel and bespoke to this investigation, its appropriateness must first be validated before the measurements collected from it can be analysed with confidence. To begin this characterisation of the rig, a sequence of baseline measurements was conducted without any resonator present, such that the intrinsic characteristics of the rig could be determined and evaluated. This initial rig characterisation was conducted according to the following scheme of investigation:

1) Evaluate Acoustic Excitation Signal
    a. Confirm that only plane waves exist
    b. Evaluate spectral distribution of excitation amplitude
    c. Evaluate effectiveness of anechoic termination
    d. Evaluate feasible sound pressure levels
2) Evaluate grazing flow
    a. Measure available grazing flow magnitudes
    b. Measure consequential flow generated noise
3) Evaluate Signal to noise ratio for maximum grazing flow magnitude

Following these baseline measurements, the Distributed Resonator section was subsequently attached, in order to extend the scheme of investigation to the following parameters:

4) Evaluate FRF sensitivity to circumferential in-duct microphone location
5) Evaluate Bias Flow
    a. Measure bias mass flow rate to corresponding integer values of percentage pressure drop across resonator *(for representative cases)*
    b. Calculate corresponding neck velocity for each bias flow condition
6) Evaluate Signal to noise ratio for maximum bias flow magnitude

Before making measurements with the distributed resonator, it is important to first investigate properties of the measurement rig and excitation signals using a blank measurement section. The blank tube replaces the HFD measurement section at the Start/End of the absorption section of the rig, as shown in Figure 124. In this configuration only the two upstream and two downstream microphones are available for measurement, as the FRF corresponding microphone ports are all specific to the HFD test section. The use of the blank tube section in the following evaluations ensures that all measured duct properties are independent of any resonator specific properties and allows the inherent test conditions for all subsequent HFD resonator measurements to be fully quantified. For

the later cases requiring an evaluation of bias flow however, a representative case must be used in order to accommodate fitment of the bias flow delivery system to the measurement rig.

7.6.1   Acoustic Excitation Methodology

For all measurements presented in this investigation, the acoustic excitation is provided in the form of white noise. White noise is used because it represents all frequencies and negates the need to synchronise the measurement equipment with the signal generator in order to ensure the capturing of all frequencies, as with a sign sweep signal for example. However, the existence of all frequencies in such a randomly generated signal as white noise, also has the disadvantage of meaning there exists frequencies above the plane wave cut off frequency of the duct.

As such if pure white noise were to be used for these experiments, then there will exist higher order modes within the duct, and thus the measurement accuracy would reduce due to location specific errors. Two different approaches to conditioning the white noise acoustic excitation signal have been evaluated for use within this investigation and are described in the following sections:

7.6.2   Truncated White Noise

One approach to effective acoustic signal conditioning is to use a truncated white noise signal, in where a statistically random Gaussian white noise signal is generated in MATLAB and then filtered using a Butterworth filter. The chosen filter properties for the signal used in this investigation can be seen in Table 37.

Variable	Value	Units
Lower Band Stop	10	Hz
Lower Band Pass	100	Hz
Upper Band Pass	1,000	Hz
Upper Band Stop	1,100	Hz
Number of points	101,300	-
Sampling Frequency	2M	Hz
Frequency	0.25	0.25
Signal Length	4	s

Table 37 - Table Showing Truncated White Noise Signal Details

The generated excitation spectrum is designed specifically to have as flat a response across the spectrum as possible, to include all frequencies within the measurement bandwidth, and to ensure that only plane waves exist within the duct. Due to the fact that the measurement rig used at Hull has a plane wave cut-off frequency of ≈1,200Hz the signal has been truncated to a maximum of 1,100Hz. The signal was also truncated at the lower end of the spectrum below the measurement range, so that

all of the excitation energy could be focused within the measurement range, therefore helping to reduce measurement noise, and allow higher sound pressure levels to be generated when needed. The resultant excitation signal can be seen in Figure 137, this signal is then digitally stored on the signal generator and passed to the amplifier and rig drivers at the sampling frequency and frequency shown in Table 37.
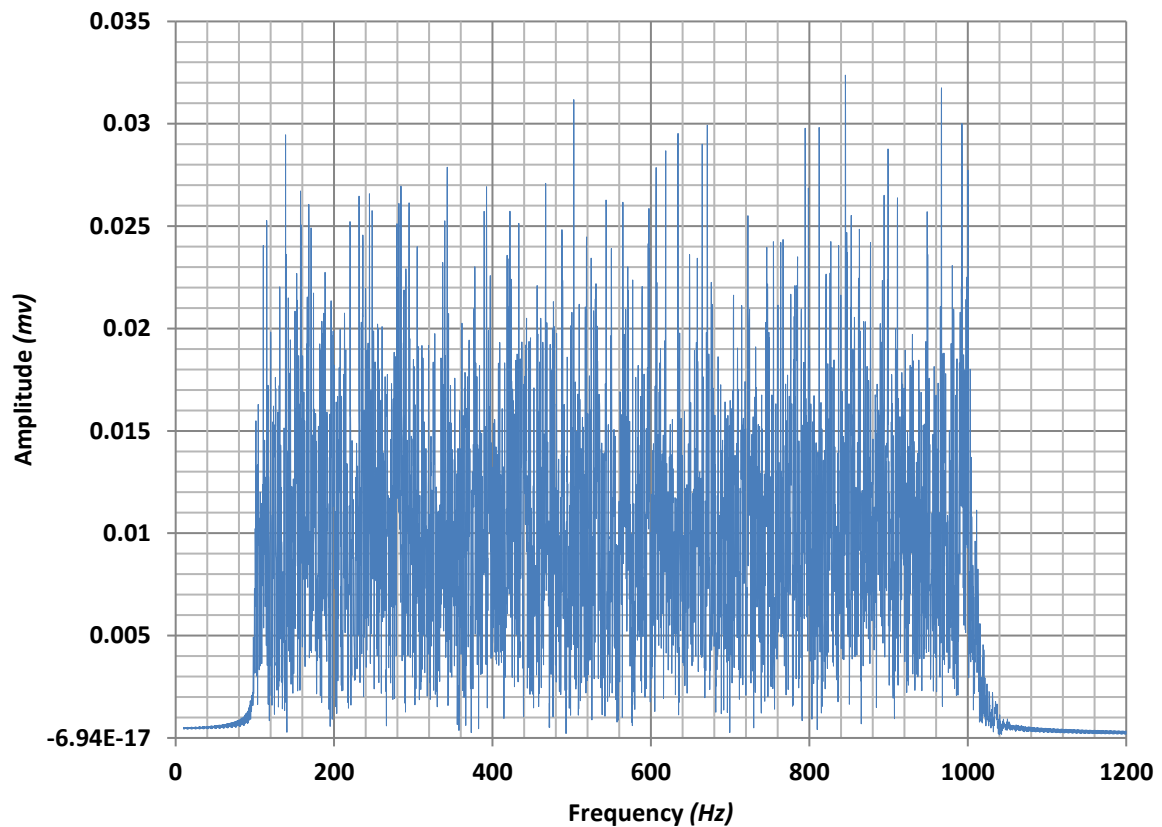
Figure 137 - FFT of Truncated White Noise Acoustic Excitation Signal

7.6.3   Multiband Filtered White Noise

During initial signal calibration exercises for the truncated white noise, the acoustic excitation spectrum measured at the test section of the rig, was disproportionally larger in magnitude at the lower frequencies than the higher frequencies, within the chosen measurement range; which can be seen from Figure 139. This was determined to be partly as a result of the acoustic driver's inherent response curve, and partly due to the intrinsic duct impedance, both of which resulted in a witnessed imbalance in signal magnitude at the location of measurement. For non-flowed and low SPL measurements the significance of this property would be negligible however, for the flowed measurements in particular, it is imperative to ensure that the acoustic excitation amplitude can be maintained at a level above the flow generated noise. Simply increasing the signal amplification only exacerbates the issue as the subsequent increase in SPL is non-linear across the frequency domain,

meaning that the practicable limit is defined by the maximum obtainable amplitude at the lowest frequency.

In order to ensure that a sufficiently high SPL can be obtained and a good signal to noise ratio across the full measurement spectrum, a more advanced multiband filter approach can be employed in place of the aforementioned band pass filter. The full details for the multiband filter design used in this investigation can be seen in *Table 38*.

Variable	Value	Units
Lower Band Stop	10	Hz
Lower Band Pass	100	Hz
Upper Band Pass	1,000	Hz
Upper Band Stop	1,100	Hz
Filter Response Type	Multiband	-
Filter Design Type	FIR -Least Squares	-
Filter Order	6555	-
Number of points	10,000	-
Sampling Frequency	2M	Hz
Signal Frequency	0.25	Hz
Signal Length	4	s

Table 38 - Table Showing Filtered White Noise Signal Details

In order to correct the signal for the duct specific properties, the employed strategy is to first begin with the aforementioned truncated white noise signal, and then apply a further high order multiband filter, where the filter coefficients for each frequency band are determined from the measured response of the original signal. After several iterations a detailed filter design can be arrived at, which demonstrates a uniform signal amplitude spectrum at the measurement section of the rig. The resultant excitation signal can be seen in *Figure 138* and as before, this signal is stored digitally on the signal generator and passed to the amplifier and rig drivers, at the sampling frequency and signal frequency shown in *Table 38*.
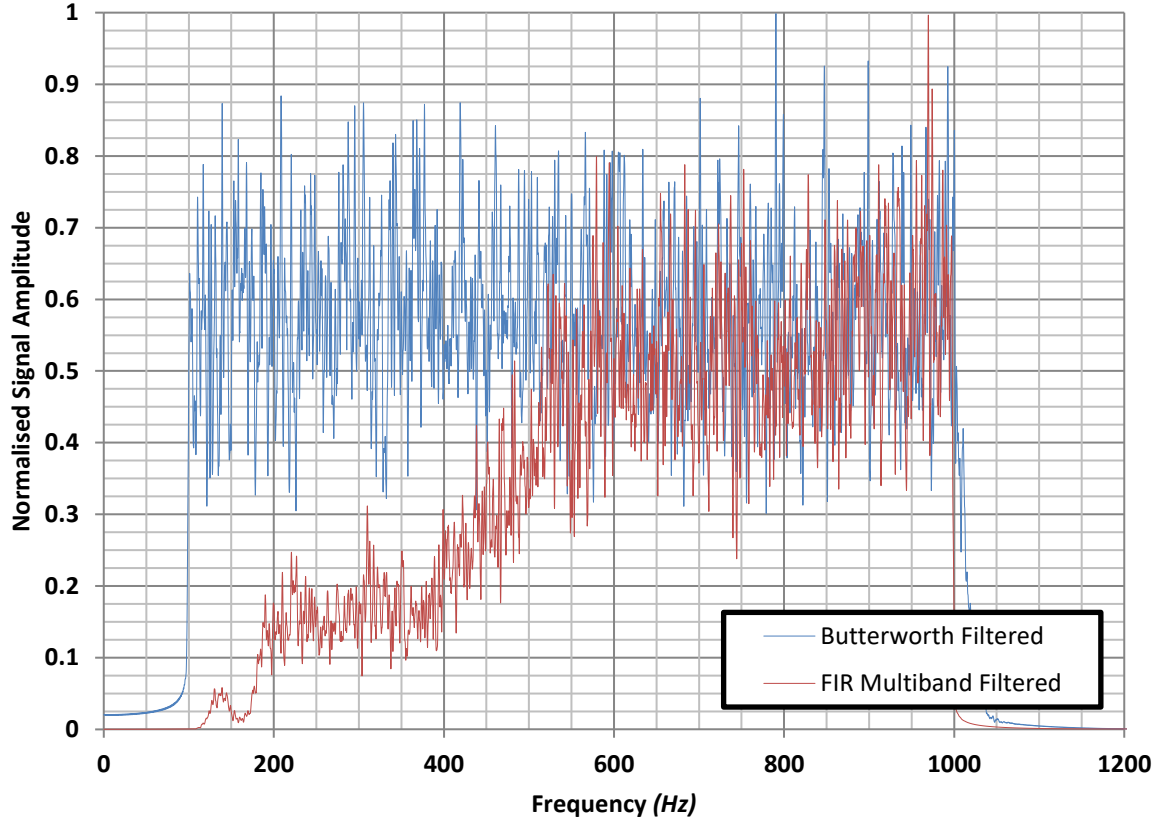
Figure 138 - FFT of Filtered White Noise Acoustic Excitation Signals

7.6.4   Acoustic Excitation Verification

As detailed in Section 7.6.1, the first step in rig & procedure evaluation is to evaluate the chosen acoustic excitation signal. An insight into the properties of the measurement rig and the acoustic excitation signal can be achieved by decomposition of the upstream and downstream acoustic pressure measurements, into their relative incident and reflected components. In order to get a consideration of the acoustic pressure and subsequent sound pressure level *(SPL)* of measurements, the measured voltage must be carefully equated to an equivalent acoustic pressure. For the measurements presented in this thesis, this is achieved by using the calibrated sensitivity of the measurement microphones (mV/Pa), the gain applied by the measurement amplifier for each case, the data acquisition V_{pp} value, and finally the appropriate amplitude scaling applied during the transforming of the data into the frequency domain. This approach allows the acoustic pressure attributed to the acoustic excitation signal to be derived for each case; which can be seen in Figure 139 & Figure 140 ,and the subsequent sound pressure level, as seen in Figure 141 & Figure 142.

By taking measurements of the blank tube under acoustic excitation only *(For a baseline 109dB SPL Truncated White Noise Signal),* and applying the decomposition method *(As specified in Section 2.4.2.3),* the spectral distribution the resultant incident and reflected acoustic pressure can be determined, as

shown in Figure 139. From an evaluation of the acoustic pressure spectral distribution observed in the duct, it is clear that the truncated signal is effective at eliminating present frequencies above the planar cut off frequency of the measurement rig. It is also however, evident that amplitude of the signal is no longer flat across the measurement spectrum, as was with the input signal. This can be accredited partly to the acoustic driver's inherent response curve, and partly to the fact that the signal source is a significant distance upstream of the measurement section; as a result, the high frequencies will succumb to a greater relative attenuation during the transmission from the acoustic source to the measurement section, due to the inherent impedance of the duct.

As discussed in Section 7.6.2, the demonstrated imbalance in spectral distribution of acoustic energy may impede the practicable ability to increase the power of the excitation signal for subsequent measurements, to a level where a sufficient signal to noise ratio can be ensured across the full measurement spectrum; hence potentially limiting the experimental effectiveness of the acoustic excitation signal, in stimulating the discrete aperture test resonator at all relevant frequencies of acoustic interest.
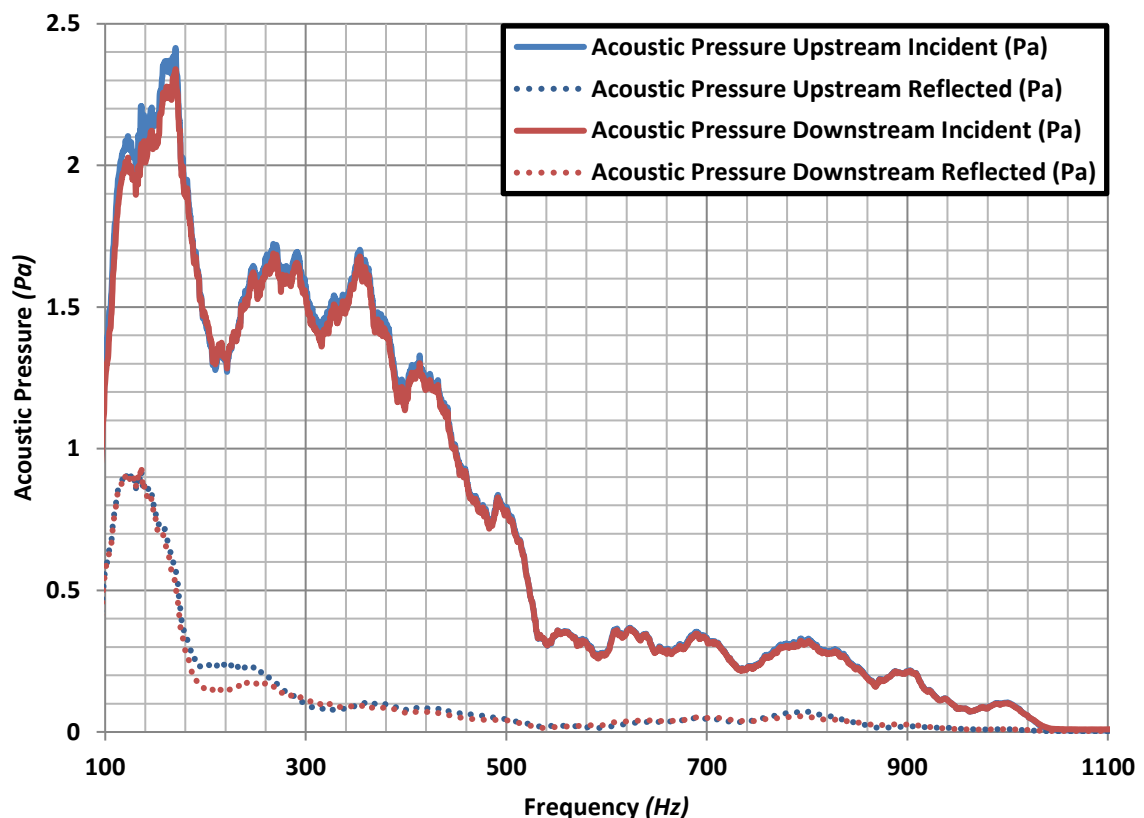
Figure 139 - Plot showing upstream and downstream incident and reflected signals with a blank measurement section, under a truncated white noise acoustic excitation only

It can be shown in Figure 140 that with the additional multiband filtering of the excitation signal, a significantly more uniform magnitude of acoustic excitation across the target measurement range can

be achieved. Similarly, it can be shown that only frequencies within the target measurement range are evident, and thus it can be subsequently determined that only plane waves exist within the measurement section for both signals. The more advanced multiband filtered signal can, however, be appreciated as preferential, as it results in a much more uniform acoustic excitation spectrum at the measurement section.
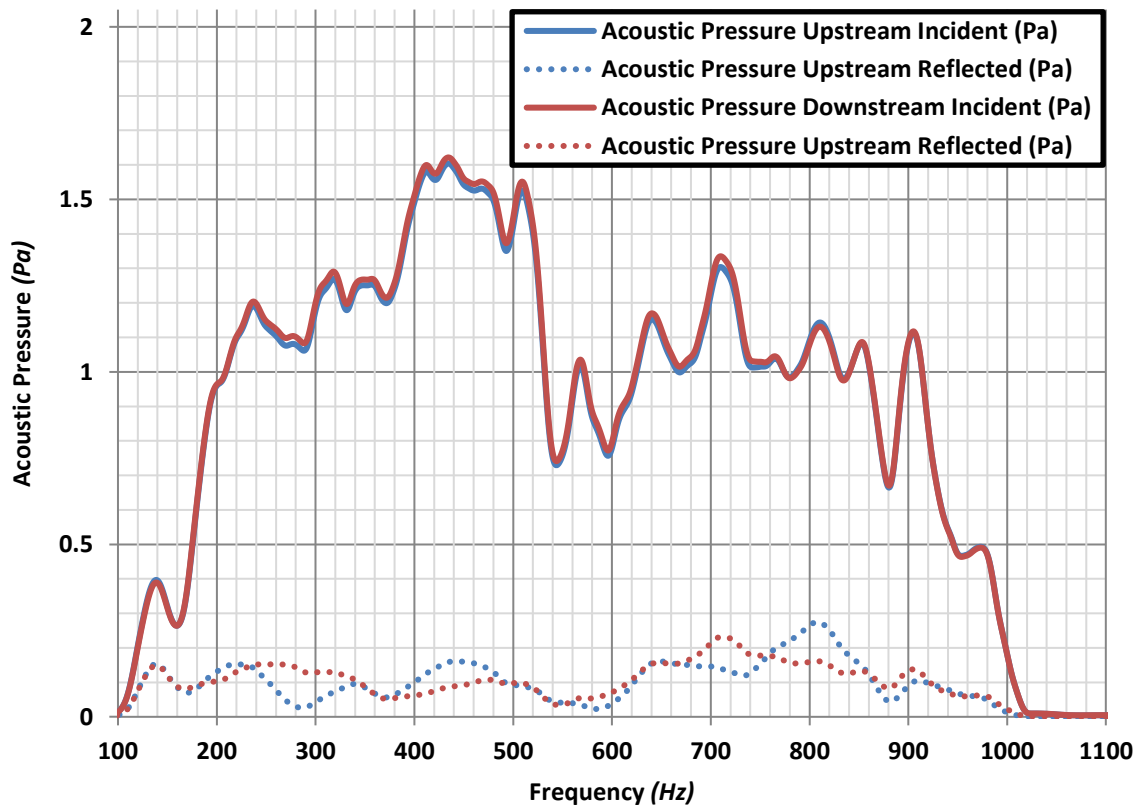
Figure 140 - Plot showing upstream and downstream incident and reflected signals with a blank measurement section, under multiband filtered white noise acoustic excitation only

With confidence that both available signals contain only dynamics within the target measurement range, and only frequencies below the plane wave cut off frequency of the rig, the obtainable sound pressure levels can subsequently be determined for each signal. Figure 141 shows the measured sound pressure level at the upstream in-duct microphone *(Mic. 1 - Figure 124),* where the signal amplitude is varied by the measurement amplifier *(Cambridge Audio Ltd. SR707)* in increments of the instrument indicated level *(0-10).*
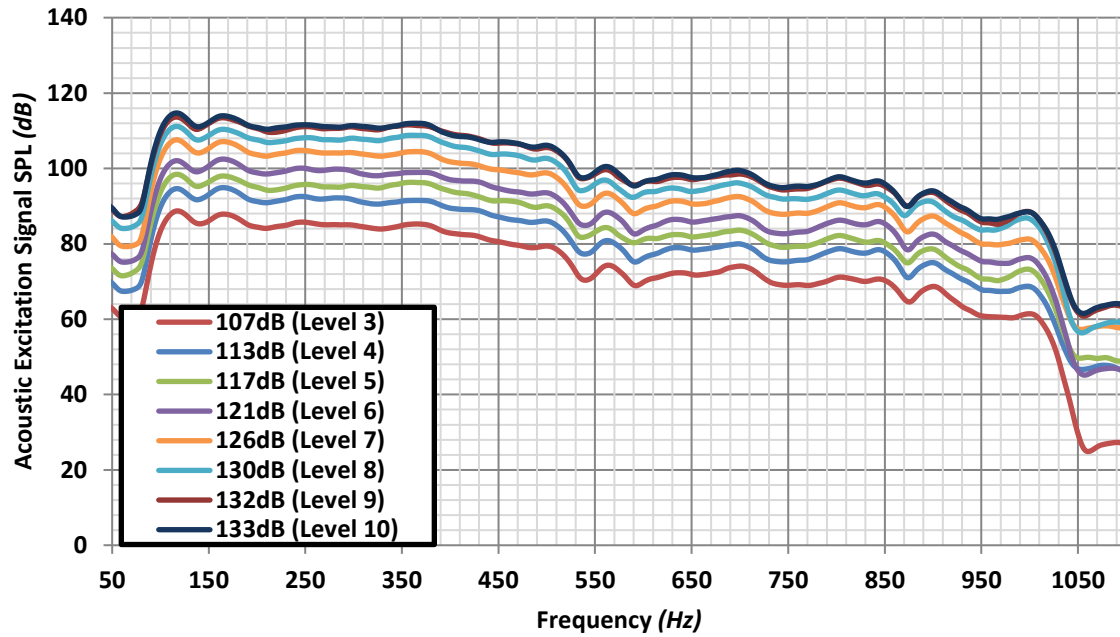
Figure 141 - Plot showing truncated white noise acoustic excitation signal SPL in the measurement section, with corresponding variations in signal amplification

The RMS values shown in the legend of Figure 141 correspond to the RMS value of SPL derived from the Time Domain, whereas the values in the plot correspond to the frequency domain SPL. Due to the nature of the white noise signal, in the time domain the amplitude of the signal at any given time, is a superposition of multiple randomly occurring frequencies, and therefore it will have a higher RMS amplitude than the frequency domain spectrum, where only the discrete frequency amplitude is given.

Figure 141 demonstrates the aforementioned imbalance in excitation signal amplitude across the measurement spectrum, whereas in Figure 142 it is apparent that the multiband filtered white noise produces the desired flat amplitude response across the measurement frequency domain. This observation serves as further validation that the multiband filtered white noise signal is the preferential choice of acoustic excitation for all distributed resonator measurements. The preferred excitation level is ultimately a compromise between the resultant signal to noise ratio, under consideration alongside the maximum flow generated noise; and the onset of any potential saturation factors; both of which are investigated further in the forthcoming sections. It is also noteworthy that; although the signal generation hardware is capable of operating with both filtered signals up to the maximum possible amplification level of 10 on the power amplifier; it was witnessed that above level 8 there was a significant increase in component temperature, and therefore it is in the interest of the equipment not to run at levels above 8 for prolonged periods of time if avoidable. Consequently, the preferable acoustic excitation condition can be concluded to be level 8 *(120dB)*, using the multiband filtered white noise signal.
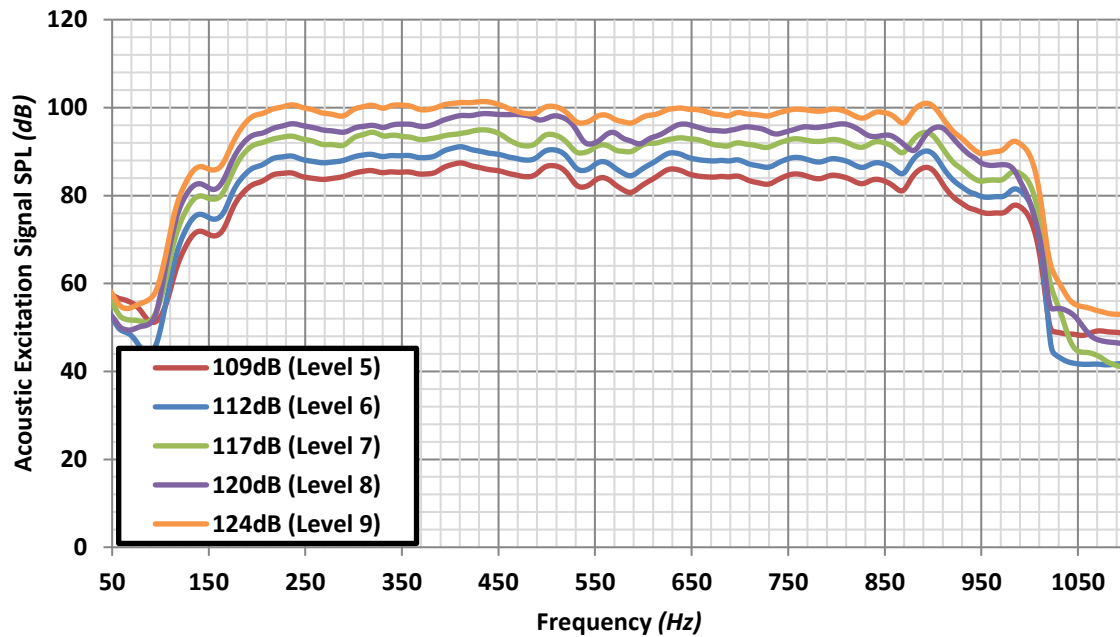
Figure 142 - Plot showing multiband filtered white noise acoustic excitation SPL in the measurement section, with corresponding variations in signal amplification

In order to successfully assume that any measured reflections are solely as a result of a fitted resonator, it is first necessary to evaluate the effectiveness of the anechoic termination. This can be achieved by determining the absorption coefficient for the measurement section with the blank tube fitted. If the Anechoic termination is perfect then it can be expected that there would be zero reflections, however a physical anechoic termination is likely to be more efficient at certain frequencies than others. Figure 143 shows the measured absorption coefficient for the anechoic termination, as determined from a multiband filtered white noise signal of 120dB. It can be seen in Figure 143 that above 200Hz almost all of the incident wave in the transmission duct is absorbed however, it is noteworthy that there are certain bandwidths within the measurement range at which a portion of the incident wave can be seen to be reflected.   As the blank measurement section is the same dimension as the rest of the transmission line, any reflections can be accounted solely to the anechoic termination.   The demonstrated absorption coefficient of generally greater than 95% is deemed acceptable, however, it cannot be considered negligible. For measured cases with very small amplitude responses, any small end reflections originating from the anechoic termination, may be of sufficient amplitude to mask or skew the measured response from that particular resonator case. As a result, even though the expected magnitude of end reflections within the measurement range are small, any successive performance evaluations, will be cleaned by removing the measured end reflections from the evaluated response, in order to improve the accuracy of subsequent resonator performance metrics.
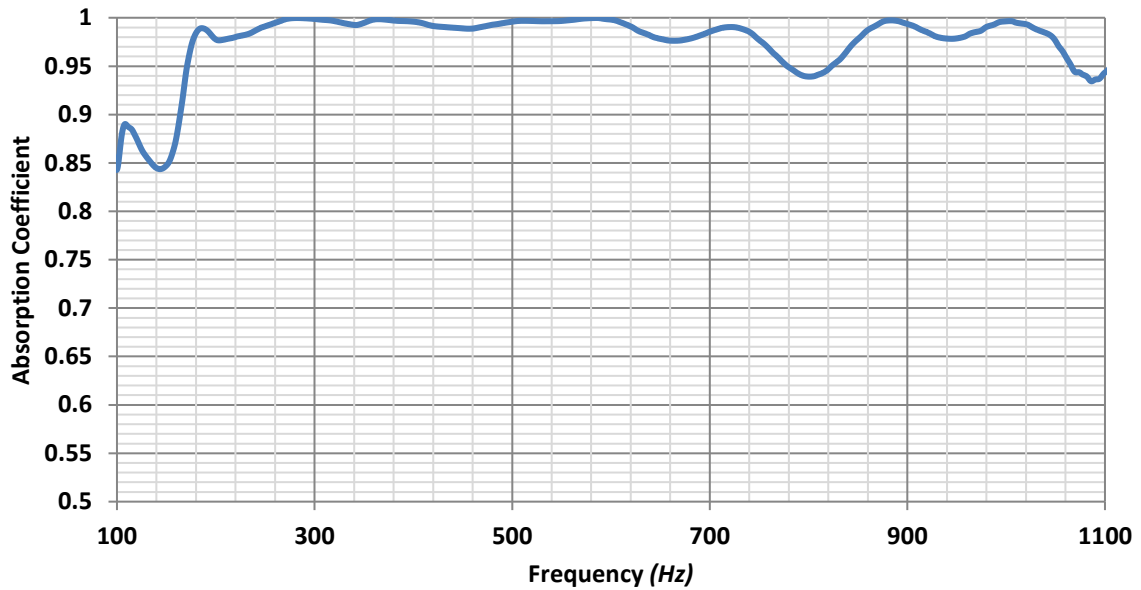
Figure 143 - Plot showing Absorption Coefficient of the Anechoic Termination

7.6.5   Grazing Flow

Following the previous evaluation of the acoustic excitation signal only, a 120dB RMS Multiband Filtered white noise signal is chosen to be the preferred baseline excitation signal, and therefore this signal will be used for the following grazing flow evaluation, and subsequent signal to noise ratio investigations.

From Figure 144 it can be seen that without the presence of grazing flow, the magnitude of the acoustic excitation seen upstream of the measurement section is consistent within the target measurement range, and produces an RMS excitation amplitude of 95dB in the frequency domain. It is noteworthy however that the true RMS acoustic pressure seen by the measurement section is 120dB, for the equivalent signal in the time domain. Unless stated otherwise, this signal will be the acoustic excitation source used for all successive measurements with and without flow.

It is important to consider the impact of grazing flow generated noise on this signal as for any given test condition the total excitation will be a sum of the acoustic signal, and any flow generated noise. The generated flow noise for the maximum grazing flow magnitude of 34m/s can be seen in Figure 144. Only the grazing flow generated noise for the maximum grazing flow condition for these tests (34m/s) is evaluated here, as the grazing flow generated noise is proportional to the grazing flow magnitude and hence this approach provides a worst-case scenario evaluation.
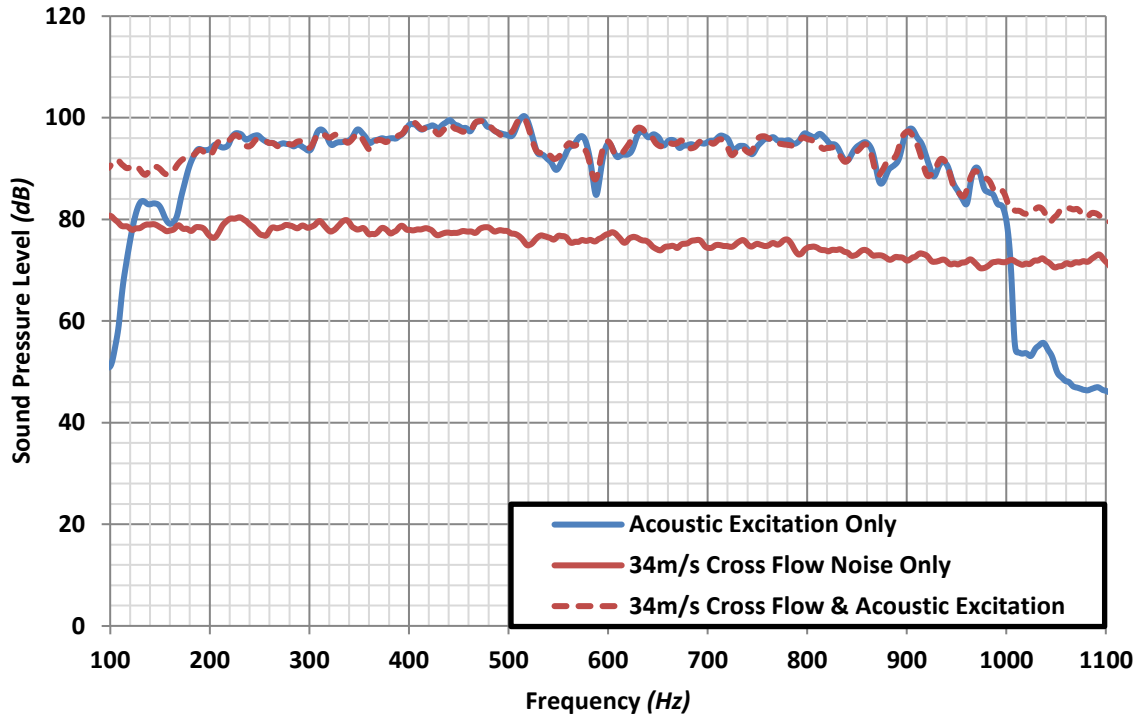
Figure 144 - Plot showing SPL across the measurement spectrum upstream of the blank section with; Acoustic Excitation only; with maximum grazing flow (34m/s) generated noise only and with acoustic excitation in the presence of maximum grazing flow.

From Figure 144 it is evident that the grazing flow generated noise is not of insignificant magnitude, and that unlike the white noise signal, it is not limited to within the measurement frequency range, nor can it be practicable filtered. Therefore, in the presence of high grazing flow, the assumption of only planar waves can no longer be exclusively applied, as ultimately the grazing flow will result in the existence of frequencies beyond the plane wave cut off frequency of the duct. With this in mind, it is imperative that the acoustic excitation signal is maintained at a sound pressure level above that of the grazing flow generated noise for all frequencies within the measurement range, so that it can be ensured that the plane wave acoustically driven frequencies are still the prominent excitation source of the resonators across all planned experimental test conditions.

7.6.6   Signal to Noise Ratio (Max grazing flow)

Figure 145 shows the signal to noise ratio *(SNR)* for the multiband white noise signal against the maximum grazing flow generated noise at 34m/s. The SNR has been calculated for each excitation signal amplitude, against the maximum grazing flow magnitude. From Figure 145 it is clear that the multiband white noise acoustic excitation signal, at the preferred 120dB RMS, is by and large, circa 15dB above the maximum flow generated noise from 200Hz - 1000Hz. As previously mentioned, given that this SNR is in relation to the maximum grazing flow magnitude, it can be assumed that this value will be larger for any lesser value of grazing flow magnitude. Furthermore, it can be appreciated that

if a higher SNR is required, then the amplitude of the signal can be increased to 124dB, resulting in a subsequent 4dB increase in SNR. These elevated sound pressure levels cannot however be maintained for prolonged periods of time, without the potential of damage to the measurement equipment. Conversely, the lower signal amplitudes can be easily maintained for prolonged periods of time however; it is evident that at reduced amplitudes the max grazing flow derived SNR is relatively low, albeit always positive within the measurement bandwidth; which subsequently erodes the assumption that the acoustic excitation signal is the primary source of driving dynamics for low SPL acoustic excitation, and high cross-flow scenarios.
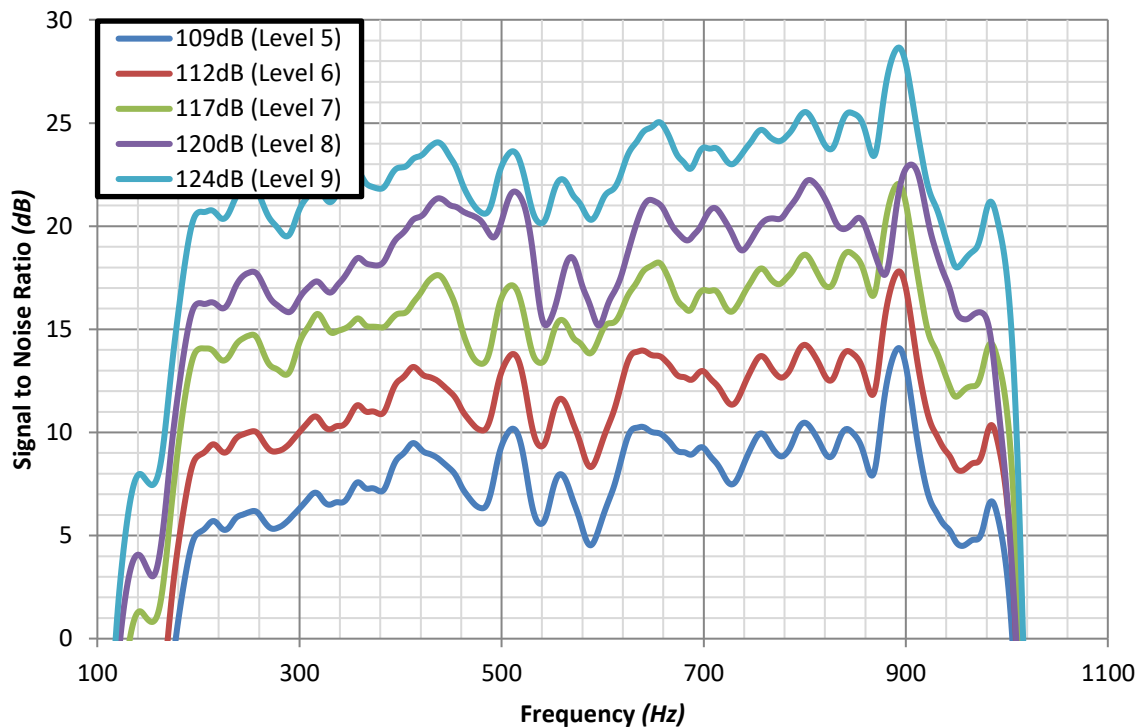
Figure 145 - Signal to Noise Ratio for various amplitudes of Multiband Filtered White Noise Acoustic Excitation, against maximum grazing flow induced noise (34m/s)

7.6.7 FRF Sensitivity to circumferential microphone location

The single hole case is a unique case detailed in Section 7.4.2, which uses test plate #13, with all holes apart from one covered. For the initial measurements of this case, all three in-plane, in-duct microphones have been used to derive three different FRF measurements. The results of this comparison can be seen in Figure 146, where it can be shown that across all three locations the peak absorption frequency differs by only 0.31Hz, whereas the magnitude of the attenuation decreases proportionally with increasing distance of the measurement location from the resonator. The truncated white noise signal was used in preference over the multiband filtered signal in this case; due to the fact that the single hole case has a much lower response frequency than the typical distributed resonator test cases; and as such the low frequency biased truncated signal is more effective at exciting

the expected response bandwidth of the resonator. The significance of this measurement is that, it confirms that with the truncated white noise signal being used, there are only planar waves being transmitted in the transmission line; which can be deduced due to the fact that the measured response does not vary significantly in the frequency domain, with varied location. The slight reduction in amplitude can be associated with inherent energy loss in the transmission of the signal from the resonator to the duct, with correspondingly increasing distance from the resonator. As such, unless otherwise stated, all future FRF metrics will be derived from the in-resonator microphone, and the nearest in-duct microphone *(A & B as shown in* Figure 146*).*
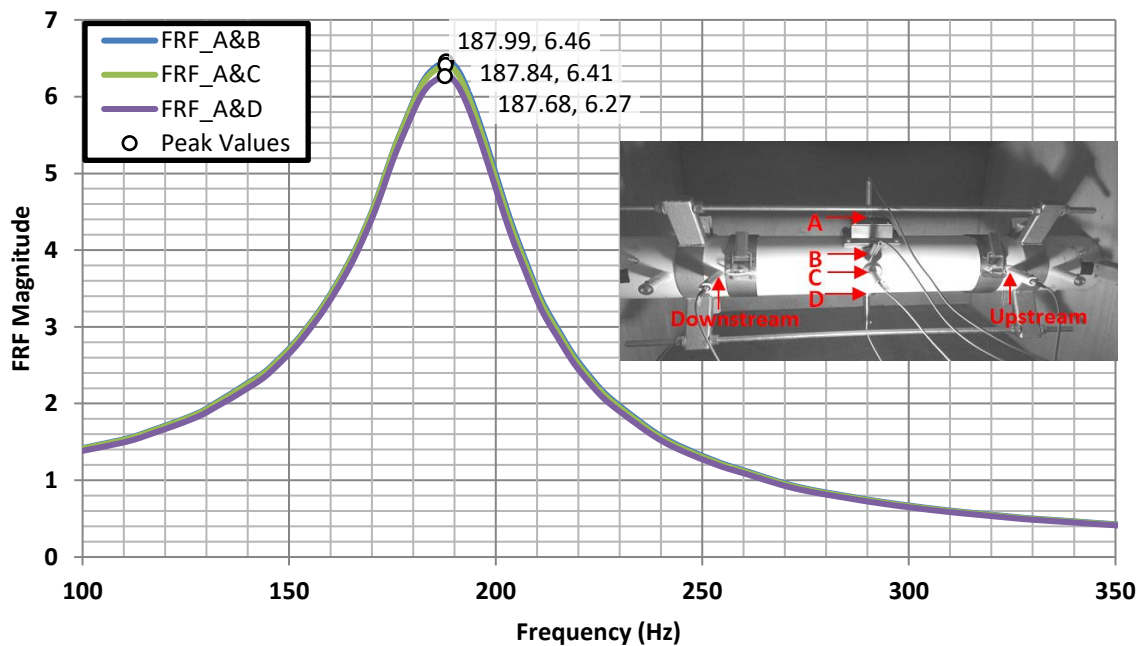
Figure 146 - Plot showing comparison of location varied FRF derivations for Plate #13, with a single hole, and a truncated acoustic white noise signal only

7.6.8   Bias Flow

As with the grazing flow, it is equally important to consider the impact of bias flow generated noise on the control acoustic excitation signal, for any given test condition. Similarly, the evaluation strategy is to analyse the maximum bias flow generated noise and assume that any lesser value of bias flow, would consequentially generate less noise. Conversely to the grazing flow however, for bias flow evaluation the blank tube cannot be used, as the distributed resonator test section is required to provide bias flow. The significance of this prerequisite is that subsequent bias flow induced noise evaluations will be resonator case specific, as will the number of holes, their diameter, and to a lesser extent, hole pattern; all of which are factors which define the bias flow characteristics, and the inevitable bias flow generated noise. In keeping with the evaluation strategy, and consideration of the values of bias mass flow rates shown in Table 34, a preferential test case can be rationalised regardless.

From Table 34 it can be seen that the Ø4mm inner neck plates, with the 20x Ø2mm outer neck plate specification can be expected to be of greatest significance, as it demonstrates the largest corresponding magnitudes of mass flow and neck velocity of all the distributed resonator test cases. As the inner plate hole pattern is expected to have little significance on the induced bias flow noise, Plate #13 is chosen for the subsequent evaluation; as it has the most conventional hole pattern, and a comparison can be made with initial qualification measurements in the absence of bias flow, which also used this common plate configuration.

The generated flow noise for the inner Plate #13, outer plate 20x Ø2mm case, with a 5%dP $(5.9\ g/s\,, U_O\ =\ 79.6m/s, U_i\ =\ 12.4\ m/s)$ can be seen in Figure 147. Similar to the previous grazing flow noise evaluation; the acoustic only SPL, the max flow noise SPL, and the combined max bias flow and acoustic excitation SPL, are all shown on Figure 147; thereby allowing a direct comparison across the measurement spectrum. As the distributed resonator test section is required for evaluation of the bias flow, the in-resonator and near-neck duct microphones can be also used in parallel with the two upstream and two downstream duct mounted microphones: allowing additional local SPL insight to be obtained.
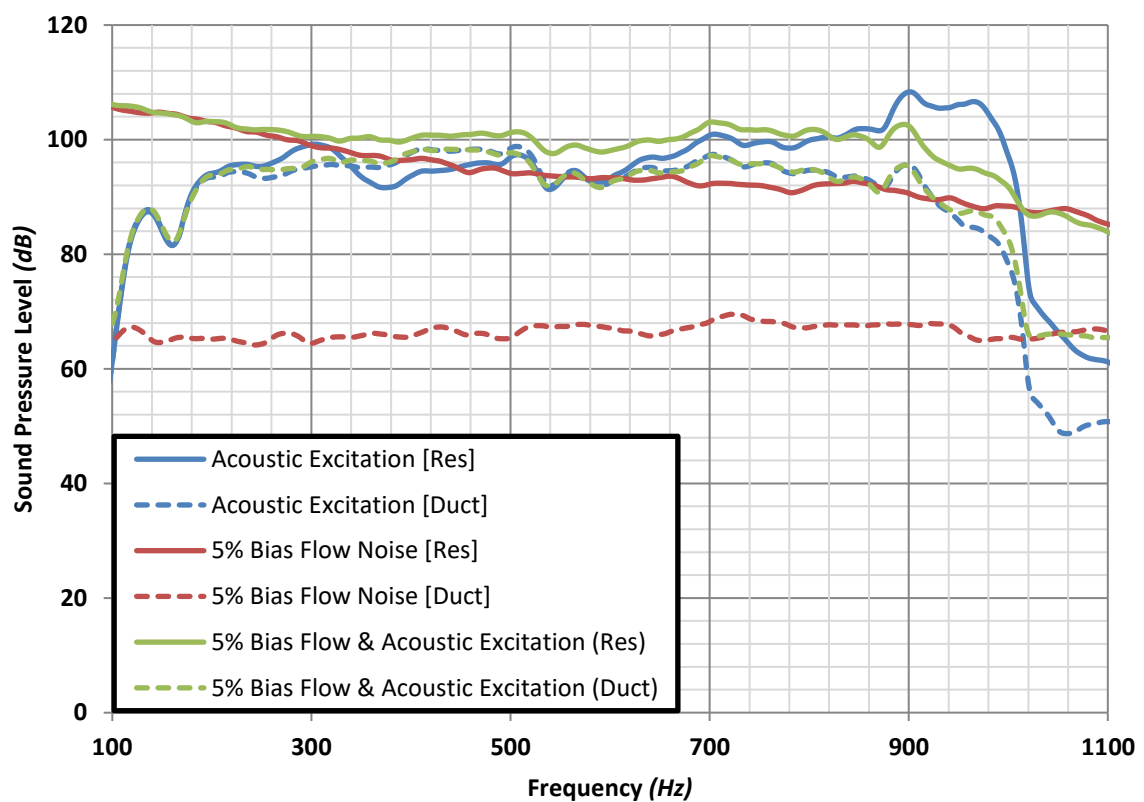
Figure 147 - Plot showing sound pressure level across the measurement spectrum for Plate #13- 20x 2mm Bias Flow holes, with; Acoustic Excitation only, with maximum bias flow (5% dP, 5.9 g/s, U_o =

79.6 m/s, U_i = 12.4 m/s) generated noise only and with acoustic excitation in the presence of maximum bias flow.

From Figure 147 it can be seen that the maximum magnitude of bias flow seen in the duct, is significantly lower than the control acoustic excitation amplitude. Inside the resonator however, the magnitude of bias flow noise is significant, and at the lower half of the measurement spectrum, is of greater amplitude than that of the acoustic excitation signal. As with the grazing flow, it can also be seen that when the bias flow is combined with the acoustic excitation signal, the flow generates noise at frequencies beyond the cut off points of the acoustic signal condition. Similarly, the significance of this is that when flow induced noise is present, there will be subsequent non-planar modes within the duct and resonator. As a result, the measurements collected in the presence of high flow magnitudes, will inevitably inherit measurement noise, due to the presence of higher order modes. It noteworthy that the requirement to use the distributed resonator test section to evaluate bias flow, will inevitably skew the magnitude of the in-resonator SPL measurements, as each specific case will exhibit a frequency dependant impedance to the transmission of acoustic excitation into the resonator cavity. For the initial evaluated case, the flow condition dependant resonant frequency is in the range of 800Hz-1,000Hz, which can be demonstrated by the difference between the duct and in-resonator SPL measurements, under acoustic excitation only.

7.6.9   Signal to Noise Ratio (Max Bias Flow)

The signal to noise ratio at each of the available measurement locations, corresponding to a 120dB Multiband Filtered White Noise acoustic excitation, and maximum 5%dP bias flow condition for Plate #13-20x2mm, can be seen in *Figure 148*. From this evaluation it is clear that at all the duct mounted microphone locations *(Including the near-neck location),* provide a suitably high signal to noise ratio, in the presence of maximum bias flow generate noise. Furthermore, the magnitude of the SNR can be seen to be larger than that of the maximum grazing flow induced noise at all frequencies, indicating the grazing flow generated noise is of greater significance than the bias flow. It is also however also evident from Figure 147 that, at the in-resonator measurement location, the magnitude of bias flow induced noise at the maximum flow condition, is of greater magnitude than the acoustic excitation signal. Consequently, this results in a negative SNR, which can be seen to occur at frequencies lower than 600Hz for this particular case. The significance of this condition is that; for distributed resonator bias flow measurements collected in this rig, it can be expected that the in-resonator FRF measurement may succumb to excess measurement noise; and as such the FRF metric could be compromised for high bias flow cases. Due to this observation, FRF will only be evaluated in parallel with duct derived metrics, where the SNR has been shown to be positive; therefore, any discrepancies or thresholds of effectiveness of the FRF metric, can be highlighted, and subsequently evaluated.

In conclusion, it can be shown that the delivery of bias flow through the resonator, has a lesser impact on duct-derived measurements, compared to flow induced noise resulting from a grazing flow; however, bias flow can be shown to have a significant impact on in-resonator acoustic pressure measurements. It is also important to consider that the in-resonator *(and to a lesser extent duct located)* measurements shown in Figure 147 & *Figure 148* are specific to the test case of Plate #13, with 20x2mm bias flow holes, and a 5% pressure drop across the resonator. It is however expected that this case will present the maximum bias flow induced noise, as it exhibits both the largest mass flow rate, and the largest neck velocities. As the chosen increment of bias flow delivery is percentage of total pressure drop, the neck velocities are similar across all cases, and only the mass flow varies significantly across hole diameter cases. All bias flow conditions can be seen in Table 34; and for common neck diameter cases, it is assumed that there will be negligible variation in bias flow properties, as a result of varied inner neck hole patters attributed to H-W & H-H investigations.
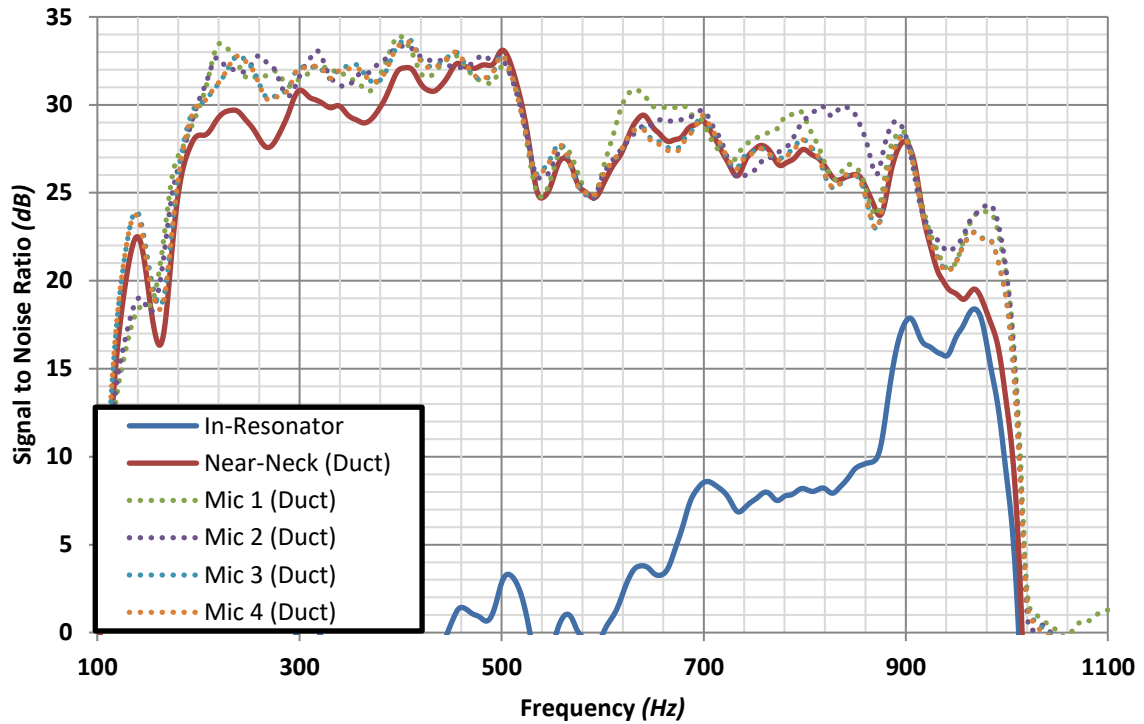
Figure 148 - SNR for 120dB Multiband Filtered White Noise Acoustic Excitation against maximum bias flow induced noise (5% dP, 5.9 g/s, U_o = 79.6 m/s, U_i = 12.4 m/s)

7.6.10 Microphone Calibration

Effective analysis from the measured data relies on accurate magnitude and phase information from all used measurement microphones. As such, an in-duct calibration method is applied; which provides accurate information about the relative magnitude and phase over the entirety of measurement spectrum. The applied method is based on the simple fact that effective measurement microphones should consistently measure identical responses in terms of both pressure magnitude and phase; if

placed at the same location, under same conditions, and exposed to the same excitation signal. In reality, however, no microphone is perfect, and as such groups of microphones are rarely unified in their measured response in real world scenarios. Consequently, it is necessary to calibrate most measurement microphones before any actual measurement takes place. The outcome from such a calibration exercise is a pair of spectral correction coefficients for both magnitude and phase for each microphone, relative to one reference microphone. Ideally frequency dependant correction factors should be obtained for the full measurement spectrum of interest, so that any frequency dependent behaviour is accounted for in the calibration. The obtained correction factors should then be applied to measured data prior to analysis.

Figure 149 shows the procedure for calibration of the four in-duct microphones used in this distributed resonator test rig; where the four microphones are joined together with their measurement surfaces aligned on a common plane and located on the axial centreline of the duct. During calibration the measurement section is removed, and a retort stand is used to project the microphones as far upstream of the open section as practically possible. If all four microphones are cohesive, these four microphones should capture same magnitude and phase information of the common incident signal.
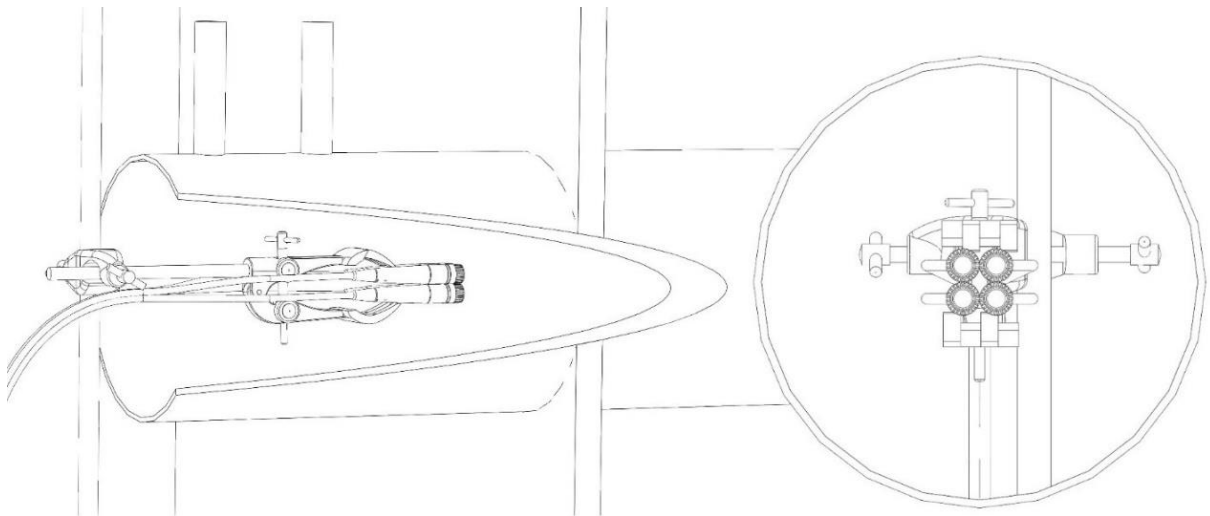
Figure 149 - Four duct microphones aligned and located at the centreline of duct, as arranged for calibration

As shown in Figure 150 & Figure 151 however, it is evident that these four microphones yield notably different responses in both magnitude and phase. From these figures it is also evident that there is frequency dependent sensitivity inherent in the measurement system, demonstrated by the spectral deviation of the transfer function from the optimal value of 1 for the magnitude, and 0 for the phase. It is these measured differences than can then be used to individually calibrate each microphone. Therefore, when these microphones are subsequently used to measure resonator performance, their

measured response can be confidently accounted to the physical properties of the experiment only and assured to be independent of any subtle differences in microphone response.
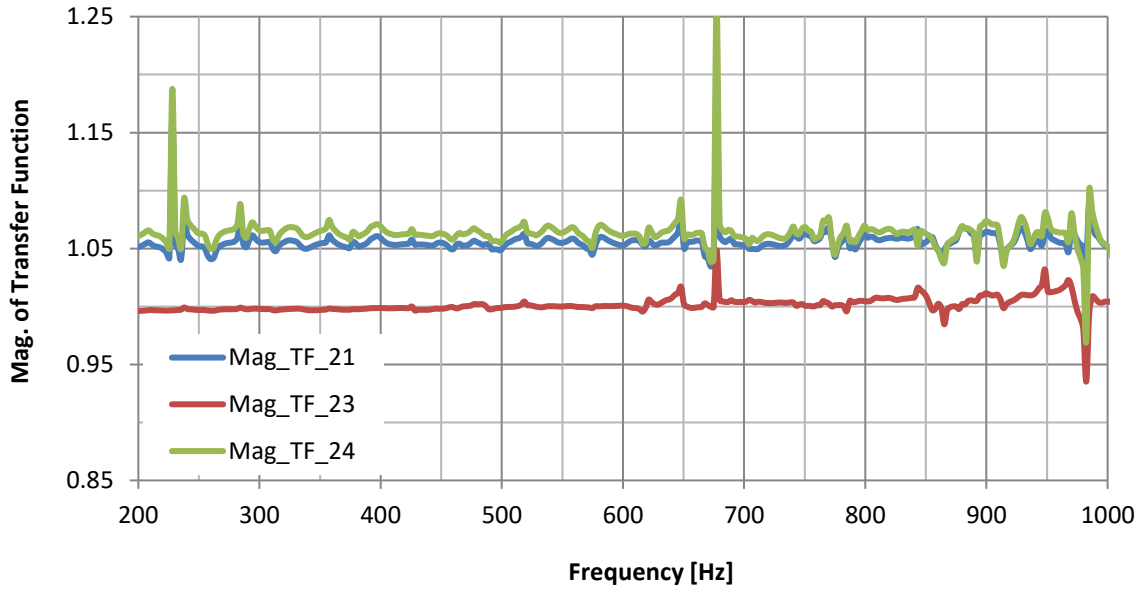
Figure 150 - Magnitude of Transfer Functions of Duct Microphones, using Microphone 2 as reference
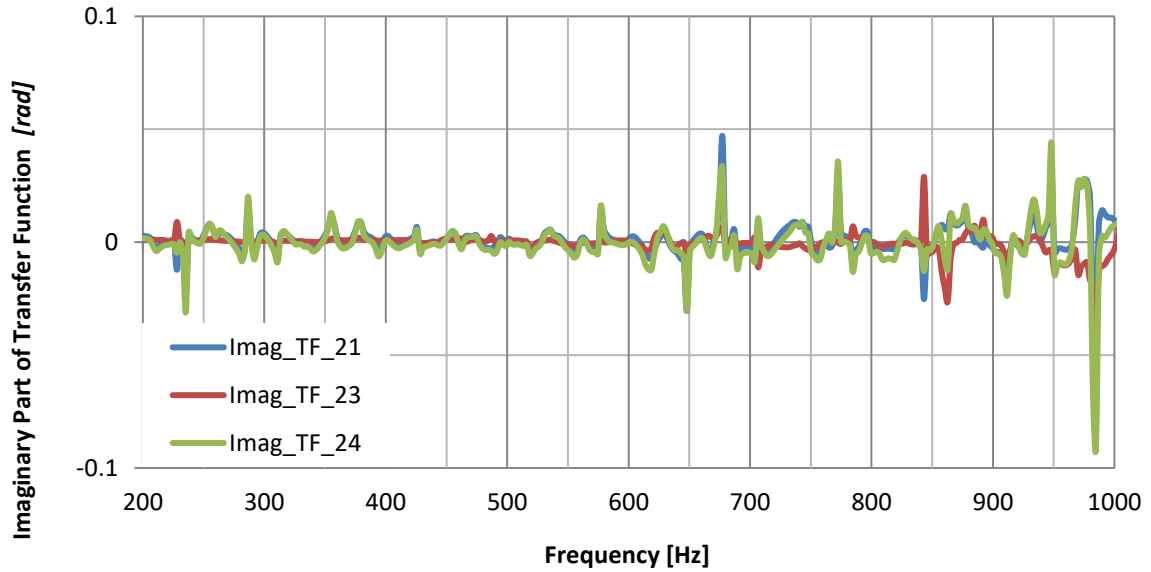
Figure 151 - Imaginary part of Transfer Functions of Duct Microphones, using Microphone 2 as reference

The numeric identifier applied to each microphone corresponds to its location within the duct, as installed for typical distributed resonator measurements, where Mic. 1 is the most upstream location, and each increasing integer corresponds to the next downstream location, with Mic. 4 being the most downstream location. It can be seen from Figure 150, that Mic. 1 and Mic. 4 tend to measure a relatively higher-pressure fluctuation amplitude compared to Mic. 2 and Mic. 3. From Figure 151 it can be seen that the phase difference, however, is more consistent between all microphones. Thus, the

transfer functions of the other three duct microphones are computed as described in Equation [173], using Mic. 2 as reference; and are subsequently applied to correct the magnitude and phase information of the corresponding microphones.

$$\text{TF}_{21} = \frac{p'_1}{p'_2} \ ; \ \text{TF}_{23} = \frac{p'_3}{p'_2} \ ; \ \text{TF}_{24} = \frac{p'_4}{p'_2} \qquad\qquad [173]$$

Where: p' is the Finite Fourier Transform of each microphone's measured acoustic pressure.

Subsequent to the application of the computed calibration coefficients according to Equation [173], the corresponding magnitude of the transfer functions for all duct microphones equates to unity, and the phase as zero respectively; when comparing measurements to the equivalent acoustic signal, and location, as per Figure 149. Therefore, it can be concluded that, after effective calibration of all duct microphones, if placed at the same location and exposed to the same conditions, it can be assured that they will all return identical pressure response across the relevant measurement spectrum. Hence any inherent inconsistency between measured microphone responses can be effectively eliminated from subsequent analysis.

7.6.11 Microphone Coherence

As discussed in Section 2.4.1.3, the pressure fluctuations measured by the microphones in the presence of cross-flow, are a superposition of the acoustic excitation signal induced sound pressure, and flow induced turbulent pressure fluctuations. Section 7.6.6 details how a concerted effort has been made to ensure a high signal to noise ratio is achieved experimentally, prior to subsequent measurements; therefore, it can be expected that the signal coherence between different microphone should be acceptable. Irrespective, it is still good practice to quantify this coherence, and to improve it as much as is practicable.

The coherence between any two signals is calculated from the auto-spectral and cross-spectral densities according to Equation [71]; whereby a calculated coherence value of unity indicates a perfect coherence between two microphones, and thus it can be concluded that both microphones are exposed to identical signals. Conversely, a low value of coherence is an indicator that flow induced noise, or other factors, are resulting in a poor cohesion between the measured pressure response captured by two microphones. The value of coherence is particularly important when utilising the two-microphone method to deduce a decomposed signal, as this method assumes that both microphones are responding to a common, in-phase signal. Figure 152 shows the calculated coherence for the four in-duct microphones, measured with a blank tube fitted in the measurement section, under acoustic

excitation only, and from this plot it can be seen that the coherence between microphones is almost perfect across the measurement range of 200-1000Hz.
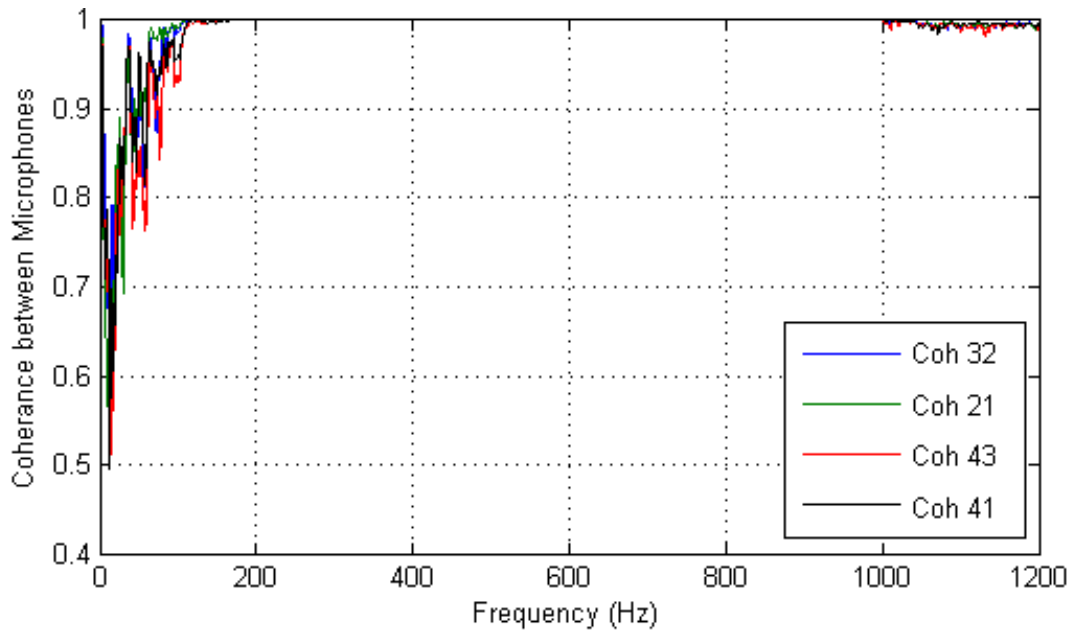
Figure 152 - Microphone Coherence for in-duct microphones, measured with blank tube (no resonator), under acoustic excitation only

Above and below these frequencies however, it can be seen that the coherence decreases, which can be attributed to the lack of acoustic excitation signal existing at these frequencies, which in turn results in a low signal to noise ratio at these frequencies.

Coherence is more significant in the presence of cross-flow however, as the flow induced noise more stochastic than the carefully filtered and truncated acoustic excitation signal. The significance of cross-flow magnitude can be seen in Figure 153, where the same measurement is repeated in the presence of the maximum cross-flow magnitude of 34m/s. As shown in Section 7.6.6, the cross-flow magnitude decreases the signal to noise ratio, and thus increases the measurement noise and subsequent error, which can be attributed to the observed notable decrease in microphone coherence.
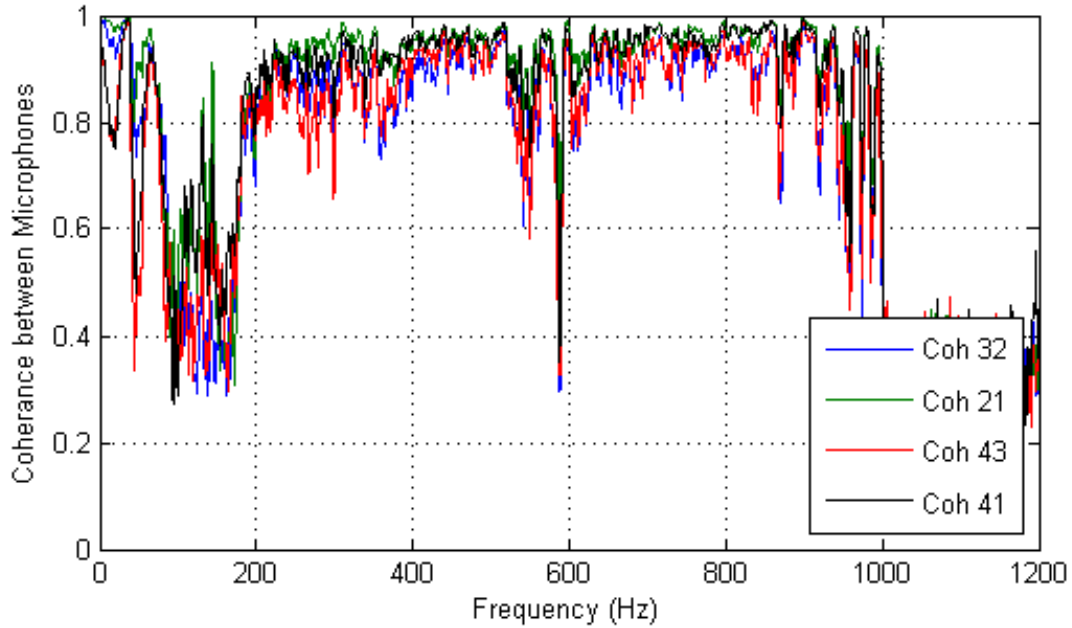
Figure 153 - Microphone Coherence for in-duct microphones, measured with blank tube (no resonator), under acoustic excitation and 34m/s cross-flow

Irrespectively, this non-coherent signal information can be removed from the measured signal prior to processing any performance metrics, as detailed in Section 2.4.1.3. Implementation of this rejection of flow noise strategy has been shown to be wholly effective at removing the non-coherent signals; whereby the application of Equation [72] results in a perfect measurement noise-free value of unity for each of the measurement microphone locations. Equation [72] results in a real valued auto spectrum however, and hence Equation [73] is applied to all subsequently processed acoustic measurement data included in this report; which adds the necessary phase information, and thereby permits subsequent plane wave decomposition according to Section 2.4.2.3. Implementation of this rejection of flow noise strategy ensures the best possible accuracy of subsequent acoustic attenuation performance evaluations under high cross-flow conditions.

7.7 Distributed Resonator Experimental Methodology Summary

Within the previous chapter a systematic experimental design methodology is applied to facilitate the development of a robust experimental regime, which is focused on gaining novel insight into fundamental distributed acoustic resonator noise attenuation characteristics; and specifically addresses the experimental objectives outlined in Section 7.1. Following a comprehensive explanation of the target investigation strategy in Section 7.2, the necessary tools and techniques required to permit effective experimental evaluation, the resultant parameters, permutations, and measurement methodologies are rationalised, and optimised.

A systematic approach is taken to design a bespoke distributed aperture test methodology which is outlined in Section 7.3, and the ensuing test matrix detailed in Section 7.4 consists of a bespoke experimental distributed test resonator with: a single fixed cavity volume; a total of 36 inner plate variations, consisting of 3 different neck diameters, each of which with 12 unique hole patterns, optimised for H-W & H-H investigations; 5 targeted grazing flow conditions, ranging from 12-34m/s; 4 outer plate variations, which permit 6 different bias flow test scenarios, ranging from 0-5% pressure drop across the resonator. Which in summary, provides a baseline test matrix with 36 geometrical variations, and 42 unique flow permutations, resulting in a total of 1,512 permissible individual experimental test permutations. The measurement strategy intended to efficiently extract the maximum insight from this systematically designed distributed resonator test matrix is detailed in Section 7.5.

Comprehensive qualification investigations are conducted and deliberated in Section 7.6 using the intended experimental methodology; which serves as a validation of the targeted design and implementation strategies; and provides additional insight into the salient characteristics of the measurement apparatus and methods. The conclusions drawn from the closing qualification exercises, serve to set the scene for an effective and rigorous evaluation of collected experimental results in the following results chapter, and the subsequent characterisation of key noise attenuation performance factors, corresponding to distributed resonators under a wide range of practical design and environmental considerations.

The breadth and depth of systematic design deployed in the realisation of the planned experimental methodologies, ensures that the subsequent results presented for evaluation, are; as academically rigorous as experimentally practicable; are presented with an innate understanding of the inherent characteristics experimental methodologies employed; and are strategically focused on adding value to the current state of the art in relation to the attenuation performance of distributed acoustic resonators.

CHAPTER 8 - RESULTS: DISTRIBUTED RESONATORS

In this chapter the experimental results obtained from the aforementioned experimental design methodology of CHAPTER 7 - EXPERIMENTAL METHODOLOGY: DISTRIBUTED RESONATORS will be presented, discussed, and evaluated; relative to coherence with the current state of the art of known acoustic resonator attenuation performance factors; and further novel insight gained from the targeted experimental investigations.

Unlike CHAPTER 5 - RESULTS & DISCUSSION: DISCRETE RESONATORS, within which FRF magnitude and phase was the sole performance metric utilised to determine attenuation performance; this chapter will call upon the full range of acoustic attenuation performance criteria detailed in section 2.4.2 for subsequent evaluation; ensuring that duct derived performance metrics supplement the local resonator dynamics observed, with an additional insight into upstream and downstream dynamics, impacted by the nuances of the respective attenuation performance factors investigated experimentally.

Whilst all possible test case permutations have been measured and archived as part of the study, only the representative cases, as specified in the measurement strategy of Section 7.5 will be presented for brevity. The sequence of presentation of key findings also following this aforementioned experimental strategy whereby: Section 8.1 evaluates the observed saturation effects resulting from elevated sound pressure level; Section 8.2 presents the findings from neck length verses diameter factors (L/D); Section 8.3 evaluates H-W & H-H factors; Section 8.4 details grazing flow factors; Section 8.5 outlines bias flow factors; Section 8.6 investigates combined flow factors; and Section 8.7 makes comparison with modelling predictions. This chapter concludes with a summary of all observed distributed resonator attenuation performance factors in Section 8.8, which serves as a preamble for the subsequent, and final CHAPTER 9 - CONCLUSIONS.

8.1 Saturation Effects by Sound Pressure Level

As discussed in Section 7.6.4, the acoustic excitation signal used for the full distributed resonator test matrix, should be a best compromise between signal to noise ratio and the onset of saturation factors. Therefore, in order to conclude the optimal signal amplitude, it is necessary to first investigate any potential saturation factors that will be inherent in the use of the chosen signal amplitude. The significance and properties of excess sound pressure saturation can be evaluated by first looking at a single hole case, as due to its inefficient design it is more probable to exhibit an earlier onset of saturation. Subsequently the available acoustic signal levels can be evaluated for representative cases

from the distributed resonator test matrix, allowing the best compromise case to be defined for subsequent measurements.

8.1.1   Single Hole Saturation

The special single hole introduced in Section 7.4.2 serves as a bassline case for subsequent CFD investigations (outside of the scope of this study), as it negates the need to have a fully resolved and complex computational mesh, physically representing all the holes of a typical distributed resonator case. This case is of little practical significance however, as it can be shown to be very inefficient, due primarily to the relatively large cavity size in relation to the neck area. Irrespectively, as it is essentially a discrete resonator case, it effectively mitigates the significance of potential H-H & H-W factors, and as such is a good basis for an initial independent investigation of saturation factors.

Due to the fact that the single hole case results in a peak attenuation frequency lower than the low frequency cut off point of the multiband filtered white noise signal, an alternative sine sweep signal has been used to excite the following cases. This signal was not filtered or calibrated to the same extent as the white noise signal intended for the full distributed resonator test matrix, as it is only for use on these specific cases. However, as the sine sweep only includes frequencies from 100Hz-400Hz, it can still be ensured that there are only plane waves present in all cases shown for analysis.

Given that the targeted distributed resonator test matrix acoustic excitation signal amplitude is defined by primarily optimal SNR; it is pertinent to investigate the effects of possible excitation sound pressure level induced saturation on the single hole case initially. In Figure 154 it can be seen that across the four SPL cases investigated, increasing the excitation signal amplitude simultaneously reduces the FRF magnitude, and shifts the peak resonance value to higher frequencies; where the magnitude of each excitation signal corresponds with the RMS acoustic pressure in the time domain. It is evident that for this single hole case, a reduction in attenuation magnitude, and shift in frequency can be seen for excitation amplitudes comparable with that of the standard multiband filtered white noise signal applied to the full distributed resonator test matrix. It is important to recall however, that this single hole resonator design is inherently inefficient; as it uses the same cavity volume as is intended for the corresponding distributed aperture test cases; and consequently, it should not be deduced that an equivalent result will be expected for the fully open distributed cases, when exposed to a corresponding amplitude of acoustic excitation.

The implication of this inefficient design, i.e. disproportionally large cavity to open hole area; is that it will be prone to the onset of saturation factors much earlier than a more proficient design, such as the standard distributed resonator test cases. This perceived design detriment does however have the

added benefit of being able to increase sensitivity to saturation factors, permitting investigation at a much lower excitation amplitude than what would be necessary to demonstrate similar results with an equivalent distributed resonator test case.
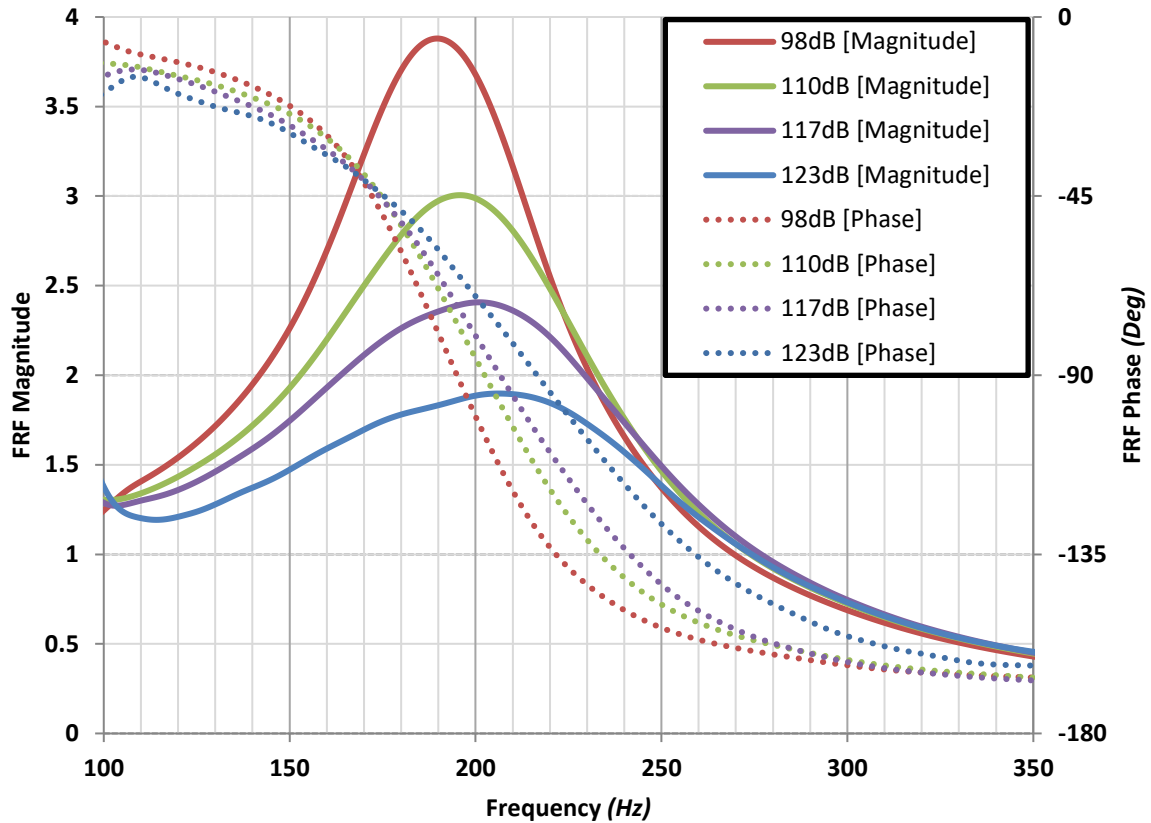
Figure 154 - Plot showing frequency response magnitude and phase for the single hole case with varying acoustic signal excitation magnitude, using a sine sweep signal, without grazing/bias flow.

As the frequency response function is only an indicator or resonator dynamics and does not wholly allow the quantification of any resultant attenuation in the duct acoustics, it is valuable to also evaluate the effects of signal excitation on the single hole case using a duct-derived performance metric.

In Figure 155 the effect of signal excitation amplitude on the resultant transmission loss of the single hole case can be seen. From this plot it is evident that the transmission loss agrees with the frequency response function, in that it can be clearly seen that with an increase in the excitation signal amplitude, the peak attenuation both decreases in magnitude, and shifts towards higher frequencies. It is also noteworthy that, even at the relatively low excitation amplitude there is still only circa 0.8dB of peak attenuation.

Previous measurements have been carried out with this single hole case in the presence of both cross-flow and bias flow, and in both cases the measured transmission loss was negligible; which with this

insight, can be attributed to the fact that the amplitude of attenuation for this case is very low, relative to the duct size, and distance between upstream and downstream microphones.
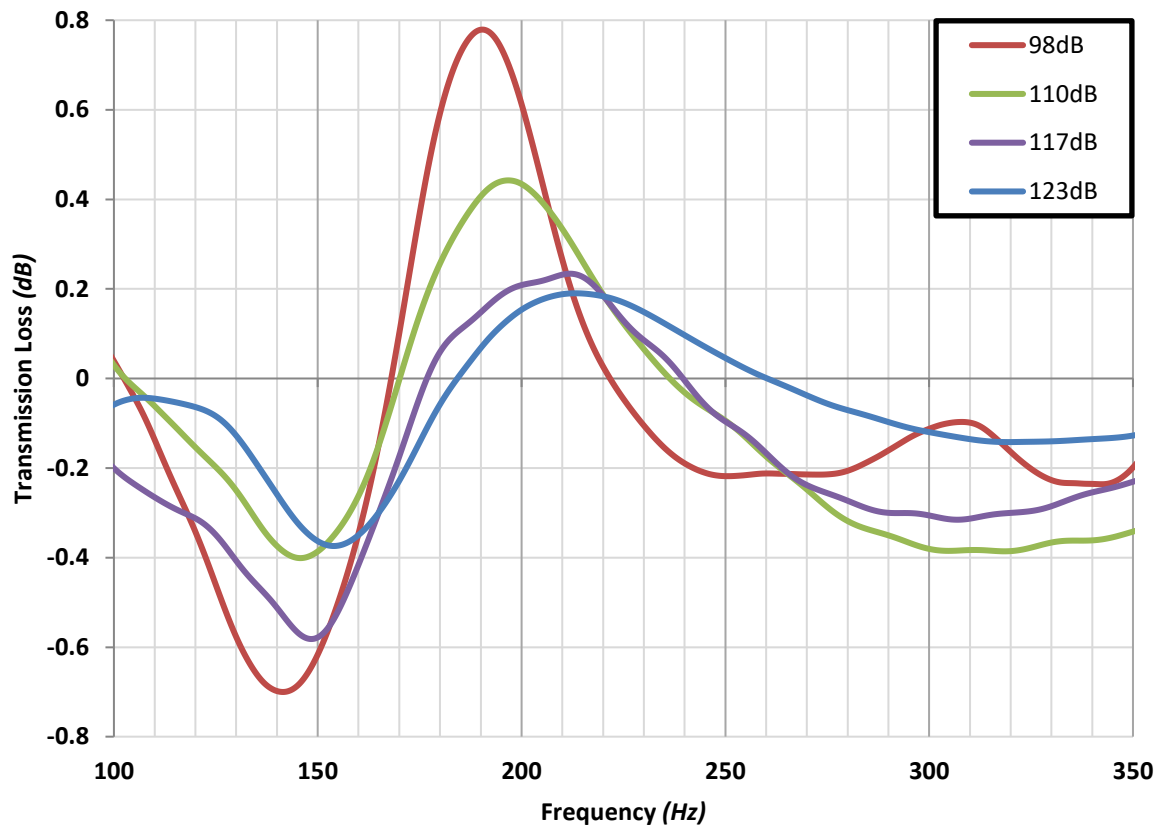
Figure 155 - Plot showing transmission loss for the single hole case, with varying acoustic signal excitation magnitude, using a sine sweep signal, without grazing/bias flow.

8.1.2 Representative Distributed Resonator Test Matrix Saturation

The previously presented results from the single hole case, showed prominent saturation as a direct result of acoustic excitation amplitude. As the primary purpose of the distributed resonator test matrix is to investigate H-W & H-H and combined flow factors, it is necessary to ensure that excitation signal induced saturation is not significant across these test matrix cases. The strategy to investigate potential saturation across the distributed resonator test matrix is to evaluate the measured response from six representative cases; consisting of each of the available hole diameters, and the two extremes of hole spacing; for each of the available excitation amplitudes. For each case, the resonator was in closed configuration with zero grazing flow, so that any measured properties are purely as a result of the acoustic excitation signal amplitude.

Figure 156 shows the measured frequency response function for Plates #01, #13 & #25; from this plot it can be seen that, as with the single hole, an increase in excitation sound pressure level can be seen to reduce the peak FRF magnitude. It is noteworthy however, that the magnitude of decrease is

significantly less prominent than it was with the single hole case, furthermore the shift in frequency is almost negligible for most measured cases.
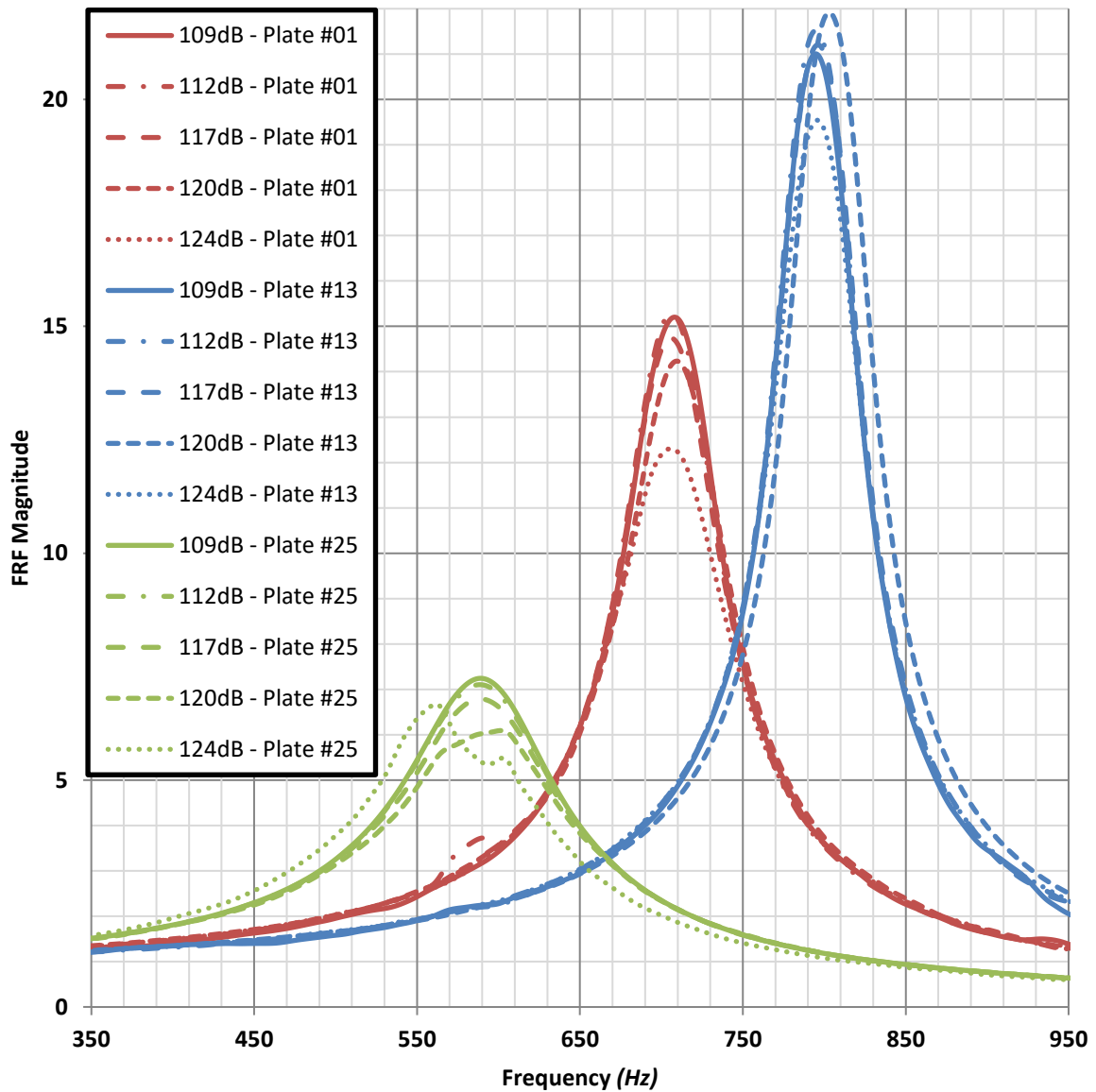
Figure 156 - FRF Magnitude for Plates #01,13 & 25; closed configuration, varying multiband filtered white noise acoustic excitation signal amplitude, and zero grazing flow

Similar to the previous single hole investigation, it is important to evaluate a duct derived quantitative performance metric alongside the FRF. It is necessary to evaluate duct derived performance metrics in order to have confidence that the witnessed trends indicated by the FRF, result in corresponding measurable responses in the duct and also to quantify the magnitude of attenuation for each case. As shown in Figure 157, the incident transmission loss for each case, shows good coherence with the FRF magnitude shown in Figure 156.
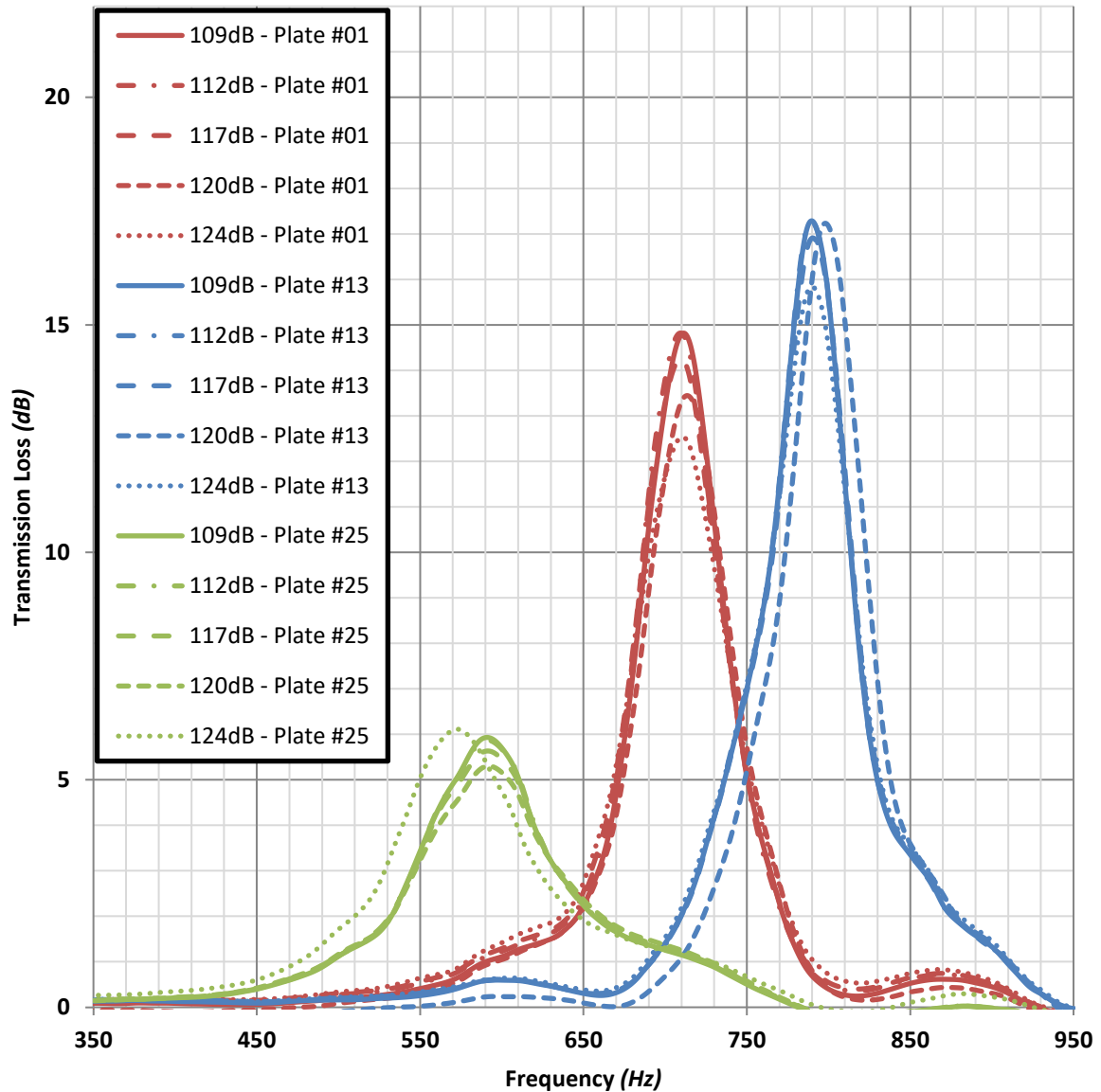
Figure 157 - Incident Transmission Loss for Plates #01,13 & 25; closed configuration, varying multiband filtered white noise acoustic excitation signal amplitude, and zero grazing flow

The FRF plot shown in *Figure 158* corresponds to the most tightly packed *(Max H-H)* case, for each of the three neck diameters, under all measured acoustic excitation signal amplitudes. These cases exhibit similar trends to those shown for the equivalent least tightly packed hole pattern *(Min H-H)*. It is however noteworthy that, for each measured case, the resultant peak attenuation frequency is significantly lower than the equivalent hole pattern and excitation amplitude, as a result of the exacerbated H-W & H-H factors. It can also be seen that the measured FRF magnitude varies between the two extreme hole patterns and neck diameters.
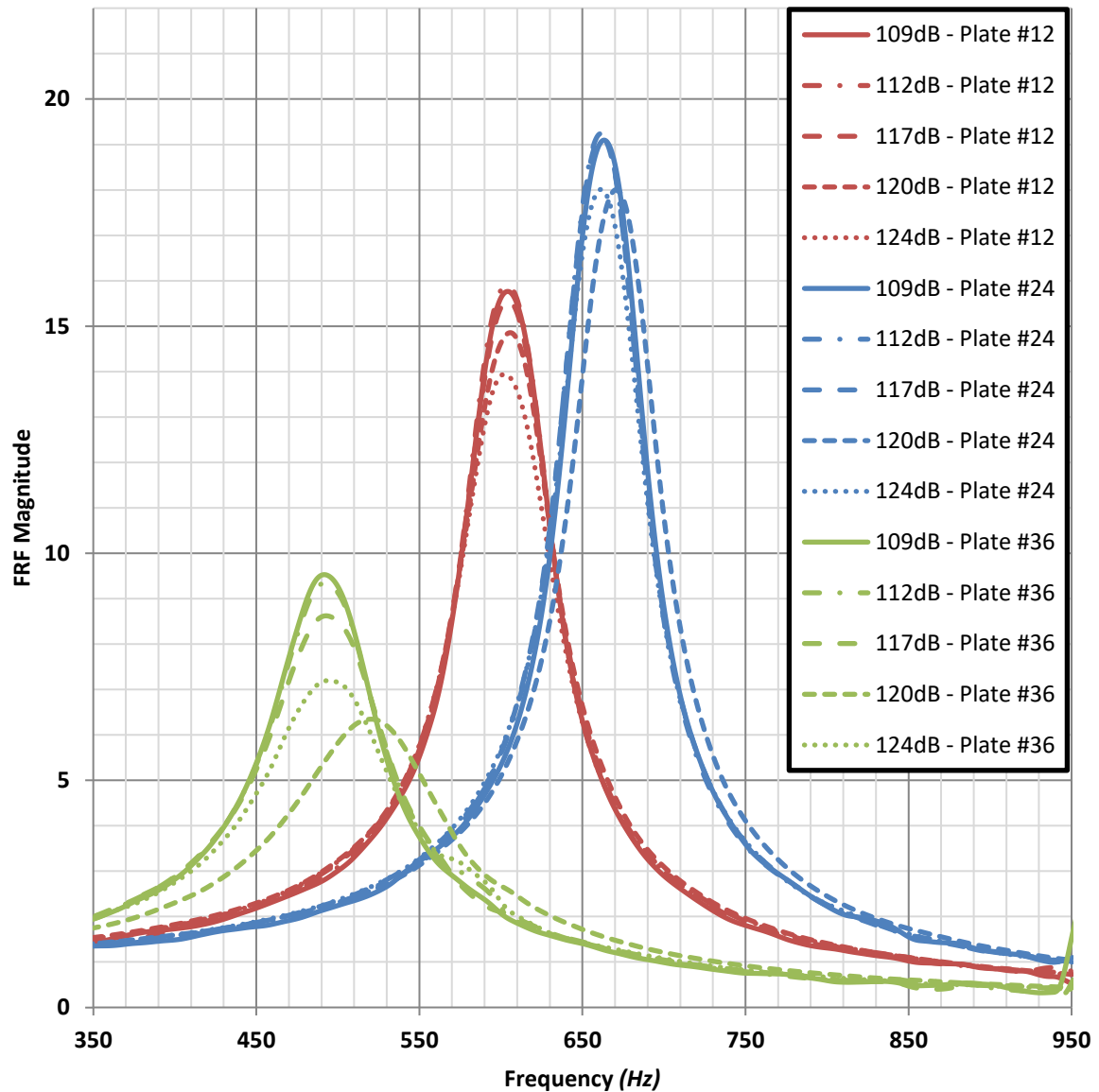
Figure 158 - FRF Magnitude for Plates #12,24 & 36; closed configuration, varying multiband filtered white noise acoustic excitation signal amplitude, and zero grazing flow

For the largest hole diameter *(4mm)* with the corresponding highest response dynamics frequency, it can be seen that a generally larger FRF magnitude is witnessed with the least densely packed cased (Plate #13), compared to most densely packed case (Plate #24). The impact of SPL across these hole pattern variations (Plate #13 & Plate #24) are however comparable. Conversely, for the smallest neck diameter *(2mm)* and the consequently lowest response dynamics frequency; the more densely packed case (Plate #36) can be seen to exhibit a stronger response magnitude. It is noteworthy however, that although an increase in magnitude can be seen in Plate #36, compared to Plate #25, so too can an increase in sensitivity to SPL induced saturation. This can be demonstrated by a comparably greater variation in measured frequency response, across the considered sound pressure levels shown for Plate #36 *(Max H-H),* compared to Plate #25 *(Min H-H)*, where the effect of SPL variation can be seen to be less significant.

As with the previous cases, the measured FRF responses shown in *Figure 158*, also shows good coherence with the corresponding measurements of Incident Transmission Loss for the equivalent cases, shown in *Figure 159*.
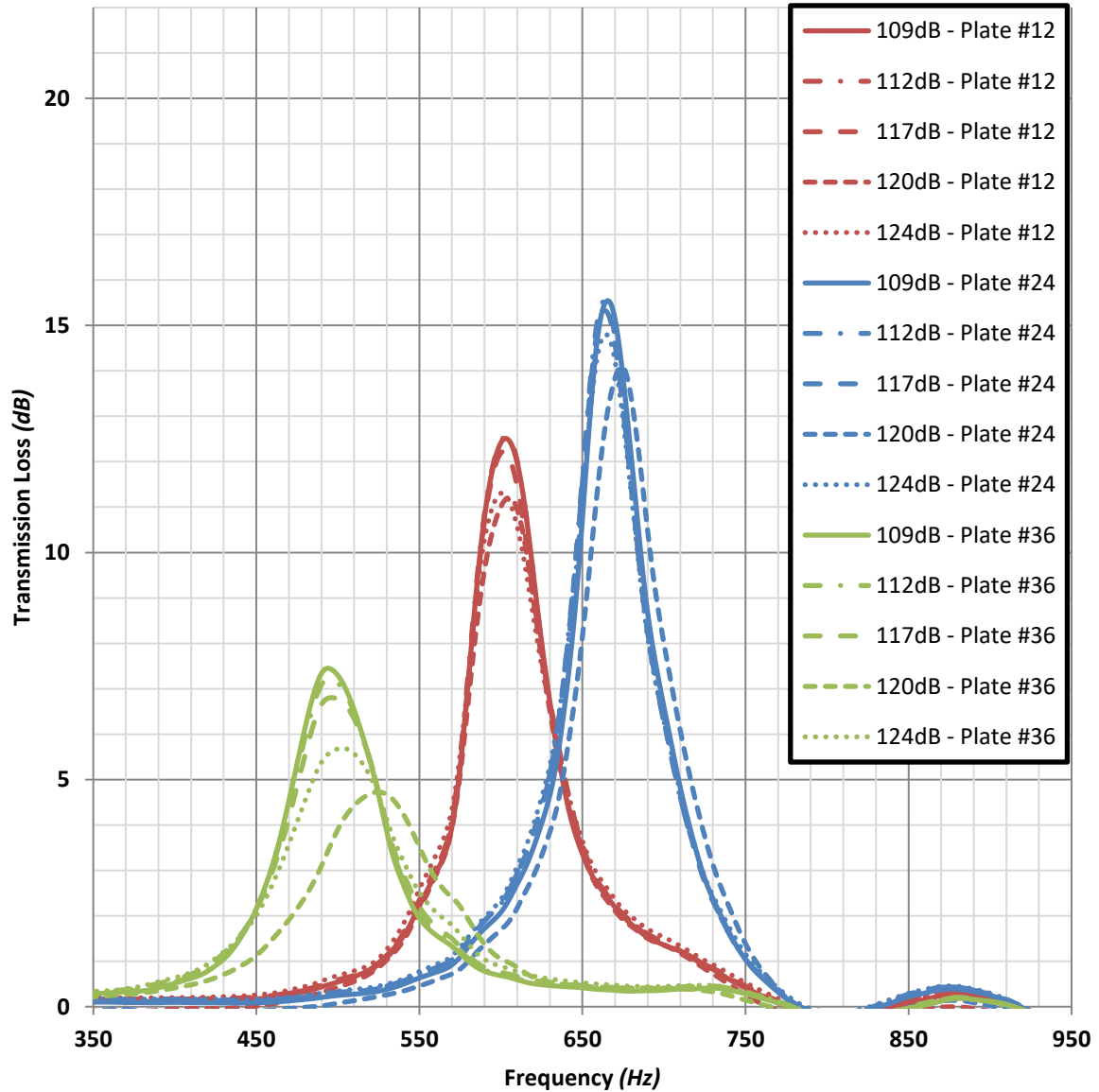
Figure 159 - Incident Transmission Loss for Plates #12,24 & 36; closed configuration, varying multiband filtered white noise acoustic excitation signal amplitude, and zero grazing flow

It can therefore be shown from these representative test case results that; when the acoustic excitation sound pressure level is of sufficient magnitude, a clear saturation of the distributed resonator can be demonstrated. Furthermore, it can be established that during the onset of any such SPL induced saturation, a subsequent increase in peak attenuation frequency and corresponding decrease in attenuation magnitude can be expected.

By evaluating SPL saturation effects on representative distributed resonator test matrix cases, it can also be confirmed that some non-linear behaviour across the test matrix may occur, if too large an acoustic excitation amplitude is used. The maximum level tested of 124dB will naturally give the best SNR value however, as any non-linear SPL factors would be detrimental to the effective independent evaluation of any H-W & H-H or flow factors, it is necessary to use a lower value than this for subsequent experimental evaluations. As such, it can be concluded that the acoustic excitation signal level of 120dB is the preferential choice for all subsequent distributed resonator measurements *(Unless otherwise specified);* as it demonstrates the best compromise between maintaining a high SNR, whilst mitigating the potential onset of high SPL resultant saturation effects.

8.2 Neck Length versus Diameter Factors (L/D)

Whilst it is of interest to experimentally investigate the significance of the relationship between neck length and diameter for the available cases; as all available inner test plates are of 2mm thickness; only three L/D ratios can be currently investigated. Irrespectively, three cases are still sufficient to indicate a trend if carefully evaluated under controlled conditions. The proposed strategy to assessing L/D significance is initiated by measuring the response of three standard representative distributed resonator cases *(Closed resonator configuration and under acoustic excitation only);* for which the measured variation in FRF magnitude and frequency resulting from varying neck diameter can be evaluated, as shown in Figure 160.
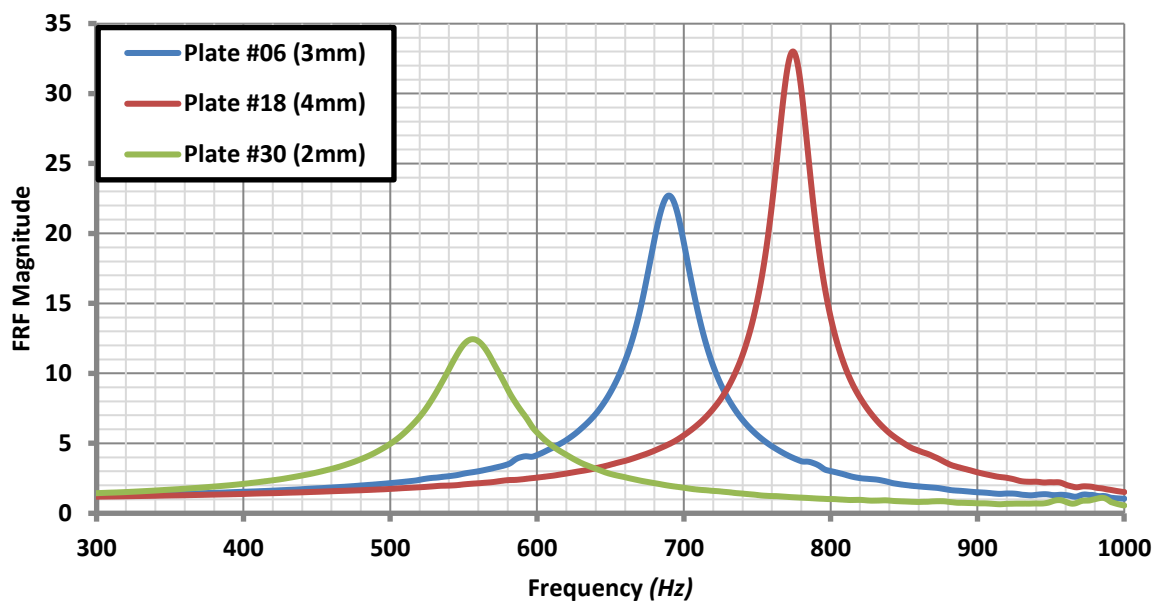
Figure 160 - Plot showing measured FRF for plates #06 (3mm), plate #18 (4mm) and plate #30 (2mm), under acoustic excitation only

The subsequent step in investigating the isolated effect of L/D on the resultant attenuation, is to fix the resonant frequency of each case; and in order to modify the resonant frequency, without modifying the inner plate properties, the resonator cavity volume is varied. As the distributed test resonator cavity cannot be increased in size, the applied experimental approach is to decrease the cavity volume by inserting a filler material, as shown in Figure 161. Because Plate #18 demonstrated the highest resonant frequency in Figure 160, it's value of 774Hz will be chosen as the target and for the Plate #06 and Plate #30 cases, the cavity volume will be decreased as shown in Figure 161. In order to know what volume of filler material is required, the analytical methods described in Section 7.2.3 were used to calculate the theoretical cavity volume which corresponds with the target dynamics frequency; then the required volume of filler material was measured using the jig shown in Figure 161. After measuring the initial response experimentally, an average of six corrective iterations were required before the desired cavity volume could be arrived at via measurement: making this a rather inefficient method of volume variation for a large data set. Furthermore, it should be noted that over time, the filler material dehydrates, and as a result its volume varies; meaning that there is a time-limited opportunity for repeatable measurements. Regardless this method still provides an effective pragmatic insight into volume effects, without the need to manufacture new bespoke components for the existing measurement rig.
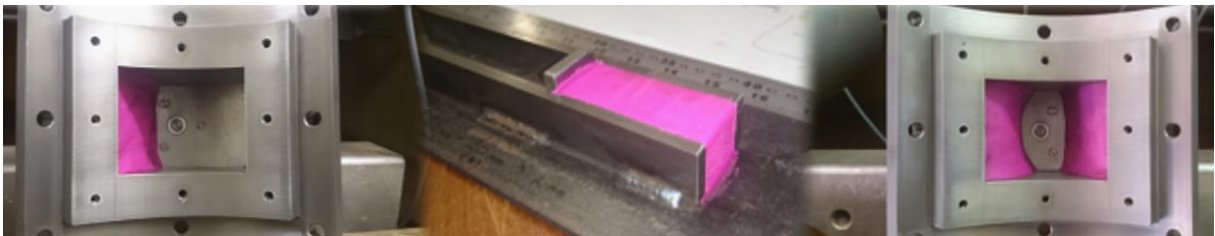
Figure 161 - Image showing distributed resonator cavity volume reduction method: Left - Plate #06 case after 41,535mm³ volume reduction; Centre - Jig for measuring volume of filler material; Right - Plate #30 case after 97,635mm³ volume reduction.

It can be clearly seen from Figure 162 that this method was effective at tuning the target resonant frequency, as both reduced volume cases matched the target frequency to within 0.15Hz. It is also evident from Figure 162 is that as expected, the reduction of the cavity volume can be seen to shift the corresponding dynamics frequencies to the higher values; it is noteworthy however, that the magnitude of the FRF can be seen to remain almost constant across the cases, irrespective of the frequency shift.

As a result of these findings, it can be concluded that for the maximum attenuation to be achieved for a given dynamics frequency, the L/D ratio should be kept as low as possible. For these cases this reads as the largest possible neck diameter, as only one neck length was available. Consequentially, it can

also be expected that if the neck diameter was constrained and the length varied, then the resultant decreasing L/D ratio would also result in a higher magnitude of attenuation.

For the test rig design used in this investigation varying the neck length is not easily achievable, due primarily to the relatively small bend radius required to fit the annular segment on the Ø165mm measurement rig, and the consequential manufacturing constraints of pre-cutting the plates and then rolling. A practicable limit of 3mm neck length could potentially be manufactured using same methods employed here for the 2mm necks however, for larger thicknesses, the inner wall will likely need to be machined from stock material.

Regardless of the practical method of neck length variation, there remains a rational argument for further experimental evaluations; as if the L/D ratio results shown in Figure 162 holds true, then improved attenuation may be achievable though optimisation of the L/D ratio.
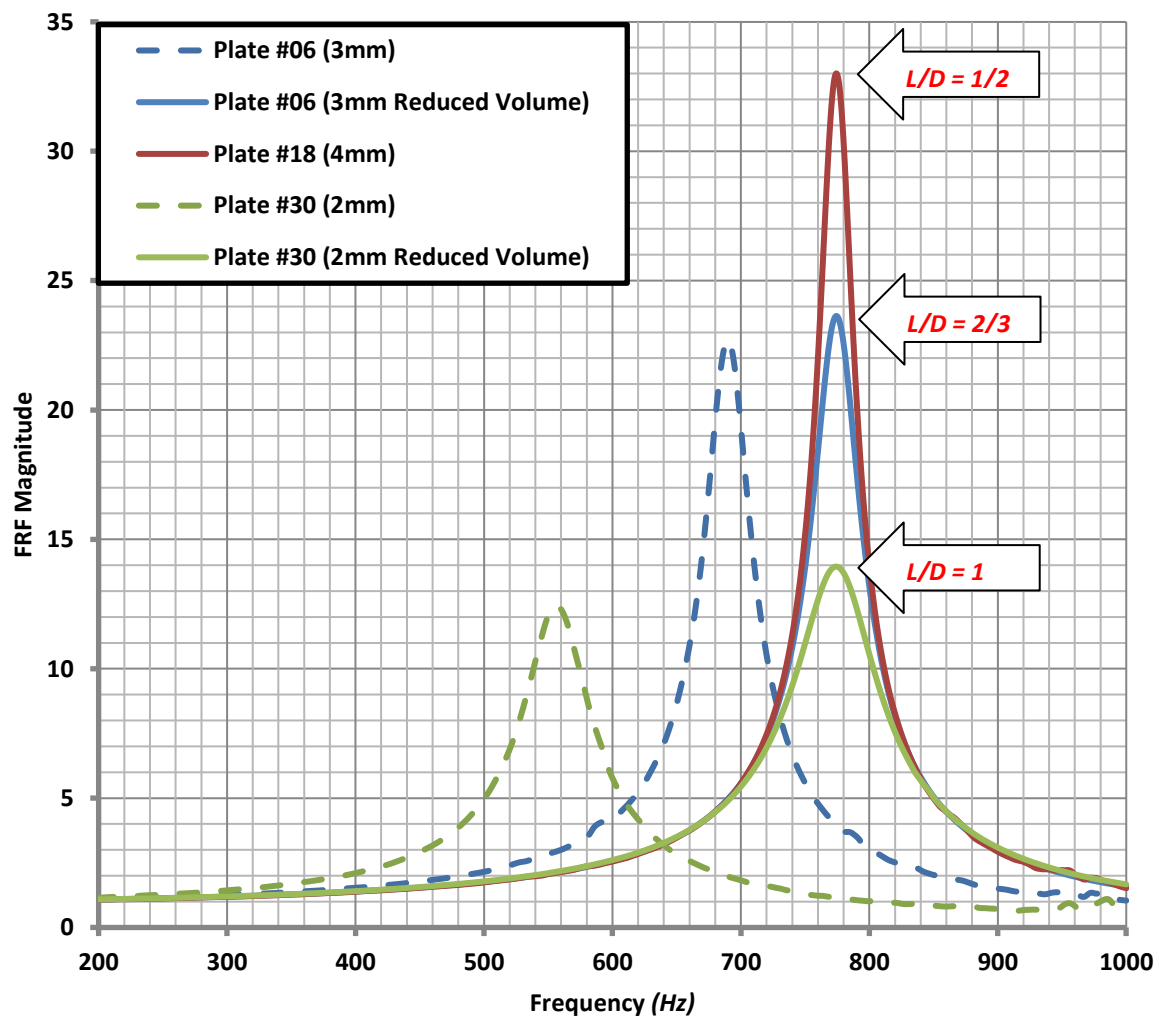
Figure 162 - Plot showing effect of L/D ratio on FRF for fixed frequency cases (Plates #06, #18 & #30), under acoustic excitation only

8.3   H-W & H-H Factors

Through the design efforts of Section 7.2.1, it is expected that the target distributed resonator test cases should demonstrate a measurable difference in peak attenuation frequency and amplitude, solely as a result of hole pattern. The resultant inner plate test matrix described in Section 7.4.1 has been developed such that there are 12 variations in hole pattern for each of the 3 available neck diameters, thus providing a comprehensive test matrix for the subsequent evaluation of H-W & H-H factors.

From an initial comparison of Figure 156 & Figure 157; the FRF and transmission loss measured for the least densely packed hole patterns; with Figure 158 & Figure 159; showing the similar performance metrics for the most densely packed hole patterns; it can be clearly seen that there is indeed a notable difference in resultant dynamics which can be attributed solely to H-W & H-H factors. Between these extreme hole pattern cases *(1/12, 13/24 & 25/36),* the only variable is hole pattern, and yet this factor alone can be seen to result in frequency shifts of over 100Hz and prominent differences in magnitude.

This observation alone is laudable, as most commonly applied analytical models do not capture such features effectively; and as such there exists great potential for significant reduction of the inaccuracies inherent in existing resonator performance predictions, if such factors can be accurately accounted for. The intended strategy for experimental evaluation of H-W & H-H factors is first to measure all 36 inner plate configurations with zero flow *(closed resonator configuration, with zero grazing flow),* and under acoustic excitation only. Following measurement and subsequent evaluation of each of the targeted test cases, the values of peak attenuation frequency and magnitude can then be holistically evaluated to support the development of additional insights, and improvements in analytical models which more accurately predict the H-W & H-H factors. Whilst in Section 5.1.2 an improvement in the analytical modelling accuracy of discrete resonators was presented; which more effectively captured some of the geometrical significance of H-W factors for discrete resonators; in this section, the goal is to provide an insight to distributed resonator relevant H-W & H-H trends and pertinent factors only. To support this goal, an initial evaluation will be facilitated through the spectral analysis of key performance factors, corresponding to all available inner plate configurations, across the targeted measurement spectrum.

Figure 163 shows the frequency response magnitude for all 12 of the 4mm neck diameter cases *(Plates #13-24)*, and from this figure it can be seen that the hole spacing alone results in a significant variation in the peak attenuation frequency, with ≈130Hz variation between Plate #13 & Plate #24. From initial evaluation of all 12 cases shown in Figure 163, it can be seen that the hole pattern density would appear to correlate with a resultant frequency shift. Furthermore, it can be seen that the highest peak

attenuation frequency occurs for the least densely packed pattern *(Plate #13)*; with the lowest corresponding to the most densely packed pattern *(Plate #24)*; and the intermediary cases distributed in the transitional region, according to their hole pattern density.

A similar trend can also be seen across the other two neck diameter conditions, with Figure 164 showing the FRF magnitude for the Ø3mm neck cases and Figure 165, the Ø2mm cases. Comparing the peak FRF frequency across the three neck diameter cases, it can also be seen that the greatest cross-case variation in frequency occurs for the Ø4mm neck cases, and the least variation occurs across the Ø2mm neck cases. This finding, along with the aforementioned relationship with hole pattern density, implies a strong correlation between H-H factors and subsequent frequency shift. The magnitude of the FRF as seen in Figure 163, for the Ø4mm neck cases, can be seen to be largest for Plate #13 and generally decrease, with increase in pattern density, to the minimum magnitude demonstrated by Plate #24. Conversely however, from Figure 164 & Figure 165 it can be seen that for the smaller neck diameter cases, the change in FRF magnitude does not follow such a clear trend. With the Ø3mm neck variations showing no obvious correlation between hole pattern and FRF magnitude, and for the Ø2mm cases the change in FRF magnitude resulting from hole pattern variations is negligible.
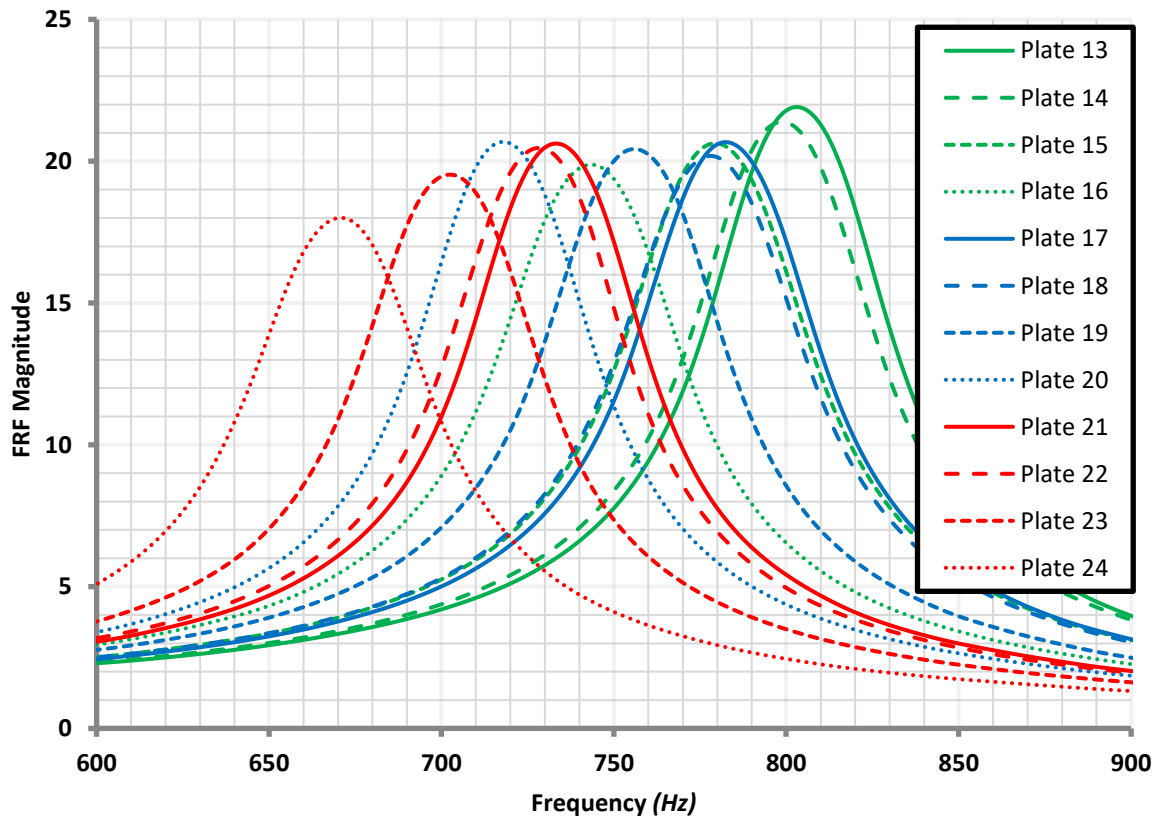
Figure 163 - FRF Mag. for Plates 13-24 (Ø4mm Neck), closed resonator, zero GF
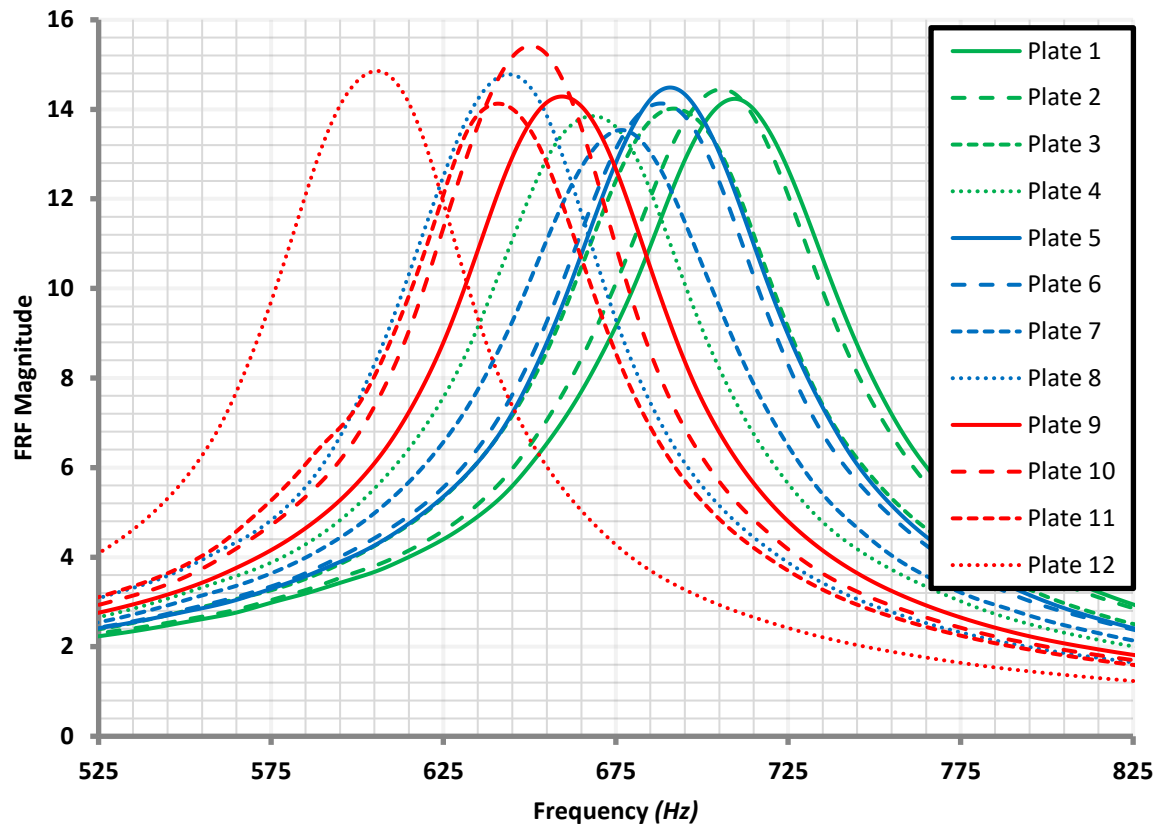
Figure 164 - FRF Magnitude for Plates 1-12 (Ø3mm Neck), closed resonator, zero GF
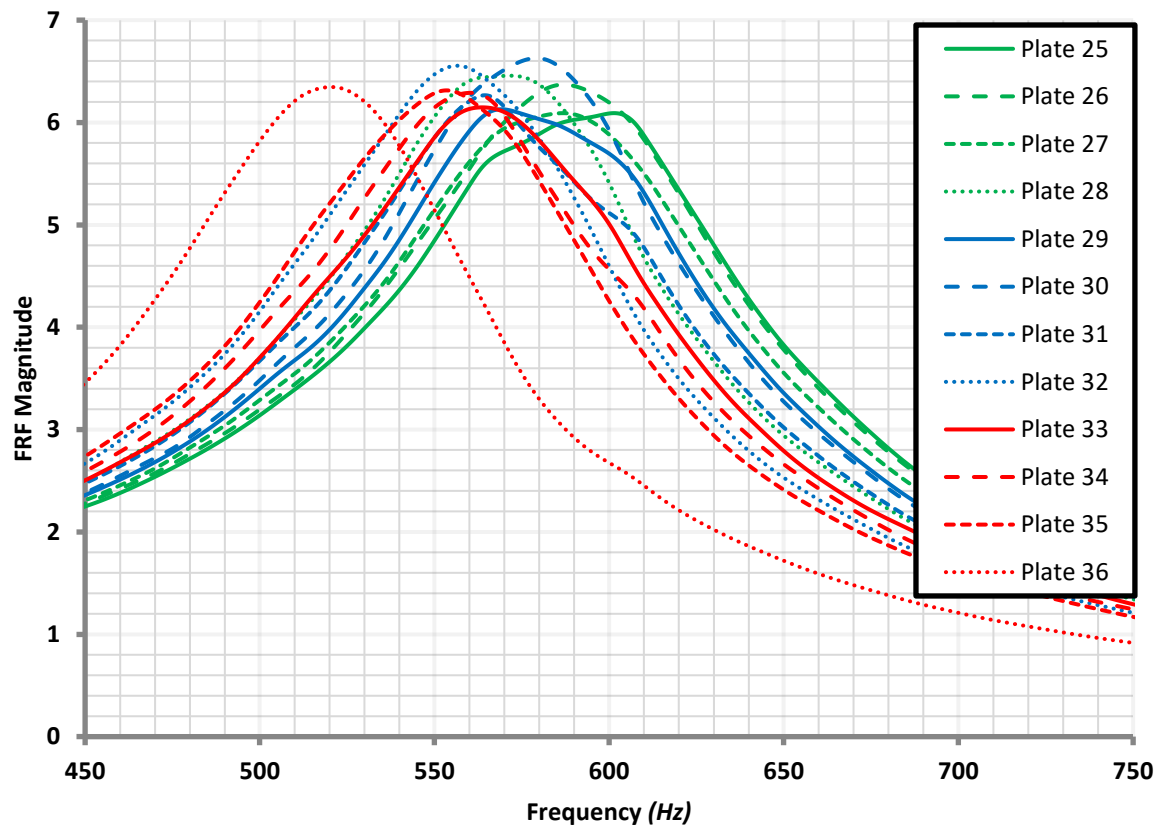
Figure 165 - FRF Magnitude for Plates 25-36 (Ø2mm Neck), closed resonator, zero GF

As mentioned in the opening to this chapter, it is important to evaluate duct derived quantitative performance metrics, alongside the FRF; in order to ensure the local response indicated by the FRF is also seen physically in the transmission line. Accordingly Figure 166, Figure 167 & Figure 168 show the measured incident transmission loss for the Ø4mm, Ø3mm & Ø2mm neck diameter H-W & H-H test cases respectively. It can be seen from these transmission loss plots, that the peak attenuation frequency trends observed, shows very good correlation with the measured peak FRF frequency for all cases measured. The magnitude trend between the FRF & Transmission loss, however, indicates some subtle noteworthy differences.

From Figure 166 it can be seen that, unlike the FRF, Plate #17 demonstrates the maximum transmission loss amplitude, and hole patterns either side of this condition *(both increased and decreased pattern density)* generally decrease in transmission loss magnitude, with increasing degree of hole pattern. From Figure 167 however, for the Ø3mm neck cases, the peak transmission loss can be seen to occur near the minimum hole pattern density *(Plate #2)*, again contrary to the FRF magnitude prediction. Furthermore, for the Ø2mm neck cases shown in Figure 168, although there was no notable difference in FRF magnitude as a result of hole pattern, it is apparent that the most densely packed case *(Plate #36)* exhibits a clear relative reduction in transmission loss magnitude.
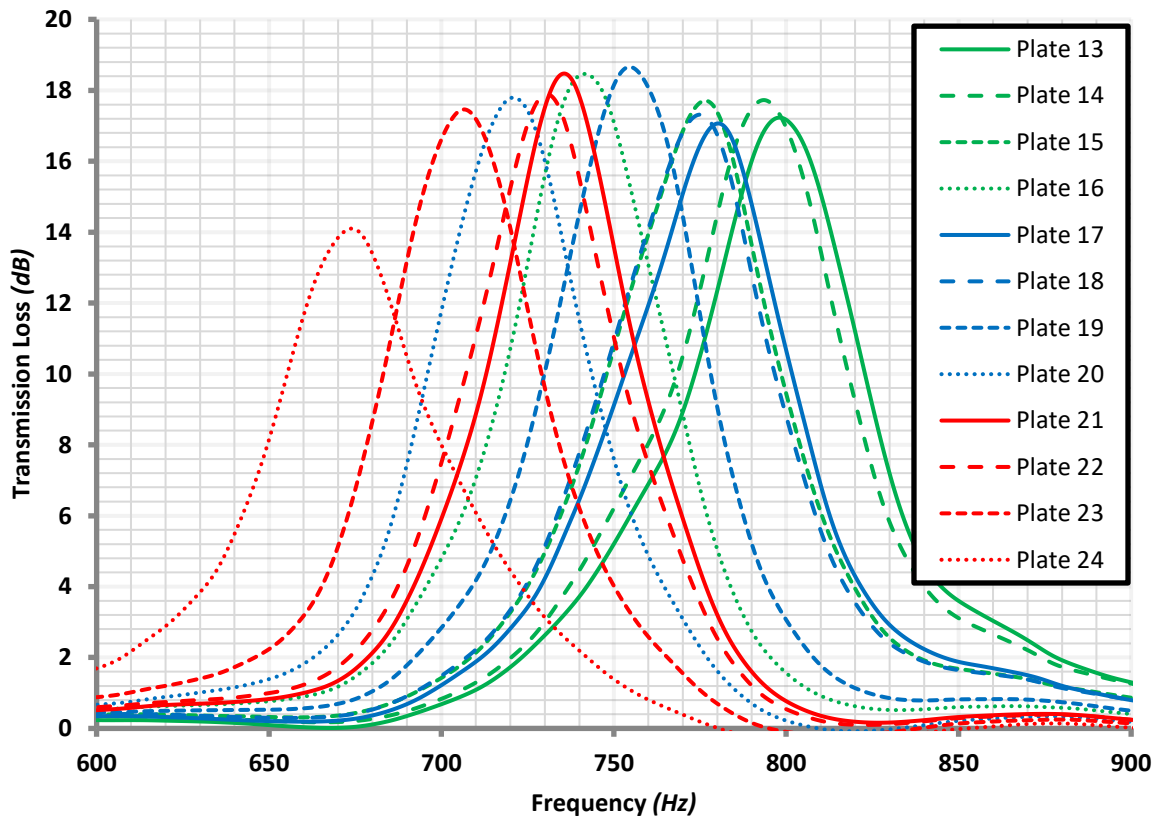
Figure 166 - Transmission Loss for Plates 13-24 (Ø4mm Neck), closed resonator, zero GF
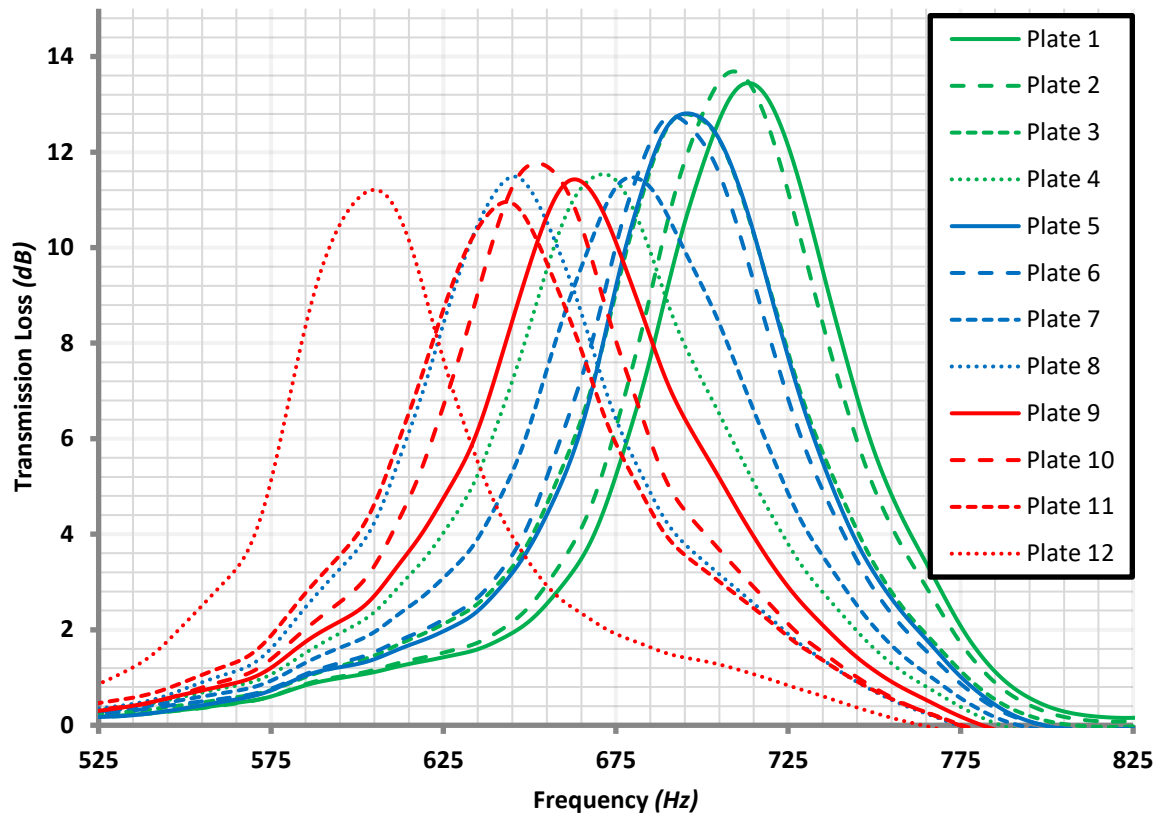
Figure 167 - Transmission Loss for Plates 1-12 (Ø3mm Neck), closed resonator, zero GF

Although it can be seen that there is little difference between the peak transmission loss magnitude across the remaining hole pattern cases for the Ø2mm neck condition, it can be appreciated that as the neck diameter is the smallest of the available cases, and as the pitch variations are constant across cases, these test cases will consequentially exhibit the smallest relative variation in H-H factors across the hole pattern test matrix.
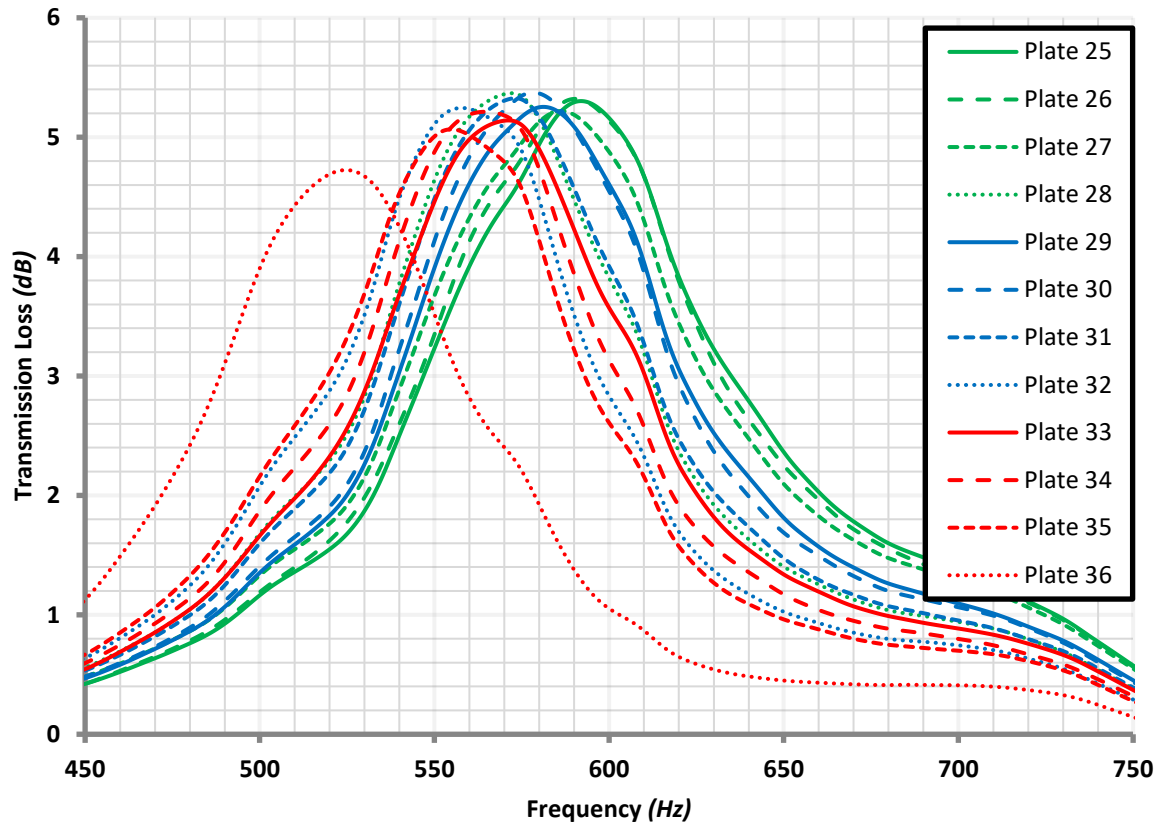
Figure 168 - Transmission Loss for Plates 25-36 (Ø2mm Neck), closed resonator, zero GF

As the transmission loss only quantifies the difference between the upstream and downstream incident components of the acoustic response, it inherently neglects the significance of any upstream reflections. In practical applications of noise attenuation using acoustic resonators however, it is often of equal importance to attenuate both downstream and upstream propagating dynamics.

Consequently, the dissipation coefficient offers an effective holistic measure of total attenuation and can be used to evaluate the attenuation characteristics for each of the measured H-W & H-H test cases, in accordance with Section 2.4.2.8. Accordingly Figure 169, Figure 170 & Figure 171 show the measured dissipation coefficient for the Ø4mm, Ø3mm & Ø2mm neck diameter H-W & H-H test cases respectively.

As with the comparison between FRF and Transmission Loss, it can be seen that the peak dissipation coefficient frequency for each case shows very good correlation with both peak FRF magnitude, and peak Transmission Loss. Similarly, it is the magnitude of the dissipation which deviates from the trends shown by the alternative performance metrics. The difference in magnitude of the dissipation coefficient, compared to the transmission loss, is a direct factor of the measured reflection coefficient considered in the derivation of this performance metric. With this in mind, from evaluation of Figure 169, it can be seen that Plate #13; which was previously shown to have the largest magnitude of FRF,

and one of the largest transmission loss magnitudes; conversely results in a relatively low value of dissipation coefficient magnitude.

This can be attributed to the fact that for such cases, the resonator is highly reactive, and much of the incident wave is reflected back upstream as opposed to being absorbed by the resonator. In such cases the transmission loss will show a high attenuation due to the large amount of energy removed from the incident wave; however, it will fail to show that a large portion of that energy may also have been reflected back upstream.

Therefore, it can be reasoned that in the context of total noise attenuation, the dissipation coefficient is a much more effective metric for appreciating the holistic attenuation performance of any given distributed resonator design against unwanted dynamics, irrespective of the direction of propagation.
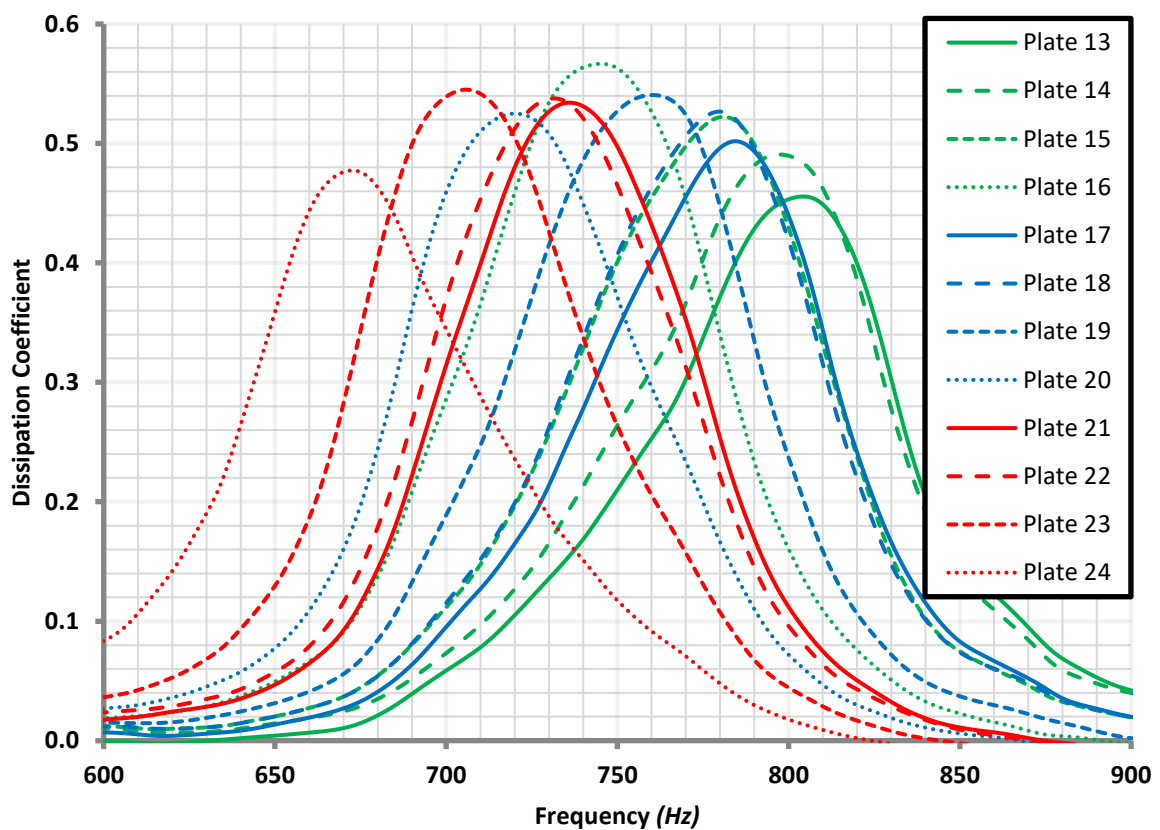
Figure 169 - Dissipation Coefficient for Plates 13-24 (Ø4mm Neck), closed resonator, zero GF
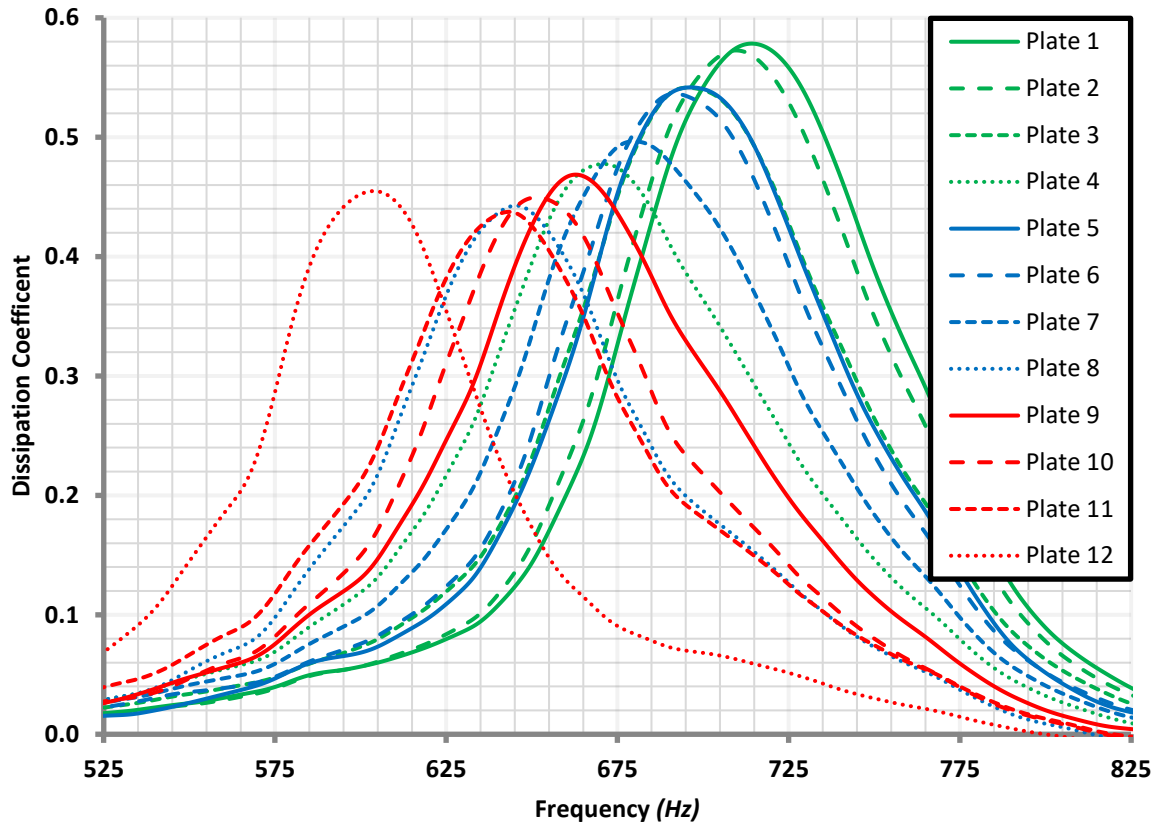
Figure 170 - Dissipation Coefficient for Plates 1-12 (Ø3mm Neck), closed resonator, zero GF
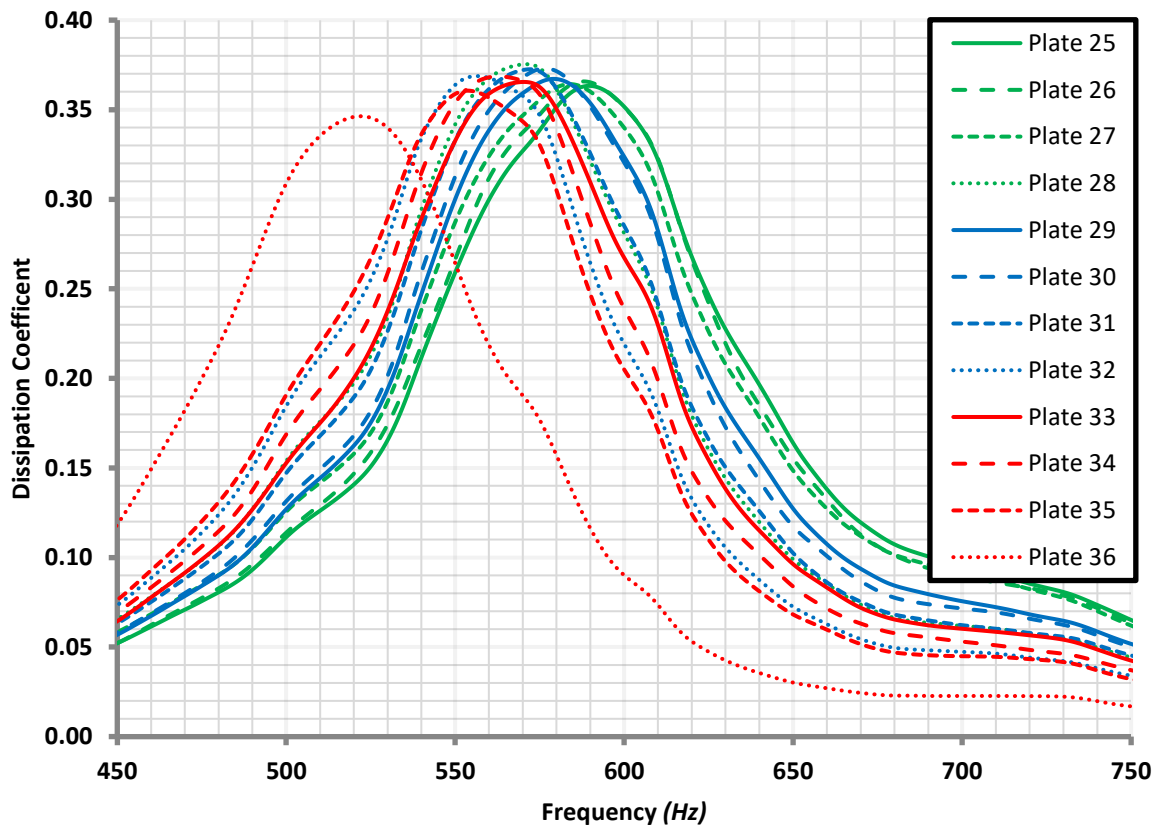
Figure 171 - Dissipation Coefficient for Plates 25-36 (Ø2mm Neck), closed resonator, zero GF

Ultimately it has been demonstrated that the H-W & H-H factors resulting from varied inner aperture hole pattern, are significant in the accurate determination of the noise attenuation performance of any given distributed resonator design. Additional insight into inherent attenuation defining characteristics attributed to H-W & H-H factors have been shown experimentally; observed trends have been identified across the test cases measured; and notable distinctions between individual cases, and performance metrics have been delineated.

8.4   Grazing Flow Effect

Whilst a total of 36 inner plate variations have been evaluated as part of the overarching comprehensive distributed resonator performance factor analysis, only three representative inner plates will be presented in the following section for brevity: in order to support a more targeted evaluation of key grazing flow factors, across the full measurement spectrum. Plate #1, #13 & #25 are chosen for subsequent investigation, as they are all of the same hole pattern *(least densely packed configuration)* and vary only in hole dimeter; with a neck diameter of Ø3mm, Ø4mm and Ø2mm. Given that the plate dimensions, and hole patterns are constant across all three cases, this results in a corresponding perforation value of 7.6%, 13.5% and 3.4% across these cases respectively. As with the previous section (8.3), which evaluated the H-W & H-H factors using a variety of performance metrics; the subsequent analysis will utilise the frequency response function (magnitude and phase), the transmission loss, the dissipation coefficient, and reflection coefficient; as acoustic attenuation performance measures.

In order to mitigate excessive information being contained in the legends of the forthcoming figures; whilst still sufficiently conveying the flow conditions of each case; a case naming convention has been established for this study. As shown in Table 39, this key describes both the grazing and bias flow conditions for each case with the letters 'b' & 'g' followed by a numerical suffix indicating the respective magnitude of the flow condition. For the six bias flow conditions measured, the number refers to the percentage of pressure drop from atmospheric pressure across the resonator, i.e. 0%dP – 5%dP. For the grazing flow, the numeric suffix refers to the increment of cross-flow measured, with g0 indicating zero cross-flow, and with g1, g2, g3, g4 & g5 referring to the average cross-flow velocities of 12m/s, 17m/s, 23m/s, 29m/s and 34m/s respectively. For example, b0g0 corresponds to a zero bias flow and zero grazing flow case; and b3g3 would be a case with a 3% pressure drop across the resonator, and an average grazing flow velocity of 23m/s.

[Plate XX]	Bias Flow (Pressure Drop)					
Grazing Flow	0%dP	1%dP	2%dP	3%dP	4%dP	5%dP
0m/s	b0g0	b1g0	b2g0	b3g0	b4g0	b5g0
12m/s	b0g1	b1g1	b2g1	b3g1	b4g1	b5g1
17m/s	b0g2	b1g2	b2g2	b3g2	b4g2	b5g2
23m/s	b0g3	b1g3	b2g3	b3g3	b4g3	b5g3
29m/s	b0g4	b1g4	b2g4	b3g4	b4g4	b5g4
34m/s	b0g5	b1g5	b2g5	b3g5	b4g5	b5g5

Table 39 - Table showing legend key for subsequent grazing/bias flowed experiments

8.4.1   Frequency Response Function

A preliminary appreciation of the impact of varying grazing flow magnitude on distributed resonator dynamics can be seen for the Ø4mm inner plate #13, in Figure 172 and Figure 173; in terms of the measured FRF magnitude, and phase variation respectively. Evaluation of Figure 172 shows that the magnitude of FRF rises initially from ≈12 under no grazing flow conditions; to a peak value of ≈23 under exposure to a 23m/s grazing flow; before then dropping quickly to a minimum of ≈7, at the maximum grazing flow magnitude of 34m/s.

The FRF phase response seen in Figure 173 reinforces these findings, where it can be seen that at a grazing flow of 34m/s, the phase change is the steepest of all the cases, and at the maximum grazing flow of 34m/s, the response flattens significantly.

Evaluation of these combined FRF evaluations allow the deduction that; a moderate value of grazing flow of 23m/s, is able to enhance the response dynamics for the inner Plate #13 case; however, increasing the grazing flow further, results in a deterioration of response dynamics.

Figure 174 and Figure 175 show similar results for plate #1, as does Figure 176 and Figure 177 for plate #25; with all three cases exhibiting a common trend of enhanced resonance as a result of a moderate grazing flow; with a diminished resonance resulting from high grazing flow magnitudes. The optimum grazing flow velocity: considered as the grazing flow magnitude which results in the largest FRF magnitude; can however be seen to vary between the respective test cases. The observed optimum grazing flow velocities are 23m/s, 17m/s, and 12m/s respectively for Plate #13, Plate #1, and Plate #25 test cases, which indicates a correlation between the neck diameter and/or perforation ratio, and the corresponding onset of resonator saturation due to grazing flow magnitude.

An additional and noteworthy observation from these results, is the shift towards higher dynamics frequencies as a result of increasing grazing flow magnitude. This effect is expected to be a result of two primary factors; firstly, the removal of some of the oscillating air mass at the duct side of the inner plate apertures, which will reduce the effective length of the necks; and secondly the grazing flow

induced neck flow, which increases the particle velocity within the aperture, and consequently reduces the end correction length (Dickey et al., 2001). The reduced reactance due to these two factors can be attributed to the observed increased in resonant frequency. These experimentally observed trends of decreasing reactance and increasing resistance; resultant from increasing grazing flow magnitude; are consistent with the observations from the previously evaluated discrete resonator cases under grazing flow, and the subsequent theoretical deductions deliberated in Section 5.3.
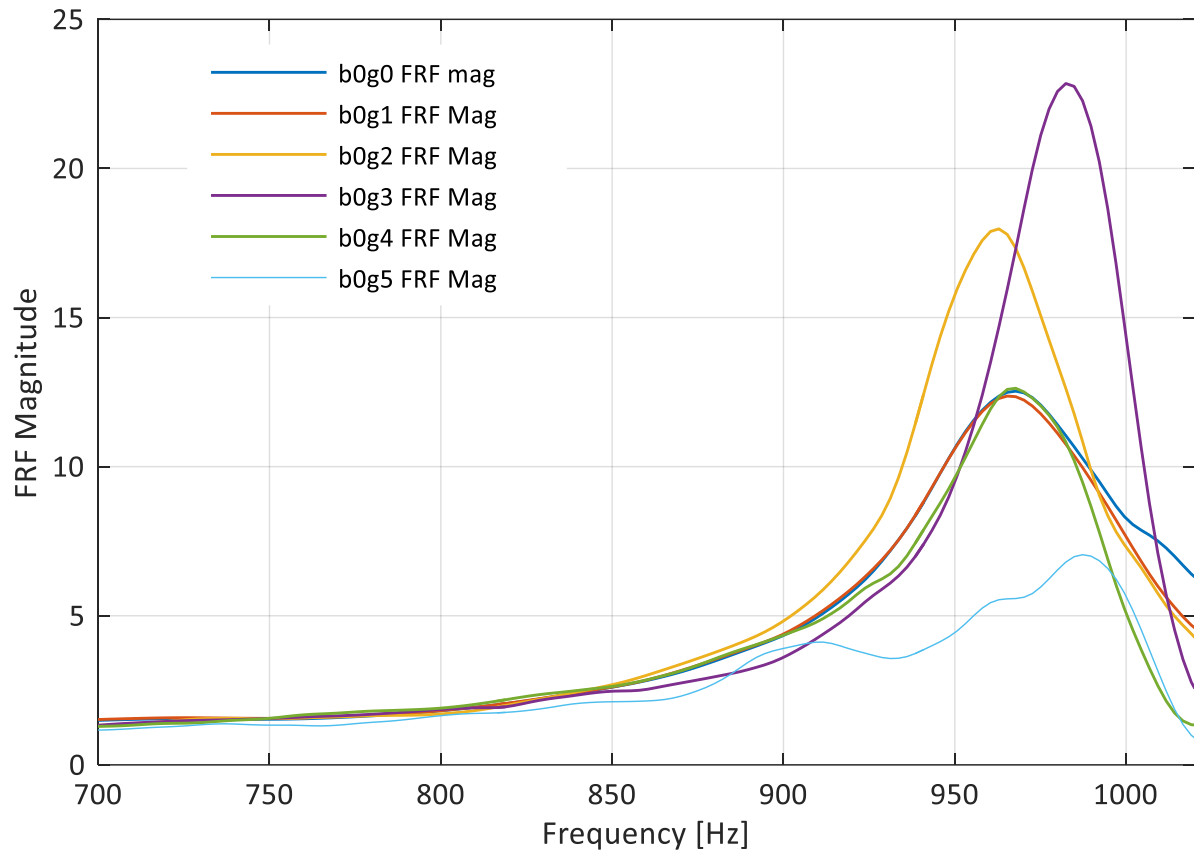
Figure 172 - FRF Magnitude for Plate #13 (Ø4mm), with varied grazing flow
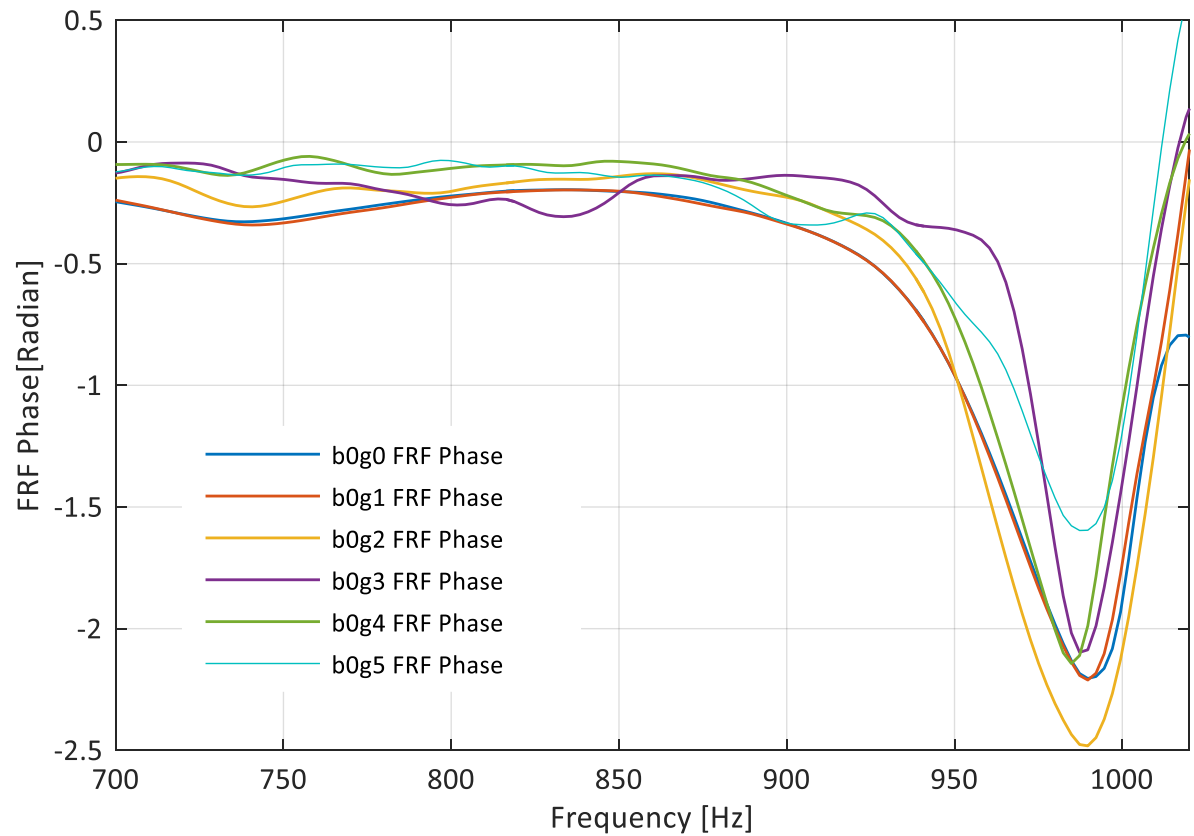
Figure 173 - FRF Phase for Plate #13 (Ø4mm), with varied grazing flow
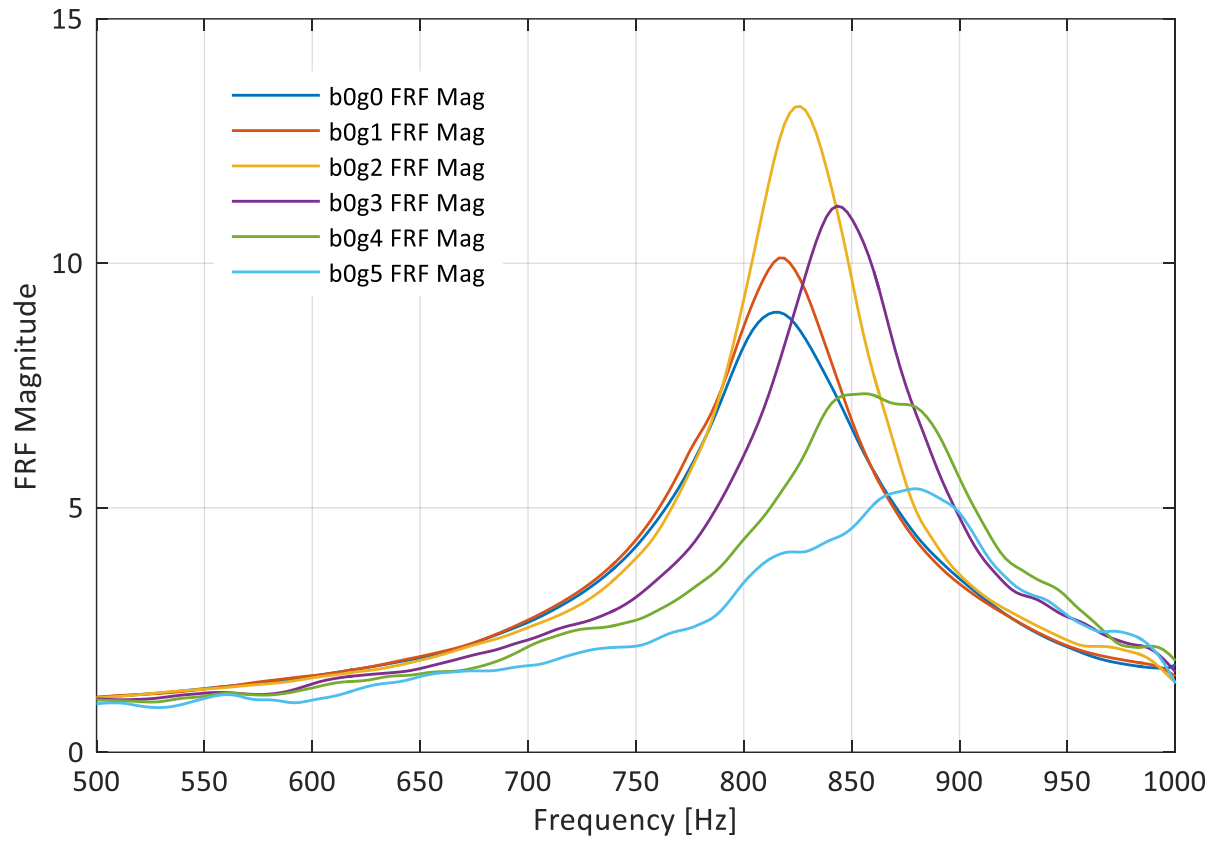
Figure 174 - FRF Magnitude for Plate #1 (Ø3mm), with varied grazing flow
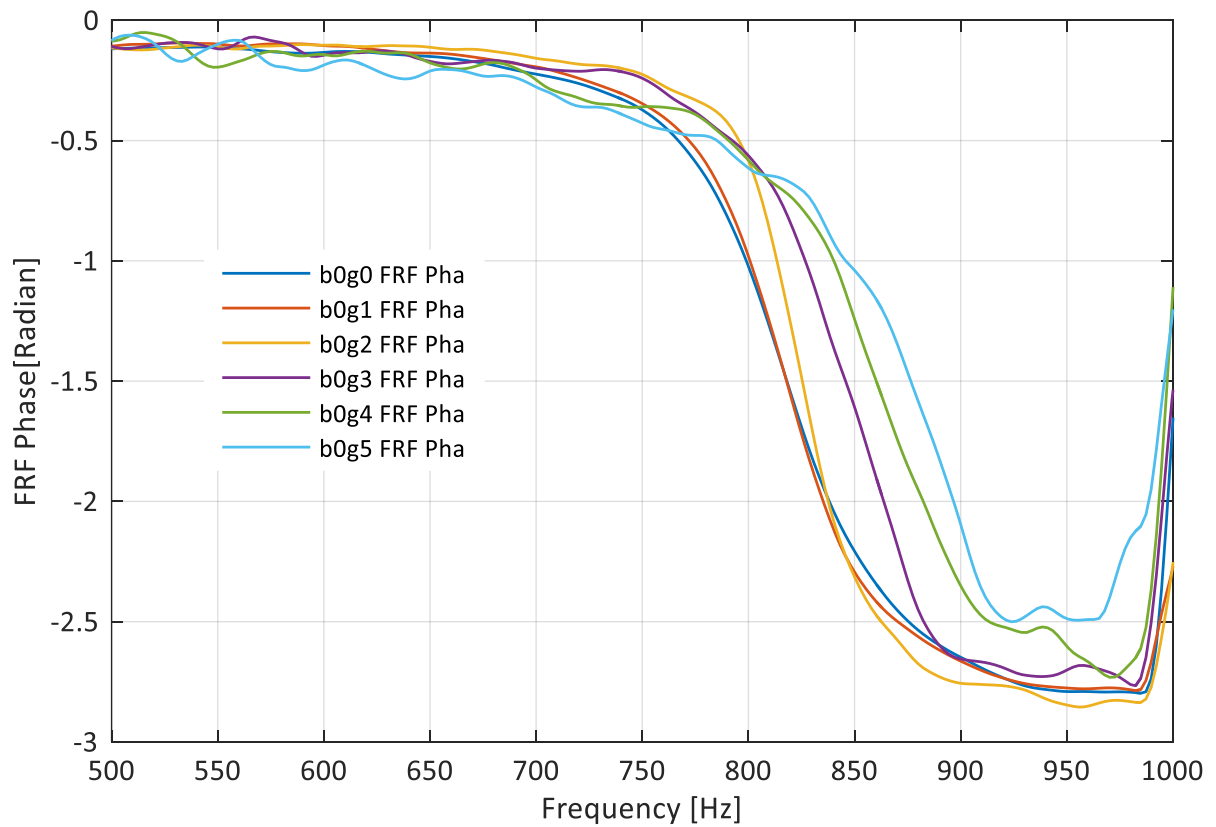
Figure 175 - FRF Phase for Plate #1 (Ø3mm), with varied grazing flow
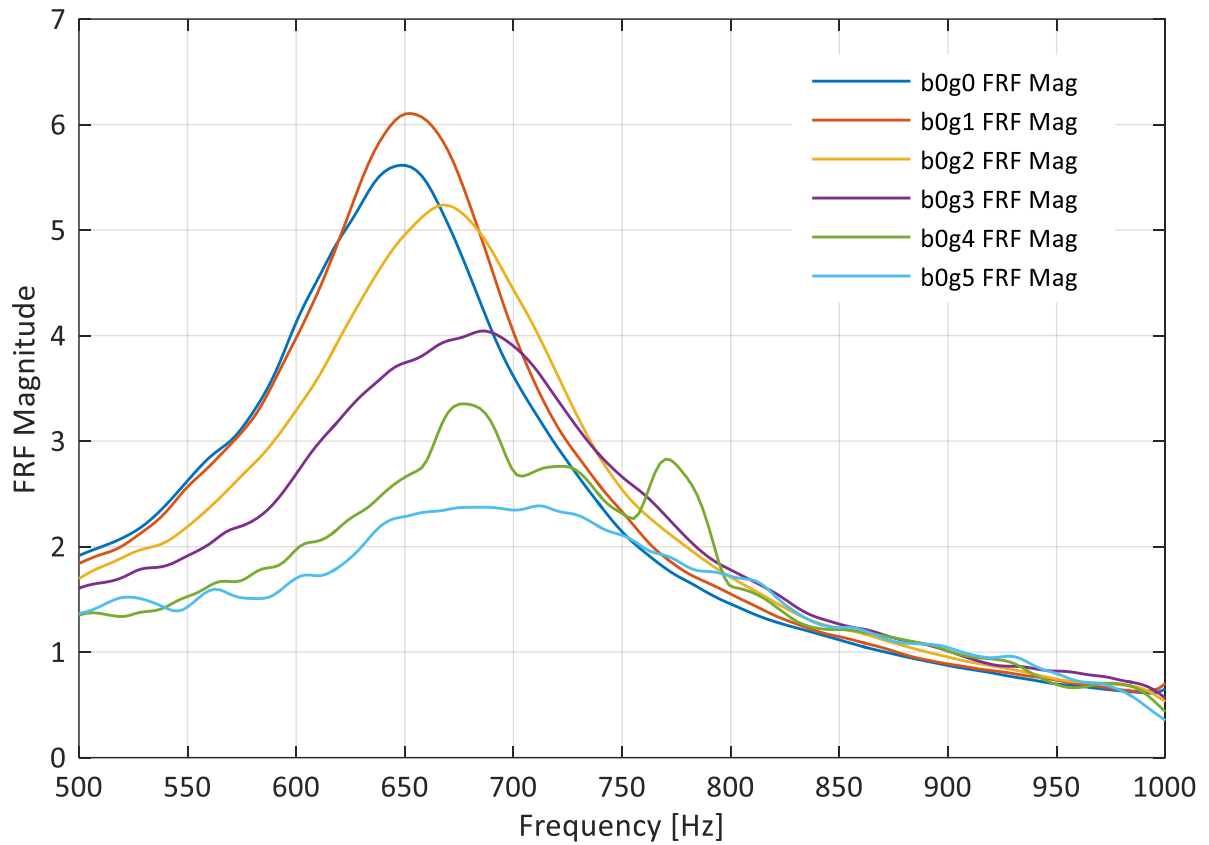
Figure 176 - FRF Magnitude for Plate #25 (Ø2mm), with varied grazing flow
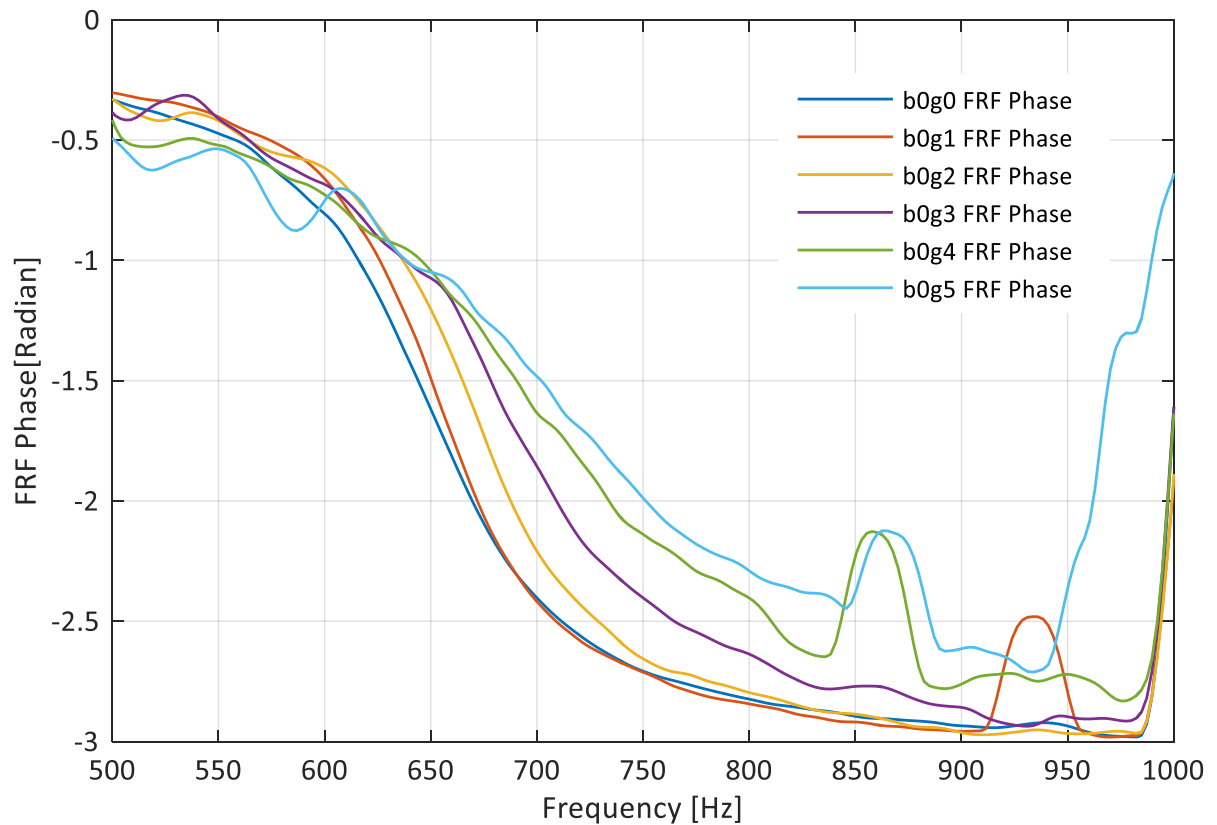
Figure 177 - FRF Phase for Plate #25 (Ø2mm), with varied grazing flow

8.4.2   Transmission Loss

Extending the evaluation of the targeted representative cases in relation to the impact of grazing flow on transmission loss, yields Figure 178, Figure 179, and Figure 180; which respectively illustrates the variation of measured transmission loss resulting from varied grazing flow magnitude; for the corresponding inner Plates #13, #1, & #25.

All three figures agree with the aforementioned conclusions drawn from an evaluation of the FRF magnitude and phase; reinforcing that a moderate grazing flow does indeed enhance the resonance effect of the distributed resonator; and similarly indicating a correlation between the neck diameter and/or perforation ratio, and the corresponding onset of resonator saturation due to grazing flow magnitude.

The optimum grazing flow velocity: considered as the grazing flow magnitude which results in the largest transmission loss magnitude, is also in agreement with the FRF deductions; where the observed optimum velocities are 23m/s, 17m/s, and 12m/s respectively, for Plate #13, Plate #1, and Plate #25 test cases.

An additional observation which can be gleaned from these representative results, is that whilst Plate #13 yields the largest peak magnitude of attenuation; according to both FRF & transmission loss metrics; it also exhibits a narrower bandwidth of attenuation, when compared to the equivalent Plate #1 & Plate #25 cases.

It can also be observed that at frequencies beyond those of peak attenuation for each case investigated, there are observed instances of small values of negative transmission loss, which indicates that the measured acoustic pressure amplitude is greater downstream, than upstream, at these frequencies. This observation infers that there is a net generation of noise at these frequencies which emanates from downstream of the upstream measurement location, and propagates downstream, where it is observed at the downstream measurement location. These artefacts can be attributed to additional noise being generated from within the measurement section, which is subsequently superimposed with the downstream propagating acoustic white noise signal, and the flow generated noise. The prevalence and amplitude of these observed negative transmission losses can be assumed to be inconsequential in relative comparison of peak attenuation characteristics.

Extraneous attenuation characteristics are observed between the frequency range of 850Hz-950Hz; which increase proportional to grazing flow magnitude; whilst subtle influences can be appreciated from Figure 178 and Figure 179, the effects are most notable in in Figure 180, as the peak attenuation of this case is furthest from the domain of interest. This phenomenon is suspected to be a rig specific

flow characteristic, which is further investigated in the subsequent section in relation to dissipation coefficient characteristics and supplemented by further delineation in Section 8.4.4.
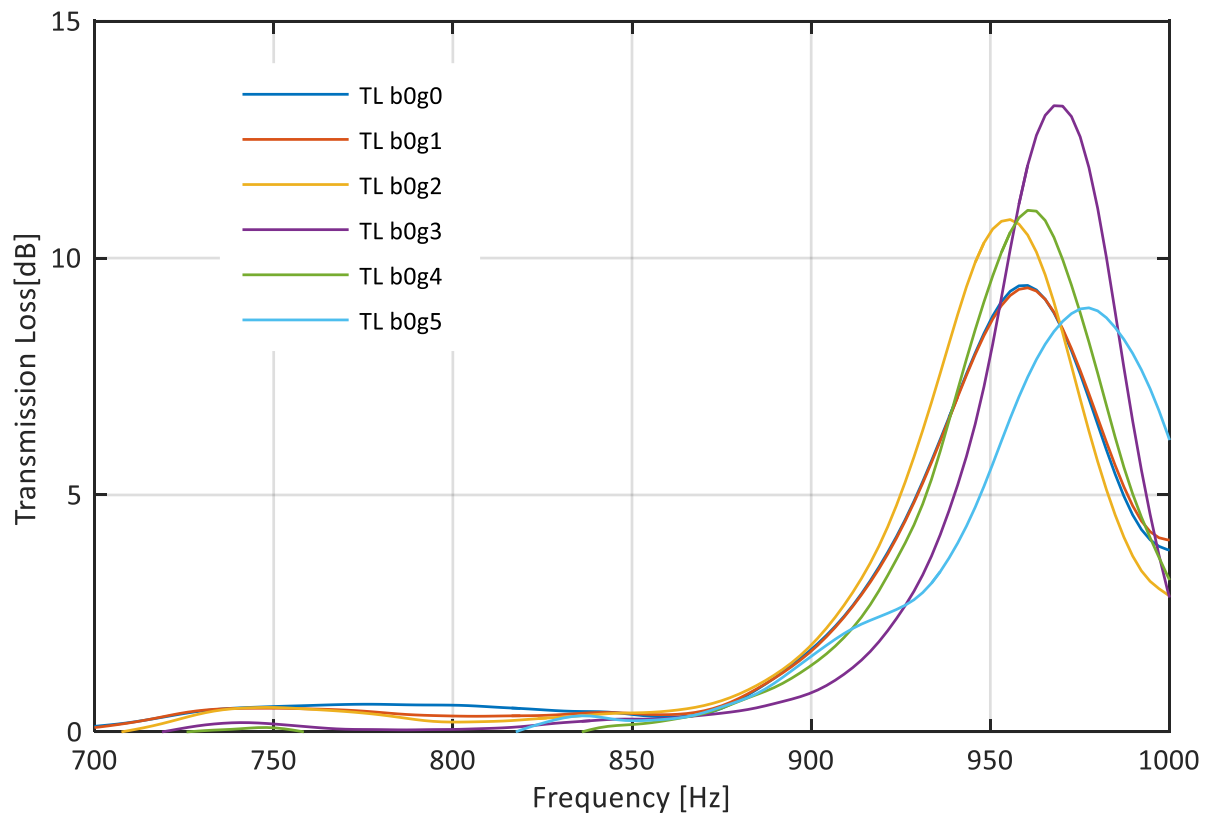
Figure 178 - Transmission Loss for Plate #13 (Ø4mm), with varied grazing flow
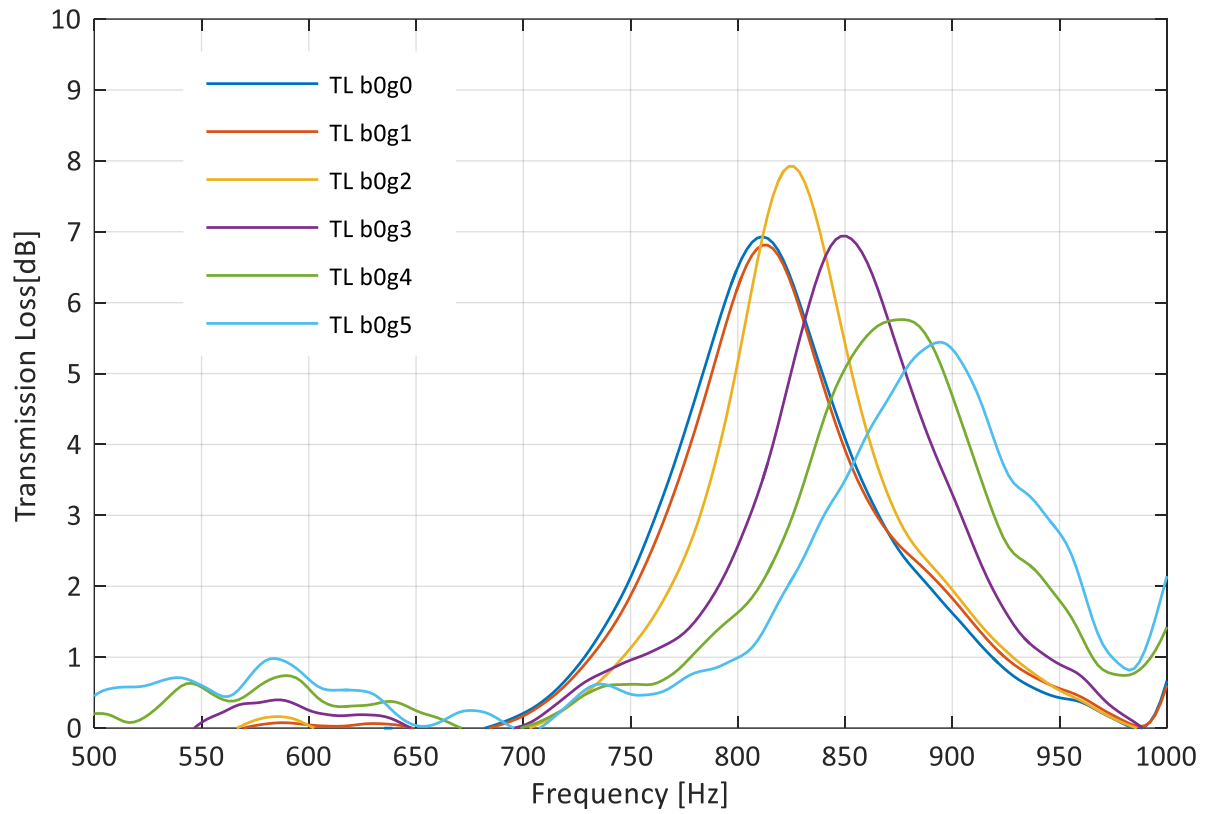
Figure 179 - Transmission Loss for Plate #1 (Ø3mm), with varied grazing flow
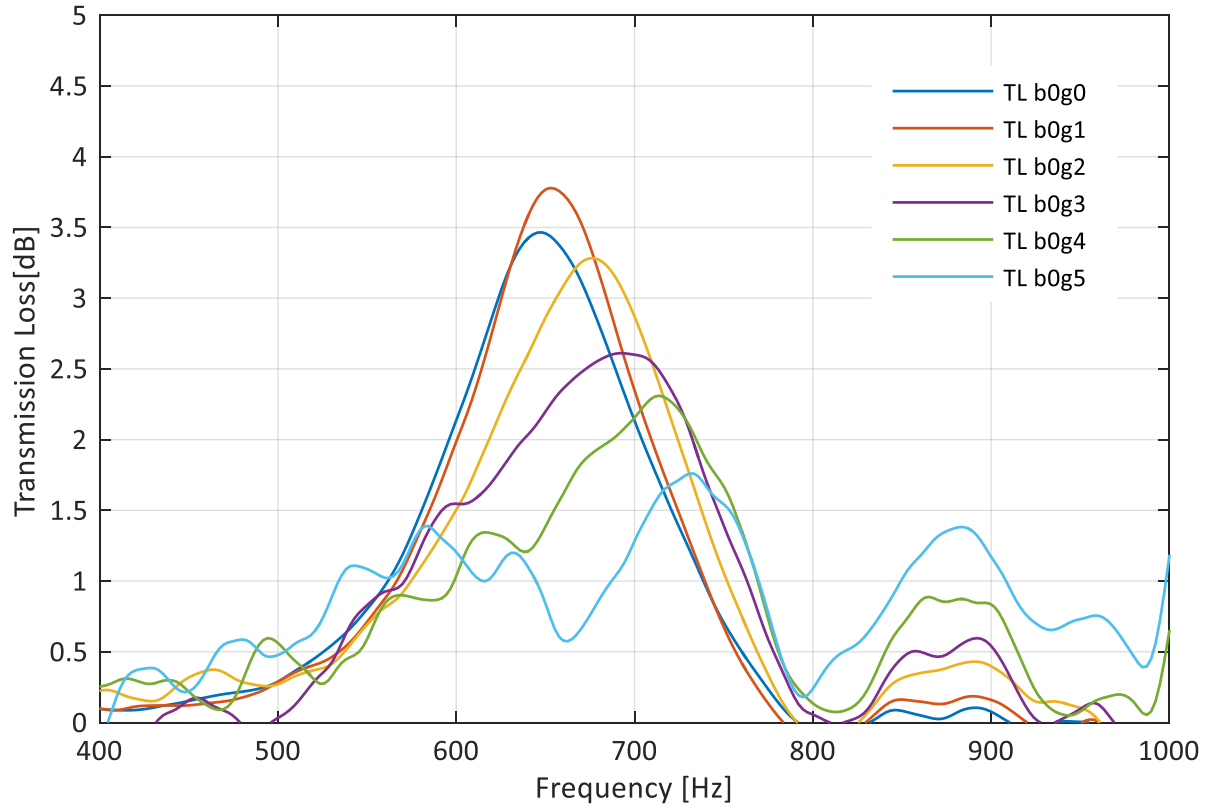
Figure 180 - Transmission Loss for Plate #25 (Ø2mm), with varied grazing flow

8.4.3   Dissipation Coefficient

As advocated in Section 8.3 in relation to the H-W & H-H factor investigations, the dissipation coefficient offers an alternative holistic measure of total attenuation, and one which also captures the significance of upstream reflections, which would otherwise be omitted in the evaluation of FRF and transmission loss alone. Furthermore, the dissipation coefficient metric can also provide supplementary insight into any additional noise generated locally at the resonator/duct interface, and quantify the net impact of any such flow dynamics factors on the net energy flow within the transmission line. Therefore, the dissipation coefficient can be used to evaluate the attenuation characteristics for each of the measured representative grazing flow test cases, in accordance with Section 2.4.2.8.

It can be seen from Figure 181, Figure 182, & Figure 183; which correspond to the measured dissipation coefficient of Plates #13, #1, & #25 respectively; under varying levels of grazing flow; that the acquired insights also differ from the aforementioned observations obtained from the FRF and transmission loss performance metrics. For example, Figure 181 shows a peak dissipation coefficient magnitude for a grazing flow of 17m/s, which differs from the observed equivalent peak FRF and transmission loss magnitude cases of 23m/s. This observation is consistent with the findings of Section 8.3; where highly reactive cases exhibited relatively low dissipation values; due to inherent upstream reflections; the same inference can be equally applied here to grazing flow associated attenuation characteristics.

Figure 182 & Figure 183 demonstrate similar findings corresponding to the Plate #1 & #25 cases respectively; whereby a decline in peak dissipation coefficient is observed from the onset, and with increasing grazing flow. Which further supports the deduction that previous FRF, and transmission loss increases in magnitude; resultant from the onset of grazing flow; can be attributed to an increase in resonator reactiveness, and a consequently greater proportion of upstream reflections; as opposed to a greater net absorption of acoustic energy.

An additional observation of interest from these findings, is that an inferred increase in acoustic energy dissipation can be seen to occur between the frequency range of 850Hz-950Hz; which increases proportional to grazing flow magnitude; and which appears across the representative cases investigated. This observation is more prevalent in Figure 182 & Figure 183, as the resonant frequency of the corresponding cases are outside of this frequency range however, the existence across all three cases infers that this observed increase in dissipation at these frequencies, may in fact be emanating from an inherent duct characteristic, and hence these nuances will be further invested in Section 8.4.4.
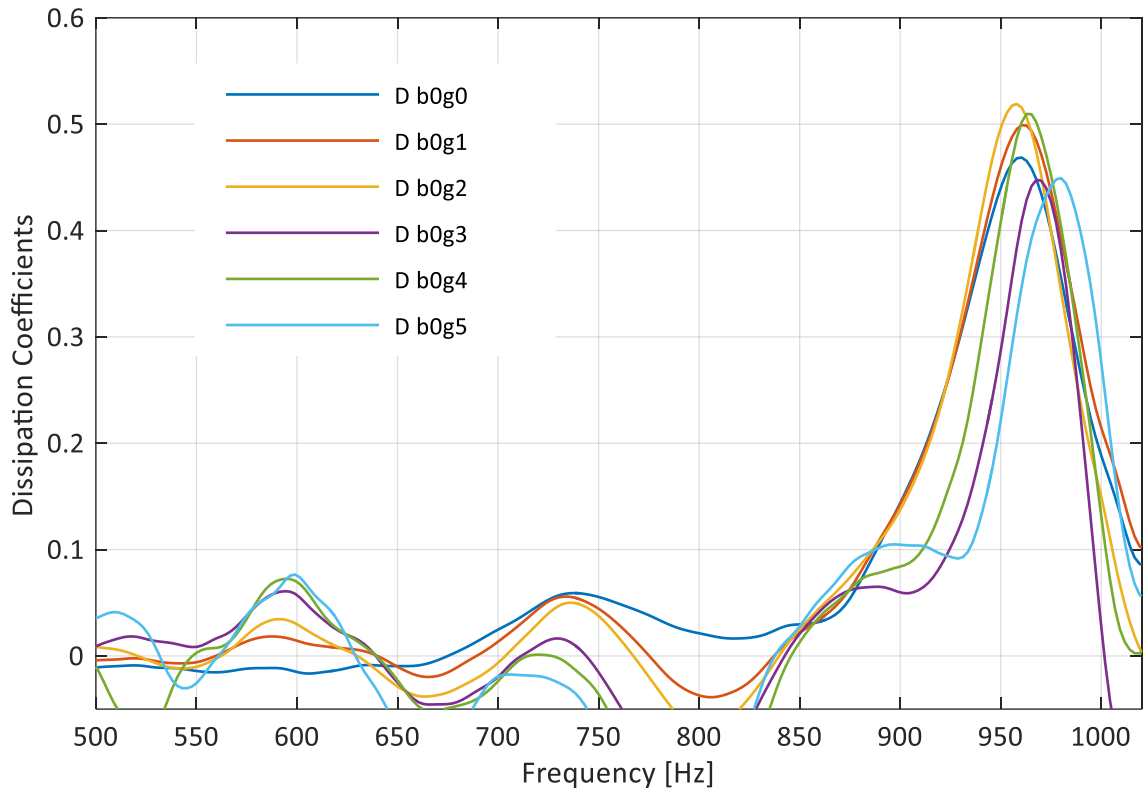
Figure 181 - Dissipation Coefficients for Plate #13 (Ø4mm), with varied grazing flow
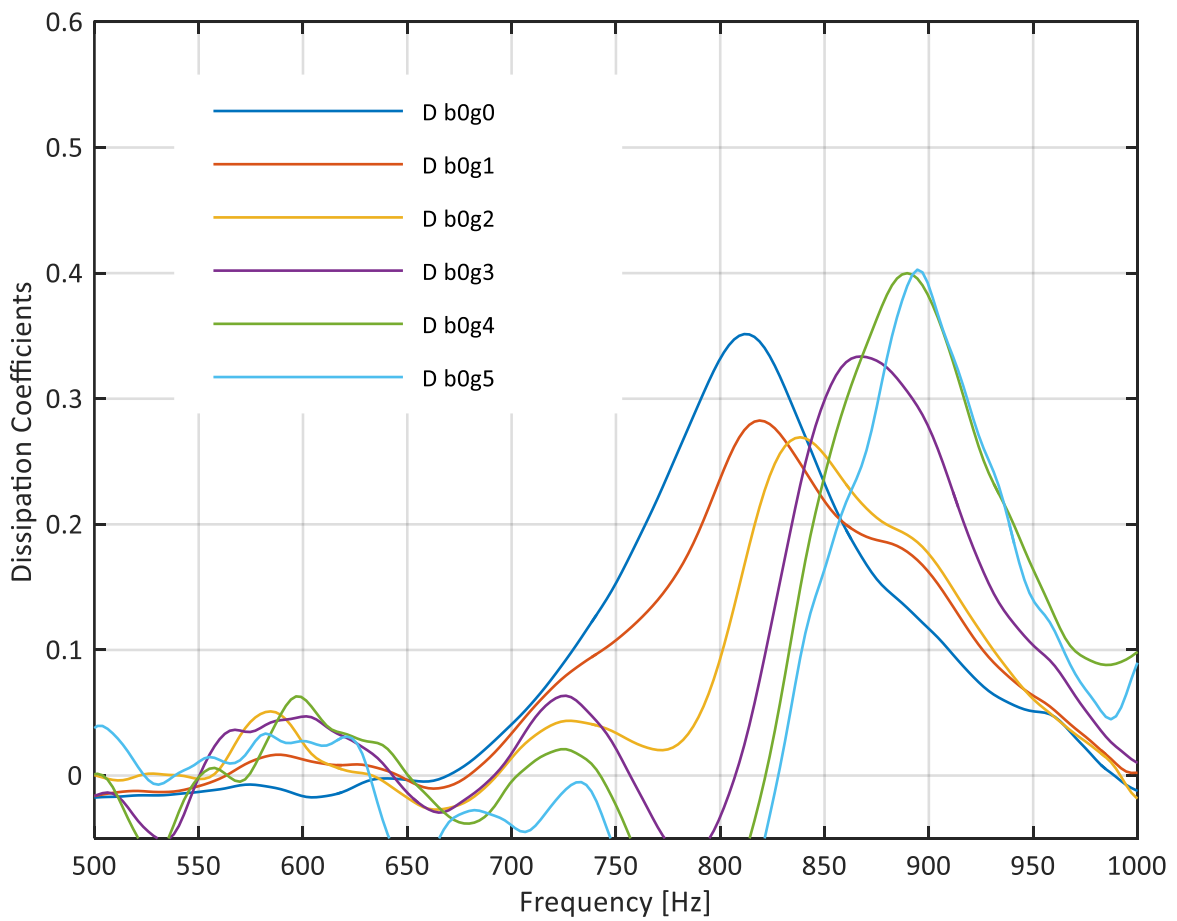
Figure 182 - Dissipation Coefficients for Plate #1 (Ø3mm), with varied grazing flow
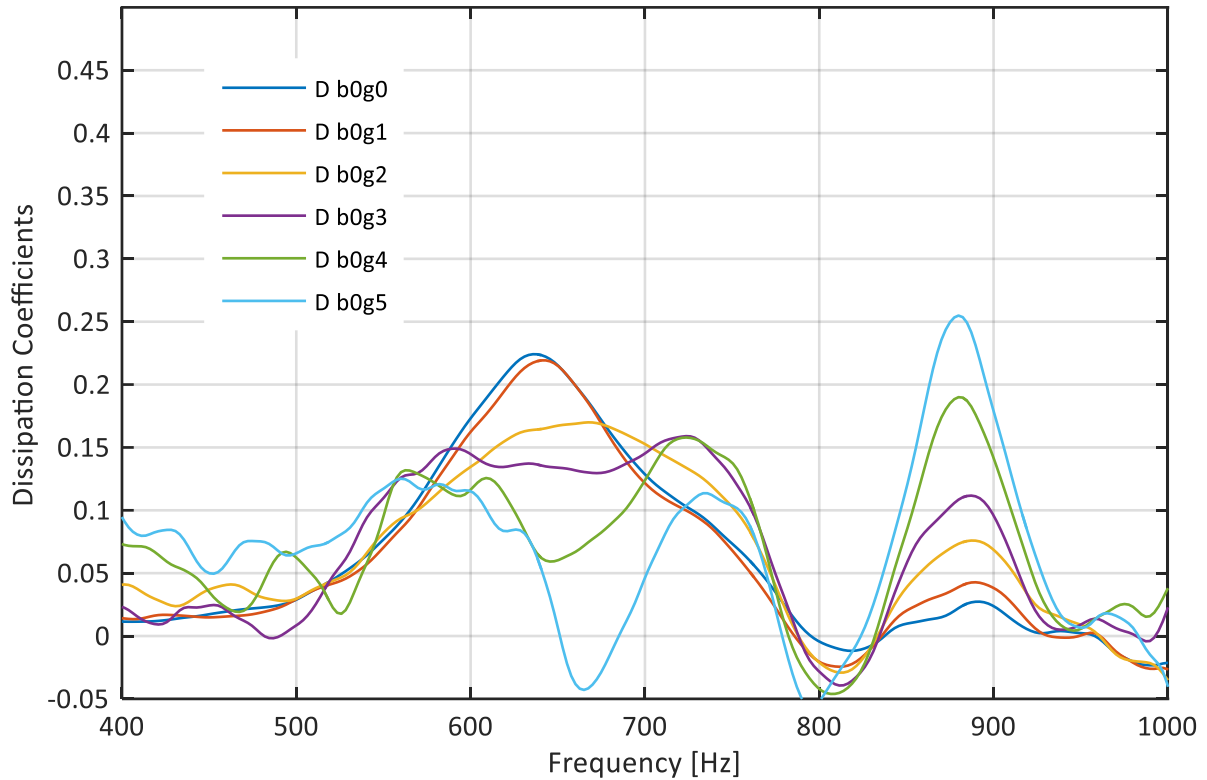
Figure 183 - Dissipation Coefficients for Plate #25 (Ø2mm), with varied grazing flow

8.4.4   Reflection Coefficient

The outlining peaks observed in the transmission loss and dissipation coefficient metrics for the previous representative cases give cause for further investigation; and whilst they can be seen across all three of the aforementioned test plate cases; they are most prominent for Plate #25; for which the resonant frequency is furthest from the observed dynamics.

As such, and in order to provide further insight, the reflection coefficient both upstream and downstream for this representative case will be investigated separately. From Figure 184 it can be seen that the downstream reflection coefficient increases proportional to the magnitude of grazing flow, with the exception of two discrete bandwidths; between 850Hz - 950Hz, and between 500Hz - 600Hz, where a disproportional increase is observed. As the downstream anechoic termination is manufactured in accordance with ISO-5136 (2003), a general increase of downstream reflection attributed to an increase in grazing flow magnitude is expected however, the peaks are not and must be therefore considered as an unintended characteristic of the practical installation. A consequence of this characteristic is that, with increasing grazing flow magnitude, there will be additional acoustic energy within these bandwidths re-entering the resonator section from downstream, which can be considered as the cause for the peaks in dissipation outside of the expected resonant frequency observed from the corresponding dissipation coefficient observations of the representative cases.
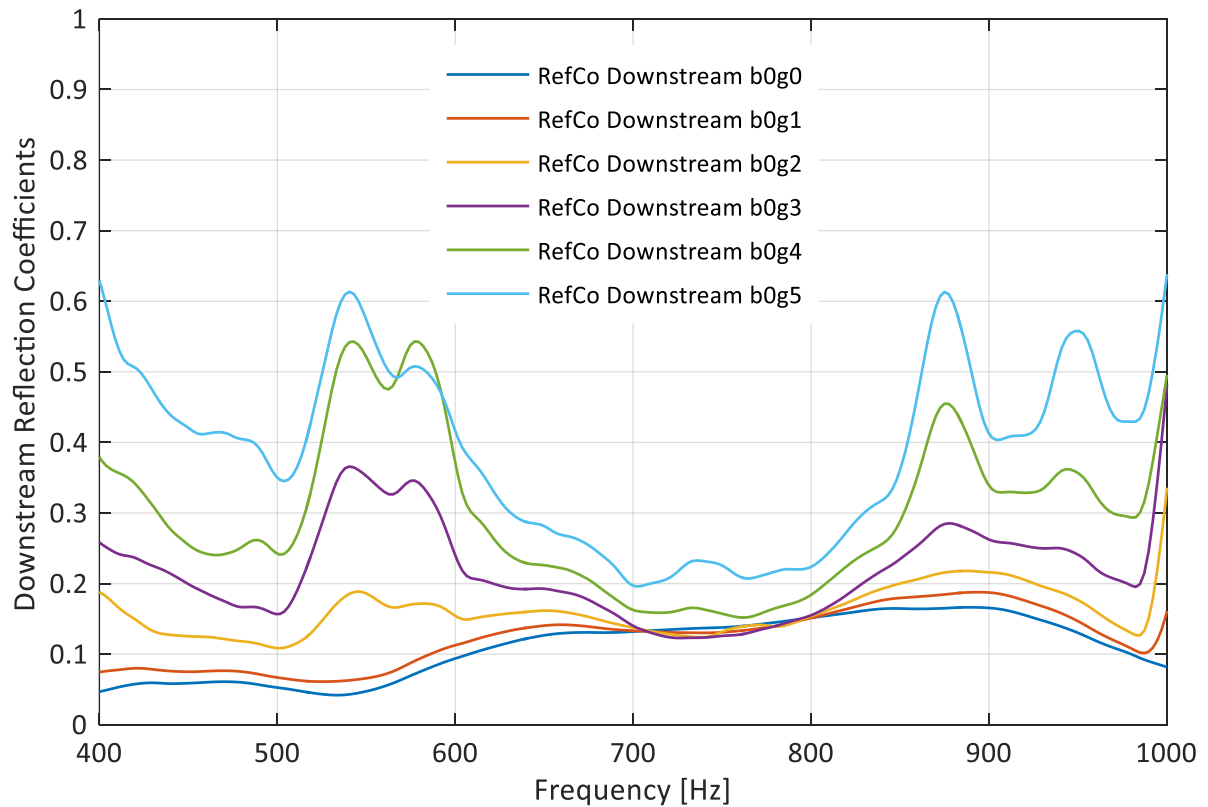
Figure 184 - Downstream Reflection Coefficients for Plate #25 (Ø2mm), with varied grazing flow

Furthermore, upon evaluation of Figure 185 it can be appreciated that the higher frequency bandwidth of duct dynamics ($850 Hz - 950 Hz$) is less prominent upstream, than downstream; indicating that part of the downstream originating dynamics, are again reflected downstream; and hence further contributing to the observed peak in transmission loss outside of the expected peak attenuation frequency of the investigated representative cases.

In section 7.6.4 the attenuation performance of the anechoic termination was investigated, and in Figure 143 it was subsequently shown that; whilst it was compliant with the expected standards, including the thresholds of absorption coefficient; as with any real world apparatus, it was not perfect. The aforementioned results are consequent to these imperfections, and testament to why it is imperative to have an innate understanding of the physical attributes of the experimental apparatus being used to investigate the attenuation performance attributes of acoustic resonators; as naivety to any intrinsic nuances, has the potential to lead to misconceptions of specific case results. Armed with the additional insights from these results however, and the prior evaluations of the representative cases, subsequent results can be confidently investigated with an aptitude to differentiate between the subtlest of acoustic resonator performance determining factors, and inherent experimental apparatus characteristics.
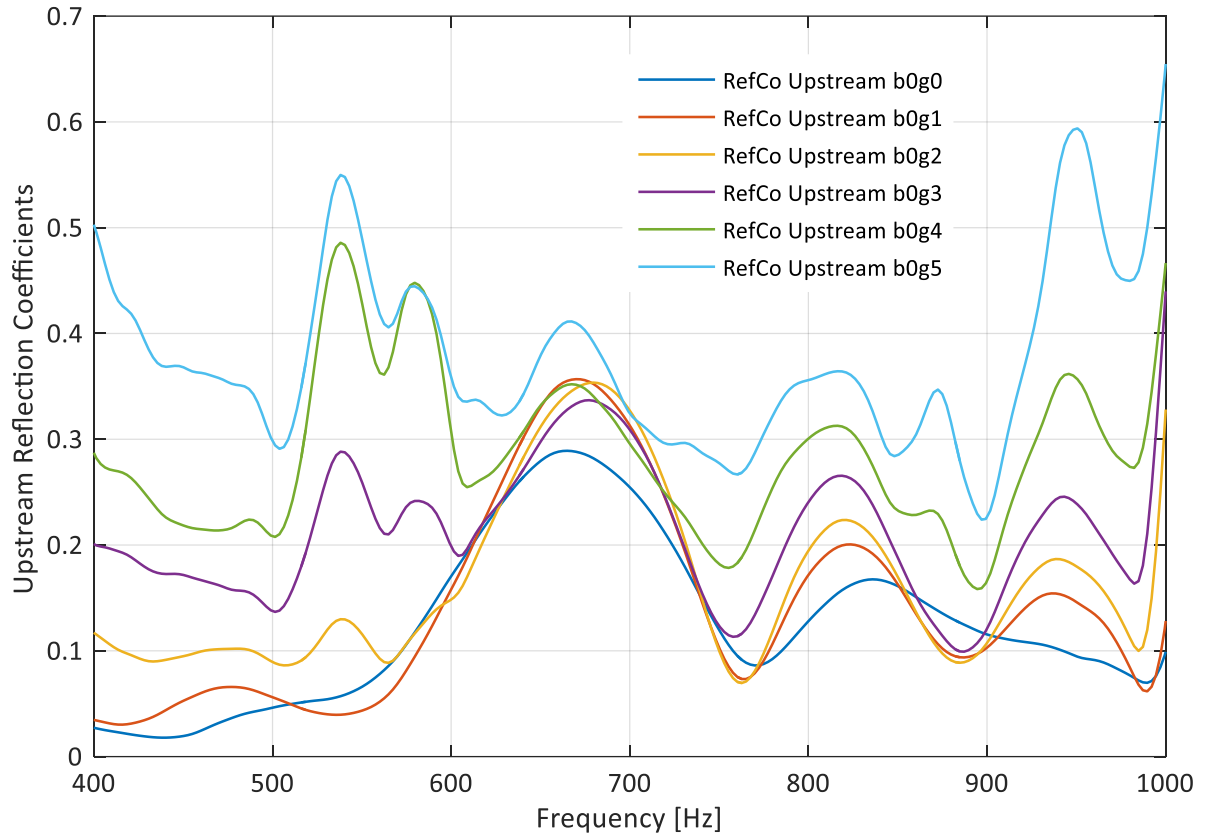
Figure 185 - Upstream Reflection Coefficients for Plate #25 (Ø2mm), with varied grazing flow

8.5 Bias Flow Effect

The impact of bias flow, i.e. a residual flow though the resonator, has been introduced in relation to resonator impedance in Section 2.3.8, and further deliberated in the context of the current state of the art of analytical modelling in CHAPTER 3 - LITERATURE REVIEW. The breadth and depth of literature reviewed and critiqued indicates that bias flow *(sometimes referred to a purge flow),* has a much stronger effect on the resonant characteristics of distributed resonators, compared with that of grazing flow (Lahiri, 2014; Dickey et al., 2001).

As with the previous section within which the impact of grazing flow on acoustic resonator attenuation performance was, by design, exclusively invested, this section will follow the measurement strategy outlined in Section 7.5.5. Similarly, a range of performance metrics will be deployed in order to gain an insight into the resultant resonator response to varied bias flow; quantified via FRF in Section 8.5.1, with additional duct derived metrics providing a holistic insight into transmission loss in Section 8.5.2; dissipation coefficient being deliberated in Section 8.5.3; and finally an equivalent appraisal of any upstream reflection nuances being evaluated in Section 8.5.4.

8.5.1   Frequency Response Function

As shown in Figure 186 and Figure 187; which correspond to the FRF magnitude and phase measured for Plate #13 respectively, with varied degrees of bias flow; unlike the equivalent grazing flow cases shown in Section 8.4.1, the immediate introduction of bias flow suppresses the observed resonant response. It can be seen that even the lowest 1%dP pressure drop across the resonator, causes a severe saturation relative to the non-flowed resonant response, and with increasing magnitude of bias flow, the FRF becomes almost linear across the frequency domain. The FRF phase shown in Figure 187, as with the previous grazing flow cases, agrees with the FRF magnitude; albeit with some anomalies evident at the highest bias flow cases, which can be likely attributed to measurement noise, as opposed to acoustic noise; this deduction should however, be validated with the subsequent duct-derived metrics.

Evaluation of the alternative representative cases of Plate #1 & #25, shown in Figure 188 and Figure 189 respectively, indicates a common trend occurring, irrespective of hole diameter and pattern. Therefore, in relation to the observed FRF measurements, it can be deduced that; the maximum resonance effect of a distributed resonator occurs in the absence of bias flow; and with the onset of bias flow the natural narrowband response of the resonator is saturated; tending towards a linear frequency response proportional to the magnitude of bias flow.
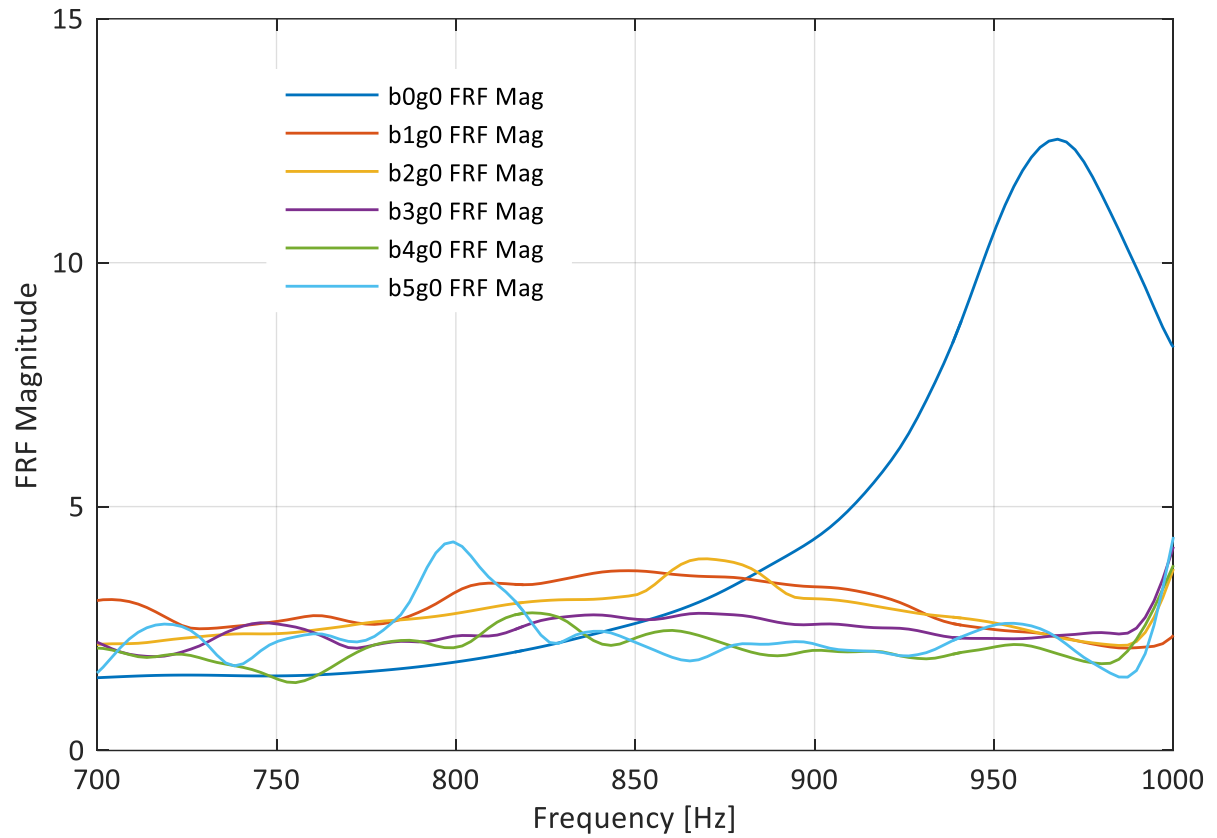
Figure 186 - FRF Magnitude for Plate #13 (Ø4mm), with varied bias flow
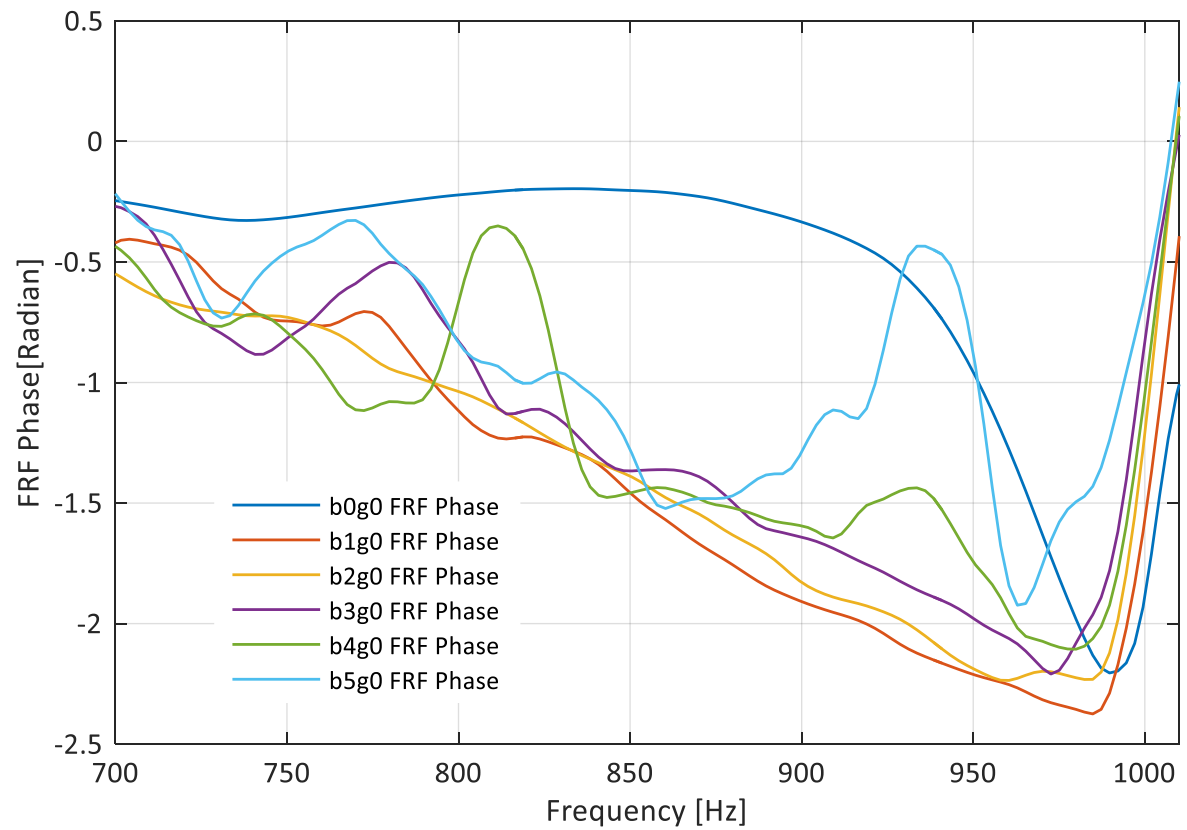
Figure 187 - FRF Phase for Plate #13 (Ø4mm), with varied bias flow
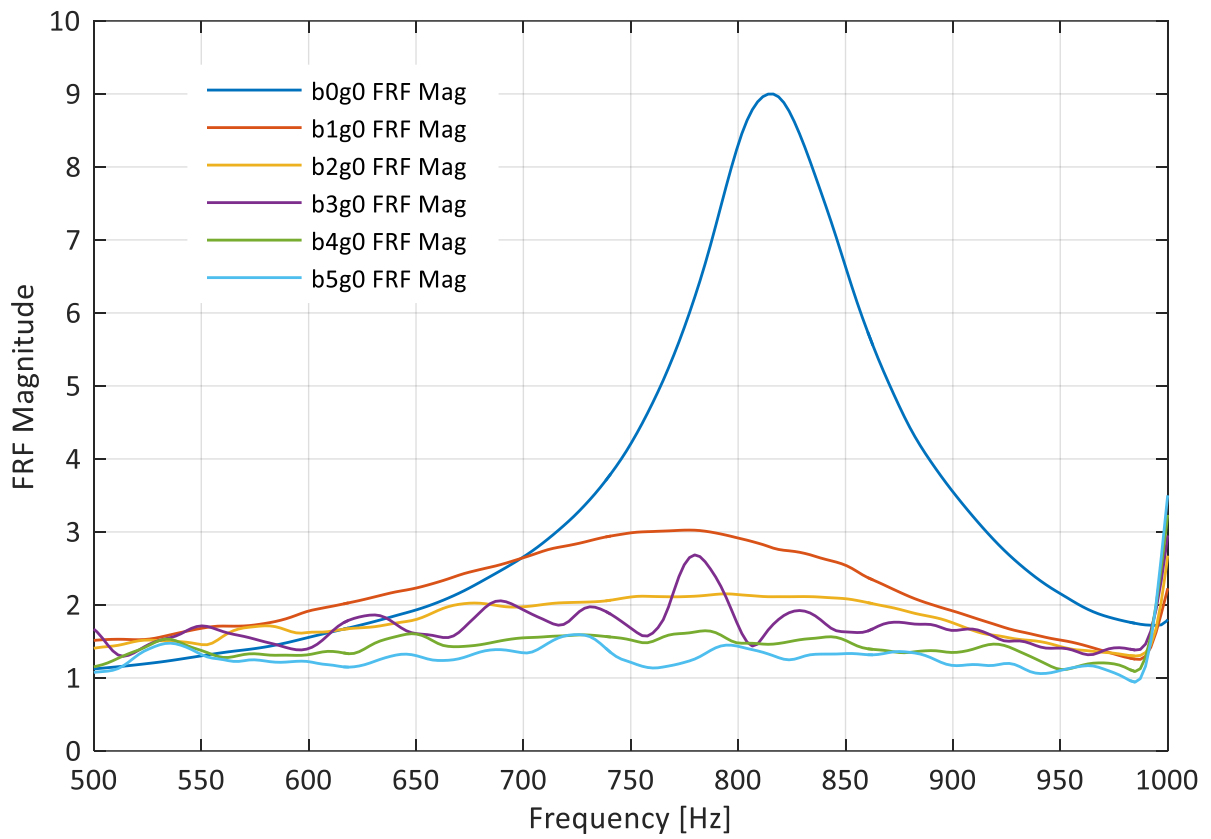
Figure 188 - FRF Magnitude for Plate #1 (Ø3mm), with varied bias flow
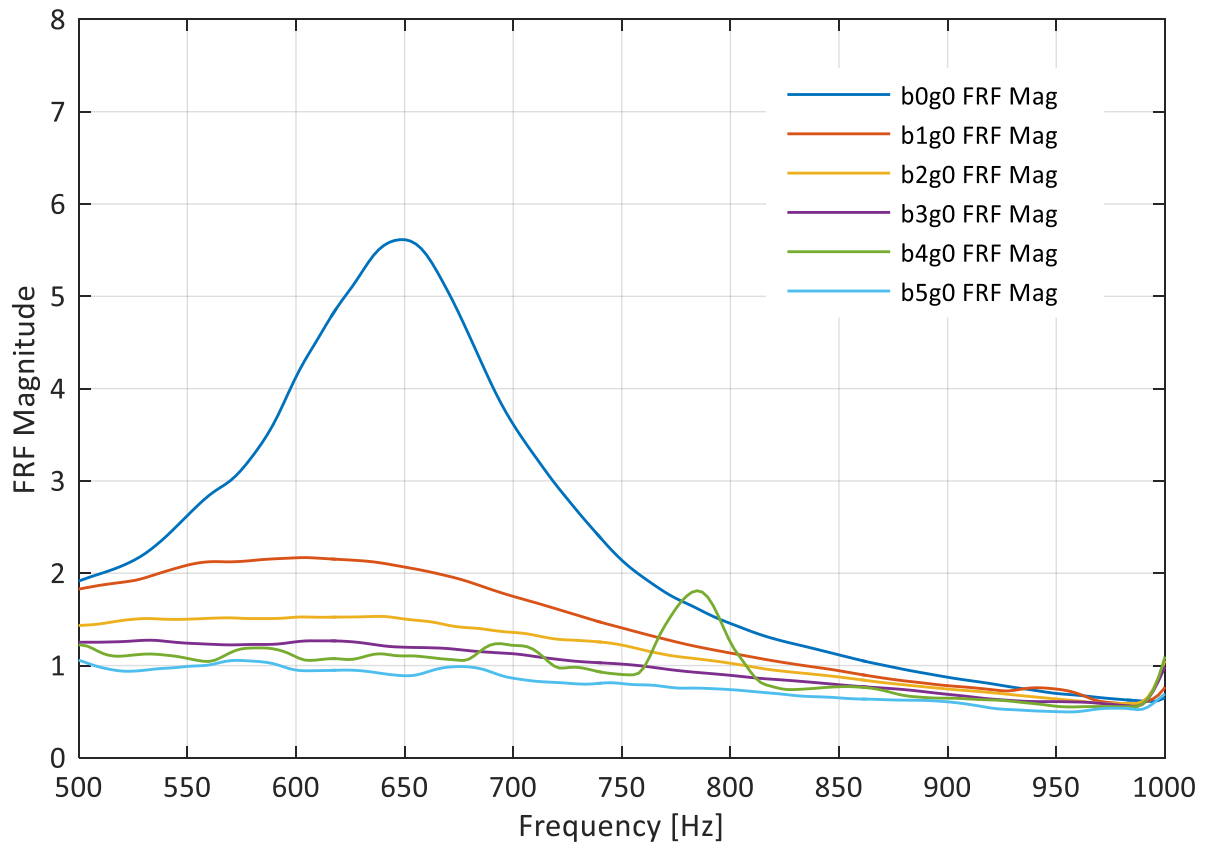
Figure 189 - FRF Magnitude for Plate #25 (Ø2mm), with varied bias flow

8.5.2 Transmission Loss

Figure 190, Figure 191 and Figure 192 show how the duct-derived transmission loss varies as a result of the measured bias flow permutations, for the representative inner Plate #13, #1 & #25 cases respectively. From these three investigated cases, it is evident that; as previously indicated by the FRF metric; introducing bias flow reduces peak sound attenuation effect significantly from the onset, and increasingly so with an increase in magnitude. Unlike the corresponding grazing flow cases, there is no evidence of an initial enhancement of resonant effects, which further enforces the deduction that bias flow driven by a pressure difference across the resonator, has a more significant effect of the inherent attenuation properties of the resonator, than a grazing flow past the resonator.

It is important to note however, that the distributed resonator cases investigated here within, are distinctly different from the perforated liners often utilised in the context of combustors; where, as discussed in Section 1.1.3, the need to provide a bias flow is driven primarily by the requirement for the provision of combustor wall cooling. This duality in functionality results in a trade of between; the amount of cooling air delivered to the combustor via the resonator; and the targeted noise absorption capabilities of the perforated liner.

In order to support such deliberations, Eldredge (2003) investigated the optimum bias flow for perforated liners in relation to their noise absorption effects, and derived the approximation seen in Equation *[174]*.

$$\left(\frac{M_{ac}}{\sigma}\right)_{opt} = \frac{CL/S}{2\sqrt{2}} \qquad\qquad \textit{[174]}$$

Where: σ is perforation ratio of the liner, C and L are the circumferential and axial length of the liner respectively, and S is cross section area of the main duct. Although Eldredge derived this formula in relation to perforated liners; which typically feature much larger plate areas, and more often surround the full circumferential area of the acoustically relevant domain; the application of Equation *[174]* in the context of these investigated cases, presents an opportunity to estimate the potential significance of the measured aperture flow velocities, on the observed attenuation characteristics. The optimum bias flow aperture velocities arrived at using Equation *[174]* for the corresponding inner Plate #13, #1 & #25 test cases are respectively $2.2m/s$, $1.3m/s$ and $0.6m/s$. These calculated optimum bias flow velocities are much lower than the minimum measured cases of 1%dP pressure driven bias flow of $5.6m/s < U_i < 5.8m/s$. In consideration of this evaluation, it can be appreciated that for the distributed resonator investigated; the lowest bias flow measured is comparatively large, relative to

the optimum value for noise attenuation; and as such it is expected that the observed early onset of saturation due to bias flow, is as prevalent as observed. Equally if the experimental resonator exhibited larger axial and circumferential dimensions, it could be expected that the impact of an equivalent bias flow, would not be so dominant on the resultant peak attenuation magnitude.

Whilst it can be seen that the presence of bias flow unanimously suppresses the maximum attenuation magnitude near the resonant frequency; the observed peak transmission loss frequency is markedly lower following the introduction of bias flow through the resonator. This observation cannot be attributed as a consequence of increased effective plate thickness; as bias flow is known to actually tend to reduce the effective length of the acoustic neck; but rather can be considered as a result of the open outer plate holes, and their corresponding porosity which facilitates the proportional introduction of bias flow; resulting in an effective enlargement of the cavity volume in such circumstances. Consequently, the larger the permeability of the outer liner, the more obvious this shift in frequency will be, for example: upon evaluation of the smallest permeability case of Plate #25, as shown in Figure 192; the observed shift in frequency is fairly insignificant; as opposed to the maximum diameter case of Plate #13, where over a 100Hz frequency shift can be observed in Figure 190.
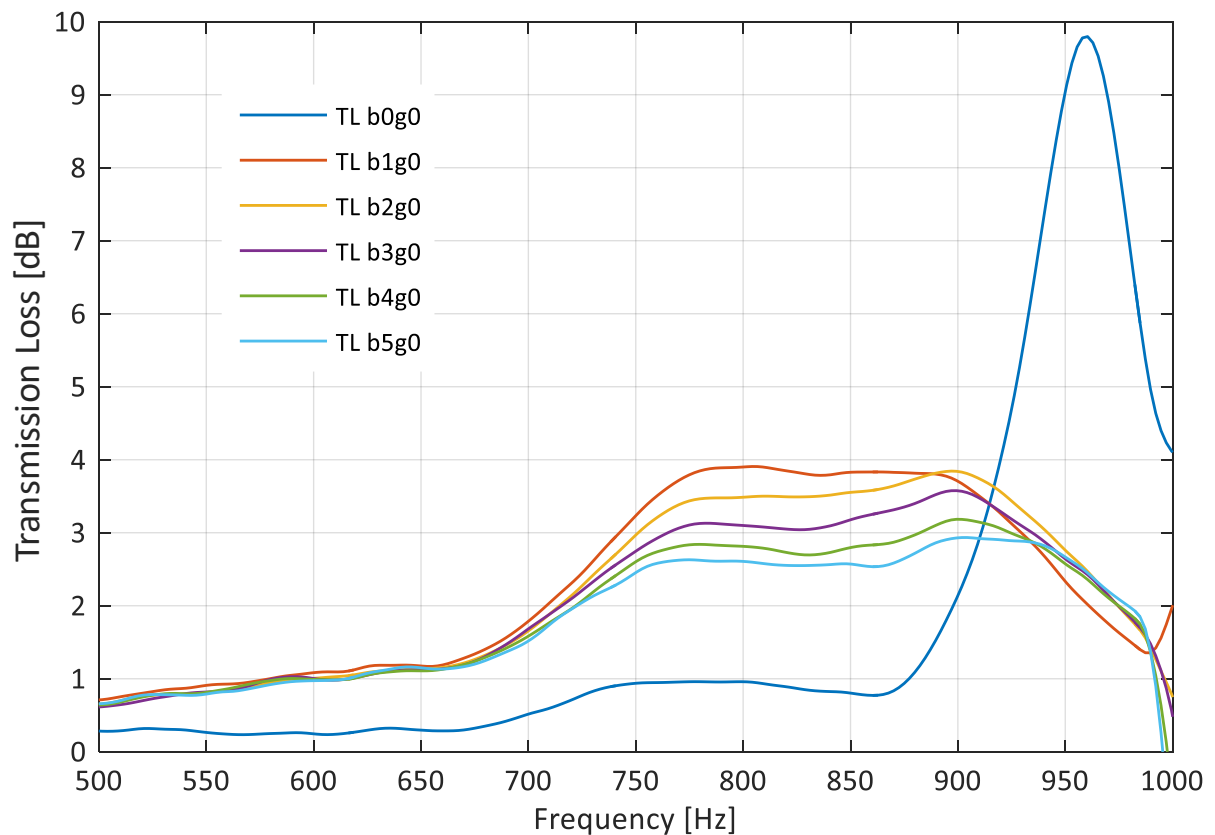
Figure 190 - Transmission Loss for Plate #13 (Ø4mm), with varied bias flow
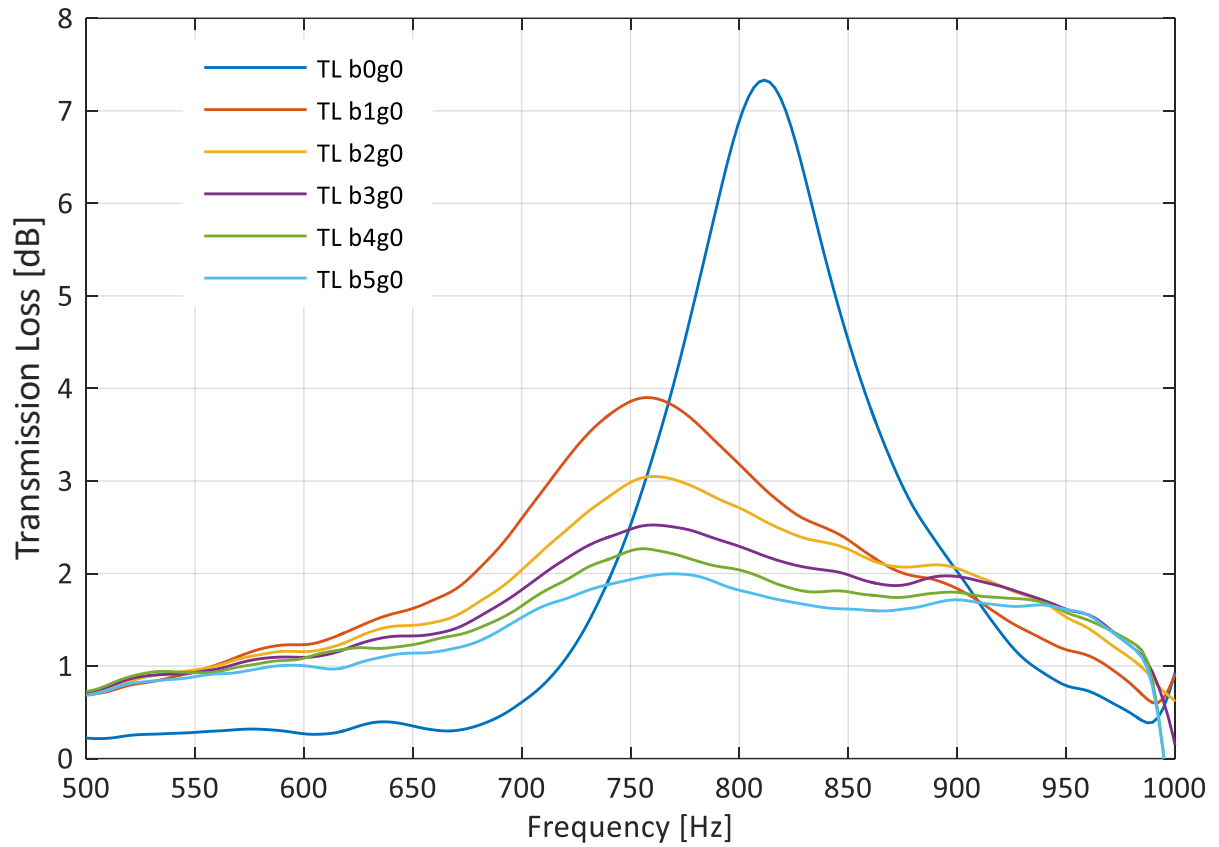
Figure 191 - Transmission Loss for Plate #1 (Ø3mm), with varied bias flow
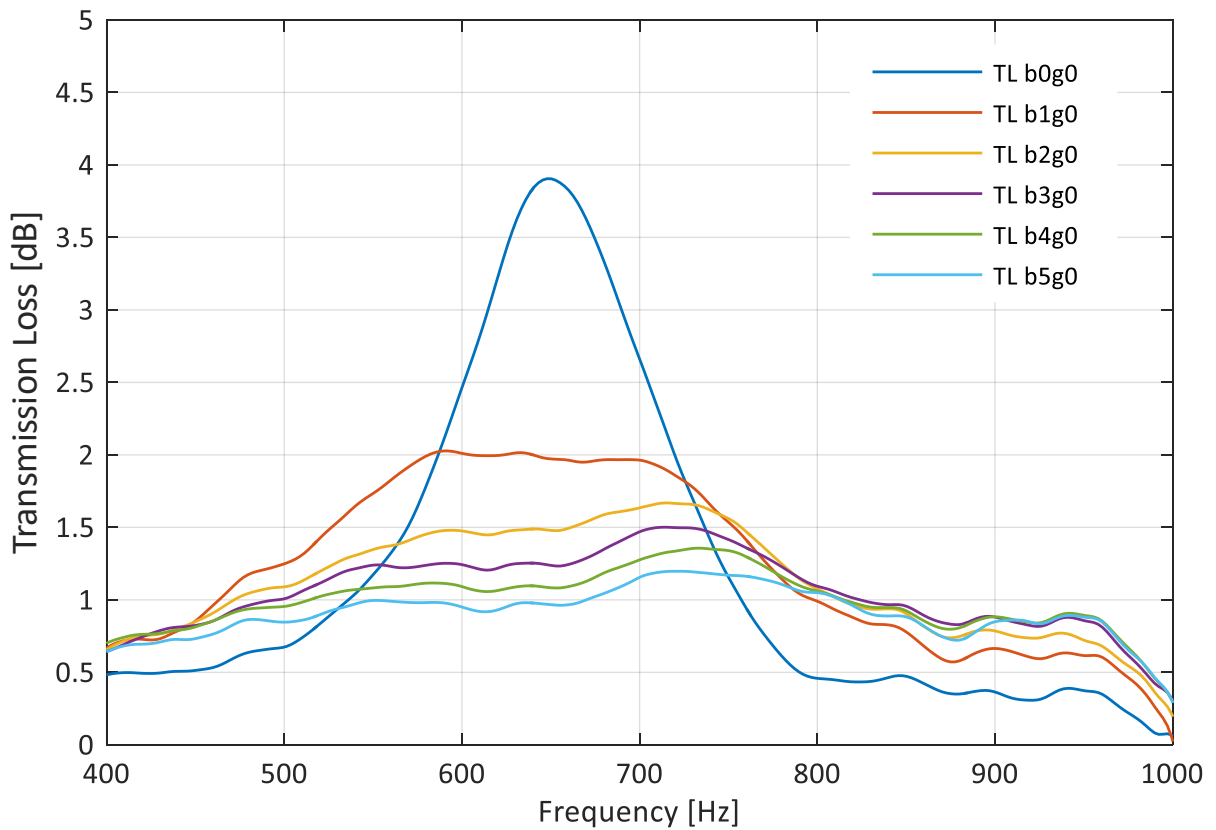
Figure 192 - Transmission Loss for Plate #25 (Ø2mm), with varied bias flow

8.5.3 Dissipation Coefficient

The measured Dissipation Coefficients of Plate #13, Plate #1 & Plate #25, under the equivalent bias flow regimes as according to Table 39, are shown in Figure 193, Figure 194 & Figure 195 respectively. Comparison between the corresponding plots of dissipation coefficient and the previously evaluated transmission loss, are coherent and supportive of common conclusions.

Consequently, it can be confidently concluded that, introducing bias flow will suppress the peak resonance effect significantly however, the absorption bandwidth can be observed to be increased in the presence of bias flow. The peak magnitude of dissipation coefficient is immediately reduced to approximately half of that in the absence of flow; and a plateau in magnitude can be observed at frequencies far from the resonant frequency, indicating a broadband attenuation effect, which is independent of resonant frequency. A general trend can be observed, whereby the larger the corresponding bias flow velocity is, the greater the reduction is dissipation magnitude is, relative to the no-flow case.

As with the equivalent grazing flow cases evaluated in Section 8.4.3, the dissipation coefficient metric provides an additional insight into overall attenuation characteristics which can be attributed to reflection back upstream of the measurement section; albeit the prevalence of upstream reflections emanating from bias flow phenomena is much less prominent than observed under closed resonator conditions.
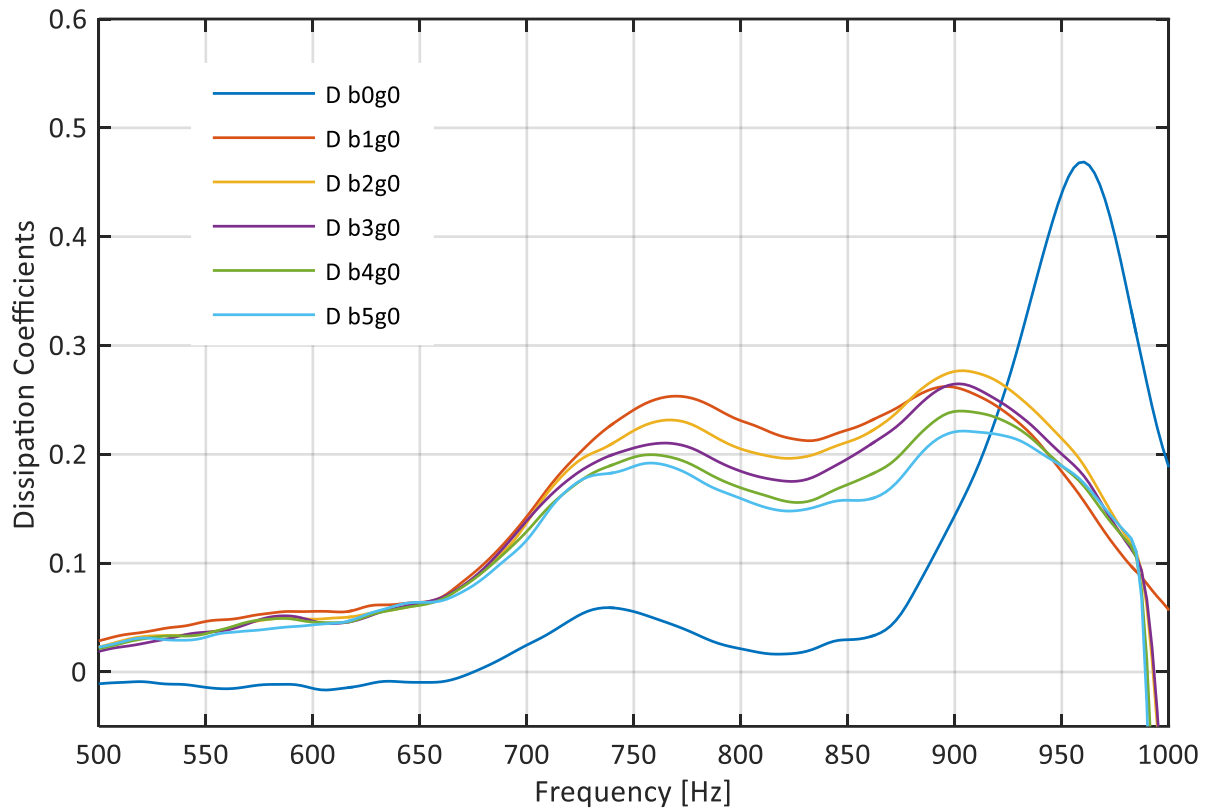
Figure 193 - Dissipation Coefficients for Plate #13 (Ø4mm), with varied bias flow
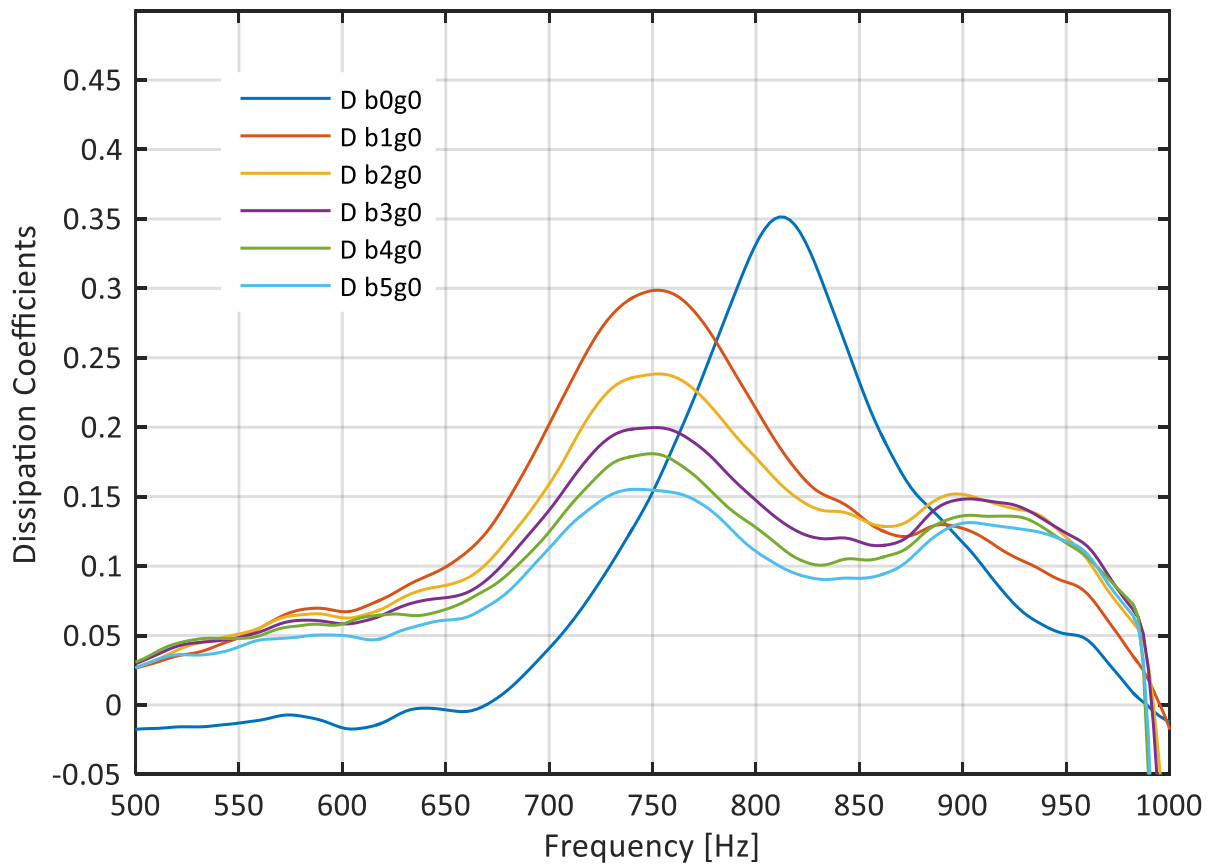
Figure 194 - Dissipation Coefficients for Plate #1 (Ø3mm), with varied bias flow
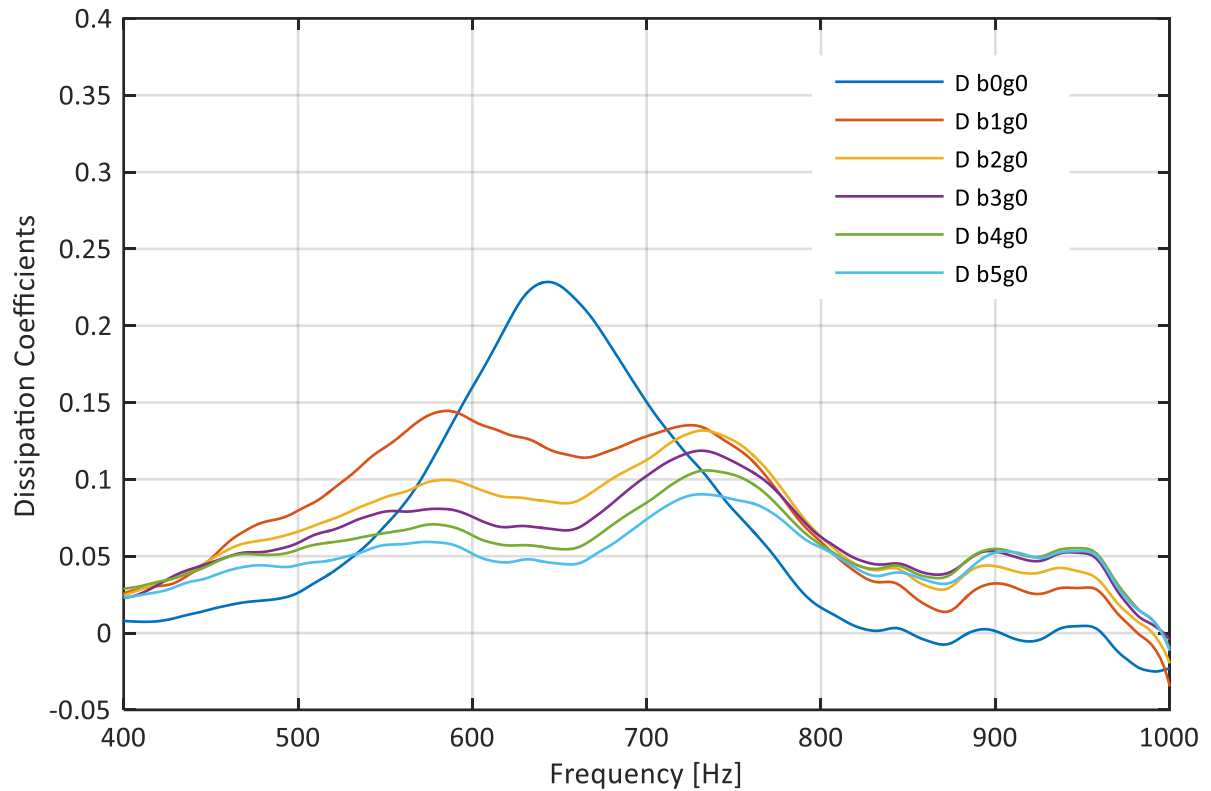
Figure 195 - Dissipation Coefficients for Plate #25 (Ø2mm), with varied bias flow

8.5.4   Upstream Reflection Coefficient

As shown in Section 8.4.4, evaluation of the upstream reflection coefficient can provide invaluable insight into any residual reflections either; originating from, or reflected by, the measurement section; which subsequently travel back upstream in the direction of the acoustic source. Figure 196, Figure 197 & Figure 198 indicate that for the representative cases investigated, the introduction of bias flow reduces the magnitude of noise reflected from the measurement section upstream; which therefore results in a greater proportion of acoustic energy entering the measurement section and traveling downstream. The transmission loss metrics shown in Section 8.5.2 confirmed that from the onset of introduction of bias flow, the peak attenuation magnitude was immediately decreased significantly, and a broadening of attenuation bandwidth could be observed. Cross evaluation with the dissipation coefficient, however, shows that there is not an equivalent increase in upstream reflections. This coherence between metrics indicates that bias flow shifts the primary attenuation mechanism from that of a reactive resonant system, towards a more frequency independent dissipative regime. As with previous cases, there are some frequencies beyond the corresponding resonant frequencies, where the introduction of additional flow generated noise, results in an increased upstream reflection from the measurement section; albeit these reflections are not so prevalent as those observed with grazing flow and acoustic excitation only, and also exhibit a more broadband characteristic response.
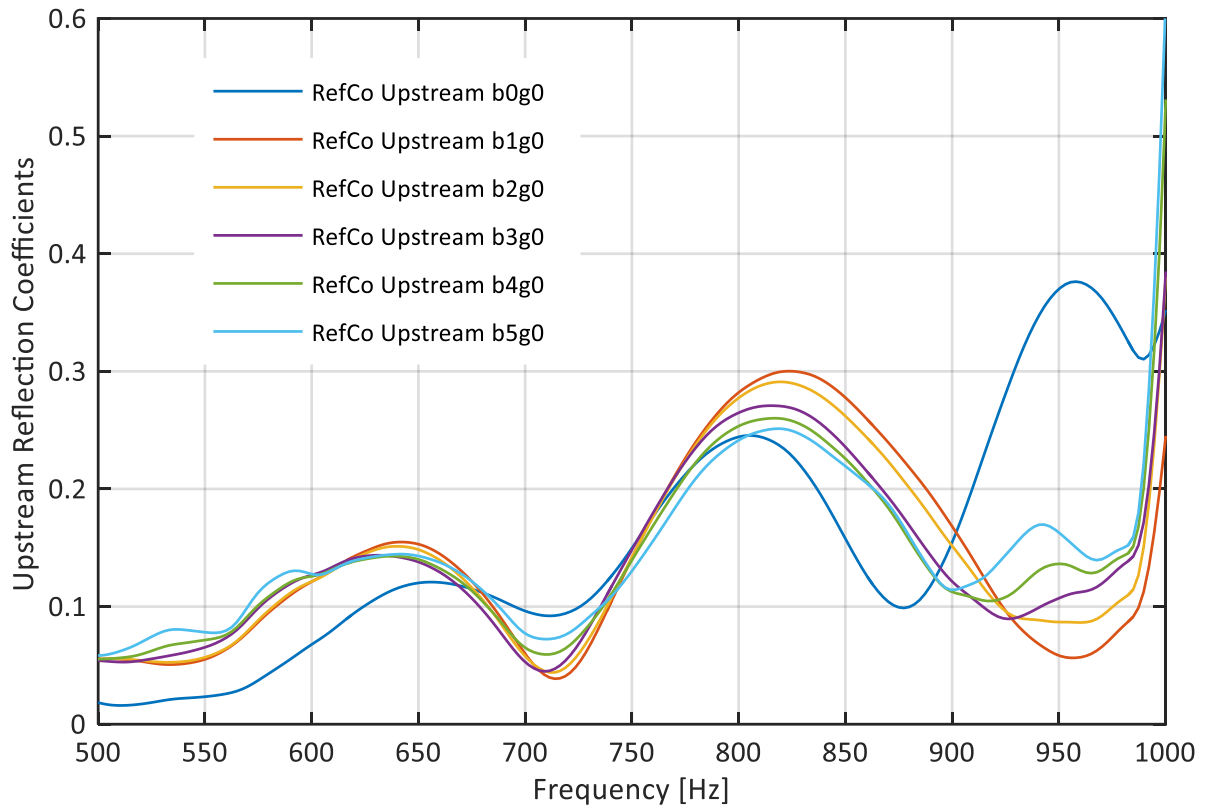
Figure 196 - Upstream Reflection Coefficients for Plate #13 (Ø4mm), with varied bias flow
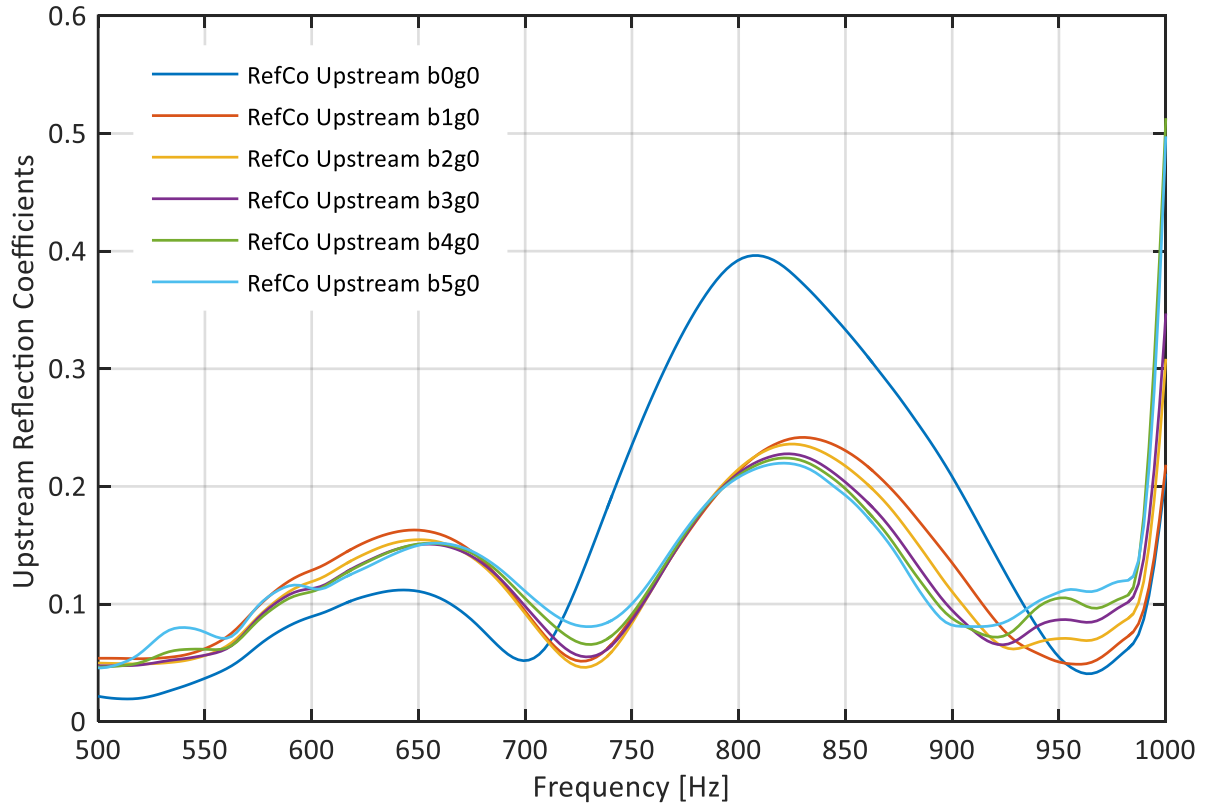
Figure 197 - Upstream Reflection Coefficients for Plate #1 (Ø3mm), with varied bias flow
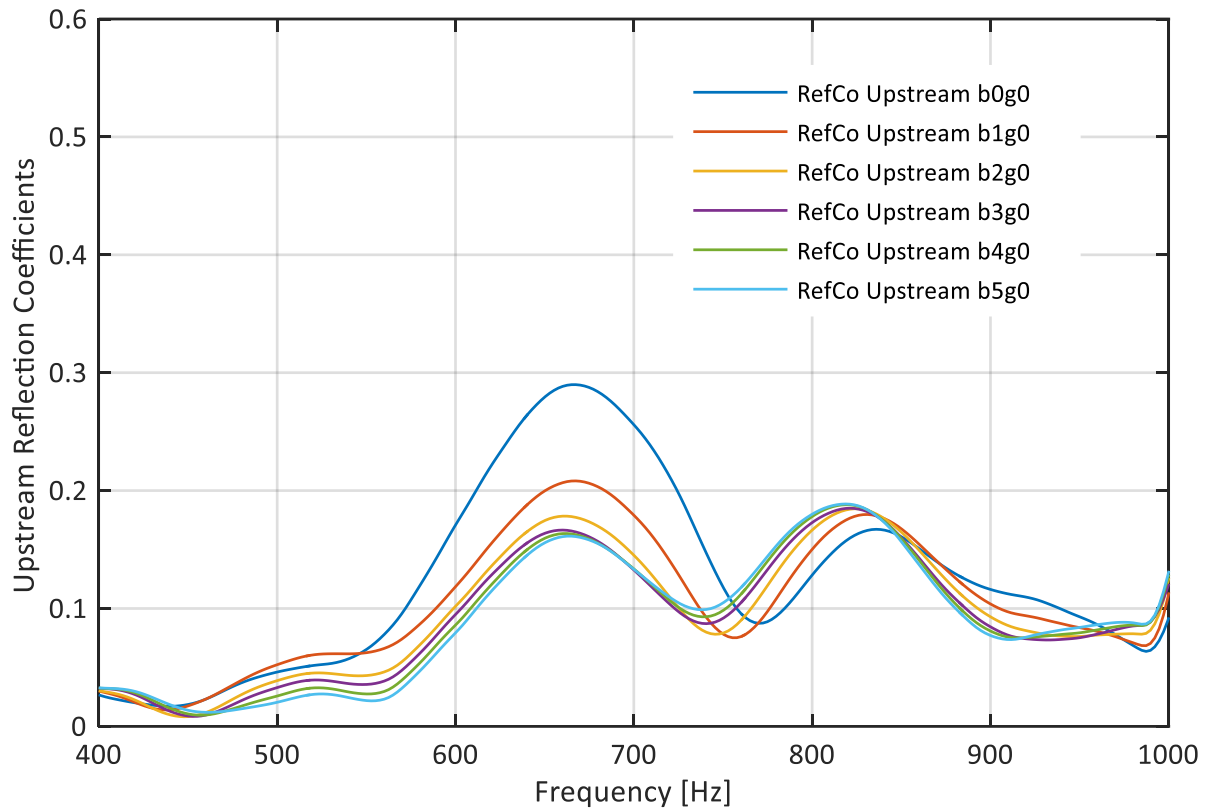
Figure 198 - Upstream Reflection Coefficients for Plate #25 (Ø2mm), with varied bias flow

8.6   Combined Grazing & Bias Flow Effect

In the previous sections the impact of varied grazing and bias flow magnitude on distributed resonators noise attenuation characteristics have been investigated and evaluated independently. In this section, the effects of simultaneous grazing and bias flow are investigated through an equivalent investigative strategy; whereby only three representative inner plates will be presented for brevity; allowing the evaluation of flow factors across the full measurement spectrum investigated. Correspondingly, Plate #1, #13 & #25 are chosen for subsequent investigation, and both transmission loss and dissipation coefficient performance metrics are evaluated for each case; with results from a 1%dP bias flow presented in Section 8.6.1; a 3%dP being presented in Section 8.6.2; and an summary of observed flow factors deliberated in Section 8.6.3.

8.6.1   1%dP Bias Flow and Varying Grazing Flows

The measured acoustic response under a constant 1%dP bias flow, and varied magnitude of grazing flow, is shown for the representative Plate #13, Plate #1 & Plate #25, in terms of both transmission loss (Figure 199, Figure 201, and Figure 203 respectively), and dissipation coefficient (Figure 200, Figure 202, and Figure 204 respectively).

Evaluation of these representative test cases indicates that the bias flow drives the primary acoustic response, and the effects of increasing gazing flow magnitude, are similar to the independent findings of grazing flow construed in Section 8.4. The effect of increasing grazing flow magnitude in the presence of bias flow retains a consequential and proportional reduction in attenuation around the peak attenuation frequency, and similar artefacts can be observed at frequencies outside of the case specific resonant response; which can be equally attributed to the aforementioned increased reflections within the measurement rig deliberated in Section 8.4. It is noteworthy however, that the observed shifts in the frequency domain attributed to an increase in grazing flow magnitude, are not so prominent as observed in the independent grazing flow investigations, which further enforces the conclusion that the bias flow dominates the resonant characteristics of the distributed resonator. Furthermore, it can be seen that; unlike the independent grazing flow investigations; there are no observed instances of a small degree of grazing flow increasing the magnitude of peak transmission loss or dissipation coefficient. It is evident however, that with combined flow the acoustic attenuation characteristics become significantly more intricate, and for cases with a naturally low peak attenuation magnitude, the additional flow factors can result in additional peaks and fluctuations which can reduce, distract, and even dominate the natural resonant response of the acoustic system.
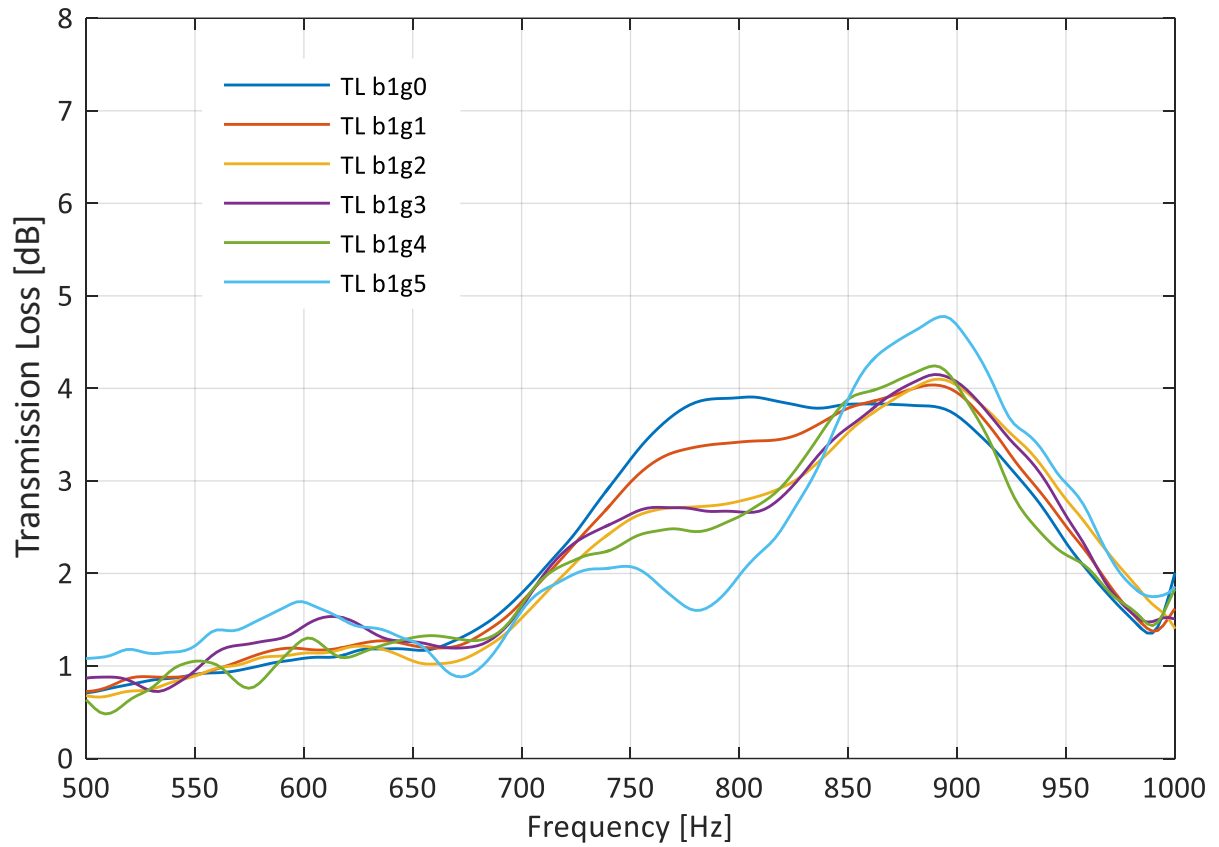
Figure 199 - Transmission Loss of Plate #13 (Ø4mm); 1%dP bias, and varied grazing flow
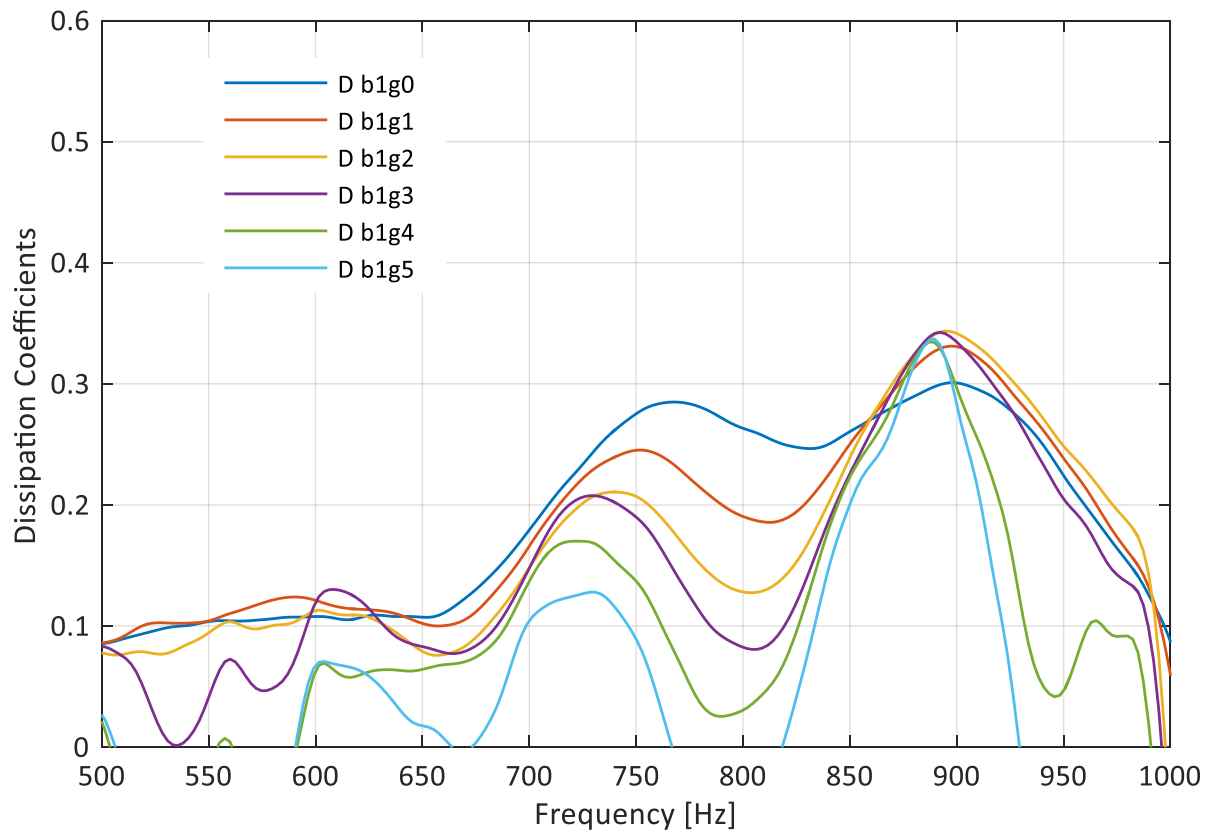
Figure 200 - Dissipation Coefficients of Plate #13 (Ø4mm); 1%dP bias, and varied grazing flow
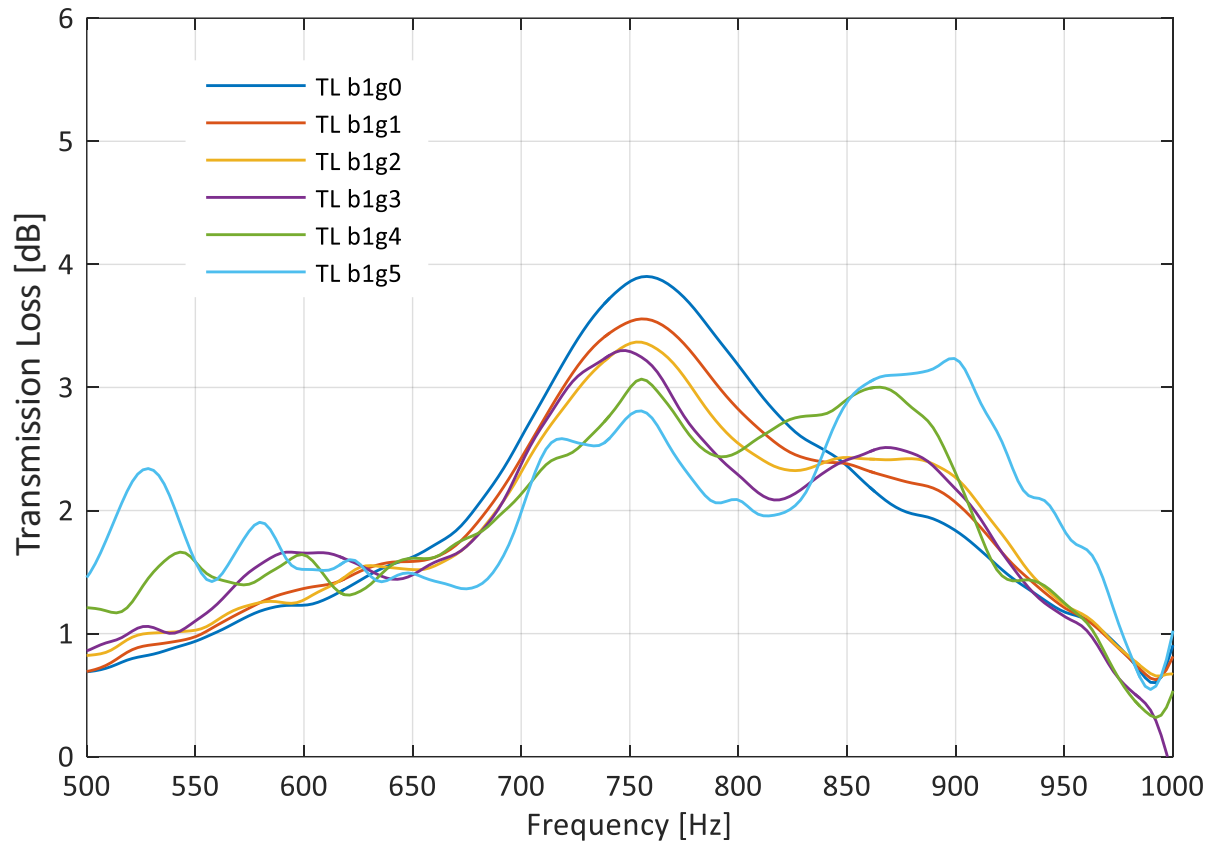
Figure 201 - Transmission Loss of Plate #1 (Ø3mm); 1%dP bias, and varied grazing flow
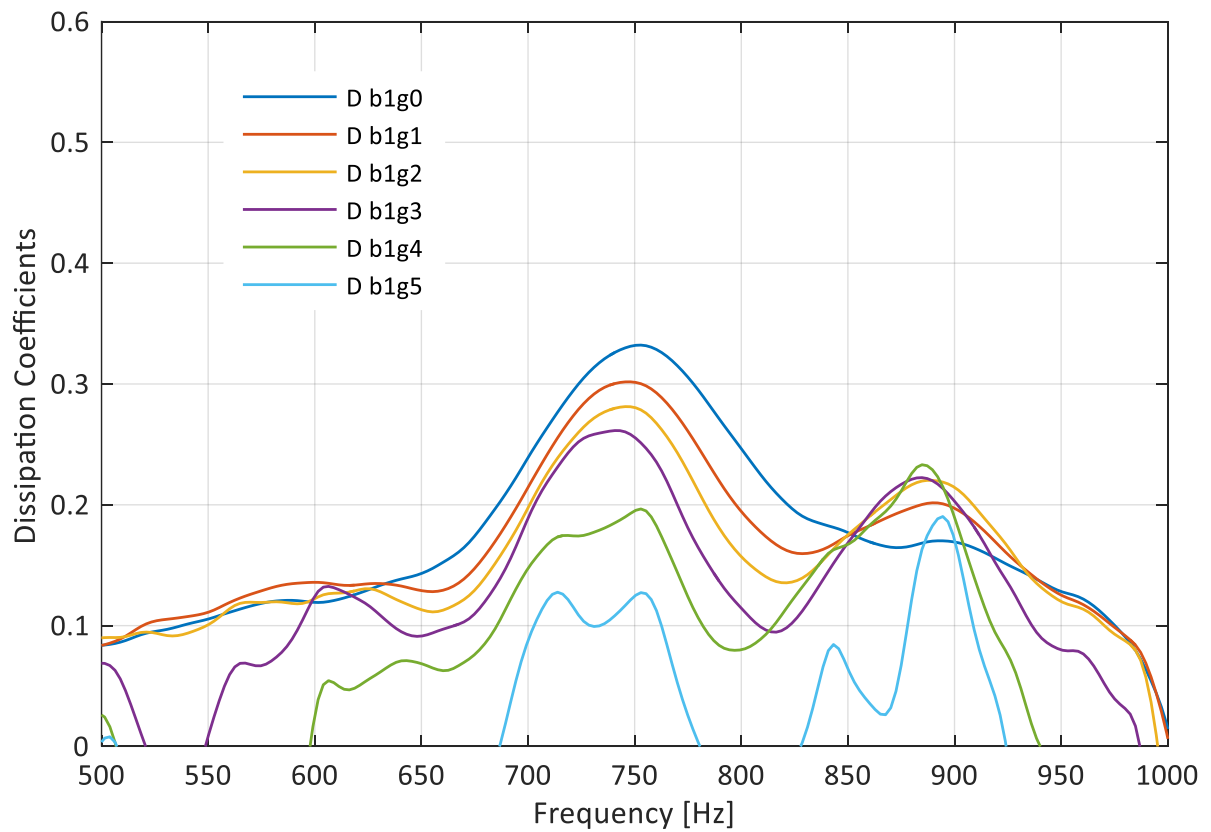
Figure 202 - Dissipation Coefficients of Plate #1 (Ø3mm); 1%dP bias, and varied grazing flow
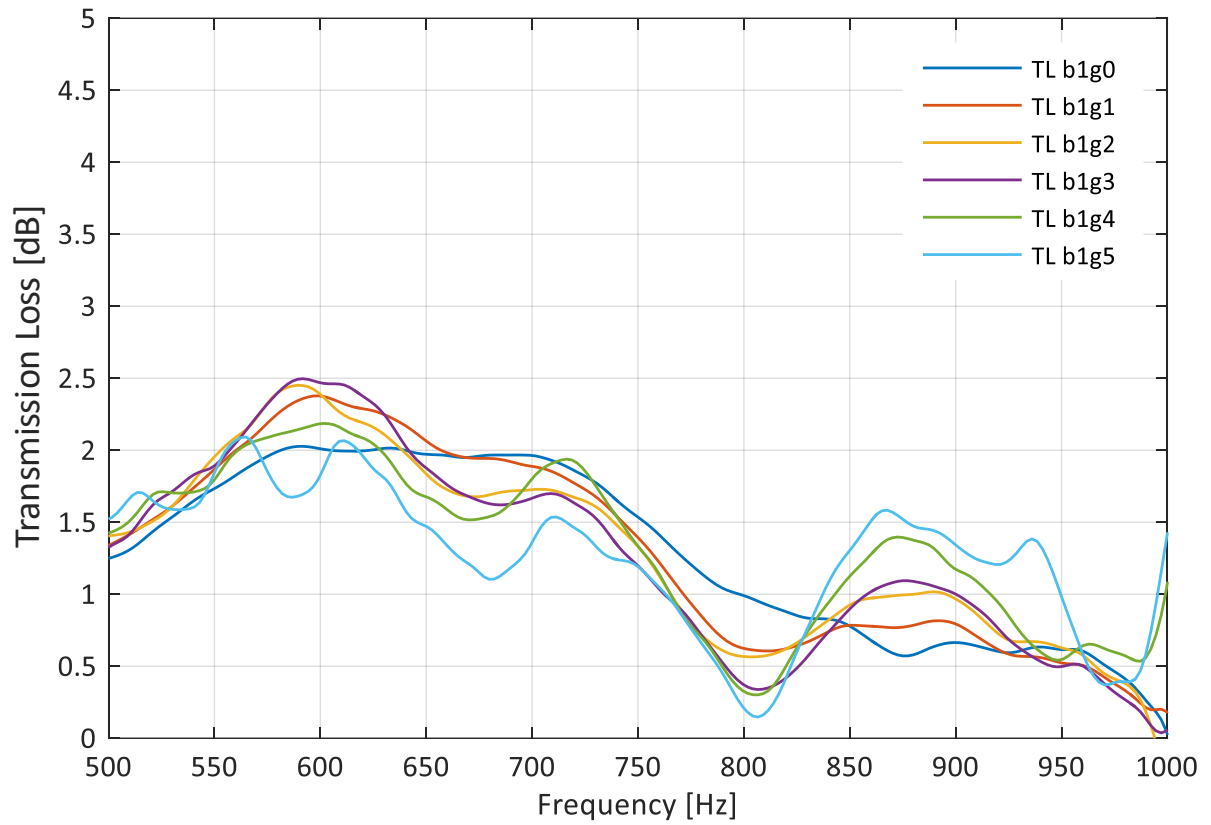
Figure 203 - Transmission Loss of Plate #25 (Ø2mm); 1%dP bias, and varied grazing flow
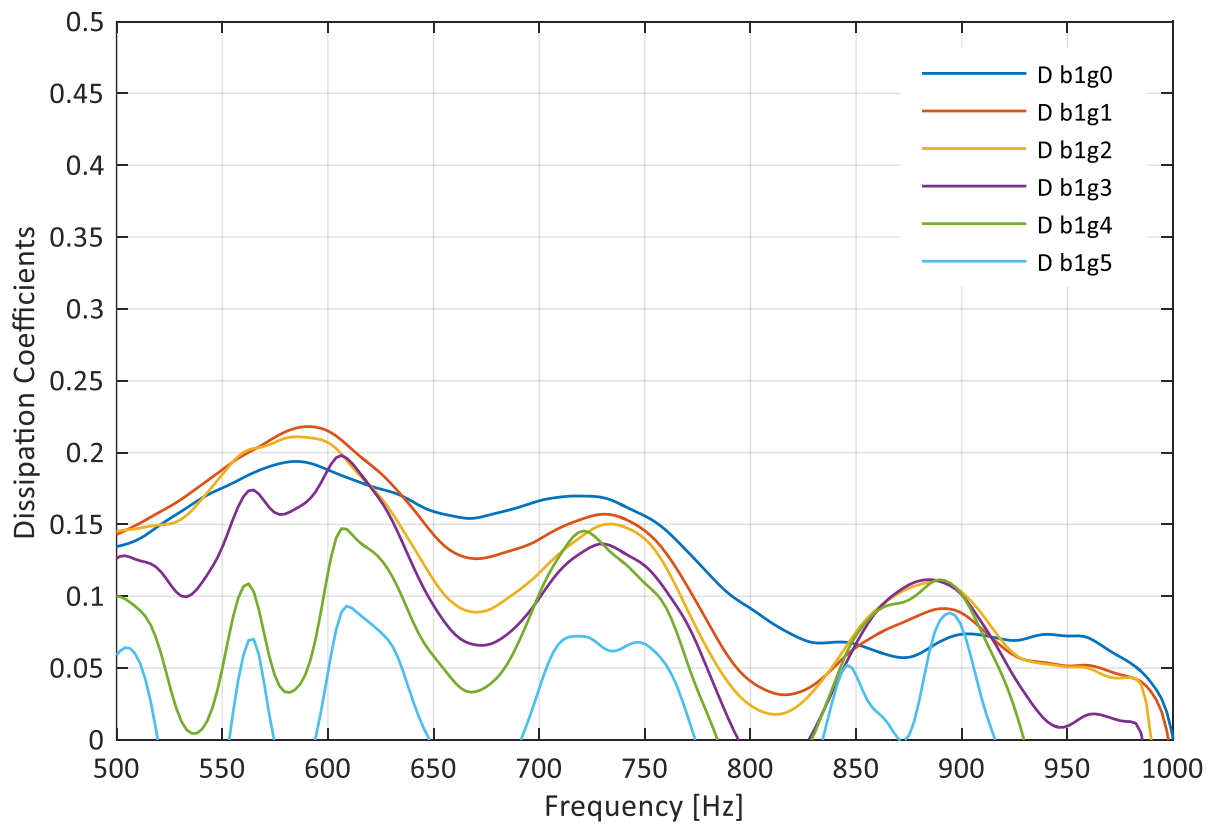
Figure 204 - Dissipation Coefficients of Plate #25 (Ø2mm); 1%dP bias, and varied grazing flow

8.6.2 3%dP Bias Flow and Varying Grazing Flows

As with the previous section, the measured acoustic response under a constant 3%dP bias flow, and varied magnitude of grazing flow, is shown for the representative Plate #13, Plate #1 & Plate #25, in terms of both transmission loss (Figure 205, Figure 207, and Figure 209 respectively), and dissipation coefficient (Figure 206, Figure 208, and Figure 210 respectively). The increased bias flow magnitude of 3%dP was shown in Section 8.5 to result in a reduced peak attenuation magnitude, and a broadening of the frequency domain of attenuation observed; a conclusion which is coherent with the observations here within, when comparing the respective transition from 1%dP, to 3%dP combined flow investigations. Similarly, it can be seen that the effect of increasing grazing flow in the presence of a 3%dP bias flow reduces the peak attenuation magnitude, albeit to a lesser extent. Equivalent secondary peaks can also be seen to result from increasing grazing flow magnitude, which can equally be attributed to altered anechoic characteristics of the measurement rig due to grazing flow, increased reflections within the measurement section, and additional flow generated noise. It can therefore be concluded that, under combined flow conditions, bias dominates grazing flow; and becomes the defining characteristic of the acoustic response of the distributed resonator, which tends towards a primarily dissipative regime under high magnitudes of bias flow.
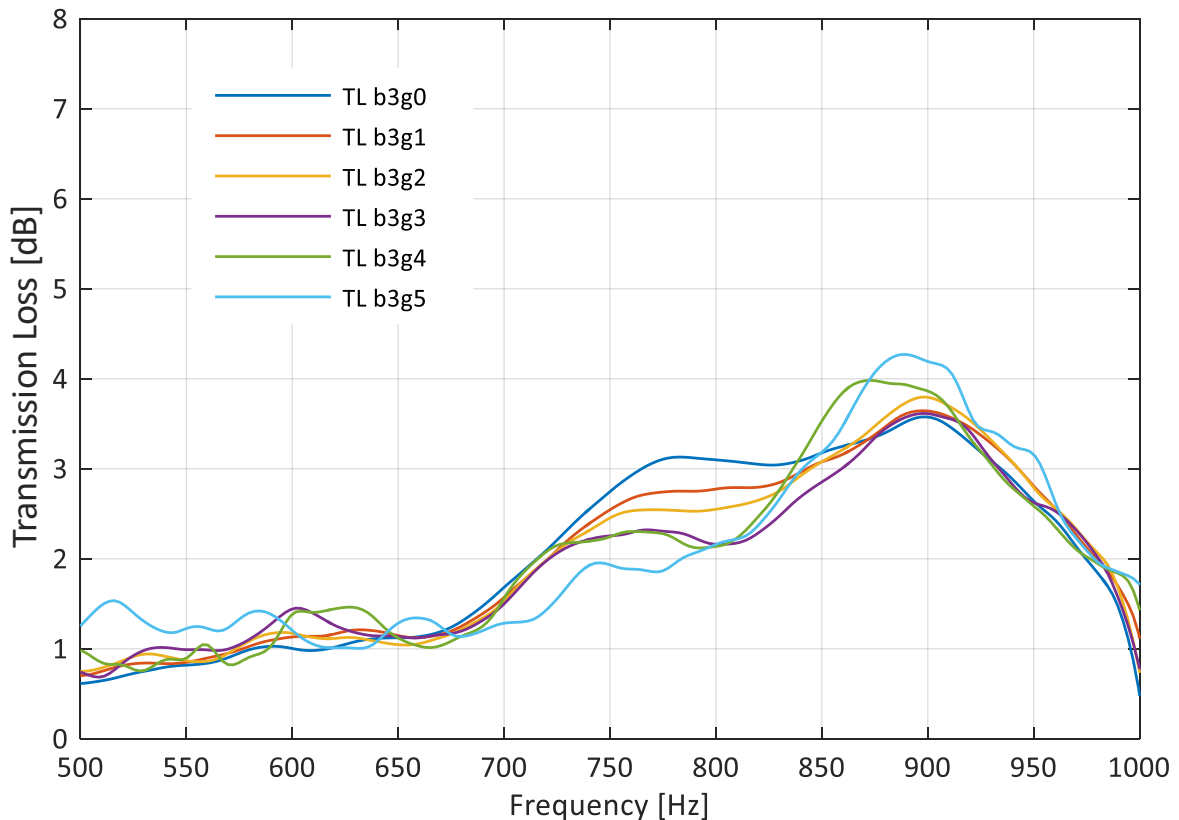
Figure 205 - Transmission Loss of Plate #13 (Ø4mm); 3%dP bias, and varied grazing flow
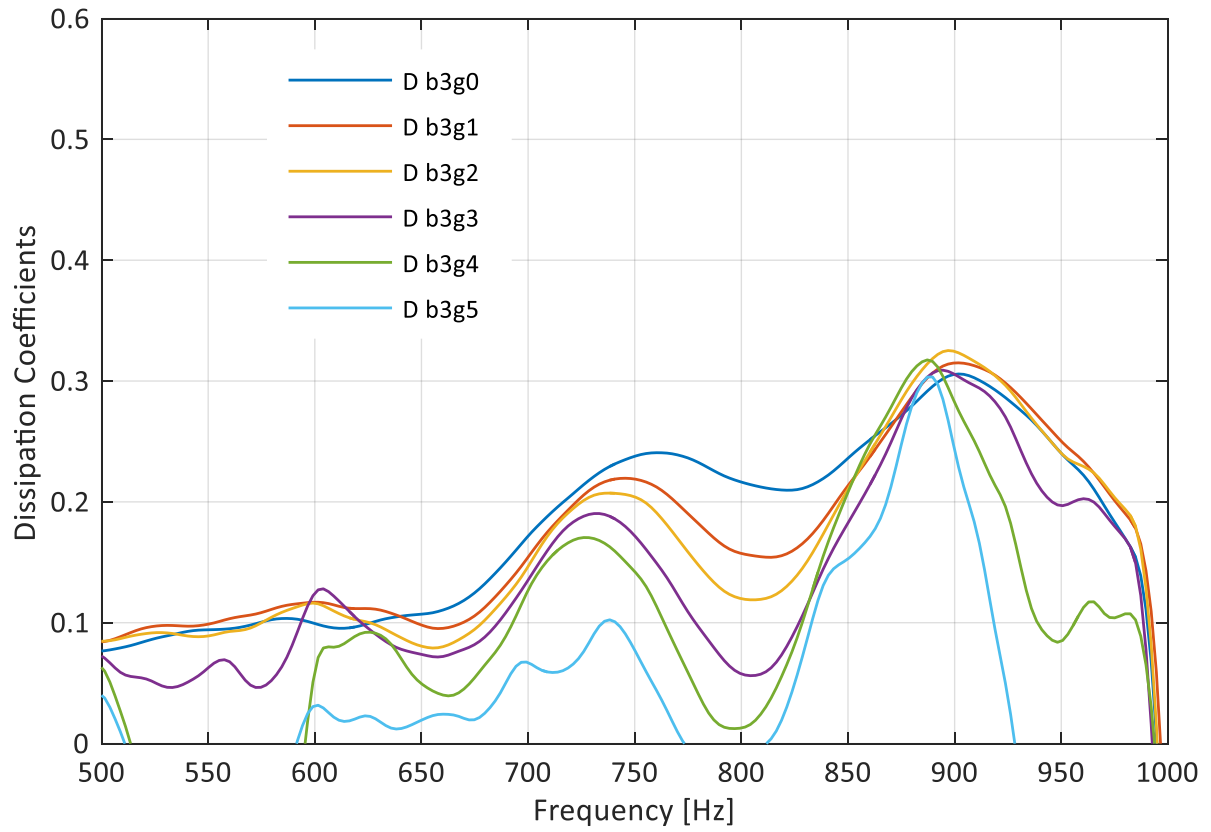
Figure 206 - Dissipation Coefficients of Plate #13 (Ø4mm); 3%dP bias, and varied grazing flow
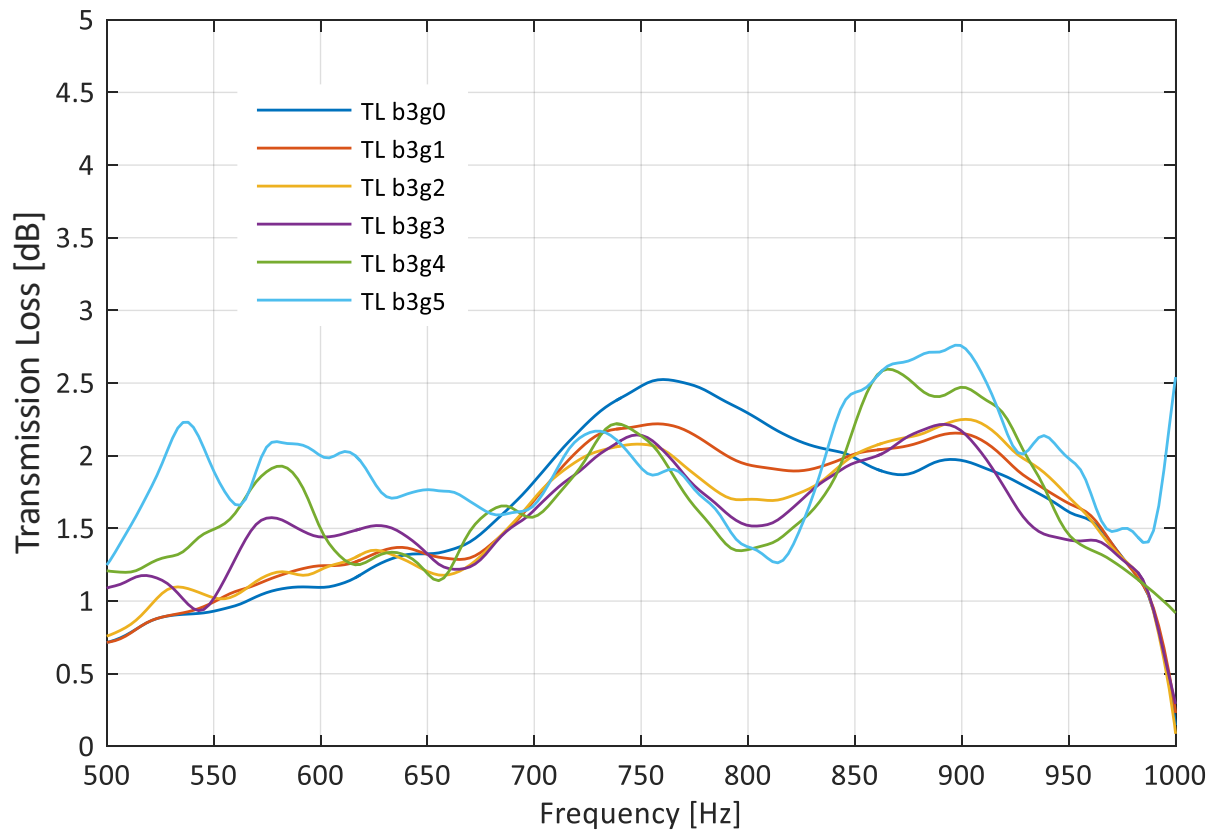
Figure 207 - Transmission Loss of Plate #1 (Ø3mm); 3%dP bias, and varied grazing flow
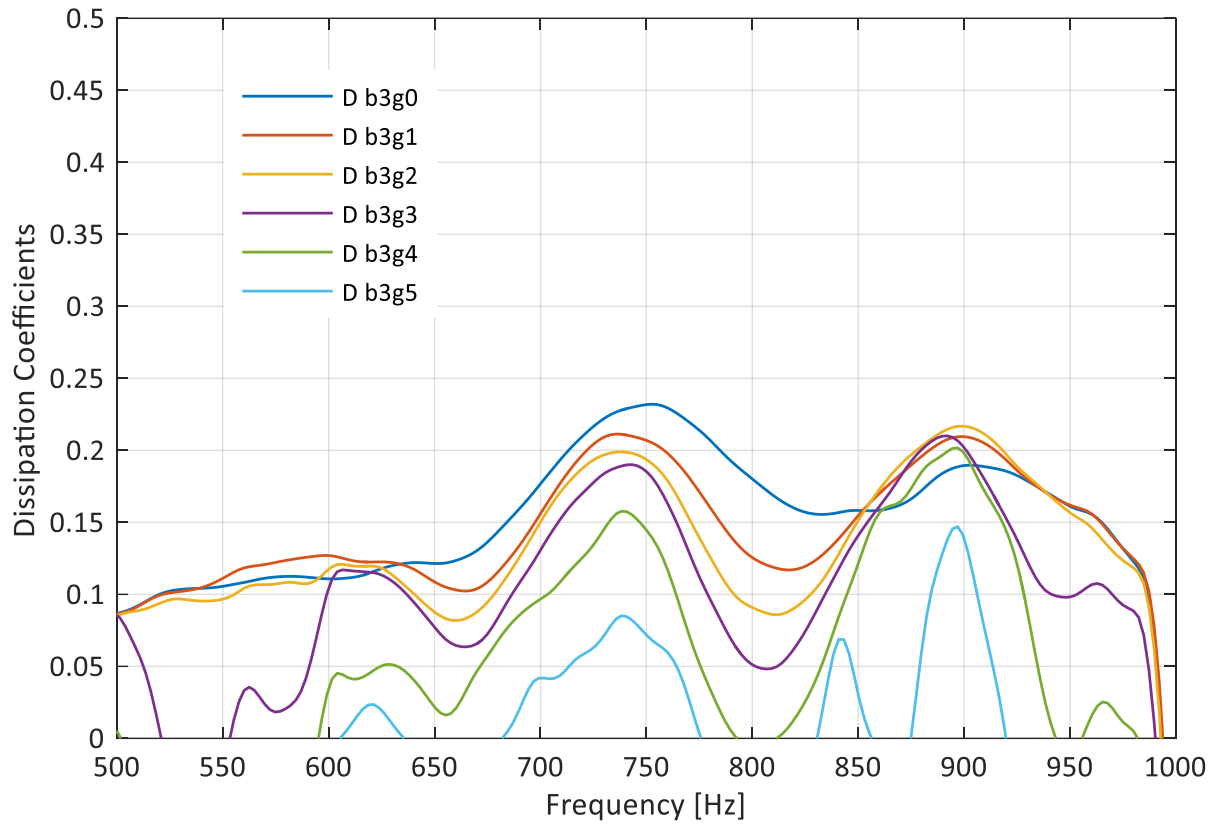
Figure 208 - Dissipation Coefficients of Plate #1 (Ø3mm); 3%dP bias, and varied grazing flow
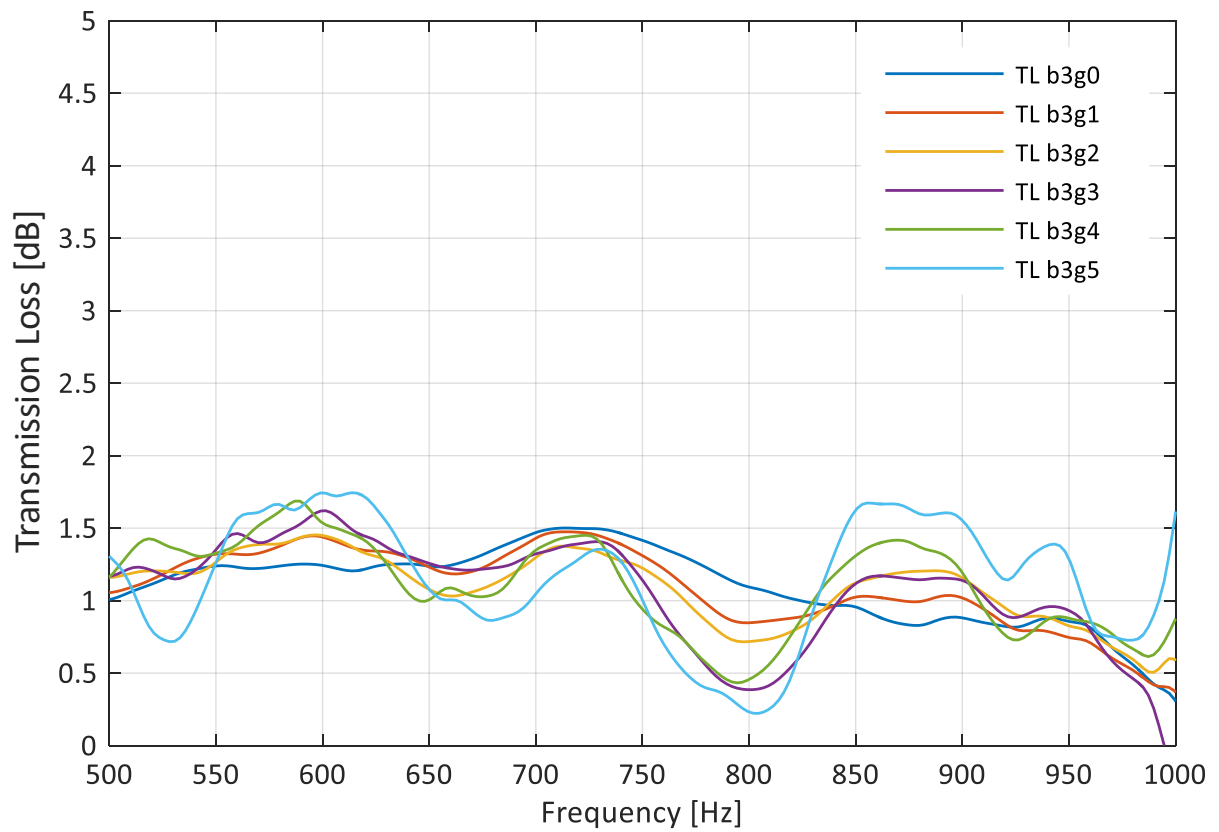
Figure 209 - Transmission Loss of Plate #25 (Ø2mm); 3%dP bias, and varied grazing flow
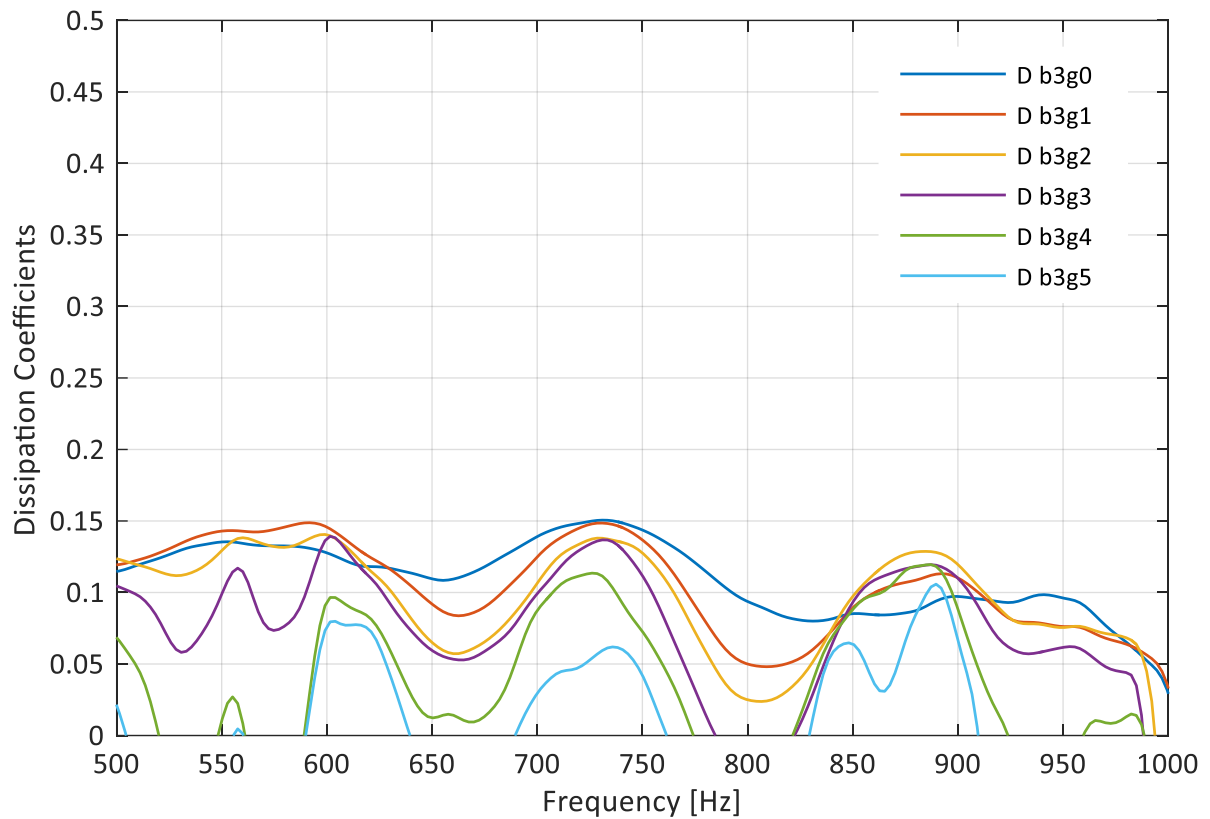
Figure 210 - Dissipation Coefficients of Plate #25 (Ø2mm); 3%dP bias, and varied grazing flow

8.6.3   Summary of Grazing and Bias Flow Effects

A moderate grazing flow, in the absence of any bias flow, can increase the resonance effect of a distributed resonator over an acoustic only excited equivalent; and as the magnitude of grazing flow is increased further, the resonance effect is diminished proportionally to the point of saturation. The optimal level of grazing flow is specific to the resonators geometric properties but can in general be considered as the flow parameters which result in the largest magnitude of resonant response. It should be noted however, that whilst FRF and transmission loss metrics are generally coherent for grazing flow measurements; evaluation of the dissipation coefficient metric shows that peak resonance conditions can exhibit sub-optimal values of dissipation; which can be attributed to a reactive resonant regime causing upstream reflections, over total attenuation. Increasing grazing flow can also be shown to impact the effective length of neck apertures, and the particle velocity within the neck; which has the net effect of shifting the resultant resonator dynamics to higher frequencies.

The introduction of a bias flow through the resonator, in the absence of any grazing flow, has been shown to both suppress the resonance effect, and reduce the magnitude of attenuation for the cases investigated; even under the lowest magnitude investigated of 1%dP. It has however been shown that for the geometry of resonator investigated, even the lowest values of bias flow, results in comparatively large values of neck velocities; therefore, early onset of resonator saturation resulting

from high magnitudes of bias flow is expected and demonstrated accordingly. In addition to the iterations of pressure drop induced bias flow investigated; the subtle variations in bias flow between the respective neck diameter cases further supports the conclusion that; the consequential reduction in resonance is proportional to the bias flow velocity. Whilst increasing bias flow magnitude reduces peak attenuation magnitude and resonant characteristics, it also can be seen to increase the attenuation bandwidth; and in general, shifts the primary attenuation mechanism of a distributed resonator from reactive, to dissipative, with increasing magnitude of bias flow.

In circumstances where both grazing and bias flow exist concurrently, it can be shown that the bias flow is the dominant factor in determining the general attenuation characteristics of the corresponding resonator. Grazing flow retains the ability to modify both the resistance and reactance of the resonator however, with increasing bias flow magnitude, the influence of any grazing flow diminishes, and tends towards negligible under high bias flow conditions.

8.7 Comparison with modelling predictions

The previous Literature review Chapter concluded with an evaluation of the work of Wang (2019); within which his empirical model derived from numerical results; was validated against eighteen experimental measurements developed for, and evaluated within, this independent study. Therefore, it is fitting to expand upon this prior art and make a common comparison with the complete test matrix of equivalent cases available. Accordingly, the expansion of Wang's (2019) model validation can be seen as: a comparison of ideal end correction length values obtained from the 36 available inner plate variations, measured under closed resonator, non-flowed, and acoustic excitation only conditions, in Figure 211; supplemented in tabular form, with the relevant parameters and relative model errors defined in Table 40.
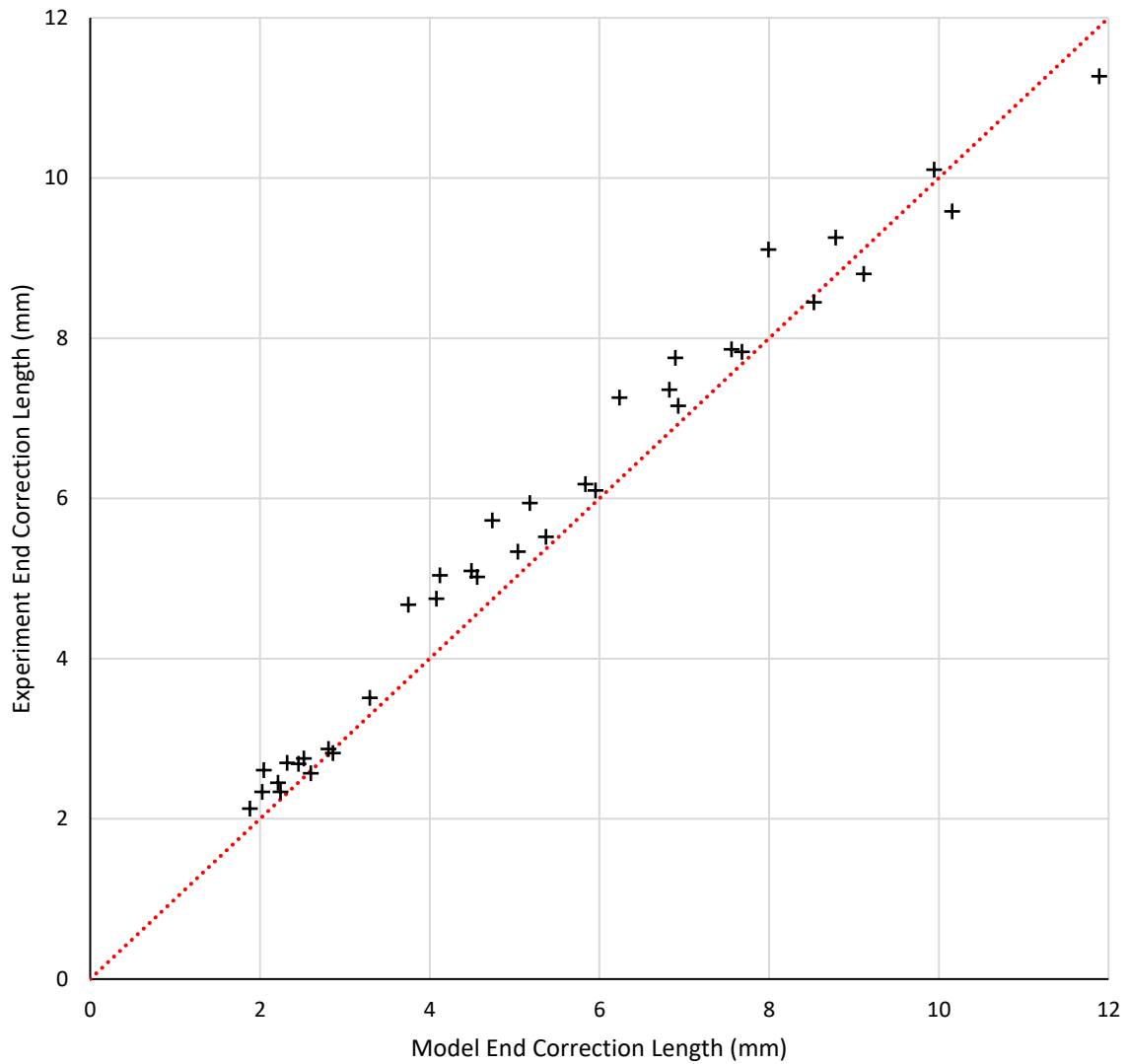
Figure 211 – Comparison of the Wang's model against full H-W & H-H test matrix; closed resonator, no flow (Wang et al., 2019)

It can be seen that the aforementioned deduction of an increase in aperture end correction length, correlated to effective porosity, and attribution to an increasing hole-to-hole interaction effects, holds true across these additional evaluated cases. These results provide further evidence contradictory to the prior art of Fok (1941); and the common consensus of analytical modelling methods of interaction effects, as delineated in Section 2.3.4.

Wang (2019) recognised that his model does not effectively capture any inherent hole-to-wall effects, and attributed his observed errors to this factor; a deduction which is further enforced by the observed results here within; which demonstrate a clear relationship between the relative error of his model, and the hole pattern pitch; which directly corresponds to an increased proximity of the plate apertures to the wall of the measurement resonator.

Plate #	$\emptyset_{neck}$ (mm)	$Pitch_Y$ (mm)	$Pitch_X$ (mm)	σ_{eff} (%)	f_r Exp. (Hz)	f_r Model. (Hz)	Relative Err. (%)	δ Exp. (mm)	δ Model (mm)	Relative Err. (%)
1	3	7.7	15	6.12%	709	764	7.73%	4.67	3.75	-19.76%
2	3	7.7	12	7.65%	705	743	5.34%	4.75	4.08	-14.06%
3	3	7.7	9	10.20%	692	715	3.44%	5.02	4.56	-9.14%
4	3	7.7	6	15.30%	668	675	1.01%	5.52	5.37	-2.71%
5	3	6	15	7.85%	691	741	7.24%	5.04	4.12	-18.22%
6	3	6	12	9.82%	688	719	4.53%	5.09	4.49	-11.81%
7	3	6	9	13.09%	676	691	2.10%	5.34	5.04	-5.59%
8	3	6	6	19.63%	644	650	0.91%	6.10	5.95	-2.38%
9	3	4.2	15	11.22%	659	706	7.09%	5.73	4.74	-17.28%
10	3	4.2	12	14.02%	650	684	5.15%	5.94	5.18	-12.78%
11	3	4.2	9	18.70%	641	655	2.17%	6.18	5.83	-5.55%
12	3	4.2	6	28.05%	606	613	1.27%	7.16	6.93	-3.19%
13	4	7.7	15	10.88%	803	851	6.00%	7.26	6.24	-14.04%
14	4	7.7	12	13.60%	799	822	2.98%	7.36	6.82	-7.26%
15	4	7.7	9	18.13%	779	785	0.76%	7.83	7.68	-1.89%
16	4	7.7	6	27.20%	743	733	-1.42%	8.80	9.12	3.56%
17	4	6	15	13.96%	782	819	4.72%	7.76	6.90	-11.07%
18	4	6	12	17.45%	778	790	1.58%	7.86	7.56	-3.87%
19	4	6	9	23.27%	756	753	-0.38%	8.45	8.53	0.95%
20	4	6	6	34.91%	718	701	-2.39%	9.58	10.16	5.98%
21	4	4.2	15	19.95%	733	773	5.43%	9.11	7.99	-12.24%
22	4	4.2	12	24.93%	728	744	2.17%	9.26	8.78	-5.11%
23	4	4.2	9	33.24%	702	707	0.67%	10.10	9.94	-1.58%
24	4	4.2	6	49.87%	671	656	-2.26%	11.27	11.89	5.50%
25	2	7.7	15	2.72%	601	620	3.13%	2.13	1.88	-11.60%
26	2	7.7	12	3.40%	587	609	3.74%	2.33	2.03	-13.15%
27	2	7.7	9	4.53%	587	593	1.12%	2.34	2.24	-4.07%
28	2	7.7	6	6.80%	571	570	-0.35%	2.57	2.60	1.24%
29	2	6	15	3.49%	569	607	6.73%	2.61	2.05	-21.57%
30	2	6	12	4.36%	579	595	2.79%	2.45	2.21	-9.72%
31	2	6	9	5.82%	564	579	2.57%	2.69	2.45	-8.64%
32	2	6	6	8.73%	556	554	-0.42%	2.82	2.86	1.44%
33	2	4.2	15	4.99%	564	588	4.29%	2.70	2.32	-14.04%
34	2	4.2	12	6.23%	560	575	2.57%	2.75	2.52	-8.54%
35	2	4.2	9	8.31%	553	557	0.69%	2.87	2.81	-2.31%
36	2	4.2	6	12.47%	520	531	2.03%	3.51	3.29	-6.17%

Table 40 – Table showing measured results from full H-W & H-H test matrix compared with Wang's model; closed resonator, no flow (Wang et al., 2019)

Irrespective of Wang's (2019) models lack of consideration of hole-to-wall factors, it shows a strong correlation between the effective porosity geometric resonator design variable, and the resultant end correction. In order to further evaluate the significance of this factor, and its inherent correlation with the end correction factor, the experimentally determined end correction factors are plotted against the effective porosity, as shown in Figure 212. Here the effective porosity is defined as per Equation [135], and the end correction is normalised according to Equation *[175]*:

$$\varepsilon = \frac{\delta}{\sqrt{Pitch_X^2 + Pitch_Y^2}} \qquad [175]$$

From these results it can be seen that the normalised end correction is approximately linear with the effective porosity, and that all measured cases are in close agreement with this underlying trend. Therefore, it can be deduced that the effective porosity is a dominant characteristic of the acoustic end correction of distributed resonators, which supports Wang's model, and validates it's use as pragmatic method for initial prediction of a resonator's peak dynamics frequency; albeit this method can only be applied in the absence of cross/bias flow.
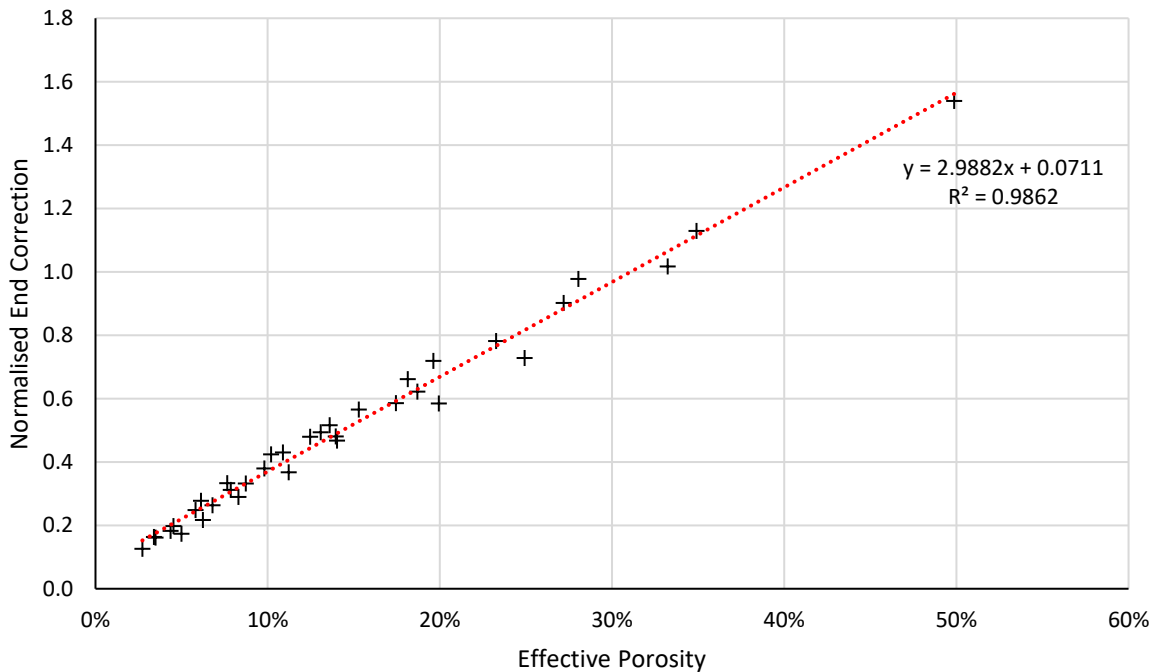
Figure 212 - Normalised experimentally determined end correction, against effective porosity

Similarly, this regression analysis itself presents an opportunity to pragmatically predict the expected peak resonance frequency of the equivalent cases, and accordingly a new model can be presented; which is derived from the experimentally derived end correction, and the aforementioned regression analysis, as shown in Equation *[176]*.

$$\delta = \sqrt{Pitch_X^2 + Pitch_Y^2} \cdot 2.9882\sigma_{eff} + 0.0711$$

[176]

An equivalent reproduction of Table 40 in which Wang's model was evaluated, can be seen in Table 41, which details a comparison between measured, and model predicted values.

Plate #	$\varnothing_{neck}$ (mm)	$Pitch_Y$ (mm)	$Pitch_X$ (mm)	σ_{eff} (%)	f_r Exp. (Hz)	f_r Model. (Hz)	Relative Err. (%)	δ Exp. (mm)	δ Model (mm)	Relative Err. (%)
1	3	7.7	15	6%	709	731	3.07%	4.67	4.28	-8.38%
2	3	7.7	12	8%	705	732	3.70%	4.75	4.27	-9.97%
3	3	7.7	9	10%	692	721	4.31%	5.02	4.45	-11.31%
4	3	7.7	6	15%	668	685	2.50%	5.52	5.16	-6.56%
5	3	6	15	8%	691	696	0.70%	5.04	4.94	-1.95%
6	3	6	12	10%	688	698	1.48%	5.09	4.89	-4.02%
7	3	6	9	13%	676	693	2.38%	5.34	5.00	-6.31%
8	3	6	6	20%	644	665	3.36%	6.10	5.58	-8.49%
9	3	4.2	15	11%	659	635	-3.70%	5.73	6.33	10.56%
10	3	4.2	12	14%	650	639	-1.78%	5.94	6.23	4.90%
11	3	4.2	9	19%	641	638	-0.48%	6.18	6.26	1.28%
12	3	4.2	6	28%	606	623	2.83%	7.16	6.66	-6.95%
13	4	7.7	15	11%	803	829	3.27%	7.26	6.68	-7.95%
14	4	7.7	12	14%	799	823	3.07%	7.36	6.81	-7.46%
15	4	7.7	9	18%	779	803	3.02%	7.83	7.26	-7.25%
16	4	7.7	6	27%	743	749	0.82%	8.80	8.63	-1.99%
17	4	6	15	14%	782	777	-0.68%	7.76	7.89	1.73%
18	4	6	12	17%	778	774	-0.45%	7.86	7.95	1.13%
19	4	6	9	23%	756	762	0.76%	8.45	8.29	-1.87%
20	4	6	6	35%	718	722	0.56%	9.58	9.45	-1.35%
21	4	4.2	15	20%	733	694	-5.33%	9.11	10.39	14.12%
22	4	4.2	12	25%	728	694	-4.63%	9.26	10.38	12.10%
23	4	4.2	9	33%	702	689	-1.89%	10.10	10.57	4.65%
24	4	4.2	6	50%	671	667	-0.61%	11.27	11.43	1.46%
25	2	7.7	15	3%	601	571	-4.95%	2.13	2.57	20.75%
26	2	7.7	12	3%	587	578	-1.45%	2.33	2.46	5.49%
27	2	7.7	9	5%	587	579	-1.25%	2.34	2.45	4.72%
28	2	7.7	6	7%	571	565	-1.17%	2.57	2.68	4.24%
29	2	6	15	3%	569	556	-2.36%	2.61	2.83	8.66%
30	2	6	12	4%	579	563	-2.74%	2.45	2.70	10.37%
31	2	6	9	6%	564	567	0.39%	2.69	2.65	-1.34%
32	2	6	6	9%	556	557	0.04%	2.82	2.82	-0.15%
33	2	4.2	15	5%	564	524	-6.97%	2.70	3.43	27.07%
34	2	4.2	12	6%	560	532	-5.06%	2.75	3.27	18.89%
35	2	4.2	9	8%	553	537	-2.94%	2.87	3.17	10.41%
36	2	4.2	6	12%	520	533	2.46%	3.51	3.25	-7.44%

Table 41 - Table showing measured results from full H-W & H-H test matrix compared with new Effective Porosity model; closed resonator, no flow

This alternative formulation detailed in Equation *[176]* incorporates the salient variables of aperture separation and effective porosity, and the redundant summation of the single hole end correction is removed, as aperture diameter is already contained within the effective porosity derivation. A statistical summary of the comparison of both models against experimental results can be seen in Table 42, which shows that the proposed model on average provides a more accurate fit to the experimental data evaluated here within. Similarly, this pragmatic approach to predicting the resonant frequency of a distributed resonator with salient H-H factors is of significant value in the initial prediction of peak dynamics frequencies, due to its ease of implementation over more advanced impedance modelling approaches. As with Wang's (2019) model however, this model's lack of consideration of underlying hole-to-wall factors remains a weakness, and a primary source of prediction error. Similarly, this model is also only valid in the absence of any grazing or bias flow.

	δ Relative Error *(%)*		f_r Relative Error *(%)*	
	Wang (2019)	Equation *[176]*	Wang (2019)	Equation *[176]*
Mean Exp. Δ	-7.2%	1.7%	2.6%	-0.3%
Max Exp. Δ	6.0%	27.1%	7.7%	4.3%
Min Exp. Δ	-21.6%	-11.3%	-2.4%	-7.0%
STD	6.9%	9.2%	2.6%	2.9%

Table 42 - Table showing comparison statistics between modelling predictions and experimental results

8.8 Summary of Distributed Resonator Results

In this chapter the acoustic attenuation performance characteristics of distributed aperture Helmholtz resonators were investigated across; a range of 36 geometric variations of inner plate configurations, focused on providing unique insight into hole-to-wall and hole-to-hole interaction effects; alongside 5 discrete grazing flow magnitude conditions, and 6 discrete bias flow conditions; which provides a combined flow experimental test matrix, consisting of 42 unique flow condition permutations, focused on providing additional insight into flow factors affecting response dynamics; equating to a comprehensive experimental database of 1,512 measured acoustic responses of distributed Helmholtz resonator performance factors.

In Section 8.1, saturation factors due to high excitation sound pressure levels was investigated, initially on a special single hole case, and later on, representative cases from the H-W and H-H test matrix. It was demonstrated that, when exposed to a sufficiently high SPL, a distributed resonator enters a non-linear regime, whereby an increase in SPL results in an increase in peak attenuation frequency, and a corresponding reduction in attenuation magnitude. Prior to the onset of SPL induced saturation effects, the corresponding resonator dynamics remain linear, and a resistance to saturation effects is observed to be proportional to the number, and diameter, of holes present; for an equivalent volume of

distributed resonator. The experiential relationship between the total neck area and resistance to saturation effects is attributed to a relative increase in attenuation magnitude; which results in a reduction of saturation significance on the overall observed response; whilst the transition from linear to non-linear remains independent of frequency and orifice diameter. While no direct comparison with any existing analytical models has been made within this study, the observations support the practical implications of the theories studied in Section 2.3.5.

Evaluation of the significance of the neck length over diameter ratio (L/D) on the resultant acoustic attenuation performance was investigated in Section 8.2; which concluded with a simple pragmatic observation; that for a given target dynamics frequency, tuning the resonator cavity volume, and reducing the L/D ratio as low as practicable to reach the target dynamics frequency; will result in an optimisation of the total attenuation potential available.

In Section 8.3 the experimental design strategy of Section 7.2.1; which sought to create a test matrix of distinguishable H-W & H-H factors; was physically implemented through the measurement, and subsequent evaluation, of key performance metrics for all targeted cases; under equivalent acoustic excitation only. From initial assessment of the extremes of hole pattern, it was shown that a measured peak attenuation frequency shift of over 100Hz could be solely attributed to H-W & H-H factors, indicating the significance of these design factors on a discrete resonator's acoustic reactance, and associated end correction values.

A piecewise investigative strategy was executed, whereby the measured acoustic response of all cases was evaluated across the frequency domain, with results presented according to the relative neck diameter, and the key performance metrics of frequency response function, transmission loss, and dissipation coefficient. This investigative strategy yielded the common deduction that, a strong correlation between observed shifts in peak attenuation frequency and magnitude, can be predominantly attributed to the effective porosity parameter. As the hole patterns investigated vary around the centroid of the test plates, the effective porosity for these cases is directly proportional to the hole-to-hole interaction; and inversely proportional to the hole-to-wall interaction. This observation has been further validated within the aforementioned modelling comparisons, detailed in Section 8.7, where the effective porosity alone has shown to be a viable method of pragmatic peak dynamics prediction. As the contributing H-W & H-H factors exist concurrently in all cases physically investigated, respective modelling validations can therefore not be made directly from these measurements, without speculative inferences of the relative contributions.

To supplement and summarise the previous piecewise spectral evaluation of the relevant performance metrics, an overview of the measured peak attenuation frequency and magnitude can be seen in Table 43; which includes all test cases and metrics evaluated.

Plate #	$\emptyset_{neck}$ (mm)	$Pitch_Y$ (mm)	$Pitch_X$ (mm)	σ_{eff} (%)	Peak Frequency			Peak Magnitude		
					FRF (Hz)	TL (Hz)	D (Hz)	FRF	TL (dB)	D
1	3	7.7	15	6.1%	709	713	714	14.23	13.44	0.58
2	3	7.7	12	7.6%	705	709	710	14.45	13.69	0.57
3	3	7.7	9	10.2%	692	695	695	14.02	13.23	0.54
4	3	7.7	6	15.3%	668	671	671	13.85	13.32	0.48
5	3	6	15	7.9%	691	696	696	14.49	12.81	0.54
6	3	6	12	9.8%	688	691	692	14.13	12.75	0.54
7	3	6	9	13.1%	676	679	680	13.54	11.63	0.50
8	3	6	6	19.6%	644	645	645	14.78	11.91	0.44
9	3	4.2	15	11.2%	659	663	663	14.29	11.43	0.47
10	3	4.2	12	14.0%	650	652	651	15.42	12.45	0.45
11	3	4.2	9	18.7%	641	643	643	14.13	12.08	0.44
12	3	4.2	6	28.0%	606	605	604	14.86	12.41	0.45
13	4	7.7	15	10.9%	803	798	804	21.91	17.23	0.46
14	4	7.7	12	13.6%	799	793	797	21.39	17.73	0.49
15	4	7.7	9	18.1%	779	776	781	20.63	17.71	0.52
16	4	7.7	6	27.2%	743	741	745	19.88	18.46	0.57
17	4	6	15	14.0%	782	780	784	20.67	17.07	0.50
18	4	6	12	17.5%	778	775	780	20.19	17.32	0.53
19	4	6	9	23.3%	756	754	760	20.43	18.66	0.54
20	4	6	6	34.9%	718	721	720	20.68	17.80	0.53
21	4	4.2	15	19.9%	733	735	736	20.62	18.47	0.53
22	4	4.2	12	24.9%	728	730	731	20.47	17.89	0.54
23	4	4.2	9	33.2%	702	706	706	19.53	17.46	0.55
24	4	4.2	6	49.9%	671	674	673	18.01	14.45	0.48
25	2	7.7	15	2.7%	601	592	590	6.09	5.30	0.36
26	2	7.7	12	3.4%	587	590	588	6.37	5.32	0.37
27	2	7.7	9	4.5%	587	586	584	6.09	5.22	0.36
28	2	7.7	6	6.8%	571	572	571	6.46	5.37	0.38
29	2	6	15	3.5%	569	581	579	6.13	5.25	0.37
30	2	6	12	4.4%	579	578	576	6.63	5.37	0.37
31	2	6	9	5.8%	564	573	572	6.27	5.33	0.37
32	2	6	6	8.7%	556	558	556	6.55	5.24	0.37
33	2	4.2	15	5.0%	564	571	570	6.15	5.14	0.37
34	2	4.2	12	6.2%	560	564	563	6.29	5.21	0.37
35	2	4.2	9	8.3%	553	555	553	6.31	5.07	0.36
36	2	4.2	6	12.5%	520	525	522	6.35	4.72	0.35

Table 43 - Table showing peak frequency and magnitude values for all measured H-W & H-H test matrix cases: Where FRF = Frequency Response Function; TL = Transmission Loss; D = Dissipation Coefficient

The effective porosity and corresponding performance metrics presented in Table 43 are conditionally formatted by column; which highlights the distribution of values across the respective cases;

graduating from the highest value in green, to the lowest values in red. It can be seen that the peak dynamics frequency values are coherent across the respective performance metrics; with common trend of inverse proportionality between the effective porosity value, and the corresponding frequency; across each discrete neck diameter sub-set.

A moderate trend of inverse proportionality between the effective porosity, and the magnitude of resonance effect, i.e. the FRF magnitude, can be seen for the largest neck diameter cases of Plate #13 - #24; the cohesion between these factors trend can however be seen to diminish with decreasing neck diameter; to the point where it is negligible for the smallest neck diameter cases of Plates #25 - #36.

A similar moderate trend of inverse proportionality between the effective porosity, and the transmission loss magnitude is evident; whereby across all neck diameters investigated, the lowest magnitude of transmission loss corresponds to the maximum effective porosity. The maximum transmission loss however, does not exclusively occur at the lowest effective porosity; but rather at the penultimate lowest porosity for the Ø3mm neck, and around the median porosity for the Ø4mm neck; observed deviations in magnitude are however subtle across the cases measured, and consequently insufficient to make any definitive deductions.

Evaluation of the dissipation across the measured cases highlights the importance of understanding the primary attenuation mechanism of an acoustic resonator in an applied context, as it can be shown that in some cases; for example, Plate #13; that a high observed magnitude of resonance, can actually coincide with a relatively low value of dissipation. The inference here is that in such circumstances, the attenuation regime is primarily reactive; which results in high downstream attenuation and consequential high transmission loss values; but simultaneously reflects much of the acoustic energy back upstream; therefore, resulting in a relatively low value of dissipation coefficient.

An imperative conclusion from these results, is the required clarity of definition in the porosity value, when used for any analytical modelling attempts; as it is irrefutable that the porosity is a key performance defining parameter however, it also presents a great potential for misinterpretation. The common definition of porosity, of the ratio between acoustically "open" and closed area, is ineffective at capturing H-H & H-W interaction effects, which has been shown to have a significant impact on distributed resonator dynamics. Furthermore, despite the more descriptive "effective porosity" having been shown to have a strong correlation with the evaluated performance factors; it's use in effective analytical modelling attempts remains heavily nuanced. For the cases investigated here within, the basic definition of porosity only varies three times across the x36 strong test matrix, in accordance with neck diameter; whereas the effective diameter varies according to the neck diameter and the corresponding separation pitch in the Cartesian coordinates and is consequently unique to each of the

cases investigated. The H-W interaction has however, been demonstrated to have a significant effect on distributed resonator dynamics, and this factor cannot be explicitly captured through the effective porosity parameter alone. For example, if the effective porosity was to be fixed, but the hole pattern skewed from the centroid of the cavity volume, the H-W interactions would consequently vary, and demonstrable differences in resonator characteristics will occur.

Section 2.3.4 presented the current analytical knowledge relating to interaction effects, i.e. H-H factors, and clarified that; despite having been studied extensively, and many analytical models existing; numerous contradictions in modelling methodologies exist, and a definitive model remains elusive for distributed resonators. All current analytical models reviewed can be shown to underpredict the experimental end correction observed from these applied cases. Furthermore, the impact of porosity on end correction has been shown to be experimentally contradictory to the analytical models discussed in Section 2.3.4 which support a reduction of the end correction proportional to the porosity.

In Section 8.4, 8.5, & 8.6 the impact of grazing flow; bias flow, and combined flow factors were evaluated respectively; and the measured results presented across the consistent measurement frequency domain of 500Hz-1,500Hz. From these investigations it was concluded that; in the absence of any bias flow, a moderate grazing flow causes an increase the observed magnitude of resonance of a distributed resonator, over an acoustically stimulated equivalent resonator; an observation which was evident across all neck diameters, and both FRF and transmission loss metrics. Beyond the peak value of attenuation magnitude, which varies according to the geometric parameters of the distributed resonator, i.e. the neck diameter in these test cases; a further increase in grazing flow magnitude, results in a proportionally diminishing resonance effect. Whilst excessive grazing flow magnitude is shown to decrease the peak attenuation magnitude of the resonator, it can be also observed to introduce an increase in broadband attenuation. Additional flow generated noise, can also be shown to decrease the performance of downstream anechoic terminations, introducing additional reflections to the measurement section; furthermore, geometrically sensitive flow induced reverberations can result in a practical net increase in noise at certain frequencies.

Cross examination of the evaluated performance metrics confirms that observed cases of peak resonance, can result in sub-optimal values of overall dissipation; which can be attributed to upstream reflections under a predominantly reactive attenuation regime; which highlights the importance of understanding the context of application, and evaluation of performance via the most appropriate metric accordingly. Additionally, increasing grazing flow magnitude can be shown to have a high correlation with a consequential shift towards higher frequency dynamics, which can be attributed to a net reduction in the in effective length of the neck apertures, and modification of the particle velocity within the neck.

Bias flow through the resonator has been shown to have a similar impact on resonator performance; where increasing magnitude of bias flow results in a decreasing resonance effect, coupled with an equivalent increase in broadband attenuation. When both grazing flow and bias flow exist concomitantly, the attenuation characteristics of the corresponding resonator are principally determined by the more dominate factor of bias flow.

In order to support a holistic appreciation of the dissipation variation attributed to the evaluated flow factors, a summary of average dissipation coefficient across the measurement spectrum is presented in Table 44. The values shown are similarly conditionally formatted by column to highlight the distribution of values across the respective cases. Through this approach additional insight can be obtained as to the combined geometric and flow properties which result in the greatest broadband attenuation. These results signify the aforementioned deductions, and highlight the nuances of combined flow conditions, such as demonstrating that a bias flow through the resonator has the ability to enhance broadband attenuation, and to dominate over grazing flow induced characteristics. A holistic appraisal of broadband attenuation does however mask the narrowband nuances evidenced in the previous spectral evaluations of key attenuation factors. Therefore, if the frequency of unwanted noise is discrete, or can be identified to be within a narrow bandwidth, a careful consideration of the frequency dependant impacts on attenuation resulting from combined flow factors should be applied.

	Grazing Flow / Bias Flow	Closed	0%dP [b0]	1%dP [b1]	2%dP [b2]	3%dP [b3]	4%dP [b4]	5%dP [b5]
Plate #1	0m/s [g0]	13.6%	11.3%	15.4%	14.2%	13.3%	11.8%	10.6%
	12m/s [g1]	10.3%	9.5%	14.0%	12.4%	11.7%	10.8%	9.2%
	17m/s [g2]	7.7%	7.2%	13.8%	12.2%	10.7%	10.5%	9.1%
	23m/s [g3]	10.9%	7.8%	11.7%	12.2%	10.4%	8.5%	7.4%
	29m/s [g4]	12.0%	9.6%	12.4%	9.0%	8.9%	7.1%	8.8%
	34m/s [g5]	11.5%	8.3%	8.6%	10.8%	7.6%	5.0%	1.9%
Plate #13	0m/s [g0]	8.0%	9.2%	16.5%	16.3%	15.7%	14.4%	14.3%
	12m/s [g1]	6.7%	8.2%	15.1%	14.8%	14.1%	13.3%	12.2%
	17m/s [g2]	0.2%	7.7%	15.0%	14.3%	13.8%	13.6%	12.1%
	23m/s [g3]	-1.8%	3.3%	13.5%	13.1%	12.6%	12.2%	11.1%
	29m/s [g4]	1.4%	4.8%	11.3%	11.7%	12.3%	11.6%	11.7%
	34m/s [g5]	3.3%	2.2%	10.2%	7.5%	10.2%	9.1%	6.2%
Plate #25	0m/s [g0]	9.4%	8.2%	9.1%	8.4%	7.7%	7.1%	8.2%
	12m/s [g1]	7.6%	6.7%	8.0%	7.4%	6.8%	5.6%	5.2%
	17m/s [g2]	8.2%	7.5%	8.1%	7.5%	6.7%	6.2%	5.4%
	23m/s [g3]	7.6%	6.9%	7.0%	5.9%	5.6%	6.0%	5.3%
	29m/s [g4]	7.1%	8.9%	6.3%	4.0%	4.6%	4.9%	4.9%
	34m/s [g5]	4.5%	4.7%	5.0%	1.8%	3.3%	2.0%	2.7%

Table 44 - Table showing average Dissipation Coefficient across measurement spectrum (500Hz - 1,000Hz) for Plate #1, #13 & #25; under varied flow conditions

CHAPTER 9 - CONCLUSIONS

From a comprehensive review of relevant acoustic literature in CHAPTER 2 -, and current analytical and empirical acoustic impedance models in CHAPTER 3 -, it can be ascertained that whilst noise attenuation characteristics can be modelled for a variety of acoustic resonator configurations; the ability to accurately describe the full fidelity and complexity of an applied context, remains aspirational. This fact can be attributed to an appreciation that in reality, the true noise attenuation characteristics of a resonator is not dependant only on the normal incident Rayleigh conductivity alone; which is an integral assumption of most analytical modelling methods; but rather is affected by varied signal incidence angles concomitantly; alongside the geometric and thermodynamic properties not only within the boundaries of the resonator itself, but also from far upstream and downstream of the device; all factors which introduce additional nuances which are not captured by any idealistic models.

Therefore, in order to support an effective evaluation of performance defining noise attenuation characteristics in an applied context, this study has focused on developing experimental investigative strategies, under carefully controlled specific conditions, optimised for the successive evaluation of key parameters of interest. This strategy has sought to serve the dual purpose of providing additional insight into performance defining characteristics, whilst also permitting an evaluation of the effectiveness of existing modelling methods.

Targeted discrete resonator experiments, for which the experiential design methodology was delineated in CHAPTER 4 -, and the subsequent results presented in CHAPTER 5 -; have shown that the use of the classic Helmholtz resonance equation of Equation [142], is limited to a narrow range of practical geometries; and significant errors in peak resonance predictions occur outside of its thresholds of applicability. The modification of the neck length l to represent the known additional acoustic radiation end effect, according to $2l' = 16r_0/3\pi$ (Kinsler & Frey, 1982), only yields an improvement in predictions when the inherent assumption of a circular piston in an infinite baffle can be applied, i.e. the neck aperture is very small compared to the resonator cavity, and the external proximity to any neighbouring wall is large. Ingard (1953) recognised that this assumption can result in considerable error in predictions when the respective cavity/duct geometry has an acoustical influence on the aperture impedance, and accordingly offered an improved model as shown in Equation *[144]*. He introduces a term to account for geometric ratios of proportionally between the aperture and surrounding walls and states a limit of applicability for his model of $\xi < 0.4$.

Experimental validation of Ingard's (1953) model on test cases with geometric ratios of proportionality of $0.04 < \xi < 0.3$ demonstrated that, even within his stated thresholds of applicability, his model

consistently overpredicted the observed resonant frequency across all 70 measured test cases. The observed errors in predictions were shown to be greater than using the idealised value of end correction for these cases, that the magnitude of error was proportional to the neck diameter, and therefore the geometric ratio of proportionality. These findings supported an observed contradiction to the inferred hole-to-wall interaction theory; however, Ingard (1953) had validated his model experimental, and shown good agreement between this theory and measurements, albeit for less extreme geometry variations. It can therefore be deduced that the primary cause of this observed discrepancy is in fact additional geometric factors, which are not represented effectively within his model.

Accordingly, in Section 5.1.2, this hypothesis was investigated, and an additional novel geometric correction factor was introduced. The assumption was made that the observed errors could be attributed to the inherent assumptions of a uniform velocity distribution, and the neglection of viscosity, therefore further limiting applicability to apertures of negligible thickness. As the length of the necks experimentally investigated were not negligible (27.15mm), and as the test cases consisted of large variations in cavity depth, these additional geometric variables were introduced into a supplementary geometric correction factor, as described in Equation *[146]*. Modification of the classic peak Helmholtz resonance frequency equation, with the summation of Ingard's (1953) hole-to-wall interaction factor, and the proposed additional spatial correction factor, yielded the new empirically derived formulation of Equation *[148]*. This novel model was validated against the equivalent measured test cases and produced a trivial average error in prediction of 0.34Hz across all 70 cases, indicating that it provides a robust solution for the improved accuracy in prediction of discrete resonators with neck diameter ratios of $0.04 < \xi < 0.3$, and length over dimeter ratios for both the neck and resonator cavity of $1.81 < L_n/D_n < 9.05$, and $0.73 < L_C/D_C < 2.91$ respectively.

In Section 5.2 the impact of alternative neck termination geometries on attenuation performance was investigated; within which conical, radial, and acoustic horn geometries were experimentally evaluated using representative discrete resonator test cases, of a consistent Ø5mm nominal neck diameter, and varied cavity volume. Experimentally obtained results for varied degrees of duct-side conical neck termination showed good cohesion with both the theory, and experimentally obtained results of Tang (2005), who considered resonator cavity-side tapered necks. Both theoretical deductions and experimentally obtained results demonstrate that a reduction of the acoustic impedance is achieved through tapering of the neck, which consequently increases the noise attenuation performance of a Helmholtz resonator. The larger the degree of taper, the greater the improvement in attenuation magnitude is observed, alongside a correspondingly proportional increase in resonant frequency, relative to the equivalent non-tapered case. A solution for the approximate

resonant frequency of a resonator with a tapered neck is presented in Equation *[150]*, which produces minimal error when used in conjunction with the depth analysis end correction of Chanaud (1997). Both the theory reviewed, and experimental results obtained, demonstrate that the comparative significance of neck tapering on the resultant absorption frequency and magnitude alteration, decreases with increasing cavity volume.

Experimental investigation of radial neck terminations demonstrated equivalent findings to those of the tapered necks, albeit with a lower magnitude of frequency and magnitude modification observed, relative to the tapered neck investigations. The lower relative difference can be attributed to the geometrical significance of these variations predominantly; whereby the largest investigated radial neck diameter case of 5mm, equates to an increase of the acoustically relevant volume within the neck of 23% over the baseline case, whereas the largest conical neck taper of 25°, is equivalent to a 111% increase over the same baseline case. In consideration of the relative alteration to the acoustically relevant volume within the neck, against the consequently increase in attenuation magnitude; it can be deduced that rounding of the neck termination is in fact, acoustically a more efficient strategy to improving attenuation potential. Similar observations have been made by Keller and Zauner (1995), who demonstrated on a resonator with a Ø9mm neck, of 100mm length, and an end termination of a 15mm radius; that a 55% relative increase in attenuation could be obtained over the equivalent case with a sharp termination.

Evaluation of the potential attenuation performance improvements obtainable from neck geometry modification was extended into the realm of acoustic horn geometries, both theoretically and experimentally. From an acoustics point of view, the aforementioned conical and radial neck terminations can equally be considered as acoustic horns; and consequently, much of the associated theory can equally be applied, however; the short supplementary investigation contained in Section 5.2.3 focused on the three unique geometries of exponential, hyperbolic, and tractrix. Review of the current state of the art indicates that theoretically the impedance at the throat of these horn geometries can be calculated, albeit only under the assumption of plane wave fronts. However, despite having been analytically addressed by Stewart & Lindsay (1930), realisation of the solutions becomes rapidly complicated. Furthermore, whilst in a uniform tube the wave fronts can exist in a planar form, it has been shown experimentally by Hall (1928; 1932) that for an exponential and conical horn, the wave fronts are spherical, with centres at the apex. The tractrix curve was first employed for horn use by P.G.A.H. Voight, and patented in 1926 (Voigt, 1926), with the theory being further investigated by Lambert (1954) and Kolbrek (2008); who ultimately demonstrated that the wave-front for this geometry was neither spherical or planar. The significance of these deductions is that integration of horn geometries within existing lumped parameter impedance models, for the *purposes of analytical*

attenuation performance predictions is not trivial. Irrespective, the experimental investigations within this study have validated the hypothesise that tangible attenuation performance improvements can be obtained through the replication of acoustic horn geometries in the neck of a resonator; with demonstrable improvements in the attenuation magnitude being validated experimentally.

The impact of a grazing flow on the attenuation performance of an acoustic resonator has be investigated in Section 5.3 and Section 8.4; in relation to both discrete, and distributed resonators respectively; with a corresponding impact on both resistance and reactance being experimentally validated. For both discrete and distributed resonators, an increase in acoustic resistance is observed with increasing grazing flow magnitude, which corresponds to a proportional decrease in peak attenuation magnitude, and an equivalent increase in broadband attenuation. The resonator reactance is shown to be modified through a reduction in acoustic radiation at the aperture interface with the grazing flow, which consequently results in a shift towards higher resonant frequencies. The shift in resonator dynamics is shown to be proportional to the grazing flow magnitude until the point of saturation; after which the grazing flow velocity dominates the acoustic particle velocity field, and the impedance becomes almost linear.

It was shown in Section 5.3 that the impact of grazing flow on end correction is less prevalent than the effects on the resistance, which agrees with comparable prior experimental studies (Goldman, A. L. & Panton, 1976; Goldman, A. & Chung, 1982; Kooi & Sarin, 1981). A comparatively large degree of scatter in peak frequency shift is also observed, which inherently reduces the effectiveness of any attempts to model the reactance with a simplified analytical solution in the presence of grazing flow. Similar observations can be seen from review of prior art, which leads to the deduction that the physics of the flow/acoustic interaction is quite complex, and that attempts to parametrise the orifice impedance will partially mask the true nature of the mean flow effects at an orifice, a view which is shared by Cummings (1986a). Irrespective, the current state of the art in relation to analytical and empirical modelling in the presence of grazing flow has been reviewed in Section 5.3.3, and has shown a general agreement with experimentally obtained results here within.

Deviations from the overserved acoustic responses and simplified analytical models in the presence of grazing flow, can be attributed to the complex fluid dynamics at the interface of the aperture and the grazing flow. Such aeroacoustics interaction factors diminish the applicability of the basic lumped parameter models which inherit the assumptions of Rayleigh's (1926) conductivity determining characteristics in their modelling of the impedance of the resonator orifice. This inference points to the ductions of Rice (1976), who drew a conclusion that the orifice inductive mass reactance end correction is not directly a function of grazing flow, but rather that the experimentally observed total inductance reduction with grazing flow, is occurring within the slug flow within the orifice itself; as

opposed to externally within the end correction. This notion is also supported by the work of Herse and Walker (1979), who attributes the vena contracta effect of the grazing flow, to the erosion of the slug-mass type oscillatory flow assumption within the orifice, under grazing flow conditions.

The interaction between the orifice of an acoustic resonator, and the grazing flow shear layer, can also be seen to result in the generation of additional tones beyond the resonant frequency. This phenomenon was evidenced in Section 5.3.2, corresponding to the smallest cavity volume with a Ø15mm neck, and has also been observed by Herse and Walker (1979) experimentally; who was able demonstrate that such tones occurred at the specific Strouhal number of 0.26. The use of the Strouhal number to predict the onset of such dynamics is prevalent in existing literature, and as shown in Section 3.2.3, can also be used to estimate the impedance of perforated plates in the presence of bias flow. Linking the aeroacoustics tones and acoustic eigenfrequencies of the cavity has been analytically attempted by Massenzio et al. (2008), who considers the wavelength of the shear layer, as opposed to the Strouhal number however; in practice, solution of this method would require the definition of the eigenfrequencies for the cavity and the momentum thickness of the flow over the cavity to be solved in advance, either analytically or numerically. Ultimately the work of Massenzio et al. (2008) highlights the high potential for many resonant interactions, and such methods only serve as estimates to roughly predict the onset of aeroacoustic resonances.

In conclusion, whilst the onset of non-linear characteristics pertaining to flow properties can be reasonably estimated by currently theory, the attenuation performance beyond this point cannot, however, be adequately predicted by existing simplified analytical solutions. Therefore, a comprehensive classification of such performance factors in the presence of aeroacoustics-acoustic coupling remains reserved for rigorous numerical or experimental investigations.

Further evaluations of the impact of flow factors on attenuation performance were conducted in Section 8.4, 8.5, & 8.6; corresponding to the impact of grazing flow; bias flow, and combined flow factors on distributed resonators respectively. These investigations supported the aforementioned deductions pertaining to grazing flow factors on discrete resonators but added additional insight into the nuances of observed attenuation performance both upstream and downstream of the acoustic resonator. Cross examination of attenuation performance as defined by frequency response magnitude, transmission loss, and dissipation coefficient; for equivalent cases; yielded the conclusion that observed cases of peak resonance magnitude, can concurrently result in sub-optimal values of overall dissipation. These findings indicate that under a predominantly reactive attenuation regime, significant amounts of acoustic energy can be reflected back upstream, as opposed to being directly attenuated by the resonator. The introduction of bias flow through the resonator was experimentally confirmed to have a similar impact on attenuation performance as grazing flow, and when grazing flow

and bias flow exist concomitantly; the bias flow is shown to be the dominant factor in the determination of attenuation characteristics.

Saturation factors due to high sound pressure levels were investigated in Section 8.1, where it was effectively demonstrated experimentally that; under exposure to a sufficiently high SPL, the resonator enters a non-linear regime, where an increase in SPL results in an increase in peak attenuation frequency, and a corresponding reduction in attenuation magnitude. A resilience to saturation is shown to be proportional to the number, and diameter of apertures; for an equivalent volume of resonator; which is attributed to a relative increase in attenuation magnitude. The onset of saturation is shown to be independent of frequency and diameter, and the experimentally obtained results agree with the theory discussed in Section 2.3.5.

The experimental design methodology intended to provide novel insight into the impact of hole-to-wall and hole-to-hole interaction effects, on the attenuation performance of distributed resonators was described in CHAPTER 7 -, and the intentions of this approach was validated in Section 8.3; where an observed shift in peak attenuation frequency of over 100Hz was attributed solely to these factors, for otherwise equivalent cases. Across the 36 discrete hole patterns measured, a strong correlation between the observed effects on peak attenuation frequency and magnitude, with the effective porosity parameter was identified. 18 of the distributed resonator test cases from this study, were used for validation the empirical model introduced by Wang (2019), for which the effective porosity parameter was used to predict the required end correction. His model was compared to all 36 of the available cases from this study, which validated the deduction that effective porosity provides a reasonable prediction of the end correction required to effectively represent hole-to-hole interaction effects. The validated trend shows an increase in end correction length that is proportional to effective porosity, which is contradictory to the prior art of Fok (1941); and the common consensus of analytical modelling methods of interaction effects, as delineated in Section 2.3.4. The errors in Wang's (2019) model was shown to corelate with the hole pattern pitch values in the cartesian coordinates, which can be attributed the hole-to-wall contribution not captured in his model. An alternative empirical model was presented in Equation *[176]* incorporating the salient variables of aperture separation, which was subsequently shown to reduce the prediction error across the measured cases. In comparison, all current analytical models reviewed have shown to consistently underpredict the required end correction required to match these experimental results. Therefore, in the absence of flow factors, empirical modelling can be concluded to be an effective pragmatic method for the initial prediction of a distributed resonator's peak dynamics frequency corresponding to hole-to-hole interaction effects.

In CHAPTER 6 - an implicit unsteady numerical modelling methodology was developed, implemented and was subsequently shown to accurately replicate the experimentally observed attenuation performance of real resonators. Beyond the evidenced precise replication of physically observed performance metrics, novel time-averaging of acoustic velocity magnitude in the vicinity of the resonator neck, has been shown to be able to provide unique insight into the intrinsic dynamics in the vicinity of the neck.

These findings highlight the significance of multi-dimensional evanescent cross modes on the effective acoustic inertial end correction; in addition to the relationship between geometric parameters and the subsequent decay of evanescent modes; including the effects of aperture edge geometry modification. The aforementioned factors outline the inherent weakness of the fundamental Rayleigh (1926) analytical end correction approach; whereby a virtual extension of the same geometry as the neck, is idealised to represent the physical additional entrained mass. Ingard (1953) adeptly identified that to truly define the end correction, the unique diffraction problem pertaining to the transmission of sound through the resonator aperture must be solved, however; as the velocity distribution in the aperture is not known a priori, a comprehensive solution is not reasonably practicable without employing a uniform velocity distribution assumption. Accordingly, a paradoxical problem remains whereby the underlying fluid dynamics in the vicinity of the neck must be masked to a rational degree, in order to reach a practicable analytical solution, which effectively describes the intrinsic effects on acoustic attenuation performance characteristics. The prior art delineated in Chapters 2 & 3 has shown that the complex entrainment traits can nonetheless be effectively translated into subsequent acoustic resistance and reactance modifications, through simplified analytical solutions. Furthermore, with the addition of novel empirical corrections it can be confidently demonstrated that, irrespective of the inherent simplified assumptions, the current state of the art can be further advanced to provide very accurate predictions of tangible acoustic attenuation performance, and across a large range of geometric conditions.

The ultimate accuracy of existing analytical and empirical models is however, significantly diminished in applications where the acoustic response is no longer primarily driven by acoustic excitation, and where the dominant physics is predominantly non-linear. Knowledge of the onset of non-linear characteristics is therefore a critical factor in enabling accurate predictions of the attenuation performance. Much work has been reviewed and is ongoing pertaining to the onset and embodiment of non-linear characteristics within impedance modelling efforts (Bolt et al., 1949; Ingard, U., 1953; Ingard, Uno & Ising, 1967; Ingård & Labate, 1950; Melling, 1973; Sivian, 1935; Tonon & Sirignano, 1970; Zinn, 1970; Zorumski & Parrott, 1971; Betts, Juan Fernando, 2000; Farooqui et al., 2016; Elnady, 2004)

however, a comprehensive characterisation of such performance defining factors remains analytically onerous and outstanding.

Many of the challenges in the ultimate obtainment of a comprehensive solution of the heavily nuanced and complex fluid dynamics which underpin acoustic attenuation performance factors, can be traditionally attributed to the complexity of numerical solutions required. With contemporary advanced numerical solvers, and increased levels of compute resource which are now more commonly obtainable, these numerical challenges of the past become increasingly trivial. Even with the most powerful modern numerical solvers remains the need for an engineer who intimately understands both the solution system, and the context of application. Failure to address either of these prerequisites results in the modern dilemma of; excessive generation of meaningless data; misinterpretation of quality data; or interpretations/applications which are out of context. Any of the aforementioned ailments can ultimately result in significant errors between acoustic resonator design intentions and observed outcomes; it is therefore imperative that solutions are both accurate, obtainable, and appropriate at the point of application.

Irrespective of ominous of statements such as: "The rigorous calculation of δ_i and δ_e for a given resonator geometry is quite involved and can in general hardly be done" (Ingard, U., 1953); and "a universal model for predicting combustion instabilities can hardly be achieved given the current state of knowledge" (Elsari & Cummings, 2003); one can rest assured, as evidenced within this work directly, and evaluation of the current state of the art; that effective solutions to such acoustic problems are in fact now obtainable. The reality is that advanced numerical methods now permit the direct solution of incredibly complex noise attenuation applications however, such solutions sustain a level of cost and complexity that makes them either unobtainable, or impractical for most tangible applications. Furthermore, even when such methods are viable and accessible, they by design must call upon a great deal of specificity in definition, and consequently the outcomes cannot be broadly applied out of this explicit context. It is therefore the aspiration of this work that that the overarching deduction be not to seek a universal analytical model, nor to endorse comprehensive numerical solutions for all applications; but rather to sustain a balance between the advanced and rigorous examination of underpinning phenomena, amidst the goal of democratisation, popularisation, and integration of findings with accessible tools and techniques, such that they can be readily applied in practice.

Within this study it has been ultimately demonstrated that, through rigorous and strategic experimental and numerical examination, the knowledge of key functional noise attenuation performance defining characteristics of acoustic resonators, has been incrementally advanced and authenticated. The case has also been presented that, idealistic analytical models; whilst in their original simplified form, can be seen to result in significant estimate error against observed applied

cases; can be effectively empirically modified to provide precise predictions within defined thresholds of applicability, whilst retaining the accessibility and ease of application of the simplified models.

9.1 Outlook & Perspectives

Despite this study covering deploying a wide range of investigative techniques; covering analytical, empirical, numerical and experimental methods; every conclusion extracted from the respective methods has involved a level of empiricism. Consequentially, an investigative method which provides irrefutable evidence of the underlying physical occurrences remains highly desirable. Contemporary advanced optical measurement methods present an exciting opportunity for high fidelity spatial, and temporal measurement of the particle movement within the vicinity of the resonator neck. Existing studies by Rupp et. al (2010; 2013), Heuwinkel et al. (2010), and ongoing work by Schulz et al. (2013; 2018) shows great promise for this techniques ability to support advancements in a physical understanding of the mechanics of acoustic attenuation performance defining characteristics.

Within this study the PolyJet™ 3D printing technique was used to effectively and efficiently manufacture neck inserts with intricate mathematically driven internal neck geometries, at a high resolution of 14-microns, which were subsequently shown to produce distinguished improvements in attenuation performance when fitted to the baseline resonator. Modern advances in manufacturing such as 3D printing therefore presents an exciting opportunity to further advance the attenuation characteristics of acoustic resonators, through exploration beyond the confines of traditional manufacturing techniques. Realisation of these possibilities is rapidly yielding revolutionary developments in new acoustic resonator designs; for example, Boulvert et. al (2022) presents a novel compact porous Asymmetric Broad target frequency bandwidth Sub-wavelength Absorber (ABSA), which demonstrated an impressive mean absorption coefficient of 99% over almost an octave, and for frequencies smaller than the quarter-wavelength corresponding to the height of the absorber. This outcome was achieved through a folded quarter-wavelength resonator principle, which was designed, optimised numerically, 3D printed, and tested experimentally. Modern 3D printing techniques and materials now means that similar acoustically optimised designs with high levels of intracity, need not be limited to prototypes, and can be viably produced as functional, highly efficient noise attenuation devices, and novel metasurfaces.

The endeavours of this multifactorial investigation have resulted in a substantial assemblage of empirical data pertaining to acoustic attenuation performance factors, of which only a strategic representation has been utilised directly within the scope of this study. As such, there remains an opportunity for future work which can employ the existing abundance of experimental data to further

advance the state of the art. In addition, the advancements in empirical modelling presented within this study are open for further extrapolation and deeper integration with the multiple performance factors identified within. For example, the improved empirical insights into hole-to-wall and hole-to-hole factors obtained yields an opportunity for an extended examination of the corresponding analytical models and presents a possibility to further advance the prediction of the constituent components affecting attenuation performance. These findings and the robust empirical data collected, ultimately presents an excellent opportunity for initial validation, and subsequent development of many additional empirical and numerical investigations into the intrinsic mechanics of the attenuation performance of acoustic resonators, which will be eagerly awaited.

References

Abramowitz, M. & Stegun, I. A. (1972) *Handbook of mathematical functions with formulas, graphs, and mathematical tables*, 10th edition. National Bureau of Standards

Acoustical Society of America. (2013) American national standard acoustical terminology. American National Standards Institute, Inc.

Ahuja, K. K. and Mendoza, J., (1995), *Effects of cavity dimensions, boundary layer, and temperature on cavity noise with emphasis on benchmark data to validate computational aeroacoustic codes.* NASA Contractor Report 4653, National Aeronautics and Space Administration,

Aiman, D. A., Muhamad, S. M. F., Abdul, K. K. & Hariz, K. M. (2018) Review on resonator and muffler configuration acoustics. *Archives of Acoustics; 2018; Vol. 43; no 3; 369-384,*

Akkerman, V. & Law, C. K. (2016) Coupling of harmonic flow oscillations to combustion instability in premixed segments of triple flames. *Combustion and Flame,* 172 342–348. https://doi.org/10.1016/j.combustflame.2016.07.019

Alimohammadi, I., Sandrock, S. & Gohari, M. R. (2013) The effects of low frequency noise on mental performance and annoyance. *Environmental Monitoring and Assessment,* 185(8), 7043–7051. https://doi.org/10.1007/s10661-013-3084-8

Altay, H. M., Speth, R. L., Hudgins, D. E. & Ghoniem, A. F. (2009) Flame–vortex interaction driven combustion dynamics in a backward-facing step combustor. *Combustion and Flame,* 156(5), 1111–1125. https://doi.org/10.1016/j.combustflame.2009.02.003

Anderson, W. E. & Yang, V. (1995) Liquid rocket engine combustion instability, vol. 169. *Progress in Astronautics and Aeronautics, AIAA, Washington, DC,*

Andreini, A., Facchini, B., Ferrari, L., Lenzi, G., Simonetti, F. & Peschiulli, A. (2012) Experimental investigation on effusion liner geometries for aero-engine combustors: Evaluation of global acoustic parameters. *Turbo Expo: Power for Land, Sea, and Air.* American Society of Mechanical Engineers.

Arenas, J. & Acevedo, S. (2009) Use of resonators for practical noise reduction. *38th International Congress and Exposition on Noise Control Engineering 2009, INTER-NOISE 2009,* 2 1102–1109.

ASHRAE (2011) *ASHRAE handbook - applications* American Society of Heating Refrigeration and Air-Conditioning Engineers.

Atalla, N. & Sgard, F. (2007) Modeling of perforated plates and screens using rigid frame porous models. *Journal of Sound and Vibration,* 303(1-2), 195–208.

Ballal, D. R. & Lefebvre, A. H. (2010) *Gas turbine combustion : Alternative fuels and emissions*, 3rd ed edition. CRC Press

Barron, R. F. (2002) *Industrial noise control and acoustics*, 1st edition. CRC Press

Bartlett, M. S. (1948) Smoothing periodograms from time-series with continuous spectra. *Nature,* 161(4096), 686–687.

Basten, T. (2001) *Noise reduction by viscothermal acousto-elastic interaction in double wall panels.* University of Twente.

Batchelor, G. K. (2000) *An introduction to fluid dynamics* Cambridge University Press

Bauer, A. B. (1977) Impedance theory and measurements on porous acoustic liners. *Journal of Aircraft,* 14(8), 720–728.

Bellucci, V., Flohr, P. & Paschereit, C. O. (2004) Numerical and experimental study of acoustic damping generated by perforated screens. *AIAA Journal,* 42(8), 1543–1549.

Bellucci, V., Paschereit, C. O. & Flohr, P. (2002) Impedance of perforated screens with bias flow. *8th AIAA/CEAS Aeroacoustics Conference & Exhibit.* Breckenridge, Colorado1719 June 2002. AIAA-2002-2437.

Bendat, J. S. & Piersol, A. G. (2011) *Random data: Analysis and measurement procedures*, 4th edition. John Wiley & Sons

Beranek, L. L. (1954) *Acoustics* McGraw-Hill

Bernoulli, J. (1690) Analysis problematis antehac porpositi, de inventione linea descensus a corpore gravi percurrendae uniformiter, sic ut temporibus aequales altitudines emetiatur: & Alterius cujusdam problematis propositio. *Acta Eruditorum,* 9: 217–219.

Betts, J. F., Follet, J. I., Kelly, J. J. & Thomas, R. H. (2000) Evaluation of an impedance model for perforates including the effect of bias flow. *6th AIAA/CEAS Aeroacoustics Conference.* Lahaina, Hawaii12-14 June 2000. AIAA-2000-31118.

Betts, J. F. (2000) *Experiments and impedance modelling of liners including the effect of bias flow.* Virginia Polytechnic Institute and State University.

Bies, D. A. & Hansen, C. H. (1997) *Engineering noise control*, 2. ed., reprint. edition. Taylor & Francis

BILLAH, K. Y. & SCANLAN, R. H. (1991) Resonance, tacoma narrows bridge failure, and undergraduate physics textbooks. *American Journal of Physics,* 59(2), 118–124. https://doi.org/10.1119/1.16590

Bisplinghoff, R. L., Ashley, H. & Halfman, R. L. (1955) *Aeroelasticity* Addison-Wesley Publishing Company

Blackman, R. B. & Tukey, J. W. (1958) The measurement of power spectra from the point of view of communications engineering—Part I. *Bell System Technical Journal,* 37(1), 185–282.

Bloxsidge, G. J., Dowling, A. P. & Langhorne, P. J. (1988) Reheat buzz: An acoustically coupled combustion instability. part 2. theory. *Journal of Fluid Mechanics,* 193 445–473. https://doi.org/10.1017/S0022112088002216

Boden, H. & Zhou, L. (2012) Acoustic properties of an in-duct orifice subjected to bias flow and high level acoustic excitation. *10th International Conference on Flow-Induced Vibration (& Flow-Induced Noise).* Dublin, Ireland2nd-6th July 2012.

Bolt, R. H., Labate, S. & Ingård, U. (1949) The acoustic reactance of small circular orifices. *The Journal of the Acoustical Society of America,* 21(2), 94–97.

Bonaldo, A., Andersson, M. & Larsson, A. (2014) Engine testing using highly reactive fuels on siemens industrial gas turbines. *Turbo Expo: Power for Land, Sea, and Air.* American Society of Mechanical Engineers.

Boulvert, J., Humbert, T., Romero-García, V., Gabard, G., Fotsing, E. R., Ross, A., Mardjono, J. & Groby, J. (2022) Perfect, broadband, and sub-wavelength absorption with asymmetric absorbers: Realization for duct acoustics with 3D printed porous resonators. *Journal of Sound and Vibration,* 523 116687.

Boyce, M. P. (2012) *Gas turbine engineering handbook*, Fourth edition. Elsevier

Boyer, C. & Merzbach, U. (2011) *A history of mathematics*, Third edition. Wiley

Bronshtein, I. N. & Semendyayev, K. A. (2013) *Handbook of mathematics* Springer Science & Business Media

Bronštejn, I. N. (2015) *Handbook of mathematics*, 6. ed. edition. Springer

Bruggeman, J. C., Hirschberg, A., van Dongen, M. E. H., Wijnands, A. P. J. & Gorter, J. (1991) Self-sustained aero-acoustic pulsations in gas transport systems: Experimental study of the influence of closed side branches. *Journal of Sound and Vibration,* 150(3), 371–393. https://doi.org/10.1016/0022-460X(91)90893-O

Brun, K. & Allison, T. (2022) *Machinery and energy systems for the hydrogen economy* Elsevier

CAI, C. & MAK, C. M. (2018) Noise attenuation capacity of a helmholtz resonator. *Advances in Engineering Software,* 116 60–66. https://doi.org/10.1016/j.advengsoft.2017.12.003

Cai, C., Mak, C. M. & Wang, X. (2017a) Noise attenuation performance improvement by adding helmholtz resonators on the periodic ducted helmholtz resonator system. *Applied Acoustics,* 122 8–15. https://doi.org/10.1016/j.apacoust.2017.02.006

Cai, C., Mak, C. & Shi, X. (2017b) An extended neck versus a spiral neck of the helmholtz resonator. *Applied Acoustics,* 115 74–80.

Candel, S. M. & Poinsot, T. J. (1988) Interactions between acoustics and combustion. *Proceedings of the Institute of Acoustics,* 10(2), 103–153.

Candel, S. (2002) Combustion dynamics and control: Progress and challenges. *Proceedings of the Combustion Institute,* 29(1), 1–28. https://doi.org/10.1016/S1540-7489(02)80007-4

Carrera, A. M., Andersson, M. & Na¨ svall, H. (2011) Experimental investigation of the 4th generation DLE burner concept: Emissions and fuel flexibility performance at atmospheric conditions. *Turbo Expo: Power for Land, Sea, and Air.*

Cattafesta, L. N., Song, Q., Williams, D. R., Rowley, C. W. & Alvi, F. S. (2008) Active control of flow-induced cavity oscillations. *Progress in Aerospace Sciences,* 44(7), 479–502. https://doi.org/10.1016/j.paerosci.2008.07.002

CD-adapco. (2011) Star CCM+.

Cerrato, G. (2009) Automotive sound quality - powertrain, road and wind noise. *Sound and Vibration,* 43(4), 16–24.

Champoux, Y. & Allard, J. (1991) Dynamic tortuosity and bulk modulus in air-saturated porous media. *Journal of Applied Physics,* 70(4), 1975–1979.

Chanaud, R. C. (1997) Effects of geometry on the resonance frequency of helmholtz resonators, part ii. *Journal of Sound and Vibration,* 204(5), 829–834. https://doi.org/10.1006/jsvi.1997.0969

Chen, Z., Yan, F., Negahban, M. & Li, Z. (2020) Resonator-based reflective metasurface for low-frequency underwater acoustic waves. *Journal of Applied Physics,* 128(5), 055305. https://doi.org/10.1063/5.0006523

Chung, J. Y. (1977) Rejection of flow noise using a coherence function method. *The Journal of the Acoustical Society of America,* 62(2), 388–395.

Clapeyron, B. E. (1834) Memoir sur la puissance motrice de la chaleur. *Journal De l'École Royale Polytechnique,* 14: 153–190.

Cooley, J. W. & Tukey, J. W. (1965) An algorithm for the machine calculation of complex fourier series. *Mathematics of Computation,* 19(90), 297–301.

Cory, W. (. (2005) *Fans and ventilation - A practical guide* Elsevier Science

Cowell, L. H., Padilla, A. & Saxena, P. (2016) Advances in using associated gases in solar turbines DLE industrial gas turbines. *The Future of Gas Turbine Technology 8th International Gas Turbine Conference, ETN.*

Cox, T. & D'Antonio, P. (2016) *Acoustic absorbers and diffusers theory, design and application*, 3rd ed edition. Spon Press

Craggs, A. (1976) A finite element method for damped acoustic systems: An application to evaluate the performance of reactive mufflers. *Journal of Sound and Vibration,* 48(3), 377–392.

Crandall, I. B. (1926) *Theory of vibrating systems and sound* D. Van Nostrand Company

Culick, F. & Yang, V. (1992) Prediction of the stability of unsteady motions in solid-propellant rocket motors.

Culick, F. E. & Yang, V. (1995) Overview of combustion instabilities in liquid-propellant rocket engines.

Cummings, A. (1984) Acoustic nonlinearities and power losses at orifices. *AIAA Journal,* 22(6), 786–792.

Cummings, A. (1986a) The effects of grazing turbulent pipe-flow on the impedance of an orifice. *Acta Acustica United with Acustica,* 61(4), 233–242.

Cummings, A. (1986b) Transient and multiple frequency sound transmission through perforated plates at high amplitude. *The Journal of the Acoustical Society of America,* 79(4), 942–951.

Cummings, A. (1994) The attenuation of sound in unlined ducts with flexible walls. *Journal of Sound and Vibration,* 174(4), 433–450.

Cummings, A. (2001) Sound transmission through duct walls. *Journal of Sound and Vibration,* 239(4), 731–765. https://doi.org/10.1006/jsvi.2000.3226

Cummings, A. (1978) Low frequency acoustic transmission through the walls of rectangular ducts. *Journal of Sound and Vibration,* 61(3), 327–345. https://doi.org/10.1016/0022-460X(78)90384-X

Cummings, A. & Eversman, W. (1983) High amplitude acoustic transmission through duct terminations: Theory. *Journal of Sound and Vibration,* 91(4), 503–518.

D'Alembert (1747) "Recherches sur la courbe que forme une corde tenduë mise en vibration (investigation of the curve formed by a vibrating string)". *Histoire De l'Académie Des Sciences Et Belles-Lettres,* 3: 214–219.

Dean, P. D. and Tester, B. J., (1975), *Duct wall impedance control as an advanced concept for acoustic suppression.* Contractor Report NASA-CR-134998, NASA,

DeMetz, F. & Farabee, T. (1977) Laminar and turbulent shear flow induced cavity resonances. *4th Aeroacoustics Conference.* Atlanta, GA, U.S.A.03 October 1977 - 05 October 1977. American Institute of Aeronautics and Astronautics. https://doi.org/10.2514/6.1977-1293

Denia, F. D., Selamet, A., Fuenmayor, F. J. & Kirby, R. (2007) Acoustic attenuation performance of perforated dissipative mufflers with empty inlet/outlet extensions. *Journal of Sound and Vibration,* 302(4), 1000–1017. https://doi.org/10.1016/j.jsv.2007.01.005

Deshmukh, N. N., Ansari, A., Degwekar, S., Paul, B. & Unnikrishnan, R. (2023) Effect of geometrical parameters and use of porous material in a helmholtz resonator on suppression of thermo-acoustic instabilities. *International Journal of Spray and Combustion Dynamics,* 15(2), 127–136. https://doi.org/10.1177/17568277231158900

Dhar, P. l. (2016) *Thermal system design and simulation* Elsevier Science

Dickey, N. S., Selamet, A. & Ciray, M. S. (2001) An experimental study of the impedance of perforated plates with grazing flow. *The Journal of the Acoustical Society of America,* 110(5), 2360–2370.

Dickey, N. S. & Selamet, A. (1996) Helmholtz resonators: One-dimensional limit for small cavity length-to-diameter ratios. *Journal of Sound and Vibration,* 195(3), 512–517. https://doi.org/10.1006/jsvi.1996.0440

Dinsdale, J. (1974) Horn loudspeaker design - three articles summarizing the development of design theories and concluded with two systems for construction . *Wireless World,*

Du, L., Abom, M., Karlsson, M. & Knutsson, M. (2016) Modelling of acoustic resonators using the linearized navier stokes equations. *9th International Styrian Noise, Vibration & Harshness Congress: The European Automotive Noise Conference.* Graz, Austria22 Jun 2016 → 24 Jun 2016. SAE International. https://doi.org/10.4271/2016-01-1821

Duhamel, M. J. M. C. (1849) Sur les vvibration des gaz dans des tuyaux cylindriques, coniques, etc. *Journal De Mathématiques Pures Et Appliquées,* 14: 49–110.

Dupe`re, I. D. J. & Dowling, A. P. (2005) The use of helmholtz resonators in a practical combustor. *Journal of Engineering for Gas Turbines and Power,* 127(2), 268–275. https://doi.org/10.1115/1.1806838

El-Sharkawy, A. I. & Nayfeh, A. H. (1978) Effect of an expansion chamber on the propagation of sound in circular ducts. *The Journal of the Acoustical Society of America,* 63(3), 667–674.

Elder, S. A., Farabee, T. M. & Demetz, F. C. (1982) Mechanisms of flow-excited cavity tones at low mach number. *The Journal of the Acoustical Society of America,* Vol. 72(No. 2), pp. 532–549. https://doi.org/10.1121/1.388034

Eldredge, J. D. & Dowling, A. P. (2003) The absorption of axial acoustic waves by a perforated liner with bias flow. *Journal of Fluid Mechanics,* 485 307–335. https://doi.org/10.1017/S0022112003004518

Eliaz, N., Shemesh, G. & Latanision, R. M. (2002) Hot corrosion in gas turbine components. *Engineering Failure Analysis,* 9(1), 31–43. https://doi.org/10.1016/S1350-6307(00)00035-2

Elnady, T. (2004) *Modelling and characterization of perforates in lined ducts and mufflers.* Kungliga Tekniska Högskolan.

Elsari, M. & Cummings, A. (2003) Combustion oscillations in gas fired appliances: Eigen-frequencies and stability regimes. *Applied Acoustics,* 64(6), 565–580.

Eriksson, L. J., Anderson, C. A., Hoops, R. H. & Jayaraman, K. (1983) Finite length effects on higher order mode propagation in silencers. *11th International Congress on Acoustics.* Paris19-27 July 1983. OFFICE OF NAVAL RESEARCH LONDON (ENGLAND).

Euler, L. (1757) Principes généraux du mouvement des fluides. *Mémoires De L'académie Des Sciences De Berlin,* 274–315.

Euler, L. (1766) "De la propagation du son (on the propagation of sound)". *Mémoires De L'académie Des Sciences De Berlin,* 15: 185–209.

Evulet, A. T., ELKady, A. M., Branda, A. R. & Chinn, D. (2009) On the performance and operability of GE's dry low NO combustors utilizing exhaust gas recirculation for PostCombustion carbon capture. *Energy Procedia,* 1(1), 3809–3816. https://doi.org/10.1016/j.egypro.2009.02.182

Fahy, F. J. (2000) *Foundations of engineering acoustics* Elsevier

Farmer, G., Brown, D. D. & Rutherford, M. E. (2003) Preferential multihole combustor liner. General Electric Company.

Farooqui, M., Elnady, T. & Akl, W. (2016) Sound attenuation in ducts using locally resonant periodic aluminum patches. *The Journal of the Acoustical Society of America,* 139(6), 3277–3287. https://doi.org/10.1121/1.4948990

Fesina, M. I., Krasnov, A. V. & Gorina, L. N. (2015) Sound-insulating linings modified constructions of technical rooms. *Procedia Engineering,* 106 296–302. https://doi.org/10.1016/j.proeng.2015.06.038

Fink, D. (2019) A new definition of noise: Noise is unwanted and/or harmful sound. noise is the new 'secondhand smoke'. *Proceedings of Meetings on Acoustics,* 39(1), https://doi.org/10.1121/2.0001186

Fok, V. A. (1941) Theoretical study of the conductance of a circular hole, in a partition across a tube. *Proceedings of the USSR Academy of Sciences,* 31(9), 875–878.

Fourier, J. B. J. (1822) Théorie analytique de la chaleur (the analytic theory of heat). F. Didot.

Fry, A. (2013) *Noise control in building services: Sound research laboratories ltd*, First Edition edition. Pergamon Press

Garrison, G. D., Schnell, A. C., Baldwin, C. D. and Russell, P. R., (1969), *Suppression of combustion oscillations with mechanical damping devices.* Interim Report PWA FR-3299, Pratt & Whitney Aircraft for NASA,

Gibbs, J. W. (. W. & Wilson, E. B. (1913) *Vector analysis : A text-book for the use of students of mathematics and physics*, First edition. Yale University Press

Goldman, A. L. & Panton, R. L. (1976) Measurement of the acoustic impedance of an orifice under a turbulent boundary layer. *The Journal of the Acoustical Society of America,* 60(6), 1397–1405.

Goldman, A. & Chung, C. H. (1982) Impedance of an orifice under a turbulent boundary layer with pressure gradient. *The Journal of the Acoustical Society of America,* 71(3), 573–579.

Goldmeer, J., Fujimoto, H. & Kihara, K. (2015) Recent advancements in gas turbine fuel flexibility. *International Gas Turbine Congress.*

Goldmeer, J. & Rozas, T. (2012) Gas turbines-burning a mixture of H2 and natural gas. *Turbomachinery International,* 53(1), 24.

Goldmeer, J., York, W. & Glaser, P. (2017) Fuel and combustion system capabilities of GE's F and HA class gas turbines. *Turbo Expo: Power for Land, Sea, and Air.* American Society of Mechanical Engineers.

Goldstein, M. E. (1976) *Aeroacoustics* McGraw-Hill

Gorain, J. & Padmanabhana, C. (2020) Broadband low-frequency noise reduction using helmholtz resonator-based metamaterial. *Noise Control Engineering Journal,* 69(4), 351–363.

Goy, C. J., James, S. R. & Rea, S. (2005) Monitoring combustion instabilities: E. ON UK's experience. *Progress in Astronautics and Aeronautics,* 210 163.

Grace, S. M., Horan, K. P. & Howe, M. S. (1998) The influence of shape on the rayleigh conductivity of a wall aperture in the presence of grazing flow. *Journal of Fluids and Structures,* 12(3), 335–351.

Green, D. & Unruh, W. G. (2006) The failure of the tacoma bridge: A physical model. *American Journal of Physics,* 74(8), 706–716. https://doi.org/10.1119/1.2201854

Guess, A. W. (1975) Calculation of perforated plate liner parameters from specified acoustic resistance and reactance. *Journal of Sound and Vibration,* 40(1), 119–137. https://doi.org/10.1016/S0022-460X(75)80234-3

Gullaud, E. & Nicoud, F. (2012) Effect of perforated plates on the acoustics of annular combustors. *AIAA Journal,* 50(12), 2629–2642.

Haeussler, M., Kobus, D. C. & Rixen, D. J. (2021) Parametric design optimization of e-compressor NVH using blocked forces and substructuring. *Mechanical Systems and Signal Processing,* 150 107217. https://doi.org/10.1016/j.ymssp.2020.107217

Hall, W. M. (1932) Comments on the theory of horns. *The Journal of the Acoustical Society of America,* 3(4), 552–561.

Hall, W. M. (1928) *An investigation of sound fields in regions restricted by finite boundaries.* Massachusetts Institute of Technology.

Halliday, D. (2005) *Fundamentals of physics* Wiley

Hannink, M. H. C. (2007) *Acoustic resonators for the reduction of sound radiation and transmission.* University of Twente.

Hansen, C. (2007) *Effects of low-frequency noise and vibration on people*, First Edition edition. Multi-Science Publishing Co. Ltd.

Harris, C. M. (1994) *Noise control in buildings*, First edition. McGraw-Hill Inc.

Harrison, M., Sykes, A. O. & Martin, M. (1952) Wave effects in isolation mounts. *The Journal of the Acoustical Society of America,* 24(1), 62–71. https://doi.org/10.1121/1.1906850

Heidelberg, L. J., Rice, E. J. and Homyak, L., (1980), *Experimental evaluation of a spinning-mode acoustic-treatment design concept for aircraft inlets.* Technical Paper NASA-TP-1613, NASA,

Helmholtz, H. v. (1954) *On the sensations of tone as a physiological basis for the theory of music* Dover Publications

Herbon, J., Aicholtz, J., Hsieh, S., Viars, P., Birmaher, S., Brown, D., Patel, N., Carper, D., Cooper, C. and Fitzgerald, R., (2017), *N+2 advanced low NOx combustor technology final report.* NASA/CR—2017-219410, National Aeronautics and Space Administration,

Herrin, D. W. & Ruan, K. (2019) A review of prior ASHRAE research efforts to characterize noise propagation in ducts. *ASHRAE Transactions,* 125 599–608.

Hersh, A. S. and Walker, B., (1979), *Effect acoustic impedance of helmholtz resonators consisting of single and clustered orifices.* NASA Contractor Report 3177, National Aeronautics and Space Administration,

Heuwinkel, C., Enghard, L., Ro¨ hle, I., Mu¨ hlbauer, B., Noll, B., Aigner, M. & Busse, S. (2008) Comparison of experimental and numerical results concerning the damping of perforated liners with bias flow. *Turbo Expo: Power for Land, Sea, and Air.* Berlin, GermanyJune 9–13, 2008.

Heuwinkel, C., Piot, E., Micheli, F., Fischer, A., Enghardt, L., Bake, F. & Röhle, I. (2010) Characterization of a perforated liner by acoustic and optical measurements. *16th AIAA/CEAS Aeroacoustics Conference.*

Higgins, B. (1802) On the sound produced by a current of hydrogen gas passing through a tube. *Journal of Natural Philosophy, Chemistry and the Arts,* 1(129-131), 2.

Houston, B., Wang, J., Qin, Q. & Rubini, P. (2015) Experimental and numerical investigation of helmholtz resonators and perforated liners as attenuation devices in industrial gas turbine combustors. *Fuel,* 151 31–39. https://doi.org/10.1016/j.fuel.2014.12.001

Howe, M. S. (1975) Contributions to the theory of aerodynamic sound, with application to excess jet noise and the theory of the flute. *Journal of Fluid Mechanics,* 71(4), 625–673.

Howe, M. S. (1979a) The influence of grazing flow on the acoustic impedance of a cylindrical wall cavity. *Journal of Sound and Vibration,* 67(4), 533–544.

Howe, M. S. (1979b) On the theory of unsteady high reynolds number flow through a circular aperture. *Proceedings of the Royal Society of London.A.Mathematical and Physical Sciences,* 366(1725), 205–223.

Howe, M. S. (1998) *Acoustics of fluid-structure interactions* Cambridge university press

Huang, Y. & Yang, V. (2009) Dynamics and stability of lean-premixed swirl-stabilized combustion. *Progress in Energy and Combustion Science,* 35(4), 293–364. https://doi.org/10.1016/j.pecs.2009.01.002

Hubbard, H. H., (1991), *Aeroacoustics of flight vehicles: Theory and practice. volume 2. noise control.* 19920005561, National Aeronautics and Space Administration, Available online: https://ntrs.nasa.gov/citations/19920005561 [Accessed: Jun 1, 2023].

Hughes, I. J. & Dowling, A. P. (1990) The absorption of sound by perforated linings. *Journal of Fluid Mechanics,* 218 299–335.

Ih, J. -. (1993) On the inertial end correction of resonators. *Acta Acustica United with Acustica,* 78(1), 1–15.

Ih, J. & Lee, B. (1985) Analysis of higher-order mode effects in the circular expansion chamber with mean flow. *The Journal of the Acoustical Society of America,* 77(4), 1377–1388.

Ingard, U. (1953) On the theory and design of acoustic resonators. *Journal of the Acoustical Society of America,* 25(6), 1037–1061. https://doi.org/10.1121/1.1907235

Ingard, U. & Ising, H. (1967) Acoustic nonlinearity of an orifice. *The Journal of the Acoustical Society of America,* 42(1), 6–17.

Ingård, U. & Labate, S. (1950) Acoustic circulation effects and the nonlinear impedance of orifices. *The Journal of the Acoustical Society of America,* 22(2), 211–218.

ISO. (1998) ISO/TR 11688-1:1998 acoustics - recommended practice for the design of low-noise machinery and equipment - part 1:Planning. International Organisation for Standardisation.

ISO 5136 (2003) Acoustics-determination of sound power radiated into a duct by fans and other air-moving devices-in-duct method. *International Organization for Standardization, Geneva, Switzerland,*

Jenkins, A. (2013) Self-oscillation. *Physics Reports,* 525(2), 167–222. https://doi.org/10.1016/j.physrep.2012.10.007

Jing, X. & Sun, X. (1999) Experimental investigations of perforated liners with bias flow. *The Journal of the Acoustical Society of America,* 106(5), 2436–2441.

Jing, X. & Sun, X. (2000) Effect of plate thickness on impedance of perforated plates with bias flow. *AIAA Journal,* 38(9), 1573–1578.

Jing, X., Sun, X., Wu, J. & Meng, K. (2001) Effect of grazing flow on the acoustic impedance of an orifice. *AIAA Journal,* 39(8), 1478–1484.

Johnson, D. L., Koplik, J. & Dashen, R. (1987) Theory of dynamic permeability and tortuosity in fluid-saturated porous media. *Journal of Fluid Mechanics,* 176 379–402.

Kang, Z. & Ji, Z. (2008) Acoustic length correction of duct extension into a cylindrical chamber. *Journal of Sound and Vibration,* 310(4-5), 782–791. https://doi.org/10.1016/j.jsv.2007.11.005

Kehtarnavaz, N. (2005) *Real-time digital signal processing*, 1st Edition edition. Elsevier

Kehtarnavaz, N. (2008) CHAPTER 3 - analog-to-digital signal conversion. In Nasser Kehtarnavaz (ed) *Digital signal processing system design (second edition).* Academic Press, 57–91.

Keller, J. J. & Zauner, E. (1995) On the use of helmholtz resonators as sound attenuators. *Zeitschrift Für Angewandte Mathematik Und Physik ZAMP,* 46(3), 297–327.

Khan, I. (2014) *Industrial application of CFD to predict high frequency noise from automotive acoustic devices.* University of Hull.

Kinsler, L. E. & Frey, A. R. (1982) *Fundamentals of acoustics*, Fourth edition. Wiley

Kirchhoff, G. (1868) Ueber den einfluss der wärmeleitung in einem gase auf die schallbewegung. *Annalen Der Physik,* 210(6), 177–193.

Kolbrek, B. (2008) Horn theory: An introduction, part 1. *Audio Xpress,* 1(269), 1–8.

Kooi, J. & Sarin, S. (1981) An experimental study of the acoustic impedance of helmholtz resonator arrays under a turbulent boundary layer. *7th AIAA Aeroacoustics Conference.* Palo Alto, California,5-7 October 1981.

Kraft, R. E., Yu, J. & Kwan, H. W. (1999) Acoustic treatment design scaling methods, volume 2: Advanced treatment impedance models for high frequency ranges. *US NASA Rep., CR-1999-209120,* 2

Kurz, R., Cowell, L., Tarver, T. & Singh, A. (2019) Hydrogen in natural Gas–Combustion and compression. *Gas Turbines for Energy Network Symposium.* Banff, Alberta, CanadaGTEN.

Kuttruff, H. (2007) *Acoustics: An introduction* CRC Press

Lahiri, C. (2014) *Acoustic performance of bias flow liners in gas turbine combustors.* Technische Universität Berlin.

Lambert, R. F. (1954) Acoustical studies of the tractrix horn part I and II.

Langhorne, P. J. (1988) Reheat buzz: An acoustically coupled combustion instability. part 1. experiment. *Journal of Fluid Mechanics,* 193 417–443. https://doi.org/10.1017/S0022112088002204

Lee, D. H. & Kwon, Y. P. (2004) Estimation of the absorption performance of multiple layer perforated panel systems by transfer matrix method. *Journal of Sound and Vibration,* 278(4-5), 847–860. https://doi.org/10.1016/j.jsv.2003.10.017

Lee, D., Jang, Y., Park, J., Kang, I. S., Li, J. & Rho, J. (2021) Underwater stealth metasurfaces composed of split-orifice-conduit hybrid resonators. *Journal of Applied Physics,* 129(10), 105103. https://doi.org/10.1063/5.0042246

Lee, I. (2005) *Acoustic characteristics of perforated dissipative and hybrid silencers.* The Ohio State University.

Lee, S. & Ih, J. (2003) Empirical model of the acoustic impedance of a circular orifice in grazing mean flow. *The Journal of the Acoustical Society of America,* 114(1), 98–113.

Lee, S., Ih, J. & Peat, K. S. (2007) A model of acoustic impedance of perforated plates with bias flow considering the interaction effect. *Journal of Sound and Vibration,* 303(3-5), 741–752. https://doi.org/10.1016/j.jsv.2007.02.001

Lewis, G. D. & Garrison, G. D. (1971) The role of acoustic absorbers in preventing combustion instability. *7th Propulsion Joint Specialist Conference.* Salt Lake City,UT,U.S.A.14 June 1971 - 18 June 1971. American Institute of Aeronautics and Astronautics.

Li, L., Liu, Y., Zhang, F. & Sun, Z. (2017) Several explanations on the theoretical formula of helmholtz resonator. *Advances in Engineering Software,* 114 361–371. https://doi.org/10.1016/j.advengsoft.2017.08.004

Li, S., Li, Q., Tang, L., Yang, B., Fu, J., Clarke, C. A., Jin, X., Ji, C. Z. & Zhao, H. (2016) Theoretical and experimental demonstration of minimizing self-excited thermoacoustic oscillations by applying anti-sound technique. *Applied Energy,* 181 399–407. https://doi.org/10.1016/j.apenergy.2016.08.069

Lieuwen, T. C. & Yang, V. (2006) Combustion instabilities in gas turbine engines: Operational experience, fundamental mechanisms, and modeling. American Institute of Aeronautics and Astronautics.

Liu, K. & Sanderson, V. (2013) The influence of changes in fuel calorific value to combustion performance for siemens SGT-300 dry low emission combustion system. *Fuel,* 103 239–246. https://doi.org/10.1016/j.fuel.2012.07.068

Luong, T., Howe, M. S. & McGowan, R. S. (2005) On the rayleigh conductivity of a bias-flow aperture. *Journal of Fluids and Structures,* 21(8), 769–778.

Maa, D. (1998) Potential of microperforated panel absorber. *The Journal of the Acoustical Society of America,* 104(5), 2861–2866.

MAK, C. M. & YANG, J. (2000) A prediction method for aerodynamic sound produced by closely spaced elements in air ducts. *Journal of Sound and Vibration,* 229(3), 743–753. https://doi.org/10.1006/jsvi.1999.2483

Mak, C. M., Wu, J., Ye, C. & Yang, J. (2009) Flow noise from spoilers in ducts. *The Journal of the Acoustical Society of America,* 125(6), 3756–3765.

Massenzio, M., Blaise, A. & Lesueur, C. (2008) Mechanisms of self-sustained oscillations induced by a flow over a cavity. *Journal of Vibration and Acoustics,* 130(5),

MasterHD (2008) *Resonance effect shown for various input frequencies and damping coefficient.* Wikipedia. https://commons.wikimedia.org/wiki/File:Resonance.PNG [Accessed Apr 9 2023].

McFee, B. (2023) *Digital signals theory* CRC Press

Mechel, F. P. (1975) Design criteria for industrial mufflers. *Inter-Noise,* 75(Sendai, Japan), 751–760.

Mechel, F., Schilz, W. & Dietz, J. (1965) Akustische impedanz einer luftdurchströmten öffnung. *Acta Acustica United with Acustica,* 15(4), 199–206.

Meissner, M. (2002) Excitation of helmholtz resonator by grazing air flow. *Journal of Sound and Vibration,* 256(2), 382–388.

Melling, T. H. (1973) The acoustic impendance of perforates at medium and high sound pressure levels. *Journal of Sound and Vibration,* 29(1), 1–65. https://doi.org/10.1016/S0022-460X(73)80125-7

Mendez, S. & Eldredge, J. D. (2009) Acoustic modeling of perforated plates with bias flow for large-eddy simulations. *Journal of Computational Physics,* 228(13), 4757–4772.

Mendez, S. & Nicoud, F. (2008) Adiabatic homogeneous model for flow around a multiperforated plate. *AIAA Journal,* 46(10), 2623–2633.

Merino-Martinez, R. & Snellen, M. (2020) Implementation of tonal cavity noise estimations in landing gear noise prediction models. *AIAA AVIATION 2020 FORUM.* Virtual EventJune 15-19. American Institute of Aeronautics and Astronautics. https://doi.org/10.2514/6.2020-2578

Mongia, H. C., Held, T. J., Hsiao, G. C. & Pandalai, R. P. (2005) Incorporation of combustion instability issues into design process: GE aeroderivative and aero engines experience. *Progress in Astronautics and Aeronautics,* 210 43.

Morfey, C. L. (1964) Rotating pressure patterns in ducts: Their generation and transmission. *Journal of Sound and Vibration,* 1(1), 60–87.

Morfey, C. L. (2000) *Dictionary of acoustics* Academic press

Morse, P. M. & Ingard, K. U. (1968) *Theoretical acoustics* McGraw Hill

Munjal, M. L. (1987) *Acoustics of ducts and mufflers* Wiley

Munjal, M. L. (1998) Analysis and design of mufflers—an overview of research at the indian institute of science. *Journal of Sound and Vibration,* 211(3), 425–433. https://doi.org/10.1006/jsvi.1997.1309

Munjal, M. L. (2014) *Acoustics of ducts and mufflers, 2nd edition*, 2nd Edition edition. Wiley

Neubauer, M., Genßler, J., Radmann, V., Fleming Kohlenberg, Pohl, M., Böhme, K., Knobloch, K., Sarradj, E., Höschler, K., Modler, N. & Enghardt, L. (2023) Experimental and numerical investigation of novel acoustic liners and their design for aero-engine applications. *Aerospace,* 10(1), 5. https://doi.org/10.3390/aerospace10010005

Nilaj, N. D. & Sharma, S. D. (2017) Experiments on heat content inside a rijke tube with suppression of thermo-acoustics instability. *International Journal of Spray and Combustion Dynamics,* 9(2), 85–101. https://doi.org/10.1177/1756827716655007

Noiray, N., Durox, D., Schuller, T. & Candel, S. (2007) Passive control of combustion instabilities involving premixed flames anchored on perforated plates. *Proceedings of the Combustion Institute,* 31(1), 1283–1290.

Norris, A. N. & Sheng, I. C. (1989) Acoustic radiation from a circular pipe with an infinite flange. *Journal of Sound and Vibration,* 135(1), 85–93.

NTi Audio, A. G. (2024) *Fast fourier transform.* https://www.nti-audio.com/en/support/know-how/fast-fourier-transform-fft [Accessed Jan 25 2024].

On, F. J. (1967) *Mechanical impedance analysis for lumped parameter multi-degree of freedom/multi-dimensional systems* National Aeronautics and Space Administration

Park, S. & Kim, J. (2019) Simulation of underwater echo reduction using miniaturized helmholtz resonators. *The Journal of the Acoustical Society of Korea,* 38(1), 67–72. https://doi.org/10.7776/ASK.2019.38.1.067

Peat, K. S. & Rathi, K. L. (1995) A finite element analysis of the convected acoustic wave motion in dissipative silencers. *Journal of Sound and Vibration,* 184(3), 529–545. https://doi.org/10.1006/jsvi.1995.0331

Peat, K. S., Ih, J. & Lee, S. (2003) The acoustic impedance of a circular orifice in grazing mean flow: Comparison with theory. *The Journal of the Acoustical Society of America,* 114(6), 3076–3086.

Peters, M., Hirschberg, A., Reijnen, A. J. & Wijnands, A. (1993) Damping and reflection coefficient measurements for an open pipe at low mach and low helmholtz numbers. *Journal of Fluid Mechanics,* 256 499–534.

Peters, T. M. & Bates, J. (1998) The discrete fourier transform and the fast fourier transform. In Anonymous *The fourier transform in biomedical engineering.* Springer, 175–194.

Pierce, A. D. (1989) *Acoustics: An introduction to its physical principles and applications*, 1989th edition. Acoustical Society of America

Plunkett, R. (1958) Interaction between a vibratory machine and its foundation. *Noise Control,* 4(1), 18–22. https://doi.org/10.1121/1.2369295

Poinsot, T. (2017) Prediction and control of combustion instabilities in real engines. *Proceedings of the Combustion Institute,* 36(1), 1–28. https://doi.org/10.1016/j.proci.2016.05.007

Poinsot, T. J., Trouve, A. C., Veynante, D. P., Candel, S. M. & Esposito, E. J. (1987) Vortex-driven acoustically coupled combustion instabilities. *Journal of Fluid Mechanics,* 177 265–292. https://doi.org/10.1017/S0022112087000958

Porges, G. (1977) *Applied acoustics*, First edition. Peninsula Publishing

Premo, J. (1999) The application of a time-domain model to investigate the impedance of perforate liners including the effects of bias flow. *AIAA/CEAS Aeroacoustics Conference and Exhibit.* 5th, Bellevue, WA,10-12 May 1999. AIAA Meeting Paper Archive 711.

Putnam, A. A. (1971) *Combustion-driven oscillations in industry* American Elsevier

Ramalingam, S. & Herrin, D. W. (2013) Using statistical energy analysis to analyze sound and vibrational energy propagation in HVAC ducts. *2013 Ashrae Winter Conference,* UNSP DA–C025.

Randeberg, R. T. (2000) *Perforated panel absorbers with viscous energy dissipation enhanced by orifice design.* Norwegian University of Science and Technology.

Rashwan, S. S., Mohany, A. & Dincer, I. (2020) Investigation of self-induced thermoacoustic instabilities in gas turbine combustors. *Energy,* 190 116362.

Rayleigh, J. W. S. (1876) On waves. *Philosophical Magazine Series 5,* 1(4), 257–279.

Rayleigh, J. W. S.,3rd Baron (1926) *The theory of sound*, 2nd revis and enlarg edition. Macmillan

Rice, E. J., (1971), *A model for the acoustic impedance of a perforated plate liner with multiple frequency excitation.* Technical Memorandum NASA-TMX-67950, NASA,

Rice, E. J. (1976) Theoretical study of the acoustic impedance of orifices in the presence of a steady grazing flow. *The Journal of the Acoustical Society of America,* 59(S1), S32.

Rienstra, S. W. (1983) A small strouhal number analysis for acoustic wave-jet flow-pipe interaction. *Journal of Sound and Vibration,* 86(4), 539–556.

ROCKWELL, D. & NAUDASCHER, E. (1978) Review - self-sustaining oscillations of flow past cavities. *Journal of Fluids Engineering-Transactions of the Asme,* 100(2), 152–165. https://doi.org/10.1115/1.3448624

Rolls-Royce (1996) *The jet engine*, Fifth edition. Rolls-Royce plc

Rona, A. (2007) The acoustic resonance of rectangular and cylindrical cavities. *Journal of Algorithms & Computational Technology,* 1(3), 329–356. https://doi.org/10.1260/174830107782424110

Rossiter, J. E., (1964), *Wind-tunnel experiments on the flow over rectangular cavities at subsonic and transonic speeds (wind tunnel experiments on the flow over rectangular cavities at subsonic and transonic speeds).* Reports and Memoranda No. 3438, Ministry of Aviation,

Rupp, J. (2013) *Acoustic absorption and the unsteady flow associated with circular apertures in a gas turbine environment.* Loughborough University.

Rupp, J., Carrotte, J. & Spencer, A. (2010) Interaction between the acoustic pressure fluctuations and the unsteady flow field through circular holes.

Sachedina, K., Lato, T., Mohany, A. & Hassan, M. (2020) Effect of incident acoustic pressure amplitude on the transmission loss of helmholtz resonators. *Vibration,* 3(1), 41. https://doi.org/10.3390/vibration3010004

Sahasrabudhe, A. D., Munjal, M. L. & Ramu, S. A. (1995) Analysis of inertance due to the higher order mode effects in a sudden area discontinuity. *Journal of Sound and Vibration,* 185(3), 515–529.

Salmon, V. (1946) Generalized plane wave horn theory. *The Journal of the Acoustical Society of America,* 17(3), 199–211.

Scarpato, A., Ducruix, S. & Schuller, T. (2013) Optimal and off-design operations of acoustic dampers using perforated plates backed by a cavity. *Journal of Sound and Vibration,* 332(20), 4856–4875.

Scarpato, A., Tran, N., Ducruix, S. & Schuller, T. (2012) Modeling the damping properties of perforated screens traversed by a bias flow and backed by a cavity at low strouhal number. *Journal of Sound and Vibration,* 331(2), 276–290.

Scheffer, C. & Girdhar, P. (2004) *Practical machinery vibration analysis and predictive maintenance* Elsevier Science

Schulz, A., Gürtler, J., Czarske, J., Bake, F. & Enghardt, L. (2018) Investigation of the modulated turbulence above bias flow liner perforations with laser-optical measurements. *2018 AIAA/CEAS Aeroacoustics Conference.*

Schulz, A., Haufe, D., Fischer, A., Czarske, J., Bake, F. & Enghardt, L. (2013) Acoustic damping analysis of bias flow liners based on spectral flow characteristics. *19th AIAA/CEAS Aeroacoustics Conference.*

Selamet, A. & Radavich, P. M. (1997) The effect of length on the acoustic attenuation performance of concentric expansion chambers: An analytical, computational and experimental investigation. *Journal of Sound and Vibration,* 201(4), 407–426.

Seybert, A. F. & Ross, D. F. (1977) Experimental determination of acoustic properties using a two-microphone random-excitation technique. *The Journal of the Acoustical Society of America,* 61(5), 1362–1370.

Shigehiko Kaneko, Tomomichi Nakamura, Fumio Inada, Minoru Kato, Kunihiko Ishihara, Takashi Nishihara & Mikael A. Langthjem (2014) Chapter 2 - vibration induced by cross-flow. In Shigehiko Kaneko, Tomomichi Nakamura, Fumio Inada, et al (eds) *Flow-induced vibrations (second edition).* Academic Press, 29–115.

Shrager, A. C., Thole, K. A. & Mongillo, D. (2019) Effects of effusion cooling pattern near the dilution hole for a double-walled combustor Liner—Part 1: Overall effectiveness measurements. *Journal of Engineering for Gas Turbines and Power,* 141(1), 011022.

Sivian, L. J. (1935) Acoustic impedance of small orifices. *The Journal of the Acoustical Society of America,* 7(2), 94–101.

Snowdon, J. C. (1979) Vibration isolation: Use and characterization. *The Journal of the Acoustical Society of America,* 66(5), 1245–1274. https://doi.org/10.1121/1.383546

Soliman, J. I. & Hallam, M. G. (1968) Vibration isolation between non-rigid machines and non-rigid foundations. *Journal of Sound and Vibration,* 8(2), 329–351. https://doi.org/10.1016/0022-460X(68)90236-8

Stewart, G. W. & Lindsay, R. B. (1930) *Acoustics - A text on theory and applications* D. Van Nostrand Company, Inc.

Stokes, G. (1849) On the theories of the internal friction of fluids in motion, and of the equilibrium and motion of elastic solids. *Transactions of the Cambridge Philosophical Society,* 8(3), 287.

Stokes, G. G. (1851) On the effect of the internal friction of fluids on the motion of pendulums.

Streeter, V. L., Wylie, E. B. & Bedford, K. W. (1985) *Fluid mechanics* , 7. ed. edition. McGraw-Hill

Sullivan, J. W. (1979) A method for modeling perforated tube muffler components. II. applications. *The Journal of the Acoustical Society of America,* 66(3), 779–788.

Sun, X., Jing, X., Zhang, H. & Shi, Y. (2002) Effect of grazing–bias flow interaction on acoustic impedance of perforated plates. *Journal of Sound and Vibration,* 254(3), 557–573. https://doi.org/10.1006/jsvi.2001.4110

Syred, N. & Beér, J. M. (1974) Combustion in swirling flows: A review. *Combustion and Flame,* 23(2), 143–201. https://doi.org/10.1016/0010-2180(74)90057-1

Taamallah, S., LaBry, Z. A., Shanbhogue, S. J. & Ghoniem, A. F. (2015) Thermo-acoustic instabilities in lean premixed swirl-stabilized combustion and their link to acoustically coupled and decoupled flame macrostructures. *Proceedings of the Combustion Institute,* 35(3), 3273–3282. https://doi.org/10.1016/j.proci.2014.07.002

Tang, S. K. (2005) On helmholtz resonators with tapered necks. *Journal of Sound and Vibration,* 279(3-5), 1085–1096. https://doi.org/10.1016/j.jsv.2003.11.032

Tayong, R. B. & Leclaire, P. (2010) Holes interaction effects under high and medium sound intensities for micro-perforated panels design. *10ème Congrès Français d'Acoustique.* Lyon, France12-16 April 2010.

The MathWorks, I. (2023) *Filtering and smoothing data - MATLAB & simulink.* https://www.mathworks.com/help/curvefit/smoothing-data.html#bq_6ys3-3 [Accessed Jan 27 2024].

Tonon, T. S. & Sirignano, W. A. (1970) The nonlinearity of acoustic liners with flow effects. *AIAA 8th Aerospace Sciences Meeting.* New York19-21 January 1970. AIAA-1970-0128.

Tran, N., Ducruix, S. & Schuller, T. (2009) Passive control of the inlet acoustic boundary of a swirled burner at high amplitude combustion instabilities. *J. Eng. Gas Turbines Power,* 131(5), 7.

Turner, J. D. & Pretlove, A. J. (1991) *Acoustics for engineers*, First edition. Macmillan Education Ltd

Tyler, J. M. & Sofrin, T. G. (1962) Axial flow compressor noise studies title. 70: 309–332.

Ungar, E. E. & Dietrich, C. W. (1966) High-frequency vibration isolation. *Journal of Sound and Vibration,* 4(2), 224–241. https://doi.org/10.1016/0022-460X(66)90123-4

University of Washington Structural Research Laboratory, Farquharson, F. B., Vincent, G. S. & Washington Toll Bridge Authority (1954) *Aerodynamic stability of suspension bridges with special reference to the tacoma narrows bridge : A report of an investigation conducted by the structural research laboratory, university of washington, under the direction of the washington toll bridge authority in cooperation with the public roads administration, federal works agency* University of Washington Press

van der Seijs, M. V., de Klerk, D. & Rixen, D. J. (2016) General framework for transfer path analysis: History, theory and classification of techniques. *Mechanical Systems and Signal Processing,* 68-69 217–244. https://doi.org/10.1016/j.ymssp.2015.08.004

Voigt, P. (1926) Improvements in horns for acoustic instruments. 278098.

von Helmholtz, H. (1863) Über den einfluss der reibung in der luft auf die schallbewegung. *Verhandlungen Des Naturhistorisch-Medizinischen Vereins Zu Heidelberg in Heidelberger Jahrbücher Der Literatur,* 56(17), 257–260.

Wang, J., Rubini, P., Qin, Q. & Houston, B. (2019) A model to predict acoustic resonant frequencies of distributed helmholtz resonators on gas turbine engines. *Applied Sciences,* 9(7), 1419. https://doi.org/10.3390/app9071419

Webb, A. R., Heller, H. T., Benson, C. B. & Lahav, A. (2015) Mother's voice and heartbeat sounds elicit auditory plasticity in the human brain before full gestation. *Proceedings of the National Academy of Sciences of the United States of America,* 112(10), 3152–3157. https://doi.org/10.1073/pnas.1414924112

Webster, A. G. (1919) Acoustical impedance and the theory of horns and of the phonograph. *Proceedings of the National Academy of Sciences,* 5(7), 275–282.

Welch, M., Igoe, B. M. & Wilson, D. (2016) Combustion, fuels and emissions for industrial gas turbines. *Asia Turbomachinery & Pump Symposium. 2016 Proceedings.* Turbomachinery Laboratories, Texas A&M Engineering Experiment Station.

Welch, P. (1967) The use of fast fourier transform for the estimation of power spectra: A method based on time averaging over short, modified periodograms. *IEEE Transactions on Audio and Electroacoustics,* 15(2), 70–73.

Wilby, J. F. (1996) Aircraft interior noise. *Journal of Sound and Vibration,* 190(3), 545–564. https://doi.org/10.1006/jsvi.1996.0078

Yang, V. (2001) Introductions: Stability characteristics and control approach. *Active Control of Engine Dynamics.Von Karman Institute for Fluid Dynamics,*

Yarwood, T. M. (1953) *Acoustics: A text book for physics and engineering students* Macmillan

Young, C. I. J. & Crocker, M. J. (1975) Prediction of transmission loss in mufflers by the finite–element method. *The Journal of the Acoustical Society of America,* 57(1), 144–148.

Young, C. J. & Crocker, M. J. (1977) Finite element acoustical analysis of complex muffler systems with and without wall vibrations. *Noise Control Engineering,* 9(2), 86–93.

Yurtseven, H. H., Yilmaz, A., Xie, Q., Li, Z., Gao, Z. & Negahban, M. (2023) Locally resonant metasurface for low-frequency transmissive underwater acoustic waves. *Frontiers in Physics,* 10 1098261. https://doi.org/10.3389/fphy.2022.1098261

Zalluhoglu, U. & Olgac, N. (2016) A study of helmholtz resonators to stabilize thermoacoustically driven pressure oscillations. *The Journal of the Acoustical Society of America,* 139(4), 1962–1973. https://doi.org/10.1121/1.4946042

Zhenjing Zhu, Zhenjing Zhu, Ning Hu, Ning Hu, Junyi Wu, Wenxin Li, Wenxin Li, Jiabao Zhao, Jiabao Zhao, Maofa Wang, Maofa Wang, Maofa Wang, Fanzong Zeng, Fanzong Zeng, Huajie Dai, Huajie Dai, Yongju Zheng & Yongju Zheng (2022) A review of underwater acoustic metamaterials for underwater acoustic equipment. *Frontiers in Physics,* 10 https://doi.org/10.3389/fphy.2022.1068833

Zhou, Y., Chen, J., Chen, R., Chen, W., Fan, Z. & Ma, Y. (2020) Ultrathin electromagnetic-acoustic amphibious stealth coats. *Advanced Optical Materials,* 8(15), 2000200. https://doi.org/10.1002/adom.202000200

Zinn, B. T. (1970) A theoretical study of non-linear damping by helmholtz resonators. *Journal of Sound and Vibration,* 13(3), 347–356.

Zorumski, W. E. and Parrott, T. L., (1971), *Nonlinear acoustic theory for rigid porous materials.* Technical Note NASA-TN-D-6196, National Aeronautics and Space Administration,